

AFRL-ML-WP-TR-2000-4057

**3D STRENGTH PREDICTION OF
ADVANCED COMPOSITES**

**GYANESHWAR P. TANDON
ALEXANDER E. BOGDANOVICH**

**ADTECH SYSTEMS RESEARCH, INC.
1342 N FAIRFIELD ROAD
BEAVERCREEK, OHIO 45432-2698**

MARCH 2000

FINAL REPORT FOR 10/01/1995 – 10/31/1999

APPROVED FOR PUBLIC RELEASE; DISTRIBUTION UNLIMITED



**MATERIALS AND MANUFACTURING DIRECTORATE
AIR FORCE RESEARCH LABORATORY
AIR FORCE MATERIEL COMMAND
WRIGHT-PATTERSON AIR FORCE BASE OH 45433-7750**

REPORT DOCUMENTATION PAGE		
1. REPORT DATE (DD-MM-YYYY) 01-03-2000	2. REPORT TYPE Final	3. DATES COVERED (FROM - TO) 01-10-1995 to 31-10-1999
4. TITLE AND SUBTITLE 3D Strength Prediction of Advanced Composites Unclassified	5a. CONTRACT NUMBER	
	5b. GRANT NUMBER	
	5c. PROGRAM ELEMENT NUMBER	
6. AUTHOR(S) Tandon, Gyaneshwar P. ; Bogdanovich, Alexander E. ;	5d. PROJECT NUMBER	
	5e. TASK NUMBER	
	5f. WORK UNIT NUMBER	
7. PERFORMING ORGANIZATION NAME AND ADDRESS Adtech Systems Research, Inc. 1342 N. Fairfield Road Beavercreek , OH 45432-2698	8. PERFORMING ORGANIZATION REPORT NUMBER	
9. SPONSORING/MONITORING AGENCY NAME AND ADDRESS Materials and Manufacturing Directorate Air Force Research Laboratory Air Force Materiel Command Wright-Patterson AFB , OH 45433-7750	10. SPONSOR/MONITOR'S ACRONYM(S)	
	11. SPONSOR/MONITOR'S REPORT NUMBER(S)	
12. DISTRIBUTION/AVAILABILITY STATEMENT A PUBLIC RELEASE Materials and Manufacturing Directorate Air Force Research Laboratory Air Force Materiel Command Wright-Patterson AFB , OH 45433-7750		
13. SUPPLEMENTARY NOTES		
14. ABSTRACT		

The goal of this program was to reduce the cost of designing advanced organic and ceramic matrix composite structures by addressing key deficiencies in state-of-the-art analytical techniques.

15. SUBJECT TERMS

3D failure analysis; bonded joints; composite; cracks; debonding; energy release rate; failure criteria; friction; interface; modeling; variational methods

16. SECURITY CLASSIFICATION OF:			17. LIMITATION OF ABSTRACT Public Release	18. NUMBER OF PAGES 367	19a. NAME OF RESPONSIBLE PERSON Fenster, Lynn lfenster@dtic.mil
a. REPORT Unclassified	b. ABSTRACT Unclassified	c. THIS PAGE Unclassified			19b. TELEPHONE NUMBER International Area Code Area Code Telephone Number 703 767-9007 DSN 427-9007

REPORT DOCUMENTATION PAGE		
1. REPORT DATE (DD-MM-YYYY) 01-03-2000	2. REPORT TYPE Final	3. DATES COVERED (FROM - TO) 01-10-1995 to 31-10-1999
4. TITLE AND SUBTITLE 3D Strength Prediction of Advanced Composites Unclassified	5a. CONTRACT NUMBER	
	5b. GRANT NUMBER	
	5c. PROGRAM ELEMENT NUMBER	
6. AUTHOR(S) Tandon, Gyaneshwar P. ; Bogdanovich, Alexander E. ;	5d. PROJECT NUMBER	
	5e. TASK NUMBER	
	5f. WORK UNIT NUMBER	
7. PERFORMING ORGANIZATION NAME AND ADDRESS Adtech Systems Research, Inc. 1342 N. Fairfield Road Beavercreek , OH 45432-2698	8. PERFORMING ORGANIZATION REPORT NUMBER	
9. SPONSORING/MONITORING AGENCY NAME AND ADDRESS Materials and Manufacturing Directorate Air Force Research Laboratory Air Force Materiel Command Wright-Patterson AFB , OH 45433-7750	10. SPONSOR/MONITOR'S ACRONYM(S)	
	11. SPONSOR/MONITOR'S REPORT NUMBER(S)	
12. DISTRIBUTION/AVAILABILITY STATEMENT A PUBLIC RELEASE Materials and Manufacturing Directorate Air Force Research Laboratory Air Force Materiel Command Wright-Patterson AFB , OH 45433-7750		
13. SUPPLEMENTARY NOTES		
14. ABSTRACT		

The goal of this program was to reduce the cost of designing advanced organic and ceramic matrix composite structures by addressing key deficiencies in state-of-the-art analytical techniques.

15. SUBJECT TERMS

3D failure analysis; bonded joints; composite; cracks; debonding; energy release rate; failure criteria; friction; interface; modeling; variational methods

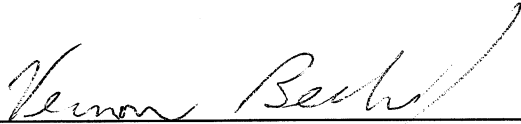
16. SECURITY CLASSIFICATION OF:			17. LIMITATION OF ABSTRACT Public Release	18. NUMBER OF PAGES 367	19a. NAME OF RESPONSIBLE PERSON Fenster, Lynn lfenster@dtic.mil
a. REPORT Unclassified	b. ABSTRACT Unclassified	c. THIS PAGE Unclassified			19b. TELEPHONE NUMBER International Area Code Area Code Telephone Number 703 767-9007 DSN 427-9007

NOTICE

Using Government drawings, specifications, or other data included in this document for any purpose other than Government procurement does not in any way obligate the U.S. Government. The fact that the Government formulated or supplied the drawings, specifications, or other data does not license the holder or any other person or corporation; or convey any rights or permission to manufacture, use, or sell any patented invention that may relate to them.

This report is releasable to the National Technical Information Service (NTIS). At NTIS, it will be available to the general public, including foreign nations.

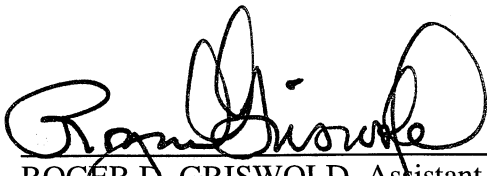
THIS TECHNICAL REPORT HAS BEEN REVIEWED AND IS APPROVED FOR PUBLICATION.



VERNON T. BECHEL, Mechanical Engineer
Mechanics Team
Structural Materials Branch



L. SCOTT THEIBERT, Chief
Structural Materials Branch
Nonmetallic Materials Division



ROGER D. GRISWOLD, Assistant Chief
Nonmetallic Materials Division
Materials and Manufacturing Directorate

Do not return copies of this report unless contractual obligations or notice on a specific document requires its return.

REPORT DOCUMENTATION PAGE			Form Approved OMB No. 0704-0188	
Public reporting burden for this collection of information is estimated to average 1 hour per response, including the time for reviewing instructions, searching existing data sources, gathering and maintaining the data needed, and completing and reviewing the collection of information. Send comments regarding this burden estimate or any other aspect of this collection of information, including suggestions for reducing this burden, to Washington Headquarters Services, Directorate for Information Operations and Reports, 1215 Jefferson Davis Highway, Suite 1204, Arlington, VA 22202-4302, and to the Office of Management and Budget, Paperwork Reduction Project (0704-0188), Washington, DC 20503.				
1. AGENCY USE ONLY (Leave blank)		2. REPORT DATE MARCH 2000		3. REPORT TYPE AND DATES COVERED FINAL REPORT FOR 10/01/1995 - 10/31/1999
4. TITLE AND SUBTITLE 3D STRENGTH PREDICTION OF ADVANCED COMPOSITES			5. FUNDING NUMBERS C F33615-95-C-5041 PE 62102 PR 4347 TA 34 WU 05	
6. AUTHOR(S) GYANESHWAR P. TANDON ALEXANDER E. BOGDANOVICH				
7. PERFORMING ORGANIZATION NAME(S) AND ADDRESS(ES) ADTECH SYSTEMS RESEARCH, INC. 1342 N FAIRFIELD ROAD BEAVERCREEK, OHIO 45432-2698			8. PERFORMING ORGANIZATION REPORT NUMBER	
9. SPONSORING/MONITORING AGENCY NAME(S) AND ADDRESS(ES) MATERIALS AND MANUFACTURING DIRECTORATE AIR FORCE RESEARCH LABORATORY AIR FORCE MATERIEL COMMAND WRIGHT-PATTERSON AFB, OH 45433-7750 POC: VERNON T. BECHEL, AFRL/MLBC, 937-255-9077			10. SPONSORING/MONITORING AGENCY REPORT NUMBER AFRL-ML-WP-TR-2000-4057	
11. SUPPLEMENTARY NOTES				
12a. DISTRIBUTION AVAILABILITY STATEMENT APPROVED FOR PUBLIC RELEASE, DISTRIBUTION UNLIMITED.			12b. DISTRIBUTION CODE	
13. ABSTRACT (Maximum 200 words) The goal of this program was to reduce the cost of designing advanced organic and ceramic matrix composite structures by addressing key deficiencies in state-of-the-art analytical techniques. Failure modes at both the fiber/matrix level and the individual lamina level were studied experimentally and with analytical modeling techniques aimed specifically at reducing design costs by reducing the need for costly empirical mechanical failure testing. The macromechanics portion of this program consisted of the development and implementation of a novel 3D variational analysis technique. This "mosaic model" was applied to predict the progressive failure of double lap composite-to-composite and composite-to-metal joints. Comparisons are made with FEM and experimental test results of failure of composite adhesive joints. Predictions of the effect of the spew fillet in adhesive joints as well as maximum stress, strain, and energy release rate and failure location in lap joints are made. The micromechanics portion of this program added significantly to the development of the cruciform test for measuring interfacial normal strength in single-fiber samples. Experimental observations of damage initiation and ultimate failure were found to be consistent with numerical predictions from a 3D FEM model. Advanced modeling techniques were also applied to the end notched flexure test, to the fiber pushout test, and for prediction of thermomechanical, conductive, and damage parameters in oxide-oxide composites for use in turbine engines.				
14. SUBJECT TERMS 3D failure analysis, bonded joints, composite, cracks, debonding, energy release rate, failure criteria, friction, interface, modeling, variational methods			15. NUMBER OF PAGES 367	
			16. PRICE CODE	
17. SECURITY CLASSIFICATION OF REPORT UNCLASSIFIED	18. SECURITY CLASSIFICATION OF THIS PAGE UNCLASSIFIED	19. SECURITY CLASSIFICATION OF ABSTRACT UNCLASSIFIED	20. LIMITATION OF ABSTRACT SAR	

TABLE OF CONTENTS

<u>SECTION</u>		<u>PAGE</u>
	EXECUTIVE SUMMARY	1
	PART A	
1.0	A CRITICAL SHEAR ENERGY RELEASE RATE CRITERIA FOR DEBONDING IN A PUSH-OUT TEST	5
1.1	Introduction	5
1.2	Initiation	5
1.3	Propagation	6
1.4	Ultimate Failure	7
2.0	STRESS FIELDS IN A SINGLE FIBER PUSH-OUT SPECIMEN CONSIDERING INTERFACIAL DAMAGE AND FRICTION	9
2.1	Introduction	9
2.2	Results and Discussion	9
2.2.1	Thermal Loading	10
2.2.2	Thermal and Push-Out Loads	11
2.2.2.1	Frictional Interface with No Adhesive Strength	12
2.2.2.2	Frictional Interface with Adhesive Strength	13
2.3	Concluding Remarks	15
3.0	INFLUENCE OF EDGE EFFECTS IN ESTIMATING INTERFACIAL NORMAL STRENGTH IN MODEL UNIDIRECTIONAL COMPOSITES	17
3.1	Introduction	17
3.2	Specimen Design, Fabrication and Test Methods	18
3.3	Experimental Results	20
3.4	Numerical Analysis	21
3.5	Asymptotic Analysis	23
3.5.1	Fiber End Exposed	23
3.5.2	Fiber End Embedded	24
3.6	Estimation of Interfacial Strength and Characteristic Failure Dimension	26
3.7	Summary	30
	REFERENCES	30
4.0	INTERFACIAL NORMAL STRENGTH EVALUATION IN MODEL UNIDIRECTIONAL COMPOSITES	32
4.1	Introduction	32
4.2	Experiment	33

TABLE OF CONTENTS (Continued)

PART A

<u>SECTION</u>		<u>PAGE</u>
	4.3 Analytical Modeling	36
	4.4 Results and Discussion	38
	4.4.1 Glass/Epoxy Composite	38
	4.4.2 SCS-0/Epoxy Composite	41
	4.4.2.1 Interface Strength Measurement	41
	4.4.2.2 Parametric Study	47
	4.4.2.3 Debond Length Measurements	52
	4.4.3 Nicalon/Epoxy Composite	53
	4.4.4 Graphite/Epoxy Composite	54
	4.5 Summary	57
	REFERENCES	59
5.0	IN SITU OBSERVATION AND MODELING OF DAMAGE MODES IN CROSS-PLY CERAMIC MATRIX COMPOSITES	61
	5.1 Introduction	61
	5.2 Experiment	61
	5.3 Analytical Background	63
	5.4 Results	64
	5.4.1 Elastic Properties	64
	5.4.2 Damage Progression	65
	5.4.3 Stress-Strain Behavior	65
	5.5 Summary	67
	REFERENCES	68
6.0	VARIATIONAL, FEM AND ASYMPTOTIC SOLUTION BEHAVIOR IN THE VICINITY OF STRESS SINGULARITIES IN CONCENTRIC CYLINDER MODEL	69
	6.1 Introduction	69
	6.2 Free-Edge Singularity	69
	6.3 Closing Remarks	73
	REFERENCES	73
7.0	LOAD TRANSFER CHARACTERISTICS IN THE VICINITY OF FIBER BREAKAGE	74
	7.1 Introduction	74
	7.2 Problem Definition	75
	7.3 Results and Discussion	75
	7.3.1 Isolated Fiber Break in an Infinite Medium	75
	7.4 Concluding Remarks	79
	REFERENCES	79

TABLE OF CONTENTS (Continued)

PART A

<u>SECTION</u>		<u>PAGE</u>
8.0	STRESS CONCENTRATIONS AT FIBER CORNERS DURING TRANSVERSE TENSION OF UNIDIRECTIONAL COMPOSITES	80
8.1	Introduction	80
8.2	Asymptotic Analysis	80
8.3	Angular Variation Matching	82
8.4	Stress Scaling Factor	82
	REFERENCES	83
9.0	ANALYSIS OF THE END-NOTCHED FLEXURE SPECIMEN FOR MODE II TESTING USING VARIATIONAL METHODS	84
9.1	Introduction	84
9.2	Methodology	85
9.3	Numerical Results and Discussion	87
9.4	Summary	94
	REFERENCES	95
10.0	CHARACTERIZATION OF INTERFACIAL FRACTURE TOUGHNESS IN MODEL POLYESTER/EPOXY COMPOSITE SYSTEM	97
10.1	Introduction	97
10.2	Specimen Preparation and Testing	97
10.3	Analytical Modeling	99
10.4	Experimental Results	101
10.5	Data Reduction & Discussion	102
	REFERENCES	105
11.0	MICROMECHANICAL RESPONSE OF A MULTI-PHASE COMPOSITE	106
11.1	Introduction	106
11.2	Methodology	107
11.3	Results & Discussion	108
11.4	Summary	110
	REFERENCES	111

TABLE OF CONTENTS (Continued)

PART B

<u>SECTION</u>		<u>PAGE</u>
1.0	THREE-DIMENSIONAL VARIATIONAL THEORY OF MOSAIC COMPOSITE STRUCTURES	113
1.1	Introduction	113
1.2	Generalized Mosaic Body Model	113
1.3	Formulation of the Variational Problem	117
1.4	Strain Energy and Work of Surface Forces for a Single Brick	120
1.5	System of Linear Simultaneous Equations for a Single Brick	123
1.6	System of Linear Simultaneous Equations for a Set of Noninteracting Bricks	126
1.7	Continuity Conditions at the Inter-Brick Boundaries in an Irregular Mosaic Structure	128
2.0	APPLICATION OF BERNSTEIN BASIS FUNCTIONS FOR 3-D ANALYSIS OF MOSAIC COMPOSITE STRUCTURES	132
2.1	Displacement Approximation	132
2.2	Continuity of Displacements Between the Bricks	134
2.3	Continuity of Transverse Stresses Between the Bricks	136
2.4	A Single-Index Form of the Continuity Relationships	141
2.5	Classification of Special Junction Lines and Points	144
2.6	Continuity of Displacements at the Interior Junction Points	145
2.7	Continuity of Displacements at the Exterior Junction Points	147
2.8	Continuity of Displacements at the Interior Junction Lines	150
2.9	External Geometric Boundary Conditions	152
2.10	Further Algorithmic Considerations	155
3.0	3-D STRESS/STRAIN AND PROGRESSIVE FAILURE ANALYSIS OF COMPOSITE BONDED JOINTS	158
3.1	Introduction	158
3.2	A "Dummy" Material Concept	159
3.3	A Comparison of the Analytical and Experimental Results for Stepped Aluminum Specimen	162
3.4	A Comparison of the Analytical and Experimental Results for Composite-to-Composite Adhesive Bonded Joints	173
3.5	The Concept of 3-D Progressive Failure Analysis	186
3.6	3-D Analysis of an Interlaminar Crack Propagation	195

TABLE OF CONTENTS (Continued)

PART B

<u>SECTION</u>		<u>PAGE</u>
4.0	3-D FINITE ANALYSIS OF COMPOSITE-TO-METAL AND COMPOSITE-TO-COMPOSITE BONDED JOINTS	204
4.1	Introduction	204
4.2	The Concept of Submodeling	206
4.3	Problem Formulation	208
4.4	Global Analysis	209
4.5	Local Analysis - Submodel 1	212
4.6	Local Analysis – Submodel 2	221
4.7	Local Analysis – Submodel 3	228
4.8	Local Stress Analysis in the Corner Region 2	229
4.9	Stress Variations in the Width and Thickness Directions	235
4.10	Stress Analysis in the Presence of Initial Debond Crack	237
4.11	Analysis of Composite-to-Composite Adhesive Bonded Joint	244
4.12	Global Analysis	247
4.13	Numerical Comparison of the Global and Submodel Analyses	257
4.14	Comparison of the Finite Element and Mosaic Model Results	265
	REFERENCES	274
5.0	CHAPTER 1 - THREE-DIMENSIONAL ANALYSIS OF CRACK PROPAGATION IN DOUBLE-LAP COMPOSITE BONDED JOINTS	275
5.1	Introduction	275
5.2	A Synopsis of 3-D Mosaic Model and Variational Analysis Approach	277
5.3	3-D Crack Propagation Analysis Using Mosaic Model Approach	289
5.4	Analysis of Double-Lap Joint with Unidirectional Composite Adherends	292
5.5	Analysis of Double-Lap Joint with Cross-Ply Composite Adherends	313
5.6	Conclusions	319
	REFERENCES	320
6.0	CHAPTER 2 – FINITE ELEMENT ANALYSIS OF COMPOSITE BONDED JOINTS WITH ACCOUNT OF A SPEW FILLET	323
6.1	Introduction	323
6.2	Analysis Approach	324
6.3	Numerical Results	327
6.4	Conclusions	334
	REFERENCES	335

TABLE OF CONTENTS (Continued)

PART B

<u>SECTION</u>		<u>PAGE</u>
7.0	THREE-DIMENSIONAL MOSAIC MODEL ANALYSIS WITH ACCOUNT OF THE ENVIRONMENTAL EFFECTS	336
7.1	Introduction	336
7.2	Incorporation of the Thermal Expansion and Moisture Swelling Effects into 3-D Mosaic Model	336
7.3	The Particular Case: Bricks Having One Plane of Elastic Symmetry	341
	REFERENCES	343

LIST OF FIGURES

PART A

FIGURE		PAGE
1-1	Estimation of debond length on initiation using critical shear energy release rate criteria	6
1-2	Comparison of force-debond length relationship during push-out test	7
1-3	Estimation of debond length at catastrophic debonding using critical shear energy release rate criteria	8
2-1	Methodology adopted to simulate the problem in both FEM and ADM	10
2-2	Comparison of shear stresses after monotonic thermal loading, $\Delta T = -48.5^{\circ}\text{C}$	11
2-3	Interface damage state at various push-in displacements	12
2-4	Comparison of ADM and FEM Results: Radial stress distribution along the interface	14
2-5	Comparison of ADM and FEM Results: Shear stress distribution along the interface	15
3-1	Straight-sided specimen with fiber ends exposed	19
3-2	Straight-sided specimen with fiber ends embedded	19
3-3	Cruciform (or cross-shaped) specimen	19
3-4	Variation of radial stress with normalized distance from center of the specimen along the length of the aluminum rod	22
3-5	Angular distribution matching of normalized stresses from finite element analysis with asymptotic solution	24
3-6	Angular distribution matching of normalized stresses from finite element analysis with asymptotic solution	25
3-7	Comparison of hoop stress from finite element analysis with asymptotic solution for straight sided specimen with fiber ends exposed	27

LIST OF FIGURES (Continued)

PART A

FIGURE		PAGE
3-8	Comparison of hoop stress from finite element analysis with asymptotic solution for straight sided specimen with fiber ends covered	28
4-1	Specimen geometry: (a) straight-sided specimen	34
4-2	Graphite fiber placement in rubber mold	34
4-3	Sample illumination	34
4-4	Portable load frame	36
4-5	Schematic of cruciform sample specimen dimensions and nomenclature	37
4-6	Stress-strain curves at various locations along the fiber length	39
4-7	Photograph showing failed specimens	39
4-8	SEM photomicrograph showing the fracture surface	40
4-9	Photomicrographs showing photoelastic fringes for the applied stresses	40
4-10	Photomicrograph showing fiber-matrix separation after failure	41
4-11	Axial variation of interfacial stresses in the matrix	42
4-12	Photomicrographs showing photoelastic fringes for the applied stresses	43
4-13	(a) Applied stress – local strain plot, and (b) Acoustic emission count respectively for SCS-0/Epoxy composite	44
4-14	Photograph showing failed specimens	46
4-15	Effect of loading arm width on the radial stress concentration factor	48

LIST OF FIGURES (Continued)

PART A

FIGURE		PAGE
4-16	Effect of wing height on the radial stress concentration factor for loading arm half-width equals (a) 3.8 mm, (b) 7.4 mm and (c) 11.2 mm	49
4-17	Photograph of the failed cruciform sample (optimized specimen geometry)	51
4-18	Images of debonding in SCS-0/epoxy	53
4-19	Shape of crack front on SCS-0 fiber surface	53
4-20	Debonding in Nicalon/epoxy	54
4-21	Effect of sample thickness	55
4-22	Effect of fiber radius	55
4-23	Effect of fillet radius	55
4-24	Effect of fiber transverse modulus	55
4-25	Fillet failure	56
4-26	Reinforced fillets	56
4-27	Failed AU4/Epoxy	57
5-1	Stress-strain relation for the $[0/90]_{3s}$ laminate at room temperature	66
5-2	Experimentally measured major Poisson's ratio as function of applied stress for $[0/90]_{3s}$ laminate at room temperature	66
6-1	Schematic of a concentric cylinder for analysis	70
6-2	Angular variation of opening stress, $\sigma_{\theta\theta}$	71
6-3	Angular variation of shear stress, $\sigma_{\rho\theta}$	71
6-4	Angular variation of radial stress, $\sigma_{\rho\rho}$	72

LIST OF FIGURES (Continued)

PART A

FIGURE		PAGE
6-5	Axial variation of radial stress, σ_{pp}	72
7-1	Schematic illustration of a single fiber fragmentation test	74
7-2	Schematic of single fiber fragmentation test for analysis	76
7-3	Axial variation of interfacial shear stress	77
7-4	Axial variation of interfacial radial stress	77
7-5	Variation of axial stress in the fiber along the Interface	78
7-6	Variation of axial stress in the matrix along the interface	78
8-1	Geometry of Test Specimens	81
8-2	Angular matching for the exposed fiber specimen	82
8-3	Angular matching for the embedded fiber specimen	83
9-1	Schematic of end-notched flexure specimen	84
9-2	Boundary conditions for analyzing ENF specimen	86
9-3	Comparison of G_{II} from various analyses	89
9-4	Comparison of beam deflection from various analyses	90
9-5	ENF mesh and close up of focused crack tip mesh	92
9-6	Variation of G_{II} in an isotropic material	93
9-7	Interfacial stresses across the specimen length in the crack plane	94
10-1	Schematic of end-notched flexure specimen	97
10-2	Three-step process for fabricating ENF specimens	98

LIST OF FIGURES (Continued)

PART A

FIGURE		PAGE
10-3	Schematic of a typical load-displacement response from the test	99
10-4	Contact stresses along specimen	100
10-5	Variation in potential energy release rate with support distance and layer refinement	101
10-6	Variation of G_{II} with crack length	102
10-7	Schematic of the observed failure paths in polyester-epoxy-composite system	103
11-1	SEM micrograph showing extensive matrix cracking in as-processed fabric	109

PART B

1.1	Example of an irregular mosaic structure	114
1.2	A “dummy” material approach applied for the irregular mosaic structure	115
1.3	Brick nomenclature for an irregular mosaic structure	116
2.1	Illustration of the junction points and lines in the mosaic body	145
2.2	Flow chart of the developed analysis and computer code 3D mosaic	157
3.1	A single-lap and double-lap adhesive bonded joints and their mosaic representations	160
3.2	Examples of adhesively bonded stiffened composite panels and their mosaic representation	162
3.3	Schematic of the test specimen (a) and mosaic representation of its 1/8 th part (b)	163
3.4	Schematic of a nonuniform mesh of the bricks	164

LIST OF FIGURES (Continued)

PART B

FIGURE		PAGE
3.5	Schematic of the strain gage placement (not in scale)	167
3.6	Variations of $\varepsilon_z / \varepsilon_x^0$ in the x direction at $y = b, z = h_1$ computed with mesh No. 8. Black bars indicate width of gages 1(a) and 2(b)	169
3.7	Variations of $\varepsilon_x / \varepsilon_x^0$ in the x direction at $y = b, z = h_1$ computed with mesh No. 8. Black bars indicate width of gages 3(a) and 4(b)	170
3.8	Variations of $\varepsilon_z / \varepsilon_x^0$ in the z direction at $x = a_1, y = 0$ computed with mesh No. 8. Black bars indicate width of gage 5 under two different magnifications	171
3.9	Variations of $\varepsilon_z / \varepsilon_x^0$ in the x direction at $y = b$, and different z -levels computed with mesh No. 8. Black bars indicates width of gage 1	172
3.10	Variations of $\varepsilon_z / \varepsilon_x^0$ in the x direction at $y = b$, and different z -levels computed with mesh No. 8. Black bars indicates width of gage 3	172
3.11	Variations of $\varepsilon_x / \varepsilon_x^0$ along the y coordinate at $x = a_1 - g_1^I / 2, z = h_1 + g_w^I / 2$ computed with meshes 7 (.....) and 8 (—)	174
3.12	Variations of $\varepsilon_z / \varepsilon_x^0$ along the y coordinate at $x = a_1 - g_w^I / 2, z = h_1 + g_1^I / 2$ computed with meshes 7 (.....) and 8 (—)	174
3.13	Variations of $\varepsilon_z / \varepsilon_x^0$ along the x coordinate at $y = b$, and different z -levels computed with meshes 7 (.....) and 8 (—)	177
3.14	Double-lap adhesive bonded joint specimen	178
3.15	The reduced bonded joint element	179
3.16	Mosaic representation of the bonded joint structural element	180
3.17	Schematic of the brick mesh	181
3.18	Schematic of the strain gage placement (not in scale)	182
3.19	Variations of $\varepsilon_z / \varepsilon_x^0$ in the x direction at $y = b$ and three z -levels. Black bars indicate width and location of gages 1 and 2.	184

LIST OF FIGURES (Continued)

PART B

FIGURE		PAGE
3.20	Variations of $\varepsilon_x / \varepsilon_x^0$ in the x direction at $y = b$ and three z -levels. Black bars indicate length and location of gages 1 and 2.	185
3.21	Double cantilever beam under peel mode loading	196
3.22	Schematic of the $1/4^{\text{th}}$ part of the double cantilever beam specimen	197
3.23	Schematic of the brick mesh pattern	198
3.24	Distribution of the strain energy density inside the specimen. Crack size $a_2 = 10 \text{ mm}$, applied peel displacement $u_0 = 0.175 \text{ mm}$. The insert shows the nomenclature of the bricks	199
3.25	Variation of the strain energy release rate on the applied peel displacement u_0 at different crack sizes	199
3.26	Dependence of the actual crack length on the applied peel displacement u_0 for different initial crack lengths a_2 .	202
3.27	Dependence of the strain energy density on the applied peel displacement u_0 for different initial crack lengths a_2 .	202
3.28	Dependence of the crack opening deflection δ on applied peel force for different initial crack sizes a_2 .	203
4-1	Schematic of a double-lap joint (a) and its $1/8^{\text{th}}$ part (b) considered in the analysis	206
4-2	Schematic of the local region locations	207
4-3	Variations of σ_x / σ_0 in Gr/Ep (a) and Al (b) adherends in local region 1 at $y/b = 1, z/h = 0.5$	225
4-4	Variations of σ_z / σ_0 in Gr/Ep (a) and Al (b) adherends in local region 1 at $y/b = 1, z/h = 0.5$	226

LIST OF FIGURES (Continued)

PART B

FIGURE		PAGE
4-5	Variations of τ_{xz} / σ_0 in Gr/Ep (a) and Al (b) adherends in local region 1 at $y / b = 1, z / h = 0.5$	226
4-6	Variations of σ_x / σ_0 in Gr/Ep (a) and Al (b) adherends in local region 2 at $y / b = 1, z / h = 0.5$	232
4-7	Variations of σ_z / σ_0 in Gr/Ep (a) and Al (b) adherends in local region 2 at $y / b = 1, z / h = 0.5$	233
4-8	Variations of τ_{xz} / σ_0 in Gr/Ep (a) and Al (b) adherends in local region 21 at $y / b = 1, z / h = 0.5$	234
4-9	Variations of σ_x / σ_0 (a), σ_z / σ_0 (b) and τ_{xz} / σ_0 (c) in the width direction for Gr/Ep and Al adherends in local region 1 at $x / a = 0.5, z / h = 0.5$	235
4-10	Variations of σ_x / σ_0 (a), σ_z / σ_0 (b) and τ_{xz} / σ_0 (c) in the thickness direction for Gr/Ep and Al adherends in local region 1 at $x / a = 0.5, y / b = 1$	236
4-11	Initial debond crack at the end of the overlap zone	238
4-12	The element mesh distortions in the x-plane without crack (a) and with initial debond crack of different length (b,c)	240
4-13	Variations of σ_x / σ_0 in Gr/Ep (a) and Al (b) adherends at $y / b = 1, z / h = 0.5$ without crack and with initial debond crack of two different lengths	241
4-14	Variations of σ_z / σ_0 in Gr/Ep (a) and Al (b) adherends at $y / b = 1, z / h = 0.5$ without crack and with initial debond crack of two different lengths	242
4.15	Variations of τ_{xz} / σ_0 in Gr/Ep (a) and Al (b) adherends at $y / b = 1, z / h = 0.5$ without crack and with initial debond crack of two different lengths	243
4.16	Schematic of a composite-to-composite adhesive bonded joint (a) and its 1/8 th part (b) considered in the analysis	244

LIST OF FIGURES (Continued)

PART B

FIGURE		PAGE
4-17	Geometry of the global and local regions in the x - y (a) and x - z (b) planes	248
4-18	Variations of σ_x / σ_0 in the adhesive (a) and middle adherend (b) along the interface at $y / b = 1, z / h = 0.3214$	259
4-19	Variations of σ_z / σ_0 in the adhesive (a) and middle adherend (b) along the interface at $y / b = 1, z / h = 0.3214$	260
4-20	Variations of τ_{xz} / σ_0 in the adhesive (a) and middle adherend (b) along the interface at $y / b = 1, z / h = 0.3214$	261
4-21	Variations of σ_x / σ_0 in the adhesive (a) and middle adherend (b) along the interface at $y / b = 1, z / h = 0.3571$	262
4-22	Variations of σ_z / σ_0 in the adhesive (a) and upper adherend (b) along the interface at $y / b = 1, z / h = 0.3571$	263
4-23	Variations of τ_{xz} / σ_0 in the adhesive (a) and upper adherend (b) along the interface at $y / b = 1, z / h = 0.3571$	264
4-24	Illustration of the brick distribution used in the Mosaic Model analysis	265
4-25	Variations of σ_x / σ_0 in Gr/Ep (a) and Al (b) adherends in the x -direction for the global region at $y / b = 1, z / h = 0.5$	267
4-26	Variations of σ_x / σ_0 in Gr/Ep (a) and Al (b) adherends in the x -direction for the local region 2 at $y / b = 1, z / h = 0.5$	268
4-27	Variations of σ_x / σ_0 in Gr/Ep (a) and Al (b) adherends in the x -direction for the local region 1 at $y / b = 1, z / h = 0.5$	269
4-28	Variations of σ_z / σ_0 in Gr/Ep (a) and Al (b) adherends in the x -direction for the global region at $y / b = 1, z / h = 0.5$	270
4-29	Variations of σ_z / σ_0 in Gr/Ep (a) and Al (b) adherends in the x -direction for the local region 1 at $y / b = 1, z / h = 0.5$	271

LIST OF FIGURES (Continued)

PART B

FIGURE		PAGE
4-30	Variations of τ_{xz} / σ_0 in Gr/Ep (a) and Al (b) adherends in the x-direction for the global region at $y/b = 1, z/h = 0.5$	272
4-31	Variations of τ_{xz} / σ_0 in Gr/Ep (a) and Al (b) adherends in the x-direction for the local region 1 at $y/b = 1, z/h = 0.5$	273
5-1	A single-lap adhesive bonded joint (a) and its mosaic model (b)	278
5-2	A double-doubler adhesive bonded joint (a) and its mosaic model (b)	279
5-3	A panel with adhesively bonded stiffener (a) and its mosaic model (b)	280
5-4	Brick nomenclature in the mosaic body model	281
5-5	Double-lap composite bonded joint (a), its 1/8 th part (b) and mosaic model (c)	294
5-6	Mesh design in the x-z (a) and y-z (b) planes	295
5-7	Brick nomenclature for the mesh variant 1 of Table 5-4	298
5-8	Histogram of the potential energy density distribution in the double-lap bonded joint with unidirectional adherends	301
5-9	Distributions of the displacements (a) u_x/u_0 (\circ), u_y/u_0 (\diamond) and u_z/u_0 (\triangle) and stresses (b) σ_z/σ_0 (\bullet), τ_{xz}/σ_0 (\blacktriangle) along the y-coordinate at $x = a_2 - h_p/2, z = h_2 - h_p/2$ calculated with mesh variants 1, 6, and 7 of Table 5-4	304
5-10	Variations of the displacement corresponding to the I-crack (a), A-crack (b) and C-crack (c) opening in the case of unidirectional Adherends	305
5-11	Variation of the displacements corresponding to the I-crack (a), A-crack (b) and C-crack (c) sliding in the case of unidirectional adherends	305

LIST OF FIGURES (Continued)

PART B

FIGURE		PAGE
5-12	Dependencies of the energy release rate on the crack length at $u_0 = 0.2 \text{ mm}$ in the case of unidirectional adherends	308
5-13	Variations of the global stiffness (1.48) with the crack length in the case of unidirectional adherends	309
5-14	Dependencies of the critical applied displacement on the crack length for the I-crack (a), A-crack (b) and C-crack (c) in the case of unidirectional adherends. Values at the curves indicate the critical strain energy release rate in J/m^2	310
5-15	Dependencies of the critical applied stress on the crack length for the I-crack (a), A-crack (b) and C-crack (c) in the case of unidirectional Adherends. Values at the curves indicate the critical strain energy Release rate in J/m^2	311
5-16	Smearing scheme of the laminated adherends	314
5-17	Variations of the displacements corresponding to the crack opening mode for the I-crack (a), A-crack (a0 and C-crack (c) in the case of $[0^\circ / 90^\circ]_{4s}$ adherends	315
5-18	Variations of the displacements corresponding to the crack sliding mode for the I-crack (a), A-crack (a0 and C-crack (c) in the case of $[0^\circ / 90^\circ]_{4s}$ adherends	315
5-19	Variations of the global stiffness (48) on the crack length in the case of $[0^\circ / 90^\circ]_{4s}$ adherends	317
5-20	Dependencies of the energy release rate on the crack length at $u_0 = 0.2 \text{ mm}$ in the case of $[0^\circ / 90^\circ]_{4s}$ adherends	317
5-21	Dependencies of the critical applied displacement on the crack length for the I- and A-cracks n the case of $[0^\circ / 90^\circ]_{4s}$ adherends. Values at the curves indicate the critical strain energy release rate in J/m^2	318

LIST OF FIGURES (Continued)

PART B

FIGURE		PAGE
5-22	Dependencies of the critical applied stress on the crack length for the I- and A-cracks in the case of $[0^\circ / 90^\circ]_{4s}$ adherends. Values at the curves indicate the critical strain energy release rate in J/m^2	319
6-1	A double-lap composite bonded joint under consideration (a) and its 1/8-th part analyzed (b)	325
6-2	Illustration of the spew fillet models in adhesive bonded joint	326
6-3	Illustration of finite element mesh used in the local analysis with the spew fillet (not in scale); the mesh of triangle elements shown differs from the actual one generated by PATRAN	327
6-4	Variations of σ_x / σ_0 (a), σ_z / σ_0 (b) and τ_{xz} / σ_0 (c) at the lower interface, $z/h = 0.3214$, from the side of adherend	329
6-5	Variations of σ_x / σ_0 (a), σ_z / σ_0 (b) and τ_{xz} / σ_0 (c) at the lower interface, $z/h = 0.3214$, from the side of adhesive	330
6-6	Variations of σ_x / σ_0 (a), σ_z / σ_0 (b) and τ_{xz} / σ_0 (c) at the upper interface, $z/h = 0.3571$, from the side of adhesive	331
6-7	Variations of σ_x / σ_0 (a), σ_z / σ_0 (b) and τ_{xz} / σ_0 (c) at the upper interface, $z/h = 0.3571$, from the side of adherend	332

LIST OF TABLES

PART A

TABLE		PAGE
3-1	Applied stress at debond initiation for model composites	21
3-2	Predicted bond strength from straight-sided specimen	29
4-1	Elastic properties of constituents	38
4-2	Experimental data from transverse testing of SCS-0/Epoxy composite	45
4-3	Maximum value of stress component s_{xx} at fiber-matrix interface and in the fillet region, for unit applied stress and varying cruciform geometry	50
5-1	Elastic properties of unidirectional laminate	64
5-2	Elastic properties of $[0/90]_{3s}$ laminate	64
10-1	Summary of test data and computed G_{II} values	104

PART B

4-1	Element meshes used in the global analysis for the x -direction convergence study	211
4-2	Element meshes used in the global analysis for the y -direction convergence study	211
4-3	Element meshes used in the global analysis for the z -direction convergence study	212
4-4	Normalized displacements at $x = 0.5a$, $y = 0.8b$, $z = 0.5h$ computed with the element meshes described in Tables 4-1 thru 4-3.	213
4-5	Element meshes used in the Submodel 1 analyses; $l_x = 20$, $l_y = 1$, $l_z = 1$	214
4-6	Normalized displacements at $x = 0.5a$, $y = 0.8b$, $z = 0.5h$ computed with the element meshes of Table 4-5.	215

LIST OF TABLES (Continued)

PART B

TABLE		PAGE
4-7	Normalized displacements at $x = 0.5a$, $y = b$, $z = 0.5h$ computed with the element meshes of Table 4-5.	216
4-8	Normalized stresses in Al and Gr/Ep adherends at $x = 0.5a$, $y = 0.8b$, $z = 0.5h$ computed with the element meshes of Table 4-5.	216
4-9	Normalized stresses in Al and Gr/Ep adherends at $x = 0.5a$, $y = b$, $z = 0.5h$ computed with the element meshes of Table 4-5.	217
4-10	Uniform meshes in the y -direction used in Submodel 1 analysis; $l_x = 20$, $l_z = 1$	218
4-11	Parametric meshes in the y -direction used in Submodel 1 analysis; $l_x = 20$, $l_z = 1$	218
4-12	Normalized stresses in Al and Gr/Ep adherends at $x = 0.5a$, $y = b$, $z = 0.5h$ computed with the element meshes of Table 4-10	219
4-13	Normalized stresses in Al and Gr/Ep adherends at $x = 0.5a$, $y = 0.8b$, $z = 0.5h$ computed with the element meshes of Table 4-10	219
4-14	Normalized stresses in Al and Gr/Ep adherends at $x = 0.5a$, $y = b$, $z = 0.5h$ computed with the element meshes of Table 4-11	220
4-15	Normalized stresses in Al and Gr/Ep adherends at $x = 0.5a$, $y = 0.8b$, $z = 0.5h$ computed with the element meshes of Table 4-11	220
4-16	Uniform element meshes in the z -direction used in Submodel 2 analysis	221
4-17	Element meshes, nonuniform in the z -direction, used in Submodel 2 analysis	221
4-18	Normalized stresses in Al and Gr/Ep adherends at $x = 0.5a$, $y = 0.8b$, $z = 0.5h$ computed with the element meshes of Tables 4-16 and 4.17	222
4-19	Normalized stresses in Al and Gr/Ep adherends at $x = 0.5a$, $y = b$, $z = 0.5h$ computed with the element meshes of Tables 4-16 and 4.17	222

LIST OF TABLES (Continued)

PART B

TABLE		PAGE
4-20	Normalized stresses in Al adherend at $x = 0.5a$, $y = b$, $z = 0.4h$ computed with the element meshes of Table 4-16	223
4-21	Normalized stresses in Gr/Ep adherend at $x = 0.5a$, $y = b$, $z = 0.6h$ computed with the element meshes of Table 4-16	223
4-22	Element meshes, nonuniform in the x -direction, used in Submodel 3 analysis	228
4-23	Normalized stresses in Al and Gr/Ep adherends at $x = 0.5a$, $y = 0.8b$, $z = 0.5h$ computed with the element meshes of Tables 4-22	229
4-24	Normalized stresses in Al and Gr/Ep adherends at $x = 0.5a$, $y = b$, $z = 0.5h$ computed with the element meshes of Tables 4-22	229
4-25	Element meshes used in Submodel 3 analyses with the debond cracks; other parameters explained in the text	239
4-26	Element meshes used in the global analysis	249
4-27	Normalized displacements at $x = 0.5444a$, $y = b$ and four z -locations, computed with different x -direction element meshes of Table 4-26	250
4-28	Normalized displacements at $x = 0.5556a$, $y = b$ and four z -locations, computed with different x -direction element meshes of Table 4-26	251
4-29	Normalized displacements at $x = 0.5667a$, $y = b$ and four z -locations, computed with different x -direction element meshes of Table 4-26	252
4-30	Normalized displacements at $x = 0.5444a$, $y = b$ and four z -locations, computed with different y -direction element meshes of Table 4-26	253
4-31	Normalized displacements at $x = 0.5556a$, $y = b$ and four z -locations, computed with different y -direction element meshes of Table 4-26	254
4-32	Normalized displacements at $x = 0.5667a$, $y = b$ and four z -locations, computed with different y -direction element meshes of Table 4-26	255

LIST OF TABLES (Continued)

PART B

TABLE		PAGE
4-33	Normalized stresses in the lower adherend at $y = b$, $z = 0.3214h$ and two x -locations, computed with different x -direction element meshes of Table 4-26	256
4-34	Normalized stresses in the adhesive layer at $x/a = 0.5444$, $y = b$, $z = 0.3214h$, computed with different x -direction element meshes of Table 4-26	256
4-35	Normalized stresses in the lower adherend at $y = b$, $z = 0.3214h$ and two x -locations, computed with different y -direction element meshes of Table 4-26	257
4-36	Normalized stresses in the adhesive layer at $x/a = 0.5444$, $y = b$, $z = 0.3214h$ computed with different y -direction element meshes of Table 4-26	257
5-1	Characteristics of the brick meshes in the x -direction	296
5-2	Characteristics of the brick meshes in the y -direction	296
5-3	Characteristics of the brick meshes in the z -direction	296
5-4	Computational variants used in the analysis	297
5-5	Convergences of the global and local potential energy densities and displacements at the corner point with the mesh refinement in the x - and z -directions	302
5-6	Convergence of the averaged stresses computed for local Regions 1, 2 and 3	303

EXECUTIVE SUMMARY

The 3D Strength Prediction of Composite Materials (3DSPC) program, sponsored by the Air Force's Materials Directorate at AFRL, focused on lowering the cost of implementing advanced composites in aerospace structures by making significant advances in design methodologies for the use of composite materials to maximize performance and material efficiency. Traditionally, many expensive coupon-level mechanical property measurement tests are conducted on candidate composite materials to provide designers with accurate thermoelastic constants to be used in design. The same mechanical tests often provide designers with less than acceptable failure information. A proven technique for applying coupon level strength properties to complicated structures with varying laminate thickness and layups does not exist. The failure modes that occur in the actual structures often do not exist in the coupons or do not exist in the same ratios and combinations. The result is that further mechanical failure testing of prototype parts is required which drives up the cost of using advanced composites.

The 3DSPC program addressed the issue of reducing mechanical testing costs by increasing the understanding of the mechanical response and progressive damage states in a range of advanced composite materials, which include high temperature brittle matrix composites (BMC) and polymer matrix composites, through the use of state-of-the-art analytical techniques. Two major routes were investigated – micromechanics (fiber/matrix level analysis) and 3D macromechanics (individual lamina level analysis) as opposed to the *laminate* level analyses that are currently being employed.

The advancements by Nicholas Pagano and G. P. Tandon over the few years prior to this program regarding global unidirectional composite behavior, material properties at the constituent level, and the boundary conditions which simulate interfacial damage, led to

increased understanding of the key mechanisms associated with failure of composite laminates. That is, the study of the response of a unidirectional layer or various micromechanical parameters such as phase geometry and interfacial properties resulted in identification of critical features that are common in fiber-reinforced composites. The current work (Part A) builds on the previous micromechanics research by Pagano and Tandon by modeling several interface strength tests, the end notched flexure (ENF) test, a high void content oxide-oxide composite for use in the hot section of turbine engines, and load transfer to the remainder of a composite from a fiber break.

The micromechanics portion of the 3DSPC yielded several important results. The cruciform geometry was utilized to evaluate the interfacial normal strength in unidirectional composite systems using single fiber specimens. The stress level at debond initiation was measured using indicators from several sources such as development of photoelastic fringes, a jump in the strain response of surface gages, the first significant occurrence of acoustic emission activity, and visual observation using a reflected light technique. The experimental observations of damage initiation and ultimate failure were found consistent with the numerical prediction using 3-D FEM. Interfacial stress distributions in the single-fiber pushout specimen were also obtained using two numerical techniques. The pushout test verified the necessity of using an elastic analysis on the order of an axisymmetric FEM model including a point-by-point representation of friction for data reduction of pushout test results.

A more rigorous elasticity model for analysis of the ENF test for characterization of Mode II fracture toughness was developed. Numerical results of this analysis were used to assess the accuracy of various solutions available in the literature, including beam theory. The ENF specimen was then used to evaluate the fracture toughness of a polyester/epoxy planar

interface, and the predictions were correlated (with mixed success) with previously obtained values from pushout testing. Finally, an oxide-oxide composite consisting of a 2-D reinforcement in a matrix consisting of alumina particles, voids, inherent cracks due to the processing conditions, and a silica bonding agent was analytically modeled. Predicted quantities are presented including the thermomechanical effective moduli, the thermal conductivity tensor, and damage due to processing conditions.

Part B of this report describes the development and implementation of a 3D variational model for predicting failure of composite adhesive joints through accurate lamina level calculation of stress, strain, and energy release rates. Prior to the 3DSPC program the Air Force and the aerospace industry utilized an outdated analysis methodology in designing composite to composite and composite to metal bonded structures. Since the approaches relied on were 2-D and 3-D FEM, and they required a prohibitive number of degrees of freedom to achieve convergence, the predicted strength and durability of adhesive joints were calculated with unknown accuracy and relied heavily on empirical data obtained at great expense. This work was conducted by Alexander Bogdanovich and builds on the recent developments in spline variational theory and its implementation (by Endle Iarve) for the prediction of failure in composite bolted joints.

A generalized version of a spline variational model referred to as the “mosaic model” was developed to accurately calculate stresses, strains, and displacements in complex shaped composite structures assembled from anisotropic parallelepipeds. The approach enforces continuity of displacements between similar material blocks and continuity of displacements and stresses between dissimilar material blocks. In addition, the model includes the effects of linear thermal expansion and moisture swelling. The theory was first applied to model double-lap

composite adhesive joints, and the results were compared to 3-D FEM results. A concept of 3-D progressive damage and fracture modeling was next proposed and illustrated on the example of interfacial crack growth in a double cantilever composite solid. The novel theoretical approach for analyzing 3-D problems of crack propagation was then applied to double and single lap composite to composite and composite to metal joints. Extensive results are documented including the locations of maximum stresses and strains as well as energy release rates as a function of joint geometry. Finally, a comprehensive discussion of the effects of the spew fillet in adhesive joints on the stress distributions near the end of the overlap is presented.

1.0 A CRITICAL SHEAR ENERGY RELEASE RATE CRITERIA FOR DEBONDING IN A PUSH-OUT TEST¹

1.1 Introduction

The objective of this study was to model the progressive debonding portion of the load-displacement response in a push-out test including initiation of debonding, propagation and eventually catastrophic debonding of the remainder of the bonded interface using a single parameter characterized as the critical shear energy release rate of the interface. In a recent study, Tandon and Pagano [1] had employed the variational model of a concentric cylinder to accurately model the fiber push-out and re-push test used for evaluation of interfacial properties. The detailed stress distributions and load-displacement solutions obtained by considering a variety of interface boundary conditions (such as adhesively bonded, frictionally sliding and debonded) were compared with a numerical elasticity solution using the material properties of polyester/epoxy system for which experimental data was available [2].

Further, to resolve the problem associated with vanishing strain energy release rate because of a weak singularity at the crack tip, a critical finite crack length extension, equal to the minimum layer thickness in the model, was suggested [1] for evaluation of the toughness of the interface using energy balance arguments. Also, the direct contribution of normal and shear tractions to the change in potential energy could be separated, although the stress components were related by the frictional law in the slip region. It was found that the model predicted the *apparent* toughness of the interface to increase with the length of the debond while the numerical contribution of shear stresses to the potential energy release rate was nearly constant.

1.2 Initiation

In this work, we have employed the critical shear energy release rate criteria ($G_r = G_{\pi}$) to predict the onset of debonding, i. e, the critical force needed to “pop-in” the debond during the

¹ (Presented at the Symposium on Micromechanics of Fiber Reinforced Composites, 5th International Conference on Composites Engineering, Las Vegas, Nevada, July 5-11, 1998)

push-out test. This is accomplished by determining the values of applied displacement (d^*) and hence, corresponding force (F^*), which result in $G_r = G_c$ for a number of debonds. As seen in Fig. 1-1, both F^* and d^* values display a minimum with debond length. Thus, according to this criterion, the length of the debond will continue to increase until stable crack growth takes place (corresponding to the minimum in the curves shown in Fig. 1-1). The debond length value at which stable propagation begins to take place is the critical debond length at initiation and the corresponding F^* value is the value of the force at which the debond will initiate. If the approach was perfectly consistent, both F^* and d^* would be minimum at the same value of the debond length. However, there is some (small) error due to the number of layers utilized ($N=10$) along with using the average value of the shear energy release rate as the critical shear energy release rate. Further, in determining d^* and F^* values as a function of debond length, a curve was fitted to approximate the relationship between G_r and force versus displacement. However, the error introduced due to this approximation is minimized by narrowing the range of interpolation

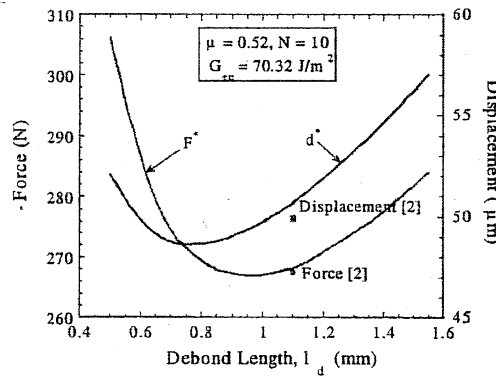


Fig. 1-1: Estimation of debond length on initiation using critical shear energy release rate criteria.

1.3 Propagation

As the debond propagates, the force-displacement response is next predicted by meeting the proposed failure criteria. This is accomplished by determining the values of applied displacement (d^*) and hence, force (F^*), which result in $G_r = G_c$ for each debond length measurement made by Bechel and Sottos [2]. This comparison with experimental data is illustrated in Fig. 1-2 and is extremely good for all debond lengths considered. During this stage the stress increases at a

decreasing rate with increasing displacement to a maximum (σ_d^*) at which point catastrophic debonding occurs along the remainder of the bonded interface.

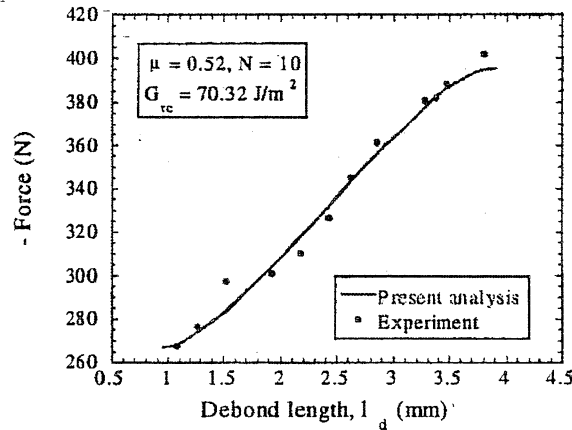


Fig. 1-2: Comparison of force-debond length relationship during push-out test

1.4 Ultimate Failure

The critical shear energy release rate criteria is also applied to estimate the maximum debond stress and the corresponding critical debond length for the push-out specimen. The variation of F^* and d^* values with the length of the debond is plotted in Fig. 1-3. It is seen that both F^* and d^* values pass through a maximum as the debond length is increased. Beyond a certain length of the debond, lesser force and displacement is needed to satisfy the critical shear energy release rate criteria and the debond becomes unstable. The debond length value at which unstable propagation begins to take place is the critical debond length for catastrophic debonding. Again, both F^* and d^* do not attain maximum values at the same value of the debond length. However, the differences are small and our estimates of the maximum debond stress, externally applied displacement and critical debond length are very close to the experimental measurements and therefore lend credence to the use of critical shear energy release rate criteria for a unite crack extension (Δa) for estimating these quantities. The predictions were also shown to be relatively independent of the magnitude of $i \sim a$ over a wide range of the latter extension.

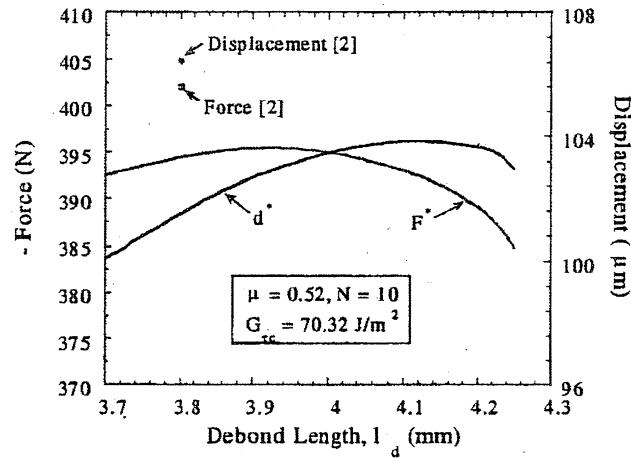


Fig. 1-3: Estimation of debond length at catastrophic debonding using critical shear release rate criteria

REFERENCES

- (1) Tandon, G. P. & Pagano, N. J., (1998), "Micromechanical Analysis of Fiber Push-Out and Re-Push Test", *Comp Sci & Techn.*, Vol 58, No. 11, pp 1709-1725
- (2) Bechel, V. & Sottos, N., (1998) "Application of Debond Length Measurements to Examine the Mechanics of Fiber Push-Out Test, *J. Mech. Phys. Solids*, Vol 46, No. 9, pp 1675-1697

2.0 STRESS FIELDS IN A SINGLE FIBER PUSH-OUT SPECIMEN CONSIDERING INTERFACIAL DAMAGE AND FRICTION¹

2.1 Introduction

Sophisticated and accurate analysis methods are required to enhance the understanding of the fiber-matrix interfacial damage evolution and the nature of mechanisms driving the damage growth. These analyses may also provide improved methods for obtaining values to the parameters characterizing the material behavior such as the adhesive bond strength and coefficient of friction from experimental data. In this work, the detailed stress distributions and load-displacement solutions obtained by using two different techniques capable of considering several interfacial conditions (bonded, sliding with friction, debonded, and sticking) are compared.

The models considered are the Axisymmetric Damage Model (ADM) [1] which produces an approximate elasticity solution with a variety of interface boundary conditions and Finite Element Method (FEM) with the fiber-matrix interface modeled as frictional contact. ADM computes the load-displacement relationship and stress fields in the model for a pre-specified state of interface damage without using load incrementation. The finite element model determines the location and extent of bonded, debonded and frictional zones on the interface as a part of the solution using an incremental loading procedure. Figure 2-1 shows the methodology used to carryout the numerical studies in this paper. In this effort, the interfacial damage zones determined from the finite element analysis are specified in ADM analyses. Then push-in displacement, corresponding load and the interfacial stress distributions obtained from the two models are compared.

2.2 Results and Discussion

Several simulations are performed for polyester fiber/epoxy matrix system with assumed

¹ (Presented at the Symposium on Processing-Structure-Property Relationships of Composite Interfaces, Annual TMS Meeting, San Antonio, TX, Feb 15-19, 1998)

coefficient of friction, a system for which experimental data is available [2].

The first case investigated (Case-I) is during the residual stress development where the loading is considered to be monotonic from a stress-free state. Then the case of superimposing push-out loading after the residual stress step is discussed as Case-II. For both of these cases the effect of adhesion on the stress fields is determined through comparison of ADM and FEM solutions. Additionally, mesh and load incrementation convergence studies are performed to independently verify the finite element solution.

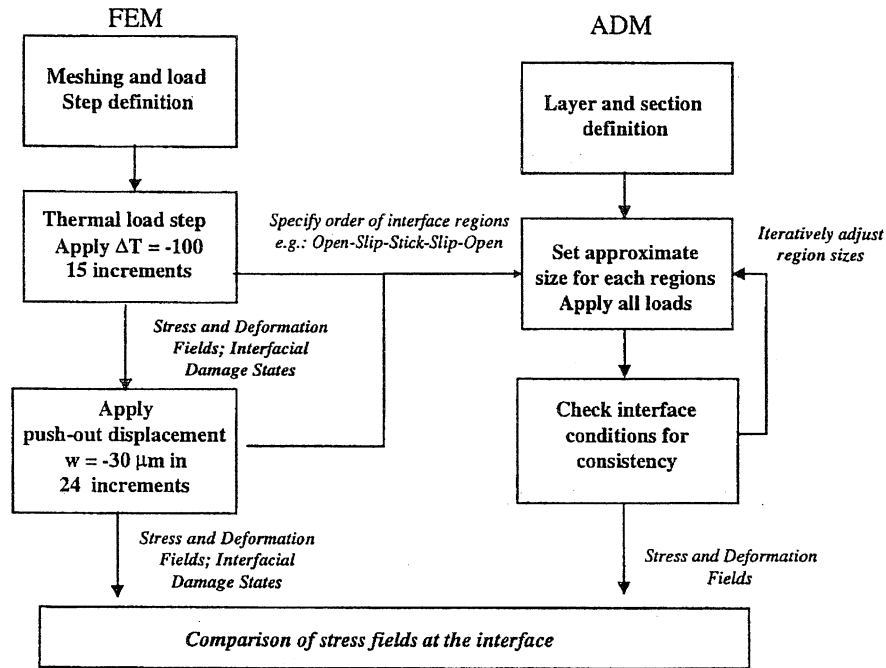


Fig. 2-1: Methodology adopted to simulate the problem in both FEM and ADM

2.2.1 Thermal Loading

The first load step considered corresponds to -48.5°C temperature difference or -0.0011 shrinkage strain. There is only thermal residual stress at this point and the load history is a monotonic decrease of temperature from the stress free state. There are no reversals of the slip direction on any portion of the interface. The stick state of the interface has the same mechanical conditions as the perfectly bonded conditions, i.e., not only the incremental displacements ΔW_f -

$\Delta W_m = 0$ but also the total displacements, $w_f - w_m = 0$. Fig. 2-2 shows the normal (σ_{RR}) and shear stress (σ_{RZ}) distributions at the fiber-matrix interface as obtained from the ADM and FEM Solutions. In this case, the stress distributions obtained for both frictional contact analyses modeling (with slip-stick zones) and adhesive bond modeling (with slip-adhesion zones) are very similar in nature. The figure also shows the $\mu\sigma_{RR}$ distribution, which is plot to distinguish between the slip and the bonded/stick regions.

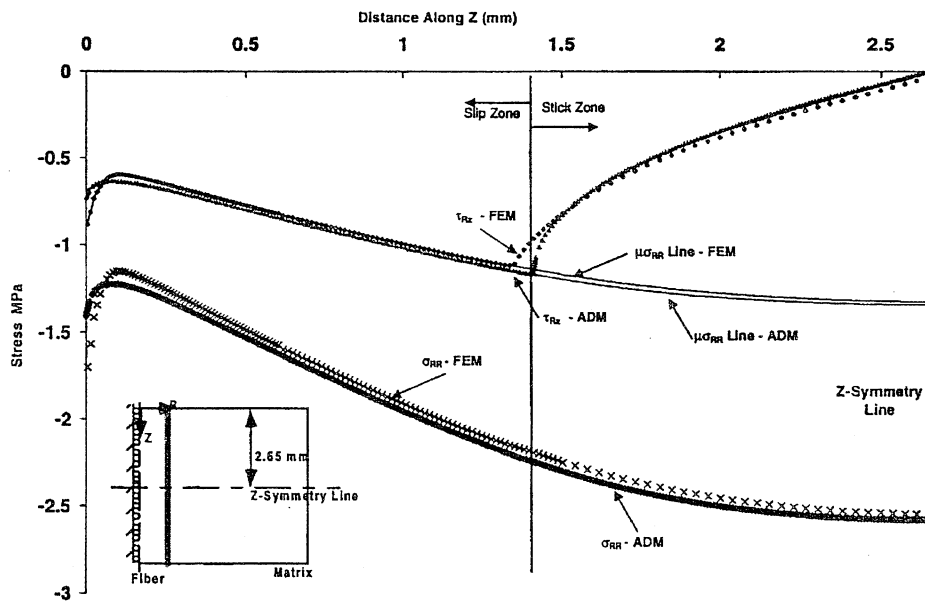


Fig. 2-2: Comparison of shear stresses after monotonic thermal loading, $\Delta T = -48.5^\circ\text{C}$

There is a small difference between the length of the slip zone obtained by ADM and that obtained by the FEM. This difference may be attributed to the element size used in FEM since ADM determines the size of the zone more precisely.

2.2.2 Thermal and Push-out Loads

Unlike Case-I, Case-II has superposition of two different types of loading applied to the model. While the chemical shrinkage causes interfacial normal compression, the push-out displacements cause interfacial shear. The results obtained from the ADM and FEM models for this case are described for two different interfacial conditions. In the first sub-section, the FEM

solution is described. The FEM solution is for interface with zero tensile adhesive strength and obeys Coulomb's law of friction under normal compression. The solutions for finite interfacial adhesive strength are described in the second sub-section

2.2.2.1 Frictional interface with no adhesive strength

The results of the FEM analysis with no adhesive tensile strength and the fiber-matrix interface maintained as frictional contact is described here. Fig. 2-3 shows the evolution of the various interface zones during the thermal loading and subsequent fiber push-out loading.

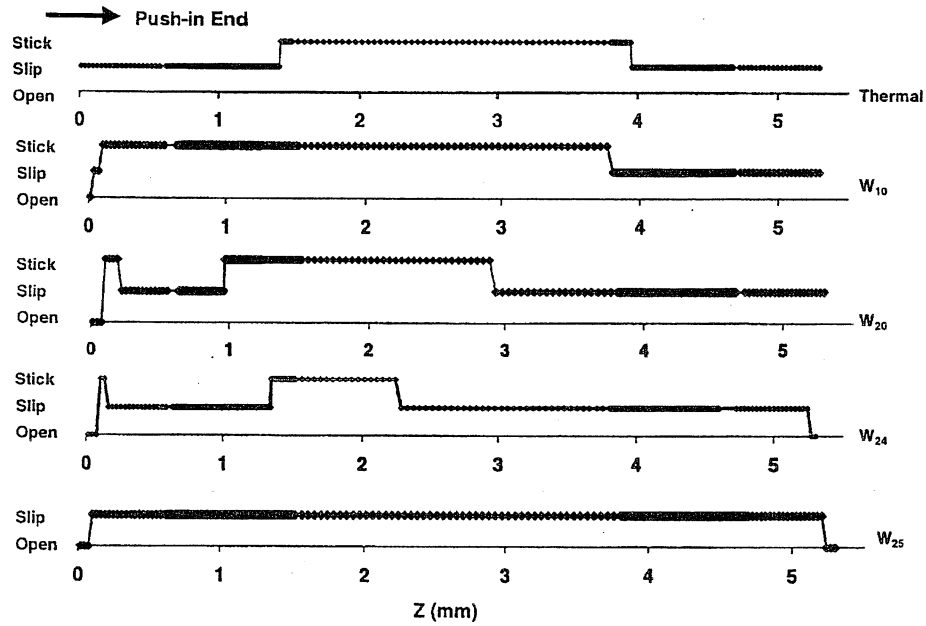


Fig. 2-3: Interface damage state at various push-in displacements

The figure describes the order of the zones and their sizes with the left end corresponding to the lower end ($Z=0$) of the fiber push-out model or the end where the push-out displacement is applied. After the thermal loading step, the order of the interface zones can be described as slip-stick-slip. The center of the model is under frictional stick (which also corresponds to adhesive bond in this case as the relative total shear displacement is also zero) and the ends have symmetric slip regions. Upon the application of 10 μm of push-out displacement, the fiber-matrix interface rearranges into open-slip-slick-slip-open zones. There is a change of direction

slip zone and hence the sign of shear stress near the fiber push-out end. At the end of the thermal loading step, the slip zone closer to the push-out end has the matrix sliding outwards (along -z axis). This direction is reversed by the applied push-out displacement. A small open zone also develops at the fiber push-out end. On further application of displacement to $w = 2011\text{m}$, the zones again rearrange to open-slip-stick-slip-open zones. An open zone develops at the opposite end of push-out. Thus, not only the size but the order of the zones also changes with incremental loading. Finally, at an applied displacement of $25\text{ }\mu\text{m}$, the entire interface is sliding with two symmetric open zones at either side of the model.

2.2.2.2 Frictional interface with adhesive strength

As mentioned earlier, the FEM model determines the length and order of the zones using an incremental loading procedure. For this part of the study, the interfacial zones determined from the FEM solution assuming frictional contact are specified in ADM and a new FEM analyses, but with one major difference. The stick zone observed in the frictional analysis is replaced by a bonded zone of equal length in both ADM and FEM analyses. This configuration corresponds to a push-out displacement of 12.4 mm applied subsequent to the residual shrinkage. Thus, three solutions are obtained for the same applied loading but with two different fiber-matrix interface conditions.

Figure 2-4 shows a comparison of the normal stress distributions from these solutions. The dashed lines with asterisks (----) show frictional-contact FEM solution, the solid line is the ADM solution and the dashed-line closely following the solid line is the FEM solution with adhesive interface conditions instead of frictional contact. These results show that the ADM solution and FEM solution correspond to each other if identical set of interfacial conditions are employed. On the other hand, the FEM frictional solution differs considerably from the adhesive solution. In the latter case, singularities [3] are encountered at the transition between open and bonded zones. Both ADM and FEM methods show the singular behavior near the bonded-open

interaction. However, the transitions from stick-to-slip regions are free of any singularities.

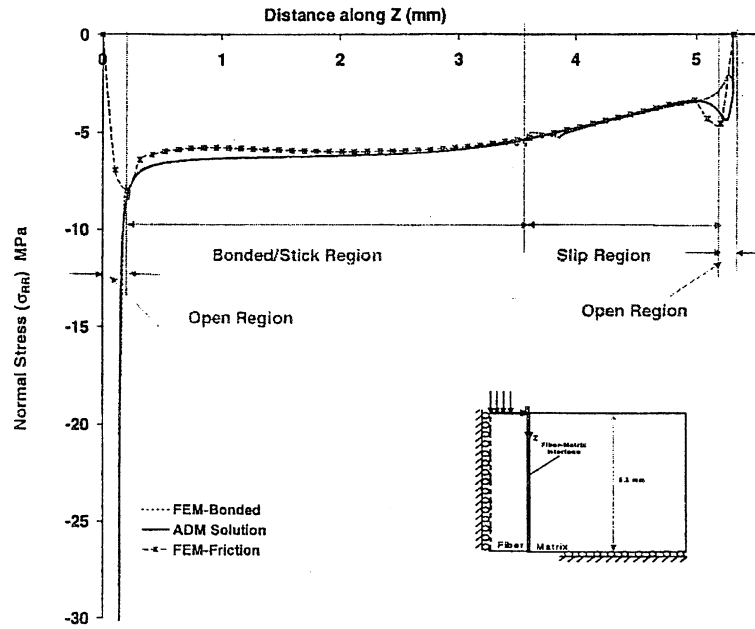


Fig. 2-4: Comparison of ADM and FEM Results: Radial stress distribution along the interface.

Fig 2-5 shows the comparison between the three analyses for the shear stress component. Again, there is a pronounced difference between frictional stick solution, the ADM solution and the FEM bonded solution for the same load set. It can be seen that ADM and FEM bonded solutions compare very well. The frictional solution, however, is completely different from the bonded and ADM solutions because of the initial interface conditions and due to the load history dependence inherent in the frictional solution. These comparisons in Figs. 2-4 and 2-5 illustrate the differences in the stress fields due to “bonded” (no shear displacement throughout the loading history) and “stick” (no shear displacement during the last load increment but has non-zero total shear displacement interface conditions. These differences can be extremely important in the interpretation of FEM friction results.

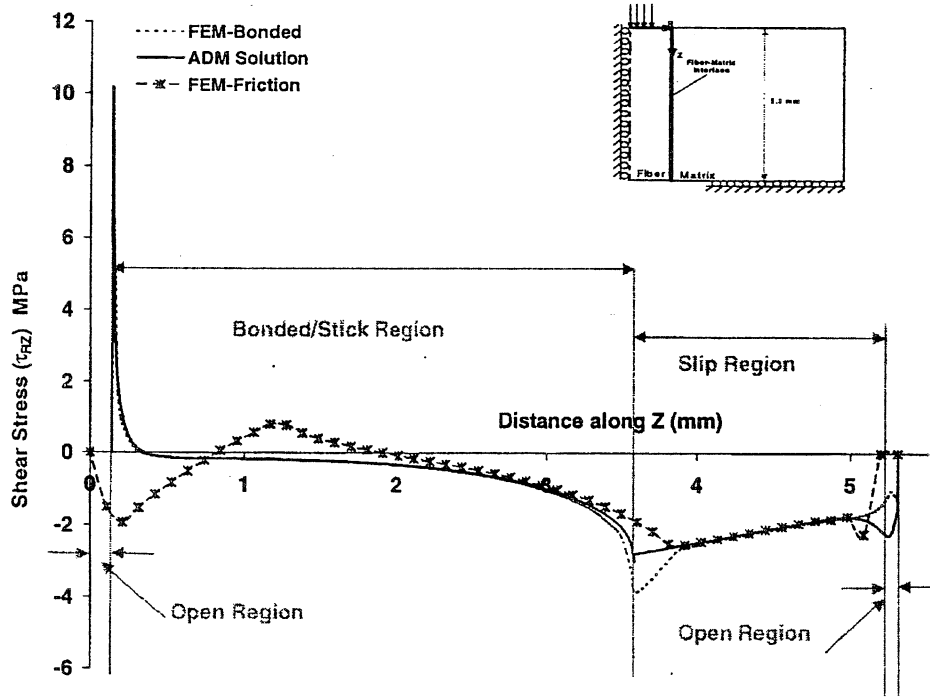


Fig. 2-5: Comparison of ADM and FEM Results: Shear stress distribution along the interface

2.3 Concluding Remarks

In this study, we have demonstrated that the predicted stress distribution in a single fiber push-out specimen is strongly dependent on the damage state (or nature of the boundary conditions) at the fiber-matrix interface. Effective simulation of damage evolution will therefore require knowledge about the initial state of the specimen. Alternately, the force required to push the fiber completely out of the matrix can be used to infer the interfacial conditions. In the presence of adhesive bonding between the fiber and matrix, Tandon and Pagano [41] have calculated the maximum fiber-end load to be 395 N using a critical value of the shear energy release rate of the interface. However, if we assume the interface to be purely frictional, the maximum push-out force is predicted as 101 N. Thus, a comparison of the predicted push-out load with assumed interface conditions and the experimental measurements will aid in determining the true nature of the interface.

REFERENCES

- (1) Pagano, N. J. (1991). Axisymmetric Micromechanical Stress Fields in Composites. *Proceedings 1991 JUTAM Symposium on Local Mechanics Concepts for Composite Materials Systems*, Springer, Verlag, 1-26.
- (2) Bechel, V. T. & Sottos, N. R., A Comparison of Calculated and Measured Debond Lengths from Fiber Push-out Tests, *Comp Sci & Techn.*, Vol 58, No. 11, pp 1727-1739
- (3) Comninou, M., Interface crack with friction in contact zone, *Journal of Applied Mechanics*, 44 (1977), pp. 780-781.
- (4) Tandon, G. P. & Pagano, N. J., (1998), Micromechanical Analysis of Fiber Push-Out and Re-Push Test", *Comp Sci & Techn.*, Vol 58, No. 11, pp 1709-1725

3.0 INFLUENCE OF EDGE EFFECTS IN ESTIMATING INTERFACIAL NORMAL STRENGTH IN MODEL UNIDIRECTIONAL COMPOSITES

3.1 Introduction

Interfacial normal strength is commonly determined by testing straight-sided single fiber composite specimens with fiber ends exposed to the free surface and interpreting debond initiation from the beginning of non-linearity or first occurrence of acoustic emission on the stress strain curve. In these specimens the free surface is a favored site for interface debonding because of stress intensification at this location and consequently, surface observation techniques and strain measurements in uniform-gage specimens may underestimate the actual interface debond stress. In order to remove the influence of the free surfaces from the test, two alternate geometries can be considered. The first design involves covering the ends of the fiber by embedding the fiber (Hu et al¹; Tandon et al²) completely inside the matrix, whereas, the second design is of a composite sample in the shape of a cruciform or cross (Gundel et al³) with an extremely large width in the gage section. It has been shown that if the fiber is completely encapsulated in matrix material, the nature of the singularity near the fiber end is reversed. The interior singularity at the fiber "corner" now manifests itself by producing a discontinuity in the axial distribution of the radial stress approaching negative infinity on the interface. Initial debonding will therefore be prevented since the residual radial stress remains compressive. With the cross-shaped geometry, the central portion of the fiber/matrix interface is highly stressed under tensile loading, thereby forcing debond initiation and propagation in the center, away from the free edges.

In this study, model single fiber composite specimens were made in the three geometrical configurations, namely, i) straight sided specimen with fiber ends exposed (Fig. 3-1), ii) straight-sided specimens with fiber ends covered (Fig. 3-2) and iii) cross-shaped design (Fig. 3-3). These model specimens are incrementally loaded in tension to failure and the fractured halves examined to identify the location of failure initiation and the extent of failure while strain and acoustic emission activity is continuously monitored. The three specimen designs have also been analyzed using 3-D finite element methods to estimate the interfacial stresses in terms of constituent material properties. Finally, some failure criteria (Whitney and Nuismer⁴) have been employed in conjunction with the experimental observations to estimate the normal bond strength of the

interface. Results indicate good correlation between experiments and the analytical predictions for test configurations considered in this study and demonstrate the importance of stress field singularities in controlling damage initiation in straight-sided samples. It is further shown that the cross-shaped design is successful in forcing debond initiation in the interior of the sample (region free of stress singularities) and therefore the results produced by testing of such specimens may be capable of providing the true transverse response of the fiber-matrix interface.

3.2 Specimen Design, Fabrication and Test Methods

In this work, model single fiber composite specimens were made in the three geometrical configurations, namely, i) straight sided specimen with fiber ends exposed, ii) straight-sided specimens with fiber ends covered and iii) cross-shaped design. The composite specimens were cast in rectangular and cruciform shaped silicone rubber molds for straight-sided and cross-shaped samples, respectively. The specimen cross-sectional dimensions are shown in Figs. 3-1 thru 3-5.

The samples were 0.198" (or 5.03 mm) thick for all three geometries considered. The composite reinforcement consisted of aluminum rods, 0.092" (or 2.34 mm) in diameter, while the matrix was an epoxy resin (Epon 828 from Shell Chemical Co.) cured with a polyetheramine (Jeffamine D-230 from Texaco, In.) for 3 days at ambient temperature. The rod surfaces were merely cleaned with acetone, which enabled the epoxy to strongly bond with the reinforcement. Rods of predetermined length were approximately positioned in the mold and epoxy resin cast around them. Curing at ambient temperature eliminated thermal residual stresses which are otherwise induced from the mismatch in coefficients of thermal expansion of fiber and matrix.

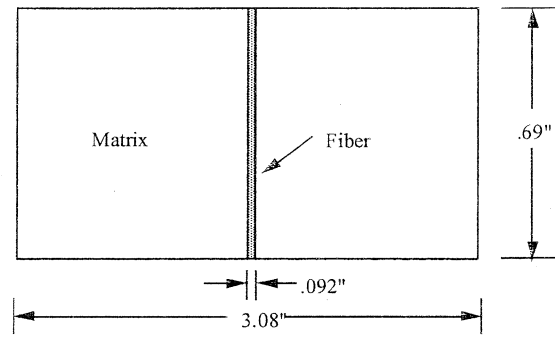


Fig. 3-1: Straight-sided specimen with fiber ends exposed

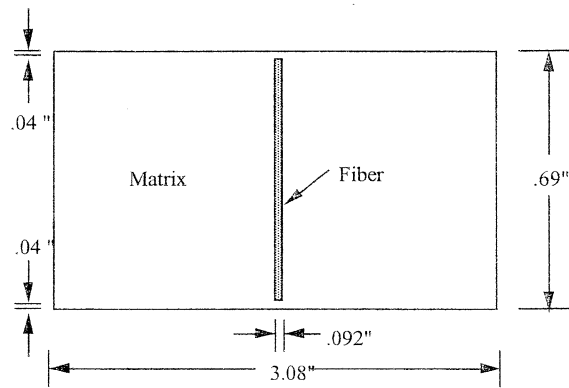


Fig. 3-2: Straight-sided specimen with fiber ends embedded

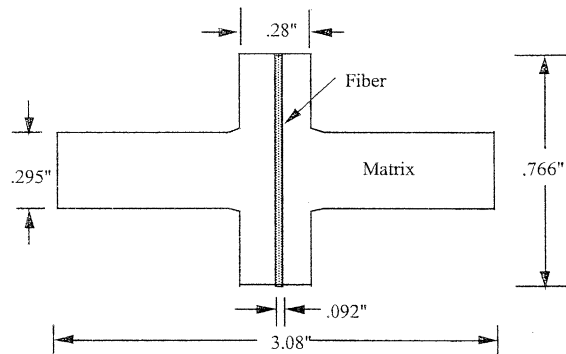


Fig. 3-3: Cruciform (or cross-shaped) specimen

The free edges of the straight-sided specimen with exposed fiber ends were progressively ground and then polished using successively smaller diameter alumina polishing powder (final size was 0.3 micrometer) in order to enhance the microscopic image for crack detection. The free

edges of the cruciform specimen and straight-sided samples with embedded fiber ends were also polished after curing. Strain gauges (gauge length 3.2 mm) were then mounted on the flat surface in the center and along the edges of the specimen perpendicular to the fiber to monitor strain during loading. An acoustic emission transducer was also attached to the specimen to monitor failure events. For straight-sided samples with fiber ends exposed, the specimen was loaded to either a prescribed level slightly higher than the expected interface debonding level or up to the first occurrence of acoustic emission on the stress strain curve. This load was held during application of a fluorescent penetrant to the polished surface, and then unloaded for microscopic examination to capture all failure events which occurred. Straight sided samples with fiber ends embedded and cruciform shaped specimen were also loaded in tension, under displacement control, to failure and the fractured halves examined to identify the locus of failure.

3.3 Experimental Results

In Table 3-1, we have listed the applied stress level at debond initiation obtained either from first occurrence of acoustic emission or beginning of non-linearity in the stress-strain curve for the three specimen designs. The values listed in Table 3-1 are the average of six specimens for each configuration considered. It was observed⁵ that for straight-sided specimen with fiber end exposed, interface debonding initiated symmetrically near the free edges in both front and back of the specimen. Subsequent loading resulted in the debond crack branching into the matrix leading to final failure. For straight-sided specimen with fiber ends covered, it was found⁵ that failure initiated at the fiber corner and propagated over some distance along the fiber length before branching into the matrix. However, for cruciform (or cross-shaped) specimen, it was observed⁵ that failure initiated in the center (region free of stress singularities) away from the fiber ends. The debond propagated for some distance along the length of the reinforcement before branching into matrix.

Table 3-1: Applied Stress At Debond Initiation For Model Composites

Model Single Fiber Specimen	Average Applied Stress at Debond Initiation	Standard Deviation (%)
Straight-sided with fiber ends exposed	1207 psi (8.3 MPa)	14.1
Straight-sided with fiber end embedded	1787 psi (12.3 MPa)	4.6
Cruciform	2832 psi (19.5 MPa)	6.7

3.4 Numerical Analysis

In this work, model single fiber composite specimens have been analyzed using 3-D finite element analysis employing the ANSYS code. The model was simplified by using symmetry planes so that only an eighth of the total specimen was required to be modeled. These planes of symmetry were constrained by symmetry boundary conditions, whereas the outer surfaces were free to move in all directions. The aluminum reinforcement and the epoxy matrix were treated as three-dimensional eight node brick elements with the following elastic properties (handbook values).

Material	E(GPa)	ν
Aluminum	72.4	0.32
Epoxy	2.9	0.35

Figure 3-4 shows the radial stress at the fiber-matrix interface in the loading direction as a function of distance along the length of the reinforcement for the three specimen geometries considered. Analysis reveals that the radial stress at the interface is the dominant stress component and is maximum in the loading direction. The local stresses are represented by the stress concentration factor (SCF), defined as the ratio of the local stress to the applied stress. The distance is normalized with respect to the radius of the aluminum rod. The SCF value is 1.2 in the center of the cruciform specimen and remains reasonably constant (within 10 percent) over two-thirds of the loading region. The SCF gradually decreases at locations further away from the center of specimen approaching zero value before increasing marginally near the free surface.

For straight-sided samples, the SCF at the center of the specimen is approximately 1.3 for both embedded and exposed fiber ends. However, as the free surface is approached for exposed rod or the edge of the embedded rod is approached, a sharp increase in the SCF is observed, although the stresses in the latter are significantly lower than the former.

The results in the previous sections for the specimens tested indicated that only in the case of the cruciform specimen did interface failure occur far from the ends and that cracking initiated at the fiber corners in both the straight sided and embedded fiber specimens. The likely explanation for this behavior is the high radial stresses that occur at the fiber corners for both the exposed-fiber and embedded-fiber specimens, as seen in Fig. 3-4. The lower far-field applied stress at debonding for these specimens, compared with the cruciform geometry, are consistent with this local elevation of radial stress at the interface. Additional insight regarding the stresses at the fiber corners is provided in the next section.

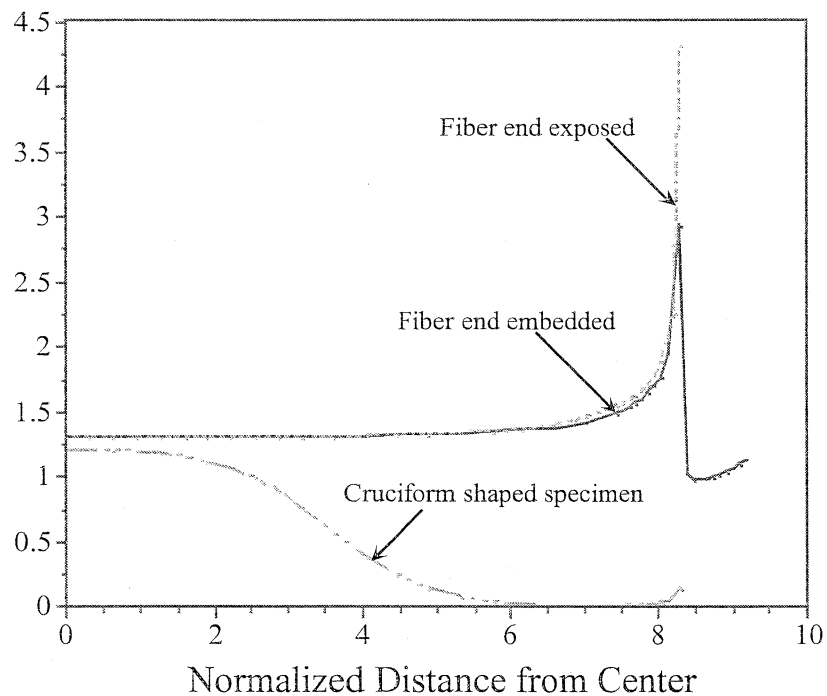


Fig. 3-4: Variation of radial stress with normalized distance from center of the specimen along the length of the aluminum rod

3.5 Asymptotic Analysis

Bogy's⁶ analysis for edge-bonded elastic wedges provides an elegant methodology for analyzing the stress concentration at the fiber corners. Using Airy's stress function approach, Bogy⁶ showed that the stresses at the corner are actually singular, and can be described in the form $\sigma_{ij} \sim r^{-\lambda}$. Here λ is the order of the singularity and is a function of the geometry and the elastic constants of the constituent materials, and r is the radial distance of a material point from the interface corner. Using Mellin's transform, and following Bogy's formulation, one obtains an 8x8 determinant, A , for both the exposed fiber and embedded fiber problem. The dominant singularity, λ , is equal to $-s-2$, where s is the eigenvalue in the domain $-2 < \text{Re}(s) < -1$ for $A=0$. Thus,

$$\sigma_{ij} = \sum K_m \rho^{-s_m-2} \Psi_{ij}^m(\theta) \quad (1)$$

where s_m represent zeroes of A and the angular variations $\Psi_{ij}^m(\theta)$ are the solution $X(s)$ for non-trivial solution to $A_{ij}(s)X_j(s) = 0$. These are obtained by a singular value decomposition method corresponding to

$$A(s_m) = 0 \quad (2)$$

3.5.1 Fiber End Exposed

Utilizing the elastic constants for epoxy matrix and aluminum fiber, we obtain one zero $s = -1.722$. Thus,

$$\sigma_{ij}(\rho, \theta) = \sum K \rho^{-0.278} \Psi_{ij}(\theta) \quad (3)$$

The scaling constant K is next determined by matching the asymptotic solution with the far-field solution obtained from finite element analysis. The matching is done using the approach of Pochiraju⁷, although we have employed some simple tools to guide us in our selection of radius r at which matching is performed. In Fig. 3-5, we have compared the angular distribution of the normalized stress components from asymptotic analysis with the finite element solution (shown as solid symbols) at $\rho/r_f = 0.17$. The stresses have been normalized such that the hoop stress $\sigma_{\theta\theta}$ is unity at the interface (i.e., at $\theta = 0^\circ$). The good agreement between our numerical calculations with the asymptotic distribution provides confidence that matching at $\rho/r_f = 0.17$ is a

good choice.

The scaling factor K is next determined by equating the hoop stress at the interface, i.e.,

$$K = \frac{[\sigma_{\theta\theta}(0^0)]_{\text{FEM}}}{\rho^{-0.278} \Psi_{\theta\theta}(0^0)} = 1.237 \quad (4)$$

3.5.2 Fiber End Embedded

For the specimen with fiber ends embedded, we obtain two zeroes, namely, $s_1 = -1.789$ and $s_2 = -1.679$. Thus,

$$\sigma_{ij}(\rho, \theta) = K_1 \rho^{-0.211} \Psi_{\theta\theta}^1(\theta) + K_2 \rho^{-0.321} \Psi_{ij}^2(\theta) \quad (5)$$

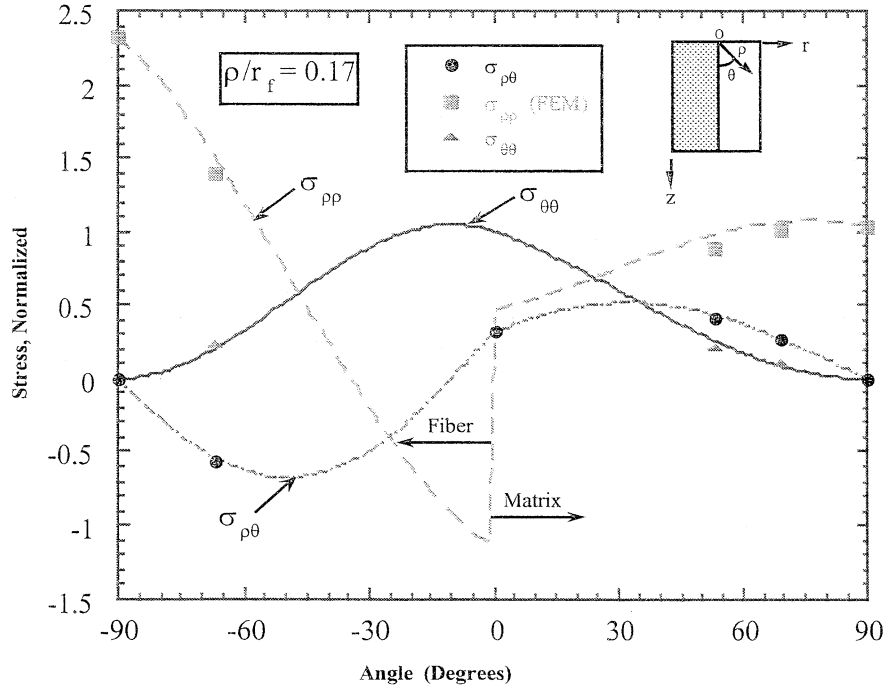


Fig. 3-5: Angular distribution matching of normalized stresses from finite element analysis with asymptotic solution

In Fig. 3-6, we compare the angular distribution of the normalized stress components from asymptotic analysis with the finite element solution (shown as solid symbols) at $\rho/r_f = 0.109$. As before, the stresses have been normalized such that the hoop stress $\sigma_{\theta\theta}$ is unity at the interface

(i.e., at $\theta = 0^\circ$).

At present, the available data from finite element solution is limited (We are in the process of generating a new solution with a much finer mesh which will give us the required angular distribution). Nevertheless, the comparison is reasonable as shown in Fig. 3-6 for the values reported. In order to evaluate the scaling constants K_1 and K_2 , we now match the hoop stress at the interface at two value of ρ/r_f , namely, 0.109 and 0.174, in a manner similar to the exposed fiber case and obtain $K_1 = 1.242$ and $K_2 = 0.065$. Thus,

$$\sigma_{ij}(\rho, \theta) = 1.242\rho^{-0.211} \Psi_{ij}^1(\theta) + 0.065\rho^{-0.321} \Psi_{ij}^2(\theta) \quad (6)$$

for the embedded fiber problem. Thus, the contribution of the term with the dominant singularity ($\lambda = -0.321$) is very small and the behavior is largely governed by the second asymptote, namely, $\lambda = -0.211$. Notice that the order of this singularity ($\lambda = -0.211$) is indeed smaller compared to the exposed fiber case ($\lambda = -0.278$) indicating that it is beneficial to embed the fiber in order to reduce the tendency towards interface failure from the fiber ends.

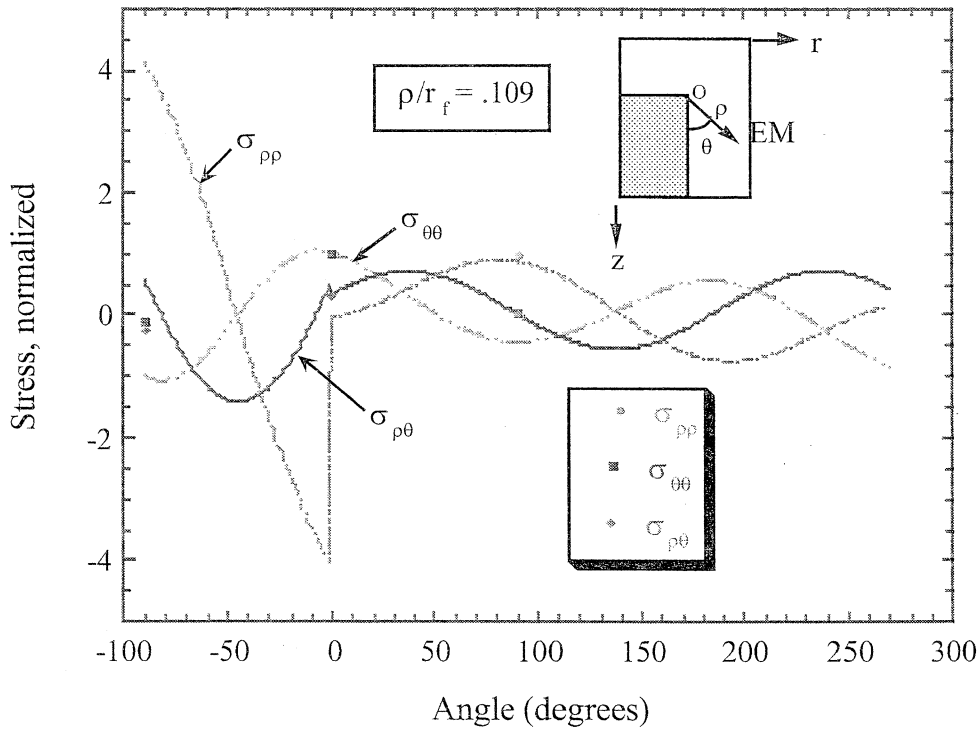


Fig. 3-6: Angular distribution matching of normalized stresses from finite element analysis with asymptotic solution

3.6 Estimation of Interfacial Strength and Characteristic Failure Dimension

In this study, we have successfully demonstrated that the cross-shaped design is successful in forcing debond initiation in the interior of the sample (region free of stress singularities). The tensile strength of the interface using the cruciform specimen results can therefore be estimated by multiplying the externally applied stress (2832 psi) with the stress concentration factor (1.2) at the interface and is calculated as 3398 psi (or 23.4 MPa). This value is significantly higher than the value of 1750 psi reported earlier (Tandon and Kim⁸) which was based on 2-D concentric cylinder model neglecting the end effects and size (specifically thickness) of the samples.

On the other hand, the singular stress profiles for the straight sided exposed-fiber and embedded fiber specimens indicate that there are two ways any useful data can be obtained from such specimens. As an extreme case, the singular stress profile can be used to imply that a crack already exists at the fiber ends at the interface, so that the maximum load in the tensile test simply reflects the attainment of criticality based on the fracture toughness of the interface. The problem with this approach is that it requires some method of determining the initial crack length. The alternate approach is to assume that the failure of the interface is governed by a probability distribution, whereby failure occurs when area integrated probability of failure reaches a critical value. Therefore, even though stress can become infinite over an infinitesimal distance, the probability of failure will remain finite, being determined by the integrated probability of failure. In this study, the focus here is to determine a characteristic distance for the exposed and embedded fiber specimens so that the apparent strength of the interface from those specimens is equal to that from the cruciform specimen.

Integrating Eq (3) for the exposed fiber case, the average hoop stress, $(\sigma_{\theta\theta})_{avg}$, at the interface over a normalized distance, ρ/r_f , is then given by

$$\frac{1}{r_f} \int \sigma_{\theta\theta} d\rho = \frac{\rho}{r_f} (\sigma_{\theta\theta})_{avg} = \frac{K}{(1-\lambda)} \left[\frac{\rho}{r_f} \right]^{(1-\lambda)}, \text{ at } \theta = 0^\circ \quad (7)$$

where we now identify ρ with the length of the fiber starting from the fiber end. Next, we plot in Fig. 3-7 the hoop stress distribution at the fiber-matrix interface in the neighborhood of the singularity from both the numerical solution and asymptotic analysis. Notice that the two

solution agree very well with each other up to $\rho/r_f = 0.17$ (point of matching) and beyond that the asymptotic solution diverges from the finite element solution. This behavior is not unexpected since the asymptotic solution is valid in a localized region only. To get the average stresses in the region which is located to the right of the point at which the two solutions were matched, we now fit the hoop stress distribution to a power law in the form

$$\sigma_{\theta\theta} = K_f \left[\frac{\rho}{r_f} \right]^{-\lambda_f}, \text{ at } \theta = 0^0 \quad (8)$$

For the exposed fiber problem, the quantities K_f and λ_f are calculated as 1.47 and 0.167, respectively, as shown in Fig. 3-7. Notice that Eq (8) is similar in form to Eq (3), and thus, the average stress under this part of the curve will be given by an expression similar to Eq (7).

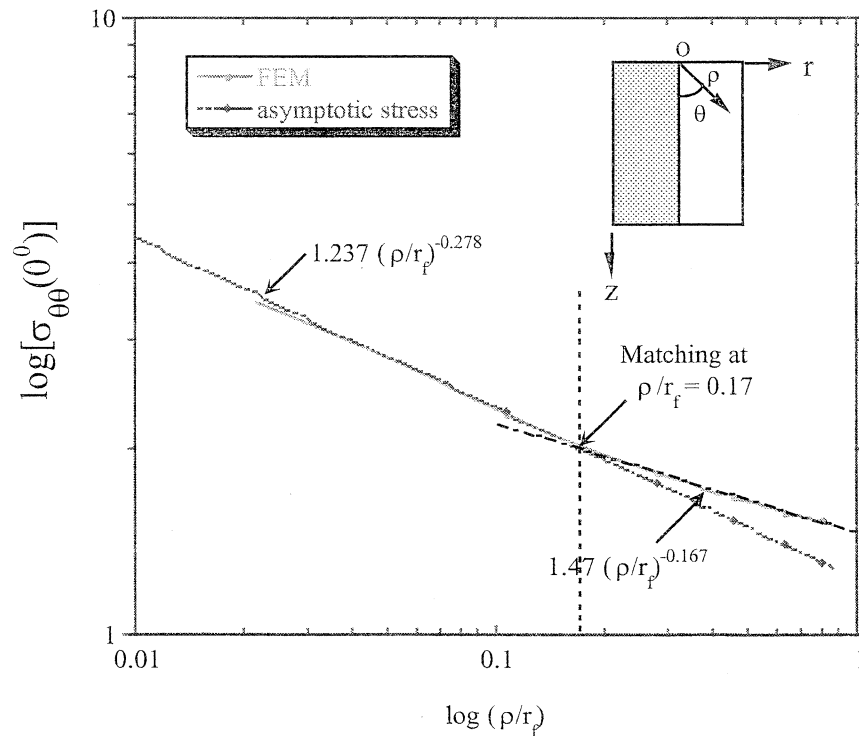


Fig. 3-7: Comparison of hoop stress from finite element analysis with asymptotic solution for straight sided specimen with fiber ends exposed

This procedure is repeated for the embedded fiber and the curve fit parameters K_f and λ_f for the FEM solution (valid beyond the point where the two solutions begin to diverge) were calculated as 1.452 and 0.148, respectively, as shown in Fig. 3-8.

In Table 3-2, we have listed the average stress values calculated over several normalized distances for straight-sided specimen in the two geometric configurations. The bond strength is then obtained by multiplying the externally applied stress level at which initiation took place with the average stress value at the interface.

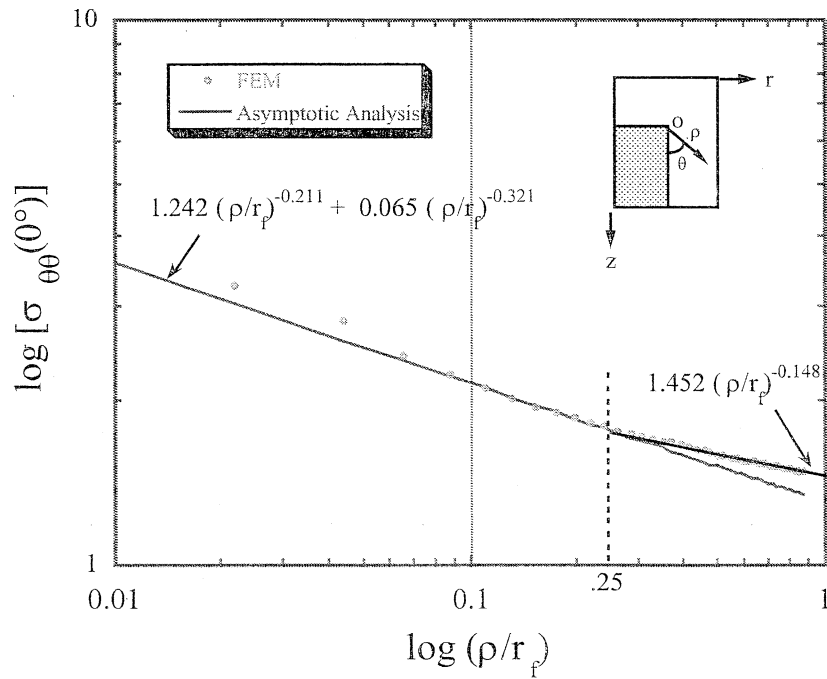


Fig. 3-8: Comparison of hoop stress from finite element analysis with asymptotic solution for straight sided specimen with fiber ends covered

Table 3-2: Predicted bond strength from straight-sided specimen

Distance	Straight-sided with fiber ends exposed		Straight-sided with fiber ends embedded	
$\left(\frac{\rho}{r_f}\right)$	$(\sigma_{\theta\theta})_{avg}$	Bond Strength*	$(\sigma_{\theta\theta})_{avg}$	Bond Strength ⁺
0.25	2.52	3042 Psi (21.0 MPa)	2.26	4036 Psi (27.8 MPa)
0.5	2.13	2571 Psi (17.7 MPa)	1.97	3523 Psi (24.3 MPa)
1.0	1.84	2221 Psi (15.3 MPa)	1.75	3120 Psi (21.5 MPa)

* Based on an average applied stress at debonding of 1207 psi

+ Based on an average applied stress at debonding of 1787 psi

As shown in Table 3-2, the stress concentration factor calculated at the exposed fiber end (for the three averaging distances considered) for straight-sided specimens are higher than the value of 1.45 used for earlier predictions⁸, which resulted in lower estimates of the bond strength of the interface. On the other hand, we have demonstrated that the cross-shaped design is successful in forcing debond initiation in the interior of the sample (region free of stress singularities) and therefore the results produced by testing of such specimens may be capable of providing the true transverse response of the fiber-matrix interface. Comparison of the interface strength value (3398 psi or 23.4 MPa) with the predicted strengths in Table 3-2 suggests that $0.5 < \rho/r_f < 1$ is a reasonably good distance over which stresses should be averaged to obtain an average strength of the interface that is representative of the material for straight-sided specimen with fiber ends embedded. However, for straight-sided specimen with fiber ends exposed, the predicted strength values are lower when averaged over the same distance. One of the possible causes for lower strength values is machining induced damage during specimen preparation prior to testing. For exposed fiber specimen, the radial stress at the interface peaks at the free edge whereas, for embedded specimen, it is at the fiber corner in the interior of the sample. These are precisely the locations where failure was found to initiate during testing of straight-sided specimen. Thus, surface damage induced during sample preparation will facilitate failure for exposed fiber specimen and will have negligible influence on specimen with fiber ends embedded.

3.7 Summary

Careful design and testing of model composites appears to be useful in estimating the normal strength of the fiber-matrix interface in unidirectional fiber composites. Two simple specimen geometries, namely, embedded fiber and cruciform design, have been considered to remove the influence of the free surfaces from tests on traditional straight-sided specimens. Results indicate good correlation between experiments and the analytical predictions and demonstrate the importance of stress field singularities in controlling damage initiation in straight-sided samples. It is further shown that only the cross-shaped design is successful in forcing debond initiation in the region free of stress singularities and therefore the results produced by testing of such specimens may be capable of providing the true transverse response of the fiber-matrix interface.

REFERENCES

- (1) Shoufeng, H., Karpur, P., Matikas, T. E., Shaw, L. & Pagano, N. J., Free Edge Effect on Residual Stresses and Debond of a Composite Fiber/Matrix Interface, *Mechanics of Composite Materials and Structures*, (1996)
- (2) Tandon, G. P., Kim, R. Y. & Dutton, R. E., Micromechanical Edge Effects in Glass Matrix Composites, presented at ASME IMECE, Atlanta, GA, Nov 17 - 22, 1996
- (3) Gundel, D. B., Majumdar, B. S. & Miracle, D. B., Evaluation of the Transverse Response of Fiber-Reinforced Composites Using a Cross-Shaped Sample Geometry, *Scripta Metallurgica et Materialia*, 33 (1995) pp 2057-2065.
- (4) Whitney, J. M. & Nuismer, R. J., Stress Fracture Criteria for Laminated Composites Containing Stress Concentrations, *Journal of Composite Materials*, 8 (1974) pp 253-265.
- (5) Tandon, G. P., Kim, R. Y., Warrier, S. G., and Majumdar, B. S., Influence of edge effects in estimating interfacial normal strength in model unidirectional composites, *Proc. Amer. Soc. Comp., 12th Tech. Conf.*, Dearborn, MI, Oct 6-9 (1997) pp 1176-1185
- (6) Bogy, D. B., Two edge bonded elastic wedges of different materials and wedge angles under surface tractions, *J. Appl. Mech.*, (1971) pp 377-386

- (7) Pochiraju, K. V., Lau, A. C. W. & Wang, A. S. D., A local-global matching method for the single fiber pullout problem with perfectly bonded interface, *Computational Mechanics*, 14 (1994) pp 84-99
- (8) Tandon, G. P. & Kim, R. Y., Test Methods for Estimation of Interfacial Normal Strength in Unidirectional Fiber Reinforced Composites, to appear in *Journal of Reinforced Plastics and Composites*, (1998)

4.0 INTERFACIAL NORMAL STRENGTH EVALUATION IN MODEL UNIDIRECTIONAL COMPOSITES

4.1 Introduction

Failure modes of fiber-reinforced composites are governed by the transfer of stress between the fiber and matrix. This transfer occurs across the interface between the constituents, and the properties of this interface, therefore, will affect the performance of the composite. The properties of the interface are, in turn, dependent upon the processing conditions employed. The literature on the characterization of interfaces in fiber-reinforced composites generally reveals a heavy emphasis on shear loading of the interface, wherein test methods such as the push-out test, the pull-out test, or the fragmentation test are widely employed. Although the shear characteristics are important under longitudinal loading, especially in polymer- and ceramic-matrix composites, there are a number of scenarios where the normal tensile strength of the interface can be more important. One of the most important cases is clearly when loading is applied perpendicular to the fiber axis, where a good fiber-matrix bond strength would significantly increase the transverse load-carrying capability of the composite. Further, under axial loading, Pagano [1] has shown that the tensile normal stress at the fiber/matrix interface plays a significant role in debonding the interface for a certain class of composites such as ceramic-matrix composites.

Unlike the interfacial shear strength, the measurement of interfacial normal strength has, to our knowledge, received only limited attention. A method that has often been used in the past to determine the interfacial normal strength has been to load a straight-sided specimen, with fiber

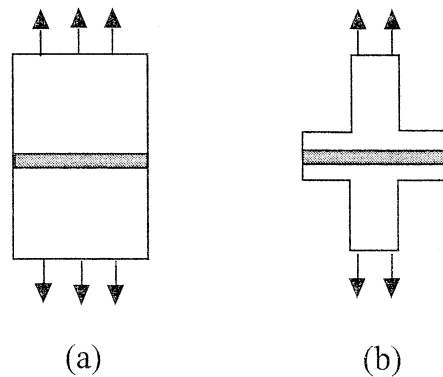


Fig. 4-1: Specimen geometry: (a) straight-sided specimen, and (b) cruciform specimen

In order to remove the influence of the free surfaces from the test, a cruciform specimen geometry was introduced by Gundel et al [3]. As shown in Fig. 4-1b, the model composite sample is in the shape of a cross with an extremely large width in the gage section. Under transverse loading, the central portion of the fiber/matrix interface is highly stressed, whereas the fiber has negligible loading in the arms/wings. Thus, interface debonding is forced to occur in the central region of the cross, so that the estimated bond strength is then free of edge effects. This is the major advantage of the cruciform geometry, as has been illustrated quite extensively in metal-matrix composites [3] and recently in polymer-matrix [4] and ceramic-matrix [5] composites. Alternately, a curved neck specimen [6] (with a reduced cross-sectional area) can be used to measure the tensile debonding strength of the interface when subjected to compressive loading. Similar to cruciform geometry, failure initiates at the center of the curved neck specimen where the stress is a maximum.

4.2 Experiment

In this work, model single fiber composite specimens were cast in a cruciform-shaped silicone rubber mold. Five different model composites were studied. The composite reinforcement consisted of glass, silicon carbide and graphite fibers, while the matrix was an epoxy resin (Epon 828 from Shell Chemical Co.) cured with a polyetheramine (Jeffamine D-230 from Texaco, Inc.) for 3 days at ambient temperature. Curing at ambient temperature eliminated thermal residual stresses which are otherwise induced from the mismatch in coefficients of thermal expansion of fiber and matrix. The optical glass fiber was obtained from Polymicron Technologies Inc. and has an inner core 125 μm in diameter and an outer polyimide layer 5 μm thick. In this work, two different silicon carbide fibers were utilized. The 140 μm diameter SiC fiber (SCS-0 from Textron) was chosen primarily because of its large size in order to establish the various test techniques utilized for detecting debond initiation. On the other hand, the smaller diameter (15 μm) SiC fiber (Nicalon) was utilized for initial testing on textile sized fibers. Finally, AS4 (Hexcel) 7 μm diameter, surface treated and sized graphite fibers and AU4 (Hexcel) graphite fibers with no surface treatment or sizing were incorporated into cruciform samples to test the interface strength in graphite epoxy specimens. The Glass, SCS-0 and Nicalon fibers were simply cleaned with acetone, positioned in the mold and then epoxy resin was cast around them. These fibers had sufficient bending stiffness to support their weight across the mold span.

However, extra care was necessary when making the graphite fiber samples to insure that the fiber was centered through the thickness of the sample. Tension was applied to the graphite fibers to prevent sagging in the mold. A schematic of the method of inserting the graphite fiber is shown in Fig. 4-2. The fiber was separated from the fiber tow without touching or cleaning the portion to be placed in the mold. Not altering the fiber surface was necessary to preserve the functionality of the sizing and to simulate actual processing of graphite/epoxy composites. Next, the fiber was tacked with wax to a lightweight cardboard “U” shape with a span greater than 2l. The U shaped fiber holder was placed on the mold, as indicated in Fig. 4-2, such that the weight of the cardboard arms placed sufficient tension on the fiber to prevent sagging without breaking the fiber. The fiber was then tacked to the rubber mold with wax, the fiber ends snipped, and the cardboard removed.

The two flat surfaces of Glass and SCS-0 specimens were progressively ground to the desired thickness, approximately 0.9 mm, while Nicalon, AS4 and AU4 samples were ground to approximately 0.5 mm. The surfaces of all samples were then polished using successively smaller diameter alumina polishing powder (final size was 0.3 micrometer) in order to enhance the microscopic image for interfacial debond detection. In order to prevent specimen failure in the grip region, fiber-glass/epoxy end tabs were adhesively bonded on the upright portion of the specimen.

The smaller fiber diameter cruciform samples, namely, Nicalon, AS4 and AU4 samples, were

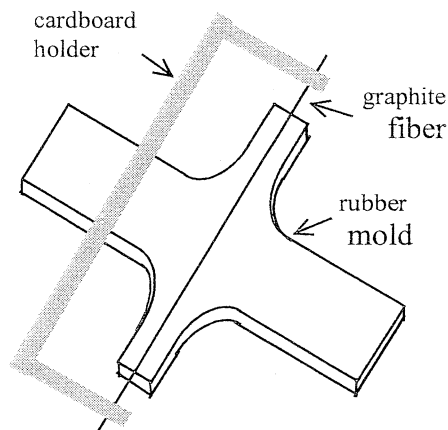


Fig. 4-2: Graphite fiber placement in rubber mold

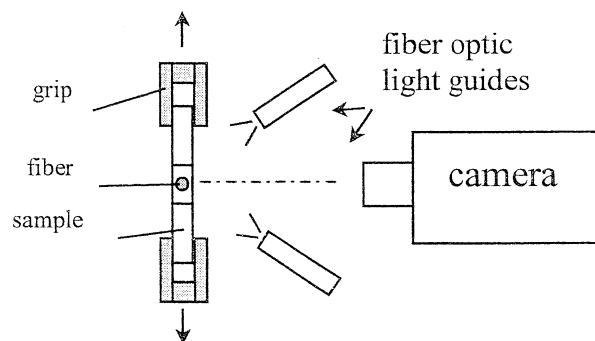


Fig. 4-3: Sample illumination

loaded using a load-frame consisting of a microstepping motor and a square rail, lead screw driven positioner. Grip velocity was maintained at 2.5 $\mu\text{m}/\text{second}$. Load was measured by sampling a piezoelectric charge transducer at 2 samples/second. The load cell signal was conditioned with a dual mode amplifier and digitized with a 16-bit A/D converter. Initiation and growth of interface debonds was detected optically by observation of variations in the intensity of light reflected from the surface of the fiber during loading. A 768H x 494V, 1/3" chip CCD camera and VCR were used to capture a video of the fiber surface at 30 frames/second. The sample was illuminated from the camera side as shown in Fig. 4-3. Two fiber optic light guides were placed at an angle to the line connecting the camera and the fiber, and the intensity of the illumination was adjusted to just below the level necessary to produce a slight shine on the fiber surface. The recorded applied loads and video images were then correlated to within ± 0.03 seconds which corresponds to $\pm 0.08 \mu\text{m}$ of applied displacement.

After completion of the test, a video capture card with accompanying software was used to select frames from the video tape record. It was possible to determine if the fiber had debonded, what portion had debonded, and to make a measurement of the debond length to within ± 0.1 fiber diameters. The resolution is reported in fiber diameters since the resolution depends on the magnification used during imaging. The magnification was adjusted to a level great enough to allow debond length to be determined accurately while being low enough to maintain the maximum field of view. The tradeoff between field of view and magnification was necessary for the best opportunity of capturing the initiation of debonding since the entire gage length could not be imaged at once.

For the larger diameter fiber specimens, namely, Glass and SCS-0 samples, strain gauges (gauge length 3.2 mm) were mounted on the flat surface of the matrix directly over the fiber and at various positions along the length of the fiber. An acoustic emission transducer was also attached to these specimen to monitor failure events. The transducer has an operating frequency range of 400 to 1000 KHz with peak sensitivity of 55 dB for the reference input of 1 V/(m/s). A polarized microscope was also employed to observe the onset and propagation of microcracks, in the form of interfacial debonding, due to applied load in some Glass and SCS-0 specimens. Fig. 4-4 shows a miniature load frame which has a capacity of 9,000 N with a resolution of 4.5 N.

Uniaxial tensile loading was applied to the specimen using this miniature loading device (hereafter referred to as straining stage) which was designed and built for *in situ* observation of damage in composite laminates. Axial force was generated by pulling the piston using nitrogen gas pressure. The straining stage is designed to be able to be mounted on the microscope stage for observation of microcracking or interfacial debond under loading. The specimen was mounted on the straining stage and loaded to the level which is slightly lower than the first expected debond level. Thereafter the specimen was loaded in increments of 9 N until final failure. At the end of each load increment, the load was held constant during which the entire

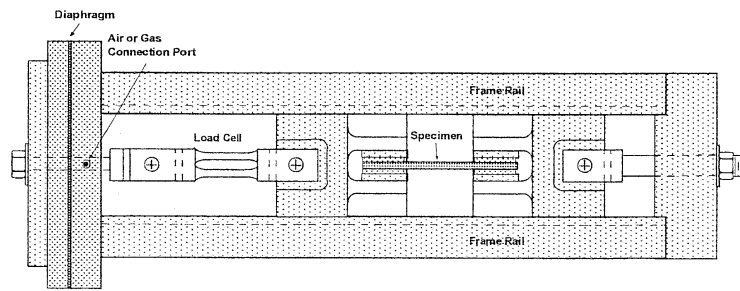


Fig. 4-4: Portable load frame

interface was microscopically examined for debonding, and the ensuing fringe pattern captured using a polaroid instant camera as well as a 35-mm camera. We have not made any effort to quantify the fringe patterns. Rather, the emphasis was to identify the location of stress intensification where failure would initiate and the stress level at which the fringes first develop in the specimen.

The large fiber diameter specimens (Glass and SCS-0 fibers) were also loaded to failure in an MTS machine while strain and acoustic emission activity were continuously monitored. The samples were initially loaded to either a prescribed level slightly higher than the expected interface debonding level or up to the first occurrence of acoustic emission on the stress strain curve. This load was then taken to failure in small increments and the fractured specimen examined to identify the locus of failure.

4.3 Analytical Modeling

The single fiber-cruciform specimen were analyzed using 3-D finite element analysis employing the ABAQUS code [7]. The specimen dimensions along with the notation that we

have used in this work are shown in Fig. 4-5. Note that the specimen thickness is indicated by " t " whereas the wing height is denoted by " $2h$ ". The models were simplified by using symmetry planes so that an eighth of the total specimen was required to be modeled. The planes of symmetry were constrained by symmetry boundary conditions, whereas the outer surfaces were reaction free. Due to the large number of elements that were anticipated (because of 3-D

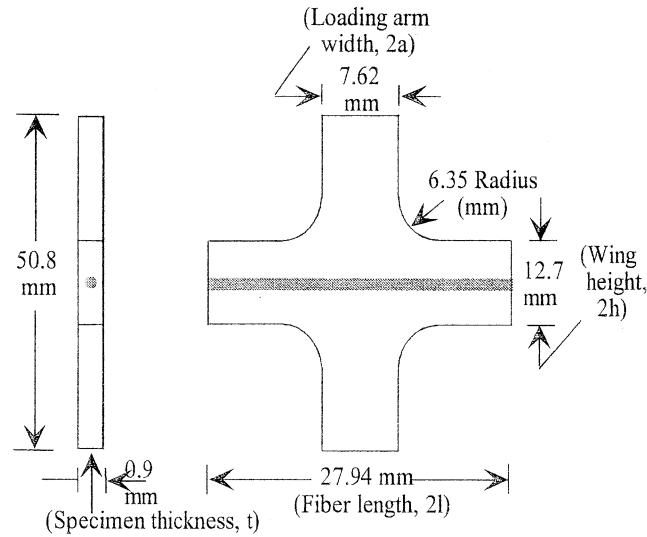


Fig. 4-5: Schematic of cruciform sample showing specimen dimensions and nomenclature

modeling), meshes were generated such that computational efficiency would be maintained without sacrificing accuracy. Finer subdivisions were employed in the regions where the stress gradient was expected to be high, such as along the fiber-matrix interface.

The FE model was loaded by applying tension perpendicular to the fiber axis by means of constant displacement of the end nodes to simulate clamped-end conditions. Both the matrix and the reinforcements were treated as three-dimensional eight-node brick elements. The epoxy matrix and Glass and SiC fibers were considered to be isotropic while graphite fibers were considered as transversely isotropic with the following elastic properties:

In Table 4-1 the subscripts A and T stand for axial and transverse, respectively. In these samples thermally-induced stresses were not anticipated, since curing was done at room

temperature¹, and therefore were not considered in the analysis. Further, the fiber matrix interface was assumed to be perfectly bonded since we wanted to examine the stress distribution in the sample prior to damage.

Table 4-1. Elastic properties of constituents

Constituents	E, Gpa	v			
Glass	65	0.25			
SCS-0	400	0.15			
Nicalon	200	0.20			
Epoxy	3.44	0.35			
Constituent	E _A , GPa	E _T , GPa	v _{AT}	v _{TT}	G _{AT} , GPa
Graphite	235	14	0.2	0.25	28

4.4 Results and Discussion

4.4.1 Glass/Epoxy Composite

Figure 4-6 shows the stress-strain curves obtained from strain gages mounted on the surface of the cruciform specimen at different distances from the central loading plane along the length of the fiber. The strain gage locations are shown in the inset in Fig. 4-6.

For the cruciform specimen, the far-field stress is equated to $P/(w_1 t)$, where P is the applied load, w_1 is the width of the loading arm and t is the specimen thickness. The measured strain values indicate that the central portion of the fiber/matrix interface is highly stressed under tensile loading, whereas the fiber is nearly unloaded in the arms/wings. This is reflected in the lower strain values recorded by strain gage 1 located near the fiber end as opposed to the remaining gages 2-4. Moreover, the strain values are nearly uniform in the center over two-thirds of the loading region (as indicated by gages 3 and 4) before they decrease with distance

¹ Chemical shrinkage in room temperature cured epoxies can be significant [8]. However, shrinkage induced strains were neglected in this study since no data was available for Epon 828 cured with polyetheramine. A value of .0022 was measured by Bechel and Sottos [8] for Epon 828 cured with diethylenetriamine (DETA). Using this value of shrinkage strain for the present system results in compressive interfacial radial stress of approximately 7 MPa which, in turn, reduces the reported interface strength by approximately 18 % for SCS-0 fiber composites.

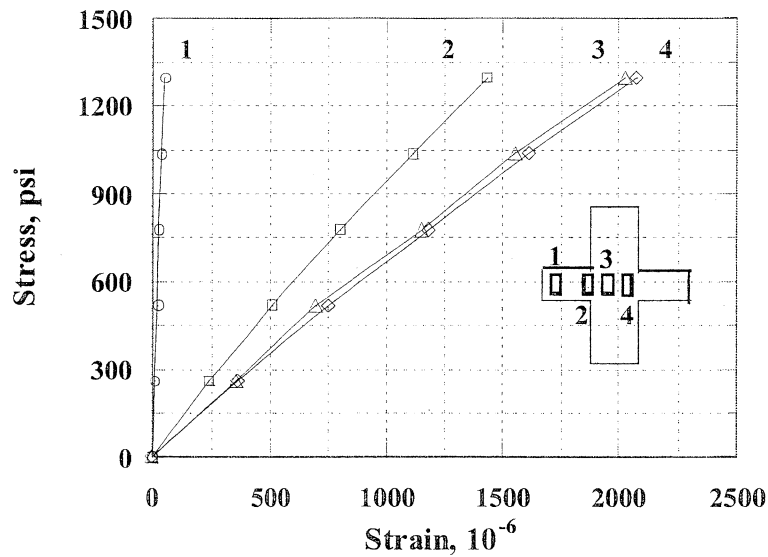


Fig. 4-6: Stress-strain curves at various locations along the fiber length

measured from the central loading plane. Further, small fillets which were provided at the junctions of the cross help in reducing the stress concentration in the matrix at these locations. This is evidenced by the lower strain measurement at gage 2 compared to gages 3 and 4 which are mounted in the central region.

Figure 4-7 is a photomicrograph of the fractured halves of two different cruciform specimens clearly indicating that failure occurred mostly in the interface. However, for some specimens without end tabs, failure occurred at the grip in the rectangular section.

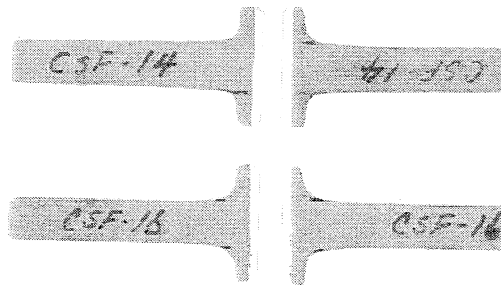


Fig. 4-7: Photograph showing failed specimens

In order to identify the failure modes under transverse loading, fracture surface analysis was next conducted using scanning electron microscopy (SEM). 4-8 shows a typical SEM photomicrograph of the fracture surface in the central region of the specimen. The fracture surface appears to be relatively smooth which is indicative of failure occurring due to radial normal stress alone. On the other hand, a rough (or hackle-like appearance) of the fracture surfaces would have been indicative of mixed-mode failure (i.e., failure due to radial normal stress in conjunction with shear stress).

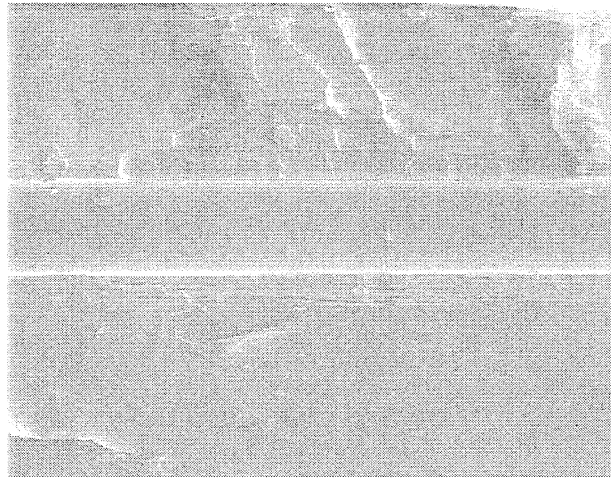
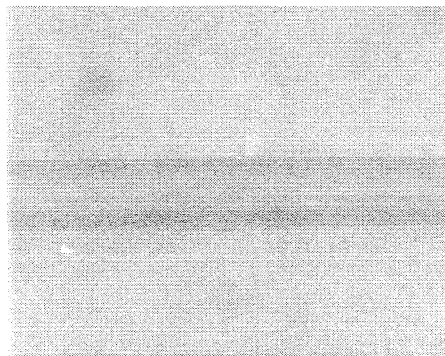
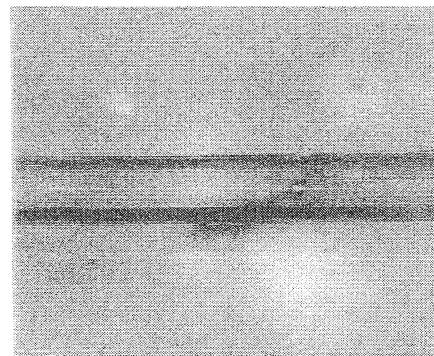


Fig. 4-8: SEM photomicrograph showing the fracture surface

We also made an attempt to identify the location of stress intensification along the fiber/matrix interface where debonding would initiate. Figure 4-9 shows the development of photoelastic fringe patterns in the central region of the cruciform specimen at two selected stress



(a) 26.1 MPa



(b) 32.7 MPa

Fig. 4-9: Photomicrographs showing photoelastic fringes for the applied stresses

levels. The first appearance of photoelastic fringe occurred at the applied stress of 26.1 MPa and was confined to a very small area. This small fringe grew in intensity with increasing load, as shown at a stress level of 32.7 MPa in Fig. 4-9(b), until failure which occurred at 36 MPa.

Figure 4-10 is a photomicrograph of the same specimen taken after failure and clearly shows that the fiber was separated from the matrix. Thus, under transverse loading, interface debonding was the dominant failure mode for single-fiber glass/epoxy cruciform specimens.

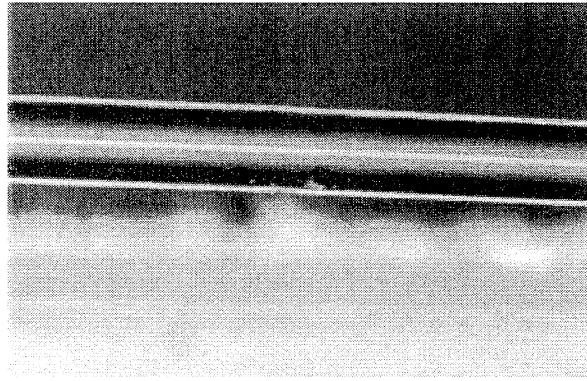


Fig. 4-10: Photomicrograph showing fiber-matrix separation after failure

4.4.2 SCS-0/Epoxy Composite

4.4.2.1 Interface Strength Measurement

Figure 4-11 shows the variation of the non-zero stress components in the matrix at the fiber matrix interface in the loading direction (i.e., $\theta = 0^\circ$) as a function of distance from the center of the cruciform specimen. These stress components have been normalized with respect to the far-field applied stress (σ_a), and thus represent the stress concentration factor (SCF), while the distance is normalized with respect to the fiber length, l .

As seen in this figure, the radial stress at the interface is the dominant stress component and remains reasonably constant (within 10 percent) over two-thirds of the loading region. The lower value (i.e., 0.9) of radial SCF at the specimen center compared with far field unit value is a result of some load shedding into the specimen wings because of their relatively large thickness, h . As a consequence, the gradients in the stress profiles shown in Fig. 4-11 across the width, a , of the loading arm are less severe compared to our observations in our earlier study on Al/epoxy system [9]. In a later section, we will demonstrate the effect of varying the width ($2a$) of the loading arm

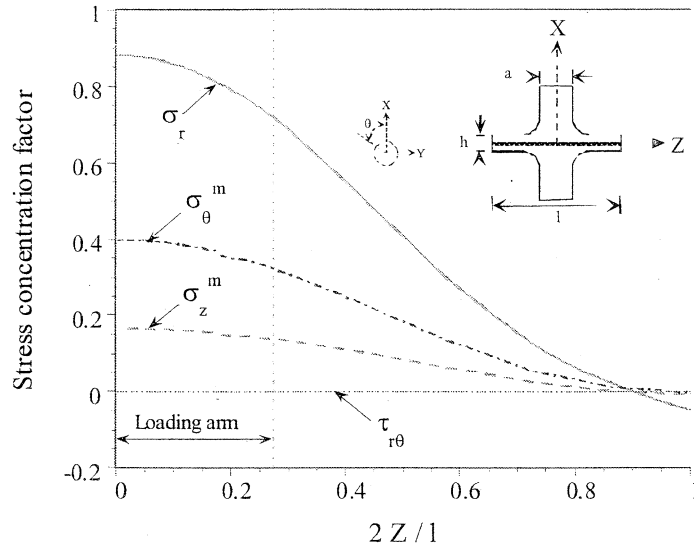


Fig. 4-11: Axial variation of interfacial stresses in the matrix

and the height ($2h$) of the wings on the radial SCF. More importantly, the present analysis does show that the radial SCF approaches zero value in the wings before increasing marginally near the free surface indicating the existence of a stress singularity at the fiber end, although the singularity is ineffective for the present geometry. Consequently, interface debonding always occurs in the central ‘gage’ section in this specimen where the radial SCF is a maximum, thus avoiding the influence of end effects on measured debond strengths. This was verified experimentally since no debonding was observed before or after loading near the free edges in the samples tested. Analytical modeling of the present geometry further indicates that the radial stress concentration factor is maximum in the loading direction, i.e., at $\theta = 0^\circ$, and that is where debonding is likely to initiate. Further, there is stress concentration in the matrix region near the fillet area. Thus, under loading applied transverse to the fiber axis, failure of the specimen is also likely to take place near the fillet region. We will demonstrate in next sub-section how this failure behavior can be modified by changing the width of the loading arm and the height of the wings.

Figure 4-12 shows the photoelastic fringe patterns in the central region of a specimen which was mounted on the straining stage of the polarized microscope and was incrementally loaded in tension to failure. The first appearance of photoelastic fringes occurred at the applied stress of

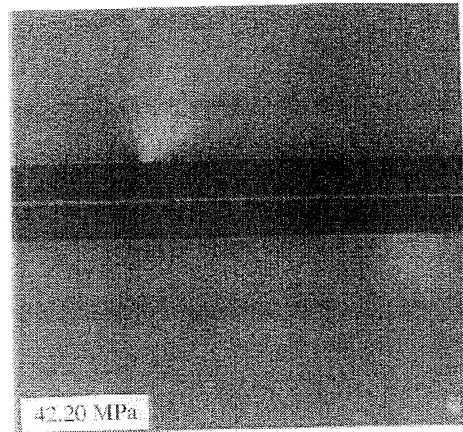
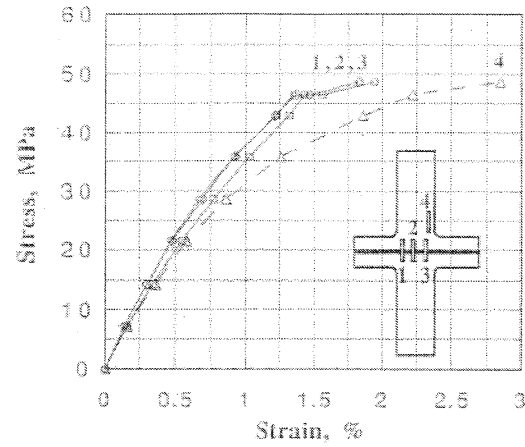


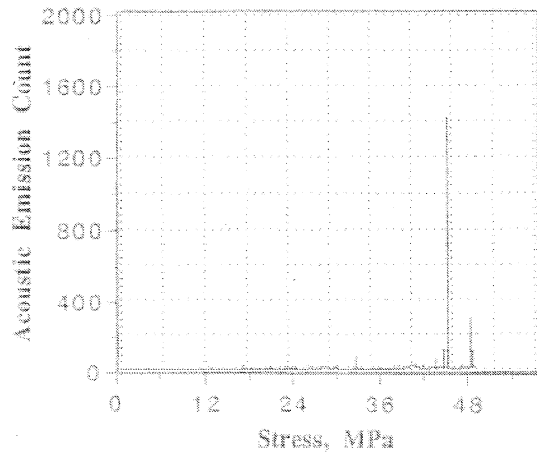
Fig. 4-12. Photomicrographs showing photoelastic fringes for the applied stresses

42.2 Mpa and was confined to three different regions along the specimen length. The first zone is a very small area near the fiber-matrix interface over the top of the fiber while the second zone is comparatively larger in size and is below the fiber surface, as seen in the micrographs in Fig. 4-12. The third zone is symmetric about the position marker with respect to zone one and is located to the right of the marker on the top of the fiber surface (but is not within the field of view of the micrographs shown). It is speculated that the first and the third zones on the top of the fiber surface are the two ends of the interfacial debond crack which has grown along the fiber length and circumference and is connected to zone 2. Using 2-D variational analysis, it has been shown in a previous study [10] with steel rods in epoxy matrix that the initial debond (caused by σ_r) propagates only along a *portion* of the cross-sectional interface and then branches into the matrix. The photomicrograph in Fig. 4-12 was taken in the loading plane and if the debond is wrapped partially around the fiber circumference, the photoelastic fringes will not indicate a well defined crack tip but will indicate just an area of higher stress. The second zone visible in the micrograph in Fig. 4-12 therefore represents the partially debonded interface in the cross-sectional plane. With an increase in the external stress level, the debond propagates axially along the interface. The external stress level at which the crack-tip fringes first appear is interpreted to be the applied stress level at debond initiation.

The model specimens are also loaded to failure in an MTS machine while strain and acoustic emission activity are continuously monitored. Figs. 4-13 (a) and 4-13(b) are a plot of the applied



(a)



(b)

Fig.4-13: (a) Applied stress - local strain plot, and (b) Acoustic emission count respectively, for SCS-0/Epoxy composite

stress – local strain response and the acoustic emission count, respectively, for SCS-0/Epoxy specimen. On this sample, multiple strain gages are utilized to monitor strain at different locations in conjunction with an acoustic emission transducer attached at the center of the specimen to detect initiation of debonding. The strain gage locations are shown in the inset in Fig. 4-13 (a).

The first evidence of acoustic emission activity occurs at a stress level of 45.1 Mpa which is seen to coincide with the strain jump in response of all three gages, 1-3, placed in the center of the specimen. This far-field stress level at the first occurrence of acoustic emission activity and/or strain jump is referred as the initial debonding stress. Moreover, the strain values are

nearly uniform in the central region as shown by gages 1-3. However, gage 4 which is located in the matrix near the fillet region records a much larger strain value relative to the remaining three gages. This signifies that there is a region of stress/strain concentration near the fillet area and is in agreement with the analytical stress predictions.

In Table 4-2, we have now listed the applied stress level at debond initiation obtained either from first occurrence of acoustic emission or strain jump in the stress-strain curve for several different cruciform samples tested on a MTS machine. As shown in Figs 13 (a) and (b), the “jump” in the stress-strain curve invariably coincides with the first occurrence of acoustic emission activity for samples on which both surface strain and acoustic emission activity measurements are conducted.

Table 4-2. Experimental data from transverse testing of SCS-0/Epoxy composite

Specimen #	Applied Stress at Debonding (Mpa)		Ultimate Failure stress (Mpa)
	Strain jump	Acoustic emission	
1	47.4	-	52.7
2	-	40.6	50.7
3	36.8	36.8	46.3
4	-	40.7	41.6
5	37.9	37.9	37.9
6	47.3	-	54.6
7	45.1	45.1	48.7

Mean Value	42.9	40.2	47.5
Std Deviation	5.2	3.2	6.0

The mean value of the external stress at which debonding initiates in samples tested on a MTS machine is calculated as 42.9 Mpa and 40.2 Mpa using indicators from strain and AE measurements, respectively. Notice that these mean values of the debond stress are in good

agreement with the stress level at which photoelastic fringes first appear in a specimen which was tested on the straining stage of a polarized microscope.

Figure 4-14 is a photomicrograph of the failed cruciform specimens indicating that ultimate failure occurs in the fillet region which is in accordance with the analytical predictions. However, for some specimens without end tabs, failure occurs at the grip in the rectangular section. Nevertheless, what is interesting to note in Fig. 4-14 is the white line in the central region of the two cruciform samples in between the strain gages. This picture was taken with the failed samples illuminated by a light source from behind and the white line that we are seeing in these images is the light which is passing through the debonded fiber-matrix interface. This micrograph is therefore a visual confirmation of fiber-matrix debonding which takes place in a cruciform specimen and the length of the illuminated region is a measurement of the extent of debonding.

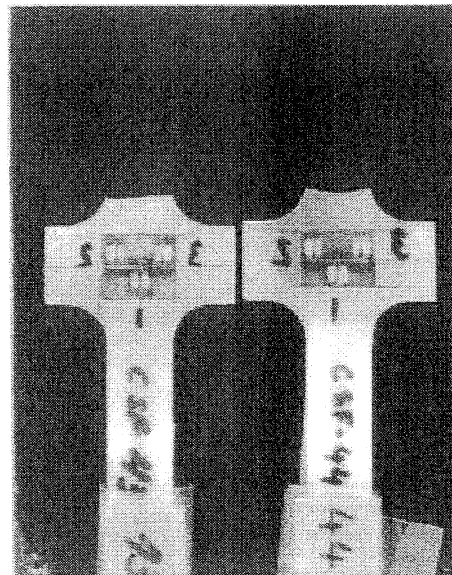


Fig. 4-14: Photograph showing failed specimens

Next, we made a section of the failed specimen in the region where we had visually observed debonding and examined the cross-section under Scanning Electron Microscope (SEM). It was observed [11] that the fiber has clearly separated from the matrix in the region which is very close to the loading direction whereas the portion of the interface, which is perpendicular to the loading direction, remains bonded. Thus, under transverse loading, debonding does not take

place over the entire circumference, but only over some portion of the interface interface and supports our hypothesis from the photoelastic fringes observed on the straining stage. As a consequence, the fiber remains attached to the matrix when the specimen fails.

The tensile strength of the interface is determined by multiplying the average value of externally applied stress at debond initiation (obtained using indicators from photoelastic, strain and AE measurements) with the radial stress concentration factor at the interface and is calculated as 36.7 Mpa. This estimated value of bond strength is independent of edge effects since we have shown that interface debonding always initiates in the central region of the cross away from fiber ends. This middle region is free of initial stress singularities and therefore the results produced by testing of these specimens are capable of providing the true transverse response of the fiber-matrix interface.

4.4.2.2. Parametric Study

While discussing the results presented in Fig. 4-11, we had noted that the radial SCF at the specimen center was lower than unity as a consequence of load shedding into the specimen wings because of their relatively large height. We had also mentioned that FEM modeling had revealed a region of large stress concentration near the circular fillet where the specimen failed. To modify the failure behavior observed using the present cruciform geometry, a parametric study was conducted in which we changed[@] the width of the loading arm (2 a) and the height of the specimen wings (2 h).

Figure 4-15 examines the effect of varying the loading arm width on the radial stress component in the loading direction, while the height of the wings remains unchanged. Note that the loading arm half-width normalized by fiber half-length is indicated as a short vertical dash-line on each one of the curves and should not be interpreted as a jump in the SCF value at that location. It is found that the radial SCF increases with an increase in the width of the loading arm and in the limit we approach the results of straight-sided geometry where failure is dominated by the free edge effects [9]. Therefore, while the stress concentration at the interface in the central region of the specimen can be significantly increased from its present value of 0.867 by increasing the width of the loading arm, there is an optimum width value beyond which stresses

evaluated at the fiber end become more dominant in the cruciform geometry. Thus, further increase of the width of the loading arm (or shortening of the length of the wings) will become counter-productive.

Figures 4-16(a), (b) and (c), are plots of the radial SCF in the loading direction along the fiber length for loading arm half-widths of 3.8 mm, 7.4 mm and 11.2 mm, respectively, while the wing height is allowed to vary. It is noted that the stress concentration at the interface increases as the height of the wings is decreased. Further, the increase in SCF is larger at smaller values of arm widths and the increment in SCF is reduced as the loading arm width increases. Thus, for $a = 7.4$ mm and 11.2 mm, there is only a marginal increase in the SCF even though the specimen half-height is reduced by one-half from 1.72 mm to 0.86 mm. Therefore, no additional advantage is obtained by further reducing the specimen height beyond a certain value. This observation is important because it becomes increasingly difficult to fabricate and handle the cruciform specimen with decreasing wing height.

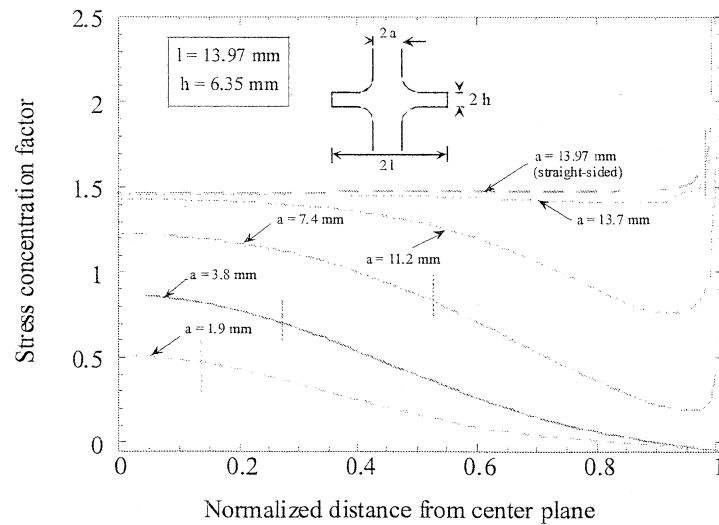
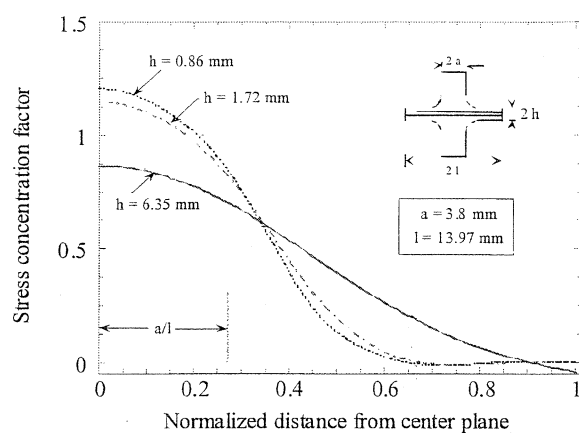
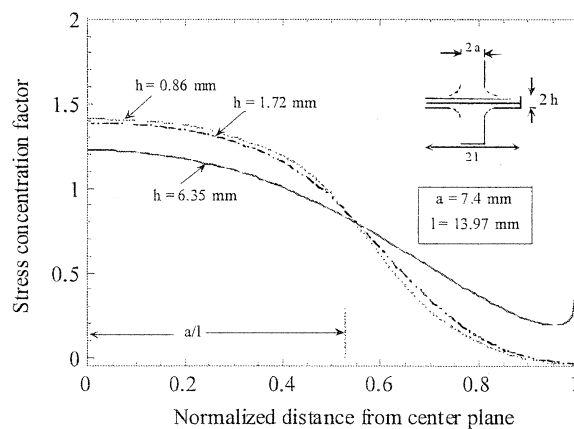


Fig. 4-15: Effect of loading arm width on the radial stress concentration factor

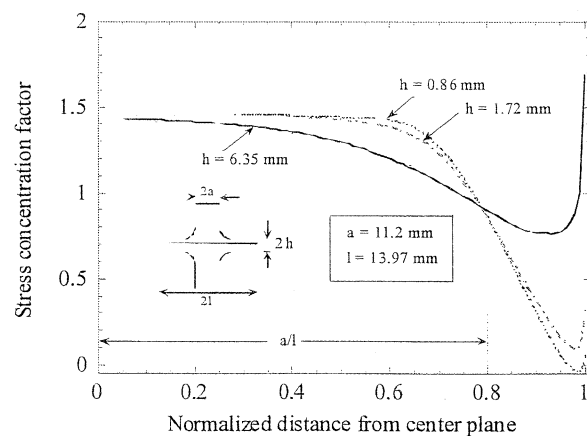
@ The fillet radius of curvature was changed from 6.35 mm to 2.54 mm and .13 mm, respectively, for loading arm half-widths of 11.2 mm and 13.7 mm. This was necessary in order to maintain a circular fillet for conducting numerical analysis.



(a)



(b)



(c)

Figure 4-16. Effect of wing height on the radial stress concentration factor for loading arm half-width equals (a) 3.8 mm, (b) 7.4 mm and (c) 11.2 mm

Table 4-3 summarizes the results of the parametric study for the maximum value of the stress component σ_{xx} in the loading direction at the fiber-matrix interface and in the fillet region, for a unit applied stress. For the geometry discussed in Table 4-3, the maximum value of interfacial stress occurs at the central plane of the specimen, while in the fillet region, σ_{xx} is maximum in the region at which the circular fillet merges into the straight section of the cruciform wing parallel to the loading direction. Recall that the present test geometry is given by $h = 6.35$ mm and $a = 3.8$ mm while the fillet radius of curvature is 6.35 mm.

Table 4-3. Maximum value of stress component σ_{xx} at fiber-matrix interface and in the fillet region, for unit applied stress and varying cruciform geometry

h (mm)	a (mm)	Stress at fiber-matrix interface	Stress in matrix in fillet region
6.35	1.9	0.508	1.138
	3.8*	0.867	1.283
	7.4	1.227	1.428
1.72	1.9	0.776	1.145
	3.8	1.149	1.278
	7.4**	1.387	1.362
0.86	1.9	0.848	1.147
	3.8	1.208	1.272
	7.4	1.409	1.339

* Original specimen geometry tested

** Optimized specimen geometry

As discussed in Figs. 4-15 and 4-16, the maximum value of the interfacial radial stress increases with an increase in the width of the loading arm and a decrease in the wing height. On the other hand, the maximum value of fillet stress is found to increase slightly with width of the loading arm while it decreases slightly with decrease in wing height at the larger value of loading arm width. As the half-width of the loading arm increases from its present value of 3.8 mm to 7.4 mm, and the wing half-height reduced from 6.35 mm to 1.72 mm, the SCF at the interface changes from 0.867 to 1.387 while the fillet stress changes from 1.283 to 1.362. Thus, by modifying the cruciform geometry, there is a significant increase in the radial SCF at the

interface, while there is only a marginal increase in the fillet stress. More importantly, the radial stress at the interface now becomes larger than the fillet stress, albeit by a small amount. These changes have a significant implication, namely, debonding will now initiate at the interface at a lower value of externally applied stress which, in turn, reduces the likelihood of failure in the fillet region. Consequently, interfacial failure will now be promoted by optimizing the cruciform geometry. This is a very simplistic interpretation of the stress field behavior. It is clear that in the fillet area, the stress distribution is influenced by the free edges, whereas, in the interior near the interface, a triaxial stress distribution exists. Nevertheless, the trends shown in Figs. 4-15, 4-16 and in Table 4-3 suggest that the new configuration given by $a = 7.4$ mm and $h = 1.72$ mm, is very close to the optimum geometry for SCS-0/epoxy system. By definition, the cruciform design which results in the largest value of interfacial radial stress in the interior of the specimen and thereby promotes interfacial failure without invoking free edge effects is considered as optimum. Moreover, these new dimensions satisfy the constraints imposed by the fabrication procedures and test methods.

To verify that the optimized geometry for SCS-0/Epoxy system would perform better, a cruciform specimen was made using the new geometric parameters and loaded to failure in an MTS machine. Figure 4-17 is the photograph of the failed specimen and clearly shows fiber-matrix debonding in the central region. The debond is seen to propagate along the fiber in the loading arm region and then runs parallel to the interface in the matrix. Eventually, the crack



Fig. 4-17: Photograph of the failed cruciform sample (optimized specimen geometry)

front bows away from the interface near the fiber end. Note that even at failure the fiber ends remain in contact with the matrix. Thus, in this new cruciform design, free edge effects are not large enough to cause failure at the fiber ends while interfacial failure is promoted, as predicted by FE analysis. For this particular sample, first occurrence of acoustic emission activity takes place at a stress level of 29.8 MPa, which in conjunction with the calculated radial SCF of 1.387, results in a debond strength of 41.3 MPa. This value is in reasonably good agreement with the average value of the predicted bond strength of 36.7 MPa using the older geometry. The fracture surface of the specimen shown in Fig. 4-17 in the central region was also examined under SEM. The inspection reveals a smooth fiber surface which is consistent with our earlier assumption that the radial stress at the interface is responsible for debond initiation. This new cruciform design, therefore, provides valid interface strength which is truly independent of edge effects.

4.4.2.3 Debond Length Measurement

The optimized cruciform geometry discussed in the previous section was utilized to make additional specimens using SCS-0 fibers for debond length measurements [12]. Initiation and growth of interface debonds was detected optically by observation of variations in the intensity of light reflected from the surface of the fiber during loading. Images showing debond initiation and debond growth from a representative test are shown in Fig. 4-18. The fiber in image (a) is black except for an area marked “debond” approximately 3.5 fiber diameters long on the bottom half of the fiber which reflects light with a greater intensity. The load increases from 193 N in image (a) to 252 N in image (d) while the debond grows over 3 mm. Surface defects in images (b), (c), and (d) can be used as position markers to compare the changing debond length.

At a higher magnification additional information can be obtained from the debonding images. For example, it is apparent from Fig. 4-19 that the crack front is not straight and perpendicular to the fiber axis but has a more complicated curved shape that extends further in the axial direction on the bottom of the fiber. As stated earlier, the illumination is set at an intensity such that before loading, the fiber surface is on the verge of being shiny. This lighting produces a bright area along the approximate centerline of the fiber that is present throughout the test. The reflective centerline area is not to be confused with the debond. As illustrated in Fig. 4-19, the height of the crack wake can be measured and used to infer the angle, α , that the debond wraps around the

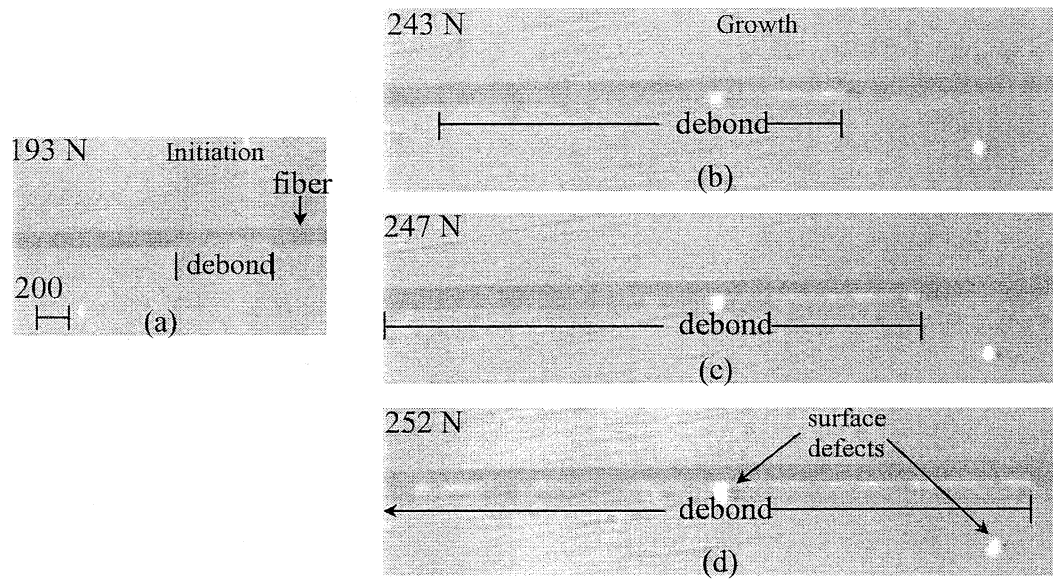


Fig. 4-18: Images of debonding in SCS-0/epoxy

fiber. On average, the value of α for SCS-0/epoxy was measured as 157.4° assuming a symmetric debond. Finally, the maximum load at which the sample completely fails can be assumed to be the load at which the debond exits the interface. From the applied load at final failure and the analytical modeling, the stress field in the sample can be determined, and the debond length and shape are known from the photomicrographs. Thus, all the required parameters are known to establish a criteria for the debond kinking out of the interface, which will be the topic of a follow on study.

4.4.3 Nicalon/Epoxy Composite

Nicalon/epoxy samples were also cruciform tested as a first attempt at testing fibers with a

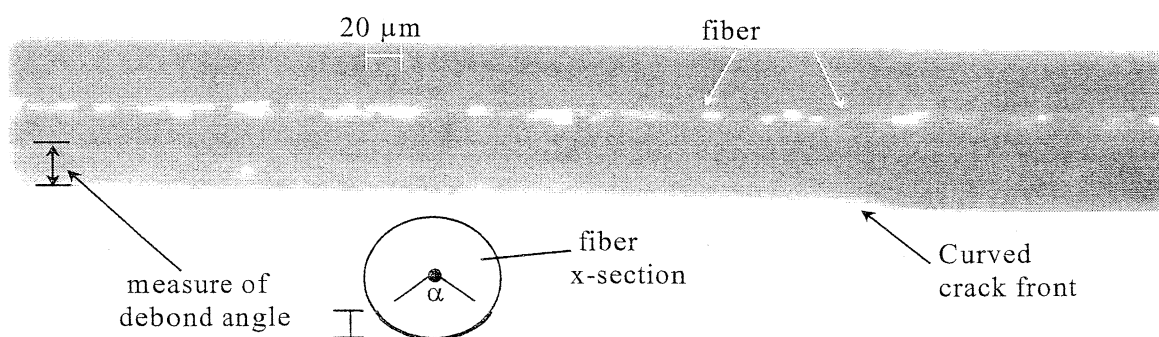


Fig. 4-19: Shape of crack front on SCS-0 fiber surface

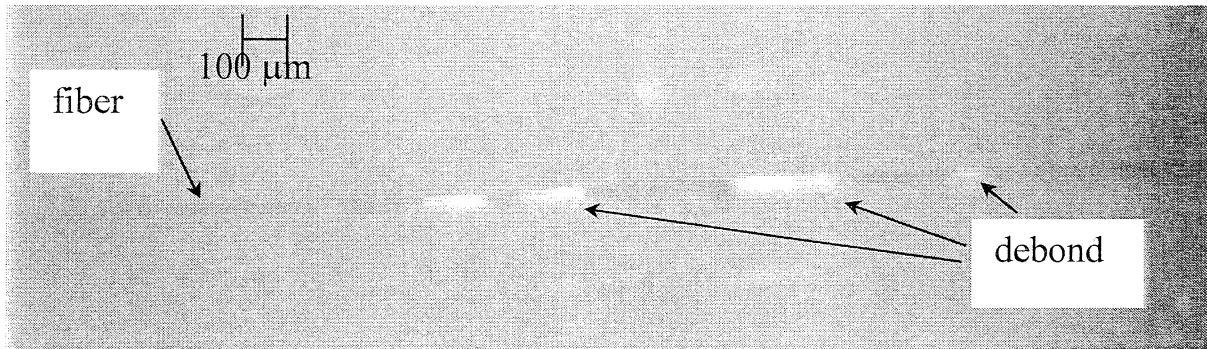


Fig. 4-20: Debonding in Nicalon/epoxy

diameter on the order of graphite fibers. Nicalon was chosen for initial studies for two reasons. Nicalon fibers can be easily placed precisely in the mold since they are stiff enough to support their own weight, and Nicalon fibers have a large transverse stiffness of 200 GPa, thus, producing a large normal stress concentration at the interface when embedded in the low modulus epoxy.

Tests on the Nicalon/epoxy system were successful in producing an interface failure using the same dimensions as the SCS-0 sample, except for the thickness which was modified ($t = 0.5\text{mm}$). In each sample one fracture surface contained a channel from the fiber while the other contained the exposed fiber. Prior to ultimate failure, debonding was imaged using reflected light. The debonds in the Nicalon tests had a distinctly different appearance than in the SCS-0 tests. As shown in Fig. 4-20, the area of high intensity reflected light is not continuous as in the SCS-0 tests but is a series of bright areas in the gage length linked together by darker areas; consequently, the moment of debond initiation was less clear. An upper bound for the strength of the Nicalon/epoxy interface was measured as 63 MPa.

4.4.4 Graphite/Epoxy Composite

Two types of graphite fibers were tested. AU4 fiber from Hexcel is an unsurface-treated and unsized fiber that has a surface comprised of weak non-structural carbon. For this reason AU4 was expected to have a low interfacial strength. Hexcel AS4 fiber was also embedded in epoxy and tested. As received, the AS4 fiber has been treated with a solvent to remove the non-structural carbon surface, and an epoxy based sizing has been applied which is optimized for

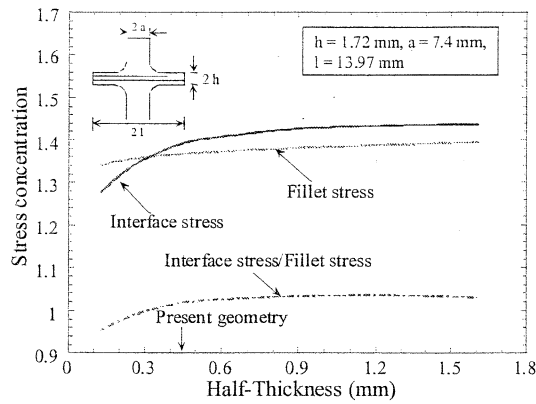


Fig. 4-21: Effect of sample thickness

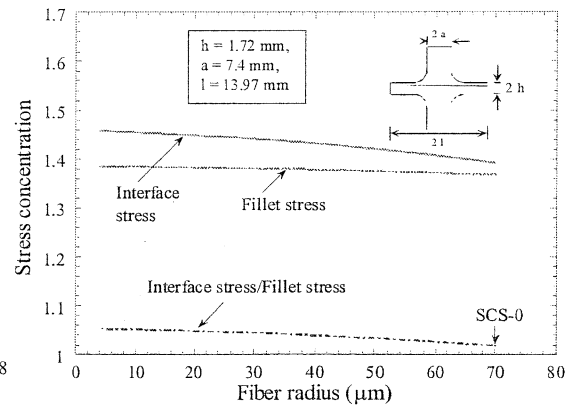


Fig. 4-22: Effect of fiber radius

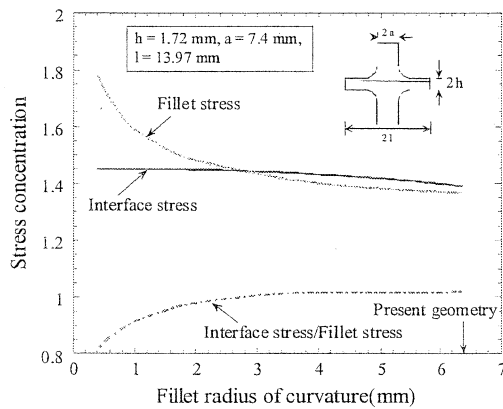


Fig. 4-23: Effect of fillet radius

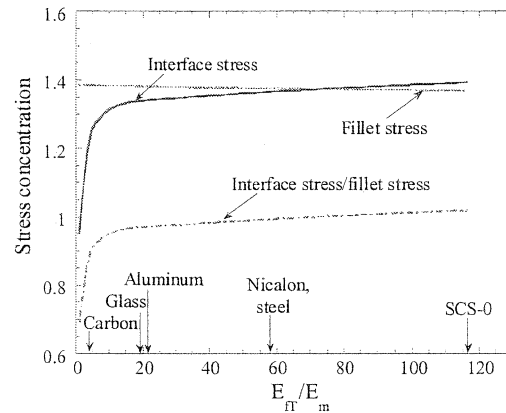


Fig. 4-24: Effect of fiber transverse modulus

adhesion to epoxy. The term “interfacial failure” is defined for the graphite fibers as failure at the epoxy/graphite interface (AU4), the graphite/sizing interface (AS4), the sizing/epoxy interface (AS4), or within the nonstructural carbon of the fiber (AU4). Madhukar and Drzal [13] tested the apparent shear strength of both AS4/epoxy and AU4/epoxy interfaces using the fragmentation test and determined that the AS4 interface was significantly stronger than the AU4 interface. The AS4 interface remained intact beyond loading that produced yielding in the epoxy.

Initial cruciform tests on the graphite/epoxy samples resulted in failure at the fillet instead of the desired failure in the gage length. The fillet failures led to a parametric study to determine the effect of sample thickness, fiber radius, fillet radius, and fiber transverse modulus — parameters

not previously studied by Tandon, *et al.*[11] In Figs. 4-21 thru 4-24 “stress concentration” is defined as the maximum interfacial normal stress, and the fillet stress is defined as the maximum stress in the loading direction on the fillet (both are normalized with respect to the applied load). The plots are based on SCS-0 properties. Figure 4-21 indicates that an increase in t results in a larger interface/fillet stress ratio, and Fig. 4-22 shows that a smaller fiber diameter will result in a more desirable ratio of interface to fillet stress. The 0.5 mm sample thickness used for the graphite/epoxy is near the optimum. Unfortunately, as is shown in Fig. 4-23, a larger fillet radius would not significantly improve the interface/fillet stress ratio. The graphite/epoxy samples failing at the fillet already had a near optimum fillet radius. Figure 4-24 illustrates the most difficult hurdle to overcome when cruciform testing the graphite fiber. The graphite/epoxy system has a ratio of transverse fiber modulus (E_{TF}) to matrix modulus (E_m) of 4.07 which is well below the transition point near $E_{TF}/E_m = 10$ below which the interface stress drops rapidly. Because of its low transverse modulus (14 GPa) the graphite fiber does not offer much resistance to deformation in the radial direction as the epoxy transfers load from the grips to the interface. A large applied load is then required to significantly load the interface. The large applied load overloads the fillet and causes fillet failure prior to interface failure. The fillet failure problem was resolved by reinforcing the fillet by extending the glass/epoxy tab material used to prevent the ends of the loading arms from being damaged by the grips. Each tab was enlarged to cover the entire loading arm, the fillets and a small portion of the wings. Figure 4-25 is an image of a sample that failed at the fillet, and Fig. 4-26 shows a sample with the reinforced fillets as well as a side view schematic of the end of one of the wings.

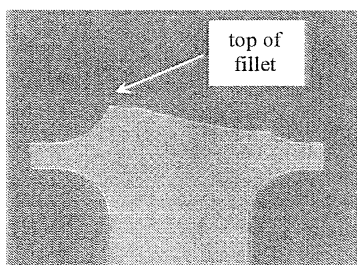


Fig. 4-25: Fillet failure

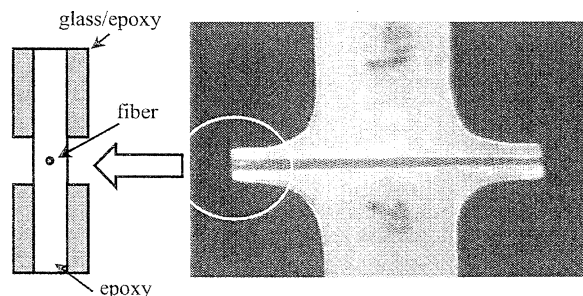


Fig. 4-26: Reinforced fillets

The graphite fiber samples with reinforced fillets failed in the gage section. Since the analysis previously developed did not include the extended tab, the interface strength was not calculated for the graphite fiber samples. Interface strengths will be included in a future publication based on a modified model. Even though quantitative results are not reported at this time, a qualitative difference in interface strength between AU4 and AS4 was established. The AS4 samples failed at an average of 30% more applied load than the AU4 samples. The failure mode was also different. Figure 4-27 shows a part of the gage section of a failed AU4 sample. The AU4 samples failed due to debonding along portions of the gage section while the AS4 samples failed several fiber diameters away from the fiber.

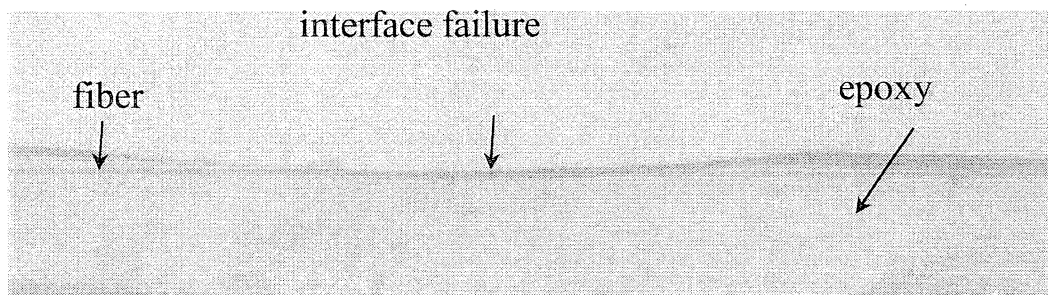


Fig. 4-27: Failed AU4/Epoxy

The interface failure in the AU4 samples and matrix failure in the AS4 samples is consistent with Madhukar *et al.*'s [13] measurement of a low apparent shear strength in AU4/epoxy and a relatively high interface strength in AS4/epoxy. The relatively large distance between the failure surface and the interface in the AS4/epoxy samples is probably a result of the chemical shrinkage of the matrix. Prior to mechanical loading, the matrix material near the interface is in compression. Upon mechanical loading, the matrix in the gage section but away from the fiber is at a greater tensile stress than the matrix adjacent to the interface.

4.5 Summary

It has been shown in this work that the single-fiber cruciform design is successful in eliminating the influence of free-edge stresses which are present in transverse testing of conventional straight-sided specimens. The experimental part of this study clearly establishes that the cruciform geometry is successful in forcing debond initiation in the central region, which is free of initial stress singularities, and therefore provides valid interfacial tensile strength data.

For Glass/Epoxy composites, inspection of photoelastic fringe pattern and stress-strain response indicates that stress intensification takes place mainly in the central loading region, while microscopic examination of the failure surface reveals that the radial stress at the interface is mainly responsible for interfacial failure.

For the large diameter SCS-0 fiber, the external stress level at debond initiation has been measured using indicators from three different sources, namely, development of photoelastic fringes, jump in strain response of surface gages and first significant occurrence of acoustic emission activity. It has been shown that the "jump" in the stress-strain curve invariably coincides with the occurrence of acoustic emission activity for samples on which both surface strain and acoustic emission activity measurements are conducted. Further, the mean values of the external stress at which debonding initiates in samples tested on a MTS agree well with the stress level at which photoelastic crack-tip fringes first appear in a specimen which is tested on the straining stage of a polarized microscope. Fiber-matrix debonding is observed visually as a white line (which is light reflected by the debonded interface) in the center of the failed specimens. Further, SEM of the cross section clearly shows that the fiber separates from the matrix in a region close to the loading direction. Additionally, inspection of photoelastic fringe pattern and stress-strain response indicates that the central portion of the fiber/matrix interface is highly stressed under tensile loading whereas the fiber carries negligible load near its ends. These experimental observations are found consistent with the numerical predictions using 3-D FEM. The analysis also reveals that the radial stress at the interface is the dominant stress component. Parametric studies on the cruciform dimensions, namely, loading arm width, wing height, sample thickness, fiber radius, fillet radius, and fiber transverse modulus yield an optimum configuration which promotes ultimate failure at the interface. Further, microscopic examination of the fracture surface reveals a smooth fiber surface which is indicative of failure occurring due to normal stress alone and is consistent with our use of maximum stress criteria for predicting failure initiation.

It has been further shown that the cruciform test can be used to determine the length and shape of the debond as a function of applied load for the large diameter SCS-0 fiber. In addition, an interface failure and an image of debonding using reflected light is obtained with smaller fiber

diameter Nicalon/epoxy samples. Qualitative differences between an AS4/epoxy and AU4/epoxy interface are demonstrated and are consistent with expected differences in normal strength (in accordance with published fragmentation results).

The results reported in this study are a part of our continuing effort to employ the cruciform geometry to estimate the tensile normal strength of the fiber-matrix interface in unidirectional composites. Such data are critical for establishing design methodologies based on micromechanical failure theories so that empirical failure diagrams obtained through extensive composite testing can be avoided.

REFERENCES

- (1) Pagano, N. J., 1998. "On the Micromechanical Failure Modes in a Class of Ideal Brittle Matrix Composites. Part I. Coated-Fiber Composites," *Composites Part B*, **29 B**, pp 93-119.
- (2) Tandon, G. P. and R. Y. Kim., 1997. "Test Methods for Estimation of Interfacial Normal Strength in Unidirectional Fiber Reinforced Composites," *Journal of Reinforced Plastics and Composites*, **16 (17)**, pp 1550-1565.
- (3) Gundel, D. B., B. S. Majumdar & D. B. Miracle, 1995. "Evaluation of the Intrinsic Transverse Response of Fiber-Reinforced Composites using a Cross-shaped Geometry," *Scripta Metall*, **33**, pp 2057.
- (4) Tandon, G. P., R. Y. Kim, S. G. Warrier and B. S. Majumdar, 1997. "Influence of Edge Effects in Estimating Interfacial Normal Strength in Model Unidirectional Composites," *Proceedings of the American Society for Composites, 12th Technical Conference*, Technomic Publishing Co. Inc., pp 1176-1185.
- (5) Majumdar, B. S., D. B. Gundel, R. E. Dutton, S. G. Warrier and N. J. Pagano, 1998. "Evaluation of the Tensile Interface Strength in Brittle Matrix Composite Systems," *Journal of American Ceramic Society*, **81 (6)**, pp. 1600-1610.
- (6) Broutman, L. J., 1969, " Measurement of the Fiber-Polymer Matrix Interfacial Strength ," *Interfaces in Composites, ASTM STP 452*, American Society for Testing and Materials, pp. 27-41.

- (7) ABAQUS/Standard User's Manual, Hibbitt, Karlsson & Sorensen, Inc., Pawtucket, RI, 1997.
- (8) Bechel, V. T. and Sottos, N. R., 1998, "Application of Debond Length Measurements to Examine the Mechanics of Fiber Pushout," *J of Mechanics and Physics of Solids*, **46** [9], pp. 1675-1697.
- (9) Tandon, G. P., Kim, R. Y., Warriar, S. G. and Majumdar, B. S., 1999, "Influence of Free Edge and Corner Singularities on Interfacial Normal Strength: Application in Model Unidirectional Composites," *Composites, Part B: Engineering* , **30**, pp. 115-134.
- (10) Tandon, G. P., Kim, R. Y. and Dutton, R. E., 1997, " Failure Modes in Unidirectional Composites Under Transverse Loading," *Journal of Reinforced Plastics and Composites*, **16**, pp. 33-49.
- (11) Tandon, G. P., Kim, R. Y. and Bechel, V. T., 2000, Evaluation of Interfacial Normal Strength in a SCS-0/Epoxy Composite Using Cruciform Specimens," *Composites Science & Technology*, in press.
- (12) Bechel, V. T., Tandon, G. P. and Kim, R. Y., 1999 " Fiber/Matrix Interface Debond Length Measurements Under Transverse Loading in the Cruciform Test," *Proceedings of the American Society for Composites, 14th Technical Conference*, Technomic Publishing Co. Inc., pp 367-376.
- (13) Madhukar, M. S. and L. T. Drzal. 1991. "Fiber-Matrix Adhesion and Its Effect on Composite Mechanical Properties: I. Inplane and Interlaminar Shear Behavior in Graphite/Epoxy Composites," *J. Composite Materials*, **25**, pp. 932-957.

5.0 IN SITU OBSERVATION AND MODELING OF DAMAGE MODES IN CROSS-PLY CERAMIC MATRIX COMPOSITES

5.1 Introduction

Ceramic-matrix composites generally exhibit matrix and/or interface damage well before final failure because of the low strain capability of the brittle matrix and weak interfacial bonding. These damages have a significant influence on the stress-strain behavior as well as on the ultimate strength of the composite. The failure process in a multidirectional laminate is further complicated by its dependence on ply orientations and stacking sequence. Reported in this study are the results of both analytical and experimental investigations carried out in an attempt to understand the initiation and propagation of damage in a $[0/90]_{3s}$ cross-ply laminate. A glass-ceramic matrix composite reinforced with silicon carbide (Nicalon) fibers is investigated at room temperature under uniaxial tensile loading. The initiation and propagation of interfacial debonding, microcracking, and fiber breaks were observed in situ, under applied load using a specially built loading device. The observed damage modes were then incorporated into existing micromechanical models to predict the laminate stress-strain behavior and compared with the experimental measurements.

5.2 Experiment

The material system considered in this study is SiC fiber(Nicalon) reinforced glass-ceramic matrix (Calcium alumino-silicate or CAS) composite supplied by Corning Incorporated in the form of panels. Both unidirectional and $[0/90]_{3s}$ cross-ply laminates are considered in this work. The fiber volume content was determined using an image analyzing technique on a square specimen with two adjacent edges polished, and its average value for 10 measurements was found to be 41 percent with a coefficient of variation of 7 percent. The average specimen thickness was approximately 0.1 inch.

Straight-sided flat specimens were then cut from the panels using a miniature diamond-impregnated saw using special care to minimize cutting edge damage. The specimens are 0.3 inch wide and 4 inch long. Thin glass-fiber end tabs (1 inch long) were mounted on both ends of

the specimen to protect them from possible gripping damage during loading. One free edge of the $[0/90]_{3s}$ specimen was progressively ground and then polished using successively smaller diameter alumina polishing powder (final size was 0.3 micrometers) in order to enhance the microscopic image for crack detection. An axial strain gage (gage length 3.2 mm) and a transverse strain gage were mounted on the mid-surface of the specimen to monitor strain during loading.

Uniaxial tensile loading was applied to the specimen of $[0/90]_{3s}$ laminate using a miniature loading device (referred to as strain stage hereafter) which was designed and built for in situ observation of damage in composite laminates. Axial force was generated by pulling the piston using nitrogen gas pressure. The straining stage is designed to be able to be mounted on the microscope stage for observation of microcracking under loading. The microcracks occurring in this class of brittle matrix composites tend to close upon removal of the applied load. This closure of the microcracks makes it very difficult to detect them using microscope. The specimen was mounted on the strain stage and loaded to a prescribed level which is slightly higher than the expected first microcracking level on the microscope stage. This load was held during microscopic examination of microcracking by scanning a predetermined area in the polished free edge, and capturing the microcracks using the image analysis device. The captured images were then transferred to a digital disc for future analysis. This procedure was repeated a few times at successive incremental load levels up to final failure. The extension of microcracks as well as their multiplication with incremental loading was assessed by observing the subsequently captured images. The average value of crack spacing was obtained from 10 measurements for a specified load level. Two specimens of a $[0/90]_{3s}$ laminate are monotonically loaded up to failure to obtain the entire stress-strain behavior of the laminate.

5.3 Analytical Background

In this work the large radius axisymmetric damage model by Schoeppner and Pagano [1] has been employed in order to approximate the thermoelastic stress field of flat laminated bodies. The model is generated by subdividing the body into regions consisting of concentric shells of constant length and satisfying Reissner's variational equation with an assumed equilibrium stress field within each region. It has been shown that in the limit as the ratio of average cylinder radius R to laminate thickness T approaches infinity, the gradient of the hoop strain through the wall thickness approaches zero, generating a stress-strain field equivalent to a flat composite coupon under a uniform axial strain. The model can be used to examine the initiation, propagation and interaction of various idealized damage such as delamination and transverse ply cracking in flat laminates containing orthotropic layers. It is assumed that transverse cracks are normal to the layer interface and extend the full depth of the ply. Furthermore, free-edge effects are neglected in this 2-D model.

In this work, we consider the effect of transverse cracking and delamination on the extensional stiffness and Poisson's ratio of a $[0/90]_{3s}$ cross-ply laminate. Under uniaxial strain in the x -direction, while the remainder of the external boundaries are traction free, the longitudinal stiffness, E_{xx} , and major Poisson's ratio, ν_{xy} , are defined as

$$E_{xx} = \frac{\bar{\sigma}_{xx}}{\bar{\epsilon}_{xx}} \quad \text{and} \quad \nu_{xy} = -\frac{\bar{\epsilon}_{yy}}{\bar{\epsilon}_{xx}} \quad (18)$$

where the bar denotes the average value of the stated quantity over the unit cell, and σ_{ij} and ϵ_{ij} are the stress and strain components in Cartesian coordinates, respectively. The constituent thermoelastic properties used for analytical calculations are given below:

$$\begin{array}{lll} E_f = 29 \text{ Msi} & \nu_f = 0.25 & \alpha_f = 1.78 \times 10^{-6} / ^\circ\text{F} \\ E_m = 14.5 \text{ Msi} & \nu_m = 0.25 & \alpha_m = 2.78 \times 10^{-6} / ^\circ\text{F} \end{array}$$

It is assumed that each constituent is isotropic. Further, E represents Young's modulus, ν the Poisson's ratio, and α the coefficient of thermal expansion (CTE), whereas subscripts f and m refer the stated quantities to fiber and matrix, respectively. The process temperature difference, ΔT , is assumed to be -1080°F .

5.4 Results

5.4.1 Elastic Properties

The elastic properties of the unidirectional ply were calculated from the constituent properties using the NDSANDS model developed by Pagano and Tandon [2]. Comparison of the initial elastic moduli between calculation and experiment is summarized in Table 5-1.

Table 5-1. Elastic properties of unidirectional laminate

<u>Property</u>	<u>Theory</u>	<u>Experiment</u>
Longitudinal modulus, Msi	20.3	19.43
Transverse modulus, Msi	18.9	17.9
Major Poisson's ratio	0.25	0.25

These ply properties are used for subsequent prediction of elastic constants of the $[0/90]_{3s}$ laminate using classical laminated plate theory. The experimental results are compared with the analytical prediction in Table 5-2.

Table 5-2. Elastic properties of $[0/90]_{3s}$ laminate

<u>Property</u>	<u>Theory</u>	<u>Experiment (Cv)</u>
Elastic modulus, Msi	19.6	16.91 (4.1)
Poisson's ratio	0.24	0.20 (12.5)

Cv: coefficient of variation, %

The measured modulus is observed to be lower compared to the theoretical predictions (assuming no damage is present) indicating that there could be some processing induced initial damage in the cross-ply laminate.

5.4.2 Damage Progression

The damage progression in the form of matrix cracking was assessed under incremental loading. The microcracks were found [3] to be initiated in the 90 degree layers as a partial debond at the interface between fiber and matrix before branching into the matrix. These microcracks propagate almost at once across the entire width of the 90 degree ply and link up with neighboring plies as the applied stress increases. The development of the transverse crack in the laminate at increasing load levels has been documented by Kim and Tandon [3]. Crack spacing between two neighboring cracks also decreases as stress level increases and appears to reach a saturation value (0.00032 inch) before final failure. Damage mechanisms such as interface debonding, matrix cracking, and fiber fracture are responsible for the nonlinear stress-strain behavior and continuous degradation of laminate properties.

5.4.3 Stress-Strain Behavior

Figure 5-1 shows typical axial and transverse stress-strain relations for the $[0/90]_{3s}$ laminate. The axial stress-strain behavior is seen to be linear both in its initial and final stages while becoming nonlinear in the transition stage. The transverse strain varies nearly linearly up to 20 Ksi and thereafter reverses its direction until final failure. This reversal of the transverse strain occurs in the nonlinear region of the axial stress-strain relation.

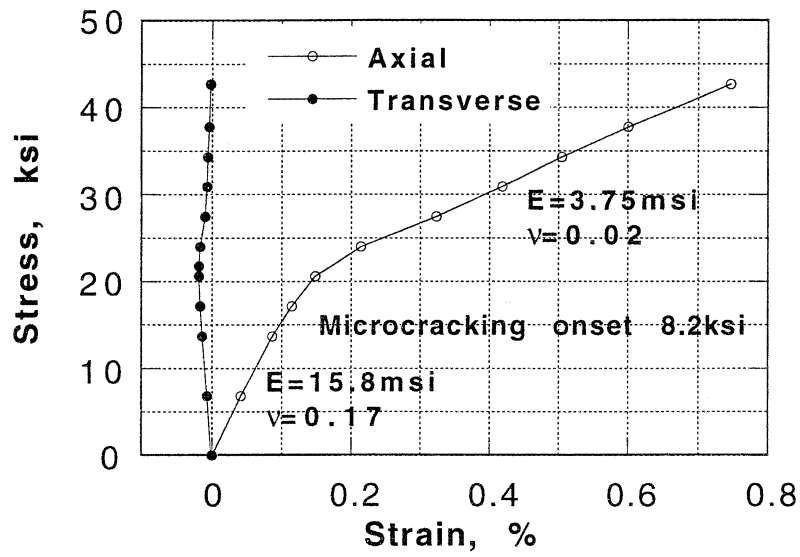


Fig. 5-1: Stress-strain relation for the $[0/90]_{3s}$ laminate at room temperature.

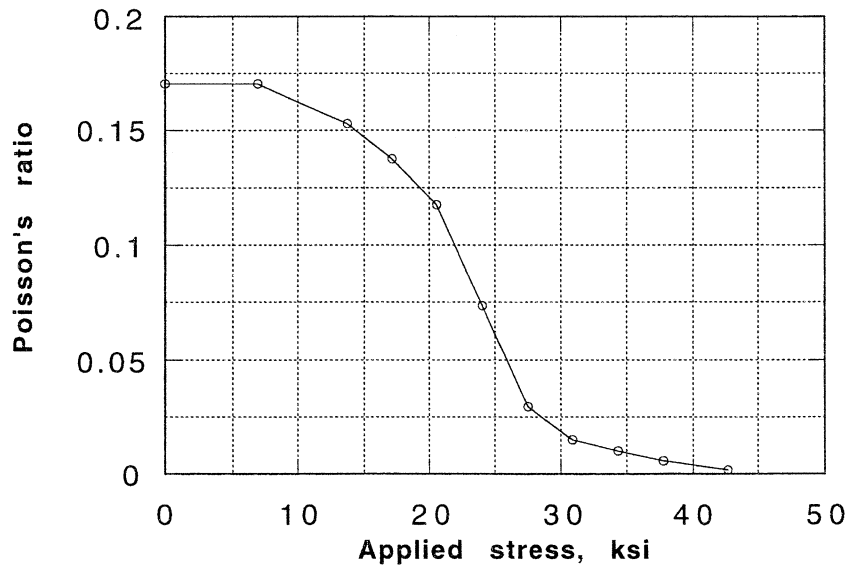


Fig. 5-2: Experimentally measured major Poisson's ratio as function of applied stress for $[0/90]_{3s}$ laminate at room temperature

Figure 5-2 shows variation of major Poisson's ratio as function of applied stress. The Poisson's ratio decreases drastically in the transition region of the stress-strain curve (Fig. 5-1) where the

transverse strain reversal occurred. Based on the observed progression of damage, we now assume the following idealized damage states and calculate the axial modulus (E_{xx}) and Poisson's ratio ν_{xy} using the large radius axisymmetric model [1].

<u>Stage of damage state</u>	<u>E_{xx}</u>	<u>ν_{xy}</u>
1. No damage present	19.6	0.24
2. Complete debonding of fiber/matrix interface in all 90° plies	13.2	0.16
3. Transverse cracking of all 90° plies in conjunction with damage stage 2(crack spacing 0.00032 inch)	10.47	0.13
4. Transverse cracking of either of inner two 0° plies in conjunction with damage stage 3	7.32	0.08
5. Transverse cracking of all plies except outer two 0° plies	3.66	0.04
6. Extension of axial crack(crack length 0.0003 inch) from the tip of the transverse cracks in damage stage 5	3.56	0.04

The predicted values of E_{xx} and ν_{xy} compare favorably with the experimental results in the initial linear region (stage 1) and final (stages 5 & 6) linear regions. In the nonlinear transition region (stages 2-4) we are unable to directly compare the predictions with experiment because of the inability to distinguish the corresponding damage stages in the present experiment. Further work is in progress to identify and capture the growth of dominant damage mechanisms with incremental loading in the transition region.

5.5 Summary

The initiation and progression of damage in the $[0/90]_{3s}$ laminate of SiC fiber (Nicalon) reinforced glass-ceramic matrix (CAS) composite have been investigated under uniaxial tension.

Damage mechanisms in the form of fiber/matrix interface debonding, matrix cracking, and longitudinal splitting are assessed at each incremental loading. Based on the observed damage states, analytical calculations were made to predict change in modulus and Poisson's ratio corresponding to the idealized states of damage. The correlation between analytical prediction and experimental results is promising.

REFERENCES

- (1) Schoeppner, G. A., and Pagano, N. J., Stress Fields and Energy Release Rates in Cross-Ply Laminates, accepted for publication in *International Journal of Solids and Structures*, 1997
- (2) Pagano, N. J. & Tandon, G. P., Elastic Response of Multidirectional Coated Fiber Composites, *Composites Science and Technology*, 31 (1988) pp 273-293
- (3) Kim, R. Y. & Tandon, G. P., In situ observation and modeling of damage modes in cross-ply ceramic matrix composites, presented at ASME IMECE, Dallas, TX, Nov 16 - 21, 1997

6.0 VARIATIONAL, FEM AND ASYMPTOTIC SOLUTION BEHAVIOR IN THE VICINITY OF STRESS SINGULARITIES IN CONCENTRIC CYLINDER MODEL

6.1 Introduction

The prediction of micro-mechanical damage initiation and growth in composite materials requires accurate stress and deformation analyses. The single fiber, axisymmetric concentric cylinder model is widely used for analyzing the thermo-elastic stress field in a composite representative volume element and for simulating fiber pullout/push-in experiments. The axisymmetric damage model (ADM) [1] was developed earlier to approximate the elastic stress field and energy release rates of bodies composed of concentric cylinders containing damaged regions either as annular or penny-shaped cracks in the constituents and/or debonds between them. The model is generated by subdividing the body into regions consisting of a core and a number of shells of constant length and satisfying the Reissner's variational equation with an assumed stress field in each region.

The present effort investigates the ability of this variational method to capture the details of the stress field in the vicinity of bi-material cracks and free-edges in the single-fiber axisymmetric model. Several example problems such as free-edge (material and geometry dependent) singularity, bi-material crack singularity (complex-valued), interface crack singularity with debonded portion of the interface sliding under frictional shear (slip-displacement direction and coefficient of friction dependent), and penny-shaped crack with square root singularity, are analyzed using the variational method, asymptotic analyses with William's type [2] stress functions, and with FEM using mesh refinement in the regions of singularity. In this study a comparison of the three solutions is presented highlighting the distance at which leading terms of asymptotic analysis are dominant and the ability of the FEM and variational methods to capture the local radial and angular distributions near cracks and free edges.

6.2 Free-Edge Singularity

As an example, we will consider the problem of thermal loading of a unidirectional fiber reinforced composite in which the classic free edge singularity is encountered. The material properties correspond to SiC fiber ($E = 410$ GPa, $\nu = 0.2$) in Borosilicate Glass matrix ($E = 63$

GPa, $\nu = 0.2$). We will assume that the fiber-matrix interface is perfectly bonded and the composite is subjected to a unit temperature change ($\Delta T = -1^\circ\text{C}$).

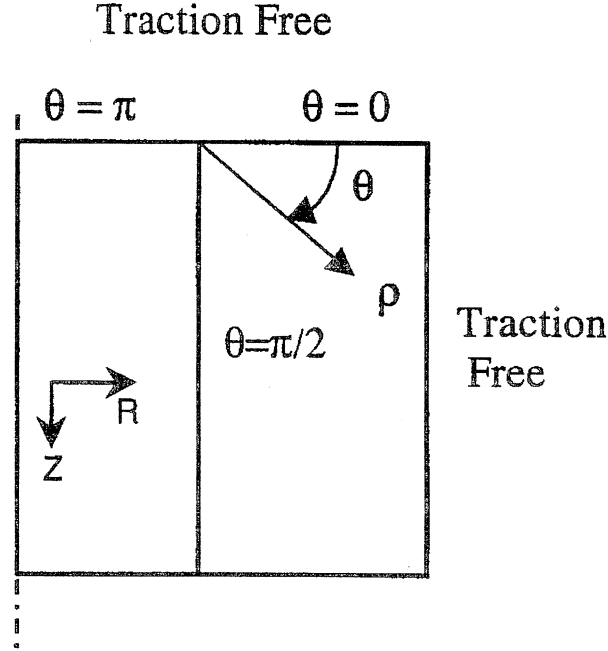


Fig. 6-1: Schematic of a concentric cylinder for analysis

An asymptotic analysis of this problem reveals the power of the radial singularity, λ , equal to -0.112 . Global stress fields are next computed using Finite Element Methods (FEM) and Axisymmetric Damage Model (ADM). In Figs. 6-2 and 6-3, we have compared the angular variation of the opening stress, $\sigma_{\theta\theta}$, and shear stress, $\sigma_{\rho\theta}$, respectively, from global analyses with the asymptotic solution of this problem. The comparison is done at a radius of $0.1 \mu\text{m}$ and the results normalized such that the opening stress is equal to unity at the fiber-matrix interface. It is seen from Figs. 6-2 and 6-3 that both FEM and ADM analyses exhibit reasonable good matching in the opening and shear stress components for all value of θ . In Fig. 6-4, we have now plotted the angular variation of the radial stress component, $\sigma_{\rho\rho}$. It is seen that the FEM solution (with sufficient mesh refinement – logarithmically increasing element sizes from 10^{-8} m), captures all the characteristics of the singular field, whereas ADM (with much coarser layering), is unable to predict the jump in the radial stress component at the interface.

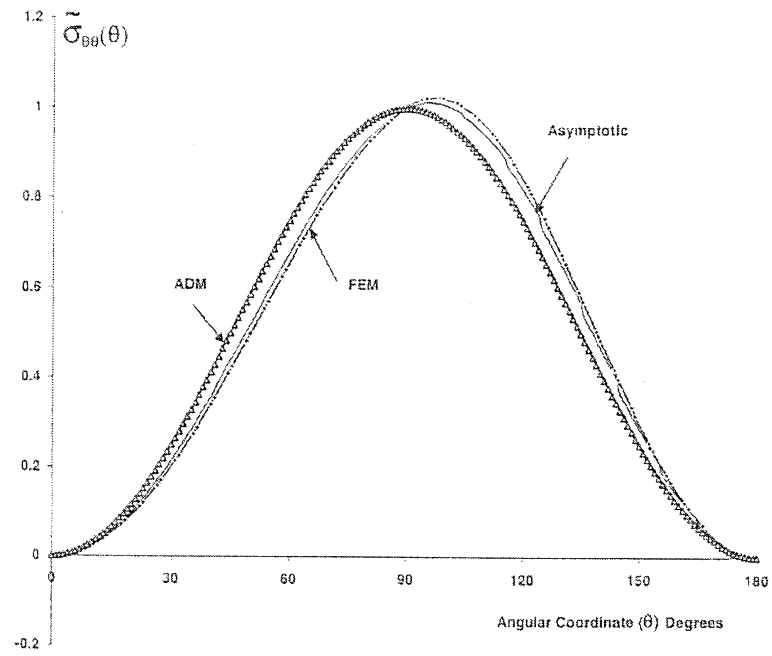


Fig. 6-2: Angular variation of opening stress, $\sigma_{\theta\theta}$

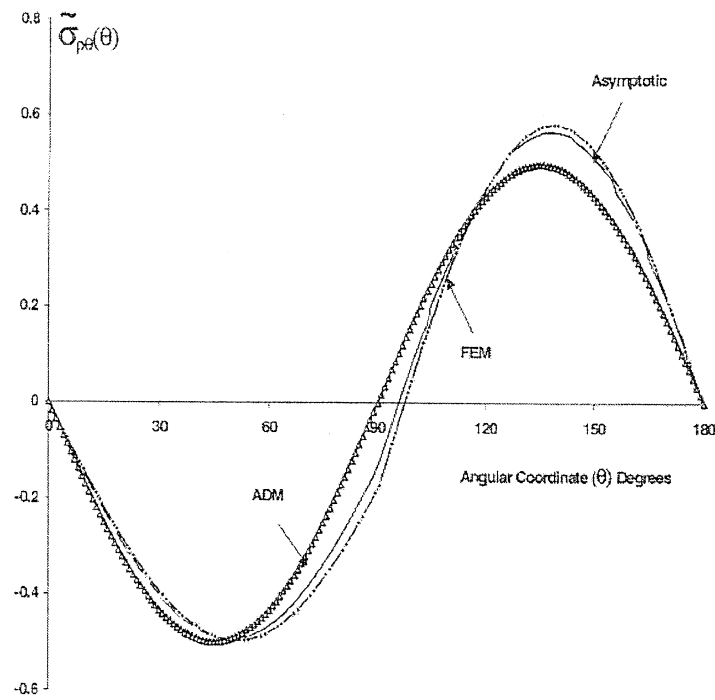


Fig. 6-3: Angular variation of shear stress, $\sigma_{\rho\theta}$

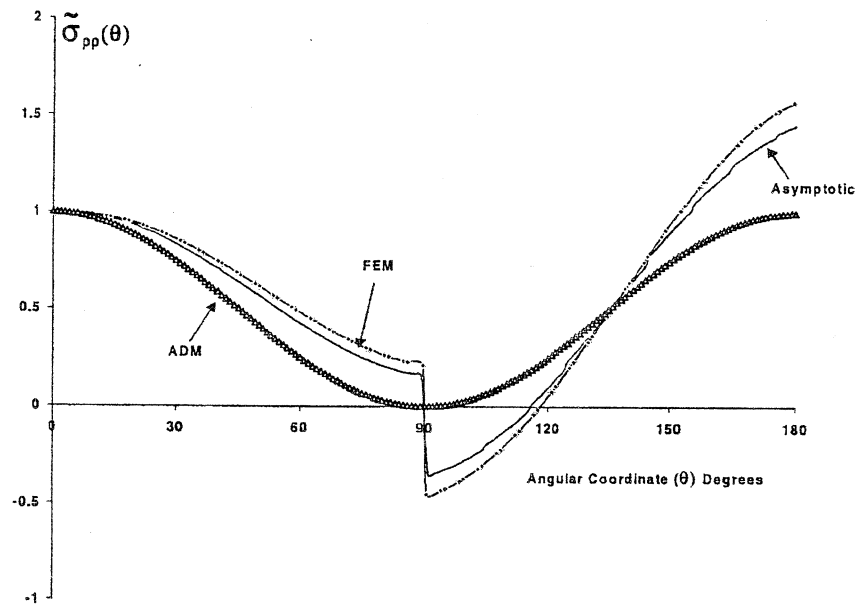


Fig. 6-4: Angular variation of radial stress, σ_{pp}

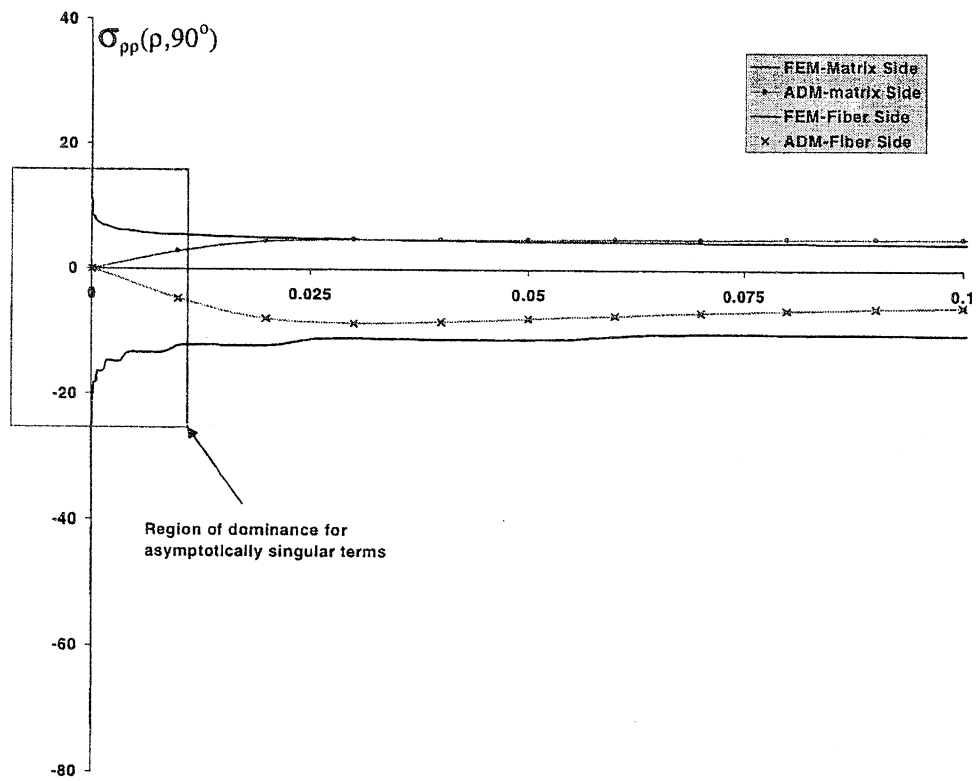


Fig. 6-5: Axial variation of radial stress, σ_{pp}

This is attributed to the fact that in ADM we do not recognize the angular dependence of the axial stress at the singular point. Both on the free edges ($\theta = 0$ and 180°) as well as at the interface ($\theta = 90^\circ$), the axial (or longitudinal) stress is equated to zero. This is illustrated in Fig. 6-5, where we have plotted the axial variation of σ_{pp} . While the FEM solution tends to $+$ and $-$ infinity (in the limit of mesh refinement), ADM solution returns a value equal to zero at the singular point, in accordance with the imposed boundary condition. We have further observed that if we compare the angular variation of σ_{pp} at a radius value which is greater than the size of zone of dominance of singular region, ADM does predict a jump in the radial stress value at the interface. For the matching done at $.1 \mu\text{m}$, the global FEM and ADM analyses yield the scaling factor as $1.922 \text{ MPa-m}^\lambda$ and $1.323 \text{ MPa-m}^\lambda$, respectively.

6.3 Closing Remarks

In this work, a combination of asymptotic, FEM, and Variational methods are used to investigate the nature of potentially singular stress fields under arbitrary loading and boundary conditions. Asymptotic analysis is used to determine the power of the radial local singularity and the angular distribution functions, whereas global stress fields are computed using FEM and ADM (Variational) methods. It is shown that FEM, with appropriate (logarithmically increasing element sizes from $\sim 10^{-8}\text{m}$) meshing, captures all the characteristics of the singular field, whereas, ADM, with coarser layering, exhibits good angular variation match in two stress components ($\sigma_{\theta\theta}$, $\sigma_{p\theta}$). Deviation from the predicted asymptotic behavior is seen in matching of radial stress component (σ_{pp}) with ADM analysis, which is attributed to the imposed boundary condition at the singular point.

REFERENCES

- (1) Pagano, N. J. (1991). Axisymmetric Micromechanical Stress Fields in Composites. *Proceedings 1991 IUTAM Symposium on Local Mechanics Concepts for Composite Materials Systems*, Springer, Verlag, 1-26.
- (2) Williams, M. L., Stress singularities resulting from various boundary conditions at angular corners of plates in extension, *J. of Applied Mechanics*, 74 (1952), pp. 526.

7.0 LOAD TRANSFER CHARACTERISTICS IN THE VICINITY OF FIBER BREAKAGE

7.1 Introduction

The single fiber, axisymmetric concentric cylinder model is widely used for analyzing the thermo-elastic stress field in a composite representative volume element. When an external stress is applied to a single fiber embedded in a matrix, the tensile stress is transferred to the fiber through an interfacial shear stress. As the tensile load increases, the tensile strain in the fiber will eventually exceed the failure strain of the fiber, and the fiber will fracture as seen in Fig. 7-1.

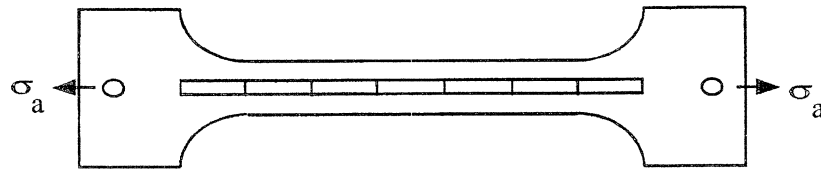


Fig. 7-1: Schematic illustration of a single fiber fragmentation test

In this study, the concentric cylinder model has been utilized to evaluate the load transfer characteristics in the immediate vicinity of a broken fiber in a unidirectional composite. A number of researchers have studied the stress distributions around discontinuous fibers. The so-called shear lag analysis is frequently used for analysis of stress transfer between fiber and matrix. However, this simplified approach leads to inaccurate predictions of shear stresses and energy release rates [1]. By developing sets of recurrence relations, McCartney [2] has extended the two cylinder stress transfer model to multiple cylinders and used the technique to study the stress transfer behavior when fiber fracture occurs. Using Reissner's variational principle, Pagano [3] has developed the axisymmetric damage model to approximate the elastic stress field and energy release rates of bodies composed of concentric cylinders containing damaged regions either as annular or penny-shaped cracks in the constituents and/or debonds between them. This variational model of a concentric cylinder [3] can be easily employed to simulate fiber breakage.

The prediction of micro-mechanical damage initiation and growth in composite materials requires accurate stress and deformation analyses. For the fiber fracture stress transfer problem, singularities are encountered for the axial stress in the matrix in the plane of fiber fracture. In

this work, the detailed stress and displacement fields in the neighborhood of fiber break are analyzed using the recursive [2] and variational [3] methods, and compared with the asymptotic stresses around the crack tip [4] and with other numerical methods such as FEM using mesh refinement in the regions of singularity. A comparison of these different solutions is presented highlighting the distance at which leading terms of asymptotic analysis are dominant and the ability of the approximate elasticity solutions to capture the local radial and angular distributions near the crack tip. Also, the assumptions of the more commonly used shear-lag analyses are critically assessed.

7.2 Problem Definition

Figure 7-2 is a schematic of the single fiber fragmentation test for analysis. The problem consists of cylindrical fiber of radius r_f embedded in a concentric cylinder of matrix material of radius r_m . The fiber axis is assumed to coincide with the z -axis and a crack is assumed present on the plane $z = 0$ within the fiber. Far away from the crack, the fiber is subjected to uniform constant displacement, w . The outer radial boundary of the concentric cylinder assemblage is considered traction free while symmetry boundary conditions are imposed on the portion of the matrix lying in the plane of the fiber break. For this work, we will assume perfect bonding at the fiber-matrix interface, although in real-life composites, there are several other micro-mechanics phenomenon such as shear yielding of the matrix, interfacial debonding and transverse matrix cracking, which are observed in conjunction with fiber fracture. These additional damage mechanisms will be treated subsequently.

7.3 Results and Discussion

7.3.1 Isolated Fiber Break in an Infinite Medium

Most analyses of stress transfer between a single fiber and a matrix can be classified as elasticity analyses, typically based on shear-lag assumptions (e.g., Cox [5]). These analyses generally neglect the contribution of radial and shear stresses, misrepresent the interfacial shear stress near the fiber break, produce an inadmissible stress state and provide poor estimates of stress transfer, especially at low fiber volume fractions. In order to provide an improved solution, Whitney and Drzal [6] have used a stress function approach based on the superposition of an exact far-field solution with an approximate local transient solution. In this study, we will

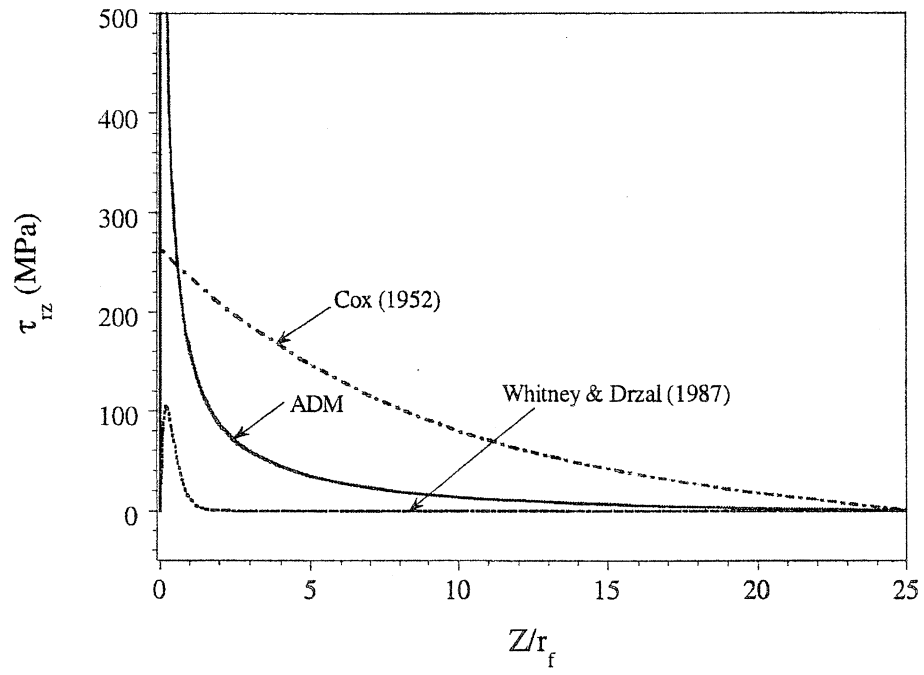


Fig. 7-3: Axial variation of interfacial shear stress

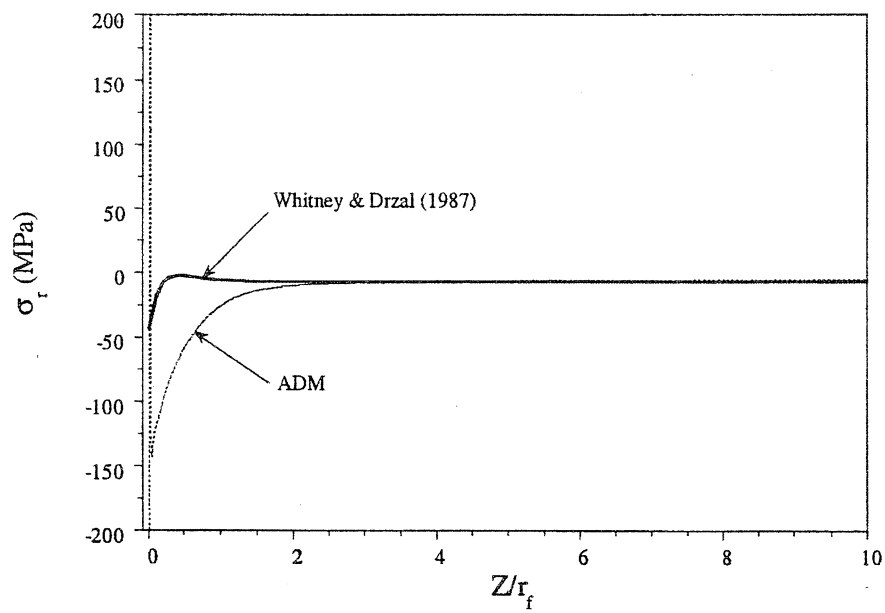


Fig. 7-4: Axial variation of interfacial radial stress

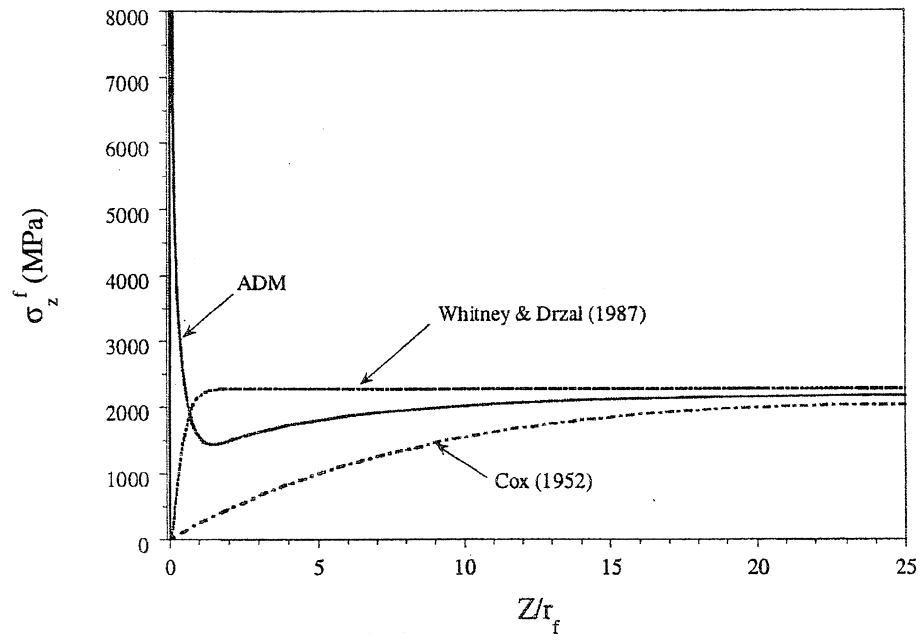


Fig. 7-5: Variation of axial stress in the fiber along the interface

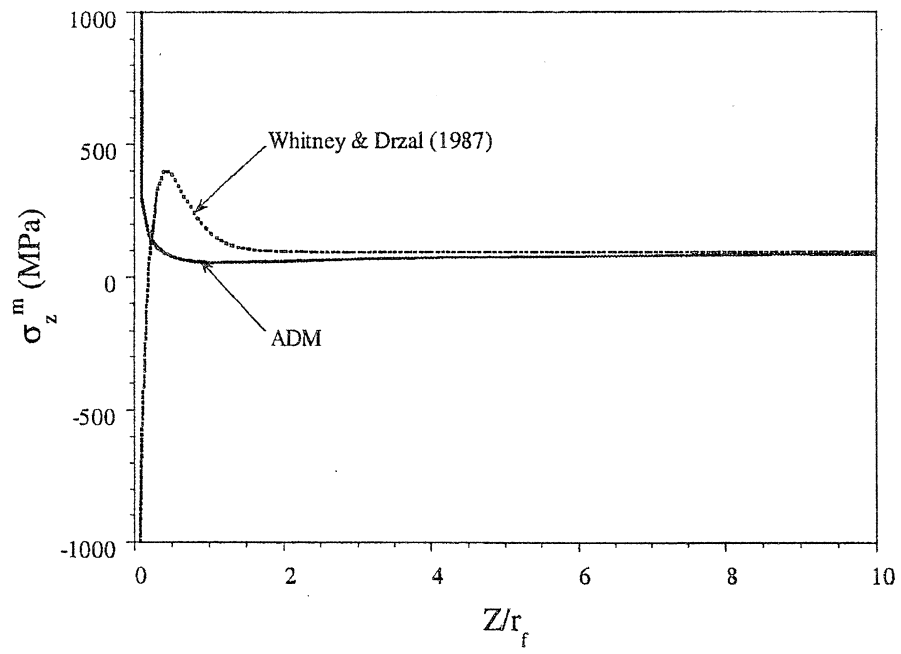


Fig. 7-6: Variation of axial stress in the matrix along the interface.

7.4 Concluding Remarks

The comparisons which we have provided in Figs. 7-3 thru 7-6 serve to illustrate the nature of the differences in the numerical stress predictions and hence stress transfer distances between simplified and more sophisticated analyses. As observed, the differences are confined mainly at the fiber end where the stress field is dominated by the presence of the singularity. We have also done exhaustive comparison of the variational results [2,3] with FEM solution and local asymptotic analyses [4] near the fiber break for both isotropic and transversely isotropic fibers which will be discussed in a manuscript currently under preparation.

REFERENCES

- (1) Nairn, J. A., "On the use of shear-lag methods for analysis of stress transfer in unidirectional composites", *Mechanics of Materials*, 26 (1997) pp. 63-80.
- (2) McCartney, L. N., "Stress transfer mechanics for systems of transverse isotropic concentric cylinders", submitted for publication (1998).
- (3) Pagano, N. J., "Axisymmetric micromechanical stress fields in composites", *Proceedings 1991 IUTAM Symposium on Local Mechanics Concepts for Composite Material Systems*, Springer, Verlag (1991) pp. 1-26.
- (4) Pagano, N. J. and Kaw, A. K. "Asymptotic stresses around a crack tip at the interface between planar or cylindrical bodies", *Int. Journal of Fracture*, 71 (1995) pp. 151-164.
- (5) Cox, H. L., "The elasticity and strength of paper and other fibrous materials", *British J. Appl. Phys.*, 3 (1952) pp. 72-92.
- (6) Whitney, J. M. and Drzal, L. T., "Axisymmetric stress distribution around an isolated fiber fragment", in *Toughened Composites* (ed. N. J. Johnson), ASTM STP 937, American Society for Testing Materials, Philadelphia, PA (1987) pp. 179-196.

8.0 STRESS CONCENTRATIONS AT FIBER CORNERS DURING TRANSVERSE TENSION OF UNIDIRECTIONAL COMPOSITES

8.1 Introduction

The transverse tensile strength (bond strength) of the fiber-matrix interface plays a key role in governing the properties of fiber-reinforced composites [1], since it affects both the transverse and longitudinal properties of the composite. Among techniques that are used to characterize the transverse bond strength, the most common one is to load a straight sided 90° specimen (Fig. 8-1a) and identify initiation of debonding either from the onset of nonlinearity in the stress-strain curve, or from surface replicas obtained from the edges of the sample under load.

Previous work on titanium matrix composites (TMCs), consisting of single SiC fibers embedded in a Ti-6Al-4V matrix showed that the replica approach failed to provide any distinction in the bond strength for a wide array of fiber coatings (including uncoated and carbon coated fibers) [2]. Stress concentrations at the exposed fiber corners were believed to be responsible for the low strengths, and failure initiation at the edges were also verified using an ultrasonic shear wave detection technique. A solution that was proposed in order to obtain valid bond strength data was to use a cruciform shaped geometry, as illustrated in Fig. 8-1b[3]. In this geometry, the fiber ends are unloaded, and fiber-matrix debonding is forced to occur in the central region of the cross, i.e., edge effects are avoided.

In subsequent work, experiments were conducted on a model Al-fiber/epoxy system, to allow visual observation of the debonding process [4]. In addition to the exposed fiber and cruciform geometry, an embedded fiber geometry (Fig. 8-1c) was also chosen, based on considerations of a lower value of stress concentration. Experiments showed that the applied stress at debonding was highest for the cruciform geometry, and lowest for the exposed fiber geometry, with an intermediate value for the embedded geometry. Fracture surfaces revealed that indeed the lower strengths were associated with failures initiating at the fiber corners.

8.2 Asymptotic Analysis

We have now completed a 2-D asymptotic analysis, and combined it with 3-D finite element method (FEM) to obtain the full-field solution for the normal stresses at the interface under transverse loading. This is similar to the approach adopted by Pochiraju et al. [5] for a push-out

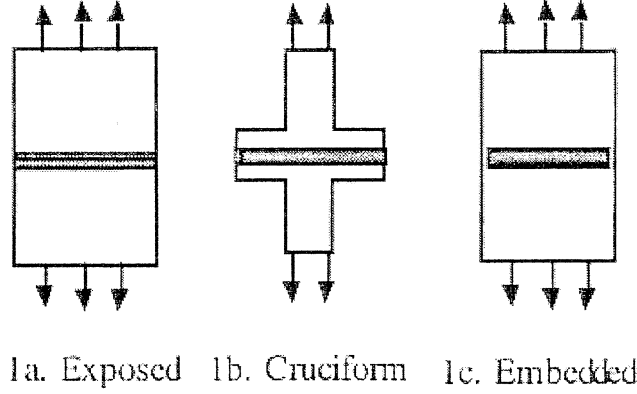


Fig. 8-1: Geometry of test specimen

problem, where they relied on the Muskhelishvili-Kolosov complex potential theory to evaluate the local stresses. The rationale here is to obtain a quantitative assessment of the effects of fiber corners on interface failure, and to compare with experimental data. The asymptotic analysis adopted here is fashioned after the work of Bogy [6], whereby a Mellin transform is used to solve the bi-harmonic equation for the Airy stress function (ϕ), namely, $\nabla^4 \phi_i = 0$, where i is either 1 or 2, depending on the two materials. The boundary conditions satisfy displacement and stress continuity at the interfaces, as well as the free-surface stress condition (for the exposed fiber specimen). For both the exposed and embedded fiber specimens, one obtains a set of 8 homogeneous equations in 8 unknowns, the latter being the constants that govern the angular variation of stresses: $A_{ij}(s) \cdot x_j(s) = 0$. Here s is the Mellin transform parameter, and a non-trivial solution, s_m , is sought in the domain $-2 \leq \text{Re}(S_m) \leq 1$. We have used the singular value decomposition method to solve the homogeneous equations, and stresses were obtained in the form:

$$\sigma_{ij} = \sum K_m \rho^{-S_m-2} \psi_{ij}^m(\theta),$$

where ρ is the distance of a field point from the fiber corner, and K_m 's are undetermined constants, to be obtained by angular matching with the 3-D FEM solution at one or two values of ρ , depending on whether there are one or two eigenvalues, S_m , respectively.

8.3 Angular Variation Matching

For the exposed fiber geometry (Fig. 8-1a) in the case of the Al/epoxy system, only one eigenvalue and one eigen function was obtained, such the order of the singularity was, $\lambda = s_m + 2 = 0.278$. Figure 8-2 illustrates the angular matching between the asymptotic and FEM results, the matching being performed at a value of ρ/r_f of 0.0773, where r_f is the fiber radius. In the case of the embedded fiber geometry, the problem was significantly more complicated by the presence of two roots, $s_1 = -1.789$ and $s_2 = -1.679$. Moreover, for $s_1 = -1.789$, there were two eigenfunctions, ψ_1 and ψ_2 . Physical considerations indicated that only one ψ was valid, and the resultant matching with FEM results are illustrated in Fig. 8-3.

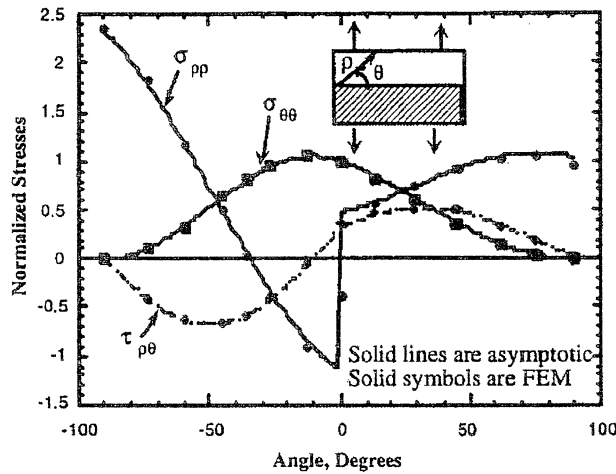


Fig. 8-2: Angular matching for the exposed fiber specimen

8.4 Stress Scaling Factor

Based on the full-field solution, the stress concentration factors were averaged over one r_f distance from the fiber ends. For the embedded fiber geometry, this averaging produced an effective bond strength that was in close agreement with the data from the cruciform geometry. For the exposed fiber specimen, the strength was still lower, and suggests that this geometry is unsuitable for fiber-matrix bond strength characterization.

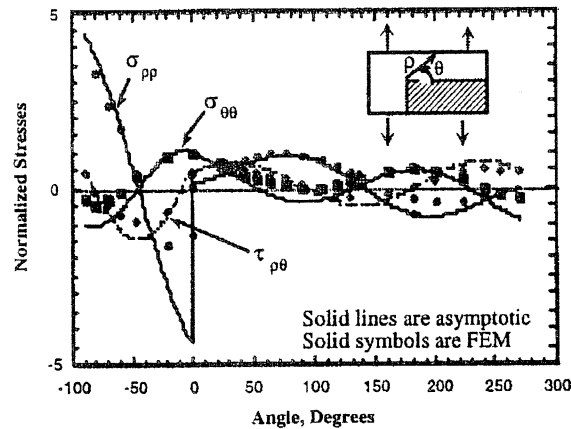


Fig. 8-3: Angular matching for the embedded fiber specimen

REFERENCES

- (1) B. S. Majumdar, "Interfaces in Metal Matrix Composites", *Titanium Matrix Composites*, S. Mall and T. Nicholas ed., Technomic Publications, pp. 113-168 (1997).
- (2) L. L. Shaw and D. B. Miracle, *Light Weight Alloys for Aerospace Applications III*, E. W. Lee, N. J. Kim, K. V. Jata and W. E. Frazer, ed., TMS, Warrendale, pp. 379-390 (1995).
- (3) D. B. Gundel, B. S. Majumdar, and D. B. Miracle, *Scripta Materialia*, 33, pp. 2057-2065 (1995).
- (4) G. P. Tandon, R. Y. Kim, S. G. Warrier, and B. S. Majumdar, "Influence of Free Edge and Corner Singularities on Interfacial Normal Strength: Application in Model Unidirectional Composites", *Composites, Part B: Engineering*, in press.
- (5) K. V. Pochiraju, A. C. Lau, and A. S. D. Wang, *Computational Mechanics*, 14, pp. 84-99 (1994).
- (6) D. B. Bogy, *ASME J. Applied Mechanics*, 38, pp. 377-386 (1971).

9.0 ANALYSIS OF THE END-NOTCHED FLEXURE SPECIMEN FOR MODE II TESTING USING VARIATIONAL METHODS

9.1 Introduction

A major source of failure in laminated composites is delamination along ply interfaces. An understanding of this behavior resides in an accurate characterization of the interlaminar fracture toughness. Tests for characterizing delamination include the double cantilever beam (DCB) for measuring the Mode I energy release rate, G_{Ic} , the end-notched flexure (ENF) specimen for measuring the Mode II energy release rate, G_{IIc} , and the end-loaded split (ELS) specimen for mixed-mode measurements.

The ENF specimen consists of a beam subjected to three-point bending with a mid-plane starter crack of desired length introduced at one end as shown in Fig. 9-1. A Mode II critical potential energy release rate is then determined by measuring the load and center deflection at the instant the starter crack propagates. Early analysis of the ENF specimen was based on simple beam theory solution by Russell and Street [1]. The beam theory solution was modified by Carlsson *et al* [2] to include the influence of interlaminar shear deformation. Subsequently, a higher order beam theory based on Reissner's variational principle was developed by Whitney [3] and the resulting field equations applied to the analysis of the ENF specimen. Additionally, Finite Element Analysis (FEA) of the ENF specimen has been performed by a number of investigators (e.g., [4 - 7]). In each of these studies significant departure from beam theory is observed over a range of values of crack length. The purpose of this study is therefore to assess the accuracy of the various solution techniques available in the literature for the analysis of the ENF specimen by using a more rigorous elasticity model.

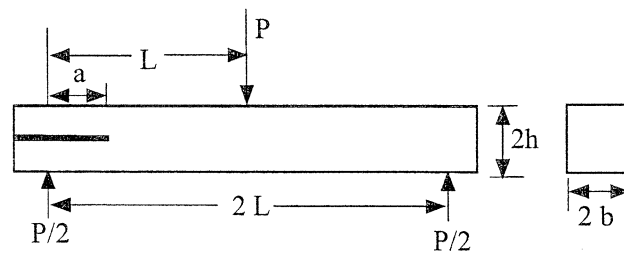


Fig. 9-1: Schematic of End-Notched Flexure Specimen

9.2 Methodology

In this work the ENF specimen is analyzed using the large radius axisymmetric damage model developed by Schoeppner and Pagano [8]. It has been shown that in the limit as the ratio of average cylinder radius R to laminate thickness T approaches infinity, the stress components and the governing equations of the large radius model are analytically equivalent to the flat laminate formulation. Using this methodology, an axisymmetric cylinder with $R \gg T$ is used to represent a flat laminate. Typical values of R/T used are in the range of 10^4 - 10^5 .

The Large Radius Axisymmetric Model (LRAM) is capable of handling discrete damage in the form of edge delamination, internal delamination and/or transverse cracking in flat laminates. Further, the material properties could be discontinuous across the laminate thickness, i.e., plies with different orthotropic material properties could be assembled in the thickness direction. This model was therefore ideally suited for the analysis of the ENF specimen. Figure 9-1 shows the configuration of the specimen with a through-width delamination at one end of the specimen. As shown in Fig. 9-1, a is the delamination length measured from the support, $2L$ is the specimen span, $2b$ is the width, and $2h$ is the thickness. Figure 9-2 shows the boundary conditions which were applied for LRAM and the coordinate convention, where z is along the specimen length and r is in the thickness direction. The concentrated load was simulated by a uniform distribution of radial stress, σ_r , over a small length, such that the resultant of the stress distribution was equivalent to the applied load. Similarly, the pin support reactions were simulated by constraining the radial displacement over a small support length while the shear traction was set equal to zero on all external boundaries. The computed potential energy release rate is sensitive to the support distance utilized in the analysis. Convergence studies were done by considering the support distance as a parameter until further variation resulted in negligible changes in the computed energy release rate values. Further, a pure mode II condition was simulated by constraining the crack faces to displace equally in the radial direction while smooth contact was maintained. The radial stress along the crack surfaces was found to be either compressive or very close to zero, as discussed later. For rigorous analysis friction needs to be considered. However, previous finite element solutions [5 - 7] have indicated that the effect of friction is to lower the energy release rate values, in general, by a small amount. Therefore, in the present

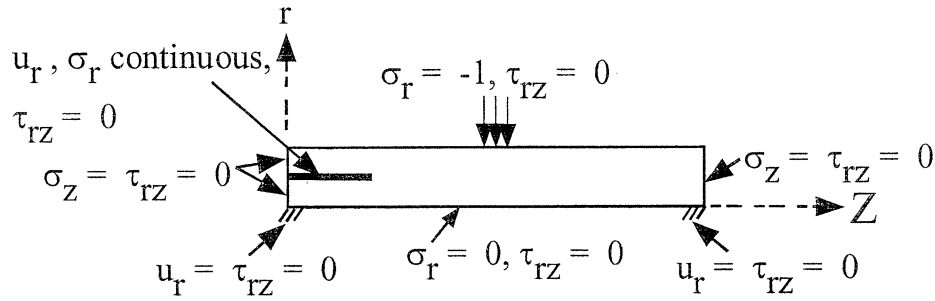


Fig. 9-2: Boundary conditions for analyzing ENF specimen

analysis, friction is neglected, i.e., smooth delamination faces are assumed.

The analytical model is generated by subdividing the body into regions consisting of a number of shells of constant thickness and length and satisfying the Reissner variational equation (1) with an assumed stress field in each region. That is, we set

$$\delta J = 0 \quad (1)$$

where

$$J = \int_V F \, dV - \int_{S'} \tilde{T}_i U_i \, dS \quad (2)$$

and

$$F = \frac{1}{2} \tau_{ij} (U_{i,j} + U_{j,i}) - W(\tau_{ij}, e_{ij}) \quad (3)$$

In these equations, W is the complementary energy, τ_{ij} and U_i are the stress and displacement components, respectively, in Cartesian coordinates, e_{ij} are the mathematical free expansional or non-mechanical strains, V is the volume enclosed by surface S , S' is the part of S on which one or more traction components are prescribed and \tilde{T}_i are the Cartesian components of the prescribed tractions. Further, a comma followed by a subscript(s) implies differentiation with respect to the appropriate coordinate(s) and the summation convention is understood. The regions are selected such that the thermoelastic properties are constant and the boundary conditions do not change character on any of the bounding surfaces within each region.

Reissner [9] has shown that the governing equations of elasticity can be obtained as a consequence of the variational equation provided both stresses and displacements are subject to variation in the application of (1). The stress field is assumed such that σ_{zz} and $\sigma_{\theta\theta}$ are linear in r within each region, while the forms of σ_{rr} and σ_{rz} are chosen to satisfy the axisymmetric

equilibrium equations of linear elasticity. The form of the boundary condition equations derived from the variational principle is given by Schoeppner and Pagano [8]. The general form of the solution for any of the dependent variables $P(z)$, namely, the stresses and weighted displacement components, is expressed by

$$P(z) = \sum_i A_i e^{\lambda_i z} + P_p(z) \quad (4)$$

within each constituent where A_i are constants, λ_i are eigenvalues of a determinant, and $P_p(z)$ is a particular solution, which in the present case is a simple polynomial. The number of regions, in particular in the radial direction, can be increased in order to improve the solution accuracy.

The potential energy release rate G then, is defined as

$$G = -d\Pi/dA \quad (5)$$

where P is the potential energy $U - W$, U is the strain energy, W is the potential energy of the prescribed tractions, and dA is the crack extension area. For analysis of the ENF specimen using LRAM, the potential energy release rate is evaluated directly using differentiation since the solution to the boundary value problem has an explicit exponential dependence along the crack length (see Eq. 4). The potential energy release rate can also be computed using various other techniques such as the virtual crack extension or virtual crack closure method. Numerical calculations for several geometry and material property combinations resulted in small differences between the various approaches.

9.3 Numerical Results and Discussion

As a numerical example, we consider the following case,

$$E_1 = 115.1 \text{ GPa}, E_3 = 9.7 \text{ GPa}, G_{13} = 4.48 \text{ GPa}, \nu_{13} = 0.3 \text{ and } L/h = 22.4$$

where 1 is the fiber direction aligned along z -axis and 2-3 is the transverse plane. These numbers are typical of graphite/epoxy unidirectional beams utilized in the ENF specimens. For analysis, the half-depth h is assumed equal to 1.7 mm while the beam half-span is taken equal to 38.1 mm. In Fig. 9-3, we have compared the Mode II potential energy release rate for various crack-length-to-semi-span ratios with available solutions [2-5, 23] from the literature. The reported values have been normalized with respect to the classical beam theory solution given by Russell and

Street [1], namely,

$$G_{II}^{\text{Beam theory}} = \frac{9 a^2 P^2}{64 E_1 b^2 h^3} \quad (6)$$

where E_1 is the effective bending modulus in the axial direction. This equation was modified by Carlsson *et al* [2] to include the effect of transverse shear deformation

$$G_{II}^{\text{CGP}} = \frac{9 a^2 P^2}{64 E_1 b^2 h^3} \left[1 + 0.2 \left(\frac{h}{a} \right)^2 \left(\frac{E_1}{G_{13}} \right) \right] \quad (7)$$

and subsequently improved by Whitney [3] using a higher order beam theory, where

$$G_{II}^{\text{W}} = \frac{9 a^2 P^2}{64 E_1 b^2 h^3} \left\{ 1 + \frac{2}{\lambda \bar{a}} + \frac{1}{60 \lambda^2 \bar{a}^2} \left[\lambda^2 \left(\frac{E_1}{G_{13}} \right) + 60 \right] \right\} \quad (8)$$

$$\lambda = 4 \sqrt{\frac{14 G_{13}}{5 E_1}}, \quad \bar{L} = L/h \quad \text{and} \quad \bar{a} = a/h \quad (9)$$

$$G_{II}^{\text{C}} = \frac{9 a^2 P^2}{64 E_1 b^2 h^3} \left[1 + 0.13 \left(\frac{E_1}{G_{13}} \right)^{1/2} \frac{h}{a} \right]^2 \quad (10)$$

Note that Eqs (8) and (9) reported in [3] have been corrected for their typographical errors. By comparing exact and approximate solutions of elastic laminates, Chatterjee [10] has derived a closed form expression for common graphite/epoxy composites

As seen in Fig. 9-3, the approximate shear deformation beam theory [2] yields up to 9 % lower G_{II} values whereas, the higher order beam theory [3] overestimates the results by up to 7 % for $a/L > 0.2$. For smaller values of crack length, the differences are even larger. It is found that both the classic beam theory solution [1] and the results of present analysis converge to zero value of energy release rate in the limit of infinitesimal crack length. However, both the shear deformation beam theory [2] and higher order beam theory [3] do not converge to zero value of energy release rate in the limiting case of zero crack length. Excellent agreement is seen between the results of present analysis and the finite element solution of Salpekar *et al* [4] using eight node isoparametric, parabolic elements. The smallest value of a/L reported, however, was 0.2.

(The finite element solution of Salpekar *et al* [4] was independently recovered by our own finite element analysis). Also, He and Evans [7] have reported good agreement between their finite element analysis using singular crack tip element and the results reported by Salpekar *et al* [4]. The approximate elasticity solution developed by Chatterjee [10] differs by less than 1 % for $a/L > 0.1$. On the other hand, the finite element results obtained by Gillespie *et al* [5] display a large discrepancy versus the other approaches. Furthermore, their results show an increase in normalized value of G_{II} with increasing values of a/L , while the other results show the opposite trend. Finally, note that all the solutions shown in Fig. 9-3 differ considerably from the classic beam theory solution [1] for short crack lengths.

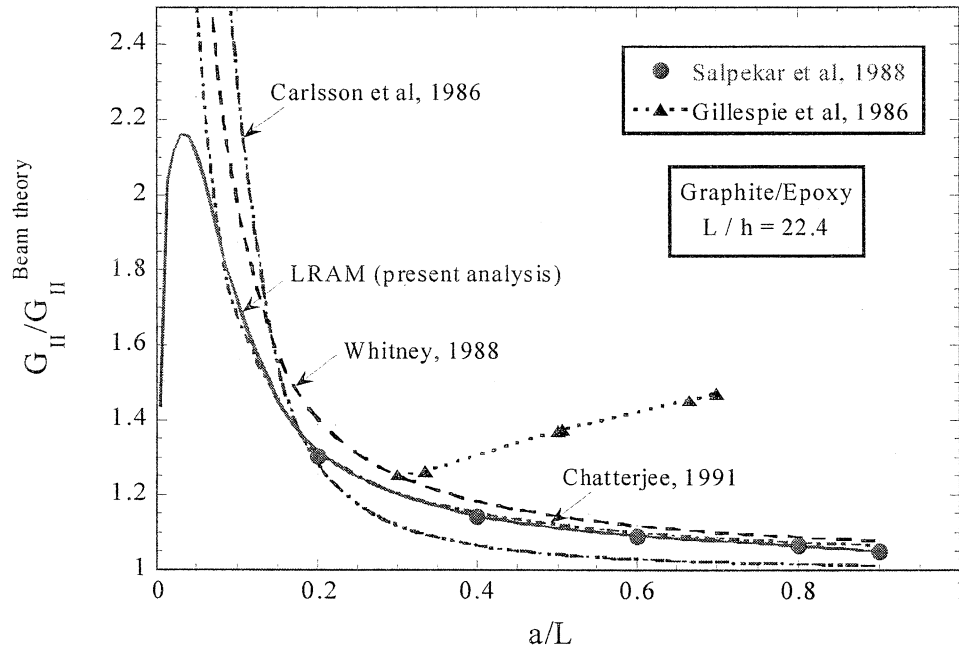


Fig. 9-3: Comparison of G_{II} from various analyses

Additionally, the deflection under a unit central concentrated load is equal to the compliance of the specimen. The compliance values predicted with LRAM, finite element analysis and those from the shear deformation beam theory are presented in Fig. 9-4. Again, all the reported values have been normalized with respect to the classical beam theory solution [1],

$$\delta^{\text{Beam theory}} = \frac{(2L^3 + 3a^3)P}{16E_1bh^3} \quad (11)$$

The shear deformation correction [2] to the classic beam theory solution is given by

$$\delta^{\text{CGP}} = \frac{(2L^3 + 3a^3)P}{16E_1bh^3} \left[1 + \frac{2(1.2L + 0.9a)h^2E_1}{(2L^3 + 3a^3)G_{13}} \right] \quad (12)$$

while the higher order beam theory solution [3] is given by

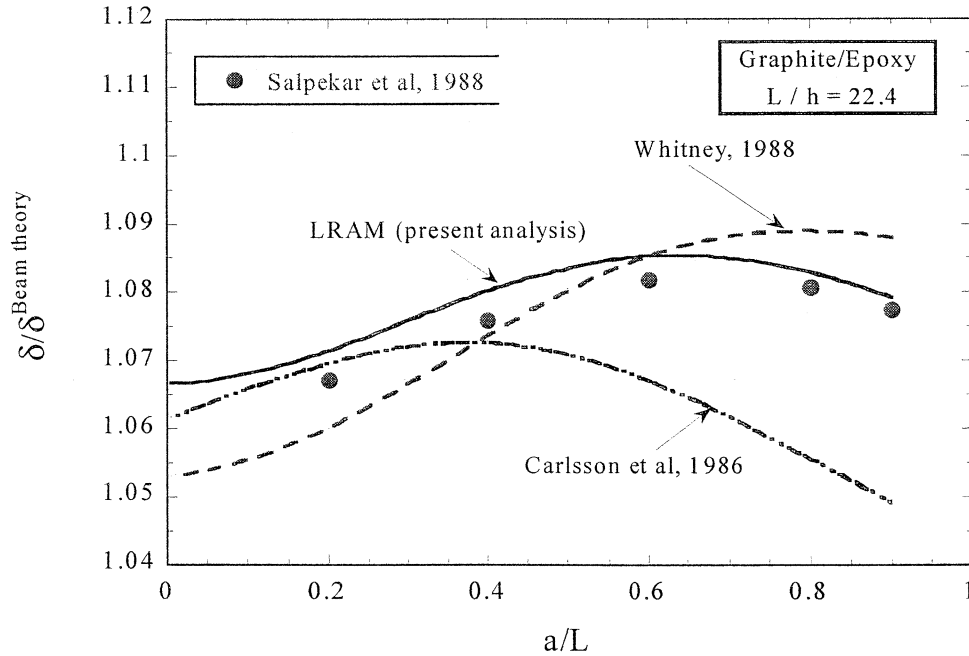


Fig. 9-4: Comparison of beam deflection from various analyses

$$\delta^w = \frac{P}{16E_1b} \left[2\bar{L}^3 + 3\bar{a}^3 + \frac{1}{340} (704\bar{L} + 51\bar{a}) \left(\frac{E_1}{G_{13}} \right) + \frac{9\bar{a}}{\lambda^2} (1 + \lambda\bar{a}) \right] \quad (13)$$

As seen in Fig. 9-4, the results of the present analysis agree with the finite element solution of Salpekar *et al* [4] reasonably well, while the beam theory solutions [2,3] differ considerably.

Next, we consider the beam to be a homogeneous isotropic material. This problem is

appropriate to study the mode II response of adhesively bonded specimens [11] provided the bond-line thickness is sufficiently small. A parametric study investigating the influence of delamination length, span, and thickness was conducted using the material properties of aluminum ($E=72.4$ GPa, $\nu=0.33$). Results from LRAM were independently verified by performing finite element analysis of the ENF specimen using ABAQUS [7] with second order, plane strain isoparametric (CPE8) elements. The crack faces were modeled using second order plane strain frictional interface (INTER3) elements. The interface elements could sustain only zero (in the case of an open crack) or compressive normal stress, σ_{nn} , while the shear stress, τ_{tz} , on the crack face was set equal to zero by using a zero coefficient of friction.

The finite element mesh designed for the ENF problem is shown in Fig. 9-5a. The regions surrounding the two bottom supports, the top loading point, and the crack tip were densely meshed, since the stresses changed rapidly with position in those areas. Typical meshes contained 2000 to 2500 elements with the larger meshes (2500 elements) required for models with a larger h . The focused mesh about the crack tip (see Fig. 9-5b) was held constant for all problems. The elements adjacent to the crack tip were $10\text{ }\mu\text{m}$ long which corresponds to a range of $0.02\% - 0.17\%$ of the crack length depending on the crack length modeled. The mesh density was considered adequate when further refinement of any portion of the model resulted in less than a 0.1% change in the energy release rate. Since friction was not modeled on the crack surface, the energy release rate could be calculated by obtaining the J integral. For computations we used 8 contours where each successive contour had an average radius about the crack tip of one element length greater than the last contour. The values for the outer 6 contours were consistently within 0.01% for all problems investigated.

Figure 9-6 shows the variation in normalized Mode II potential energy release rate with normalized crack length for two different values of span-to-thickness ratio, namely, $L/h = 4$ and 22.4 , the latter was the case examined earlier using the material properties of unidirectional graphite/epoxy composite. Reasonably good agreement is obtained between LRAM and FEM analyses for all cases considered, which gives us confidence in the reported solutions. However, it is seen that for L/h equals 22.4 (where $h=1.7$ and $L=38.1$ mm), the disparity between the present analysis and the beam theory solutions is greater if the beam is considered to be a

homogeneous isotropic material, e.g the shear deformation beam theory [2] and the higher order beam theory [3] now overestimate the results by up to 10 % and 15 %, respectively, for $a/L > 0.2$. Further, the present analysis predicts G_{II} values which are lower than the classic beam theory result [1] in this range of crack length for $L/h=22.4$. On the other hand, for the lower

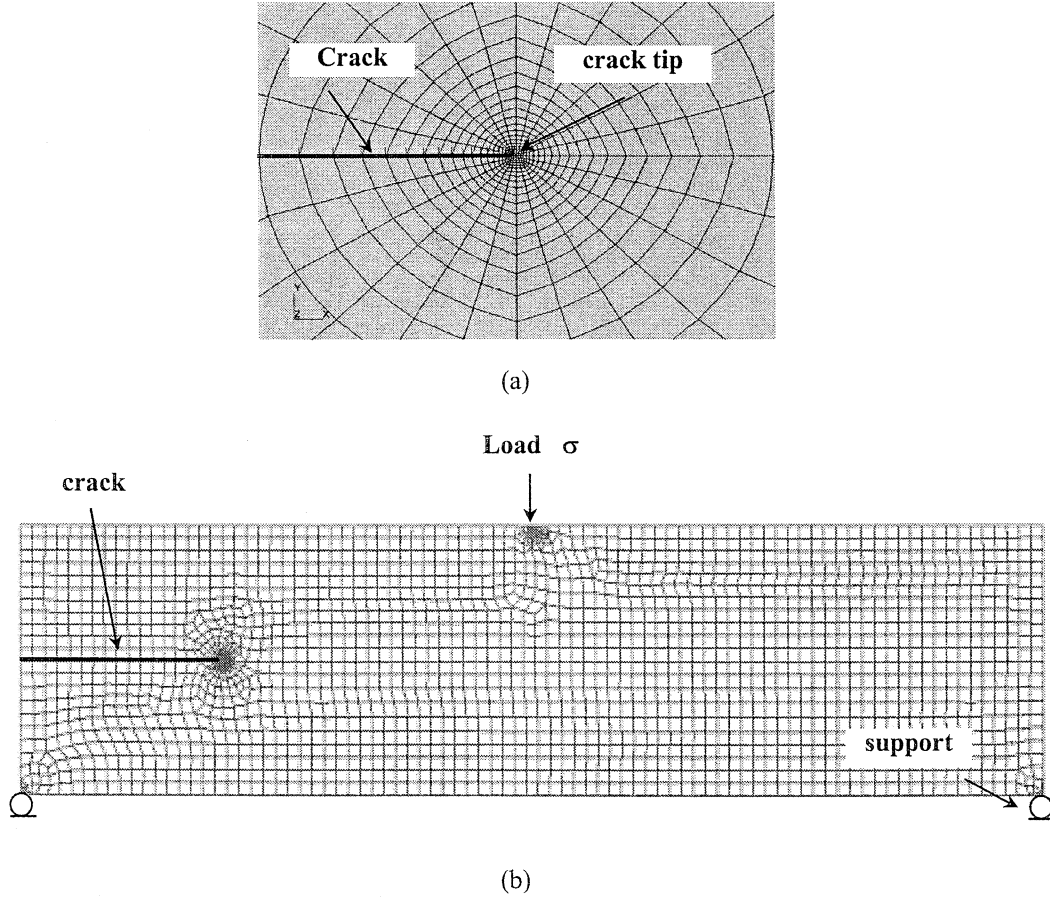


Fig. 9-5: ENF mesh and close up of focused crack tip mesh

span-to-thickness ratio, namely, $L/h = 4$, the present solution is found to be larger than the classic beam theory solution [1], while greater differences are obtained between the present analysis and modified beam theory solutions [15, 16]. These reported comparisons of potential energy release rate calculations, therefore, serve to establish the limits of applicability of beam theory expressions for analyzing the end-notched flexure specimen.

We also consider the interfacial stresses acting on the crack surfaces to explore the conditions under which the ENF specimen represents a pure Mode II response. As an example, we show in Fig.9-7 the interfacial stresses σ_r and τ_{rz} across the specimen length in the crack plane. We have

used the material properties of Aluminum with $a = 19.3$ mm, $h=1.7$ mm and $L=38.1$ mm for these calculations. Results from LRAM are compared with the finite element solution and show excellent agreement with each other. This is particularly significant in view of the fact that we had slightly different boundary conditions on crack surfaces for the two analyses. The shear stress was prescribed equal to zero in both solutions. However, in LRAM the crack faces were constrained to displace equally in the radial direction, thus, allowing for no crack opening, whereas, in finite element analysis, the radial stress determined whether the interface was in contact or open. Notice that the radial stress component is nearly zero along the mid-plane except near points of singularity or directly underneath the load nose. The variational model, LRAM, predicts a small tensile value of radial stress near the left end support which may be an artifact of the solution technique (notice that a similar peak is observed near the other support in both the solution techniques). The shear stress is singular at the crack tip with the characteristic inverse square root type singularity, although neither method explicitly recognizes the singularity, and is nearly uniform along the bonded portion of the specimen length. The

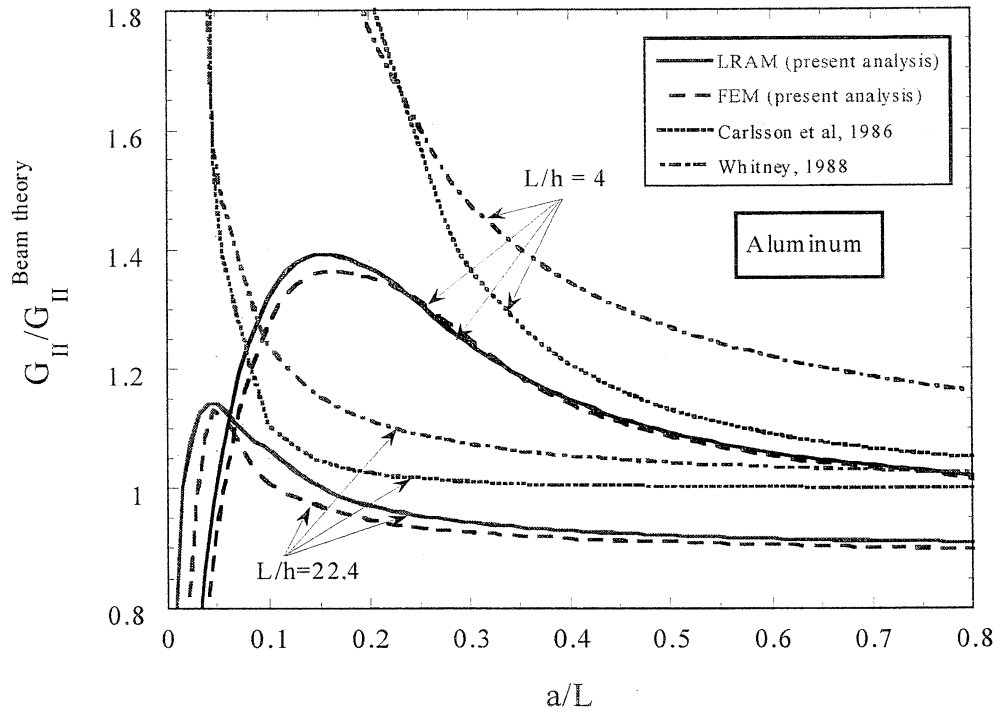


Fig. 9-6: Variation of G_{II} in an isotropic material

reported comparisons of the stress distributions shown in Fig. 9-7 give us confidence in using the ENF specimen to evaluate the mode II toughness of the interface. Similar stress distributions were obtained [12] for other crack length values, specimen dimensions and material properties utilized.

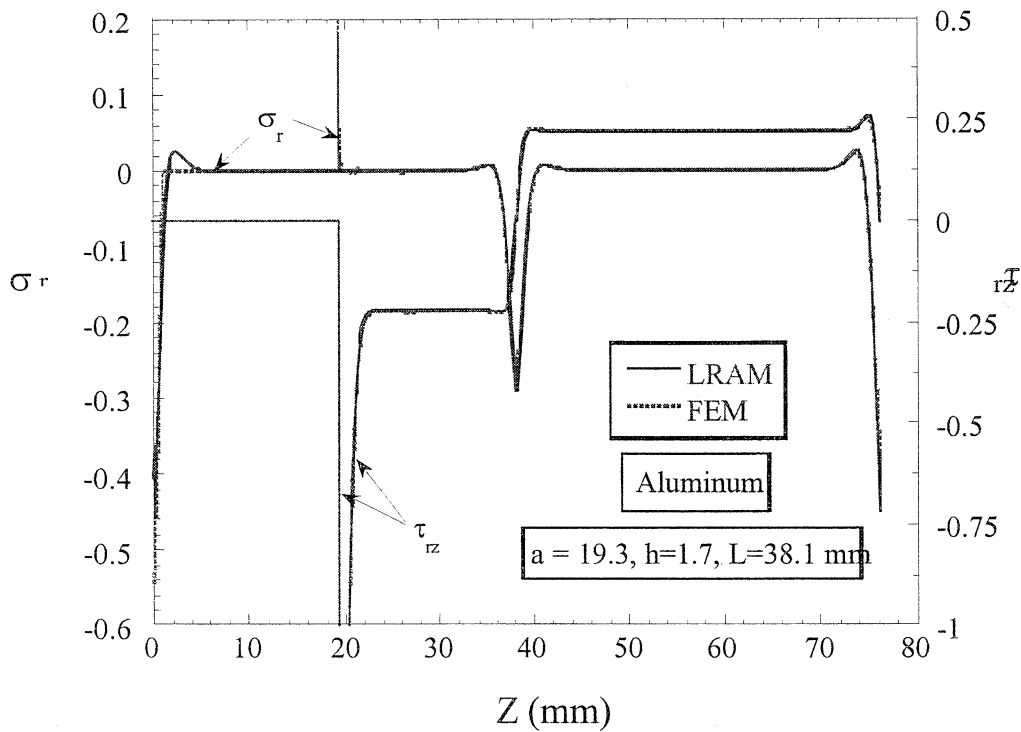


Fig. 9-7: Interfacial stresses across the specimen length in the crack plane

9.4 Summary

The end-notched flexure (ENF) specimen is analyzed in this study using LRAM and finite element analyses. An examination of the interfacial stresses acting along the crack surfaces reveals that the ENF specimen represents nearly a pure Mode II response if the crack surfaces are in smooth contact. Various approximate solutions available in the literature are assessed for their accuracy using the properties and dimensions of typical graphite/epoxy unidirectional beams. The results of the present analysis are seen to agree very well with the finite element solutions of Salpekar et al [4], He and Evans [7], and an approximate elasticity solution by Chatterjee [10]. However, both the shear deformation beam theory [2] and higher order beam theory [3] overestimate the Mode II energy release rate with the differences being larger at shorter crack

lengths. The discrepancies are even greater if the beam is considered as a homogeneous isotropic material (such as in the study of mode II response of adhesively bonded specimens [11] where the bond-line thickness is sufficiently small). These reported comparisons of potential energy release rate calculations therefore serve to establish the limits of applicability of beam theory and other approximate expressions for analyzing the ENF specimen.

REFERENCES

- (1) Russell, A. J. and K. N. Street. 1984. "Factors Affecting the Interlaminar Fracture Energy of Graphite/Epoxy Laminates," *Proc. 4th Int. Conf. On Composite Materials*, North Holland, Amsterdam, pp. 279-286.
- (2) Carlsson, L. A., J. W. Gillespie, and R. B. Pipes. 1986. "On The Analysis and Design of the End Notched Flexure Specimen for Mode II Testing," *J. Composite Materials*, **20**, pp. 594-604.
- (3) Whitney, J. M. 1988. "Analysis of The End-Notch Flexure Specimen Using a Higher Order Beam Theory Based On Reissner's Principle," *Proc. 3rd Conf. On Composite Materials*, American Society for Composites, Lancaster, Pa: Technomic Publishing Co. Inc., pp. 103-112. Also, Whitney, J. M., 1989. "Experimental Characterization of Delamination Fracture in Interlaminar Response of Composite Materials," N. J. Pagano, ed., Amsterdam: Elsevier Science Publishers B. V., pp. 213-223.
- (4) Salpekar, S. A., I. S. Raju, and T. K. O'Brein. 1988. "Strain Energy Release rate Analysis of the End-Notched Flexure Specimen Using The Finite Element Method," *J. Compos Techn. & Research*, **10**, pp. 133-139.
- (5) Gillespie, J. W., L. A. Carlsson, and R. B. Pipes. 1986. "Finite Element Analysis of the End Notched Flexure Specimen for Measuring Mode II Fracture Toughness," *Comp Science & Techn.*, **27**, pp. 177-197.
- (6) Mall, S. and N. K. Kochhar. 1986. "Finite Element Analysis of End-Notch Flexure Specimens," *J. Comp. Techn. & Research*, **8**, pp. 54-57.
- (7) He, M. Y. and A. G. Evans. 1992. "Finite Element Analysis of Beam Specimens Used to Measure the Delamination Resistance of Composites," *J. Comp. Techn. Res.*, **14**: 235-240.

- (8) Schoeppner, G. A. and N. J. Pagano. 1998. "Stress Fields and Energy Release Rates in Cross-Ply Laminates," *Int. J. Solids Structures*, **35**, pp. 1025-1055
- (9) Reissner, E. 1950. "On a variational theorem in elasticity," *J Math. Phys.* **29**, p. 90.
- (10) Chatterjee, S. N. 1991."Analysis of Test Specimens for Interlaminar Mode II fracture Toughness, Part 1. Elastic Laminates," *J. Comp. Matl.*, **25**, pp. 470-493.
- (11) Forte, M. 1999. "A Controlled Study of The Effects of Bondline Reinforcement on the Fracture Behavior of a Brittle Epoxy Adhesive," Ph.D. Thesis, Univ. of Dayton, OH.
- (12) Tandon, G. P., N. J. Pagano and V. T. Bechel, 1999. "Analysis of the End-Notched Flexure Specimen for Mode II Testing Using Variational Methods," *Proceedings of the American Society for Composites, 14th Technical Conference*, Technomic Publishing Co. Inc., pp. 265-274.
- (13) Tandon, G. P. and N. J. Pagano, 1998. "Micromechanical Analysis of Fiber Push-Out and Re-Push Test," *Comp Sci & Techn.*, **58**, No. 11, pp. 1709-1725

10.0 CHARACTERIZATION OF INTERFACIAL FRACTURE TOUGHNESS IN MODEL POLYESTER / EPOXY COMPOSITE SYSTEM

10.1 Introduction

The objective of the present study is to evaluate interfacial fracture toughness in a polyester/epoxy composite system. This model system was recently investigated by Bechel and Sottos [1] and Tandon and Pagano [2] in a push-out test. In [2], the *apparent* debond toughness of this composite system was defined using energy balance arguments during a critical finite crack extension. It was shown that as the debond propagates along the fiber-matrix interface, the force/displacement can be predicted by meeting the critical shear energy release rate criteria ($G_\tau = G_{\tau c}$, see [2] for further details). The aim of the present study is to provide an independent measure of the Mode II toughness of the polyester/epoxy interface and to correlate the fracture toughness value with the push-out data. To this effect, we have used the end-notch flexure (ENF) specimen as shown in Figure 10-1. In this test method, Mode II critical potential energy release rate (G_{IIc}) is determined using the load at the instant the starter crack propagates from the load-deflection data.

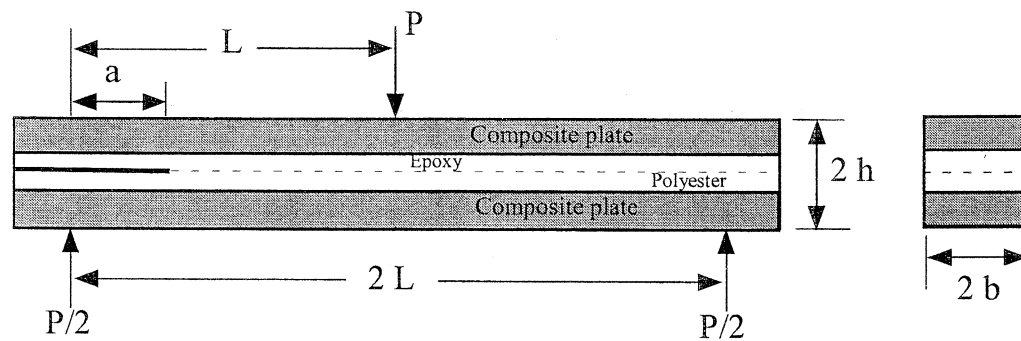


Figure 10-1. Schematic of End-Notched Flexure Specimen

10.2 Specimen Preparation And Testing

Model End-Notched Flexure specimens, consisting of polyester and epoxy rectangular plates (.01 inch thick) sandwiched between composite adherents (.09 inch thick), with a non-adhesive insert on the interface (mid plane) as a starter crack, were cast in a silicone rubber mold. The three-step process for fabricating the test specimens is illustrated in Fig 10-1. In step 1, the epoxy resin (Epon 828 from Shell Chemical Co.) is cured with polyetheramine (Jeffamine D-230

from Texaco, Inc.) for 72 hours at ambient temperature between risers placed on top of a quasi-isotropic plate of AS4/H3501-6 composite, which serves as a stiff adherent. Curing at ambient temperature eliminates thermal residual stresses that are otherwise induced from the mismatch in coefficients of thermal expansion. In step 2, a teflon insert approximately 1 inch long is placed on the cured epoxy plate at one end of the specimen. Finally, in step 3, risers are placed on top of the epoxy plate and polyester resin is poured within the mould and cured for 24 hrs at room temperature along with another composite plate on the outside.

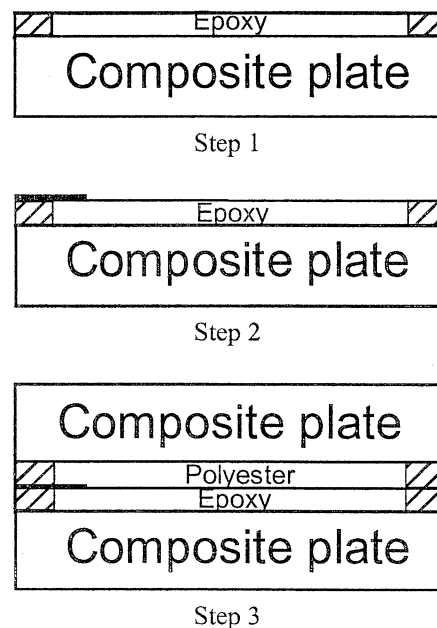


Figure 10-2. Three-step process for fabricating ENF specimens

A three point bending fixture with a total span of 5 inches is then installed in a load frame and tested in a displacement control mode. Crack propagation in the ENF specimen generally tends to be unstable. In this work it is found, in majority of the test specimens, that the use of composite adherents on the outside prevents the starter crack from jumping from the mid-plane to the outer interface while crack propagation is limited along the polyester/epoxy interface.

Loading is interrupted when the applied load reaches a maximum. At this point, the starter crack propagates up to an inch along the interface. The load-deflection response shows some non-linearity. For each test specimen, the point of crack initiation is defined by the crossing of the load-displacement curve with the slope at origin minus 5 % as shown in Fig 10-3. This offset

method is utilized in this study for identification of critical load at the instant the starter crack propagates.

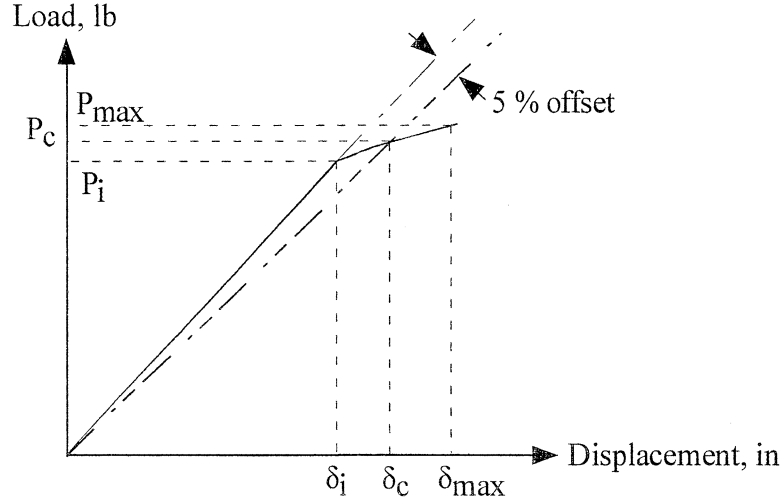


Fig. 10-3: Schematic of a typical load-displacement response from the test.

10.3 Analytical Modeling

Early analysis of the ENF specimen was based on simple beam theory solution by Russell and Street [3]. The beam theory solution was modified by Carlsson et al [4] to include the influence of interlaminar shear deformation. Subsequently, a higher order beam theory based on Reissner's variational principle was developed by Whitney [5] and the resulting field equations applied to the analysis of the ENF specimen. These analyses are however restricted to homogeneous orthotropic beams. In this study, the end-notch flexure specimen is analyzed using the large radius axisymmetric damage model (LRAM) by Schoeppner and Pagano [6]. It has been shown that in the limit as the ratio of average cylinder radius R to laminate thickness T approaches infinity, the stress components and the governing equations of the large radius model are analytically equivalent to the flat laminate formulation. The variational model [6] is also capable of handling the material variation (or discontinuity) across the beam thickness and is capable of handling discrete damage in the form of edge delamination, internal delamination and/or transverse cracking in flat laminates. This model was therefore ideally suited for the analysis of the proposed ENF specimen. For modeling purposes, the concentrated load was simulated by a uniform distribution of radial stress, σ_r , over a small length, such that the resultant

of the stress distribution was equivalent to the applied load. Similarly, the pin support reactions were simulated by constraining the radial displacement over a small support length while the shear traction was set equal to zero on all external boundaries. Further, a pure mode II condition was simulated by constraining the crack faces to displace equally in the radial direction while smooth contact was maintained.

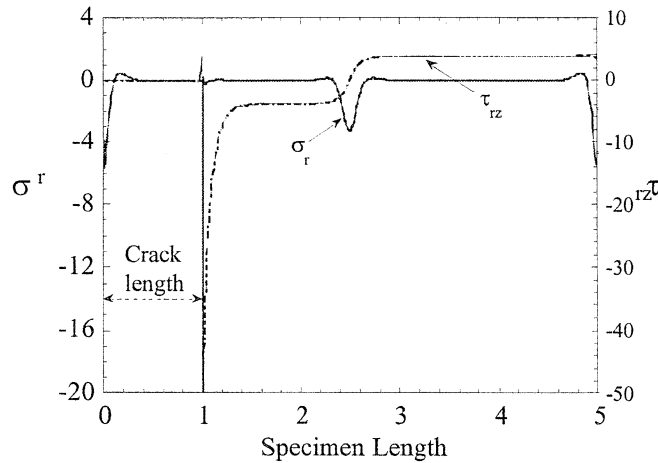


Fig. 10-4: Contact stresses along specimen

We first consider the contact stresses acting on the crack surfaces and along the crack plane to explore the conditions under which the ENF specimen represents a pure Mode II response. Figure 10-4 shows the variation of the normal and shear stress components along the specimen length in the crack plane. For the results shown in Fig. 10-4, the crack length, a , was set equal to 1 while the specimen length between supports, $2L$, was equal to 5. Notice that the normal stress component is nearly zero along the mid-plane except near points of singularity or directly underneath the load nose. The variational model predicts a small tensile value of radial stress near the left end support which may be an artifact of the solution technique (notice that a similar peak is observed near the other support). The shear stress is singular at the crack tip with the characteristic inverse square root type singularity, although the variational method does not explicitly recognize the singularity, and is nearly uniform along the bonded portion of the specimen length. The stress distributions shown in Fig. 10-4 therefore give us confidence in using the ENF specimen to evaluate the mode II toughness of the interface.

Next, the variational method is utilized to evaluate the potential energy release rate. This computation is performed directly using differentiation of the potential energy since the solution to the boundary value problem has an explicit exponential dependence along the crack length. The computed potential energy release rate is sensitive to the support distance utilized in the analysis as shown in Fig. 10-5. Convergence studies were done by considering the support distance as a parameter in conjunction with layer refinement to improve the solution accuracy until further variation resulted in negligible changes in the computed energy release rate values.

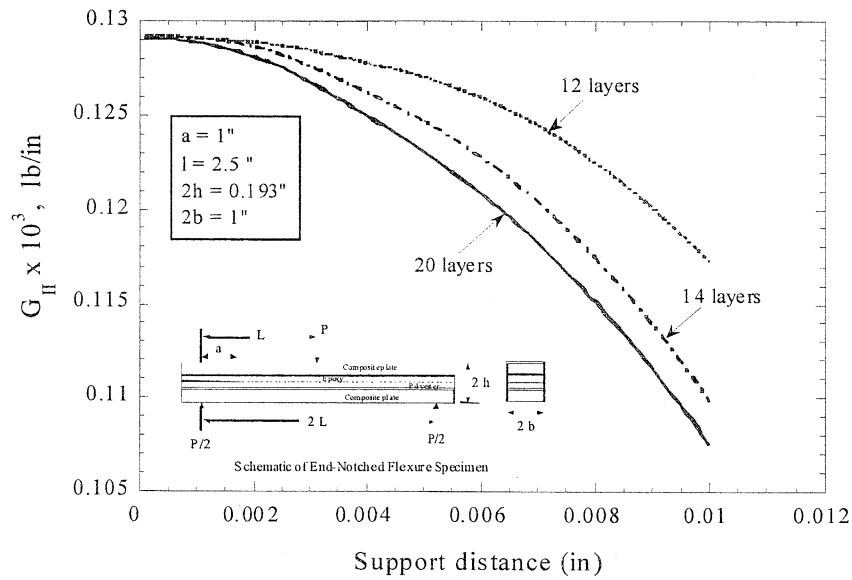


Fig. 10-5: Variation in potential energy release rate with support distance and layer refinement

Figure 10-6 shows the comparisons for various crack-length-to-semi-span ratios (ranging from 0.1 to 0.9) with the beam theory equations under a unit applied load. The comparative solutions using beam theory equations (1 – 3) were obtained using rule of mixtures computed effective modulus. The reported comparisons of potential energy release rate calculations serve to establish the limits of applicability of beam theory expressions for analyzing the end-notched flexure specimen using homogenized beam modulus.

10.4 Experimental Results

As mentioned earlier, crack propagation in the ENF specimen generally tends to be unstable.

Figure 10-7 is a schematic of the various failure paths observed [7] in the 3-point flexure testing of polyester/epoxy composite system. As shown in Fig.10-7a, the use of composite adherents on

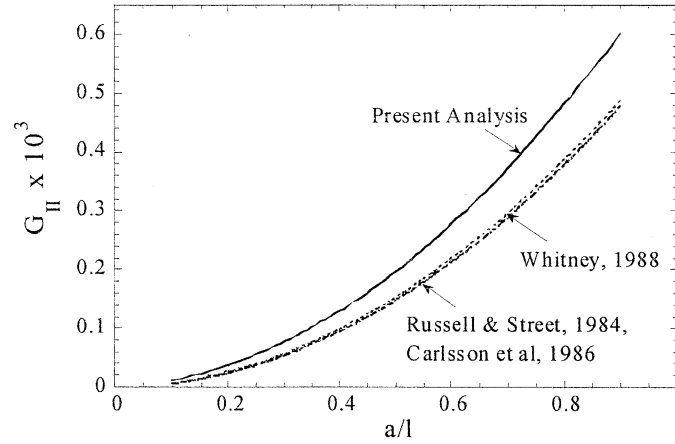


Fig. 10-6. Variation of G_{II} with crack length

the outside prevents the starter crack from jumping from the mid-plane to the outer interface while crack propagation is limited along the polyester/epoxy interface. This is the desirable failure mode since we are interested in evaluating the toughness of the polyester/epoxy interface. Majority of the specimens tested in this study fail in this particular manner. However, specimen failure is not always restricted to this configuration alone. Figures 10-7b-d are some of the other failure paths observed in this work and show crack jumping/deflection from the mid-plane to the outer interface. Experimental data from the specimens that fail in the configuration other than shown in Fig. 10-7a is therefore not included in the results reported here.

10.5 Data Reduction & Discussion

Mode II potential energy release rate (G_{II}) is then determined using the beam theory [3] and variational [6] analyses. The classical beam theory solution for G_{II} obtained by Russell and Street [4] is given by

$$G_{II}^{Beam\ theory} = \frac{9a^2 P_c^2}{4b(2L^3 + 3a^3)} \frac{\delta}{P} \quad (1)$$

where a is the delamination length measured from the support, $2L$ is the specimen span, $2b$ is the width, δ/P is the measured slope from the load-displacement data and P_c is the critical load at the

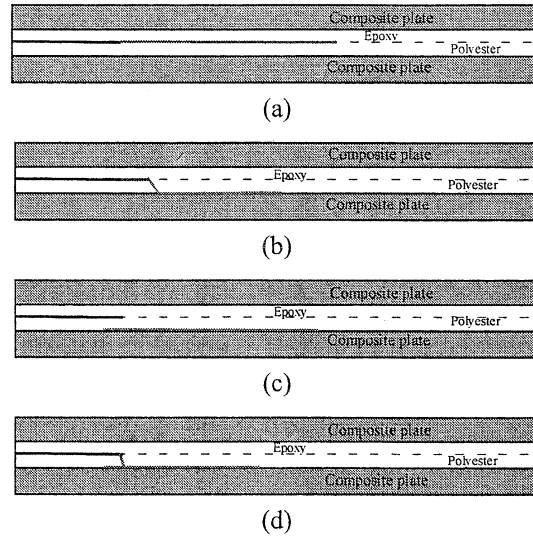


Fig. 10-7: Schematic of the observed failure paths in polyester-epoxy-composite system

instant the starter crack propagates. Alternately, the compliance calibration method (CCM) can be employed to determine the energy release rate that is given by

$$G_{II}^{CCM} = \frac{3ma^2 P_c^2}{4b} \quad (2)$$

where δ_i and P_i are the measured deflection and load level recorded for several values of

$$m = \frac{\delta_i / P_i}{a_i^3} \quad (3)$$

delamination length, a_i . For the variational model [6], potential energy release rate G (equal to G_{II} for ENF specimen) is defined as

$$G = -d\Pi/dA \quad (4)$$

where Π is the potential energy $U - W$, U is the strain energy, W is the potential energy of the prescribed tractions, and dA is the crack extension area. Table 10-1 is a summary of the limited test data along with the computed values of energy release rates using the three methods outlined here.

As seen in Table 10-1, there is a large amount of scatter in the computations with the compliance calibration method predicting the largest values of G_{II} and the variational analysis

providing the most conservative estimates. Nevertheless, the average value of G_{II} with the present analysis (2.1 lb/in) is still considerably larger than the value of $G_{tc} = 0.4$ lb/in which was used to predict the progressive debonding of the polyester/epoxy interface in the push-out test [2]. The reason for this discrepancy is not clear at present though several issues come to mind such as sample preparation, influence of surface roughness, effect of adherent, planar versus curved interface and mode mixity under combined loading in the push-out test. The experimental data is also rather limited and has a large scatter with inconsistency between beam theory data reduction techniques, namely, using the critical load at onset of crack propagation versus compliance calibration method. Finally, we need to resolve the issue of whether the Mode II toughness, G_{II} , measured in a ENF test is the same as the critical value of the shear energy release rate, G_{tc} , in the push-out test. Obviously, there are several unanswered questions at present which need further investigation. We are also in the process of testing some more test specimens which should reduce the scatter in the data and narrow the error range in the predictions.

Table 10-1. Summary of test data and computed G_{II} values

Specimen #	Width, 2b (in)	Thickness, 2h (in)	Length, 2L (in)	Mode II Energy Release rate, lb/in		
				Compliance Calibration Method	Beam Theory	LRAM (present analysis)
1	1.006	0.193	5	4.782	3.295	3.102
2	1.007	0.193	5	3.491	2.405	2.267
3	1.012	0.193	5	2.482	1.954	1.620
4	1.013	0.193	5	2.392	1.883	1.563
5	0.994	0.233	4	4.672	3.244	1.922
Average	-	-	-	3.564	2.556	2.095

REFERENCES

- (1) Bechel, V. T. and Sottos, N. R., 1998, "Application of Debond Length Measurements to Examine the Mechanics of Fiber Pushout," *J of Mechanics and Physics of Solids*, **46** [9], pp. 1675-1697.
- (2) Tandon, G. P. and N. J. Pagano, 1998. "Micromechanical Analysis of Fiber Push-Out and Re-Push Test," *Comp Sci & Techn.*, **58**, No. 11, pp. 1709-1725
- (3) Russell, A. J. and K. N. Street. 1984. "Factors Affecting the Interlaminar Fracture Energy of Graphite/Epoxy Laminates," *Proc. 4th Int. Conf. On Composite Materials*, North Holland, Amsterdam, pp. 279-286.
- (4) Carlsson, L. A., J. W. Gillespie, and R. B. Pipes. 1986. "On The Analysis and Design of the End Notched Flexure Specimen for Mode II Testing," *J. Composite Materials*, **20**, pp. 594-604.
- (5) Whitney, J. M. 1988. "Analysis of The End-Notch Flexure Specimen Using a Higher Order Beam Theory Based On Reissner's Principle," *Proc. 3rd Conf. On Composite Materials*, American Society for Composites, Lancaster, Pa: Technomic Publishing Co. Inc., pp. 103-112. Also, Whitney, J. M., 1989. "Experimental Characterization of Delamination Fracture in Interlaminar Response of Composite Materials," N. J. Pagano, ed., Amsterdam: Elsevier Science Publishers B. V., pp. 213-223.
- (6) Schoeppner, G. A. and N. J. Pagano. 1998. "Stress Fields and Energy Release Rates in Cross-Ply Laminates," *Int. J. Solids Structures*, **35**, pp. 1025-1055
- (7) Tandon, G. P. and R. Y. Kim, 1999. "Analysis and Characterization of Interfacial Fracture Toughness in Model Composite," *Proceedings 6th International Conference on Composites Engineering*, David Hui, ed., Orlando, Florida, June 27 - July 3, (1999) pp. 827-828.

11.0 MICROMECHANICAL RESPONSE OF A MULTI-PHASE COMPOSITE

11.1 Introduction

The objectives of this mechanics effort are to support the development of a revolutionary turbine burner in the areas of material selection and analytical modeling. Specifically, we initially consider an oxide-oxide composite consisting of 2D reinforcement (Nextel 610 or 720 fibers) in a matrix consisting of alumina particles, voids, inherent cracks due to the processing conditions, and a silica bonding agent. Predicted quantities include the thermomechanical effective moduli, thermal conductivity tensor, phase stresses, and damage due to processing and service loading conditions. Initial work will focus on elastic behavior while subsequent research will treat the composite creep response. The effective composite properties, in turn, will serve as input parameters in a 3D FEM to analyze the stress fields in the turbine burner under operational conditions (this work will be done by others). A feedback loop between the FEM and the micromechanical model will be established to define the evolution of the service-induced damage. The overall program objectives are to establish the scientific knowledge needed to develop an ultra-compact, high-energy-density turbine burner that will enable aero propulsion systems to operate on a constant temperature cycle and also to establish a science-based methodology in which the development of new hot section components (turbine burner) and the enabling materials evolve through interactive studies that couple the component, structure, and material requirements.

The basic research issues in mechanics include the model details for such a complex multi-phase composite material. In particular, calculation of phase stresses as well as “homogenized” matrix properties, and the resulting failure initiation and fracture mechanics laws to govern crack distribution. The homogenized matrix properties are of concern from both theoretical and experimental viewpoints. For example, no experimental samples of the multi-phase matrix exist. In fact, it is not known whether such specimens are even possible to manufacture in any cost-effective manner. It is therefore essential to determine the moduli and strength properties of the matrix by analysis and correlate these predictions with experimental observations of stiffness and damage in the *composite* material. The scale at which this modeling can be successfully accomplished is not known *apriori* and will pose severe challenges to the experimentalist as

well. Fortunately, previous work funded by AFOSR has provided us with a good background in studying microfracture theoretically and conducting the detailed experiments to query the quality of the predictions in a realistic manner.

11.2 Methodology

The approach will follow a building block scenario in which the microstructure is homogenized at various levels depending on the particular quantities being sought. Firstly, the effective moduli of the multi-phase matrix material will be computed by use of a three-phase version of the Mori-Tanaka scheme [1-3]. These results will also be compared with multi-level representations of particles, voids, and binder possible with the NDSANDS [4] model. Secondly, the effect of yarn crimp on the 3D effective moduli of a composite will be determined by comparison of a fabric reinforcement model [5] with that for a cross-ply laminate and also with the straight-fiber micromechanical stiffness model NDSANDS. The homogenized matrix moduli will be assumed in this comparison. Since the as-processed composite is known to contain a fairly well defined distribution of cracks normal to the fiber directions, we next determine the effective moduli of a damaged ply using the known crack spacing in the Schoeppner-Pagano [6] model and the moduli from Pagano's [7] 3D exact laminate elasticity theory. Finally, the two cracked layers are assembled and the moduli computed from the exact laminate theory and also by volume averaging of the stiffness and compliance tensors. These are upper and lower bounds of the moduli and are free from the bias caused by a lamination scheme. It is these results which can be compared to experiment. They are also used to assess the quality of the various assumptions invoked in the calculations and to define the influence of the damage on the effective moduli. This modeling approach can be shown to produce very good agreement with the experiments for effective moduli, however, the prediction of phase stress distributions is not expected to be accurate. In order to calculate more accurate phase stresses so that the failure characteristics can be predicted, we replace the previous layer models with a concentric cylinder model [8] in which the distinct fiber and homogenized matrix phases are recognized, along with a micromechanical representation of the damage. The latter damage mode consists of fiber-matrix debonding coupled with matrix cracks emanating from the debond tips. This model will provide a more accurate prediction of the stresses in the fibers and "homogenized" matrix and can also be checked for consistency with the damage observations. It will also permit one to

return to the undamaged homogenized matrix and estimate an upper bound on the residual stress state leading to cracking. Thus, a true strength property of the homogenized matrix will have been established. If the details of the local cracks can be established at the particle, void, and binder scale, we hope to formulate an effective field model in which the stress in the weakest (most likely the binder) constituent can be estimated. If correlations with experiment are successful, we will be in a position to vary the composition and/or ratios of constituents to provide improved performance. Some of these steps will now be demonstrated below as significant results.

11.3 Results & Discussion

Based on Mori and Tanaka's concept of "average stress" in the matrix and Eshelby's solution of an ellipsoidal inclusion, an approximate theory was developed by Weng [1] to evaluate the overall moduli of a general multiphase, anisotropic composite with arbitrarily oriented anisotropic inclusions. For the material system under consideration, the "homogenized matrix" consists of stiff alumina particles finely dispersed in silica. Additionally, the matrix has a significant amount of porosity. We will assume that both the alumina particles and the pores are spherical in shape and evaluate the elastic properties of the effective matrix (i.e., alumina + voids in silica) using the expressions developed by Weng [1]. The solutions to the effective coefficient of thermal expansion of the three-phase solid and effective thermal conductivity of a multiphase isotropic composite, are given by Pan and Weng [2] and Norris [3], respectively, using the Mori-Tanaka approximation. Using the material properties of alumina ($E=310$ GPa, $\nu=0.15$, $\alpha=8.5 \times 10^{-6}/^\circ\text{C}$, $\mu=10$ W/m-K) and silica ($E=72$ GPa, $\nu=0.16$, $\alpha=0.5 \times 10^{-6}/^\circ\text{C}$, $\mu=1.75$ W/m-K), the effective matrix properties are evaluated as,

$$E_m = 69.8 \text{ GPa}, \nu_m = 0.18, \alpha_m = 7.44 \times 10^{-6}/^\circ\text{C}, \mu_m = 2.66 \text{ W/m-K}$$

using particle and void content of 0.52 and 0.34, respectively, in the matrix.

The fabric itself is an 8 Harness satin which could be approximated by a cross-ply laminate. Pagano and Tandon [4] have developed a theoretical model to approximate the thermo-elastic response of multi-directional coated fiber composites. In order to employ their model, we will approximate the 8 Harness fabric by orienting the fiber tows in 0 and 90 degree orientations in the cross-sectional plane of the effective matrix, the properties of which have been earlier

determined. Assuming that no initial damage is present and using $E_f=262$ GPa, $\nu_f=0.25$, $\alpha_f=6.0$ e-6/ $^{\circ}$ C, $\mu_f=6.5$ W/m-K, for Nextel 720 fiber, we evaluate the following properties for the undamaged fabric,

$$E_x = E_y = 136.3 \text{ GPa}, E_z = 116 \text{ GPa}, \nu_{xy}=0.1859, \nu_{xz} = \nu_{yz} = 0.2130$$

$$G_{xy} = 49.42 \text{ GPa}, G_{xz} = G_{yz} = 48.75 \text{ GPa}, \alpha_x = \alpha_y = 6.502 \text{ e-6}/^{\circ}\text{C}, \alpha_z = 6.719 \text{ e-6}/^{\circ}\text{C}$$

$$\mu_x = \mu_y = 4.141 \text{ W/m-K and } \mu_z = 3.895 \text{ W/m-K}$$

where x-y is the fabric plane and z is the thickness direction, and the fiber volume fraction is 0.45. These computed thermo-elastic constants using NDSANDS [4] are in very good agreement with the analytical results of Naik [5], where the actual fiber architecture is considered in a unit cell, thereby, supporting our approximation of the 8 Harness satin weave. The in-plane properties also agree with the classical lamination plate theory results where the fabric composite is approximated as a $[0/90]_s$ laminate. The experimental measurements are:

$$E_x = 80 \text{ GPa}, \nu_{xy} = .05 - .08, G_{xy} = 15 - 23 \text{ GPa}, \alpha_x = 6.2 \text{ e-6}/^{\circ}\text{C}$$

so that the stiffness predictions are much too high. However, on close examination, extensive damage in the form of transverse matrix cracking is observed (see Fig.11-1). This is simulated

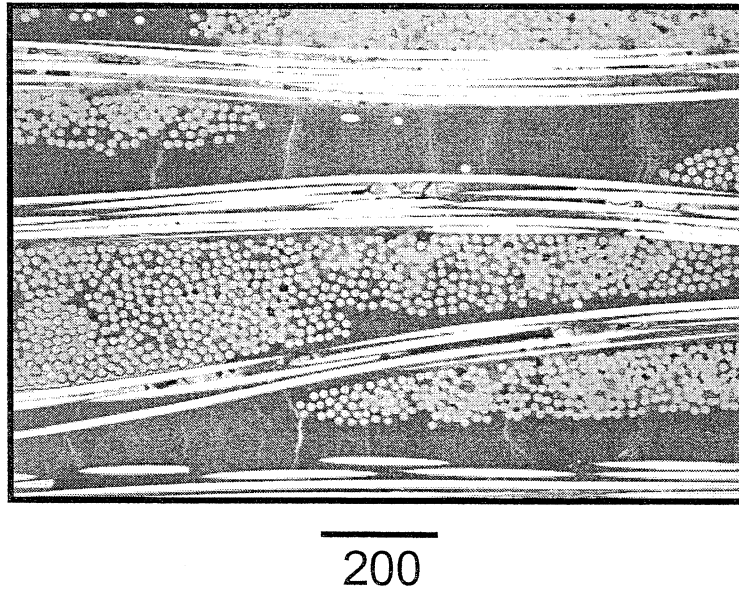


Fig. 11-1: SEM micrograph showing extensive matrix cracking in as-processed fabric

using Large Radius Axisymmetric Damage Model [6] for the average crack spacing observed in the interior ply of a cross-ply laminate:

$$\begin{aligned} E_x &= 90.4 \text{ GPa}, E_y = 136.18 \text{ GPa}, E_z = 115.98 \text{ GPa}, \nu_{yx} = 0.1687, \nu_{zx} = 0.1704, \\ \nu_{yz} &= 0.2124, G_{xy} = 34.53 \text{ GPa}, G_{xz} = 43.29 \text{ GPa}, G_{yz} = 48.75 \text{ GPa}, \\ \alpha_x &= 6.41 \text{ e-6/}^\circ\text{C}, \alpha_y = 6.50 \text{ e-6/}^\circ\text{C}, \alpha_z = 6.72 \text{ e-6/}^\circ\text{C} \end{aligned}$$

Using the 3-D Lamination Theory [7] to evaluate the effective properties of the damaged ply, we get

$$\begin{aligned} E_L &= 156.4 \text{ GPa}, E_T = 21.99 \text{ GPa}, E_z = 115.9 \text{ GPa}, \nu_{LT} = 0.2185, \nu_{Lz} = 0.2185, \\ \nu_{Tz} &= 0.0391, G_{LT} = 19.64 \text{ GPa}, G_{Lz} = 49.45 \text{ GPa}, G_{Tz} = 38.51 \text{ GPa}, \\ \alpha_L &= 6.33 \text{ e-6/}^\circ\text{C}, \alpha_T = 6.67 \text{ e-6/}^\circ\text{C}, \alpha_z = 6.76 \text{ e-6/}^\circ\text{C} \end{aligned}$$

The damaged plies are now arranged in a $[0/90]_s$ orientation to obtain effective laminate properties:

$$\begin{aligned} E_x &= E_y = 89.54 \text{ GPa}, E_z = 115.94 \text{ GPa}, \nu_{yx} = 0.0539, \nu_{zx} = 0.1682, \\ \nu_{yz} &= 0.1299, G_{xy} = 19.64 \text{ GPa}, G_{xz} = G_{yz} = 43.30 \text{ GPa}, \\ \alpha_x &= \alpha_y = 6.38 \text{ e-6/}^\circ\text{C}, \alpha_z = 6.76 \text{ e-6/}^\circ\text{C} \end{aligned}$$

which are in good agreement with the experimental measurements.

11.4 Summary

From the mechanics viewpoint, success of our effort will provide the Air Force with the analytical tools and experimental protocol to enact true composite material design for high temperature applications. Aside from the oxide-oxide class of composites (or possibly another form of ceramic matrix composite), the methodology will also be appropriate for application to structural carbon-carbon composites which have numerous functions in thermal protection systems and other space vehicle applications. In terms of the overall program itself, if successful, it will provide a key technology essential for the development of a propulsion system that operates on a constant temperature (CT) cycle -- an ultra-compact combustion system that will efficiently add heat between the turbine stages and is constructed of advanced, light-weight

composite materials. The lack of an ultra-compact turbine burner constructed of high temperature materials has been the major obstacle to the development of a propulsion system operating on a CT cycle.

REFERENCES

- (1) Schoeppner, G. A. and N. J. Pagano. 1998. "Stress Fields and Energy Release Rates in Cross-Ply Laminates," *Int. J. Solids Structures*, **35**, pp. 1025-1055
- (2) Weng, G. J., 1984. "Some Elastic Properties of Reinforced Solids, With Special Reference to Isotropic Ones Containing Spherical Inclusions," *Int. J. Engng Sci.*, **22**[7], pp. 845-856
- (3) Pan, H. H and Weng, G. J., 1992. "Thermal Stress and Volume Change During a Cooling Process Involving Phase Transformation," *J. Thermal Stress*, **15**, pp. 1-23.
- (4) Norris, A. N., 1989. "An Examination of the Mori-Tanaka Effective Medium Approximation for Multiphase Composites," *J. Applied Mechanics*, **56**, pp. 83-88.
- (5) Pagano, N. J. and Tandon, G. P., 1988. "Elastic Response of Multi-Directional Coated Fiber Composites," *Comp. Sci & Techn.*, **31**, pp. 273-293.
- (6) Naik, R. A., 1994, "Analysis of Woven and braided fabric reinforced Composites," NASA Contractor Report 194930, NASA Langley Research Center, Hampton, VA.
- (7) Pagano, N. J., 1974. "Exact Moduli of Anisotropic Laminates," in *Composite Materials*, L. J. Broutman and R. H. Krock eds., Vol. 2: *Mechanics of Composite materials*. G. P. Sendeckyj, ed., pp. 23-44.
- (8) Pagano, N. J. and G. P. Tandon, 1994. "2-D Damage Model for Unidirectional Composites Under transverse tension and/or Shear," *Mechanics of Composite Materials and Structures*, **1**, pp. 119-155

PART B

MACROMECHANICS

1.0 THREE-DIMENSIONAL VARIATIONAL THEORY OF MOSAIC COMPOSITE STRUCTURES

1.1 Introduction

A generalized theory aimed at three-dimensional (3-D) stress analysis of composite structures is presented in this section. The generalization of the theoretical development has been performed in three directions:

- (i) considering arbitrary *irregular* assemblage of the bricks, not necessarily a complete mosaic parallelepiped;
- (ii) obtaining all equations for the general case of anisotropy, so as any of the bricks could be characterized by 21 independent elastic constants;
- (iii) elaborating the variational equations, internal and external boundary conditions for a single brick for the full mosaic body.

The theory presented in this section is allowing to apply any set of basis functions (various types of polynomials, power series, trigonometric functions, etc.) which may be chosen independently for each coordinate direction and each displacement component. In Section 2 this theory will be specified for the case of Bernstein basis functions.

1.2 Generalized Mosaic Body Model

A mosaic composite body which has been considered was assumed to be a regular parallelepiped. This assumption imposes obvious limitation on the class of problems which can be solved using the developed 3-D variational Mosaic Model. For example, the irregular mosaic structure shown in Fig. 1.2 (as well as any other structure having “gaps”) cannot be solved directly using previous Mosaic approaches.

One possible approach allowing to avoid this limitation of the model is to complete an irregular structure to a respective regular mosaic parallelepiped by adding “dummy” material bricks, as was proposed in [2]. Using this approach, the structure shown in Fig. 1.1, for example, is transformed into the regular mosaic parallelepiped shown in Fig. 1.2.

Application of this approach for 3-D stress analysis of bonded joints has been previously illustrated. The approach has huge advantage from the point of simplicity, which is especially important for the engineering applications. Namely, this enables to solve rather complex and diverse geometries using very simple, *unified* input. However, the approach also shows two rather significant drawbacks: (I) only external displacements, not external surface forces can be applied to the dummy material bricks (this narrows the circle of possible loading cases) and (II) a number of additional degrees of freedom have to be used, because the dummy material bricks should also be discretized (this unnecessarily increases computational expenses).

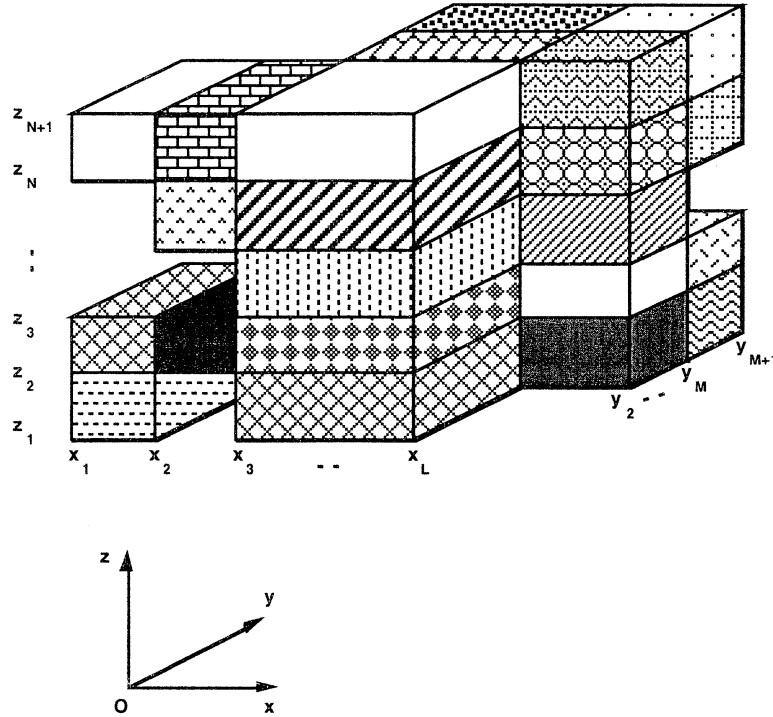


Fig. 1.1: Example of an irregular mosaic structure

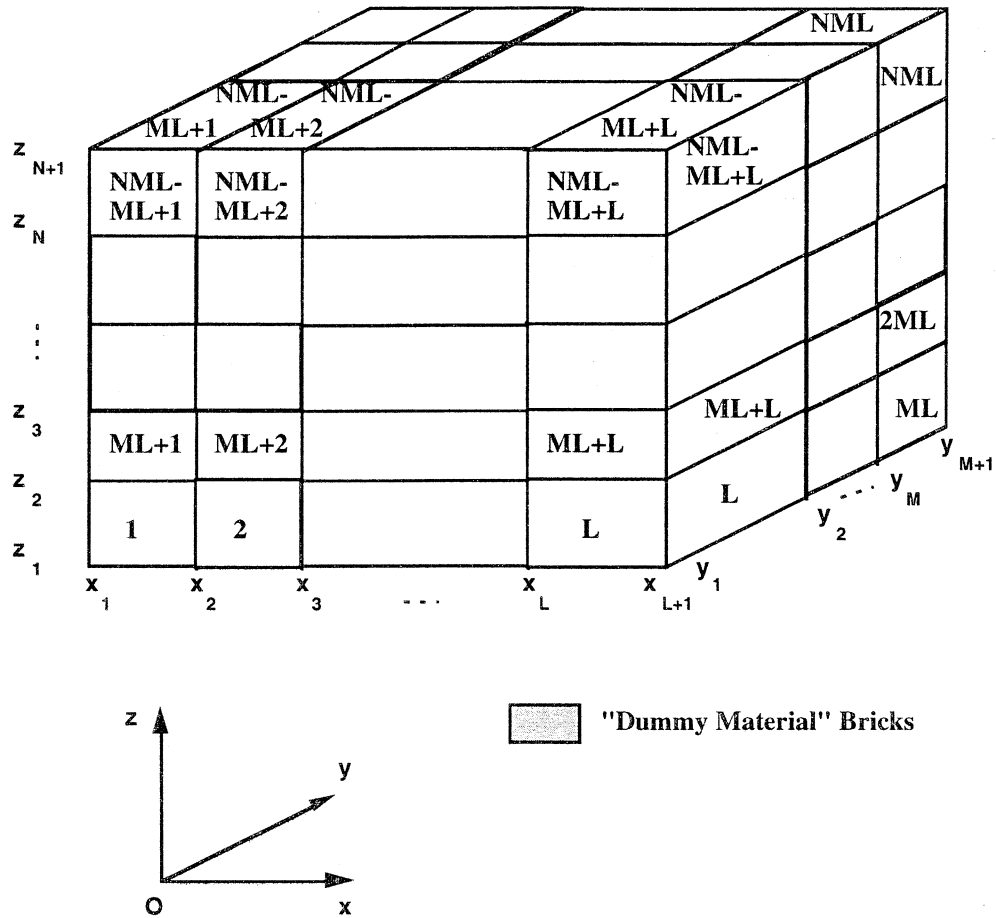


Fig. 1.2: A "dummy" material approach applied for the irregular mosaic structure

When comparing mosaic structures shown in Figs. 1.1 and 1.2, it becomes clear that the basic problem formulation can be extended for the case of an arbitrary irregular brick assemblage. The required modifications are illustrated in Fig. 1.3 and can be outlined as the following steps:

(iii) All material bricks are then renumbered in a through-sequence, using index $s = 1, \dots, S$. And all empty bricks are renumbered in a through-sequence using index $s^0 = S+1, \dots, \hat{S}$. So, $S = \hat{S} - S^0$, where $\hat{S} = L \cdot M \cdot N$, and S and S^0 are total numbers of the material and empty bricks in the regular mosaic parallelepiped, respectively. After that, all empty bricks are excluded from the consideration by simply mentioning that total number of bricks in the model is S , and only those bricks are regarded which correspond to $s = 1, \dots, S$.

1.3 Formulation Of The Variational Problem

In the further considerations we assume that each of S material bricks may have linearly elastic anisotropic properties. Stress-strain equations for the s^{th} brick are written in the form:

$$\begin{aligned}
 \sigma_x^{(s)}(\mathbf{r}) &= C_{11}^{(s)} \varepsilon_x^{(s)}(\mathbf{r}) + C_{12}^{(s)} \varepsilon_y^{(s)}(\mathbf{r}) + C_{13}^{(s)} \varepsilon_z^{(s)}(\mathbf{r}) + C_{14}^{(s)} \gamma_{yz}^{(s)}(\mathbf{r}) + C_{15}^{(s)} \gamma_{xz}^{(s)}(\mathbf{r}) + C_{16}^{(s)} \gamma_{xy}^{(s)}(\mathbf{r}) \\
 \sigma_y^{(s)}(\mathbf{r}) &= C_{12}^{(s)} \varepsilon_x^{(s)}(\mathbf{r}) + C_{22}^{(s)} \varepsilon_y^{(s)}(\mathbf{r}) + C_{23}^{(s)} \varepsilon_z^{(s)}(\mathbf{r}) + C_{24}^{(s)} \gamma_{yz}^{(s)}(\mathbf{r}) + C_{25}^{(s)} \gamma_{xz}^{(s)}(\mathbf{r}) + C_{26}^{(s)} \gamma_{xy}^{(s)}(\mathbf{r}) \\
 \sigma_z^{(s)}(\mathbf{r}) &= C_{13}^{(s)} \varepsilon_x^{(s)}(\mathbf{r}) + C_{23}^{(s)} \varepsilon_y^{(s)}(\mathbf{r}) + C_{33}^{(s)} \varepsilon_z^{(s)}(\mathbf{r}) + C_{34}^{(s)} \gamma_{yz}^{(s)}(\mathbf{r}) + C_{35}^{(s)} \gamma_{xz}^{(s)}(\mathbf{r}) + C_{36}^{(s)} \gamma_{xy}^{(s)}(\mathbf{r}) \\
 \tau_{yz}^{(s)}(\mathbf{r}) &= C_{14}^{(s)} \varepsilon_x^{(s)}(\mathbf{r}) + C_{24}^{(s)} \varepsilon_y^{(s)}(\mathbf{r}) + C_{34}^{(s)} \varepsilon_z^{(s)}(\mathbf{r}) + C_{44}^{(s)} \gamma_{yz}^{(s)}(\mathbf{r}) + C_{45}^{(s)} \gamma_{xz}^{(s)}(\mathbf{r}) + C_{46}^{(s)} \gamma_{xy}^{(s)}(\mathbf{r}) \\
 \tau_{xz}^{(s)}(\mathbf{r}) &= C_{15}^{(s)} \varepsilon_x^{(s)}(\mathbf{r}) + C_{25}^{(s)} \varepsilon_y^{(s)}(\mathbf{r}) + C_{35}^{(s)} \varepsilon_z^{(s)}(\mathbf{r}) + C_{45}^{(s)} \gamma_{yz}^{(s)}(\mathbf{r}) + C_{55}^{(s)} \gamma_{xz}^{(s)}(\mathbf{r}) + C_{56}^{(s)} \gamma_{xy}^{(s)}(\mathbf{r}) \\
 \tau_{xy}^{(s)}(\mathbf{r}) &= C_{16}^{(s)} \varepsilon_x^{(s)}(\mathbf{r}) + C_{26}^{(s)} \varepsilon_y^{(s)}(\mathbf{r}) + C_{36}^{(s)} \varepsilon_z^{(s)}(\mathbf{r}) + C_{46}^{(s)} \gamma_{yz}^{(s)}(\mathbf{r}) + C_{56}^{(s)} \gamma_{xz}^{(s)}(\mathbf{r}) + C_{66}^{(s)} \gamma_{xy}^{(s)}(\mathbf{r})
 \end{aligned} \tag{1}$$

where $\mathbf{r} = \{x, y, z\}$ is a position vector. It is assumed that material properties are homogeneous inside each brick, hence the stiffnesses in (1) do not depend on the coordinates. Generally, all 21 stiffness components may be independent nonzero values. In order to present forthcoming equations in a concise form, the following notations are introduced:

$$\begin{aligned}
 \sigma_x^{(s)} &= \sigma_1^{(s)}, \quad \sigma_y^{(s)} = \sigma_2^{(s)}, \quad \sigma_z^{(s)} = \sigma_3^{(s)}, \quad \tau_{yz}^{(s)} = \sigma_4^{(s)}, \quad \tau_{xz}^{(s)} = \sigma_5^{(s)}, \quad \tau_{xy}^{(s)} = \sigma_6^{(s)} \\
 \varepsilon_x^{(s)} &= \varepsilon_1^{(s)}, \quad \varepsilon_y^{(s)} = \varepsilon_2^{(s)}, \quad \varepsilon_z^{(s)} = \varepsilon_3^{(s)}, \quad \gamma_{yz}^{(s)} = \varepsilon_4^{(s)}, \quad \gamma_{xz}^{(s)} = \varepsilon_5^{(s)}, \quad \gamma_{xy}^{(s)} = \varepsilon_6^{(s)}
 \end{aligned} \tag{2}$$

After that equations (1) take the form

$$\sigma_i^{(s)}(\mathbf{r}) = C_{ij}^{(s)} \varepsilon_j^{(s)}(\mathbf{r}) \quad i, j = 1, \dots, 6 \quad (3)$$

Further, assuming that both the displacements and strains are small, we adopt linear strain-displacement relations for all of the bricks in the mosaic body:

$$\begin{aligned} \varepsilon_1^{(s)} &= \frac{\partial u_x^{(s)}}{\partial x}, \quad \varepsilon_2^{(s)} = \frac{\partial u_y^{(s)}}{\partial y}, \quad \varepsilon_3^{(s)} = \frac{\partial u_z^{(s)}}{\partial z}, \quad \varepsilon_4^{(s)} = \frac{\partial u_y^{(s)}}{\partial z} + \frac{\partial u_z^{(s)}}{\partial y}, \quad \varepsilon_5^{(s)} = \frac{\partial u_x^{(s)}}{\partial z} + \frac{\partial u_z^{(s)}}{\partial x}, \\ \varepsilon_6^{(s)} &= \frac{\partial u_x^{(s)}}{\partial y} + \frac{\partial u_y^{(s)}}{\partial x} \end{aligned} \quad (4)$$

Unknown displacement field in the s^{th} brick is assumed in the form of triple series

$$\begin{aligned} u_x^{(s)} &= \sum_{i=0}^{I_x} \sum_{j=0}^{J_x} \sum_{k=0}^{K_x} U_{ijk}^{1(s)} X_i^u(x) Y_j^u(y) Z_k^u(z) \\ u_y^{(s)} &= \sum_{i=0}^{I_y} \sum_{j=0}^{J_y} \sum_{k=0}^{K_y} U_{ijk}^{2(s)} X_i^v(x) Y_j^v(y) Z_k^v(z) \\ u_z^{(s)} &= \sum_{i=0}^{I_z} \sum_{j=0}^{J_z} \sum_{k=0}^{K_z} U_{ijk}^{3(s)} X_i^w(x) Y_j^w(y) Z_k^w(z) \end{aligned} \quad (5)$$

where $U_{ijk}^{1(s)}$, $U_{ijk}^{2(s)}$ and $U_{ijk}^{3(s)}$ are unknown approximation coefficients; $X_i^u(x)$, $X_i^v(x)$, $X_i^w(x)$ are three (generally independent) sets of basis functions in the x -direction; similarly, $Y_j^u(y)$, $Y_j^v(y)$, $Y_j^w(y)$ and $Z_k^u(z)$, $Z_k^v(z)$, $Z_k^w(z)$ are (generally independent) sets of basis functions in the y and z -directions, respectively. The upper summation limits I_x , J_x , K_x , I_y , J_y , K_y , I_z , J_z and K_z can be chosen independently. Here, we only assume that identical sets of basis functions are used for all of the bricks, so (5) is valid for all $s = 1, \dots, S$.

It should be emphasized that primary form of the displacement approximation (1.5) does not account for any specific kinematic boundary conditions which may be imposed at the exterior of

each individual brick. When considering any specific boundary value problem, an *admissible* displacement field, which accounts for the essential boundary conditions, has first to be defined by modifying (5). Consequently, certain coefficients from the primary sets $U_{ijk}^{1(s)}$, $U_{ijk}^{2(s)}$ and $U_{ijk}^{3(s)}$ may become *known* or *mutually interrelated* values. However, using primary form (5) of the displacement approximation is most suitable at this stage of our theoretical development.

Variational principle of minimum total potential energy will be applied here; this is written as

$$\delta\Pi = \delta(P - A) = 0 \quad (6)$$

where P is strain energy of the mosaic body and A is work of surface forces acting on its exterior. Total potential energy Π can be represented as sum of potential energies $\Pi^{(s)}$ of all of the bricks in the body:

$$\Pi = \sum_{s=1}^S \Pi^{(s)} = \sum_{s=1}^S (P^{(s)} - A^{(s)}) \quad (7)$$

The consequence of (6) are Ritz-type equations which are written in the form:

$$\frac{\partial\Pi}{\partial U_{pqr}^{1(f)}} = 0, \quad \frac{\partial\Pi}{\partial U_{pqr}^{2(f)}} = 0, \quad \frac{\partial\Pi}{\partial U_{pqr}^{3(f)}} = 0 \quad (8)$$

where four indices p , q , r and f identify all *independent* unknowns remaining in the displacement approximations (5) after applying the imposed internal and external kinematic boundary conditions.

In the view of (7), equations (8) take the form

$$\sum_{s=1}^S \left(\frac{\partial P^{(s)}}{\partial U_{pqr}^{1(f)}} - \frac{\partial A^{(s)}}{\partial U_{pqr}^{1(f)}} \right) = 0, \quad \sum_{s=1}^S \left(\frac{\partial P^{(s)}}{\partial U_{pqr}^{2(f)}} - \frac{\partial A^{(s)}}{\partial U_{pqr}^{2(f)}} \right) = 0, \quad \sum_{s=1}^S \left(\frac{\partial P^{(s)}}{\partial U_{pqr}^{3(f)}} - \frac{\partial A^{(s)}}{\partial U_{pqr}^{3(f)}} \right) = 0 \quad (9)$$

It should be emphasized that after imposing certain continuity conditions between the bricks, strain energy of the s^{th} brick may become a function of some unknowns which belong to the other bricks in the primary displacement approximation (5). However, in the case of noninteracting bricks equations (9) split into a series of independent equations

$$\frac{\partial P^{(s)}}{\partial U_{pqr}^{1(s)}} - \frac{\partial A^{(s)}}{\partial U_{pqr}^{1(s)}} = 0, \quad \frac{\partial P^{(s)}}{\partial U_{pqr}^{2(s)}} - \frac{\partial A^{(s)}}{\partial U_{pqr}^{2(s)}} = 0, \quad \frac{\partial P^{(s)}}{\partial U_{pqr}^{3(s)}} - \frac{\partial A^{(s)}}{\partial U_{pqr}^{3(s)}} = 0, \quad s = 1, \dots, S \quad (10)$$

Our next objective is to express $P^{(s)}$ and $A^{(s)}$ in terms of the unknowns $U_{ijk}^{1(s)}$, $U_{ijk}^{2(s)}$ and $U_{ijk}^{3(s)}$.

1.4 Strain Energy And Work Of Surface Forces For A Single Brick

Generally, strain energy of an anisotropic body can be written in the form

$$P^{(s)} = P^{(s)}(\varepsilon_1^{(s)}, \varepsilon_2^{(s)}, \varepsilon_3^{(s)}, \varepsilon_4^{(s)}, \varepsilon_5^{(s)}, \varepsilon_6^{(s)}) = \frac{1}{2} \iiint_{V_s} \sum_{\alpha, \beta=1}^6 C_{\alpha\beta}^{(s)} \varepsilon_{\alpha}^{(s)} \varepsilon_{\beta}^{(s)} dV_s \quad (11)$$

Taking into account Hooke's law for a generally anisotropic material (1) and then substituting (4) and (5) in (11) we obtain the following expression:

$$\begin{aligned} P^{(s)} = & \frac{1}{2} \sum_{i=0}^{I_x} \sum_{j=0}^{J_x} \sum_{k=0}^{K_x} \sum_{p=0}^{I_x} \sum_{q=0}^{J_x} \sum_{r=0}^{K_x} a_{ijk,pqr}^{11(s)} U_{ijk}^{1(s)} U_{pqr}^{1(s)} + \frac{1}{2} \sum_{i=0}^{I_y} \sum_{j=0}^{J_y} \sum_{k=0}^{K_y} \sum_{p=0}^{I_x} \sum_{q=0}^{J_x} \sum_{r=0}^{K_x} a_{ijk,pqr}^{12(s)} U_{ijk}^{2(s)} U_{pqr}^{1(s)} \\ & + \frac{1}{2} \sum_{i=0}^{I_z} \sum_{j=0}^{J_z} \sum_{k=0}^{K_z} \sum_{p=0}^{I_x} \sum_{q=0}^{J_x} \sum_{r=0}^{K_x} a_{ijk,pqr}^{13(s)} U_{ijk}^{3(s)} U_{pqr}^{1(s)} + \frac{1}{2} \sum_{i=0}^{I_x} \sum_{j=0}^{J_x} \sum_{k=0}^{K_x} \sum_{p=0}^{I_y} \sum_{q=0}^{J_y} \sum_{r=0}^{K_y} a_{ijk,pqr}^{21(s)} U_{ijk}^{1(s)} U_{pqr}^{2(s)} \\ & + \frac{1}{2} \sum_{i=0}^{I_y} \sum_{j=0}^{J_y} \sum_{k=0}^{K_y} \sum_{p=0}^{I_y} \sum_{q=0}^{J_y} \sum_{r=0}^{K_y} a_{ijk,pqr}^{22(s)} U_{ijk}^{2(s)} U_{pqr}^{2(s)} + \frac{1}{2} \sum_{i=0}^{I_z} \sum_{j=0}^{J_z} \sum_{k=0}^{K_z} \sum_{p=0}^{I_y} \sum_{q=0}^{J_y} \sum_{r=0}^{K_y} a_{ijk,pqr}^{23(s)} U_{ijk}^{3(s)} U_{pqr}^{2(s)} \\ & + \frac{1}{2} \sum_{i=0}^{I_x} \sum_{j=0}^{J_x} \sum_{k=0}^{K_x} \sum_{p=0}^{I_z} \sum_{q=0}^{J_z} \sum_{r=0}^{K_z} a_{ijk,pqr}^{31(s)} U_{ijk}^{1(s)} U_{pqr}^{3(s)} + \frac{1}{2} \sum_{i=0}^{I_y} \sum_{j=0}^{J_y} \sum_{k=0}^{K_y} \sum_{p=0}^{I_z} \sum_{q=0}^{J_z} \sum_{r=0}^{K_z} a_{ijk,pqr}^{32(s)} U_{ijk}^{2(s)} U_{pqr}^{3(s)} \\ & + \frac{1}{2} \sum_{i=0}^{I_z} \sum_{j=0}^{J_z} \sum_{k=0}^{K_z} \sum_{p=0}^{I_z} \sum_{q=0}^{J_z} \sum_{r=0}^{K_z} a_{ijk,pqr}^{33(s)} U_{ijk}^{3(s)} U_{pqr}^{3(s)} \end{aligned} \quad (12)$$

Here

$$\begin{aligned} a_{ijk,pqr}^{11(s)} = & C_{11}^{(s)} X_{ip}^{uu} Y_{jq}^{uu} Z_{kr}^{uu} + C_{66}^{(s)} X_{ip}^{uu} Y_{jq}^{uu} Z_{kr}^{uu} + C_{55}^{(s)} X_{ip}^{uu} Y_{jq}^{uu} Z_{kr}^{uu} + C_{56}^{(s)} (X_{ip}^{uu} Y_{jq}^{uu} Z_{kr}^{uu} + X_{ip}^{uu} Y_{jq}^{uu} Z_{kr}^{uu}) \\ & + C_{16}^{(s)} (X_{ip}^{uu} Y_{jq}^{uu} Z_{kr}^{uu} + X_{ip}^{uu} Y_{jq}^{uu} Z_{kr}^{uu}) + C_{15}^{(s)} (X_{ip}^{uu} Y_{jq}^{uu} Z_{kr}^{uu} + X_{ip}^{uu} Y_{jq}^{uu} Z_{kr}^{uu}) \end{aligned}$$

$$\begin{aligned}
a_{ijk,pqr}^{12(s)} = & C_{12}^{(s)} X_{ip}^{vu} Y_{jq}^{vu} Z_{kr}^{vu} + C_{66}^{(s)} X_{ip}^{vu} Y_{jq}^{vu} Z_{kr}^{vu} + C_{26}^{(s)} X_{ip}^{vu} Y_{jq}^{vu} Z_{kr}^{vu} + C_{16}^{(s)} X_{ip}^{vu} Y_{jq}^{vu} Z_{kr}^{vu} \\
& + C_{45}^{(s)} X_{ip}^{vu} Y_{jq}^{vu} Z_{kr}^{vu} + C_{25}^{(s)} X_{ip}^{vu} Y_{jq}^{vu} Z_{kr}^{vu} + C_{14}^{(s)} X_{ip}^{vu} Y_{jq}^{vu} Z_{kr}^{vu} + C_{46}^{(s)} X_{ip}^{vu} Y_{jq}^{vu} Z_{kr}^{vu} + C_{56}^{(s)} X_{ip}^{vu} Y_{jq}^{vu} Z_{kr}^{vu}
\end{aligned} \tag{13}$$

$$\begin{aligned}
a_{ijk,pqr}^{13(s)} = & C_{13}^{(s)} X_{ip}^{wu} Y_{jq}^{wu} Z_{kr}^{wu} + C_{55}^{(s)} X_{ip}^{wu} Y_{jq}^{wu} Z_{kr}^{wu} + C_{36}^{(s)} X_{ip}^{wu} Y_{jq}^{wu} Z_{kr}^{wu} + C_{45}^{(s)} X_{ip}^{wu} Y_{jq}^{wu} Z_{kr}^{wu} \\
& + C_{35}^{(s)} X_{ip}^{wu} Y_{jq}^{wu} Z_{kr}^{wu} + C_{14}^{(s)} X_{ip}^{wu} Y_{jq}^{wu} Z_{kr}^{wu} + C_{46}^{(s)} X_{ip}^{wu} Y_{jq}^{wu} Z_{kr}^{wu} + C_{15}^{(s)} X_{ip}^{wu} Y_{jq}^{wu} Z_{kr}^{wu} \\
& + C_{56}^{(s)} X_{ip}^{wu} Y_{jq}^{wu} Z_{kr}^{wu}
\end{aligned}$$

Rest of the coefficients entering in (12) is defined as follows. The coefficients $a_{ijk,pqr}^{22(s)}$, $a_{ijk,pqr}^{23(s)}$ and $a_{ijk,pqr}^{21(s)}$ are obtained from $a_{ijk,pqr}^{11(s)}$, $a_{ijk,pqr}^{12(s)}$ and $a_{ijk,pqr}^{13(s)}$, respectively, by the following cyclic permutations: 2 for 1, 3 for 2, 1 for 3, 5 for 4, 6 for 5, 4 for 6, j for i , k for j , i for k , q for p , r for q , p for r , v for u , w for v , u for w , Y for X , Z for Y , and X for Z . Then, coefficients $a_{ijk,pqr}^{33(s)}$, $a_{ijk,pqr}^{31(s)}$ and $a_{ijk,pqr}^{32(s)}$ are obtained from $a_{ijk,pqr}^{22(s)}$, $a_{ijk,pqr}^{23(s)}$ and $a_{ijk,pqr}^{21(s)}$, respectively, by the same cyclic permutations.

Notations introduced in (13) are defined in Appendix A. Note that the coefficients possess the following important symmetry properties

$$\begin{aligned}
a_{ijk,pqr}^{11(s)} &= a_{pqr,ijk}^{11(s)}, & a_{ijk,pqr}^{22(s)} &= a_{pqr,ijk}^{22(s)}, & a_{ijk,pqr}^{33(s)} &= a_{pqr,ijk}^{33(s)}, \\
a_{ijk,ijk}^{12(s)} &= a_{ijk,ijk}^{21(s)}, & a_{ijk,ijk}^{13(s)} &= a_{ijk,ijk}^{31(s)}, & a_{ijk,ijk}^{23(s)} &= a_{ijk,ijk}^{32(s)}, \\
a_{ijk,pqr}^{12(s)} &= a_{pqr,ijk}^{21(s)}, & a_{ijk,pqr}^{13(s)} &= a_{pqr,ijk}^{31(s)}, & a_{ijk,pqr}^{23(s)} &= a_{pqr,ijk}^{32(s)}
\end{aligned} \tag{14}$$

In the particular case of $I_x = I_y = I_z = I$, $J_x = J_y = J_z = J$ and $K_x = K_y = K_z = K$, expression (11) is reduced to the less cumbersome form

$$\begin{aligned}
P^{(s)} = & \frac{1}{2} \sum_{i=0}^I \sum_{j=0}^J \sum_{k=0}^K \sum_{p=0}^I \sum_{q=0}^J \sum_{r=0}^K \left\{ a_{ijk,pqr}^{11(s)} U_{ijk}^{1(s)} U_{pqr}^{1(s)} + a_{ijk,pqr}^{12(s)} U_{ijk}^{2(s)} U_{pqr}^{1(s)} + a_{ijk,pqr}^{13(s)} U_{ijk}^{3(s)} U_{pqr}^{1(s)} \right. \\
& + a_{ijk,pqr}^{21(s)} U_{ijk}^{1(s)} U_{pqr}^{2(s)} + a_{ijk,pqr}^{22(s)} U_{ijk}^{2(s)} U_{pqr}^{2(s)} + a_{ijk,pqr}^{23(s)} U_{ijk}^{3(s)} U_{pqr}^{2(s)} + a_{ijk,pqr}^{31(s)} U_{ijk}^{1(s)} U_{pqr}^{3(s)} \\
& \left. + a_{ijk,pqr}^{32(s)} U_{ijk}^{2(s)} U_{pqr}^{3(s)} + a_{ijk,pqr}^{33(s)} U_{ijk}^{3(s)} U_{pqr}^{3(s)} \right\}
\end{aligned} \tag{15}$$

Note that expressions (12) and (14) do not account for any kinematic boundary conditions. Hence, when solving any specific boundary value problem they would take some modified form.

Next consider expression of the work of external surface forces. For a single brick this is defined by:

$$A^{(s)} = \sum_{i=0}^{I_x} \sum_{j=0}^{J_x} \sum_{k=0}^{K_x} U_{ijk}^{1(s)} Q_{ijk}^{1(s)} + \sum_{i=0}^{I_y} \sum_{j=0}^{J_y} \sum_{k=0}^{K_y} U_{ijk}^{2(s)} Q_{ijk}^{2(s)} + \sum_{i=0}^{I_z} \sum_{j=0}^{J_z} \sum_{k=0}^{K_z} U_{ijk}^{3(s)} Q_{ijk}^{3(s)} \tag{16}$$

where

$$\begin{aligned}
Q_{ijk}^{1(s)} = & X_i^u(x_l) Y_{(xx)j}^{(s)u,l} Z_{(xx)k}^{(s)u,l} Q_{xx}^{(s)l} + X_i^u(x_{l+1}) Y_{(xx)j}^{(s)u,l+1} Z_{(xx)k}^{(s)u,l+1} Q_{xx}^{(s)l+1} \\
& + Y_j^u(y_m) X_{(xy)i}^{(s)u,m} Z_{(xy)k}^{(s)u,m} Q_{xy}^{(s)m} + Y_j^u(y_{m+1}) X_{(xy)i}^{(s)u,m+1} Z_{(xy)k}^{(s)u,m+1} Q_{xy}^{(s)m+1} \\
& + Z_k^u(z_n) X_{(xz)i}^{(s)u,n} Y_{(xz)j}^{(s)u,n} Q_{xz}^{(s)n} + Z_k^u(z_{n+1}) X_{(xz)i}^{(s)u,n+1} Y_{(xz)j}^{(s)u,n+1} Q_{xz}^{(s)n+1}
\end{aligned} \tag{17}$$

$$\begin{aligned}
Q_{ijk}^{2(s)} = & X_i^v(x_l) Y_{(yx)j}^{(s)v,l} Z_{(yx)k}^{(s)v,l} Q_{yx}^{(s)l} + X_i^v(x_{l+1}) Y_{(yx)j}^{(s)v,l+1} Z_{(yx)k}^{(s)v,l+1} Q_{yx}^{(s)l+1} \\
& + Y_j^v(y_m) X_{(yy)i}^{(s)v,m} Z_{(yy)k}^{(s)v,m} Q_{yy}^{(s)m} + Y_j^v(y_{m+1}) X_{(yy)i}^{(s)v,m+1} Z_{(yy)k}^{(s)v,m+1} Q_{yy}^{(s)m+1} \\
& + Z_k^v(z_n) X_{(yz)i}^{(s)v,n} Y_{(yz)j}^{(s)v,n} Q_{yz}^{(s)n} + Z_k^v(z_{n+1}) X_{(yz)i}^{(s)v,n+1} Y_{(yz)j}^{(s)v,n+1} Q_{yz}^{(s)n+1}
\end{aligned} \tag{18}$$

$$\begin{aligned}
Q_{ijk}^{3(s)} = & X_i^w(x_l) Y_{(zx)j}^{(s)w,l} Z_{(zx)k}^{(s)w,l} Q_{zx}^{(s)l} + X_i^w(x_{l+1}) Y_{(zx)j}^{(s)w,l+1} Z_{(zx)k}^{(s)w,l+1} Q_{zx}^{(s)l+1} \\
& + Y_j^w(y_m) X_{(zy)i}^{(s)w,m} Z_{(zy)k}^{(s)w,m} Q_{zy}^{(s)m} + Y_j^w(y_{m+1}) X_{(zy)i}^{(s)w,m+1} Z_{(zy)k}^{(s)w,m+1} Q_{zy}^{(s)m+1} \\
& + Z_k^w(z_n) X_{(zz)i}^{(s)w,n} Y_{(zz)j}^{(s)w,n} Q_{zz}^{(s)n} + Z_k^w(z_{n+1}) X_{(zz)i}^{(s)w,n+1} Y_{(zz)j}^{(s)w,n+1} Q_{zz}^{(s)n+1}
\end{aligned} \tag{19}$$

In these expressions, $Q_{xx}^{(s)l}, \dots, Q_{zz}^{(s)n+1}$ are 18 (in most general case) sets of the external surface

force amplitudes, which have to be obtained from the given surface force distribution laws. Other notations used in (17)-(19) are also possible. By using (16)-(19), one can derive work of external surface forces acting on the brick for any given surface load distribution. This can be done for *any* system of basis functions adopted for the displacements in the x , y , and z -coordinate directions.

1.5 System Of Linear Simultaneous Equations For A Single Brick

Now, having equations (10) and expressions (12), (16), it is easy to derive general form of linear system of simultaneous equations for a single brick. The system has been below:

$$\sum_{i=0}^{I_x} \sum_{j=0}^{J_x} \sum_{k=0}^{K_x} a_{ijk,pqr}^{11(s)} U_{ijk}^{1(s)} + \sum_{i=0}^{I_y} \sum_{j=0}^{J_y} \sum_{k=0}^{K_y} a_{ijk,pqr}^{12(s)} U_{ijk}^{2(s)} + \sum_{i=0}^{I_z} \sum_{j=0}^{J_z} \sum_{k=0}^{K_z} a_{ijk,pqr}^{13(s)} U_{ijk}^{3(s)} = Q_{pqr}^{1(s)}$$

for $p = 0, 1, \dots, I_x$; $q = 0, 1, \dots, J_x$; $r = 0, 1, \dots, K_x$

$$\sum_{i=0}^{I_x} \sum_{j=0}^{J_x} \sum_{k=0}^{K_x} a_{ijk,pqr}^{21(s)} U_{ijk}^{1(s)} + \sum_{i=0}^{I_y} \sum_{j=0}^{J_y} \sum_{k=0}^{K_y} a_{ijk,pqr}^{22(s)} U_{ijk}^{2(s)} + \sum_{i=0}^{I_z} \sum_{j=0}^{J_z} \sum_{k=0}^{K_z} a_{ijk,pqr}^{23(s)} U_{ijk}^{3(s)} = Q_{pqr}^{2(s)} \quad (20)$$

for $p = 0, 1, \dots, I_y$; $q = 0, 1, \dots, J_y$; $r = 0, 1, \dots, K_y$

$$\sum_{i=0}^{I_x} \sum_{j=0}^{J_x} \sum_{k=0}^{K_x} a_{ijk,pqr}^{31(s)} U_{ijk}^{1(s)} + \sum_{i=0}^{I_y} \sum_{j=0}^{J_y} \sum_{k=0}^{K_y} a_{ijk,pqr}^{32(s)} U_{ijk}^{2(s)} + \sum_{i=0}^{I_z} \sum_{j=0}^{J_z} \sum_{k=0}^{K_z} a_{ijk,pqr}^{33(s)} U_{ijk}^{3(s)} = Q_{pqr}^{3(s)};$$

for $p = 0, 1, \dots, I_z$; $q = 0, 1, \dots, J_z$; $r = 0, 1, \dots, K_z$

Superscript (s) in (20) can take any value from the set $s = 1, 2, \dots, S$.

It should be pointed out that system of simultaneous equations (20) is generic in nature: it has singular matrix and, therefore, can not be readily solved. This statement has clear mechanical explanation: no kinematic boundary conditions have yet been imposed on the bricks, hence, a rigid body translation and rotation were not restrained. Due to that, any infinitesimal surface force entering in the right hand side of (20) would cause infinite displacements. In order to obtain a finite-valued solution for any specific boundary value problem, some minimal set of geometric constraints should be imposed.

Equations (20) can be further written in the following concise form:

$$a_{ijk,pqr}^{\alpha\beta(s)} U_{ijk}^{\beta(s)} = Q_{pqr}^{\alpha(s)} \quad (21)$$

where $\alpha = 1, 2, 3$; $\beta = 1, 2, 3$; $s = 1, \dots, S$ and the following ranges of the other indices apply:

$$\begin{aligned} p = 0, 1, \dots, I_x; \quad q = 0, 1, \dots, J_x; \quad r = 0, 1, \dots, K_x & \quad \text{for } \alpha = 1 \\ p = 0, 1, \dots, I_y; \quad q = 0, 1, \dots, J_y; \quad r = 0, 1, \dots, K_y & \quad \text{for } \alpha = 2 \\ p = 0, 1, \dots, I_z; \quad q = 0, 1, \dots, J_z; \quad r = 0, 1, \dots, K_z & \quad \text{for } \alpha = 3 \end{aligned}$$

Summation convention over β, i, j , and k applies in (21).

System of equations (21) can be also written in a matrix form

$$\mathbf{A}^{(s)} \mathbf{U}^{(s)} = \mathbf{Q}^{(s)} \quad (22)$$

For the sake of compactness the vectors and matrices in (22) are further written explicitly for the particular case

$$I_x = I_y = I_z = I, \quad J_x = J_y = J_z = J, \quad K_x = K_y = K_z = K \quad (23)$$

which allows to obtain the following:

$$\mathbf{U}^{(s)} = \begin{Bmatrix} \mathbf{U}^{1(s)} \\ \mathbf{U}^{2(s)} \\ \mathbf{U}^{3(s)} \end{Bmatrix}; \quad \mathbf{U}^{\alpha(s)} = \begin{Bmatrix} U_{000}^{\alpha(s)} \\ \vdots \\ U_{00K}^{\alpha(s)} \\ \vdots \\ U_{0JK}^{\alpha(s)} \\ \vdots \\ U_{IJK}^{\alpha(s)} \end{Bmatrix} = \begin{Bmatrix} U_1^{\alpha(s)} \\ \vdots \\ U_{K+1}^{\alpha(s)} \\ \vdots \\ U_{(J+1)(K+1)}^{\alpha(s)} \\ \vdots \\ U_{(I+1)(J+1)(K+1)}^{\alpha(s)} \end{Bmatrix} \quad (24)$$

with $\alpha = 1, 2, 3$.

The following notation is further introduced:

$$\mathbf{U}^{(s)} = \{U_f^{(s)}\} \quad (25)$$

where

$$f = f(i, j, k, \alpha) = 1 + i + j(J+1) + k(J+1)(K+1) + (\alpha-1)(I+1)(J+1)(K+1) \quad (26)$$

As before, $i = 0, 1, \dots, I$; $j = 0, 1, \dots, J$; $k = 0, 1, \dots, K$ and $\alpha = 1, 2, 3$.

The vector of known right hand sides is

$$\mathbf{Q}^{(s)} = \begin{Bmatrix} \mathbf{Q}^{1(s)} \\ \mathbf{Q}^{2(s)} \\ \mathbf{Q}^{3(s)} \end{Bmatrix}; \quad \mathbf{Q}^{\alpha(s)} = \begin{Bmatrix} Q_{000}^{\alpha(s)} \\ \vdots \\ Q_{00K}^{\alpha(s)} \\ \vdots \\ Q_{0JK}^{\alpha(s)} \\ \vdots \\ Q_{IJK}^{\alpha(s)} \end{Bmatrix} = \begin{Bmatrix} Q_1^{\alpha(s)} \\ \vdots \\ Q_{K+1}^{\alpha(s)} \\ \vdots \\ Q_{(J+1)(K+1)}^{\alpha(s)} \\ \vdots \\ Q_{(I+1)(J+1)(K+1)}^{\alpha(s)} \end{Bmatrix} \quad (27)$$

where

$$g = g(p, q, r, \beta) = 1 + p + q(J+1) + r(J+1)(K+1) + (\beta-1)(I+1)(J+1)(K+1) \quad (28)$$

with $p = 0, 1, \dots, I$, $q = 0, 1, \dots, J$; $r = 0, 1, \dots, K$ and $\beta = 1, 2, 3$.

The following notation is further introduced :

$$\mathbf{Q}^{(s)} = \{Q_g^{(s)}\} \quad (29)$$

Next, the following matrix is defined:

$$\mathbf{A}^{(s)} = \begin{bmatrix} \mathbf{A}^{11(s)} & \mathbf{A}^{12(s)} & \mathbf{A}^{13(s)} \\ \mathbf{A}^{21(s)} & \mathbf{A}^{22(s)} & \mathbf{A}^{23(s)} \\ \mathbf{A}^{31(s)} & \mathbf{A}^{32(s)} & \mathbf{A}^{33(s)} \end{bmatrix} \quad (30)$$

where

$$\mathbf{A}^{\alpha\beta(s)} = \begin{bmatrix} a_{000,000}^{\alpha\beta(s)} & \cdots & a_{00K,000}^{\alpha\beta(s)} & \cdots & a_{IJK,000}^{\alpha\beta(s)} \\ \vdots & \vdots & \vdots & \vdots & \vdots \\ a_{000,00K}^{\alpha\beta(s)} & \cdots & a_{00K,00K}^{\alpha\beta(s)} & \cdots & a_{IJK,00K}^{\alpha\beta(s)} \\ \vdots & \vdots & \vdots & \vdots & \vdots \\ a_{000,IJK}^{\alpha\beta(s)} & \cdots & a_{00K,IJK}^{\alpha\beta(s)} & \cdots & a_{IJK,IJK}^{\alpha\beta(s)} \end{bmatrix}$$

$$= \begin{bmatrix} a_{1,1}^{\alpha\beta(s)} & \cdots & a_{(K+1),1}^{\alpha\beta(s)} & \cdots & a_{(I+1)(J+1)(K+1),1}^{\alpha\beta(s)} \\ \vdots & \vdots & \vdots & \vdots & \vdots \\ a_{1,(K+1)}^{\alpha\beta(s)} & \cdots & a_{(K+1),(K+1)}^{\alpha\beta(s)} & \cdots & a_{(I+1)(J+1)(K+1),1}^{\alpha\beta(s)} \\ \vdots & \vdots & \vdots & \vdots & \vdots \\ a_{1,(I+1)(J+1)(K+1)}^{\alpha\beta(s)} & \cdots & a_{(K+1),(I+1)(J+1)(K+1)}^{\alpha\beta(s)} & \cdots & a_{(I+1)(J+1)(K+1),(I+1)(J+1)(K+1)}^{\alpha\beta(s)} \end{bmatrix} \quad (31)$$

So, (30) is of the form

$$\mathbf{A}^{(s)} = \left[a_{fg}^{(s)} \right] \quad (32)$$

where f and g are defined by (26) and (28), respectively.

Thus, at any s value (22) represents a system of $3(I+1)(J+1)(K+1)$ linear equations with the same number of unknowns. It is easy to check that due to the properties (14) matrix $\mathbf{A}^{(s)}$ is *symmetric*. It has to be emphasized again that system of simultaneous equations (22) does not incorporate any geometric boundary conditions.

1.6 System Of Linear Simultaneous Equations For A Set Of Noninteracting Bricks

Next step is to derive a generic form of resulting system for a mosaic body containing S noninteracting bricks. The system is written in the form

$$\mathbf{AU} = \mathbf{Q} \quad (33)$$

where

$$\mathbf{U} = \{U_\phi\} \quad (34)$$

with

$$\begin{aligned} \phi = \phi(i, j, k, \alpha, s') &= 1 + i + j(J+1) + k(J+1)(K+1) + (\alpha-1)(I+1)(J+1)(K+1) \\ &+ 3(s'-1)(I+1)(J+1)(K+1) \end{aligned} \quad (35)$$

where s' runs values $1, 2, \dots, S$. Further,

$$\mathbf{Q} = \{Q_\varphi\} \quad (36)$$

where

$$\begin{aligned} \varphi = \varphi(p, q, r, \beta, s'') &= 1 + p + q(J+1) + r(J+1)(K+1) + (\beta-1)(I+1)(J+1)(K+1) \\ &+ 3(s''-1)(I+1)(J+1)(K+1) \end{aligned} \quad (37)$$

with s'' running values $1, 2, \dots, S$.

The matrix entering in (33) is written in the form

$$\mathbf{A} = [a_{\phi\varphi}] \quad (38)$$

where ϕ and φ are defined by (35) and (37), respectively.

The column vectors \mathbf{U} and \mathbf{Q} each has $D = 3S(I+1)(J+1)(K+1)$ components, and \mathbf{A} is a *symmetric* square matrix. Equations (33) are reminiscent with the standard type matrix equations common in the finite element analysis. Indeed, \mathbf{A} recalls a global stiffness matrix, \mathbf{U} recalls a nodal displacement vector, and \mathbf{Q} a nodal external force vector. However, there are substantial differences: the vector of unknowns \mathbf{U} defined by (34) contains *coefficients of the displacement approximation* (5), which are not necessarily *nodal displacements* as in a customary finite element analysis. Also, components of the right hand side vector \mathbf{Q} have, generally, different physical meaning than nodal forces in a customary finite element analysis. Nevertheless, if using special types of basis functions (“shape functions”) in the displacement approximation (5), equations (33) can be directly related to the result of derivations performed for the respective 3-D hexahedral finite elements. This emphasizes a generic value of the developed variational analysis approach.

It is worthwhile pointing out again that no *a priori* assumptions have been yet made regarding specific type of basis functions in the displacement approximation (5). In principle, the developed theory can be applied with any system of basis functions. For example, trigonometric functions, power series, splines, Chebyshev, Legendre, Bessel, Laguerre, Lagrange, Bernstein and other polynomials can be utilized. Furthermore, the theory allows one to use different type of basis functions in the x , y and z -directions. Specific choice of the basis functions can be motivated by their preferable order of continuity, analytical convenience, higher convergence rate, minimal roundoff errors, and other computational considerations.

Further development of this theory will address formulation of the internal continuity conditions for the mosaic body. The conditions of continuity of displacements and transverse stresses at the boundaries between the bricks are presented in the next section.

1.7 Continuity Conditions at the Inter-Brick Boundaries in an Irregular Mosaic Structure

Now we return to Fig. 1.3 and consider interaction between the bricks in a general case of irregular mosaic structure. Following the approach developed in Section 1.2, all internal boundaries between the bricks are segregated into three groups:

- (a) The boundaries between any *two material* bricks are further treated as *internal boundaries* of the mosaic body. Accordingly, the conditions of displacement continuity and transverse stress continuity will be imposed there.
- (b) The boundaries between a *material* brick and an *empty* brick are further treated as *external boundaries* of the mosaic body. Accordingly, external kinematic or static boundary conditions may be imposed there.
- (c) The boundaries between any *two empty* bricks are just ignored in the further considerations.

Further, all those exterior surfaces of the bricks which are, at the same time, parts of the exterior of the mosaic body, are segregated into two groups:

- (d) those which belong to any material brick and
- (e) those which belong to any empty brick.

The surfaces of group (d) may be exposed to external kinematic or static boundary conditions. The surfaces of group (e) are ignored in the further considerations. Segregation of the surfaces between the groups (a)-(e) may be performed in the computer code using “pointer” technique.

Now it is clear that the internal boundary conditions have to be formulated *only* for the surfaces belonging to group (a), and the external boundary conditions can be formulated only for the surfaces belonging to groups (b) and (d). Next we elaborate one possible approach to formulating internal displacement and stress continuity conditions in the presence of empty bricks.

First of all, it is recognized that there are three sets of internal plane elements in the mosaic parallelepiped shown in Fig. 1.3. The first set contains all plane elements perpendicular to the x -

axis and having coordinates x_l , $l=2,3,\dots,L$. The second set contains all plane elements perpendicular to the y -axis and having coordinates y_m , $m=2,3,\dots,M$. And the third set contains all plane elements perpendicular to the z -axis and having coordinates z_n , $n=2,3,\dots,N$. The internal displacement and stress continuity conditions for the case of a regular mosaic parallelepiped have been derived in Sections 1.4 and 1.5 of [1]. Now we need to modify them taking into account that at any location in the mosaic structure there can be empty brick.

All those plane elements which are perpendicular to the x axis and separate two *material* bricks are now identified by numbers \hat{l}_{mn} , where $m=2,3,\dots,M+1$ and $n=2,3,\dots,N+1$. For each specific combination of m and n , the numbers \hat{l}_{mn} belong to some subset of the sequence of numbers $2,3,\dots,L$. The sequence \hat{l}_{mn} is determined by the architecture of specific mosaic body under consideration. In particular, if some row of bricks corresponding to $m=m^*$, $n=n^*$ does not contain any empty bricks, then $\hat{l}_{m^*n^*}=2,3,\dots,L$. However, generally \hat{l}_{mn} does not run *all* terms of the sequence $2,3,\dots,L$. Nevertheless, one can rearrange the terms using through notation, and get the sequence $2,3,\dots,\hat{L}$, where $\hat{L}\leq L$. For the latter sequence we will use index \hat{l} which runs values $\hat{l}=2,3,\dots,\hat{L}$.

Analogously, all those plane elements which are perpendicular to the y -axis and separate two *material* bricks are identified by numbers \hat{m}_{ln} , where $l=2,3,\dots,L+1$ and $n=2,3,\dots,N+1$. For each combination of l and n , the numbers \hat{m}_{ln} belong to some subset of the sequence of numbers $2,3,\dots,M$. Analogously to the above consideration, the sequence of numbers \hat{m}_{ln} is rearranged as $\hat{m}=2,3,\dots,\hat{M}$.

Finally, all those plane elements which are perpendicular to the z -axis and separate two *material* bricks are identified by numbers \hat{n}_{lm} , where $l=2,3,\dots,L+1$ and $m=2,3,\dots,M+1$. For each combination of l and m the numbers \hat{n}_{lm} belong to some subset of the set of numbers $2,3,\dots,N$. Again, the sequence of numbers \hat{n}_{lm} is rearranged as $\hat{n}=2,3,\dots,\hat{N}$.

Now it is easy to generalize the equations. The displacement continuity conditions are expressed as the following sets of equations. For the inter-brick boundaries perpendicular to the x -axis

$$u_x^{s(\hat{l},m,n)}(x_{\hat{l}},y,z) = u_x^{s(\hat{l}+1,m,n)}(x_{\hat{l}},y,z); u_y^{s(\hat{l},m,n)}(x_{\hat{l}},y,z) = u_y^{s(\hat{l}+1,m,n)}(x_{\hat{l}},y,z); \quad (39)$$

$$u_z^{s(\hat{l},m,n)}(x_{\hat{l}},y,z) = u_z^{s(\hat{l}+1,m,n)}(x_{\hat{l}},y,z)$$

where

$$s(\hat{l},m,n) = 1 + (\hat{l} - 2) + (m - 2)L + (n - 2)L \cdot M \quad (40)$$

and

$$\hat{l} = 2, 3, \dots, \hat{L}; \quad m = 2, 3, \dots, M + 1; \quad n = 2, 3, \dots, N + 1 \quad (41)$$

For the inter-brick boundaries perpendicular to the y -axis

$$u_x^{s(l,\hat{m},n)}(x,y_{\hat{m}},z) = u_x^{s(l,\hat{m}+1,n)}(x,y_{\hat{m}},z); u_y^{s(l,\hat{m},n)}(x,y_{\hat{m}},z) = u_y^{s(l,\hat{m}+1,n)}(x,y_{\hat{m}},z); \quad (42)$$

$$u_z^{s(l,\hat{m},n)}(x,y_{\hat{m}},z) = u_z^{s(l,\hat{m}+1,n)}(x,y_{\hat{m}},z)$$

where

$$s(l,\hat{m},n) = 1 + (l - 2) + (\hat{m} - 2)L + (n - 2)L \cdot M \quad (43)$$

and

$$l = 2, 3, \dots, L + 1; \quad \hat{m} = 2, 3, \dots, \hat{M}; \quad n = 2, 3, \dots, N + 1 \quad (44)$$

And for the inter-brick boundaries perpendicular to the z -axis

$$u_x^{s(l,m,\hat{n})}(x,y,z_{\hat{n}}) = u_x^{s(l,m,\hat{n}+1)}(x,y,z_{\hat{n}}); u_y^{s(l,m,\hat{n})}(x,y,z_{\hat{n}}) = u_y^{s(l,m,\hat{n}+1)}(x,y,z_{\hat{n}}); \quad (45)$$

$$u_z^{s(l,m,\hat{n})}(x,y,z_{\hat{n}}) = u_z^{s(l,m,\hat{n}+1)}(x,y,z_{\hat{n}})$$

where

$$s(l,m,\hat{n}) = 1 + (l - 2) + (m - 2)L + (\hat{n} - 2)L \cdot M \quad (46)$$

and

$$l = 2, 3, \dots, L + 1; \quad m = 2, 3, \dots, M + 1; \quad \hat{n} = 2, 3, \dots, \hat{N} \quad (47)$$

Using analogous considerations, the conditions of transverse stress continuity are formulated as follows. For the inter-brick boundaries perpendicular to the x -axis those are

$$\begin{aligned}\sigma_x^{s(\hat{l},m,n)}(x_{\hat{l}},y,z) &= \sigma_x^{s(\hat{l}+1,m,n)}(x_{\hat{l}},y,z); \quad \tau_{xy}^{s(\hat{l},m,n)}(x_{\hat{l}},y,z) = \tau_{xy}^{s(\hat{l}+1,m,n)}(x_{\hat{l}},y,z); \\ \tau_{xz}^{s(\hat{l},m,n)}(x_{\hat{l}},y,z) &= \tau_{xz}^{s(\hat{l}+1,m,n)}(x_{\hat{l}},y,z)\end{aligned}\tag{48}$$

with $s(\hat{l},m,n)$ defined by (40), and \hat{l} , m and n defined by (41).

For the inter-brick boundaries perpendicular to the y -axis one obtains

$$\begin{aligned}\sigma_y^{s(l,\hat{m},n)}(x,y_{\hat{m}},z) &= \sigma_y^{s(l,\hat{m}+1,n)}(x,y_{\hat{m}},z); \quad \tau_{xy}^{s(l,\hat{m},n)}(x,y_{\hat{m}},z) = \tau_{xy}^{s(l,\hat{m}+1,n)}(x,y_{\hat{m}},z); \\ \tau_{yz}^{s(l,\hat{m},n)}(x,y_{\hat{m}},z) &= \tau_{yz}^{s(l,\hat{m}+1,n)}(x,y_{\hat{m}},z)\end{aligned}\tag{49}$$

with $s(l,\hat{m},n)$ defined by (43), and l , \hat{m} and n defined by (44).

Finally, for the inter-brick boundaries perpendicular to the z -axis the following is written:

$$\begin{aligned}\sigma_z^{s(l,m,\hat{n})}(x,y,z_{\hat{n}}) &= \sigma_z^{s(l,m,\hat{n}+1)}(x,y,z_{\hat{n}}), \quad \tau_{xz}^{s(l,m,\hat{n})}(x,y,z_{\hat{n}}) = \tau_{xz}^{s(l,m,\hat{n}+1)}(x,y,z_{\hat{n}}); \\ \tau_{yz}^{s(l,m,\hat{n})}(x,y,z_{\hat{n}}) &= \tau_{yz}^{s(l,m,\hat{n}+1)}(x,y,z_{\hat{n}})\end{aligned}\tag{50}$$

with $s(l,m,\hat{n})$ defined by (46), and l , m and \hat{n} defined by (47). It is seen that the index notations in all above equations are consistent. The following index values take place:

$$\begin{aligned}l &= 2, 3, \dots, L+1; \quad m = 2, 3, \dots, M+1; \quad n = 2, 3, \dots, N+1; \\ \hat{l} &= 2, 3, \dots, \hat{L}; \quad \hat{m} = 2, 3, \dots, \hat{M}; \quad \hat{n} = 2, 3, \dots, \hat{N}\end{aligned}\tag{51}$$

Equations (39), (42), (45) and (48)-(50) provide a complete formulation of all necessary internal continuity conditions for the displacements and stresses inside an arbitrary irregular mosaic body. Further development of the theory, which will be focused on incorporating these conditions in the variational solution is presented in Section 2.

2.0 APPLICATION OF BERNSTEIN BASIS FUNCTIONS FOR 3-D ANALYSIS OF MOSAIC COMPOSITE STRUCTURES

2.1 Displacement Approximation

Three-dimensional dynamic and static variational analysis methodology developed in Section 1 for a mosaic body composed of anisotropic bricks is further elaborated here for the case of Bernstein basis functions of an arbitrary degree applied for displacement approximation in all three coordinate directions.

Bernstein basis functions of degree N are defined as follows:

$$B_n^N(\xi) = \frac{N!}{n!(N-n)!} \xi^n (1-\xi)^{N-n}; \quad \xi \in [0,1]; \quad n = 0, 1, \dots, N \quad (1)$$

where N may be any integer number. For any value of n , definition (1) represents the N^{th} degree polynomial. It is well known that all algebraic polynomials of degree $\leq N$ constitute a linear space of dimension $N+1$. Since the $N+1$ functions $B_n^N(\xi)$, $n = 0, 1, \dots, N$ are linearly independent, they form a basis. Note that linear form of Bernstein basis functions

$$B^N(\xi) = \sum_{n=0}^N b_n \frac{N!}{n!(N-n)!} \xi^n (1-\xi)^{N-n}, \quad \xi \in [0,1] \quad (2)$$

is known as Bezier curve.

The assumed displacement approximation for the s^{th} brick (Section 1, Eq.(5)) is written, with account of notations (Section 1, Eq. (23)), in the following form

$$\begin{aligned} u_x^{(s)}(x, y, z) &= \sum_{i=0}^I \sum_{j=0}^J \sum_{k=0}^K U_{ijk}^{1(s)} X_i^u(x) Y_j^u(y) Z_k^u(z) \\ u_y^{(s)}(x, y, z) &= \sum_{i=0}^I \sum_{j=0}^J \sum_{k=0}^K U_{ijk}^{2(s)} X_i^v(x) Y_j^v(y) Z_k^v(z) \\ u_z^{(s)}(x, y, z) &= \sum_{i=0}^I \sum_{j=0}^J \sum_{k=0}^K U_{ijk}^{3(s)} X_i^w(x) Y_j^w(y) Z_k^w(z) \end{aligned} \quad (3)$$

In principle, the basis functions (their degree, specifically) can be different for each coordinate direction. It is further assumed that same form of the displacement approximation (3) applies for all bricks in the mosaic body.

When using Bernstein basis functions (1), the following displacement approximation is obtained from (3):

$$u_x^{(s)}(x, y, z) = \sum_{i=0}^I \sum_{j=0}^J \sum_{k=0}^K U_{ijk}^{1(s)} P_i^I(x) P_j^J(y) P_k^K(z)$$

$$u_y^{(s)}(x, y, z) = \sum_{i=0}^I \sum_{j=0}^J \sum_{k=0}^K U_{ijk}^{2(s)} P_i^I(x) P_j^J(y) P_k^K(z) \quad (4)$$

$$u_z^{(s)}(x, y, z) = \sum_{i=0}^I \sum_{j=0}^J \sum_{k=0}^K U_{ijk}^{3(s)} P_i^I(x) P_j^J(y) P_k^K(z)$$

where

$$P_i^I(x) = \frac{I!}{i!(I-i)!} \left(\frac{x - x_l}{x_{l+1} - x_l} \right)^i \left(\frac{x_{l+1} - x}{x_{l+1} - x_l} \right)^{I-i} \quad \text{for } x \in [x_l, x_{l+1}]; \quad (5)$$

$$P_i^I(x) = 0 \quad \text{else}$$

$$P_j^J(y) = \frac{J!}{j!(J-j)!} \left(\frac{y - y_m}{y_{m+1} - y_m} \right)^j \left(\frac{y_{m+1} - y}{y_{m+1} - y_m} \right)^{J-j} \quad \text{for } y \in [y_m, y_{m+1}]; \quad (6)$$

$$P_j^J(y) = 0 \quad \text{else}$$

$$P_k^K(z) = \frac{K!}{k!(K-k)!} \left(\frac{z - z_n}{z_{n+1} - z_n} \right)^k \left(\frac{z_{n+1} - z}{z_{n+1} - z_n} \right)^{K-k} \quad \text{for } z \in [z_n, z_{n+1}]; \quad (7)$$

$$P_k^K(z) = 0 \quad \text{else}$$

Bernstein basis functions possess certain useful properties which make them suitable for developing rather simple and elegant mathematical solutions and computational algorithms for various boundary value problems of elasticity. The following property is especially valuable:

$$\sum_{n=0}^N B_n^N(\xi) = 1 \quad \text{for any } \xi \in [0.1] \quad (8)$$

It was shown that applying (8) allows one to *exactly* satisfy external boundary conditions in terms of *uniform* displacements and/or their first derivatives imposed on the brick. Besides that, Bernstein basis functions provide an opportunity of obtaining almost all parts of the solution in the form of *analytical expressions*, without using numerical evaluations of the integrals or other approximate procedures. This allows one to derive *explicit* form of the resulting systems of linear simultaneous equations (Section 1, Eq. (33)) and *analytically* formulate kinematic constraints in terms of linear relationships between the unknowns for various types of external and internal boundary conditions.

2.2 Continuity of Displacements Between the Bricks

Now the displacement approximation (4) can be used to specify the displacement continuity conditions formulated in Section 1.7. By substituting (4) in (Section 1, Eq. (39)) it is obtained

$$\begin{aligned} \sum_{j=0}^J \sum_{k=0}^K \left[U_{ljk}^{1,s(\hat{l},m,n)} - U_{0jk}^{1,s(\hat{l}+1,m,n)} \right] P_j^J(y) P_k^K(z) &= 0 \\ \sum_{j=0}^J \sum_{k=0}^K \left[U_{ljk}^{2,s(\hat{l},m,n)} - U_{0jk}^{2,s(\hat{l}+1,m,n)} \right] P_j^J(y) P_k^K(z) &= 0 \\ \sum_{j=0}^J \sum_{k=0}^K \left[U_{ljk}^{3,s(\hat{l},m,n)} - U_{0jk}^{3,s(\hat{l}+1,m,n)} \right] P_j^J(y) P_k^K(z) &= 0 \end{aligned} \quad (9)$$

Due to a linear independence of Bernstein basis functions corresponding to different values of their subscript, these conditions can be satisfied if only

$$U_{ijk}^{1,s(\hat{l},m,n)} = U_{0jk}^{1,s(\hat{l}+1,m,n)}, \quad U_{ijk}^{2,s(\hat{l},m,n)} = U_{0jk}^{2,s(\hat{l}+1,m,n)}, \quad U_{ijk}^{3,s(\hat{l},m,n)} = U_{0jk}^{3,s(\hat{l}+1,m,n)} \quad (10)$$

where $j = 0, 1, \dots, J$ and $k = 0, 1, \dots, K$.

Analogous considerations applied to the continuity conditions (Section 1, Eq. (42)) result in the following relations:

$$U_{ijk}^{1,s(l,\hat{m},n)} = U_{i0k}^{1,s(l,\hat{m}+1,n)}, \quad U_{ijk}^{2,s(l,\hat{m},n)} = U_{i0k}^{2,s(l,\hat{m}+1,n)}, \quad U_{ijk}^{3,s(l,\hat{m},n)} = U_{i0k}^{3,s(l,\hat{m}+1,n)} \quad (11)$$

where $i = 0, 1, \dots, I$ and $k = 0, 1, \dots, K$.

Finally, the continuity conditions (Section 1, Eq. (45)) are reduced to the following:

$$U_{ijk}^{1,s(l,m,\hat{n})} = U_{ij0}^{1,s(l,m,\hat{n}+1)}, \quad U_{ijk}^{2,s(l,m,\hat{n})} = U_{ij0}^{2,s(l,m,\hat{n}+1)}, \quad U_{ijk}^{3,s(l,m,\hat{n})} = U_{ij0}^{3,s(l,m,\hat{n}+1)} \quad (12)$$

where $i = 0, 1, \dots, I$ and $j = 0, 1, \dots, J$.

All three groups of relations (10) can be further written in the following unified form:

$$U_{ijk}^{\alpha,s(\hat{l},m,n)} = U_{0jk}^{\alpha,s(\hat{l}+1,m,n)}, \quad \alpha = 1, 2, 3; \quad j = 0, 1, \dots, J; \quad k = 0, 1, \dots, K \quad (13)$$

All three groups of relations (11) can be represented as

$$U_{ijk}^{\beta,s(l,\hat{m},n)} = U_{i0k}^{\beta,s(l,\hat{m}+1,n)}, \quad \beta = 1, 2, 3; \quad i = 0, 1, \dots, I; \quad k = 0, 1, \dots, K \quad (14)$$

And all three groups of relations (12) can be written in the form

$$U_{ijk}^{\gamma,s(l,m,\hat{n})} = U_{ij0}^{\gamma,s(l,m,\hat{n}+1)}, \quad \gamma = 1, 2, 3; \quad i = 0, 1, \dots, I; \quad j = 0, 1, \dots, J \quad (15)$$

The expressions for $s(\hat{l}, m, n)$, $s(l, \hat{m}, n)$ and $s(l, m, \hat{n})$ entering in (13), (14) and (15) are given by Section 1, Eqs. (40), (43) and (46), respectively. The values of l , m , n , \hat{l} , \hat{m} and \hat{n} are defined

by the respective expressions Section 1, Eqs. (41), (44) and (47). Relations (13)-(15) provide part of the whole necessary set of relations which need to be satisfied as to obtain solutions of boundary value problems for mosaic structures with continuous displacement field. Another types of the required relations will be derived in Sections 2.5 - 2.8.

2.3 Continuity of Transverse Stresses Between the Bricks

Next we consider the inter-brick stress boundary conditions Section 1, Eqs. 48 - 50. Formulation of these conditions is more complex than formulation of the displacement continuity conditions.

We start with the first condition from the set Section 1, Eq. (48). By using strain-displacement relations Section 1, Eq. (4) and stress-strain relations Section 1, Eq. (1), written here for the case of an orthotropic material, the following is obtained:

$$\begin{aligned}
& C_{11}^{s(\hat{l},m,n)} \left(\frac{\partial u_x^{s(\hat{l},m,n)}(x,y,z)}{\partial x} \right)_{x=x_{\hat{l}}} + C_{12}^{s(\hat{l},m,n)} \left(\frac{\partial u_y^{s(\hat{l},m,n)}(x,y,z)}{\partial y} \right)_{x=x_{\hat{l}}} \\
& + C_{13}^{s(\hat{l},m,n)} \left(\frac{\partial u_z^{s(\hat{l},m,n)}(x,y,z)}{\partial z} \right)_{x=x_{\hat{l}}} \\
& = C_{11}^{s(\hat{l}+1,m,n)} \left(\frac{\partial u_x^{s(\hat{l}+1,m,n)}(x,y,z)}{\partial x} \right)_{x=x_{\hat{l}}} + C_{12}^{s(\hat{l}+1,m,n)} \left(\frac{\partial u_y^{s(\hat{l}+1,m,n)}(x,y,z)}{\partial y} \right)_{x=x_{\hat{l}}} \\
& + C_{13}^{s(\hat{l}+1,m,n)} \left(\frac{\partial u_z^{s(\hat{l}+1,m,n)}(x,y,z)}{\partial z} \right)_{x=x_{\hat{l}}}
\end{aligned} \tag{16}$$

Further, by applying (4) in (16) and using properties of $\left(\frac{dP_i^I(x)}{dx}\right)_{x=x_{\hat{l}}}$ and $(P_i^I(x))_{x=x_{\hat{l}}}$ in the

intervals $x \in [x_{\hat{l}-1}, x_{\hat{l}}]$ and $x \in [x_{\hat{l}}, x_{\hat{l}+1}]$, Eq. (16) is transformed to the form:

$$\begin{aligned} & \sum_{j=0}^J \sum_{k=0}^K \left\{ \left[C_{11}^{s(\hat{l}, m, n)} \frac{I}{x_{\hat{l}} - x_{\hat{l}-1}} \left(U_{ljk}^{1, s(\hat{l}, m, n)} - U_{l-1, jk}^{1, s(\hat{l}, m, n)} \right) \right. \right. \\ & \left. \left. - C_{11}^{s(\hat{l}+1, m, n)} \frac{I}{x_{\hat{l}+1} - x_{\hat{l}}} \left(U_{1jk}^{1, s(\hat{l}+1, m, n)} - U_{0jk}^{1, s(\hat{l}+1, m, n)} \right) \right] P_j^J(y) P_k^K(z) \right. \\ & \left. + \left[C_{12}^{s(\hat{l}, m, n)} U_{ljk}^{2, s(\hat{l}, m, n)} - C_{12}^{s(\hat{l}+1, m, n)} U_{0jk}^{2, s(\hat{l}+1, m, n)} \right] \frac{dP_j^J(y)}{dy} P_k^K(z) \right. \\ & \left. + \left[C_{13}^{s(\hat{l}, m, n)} U_{ljk}^{3, s(\hat{l}, m, n)} - C_{13}^{s(\hat{l}+1, m, n)} U_{0jk}^{3, s(\hat{l}+1, m, n)} \right] P_j^J(y) \frac{dP_k^K(z)}{dz} \right\} = 0 \end{aligned} \quad (17)$$

Next step is to incorporate relations (13), which express displacement continuity between the bricks, into (17). This results in the following equation:

$$\begin{aligned} & \sum_{j=0}^J \sum_{k=0}^K \left\{ \left[C_{11}^{s(\hat{l}, m, n)} \frac{I}{x_{\hat{l}} - x_{\hat{l}-1}} \left(U_{ljk}^{1, s(\hat{l}, m, n)} - U_{l-1, jk}^{1, s(\hat{l}, m, n)} \right) \right. \right. \\ & \left. \left. - C_{11}^{s(\hat{l}+1, m, n)} \frac{I}{x_{\hat{l}+1} - x_{\hat{l}}} \left(U_{1jk}^{1, s(\hat{l}+1, m, n)} - U_{ljk}^{1, s(\hat{l}, m, n)} \right) \right] P_j^J(y) P_k^K(z) \right. \\ & \left. + \left[C_{12}^{s(\hat{l}, m, n)} - C_{12}^{s(\hat{l}+1, m, n)} \right] U_{ljk}^{2, s(\hat{l}, m, n)} \frac{dP_j^J(y)}{dy} P_k^K(z) \right. \\ & \left. + \left[C_{13}^{s(\hat{l}, m, n)} - C_{13}^{s(\hat{l}+1, m, n)} \right] U_{ljk}^{3, s(\hat{l}, m, n)} P_j^J(y) \frac{dP_k^K(z)}{dz} \right\} = 0 \end{aligned} \quad (18)$$

This equation relates the displacement approximation coefficients $U_{ljk}^{1,s(\hat{l},m,n)}$, $U_{l-1,jk}^{1,s(\hat{l},m,n)}$,

$U_{ljk}^{1,s(\hat{l}+1,m,n)}$, $U_{ljk}^{2,s(\hat{l},m,n)}$, and $U_{ljk}^{3,s(\hat{l},m,n)}$.

The task to exactly satisfy Eq. (18) seems very difficult, may be even impossible. What could be tried is to first express the derivatives through the corresponding functions using the differentiation formula for Bernstein polynomials. Then the terms in the series can be rearranged, what will finally result in a very complex system of relationships between the displacement approximation coefficients. It is not clear if the system would be solvable without involving numerical procedures. So, it seems that only one opportunity exists to avoid this complexity. Namely, Eq.

(18) is substantially simplified in the case when adjacent bricks $s(\hat{l},m,n)$ and $s(\hat{l}+1,m,n)$ have identical elastic characteristics, i.e., when $C_{11}^{s(\hat{l},m,n)} = C_{11}^{s(\hat{l}+1,m,n)}$, $C_{12}^{s(\hat{l},m,n)} = C_{12}^{s(\hat{l}+1,m,n)}$ and $C_{13}^{s(\hat{l},m,n)} = C_{13}^{s(\hat{l}+1,m,n)}$. The following equation is then obtained:

$$\sum_{j=0}^J \sum_{k=0}^K I \cdot C_{11}^{s(\hat{l},m,n)} \left[\frac{1}{x_{\hat{l}} - x_{\hat{l}-1}} \left(U_{ljk}^{1,s(\hat{l},m,n)} - U_{l-1,jk}^{1,s(\hat{l},m,n)} \right) - \frac{1}{x_{\hat{l}+1} - x_{\hat{l}}} \left(U_{ljk}^{1,s(\hat{l}+1,m,n)} - U_{ljk}^{1,s(\hat{l},m,n)} \right) \right] P_j^J(y) P_k^K(z) = 0 \quad (19)$$

Taking into account that all basis functions are linearly independent, and that $I \neq 0$ and $C_{11}^{s(\hat{l},m,n)} \neq 0$, the following is obtained from (19):

$$\frac{1}{x_{\hat{l}} - x_{\hat{l}-1}} \left(U_{ljk}^{1,s(\hat{l},m,n)} - U_{l-1,jk}^{1,s(\hat{l},m,n)} \right) - \frac{1}{x_{\hat{l}+1} - x_{\hat{l}}} \left(U_{ljk}^{1,s(\hat{l}+1,m,n)} - U_{ljk}^{1,s(\hat{l},m,n)} \right) = 0 \quad (20)$$

for $j = 0, 1, \dots, J$ and $k = 0, 1, \dots, K$. After some manipulations this equation is written in the form

$$U_{ljk}^{1,s(\hat{l}+1,m,n)} = \frac{x_{\hat{l}+1} - x_{\hat{l}-1}}{x_{\hat{l}} - x_{\hat{l}-1}} U_{ljk}^{1,s(\hat{l},m,n)} - \frac{x_{\hat{l}+1} - x_{\hat{l}}}{x_{\hat{l}} - x_{\hat{l}-1}} U_{l-1,jk}^{1,s(\hat{l},m,n)} \quad (21)$$

Thus, if all bricks have identical material properties, the σ_x continuity condition is tremendously simplified. Note that relationships (2.21) also guarantee continuity of the *strain* ε_x at $x = x_{\hat{l}}$.

Analogous considerations can be applied for the other stress continuity conditions in Section 1, Eqs. (48) - (50). We do not present here the corresponding equations for the case of dissimilar material bricks. In the case of identical material bricks the following relationships providing continuity of *stresses* and *strains* take place:

Continuity of τ_{xy} and γ_{xy} at $x = x_{\hat{l}}$:

$$U_{1jk}^{2,s(\hat{l}+1,m,n)} = \frac{x_{\hat{l}+1} - x_{\hat{l}-1}}{x_{\hat{l}} - x_{\hat{l}-1}} U_{ijk}^{2,s(\hat{l},m,n)} - \frac{x_{\hat{l}+1} - x_{\hat{l}}}{x_{\hat{l}} - x_{\hat{l}-1}} U_{l-1jk}^{2,s(\hat{l},m,n)} \quad (22)$$

Continuity of τ_{xz} and γ_{xz} at $x = x_{\hat{l}}$:

$$U_{1jk}^{3,s(\hat{l}+1,m,n)} = \frac{x_{\hat{l}+1} - x_{\hat{l}-1}}{x_{\hat{l}} - x_{\hat{l}-1}} U_{ijk}^{3,s(\hat{l},m,n)} - \frac{x_{\hat{l}+1} - x_{\hat{l}}}{x_{\hat{l}} - x_{\hat{l}-1}} U_{l-1jk}^{3,s(\hat{l},m,n)} \quad (23)$$

Continuity of σ_y and ε_y at $y = y_{\hat{m}}$:

$$U_{ilk}^{2,s(l,\hat{m}+1,n)} = \frac{y_{\hat{m}+1} - y_{\hat{m}-1}}{y_{\hat{m}} - y_{\hat{m}-1}} U_{ijk}^{2,s(l,\hat{m},n)} - \frac{y_{\hat{m}+1} - y_{\hat{m}}}{y_{\hat{m}} - y_{\hat{m}-1}} U_{ij-1k}^{2,s(l,\hat{m},n)} \quad (24)$$

Continuity of τ_{xy} and γ_{xy} at $y = y_{\hat{m}}$:

$$U_{ilk}^{1,s(l,\hat{m}+1,n)} = \frac{y_{\hat{m}+1} - y_{\hat{m}-1}}{y_{\hat{m}} - y_{\hat{m}-1}} U_{ijk}^{1,s(l,\hat{m},n)} - \frac{y_{\hat{m}+1} - y_{\hat{m}}}{y_{\hat{m}} - y_{\hat{m}-1}} U_{ij-1k}^{1,s(l,\hat{m},n)} \quad (25)$$

Continuity of τ_{yz} and γ_{yz} at $y = y_{\hat{m}}$:

$$U_{ilk}^{3,s(l,\hat{m}+1,n)} = \frac{y_{\hat{m}+1} - y_{\hat{m}-1}}{y_{\hat{m}} - y_{\hat{m}-1}} U_{ijk}^{3,s(l,\hat{m},n)} - \frac{y_{\hat{m}+1} - y_{\hat{m}}}{y_{\hat{m}} - y_{\hat{m}-1}} U_{ij-1k}^{3,s(l,\hat{m},n)} \quad (26)$$

Continuity of σ_z and ε_z at $z = z_{\hat{n}}$:

$$U_{ijl}^{3,s(l,m,\hat{n}+1)} = \frac{z_{\hat{n}+1} - z_{\hat{n}-1}}{z_{\hat{n}} - z_{\hat{n}-1}} U_{ijk}^{3,s(l,m,\hat{n})} - \frac{z_{\hat{n}+1} - z_{\hat{n}}}{z_{\hat{n}} - z_{\hat{n}-1}} U_{ijK-1}^{3,s(l,m,\hat{n})} \quad (27)$$

Continuity of τ_{xz} and γ_{xz} at $z = z_{\hat{n}}$:

$$U_{ijl}^{1,s(l,m,\hat{n}+1)} = \frac{z_{\hat{n}+1} - z_{\hat{n}-1}}{z_{\hat{n}} - z_{\hat{n}-1}} U_{ijk}^{1,s(l,m,\hat{n})} - \frac{z_{\hat{n}+1} - z_{\hat{n}}}{z_{\hat{n}} - z_{\hat{n}-1}} U_{ijK-1}^{1,s(l,m,\hat{n})} \quad (28)$$

Continuity of τ_{yz} and γ_{yz} at $z = z_{\hat{n}}$:

$$U_{ijl}^{2,s(l,m,\hat{n}+1)} = \frac{z_{\hat{n}+1} - z_{\hat{n}-1}}{z_{\hat{n}} - z_{\hat{n}-1}} U_{ijk}^{2,s(l,m,\hat{n})} - \frac{z_{\hat{n}+1} - z_{\hat{n}}}{z_{\hat{n}} - z_{\hat{n}-1}} U_{ijK-1}^{2,s(l,m,\hat{n})} \quad (29)$$

All three groups of relations (21) - (23) can be written in the following unified form:

$$U_{ljk}^{\alpha,s(\hat{l}+1,m,n)} = \frac{x_{\hat{l}+1} - x_{\hat{l}-1}}{x_{\hat{l}} - x_{\hat{l}-1}} U_{ljk}^{\alpha,s(\hat{l},m,n)} - \frac{x_{\hat{l}+1} - x_{\hat{l}}}{x_{\hat{l}} - x_{\hat{l}-1}} U_{l-1jk}^{\alpha,s(\hat{l},m,n)} \quad (30)$$

where $\alpha = 1,2,3$; $j = 0,1,\dots,J$; $k = 0,1,\dots,K$.

All three groups of relations (24) - (26) are written as

$$U_{ilk}^{\beta,s(l,\hat{m}+1,n)} = \frac{y_{\hat{m}+1} - y_{\hat{m}-1}}{y_{\hat{m}} - y_{\hat{m}-1}} U_{ijk}^{\beta,s(l,\hat{m},n)} - \frac{y_{\hat{m}+1} - y_{\hat{m}}}{y_{\hat{m}} - y_{\hat{m}-1}} U_{iJ-1k}^{\beta,s(l,\hat{m},n)} \quad (31)$$

where $\beta = 1,2,3$; $i = 0,1,\dots,I$; $k = 0,1,\dots,K$.

And all three groups of relations (27) - (29) are unified as follows:

$$U_{ijl}^{\gamma,s(l,m,\hat{n}+1)} = \frac{z_{\hat{n}+1} - z_{\hat{n}-1}}{z_{\hat{n}} - z_{\hat{n}-1}} U_{ijk}^{\gamma,s(l,m,\hat{n})} - \frac{z_{\hat{n}+1} - z_{\hat{n}}}{z_{\hat{n}} - z_{\hat{n}-1}} U_{ijK-1}^{\gamma,s(l,m,\hat{n})} \quad (32)$$

where $\gamma = 1,2,3$; $i = 0,1,\dots,I$; $j = 0,1,\dots,J$.

The whole set of Eqs. (30) - (32) with the respective index values defined by Section 1, Eq.(51) can be only used if *all* of the brick in the mosaic body are made from the same material. If some of the bricks are made from distinct materials, then respective values of \hat{l} in (30), \hat{m} in (31) and \hat{n} in (32) should be excluded from consideration.

Thus, in the algorithm and computer code developed, all boundaries between the bricks are first segregated into two groups: the first contains all boundaries between *distinct* material bricks and the second incorporates all boundaries between *identical* material bricks. Then, relations (13) - (15) are applied to both groups and relations (30) - (32) to the second group only.

2.4 A Single-Index Form of the Continuity Relationships

For the sake of compactness, equations (13) - (15) and (30) - (32) can be further written in a single-index notation. The equivalent of (13) - (15) is obtained as follows:

$$U_{\lambda^- (\hat{l},m,n,\psi,\delta,\alpha)} = U_{\lambda^+ (\hat{l}+1,m,n,\psi,\delta,\alpha)} \quad (33)$$

$$U_{\mu^-(l,\hat{m},n,\chi,\delta,\beta)} = U_{\mu^+(l,\hat{m}+1,n,\chi,\delta,\beta)} \quad (34)$$

$$U_{v^-(l,m,\hat{n},\chi,\psi,\gamma)} = U_{v^+(l,m,\hat{n}+1,\chi,\psi,\gamma)} \quad (35)$$

where

$$\begin{aligned} \lambda^-(\hat{l},m,n,\psi,\delta,\alpha) &= \delta + (\psi - 1)(K + 1) + I(J + 1)(K + 1) \\ &+ \{(\alpha - 1) + 3[s(\hat{l},m,n) - 1]\}(I + 1)(J + 1)(K + 1) \end{aligned} \quad (36)$$

$$\begin{aligned} \lambda^+(\hat{l},m,n,\psi,\delta,\alpha) &= \delta + (\psi - 1)(K + 1) \\ &+ \{(\alpha - 1) + 3[s(\hat{l},m,n) - 1]\}(I + 1)(J + 1)(K + 1) \end{aligned} \quad (37)$$

$$\begin{aligned} \mu^-(l,\hat{m},n,\chi,\delta,\beta) &= \delta + J(K + 1) + (\chi - 1)(J + 1)(K + 1) \\ &+ \{(\beta - 1) + 3[s(l,\hat{m},n) - 1]\}(I + 1)(J + 1)(K + 1) \end{aligned} \quad (38)$$

$$\begin{aligned} \mu^+(l,\hat{m},n,\chi,\delta,\beta) &= \delta + (\chi - 1)(J + 1)(K + 1) \\ &+ \{(\beta - 1) + 3[s(l,\hat{m},n) - 1]\}(I + 1)(J + 1)(K + 1) \end{aligned} \quad (39)$$

$$\begin{aligned} v^-(l,m,\hat{n},\chi,\psi,\gamma) &= \psi(K + 1) + (\chi - 1)(J + 1)(K + 1) \\ &+ \{(\gamma - 1) + 3[s(l,m,\hat{n}) - 1]\}(I + 1)(J + 1)(K + 1) \end{aligned} \quad (40)$$

$$\begin{aligned} v^+(l,m,\hat{n},\chi,\psi,\gamma) &= \psi(K + 1) - K + (\chi - 1)(J + 1)(K + 1) \\ &+ \{(\gamma - 1) + 3[s(l,m,\hat{n}) - 1]\}(I + 1)(J + 1)(K + 1) \end{aligned} \quad (41)$$

Here, $\alpha, \beta, \gamma = 1, 2, 3$ and the values of $l, m, n, \hat{l}, \hat{m}$ and \hat{n} follow the respective expressions Section 1, Eqs. (41), (44) and (47). In addition, the following integer variables have been introduced:

$$\chi = 1, 2, \dots, I + 1; \quad \psi = 1, 2, \dots, J + 1; \quad \delta = 1, 2, \dots, K + 1 \quad (42)$$

The earlier derived stress/strain continuity relations (2.30)-(2.32) are now transformed to the form

$$U_{\lambda^+(\hat{l}+1, m, n, \psi, \delta, \alpha) + (J+1)(K+1)} = A_1 U_{\lambda^-(\hat{l}, m, n, \psi, \delta, \alpha)} - A_2 U_{\lambda^-(\hat{l}, m, n, \psi, \delta, \alpha) - (J+1)(K+1)} \quad (43)$$

$$U_{\mu^+(l, \hat{m}+1, n, \chi, \delta, \beta) + (K+1)} = B_1 U_{\mu^-(l, \hat{m}, n, \chi, \delta, \beta)} - B_2 U_{\mu^-(l, \hat{m}, n, \chi, \delta, \beta) - (K+1)} \quad (44)$$

$$U_{v^+(l, m, \hat{n}+1, \chi, \psi, \gamma) + 1} = C_1 U_{v^-(l, m, \hat{n}, \chi, \psi, \gamma)} - C_2 U_{v^-(l, m, \hat{n}, \chi, \psi, \gamma) - 1} \quad (45)$$

where

$$\begin{aligned} A_1 &= \frac{x_{\hat{l}+1} - x_{\hat{l}-1}}{x_{\hat{l}} - x_{\hat{l}-1}}, \quad A_2 = \frac{x_{\hat{l}+1} - x_{\hat{l}}}{x_{\hat{l}} - x_{\hat{l}-1}}, \\ B_1 &= \frac{y_{\hat{m}+1} - y_{\hat{m}-1}}{y_{\hat{m}} - y_{\hat{m}-1}}, \quad B_2 = \frac{y_{\hat{m}+1} - y_{\hat{m}}}{y_{\hat{m}} - y_{\hat{m}-1}}, \\ C_1 &= \frac{z_{\hat{n}+1} - z_{\hat{n}-1}}{z_{\hat{n}} - z_{\hat{n}-1}}, \quad C_2 = \frac{z_{\hat{n}+1} - z_{\hat{n}}}{z_{\hat{n}} - z_{\hat{n}-1}} \end{aligned} \quad (46)$$

Yet, the derived continuity relations (33) - (35) and (43) - (45) are not sufficient for solving boundary value problems for 3-D mosaic structures. Some additional considerations are required.

2.5 Classification of Special Junction Lines and Points

The derived relationships expressing the displacement continuity (33) - (35) and stress/strain continuity (43) - (45) conditions, written for the interfaces in the mosaic body, each represents an *ordinary* equality. However, it is easy to recognize that there are also certain lines and points in the mosaic body where the continuity conditions are expressed as *multiple* equalities. Thus, further algorithmic considerations require first to reveal all types of special lines and points and then derive additional continuity relationships for them.

Considering generic illustration presented in Fig. 2.1, the following three distinct groups of points and lines are identified:

- (i) Interior junction points (represented by the point “A” in the figure). These are the points of *eight brick junction*; all of these points are inside the mosaic body.

- (ii) Exterior junction points (represented by the points “a”, “b”, “c”, “d”, “e” and “f” in the figure). These are the points of *four brick junction*; all of these points belong to the exterior of the mosaic body.

- (iii) Interior junction lines (represented by the open end lines “aA”, “Ab”, “cA”, “Ad”, “fA” and “Ae” in the figure). These are the lines of *four brick junction*; all of them are inside the mosaic body.

It is easy to check that the groups (i), (ii) and (iii) cover all of the special points and lines which are possible in the case of a regular mosaic parallelepiped. However, for an arbitrary *irregular* mosaic structure there can be a number of additional cases (for example, the exterior junction point of *seven* bricks, the exterior junction line of *three* bricks, etc.). All of them require special consideration and provide their specific type of the continuity relations. Here, for the purpose of brevity we only address the above cases (i), (ii) and (iii).

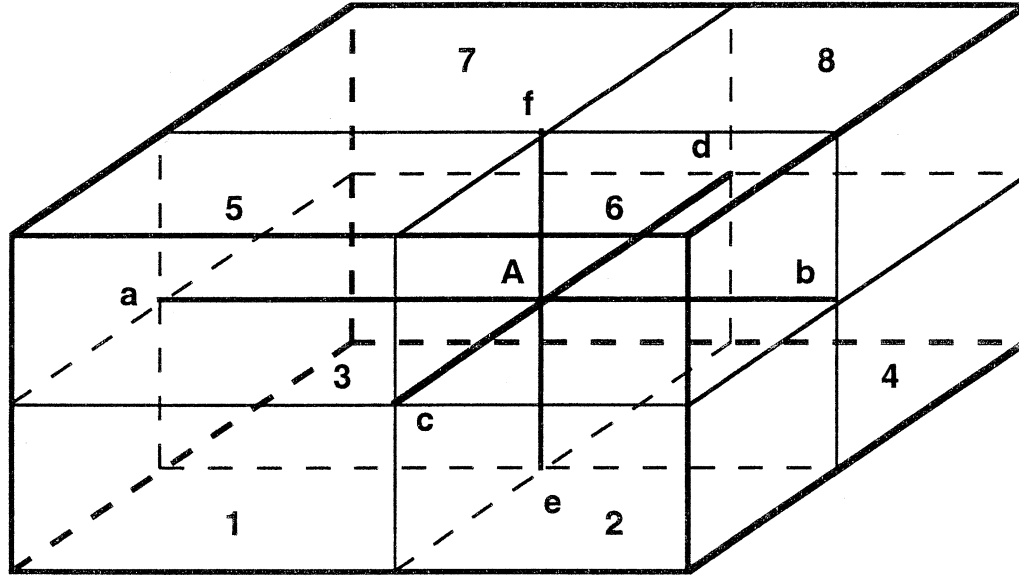


Fig. 2.1: Illustration of the junction points and lines in the mosaic body.

2.6 Continuity of Displacements at the Interior Junction Points

First consider continuity of displacements at the interior junction points of a regular mosaic parallelepiped. These class of points is represented by “A” in Fig. 2.1. The following *twelve* equations should be simultaneously satisfied at each of the points:

$$\begin{aligned}
 U_{\lambda^- (l^*, m^*, n^*, J+1, K+1, \alpha)} &= U_{\lambda^+ (l^*+1, m^*, n^*, J+1, K+1, \alpha)} \\
 U_{\lambda^- (l^*, m^*+1, n^*, 1, K+1, \alpha)} &= U_{\lambda^+ (l^*+1, m^*+1, n^*, 1, K+1, \alpha)} \\
 U_{\lambda^- (l^*, m^*, n^*+1, J+1, 1, \alpha)} &= U_{\lambda^+ (l^*+1, m^*, n^*+1, J+1, 1, \alpha)} \\
 U_{\lambda^- (l^*, m^*+1, n^*+1, 1, 1, \alpha)} &= U_{\lambda^+ (l^*+1, m^*+1, n^*+1, 1, 1, \alpha)} \\
 U_{\mu^- (l^*, m^*, n^*, I+1, K+1, \alpha)} &= U_{\mu^+ (l^*, m^*+1, n^*, I+1, K+1, \alpha)} \\
 U_{\mu^- (l^*+1, m^*, n^*, 1, K+1, \alpha)} &= U_{\mu^+ (l^*+1, m^*+1, n^*, 1, K+1, \alpha)} \\
 U_{\mu^- (l^*, m^*, n^*+1, I+1, 1, \alpha)} &= U_{\mu^+ (l^*, m^*+1, n^*+1, I+1, 1, \alpha)}
 \end{aligned} \tag{47}$$

$$\begin{aligned}
U_{\mu^{-}(l^{*}+1,m^{*},n^{*}+1,1,1,\alpha)} &= U_{\mu^{+}(l^{*}+1,m^{*}+1,n^{*}+1,1,1,\alpha)} \\
U_{v^{-}(l^{*},m^{*},n^{*},I+1,J+1,\alpha)} &= U_{v^{+}(l^{*},m^{*},n^{*}+1,I+1,J+1,\alpha)} \\
U_{v^{-}(l^{*}+1,m^{*},n^{*},1,J+1,\alpha)} &= U_{v^{+}(l^{*}+1,m^{*},n^{*}+1,1,J+1,\alpha)} \\
U_{v^{-}(l^{*},m^{*}+1,n^{*},I+1,1,\alpha)} &= U_{v^{+}(l^{*},m^{*}+1,n^{*}+1,I+1,1,\alpha)} \\
U_{v^{-}(l^{*}+1,m^{*}+1,n^{*},1,1,\alpha)} &= U_{v^{+}(l^{*}+1,m^{*}+1,n^{*}+1,1,1,\alpha)}
\end{aligned} \tag{47}$$

where $\alpha = 1, 2, 3$; $l^{*} = 2, \dots, L$; $m^{*} = 2, \dots, M$; $n^{*} = 2, \dots, N$.

It is easy to show that *not all* of the above equations are independent. This can be seen, for example, if considering the following equalities obtained from the definitions (36) - (41):

$$\begin{aligned}
\lambda^{-}(l^{*},m^{*},n^{*},J+1,K+1,\alpha) &= \mu^{-}(l^{*},m^{*},n^{*},I+1,K+1,\alpha) \\
\lambda^{-}(l^{*},m^{*}+1,n^{*},1,K+1,\alpha) &= \mu^{+}(l^{*},m^{*}+1,n^{*},I+1,K+1,\alpha) \\
\lambda^{+}(l^{*}+1,m^{*},n^{*},J+1,K+1,\alpha) &= \mu^{-}(l^{*}+1,m^{*},n^{*},1,K+1,\alpha) \\
\lambda^{+}(l^{*}+1,m^{*}+1,n^{*},1,K+1,\alpha) &= \mu^{+}(l^{*}+1,m^{*}+1,n^{*},1,K+1,\alpha) \\
\lambda^{-}(l^{*},m^{*},n^{*}+1,J+1,1,\alpha) &= \mu^{-}(l^{*},m^{*},n^{*}+1,I+1,1,\alpha) \\
\lambda^{-}(l^{*},m^{*}+1,n^{*}+1,1,1,\alpha) &= \mu^{+}(l^{*},m^{*}+1,n^{*}+1,I+1,1,\alpha) \\
\lambda^{+}(l^{*}+1,m^{*},n^{*}+1,J+1,1,\alpha) &= \mu^{-}(l^{*}+1,m^{*},n^{*}+1,1,1,\alpha) \\
\lambda^{+}(l^{*}+1,m^{*}+1,n^{*}+1,1,1,\alpha) &= \mu^{+}(l^{*}+1,m^{*}+1,n^{*}+1,1,1,\alpha)
\end{aligned} \tag{48}$$

$$\begin{aligned}
\lambda^{-}(l^{*},m^{*},n^{*},J+1,K+1,\alpha) &= v^{-}(l^{*},m^{*},n^{*},I+1,J+1,\alpha) \\
\lambda^{-}(l^{*},m^{*},n^{*}+1,J+1,1,\alpha) &= v^{+}(l^{*},m^{*},n^{*}+1,I+1,J+1,\alpha) \\
\lambda^{+}(l^{*}+1,m^{*},n^{*},J+1,K+1,\alpha) &= v^{-}(l^{*}+1,m^{*},n^{*},1,J+1,\alpha) \\
\lambda^{+}(l^{*}+1,m^{*},n^{*}+1,J+1,1,\alpha) &= v^{+}(l^{*}+1,m^{*},n^{*}+1,1,J+1,\alpha)
\end{aligned}$$

$$\begin{aligned}
\mu^+(l^*, m^*+1, n^*, I+1, K+1, \alpha) &= v^-(l^*, m^*+1, n^*, I+1, 1, \alpha) \\
\mu^+(l^*, m^*+1, n^*+1, I+1, 1, \alpha) &= v^+(l^*, m^*+1, n^*+1, I+1, 1, \alpha) \\
\lambda^+(l^*+1, m^*+1, n^*, 1, K+1, \alpha) &= v^-(l^*+1, m^*+1, n^*, 1, 1, \alpha) \\
\lambda^+(l^*+1, m^*+1, n^*+1, 1, 1, \alpha) &= v^+(l^*+1, m^*+1, n^*+1, 1, 1, \alpha)
\end{aligned} \tag{48}$$

There are different possibilities of combining (47) and (48). One of them leads to the following chain of *seven* equations:

$$\begin{aligned}
U_{\lambda^-(l^*, m^*, n^*, J+1, K+1, \alpha)} &= U_{\lambda^+(l^*+1, m^*, n^*, J+1, K+1, \alpha)} = U_{\mu^+(l^*, m^*+1, n^*, I+1, K+1, \alpha)} \\
&= U_{\lambda^+(l^*+1, m^*+1, n^*, 1, K+1, \alpha)} = U_{\lambda^-(l^*, m^*, n^*+1, J+1, 1, \alpha)} = U_{\lambda^+(l^*+1, m^*, n^*+1, J+1, 1, \alpha)} \\
&= U_{\mu^+(l^*, m^*+1, n^*+1, I+1, 1, \alpha)} = U_{\lambda^+(l^*+1, m^*+1, n^*+1, 1, 1, \alpha)}
\end{aligned} \tag{49}$$

If equations (2.49) are satisfied, then the displacements are continuous at all of the interior junction points.

2.7 Continuity of Displacements at the Exterior Junction Points

Consider next continuity of displacements at the points of four brick junctions at the exterior surfaces of the mosaic body. This class of points is represented by “a”, “b”, “c”, “d”, “e” and “f” in Fig. 2.1. In all equations of this section $\beta = 1, 2, 3$.

At the left exterior surface ($x = x_1$) the following *four* relations should be satisfied:

$$\begin{aligned}
U_{\mu^-(2, m^*, n^*, 1, K+1, \beta)} &= U_{\mu^+(2, m^*+1, n^*, 1, K+1, \beta)} \\
U_{\mu^-(2, m^*, n^*+1, 1, 1, \beta)} &= U_{\mu^+(2, m^*+1, n^*+1, 1, 1, \beta)} \\
U_{v^-(2, m^*, n^*, 1, J+1, \beta)} &= U_{v^+(2, m^*, n^*+1, 1, J+1, \beta)} \\
U_{v^-(2, m^*+1, n^*, 1, 1, \beta)} &= U_{v^+(2, m^*+1, n^*+1, 1, 1, \beta)}
\end{aligned} \tag{50}$$

By using certain relations which follow from the definitions (36) - (41), Eq. (50) are reduced to

$$U_{\mu^- (2, m^*, n^*, 1, K+1, \beta)} = U_{\mu^+ (2, m^*+1, n^*, 1, K+1, \beta)} = U_{\mu^- (2, m^*, n^*+1, 1, 1, \beta)} = U_{\mu^+ (2, m^*+1, n^*+1, 1, 1, \beta)} \quad (51)$$

If (51) is satisfied, then displacements are continuous at all junction points belonging to the surface $x=x_l$.

The following displacement continuity relations should be satisfied at the exterior junction points belonging to $x = x_{L+1}$:

$$\begin{aligned} U_{\mu^- (L+1, m^*, n^*, I+1, K+1, \beta)} &= U_{\mu^+ (L+1, m^*+1, n^*, I+1, K+1, \beta)} \\ U_{\mu^- (L+1, m^*, n^*+1, I+1, 1, \beta)} &= U_{\mu^+ (L+1, m^*+1, n^*+1, I+1, 1, \beta)} \\ U_{\nu^- (L+1, m^*, n^*, I+1, J+1, \beta)} &= U_{\nu^+ (L+1, m^*, n^*+1, I+1, J+1, \beta)} \\ U_{\nu^- (L+1, m^*+1, n^*, I+1, 1, \beta)} &= U_{\nu^+ (L+1, m^*+1, n^*+1, I+1, 1, \beta)} \end{aligned} \quad (52)$$

which are reduced to

$$\begin{aligned} U_{\mu^- (L+1, m^*, n^*, I+1, K+1, \beta)} &= U_{\mu^+ (L+1, m^*+1, n^*, I+1, K+1, \beta)} = U_{\mu^- (L+1, m^*, n^*+1, I+1, 1, \beta)} \\ &= U_{\mu^+ (L+1, m^*+1, n^*+1, I+1, 1, \beta)} \end{aligned} \quad (53)$$

Next, it is written for the exterior junction points belonging to the side $y = y_1$:

$$\begin{aligned} U_{\lambda^- (l^*, 2, n^*, 1, K+1, \beta)} &= U_{\lambda^+ (l^*+1, 2, n^*, 1, K+1, \beta)} \\ U_{\lambda^- (l^*, 2, n^*+1, 1, 1, \beta)} &= U_{\lambda^+ (l^*+1, 2, n^*+1, 1, 1, \beta)} \\ U_{\nu^- (l^*, 2, n^*, I+1, 1, \beta)} &= U_{\nu^+ (l^*, 2, n^*+1, I+1, 1, \beta)} \\ U_{\nu^- (l^*+1, 2, n^*, 1, 1, \beta)} &= U_{\nu^+ (l^*+1, 2, n^*+1, 1, 1, \beta)} \end{aligned} \quad (54)$$

These equations are reduced to

$$U_{\lambda^- (l^*, 2, n^*, 1, K+1, \beta)} = U_{\lambda^+ (l^*+1, 2, n^*, 1, K+1, \beta)} = U_{\lambda^- (l^*, 2, n^*+1, 1, 1, \beta)} = U_{\lambda^+ (l^*+1, 2, n^*+1, 1, 1, \beta)} \quad (55)$$

Considering the exterior junction points at $y = y_{M+1}$, the following relations should be satisfied:

$$\begin{aligned}
U_{\lambda^- (l^*, M+1, n^*, J+1, K+1, \beta)} &= U_{\lambda^+ (l^*+1, M+1, n^*, J+1, K+1, \beta)} \\
U_{\lambda^- (l^*, M+1, n^*+1, J+1, 1, \beta)} &= U_{\lambda^+ (l^*+1, M+1, n^*+1, J+1, 1, \beta)} \\
U_{\nu^- (l^*, M+1, n^*, I+1, J+1, \beta)} &= U_{\nu^+ (l^*, M+1, n^*+1, I+1, J+1, \beta)} \\
U_{\nu^- (l^*+1, M+1, n^*, 1, J+1, \beta)} &= U_{\nu^+ (l^*+1, M+1, n^*+1, 1, J+1, \beta)}
\end{aligned} \tag{56}$$

These equations are reduced to

$$\begin{aligned}
U_{\lambda^- (l^*, M+1, n^*, J+1, K+1, \beta)} &= U_{\lambda^+ (l^*+1, M+1, n^*, J+1, K+1, \beta)} = U_{\lambda^- (l^*, M+1, n^*+1, J+1, 1, \beta)} \\
&= U_{\lambda^+ (l^*+1, M+1, n^*+1, J+1, 1, \beta)}
\end{aligned} \tag{57}$$

When considering external junction points belonging to $z = z_1$, one obtains

$$\begin{aligned}
U_{\lambda^- (l^*, m^*, 2, J+1, 1, \beta)} &= U_{\lambda^+ (l^*+1, m^*, 2, J+1, 1, \beta)} \\
U_{\lambda^- (l^*, m^*+1, 2, 1, 1, \beta)} &= U_{\lambda^+ (l^*+1, m^*+1, 2, 1, 1, \beta)} \\
U_{\mu^- (l^*, m^*, 2, I+1, 1, \beta)} &= U_{\mu^+ (l^*, m^*+1, 2, I+1, 1, \beta)} \\
U_{\mu^- (l^*+1, m^*, 2, 1, 1, \beta)} &= U_{\mu^+ (l^*+1, m^*+1, 2, 1, 1, \beta)}
\end{aligned} \tag{58}$$

These equations reduce to

$$U_{\lambda^- (l^*, m^*, 2, J+1, 1, \beta)} = U_{\lambda^+ (l^*+1, m^*, 2, J+1, 1, \beta)} = U_{\lambda^- (l^*, m^*+1, 2, 1, 1, \beta)} = U_{\lambda^+ (l^*+1, m^*+1, 2, 1, 1, \beta)} \tag{59}$$

Finally, in the case of exterior junction points at $z = z_{N+1}$ the displacement continuity relationships are:

$$\begin{aligned}
U_{\lambda^- (l^*, m^*, N+1, J+1, K+1, \beta)} &= U_{\lambda^+ (l^*+1, m^*, N+1, J+1, K+1, \beta)} \\
U_{\lambda^- (l^*, m^*+1, N+1, 1, K+1, \beta)} &= U_{\lambda^+ (l^*+1, m^*+1, N+1, 1, K+1, \beta)} \\
U_{\mu^- (l^*, m^*, N+1, I+1, K+1, \beta)} &= U_{\mu^+ (l^*, m^*+1, N+1, I+1, K+1, \beta)} \\
U_{\mu^- (l^*+1, m^*, N+1, 1, K+1, \beta)} &= U_{\mu^+ (l^*+1, m^*+1, N+1, 1, K+1, \beta)}
\end{aligned} \tag{60}$$

These are reduced to

$$\begin{aligned} U_{\lambda^-(l^*, m^*, N+1, J+1, K+1, \beta)} &= U_{\lambda^+(l^*+1, m^*, N+1, J+1, K+1, \beta)} = U_{\lambda^-(l^*, m^*+1, N+1, 1, K+1, \beta)} \\ &= U_{\lambda^+(l^*+1, m^*+1, N+1, 1, K+1, \beta)} \end{aligned} \quad (61)$$

The obtained Eqs. (51), (53), (55), (57), (59) and (61) guarantee continuity of displacements at the whole exterior of a regular mosaic parallelepiped.

2.8 Continuity Of Displacements At The Interior Junction Lines

Next consider interior junction lines which are represented in Fig. 2.1 by the lines “aA”, “Ab”, “cA”, “Ad”, “eA” and “AF”. In all equations of this section $\gamma = 1, 2, 3$.

The following displacement continuity conditions should be satisfied at the interior junction lines parallel to the x -axis:

$$\begin{aligned} U_{\mu^-(l^*, m^*, n^*, \chi, K+1, \gamma)} &= U_{\mu^+(l^*, m^*+1, n^*, \chi, K+1, \gamma)} \\ U_{\mu^-(l^*, m^*, n^*+1, \chi, 1, \gamma)} &= U_{\mu^+(l^*, m^*+1, n^*+1, \chi, 1, \gamma)} \\ U_{\nu^-(l^*, m^*, n^*, \chi, J+1, \gamma)} &= U_{\nu^+(l^*, m^*, n^*+1, \chi, J+1, \gamma)} \\ U_{\nu^-(l^*, m^*+1, n^*, \chi, 1, \gamma)} &= U_{\nu^+(l^*, m^*+1, n^*+1, \chi, 1, \gamma)} \end{aligned} \quad (62)$$

where $l^* = 2, \dots, L+1$; $m^* = 2, \dots, M$; $n^* = 2, \dots, N$; $\chi = 2, \dots, I$. It can be recognized that not all of the above relations are independent. By using certain relations following from (36) - (41), the following is obtained:

$$\begin{aligned} U_{\mu^-(l^*, m^*, n^*, \chi, K+1, \gamma)} &= U_{\mu^+(l^*, m^*+1, n^*, \chi, K+1, \gamma)} = U_{\mu^-(l^*, m^*, n^*+1, \chi, 1, \gamma)} \\ &= U_{\mu^+(l^*, m^*+1, n^*+1, \chi, 1, \gamma)} \end{aligned} \quad (63)$$

The following displacement continuity relations should be satisfied at the interior junction lines parallel to the y -axis:

$$\begin{aligned}
U_{\lambda^-(l^*, m^*, n^*, \psi, K+1, \gamma)} &= U_{\lambda^+(l^*+1, m^*, n^*, \psi, K+1, \gamma)} \\
U_{\lambda^-(l^*, m^*, n^*+1, \psi, 1, \gamma)} &= U_{\lambda^+(l^*+1, m^*, n^*+1, \psi, 1, \gamma)} \\
U_{\nu^-(l^*, m^*, n^*, I+1, \psi, \gamma)} &= U_{\nu^+(l^*, m^*, n^*+1, I+1, \psi, \gamma)} \\
U_{\nu^-(l^*+1, m^*, n^*, 1, \psi, \gamma)} &= U_{\nu^+(l^*+1, m^*, n^*+1, 1, \psi, \gamma)}
\end{aligned} \tag{64}$$

where $l^* = 2, \dots, L$; $m^* = 2, \dots, M+1$; $n^* = 2, \dots, N$; $\psi = 2, \dots, J$. The above equations are reduced to

$$\begin{aligned}
U_{\lambda^-(l^*, m^*, n^*, \psi, K+1, \gamma)} &= U_{\lambda^+(l^*+1, m^*, n^*, \psi, K+1, \gamma)} = U_{\lambda^-(l^*, m^*, n^*+1, \psi, 1, \gamma)} \\
&= U_{\lambda^+(l^*+1, m^*, n^*+1, \psi, 1, \gamma)}
\end{aligned} \tag{65}$$

Finally, consider the interior junction lines parallel to the z -axis. The following displacement continuity relations should be satisfied there:

$$\begin{aligned}
U_{\lambda^-(l^*, m^*, n^*, J+1, \delta, \gamma)} &= U_{\lambda^+(l^*+1, m^*, n^*, J+1, \delta, \gamma)} \\
U_{\lambda^-(l^*, m^*+1, n^*, 1, \delta, \gamma)} &= U_{\lambda^+(l^*+1, m^*+1, n^*, 1, \delta, \gamma)} \\
U_{\mu^-(l^*, m^*, n^*, I+1, \delta, \gamma)} &= U_{\mu^+(l^*, m^*+1, n^*, I+1, \delta, \gamma)} \\
U_{\mu^-(l^*+1, m^*, n^*, 1, \delta, \gamma)} &= U_{\mu^+(l^*+1, m^*+1, n^*, 1, \delta, \gamma)}
\end{aligned} \tag{66}$$

where $l^* = 2, \dots, L$; $m^* = 2, \dots, M$; $n^* = 2, \dots, N+1$; $\delta = 2, \dots, K$. The above relations are reduced to

$$U_{\lambda^-(l^*, m^*, n^*, J+1, \delta, \gamma)} = U_{\lambda^+(l^*+1, m^*, n^*, J+1, \delta, \gamma)} = U_{\lambda^-(l^*, m^*+1, n^*, 1, \delta, \gamma)} = U_{\lambda^+(l^*+1, m^*+1, n^*, 1, \delta, \gamma)} \tag{67}$$

Now it is easy to recognize that Eqs. (51) and (53) can be formally obtained from (63) by substituting $l^* = 2$, $\chi = 1$ and $l^* = L+1$, $\chi = I+1$, respectively. Equations (55) and (57) can be obtained from (65) by substituting $m^* = 2$, $\psi = 1$ and $m^* = M+1$, $\psi = J+1$, respectively. And Eqs. (59) and (61) can be obtained from (67) by substituting $n^* = 2$, $\delta = 1$ and $n^* = N+1$, $\delta = K+1$, respectively. However, it is suitable to consider (51), (53), (55), (57), (59) and (61)

separately from (63), (65) and (67). The reason is that the latter group of equations provides the displacement continuity conditions along the (open-ended) junction lines and, thus, would not interact with external geometric boundary conditions. At the same time, the former group of equations provides the displacement continuity conditions at the exterior junction points, so these equations may interact with the imposed external geometric boundary conditions.

The obtained “multiple” displacement continuity relations at the interior junction points (49), exterior junction points (51), (53), (55), (57), (59), (61) and interior junction lines (63), (65) and (67) should complement the “ordinary” displacement continuity relations (33) - (35). Their use allows one to avoid repetitive kinematic constraints and, at the same time, guarantee continuity of displacements everywhere in a regular mosaic parallelepiped. As mentioned before, when solving irregular mosaic structures, some additional continuity relations should be applied. All of the necessary displacement continuity relations have been implemented in the developed computer code 3D MOSAIC.

Analogous derivations have been performed for the strain/stress continuity relations at the interior junction points, exterior junction points and interior junction lines. Those relations complement (2.43)-(2.45) and can be applied between identical material bricks. However, those have not been yet implemented in the computer code.

2.9 External Geometric Boundary Conditions

Now we will generalize the study where a single brick has been treated under various combinations of geometric boundary conditions formulated in terms of uniform displacements.

Consider s^{th} brick which exterior surfaces are defined by the coordinate values x_l , x_{l+1} , y_m , y_{m+1} , z_n and z_{n+1} . If the definition $s = 1 + (l - 2) + (m - 2)L + (n - 2)L \cdot M$ is used, where $l = 2, \dots, L + 1$; $m = 2, \dots, M + 1$; $n = 2, \dots, N + 1$, then each brick is uniquely identified in the mosaic body shown in Fig. 1.3. The maximum possible set of displacement boundary conditions for the s^{th} brick is formulated as follows:

$$u_x^{(s)}(x_l, y, z) = u_{x_l}^{1(s)}(y, z), \quad u_y^{(s)}(x_l, y, z) = u_{x_l}^{2(s)}(y, z), \quad u_z^{(s)}(x_l, y, z) = u_{x_l}^{3(s)}(y, z) \quad (68)$$

$$u_x^{(s)}(x_{l+1}, y, z) = u_{x_{l+1}}^{1(s)}(y, z), \quad u_y^{(s)}(x_{l+1}, y, z) = u_{x_{l+1}}^{2(s)}(y, z), \quad u_z^{(s)}(x_{l+1}, y, z) = u_{x_{l+1}}^{3(s)}(y, z) \quad (69)$$

$$u_x^{(s)}(x, y_m, z) = u_{y_m}^{1(s)}(x, z), \quad u_y^{(s)}(x, y_m, z) = u_{y_m}^{2(s)}(x, z), \quad u_z^{(s)}(x, y_m, z) = u_{y_m}^{3(s)}(x, z) \quad (70)$$

$$u_x^{(s)}(x, y_{m+1}, z) = u_{y_{m+1}}^{1(s)}(x, z), \quad u_y^{(s)}(x, y_{m+1}, z) = u_{y_{m+1}}^{2(s)}(x, z), \quad u_z^{(s)}(x, y_{m+1}, z) = u_{y_{m+1}}^{3(s)}(x, z) \quad (71)$$

$$u_x^{(s)}(x, y, z_n) = u_{z_n}^{1(s)}(x, y), \quad u_y^{(s)}(x, y, z_n) = u_{z_n}^{2(s)}(x, y), \quad u_z^{(s)}(x, y, z_n) = u_{z_n}^{3(s)}(x, y) \quad (72)$$

$$u_x^{(s)}(x, y, z_{n+1}) = u_{z_{n+1}}^{1(s)}(x, y), \quad u_y^{(s)}(x, y, z_{n+1}) = u_{z_{n+1}}^{2(s)}(x, y), \quad u_z^{(s)}(x, y, z_{n+1}) = u_{z_{n+1}}^{3(s)}(x, y) \quad (73)$$

where $u_{x_l}^{\alpha(s)}(y, z)$, $u_{x_{l+1}}^{\alpha(s)}(y, z)$, $u_{y_m}^{\beta(s)}(x, z)$, $u_{y_{m+1}}^{\beta(s)}(x, z)$, $u_{z_n}^{\gamma(s)}(x, y)$, and $u_{z_{n+1}}^{\gamma(s)}(x, y)$ are given

functions of the corresponding two coordinates; indices α , β and γ may take any combination of 1, 2 and 3. The maximum number of boundary conditions allowed by (68) - (73) is 18.

Now consider one specific case, when *uniform* displacements are applied on each of those sides of the bricks which belong to the exterior of the mosaic body. So,

$$u_{x_l}^{\alpha(s)}(y, z) = u_{x_l}^{\alpha, s(2, m, n)}, \quad u_{x_{l+1}}^{\alpha(s)}(y, z) = u_{x_{l+1}}^{\alpha, s(L+1, m, n)} \quad (74)$$

where m and n take all values from (1.41);

$$u_{y_m}^{\beta(s)}(x, z) = u_{y_l}^{\beta, s(l, 2, n)}, \quad u_{y_{m+1}}^{\beta(s)}(x, z) = u_{y_{M+1}}^{\beta, s(l, M+1, n)} \quad (75)$$

where l and n take all values from Section 1, Eq. (44), and

$$u_{z_n}^{\gamma(s)}(x, y) = u_{z_1}^{\gamma, s(l, m, 2)}, \quad u_{z_{n+1}}^{\gamma(s)}(x, y) = u_{z_{N+1}}^{\gamma, s(l, m, N+1)} \quad (76)$$

where l and m take all values from Section 1, Eq. (47). The values of s in (74) - (76) are defined as $s = 1 + (l - 2) + (m - 2)L + (n - 2)L \cdot M$. The right hand sides are *given* values.

After substituting displacement approximation (4) in (68) - (73), using the property of Bernstein basis functions (8) and accounting for (74) - (76), the following equations are obtained:

$$U_{\lambda^+(2, m, n, \varphi, \delta, \alpha)} = u_{x_1}^{\alpha, s(2, m, n)} \quad (77)$$

$$U_{\lambda^-(L+1, m, n, \varphi, \delta, \alpha)} = u_{x_{L+1}}^{\alpha, s(L+1, m, n)} \quad (78)$$

$$U_{\mu^+(l, 2, n, \chi, \delta, \beta)} = u_{y_1}^{\beta, s(l, 2, n)} \quad (79)$$

$$U_{\mu^-(l, M+1, n, \chi, \delta, \beta)} = u_{y_{M+1}}^{\beta, s(l, M+1, n)} \quad (80)$$

$$U_{v^+(l, m, 2, \chi, \varphi, \gamma)} = u_{z_1}^{\gamma, s(l, m, 2)} \quad (81)$$

$$U_{v^-(l, m, N+1, \chi, \varphi, \gamma)} = u_{z_{N+1}}^{\gamma, s(l, m, N+1)} \quad (82)$$

with the notations earlier introduced in (36) - (41). The obtained Eqs. (77) - (82) cover all possible combinations of external geometric boundary conditions for a mosaic body.

2.10 Further Algorithmic Considerations

Our next task is to develop mathematical algorithms allowing to derive specific forms of the generic system of linear simultaneous equations (1.33) with account for the internal continuity conditions and external geometric boundary conditions. When incorporating external geometric boundary conditions, the required procedures can be outlined as follows. There are two steps of modifications of (1.33) which take place:

- (i) certain equations are dropped in the system and
- (ii) some additional terms are added to the right hand sides of the system remaining after step (i).

The result is the following system of simultaneous equations:

$$\left[a_{\bar{\phi}\bar{\phi}} \right] \left\{ U_{\bar{\phi}} \right\} = \left\{ Q_{\bar{\phi}} \right\} - \left[a_{\phi'\bar{\phi}} \right] \left\{ U_{\phi'} \right\} \quad (83)$$

Set of numbers $\Phi' = (\phi')$ depends on the specific case of external geometric boundary conditions.

Set of numbers $\bar{\Phi} = (\bar{\phi})$ is defined through the relationship

$$\bar{\Phi} \cup \Phi' = \Phi \quad (84)$$

where $\Phi = (\phi)$, and values of ϕ were defined in Section 1, Eq. (35). Set of numbers $(\bar{\phi})$ is the same as $(\bar{\phi})$, i.e., $\bar{\Phi} = (\bar{\phi})$. Having relationship (84), it is easy to derive any specific form of (83); the only question is to identify $\Phi' = (\phi')$.

Next step is to modify the strain energy expressions Section 1, Eqs. (12) or (15) by incorporating the continuity relations derived in Sections 2.4 and 2.6 - 2.8. The corresponding modifications consist of a rather straightforward, but very cumbersome algebraic manipulations, which are dropped here.

As is seen, the developed variational theory and mathematical algorithms allow one to obtain *analytical* expressions of the matrix elements in (83) and, in some cases also analytically derive the right-hand side vector. The only essentially *non-analytical* procedures are required for numerical integration of the above system of equations.

Driver *CDRV* [3] was used in the current version of computer code 3D MOSAIC for solving sparse systems of linear simultaneous equations (83). Compressed pointer storage of the *non-zero* elements of matrix \mathbf{A} is utilized, which provides huge savings of the RAM space and, accordingly, allows one to significantly increase number of bricks in the computational model using the same computer. The adopted compressed storage scheme is identical to that used in Yale Sparse Matrix Package [4]. Solution algorithm is based on *LDU* decomposition of matrix \mathbf{A} , which is presented as $\mathbf{L} \cdot \mathbf{D} \cdot \mathbf{U} = \mathbf{A}$, where \mathbf{L} is unit lower triangular matrix, \mathbf{D} is diagonal matrix, and \mathbf{U} is unit upper triangular matrix.

After the vector \mathbf{U} is found, the displacements are computed directly from the approximation (4) by the triple series summation. Then, strains are directly computed from the strain-displacement Section 1, Eq. (4). Finally, the stresses are directly computed from the stress-strain Section 1, Eq. (1). Thus, any displacement, strain or stress component is obtained in the form of respective triple series. By prescribing three coordinate values, any strain/stress characteristic can be obtained for any point of the mosaic structure. Flow chart of the developed algorithm and computer code is shown in Fig. 2.2.

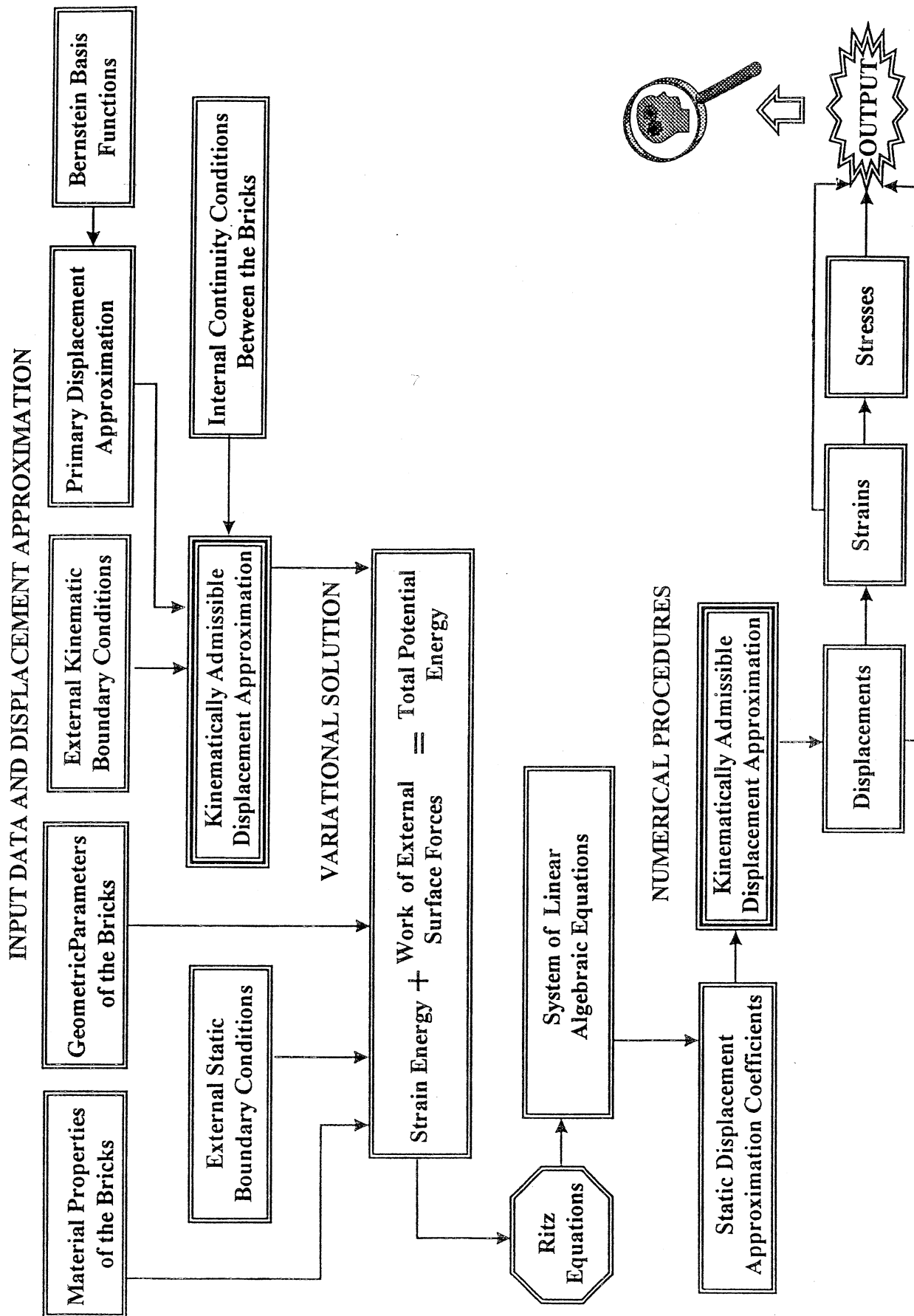


Fig. 2.2: Flow chart of the developed analysis and computer code 3D MOSAIC.

3.0 3-D STRESS/STRAIN AND PROGRESSIVE FAILURE ANALYSIS OF COMPOSITE BONDED JOINTS

3.1 Introduction

This section presents applications of 3-D variational Mosaic Model to stress/strain and progressive failure predictions in composite bonded joints. Theoretical background of the model, mathematical algorithms and specific computational routines utilized in the analysis have been described in detail in Sections 1 and 2. From the standpoint of a stress/strain analysis, the approach reported there can be viewed as a generalization of previous Mosaic approaches. The following *new* developments have to be mentioned:

- (i) an algorithm allowing to avoid “dummy” material bricks and thus solve irregular mosaic structures has been elaborated;
- (ii) a full system of the stress continuity conditions has been formulated for all three sets of the interfaces between the bricks;
- (iii) an algorithm allowing to incorporate the stress/strain continuity conditions between adjacent bricks made from the same material have been developed;
- (iv) a full set of multiple-type continuity relations at the specific points and lines inside the mosaic body has been derived;
- (v) the previous methodology, applicable for orthotropic bricks only, is now extended for the general case of anisotropy.

A new computer code 3D MOSAIC was developed by Dr. Sergei Yushanov. The algorithmic developments (iii) and (iv) have been already incorporated in the code. The aspects (i) and (v) are underway. Besides, the code is significantly more capable than the previous version reported in [1]: instead of storing in the computer RAM the whole two-dimensional *matrix* of the resulting system of simultaneous equations, containing substantial portion of zero elements, the matrix is first transformed to the one-dimensional *vector* format, with all zero elements being eliminated. This allows one to substantially increase computational capability of the model (specifically, to increase the number of bricks or degree of the basis functions) on PC's, without

asking for a more powerful computer. For example, with a 1-D vector storage technique, it is possible to solve about 150 brick model with third degree Bernstein basis functions in all three coordinate directions on a PC with 128 MB RAM, while with a 2-D matrix storage the computer memory was exceeded when considering about 30 bricks. All numerical results presented in this section were obtained on the aforementioned PC's.

As mentioned before, the new algorithm allowing to consider irregular mosaic structures has not been yet incorporated in the computer code. Thus, a dummy material bricks are used here to solve example problems for bonded joints. It is worthwhile to provide some explanation of this concept (which was originally proposed and illustrated on some examples in [2]), presented in Section 3.2. Sections 3.3 and 3.4 are devoted to the experimental validation of 3-D Mosaic Model approach. The experimental data (strain gage readings) have been provided by Dr. Ajit K. Roy. Two specific examples are considered: (a) a stepped solid Al specimen under uniaxial extension and (b) composite-to-composite adhesive bonded joint. A concept of application of the Mosaic Model approach for the problems of progressive intralaminar damage and interlaminar crack propagation is outlined in Section 3.5. This is based on the energy release rate analysis and uses the strain energy expression and other theoretical aspects of Section 1 as well as the capability to detach any adjacent bricks (of the same or distinct materials) inside the mosaic composite structure provided by the algorithm of Section 2. Section 3.6 presents illustration of this theoretical approach to 3-D analysis of crack growth in a double cantilever composite specimen.

3.2 A "Dummy" Material Concept

Schematics of a single-lap and double-lap (using different terminology, a double-doubler) adhesive joints and their Mosaic Model representations is shown in Fig. 3.1.

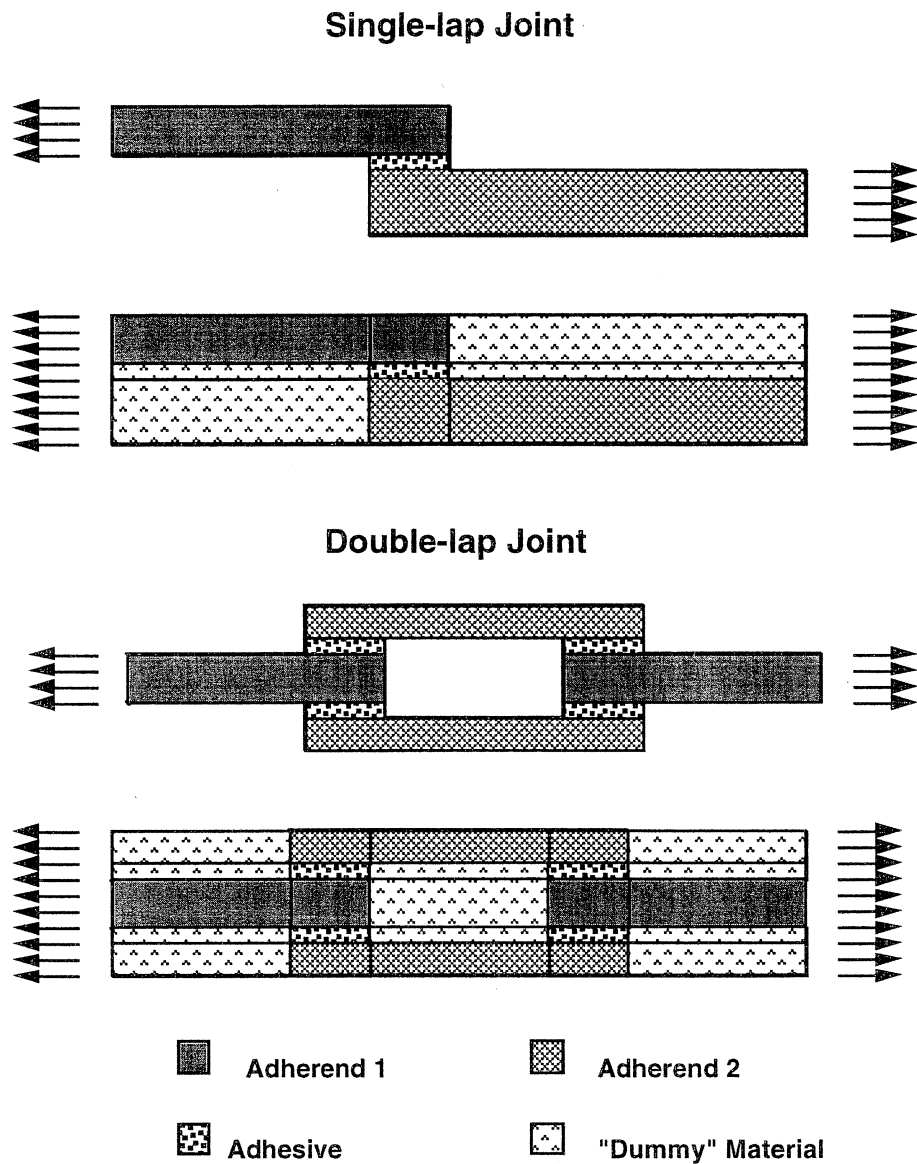


Fig. 3.1: A single-lap and double-lap adhesive bonded joints and their mosaic representations

Thus, when adding a dummy material (which has to be sufficiently “soft” as to make no effect on the stress/strain state in the primary structure), the original boundary value problem is replaced by the boundary value problem for a full mosaic parallelepiped. The parallelepiped contains *four* different materials. Total number of bricks seen here is 9 for a single-lap joint (with 4 dummy material bricks) and 25 for a double-lap joint (with 11 dummy material bricks).

Two more complex structural analysis problems, which can also be replaced by a full mosaic parallelepiped analysis, are illustrated in Fig. 3.2. In these cases, the parallelepiped is an assemblage of *four* and *five* distinct materials, respectively. The number of bricks seen here is 9 (with 4 dummy material bricks) and 35 (with 12 dummy material bricks), respectively. There is a number of internal boundaries between the same material bricks as well as between distinct material bricks.

One interesting peculiarity of the model can be recognized in Figs. 3.1 and 3.2: the more complex is shape of the primary structure, the less is *relative* number of dummy material bricks in the corresponding mosaic parallelepiped. In the other words, a computation efficiency of the dummy material concept would increase with increasing complexity of the geometric configurations.

The advantages and disadvantages of the dummy material approach have been discussed in Section 1.

Stiffened Composite Panels

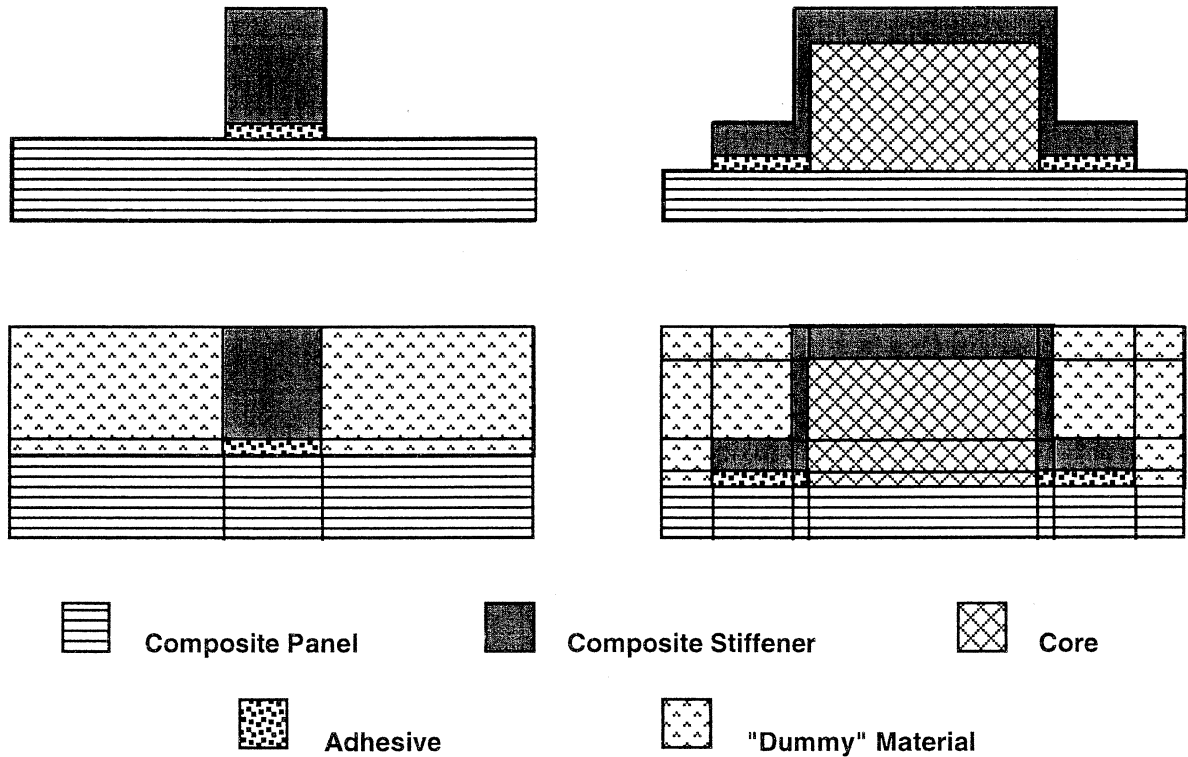


Figure 3.2. Examples of adhesively bonded stiffened composite panels and their mosaic representations

3.3 A Comparison of the Analytical and Experimental Results for Stepped Aluminum Specimen

In this section we compare analytical results obtained with 3-D Mosaic Model approach and experimental data provided by Dr. Ajit K. Roy for experimental specimen shown in Fig. 3.3.

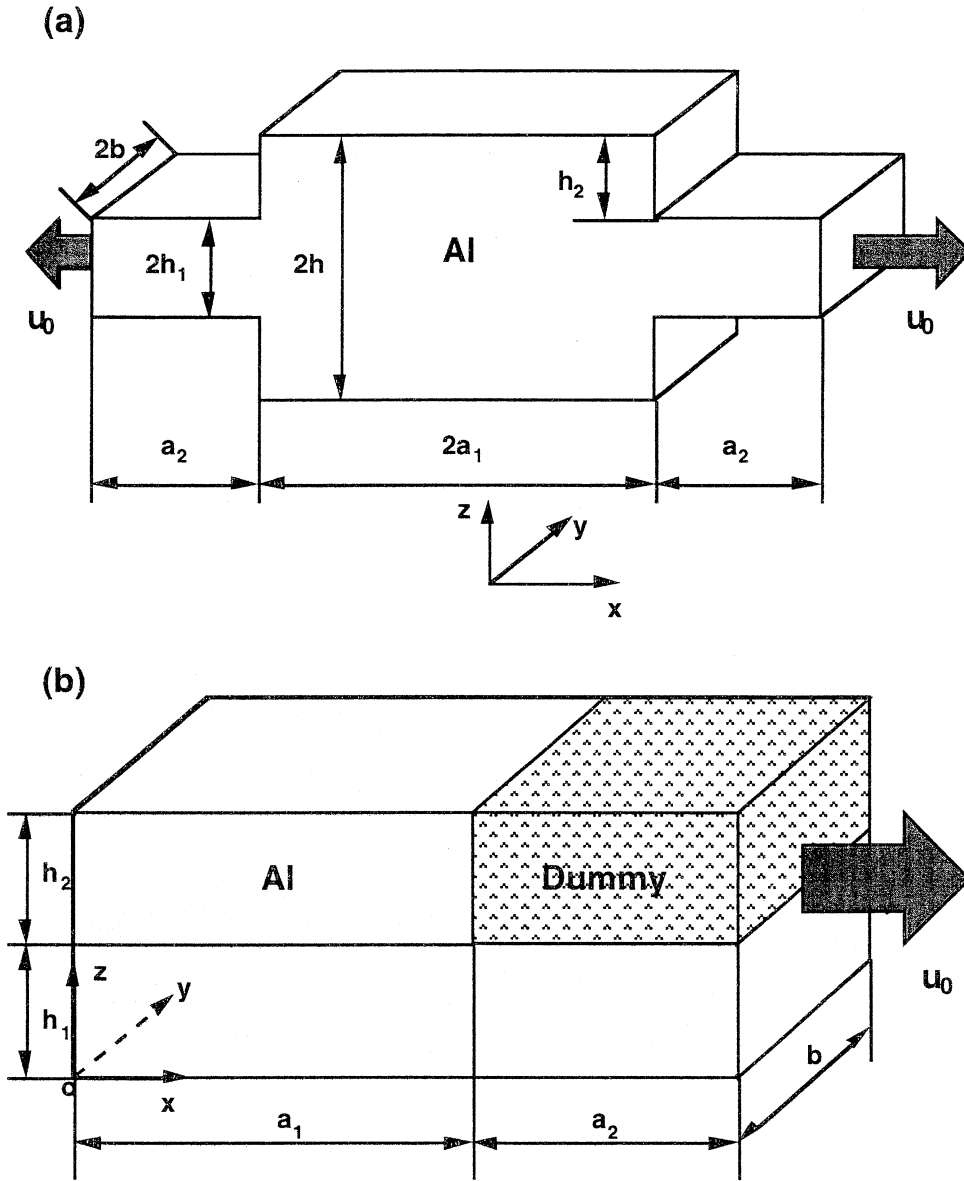


Fig. 3.3: Schematic of the test specimen (a) and mosaic representation of its 1/8th part (b).

The following geometric parameters are used:

$$a = 4in., \quad a_1 = a_2 = 2in., \quad b = 0.5in., \quad h = 0.405in., \quad h_1 = 0.1275in. \quad (1)$$

Properties of the materials used in the analysis are:

$$E = 10.15Msi, \quad \nu = 0.33 \quad (2)$$

for Al and

$$E_d = 10.15Ksi, \quad \nu_d = 0.33 \quad (3)$$

for the dummy material.

Third degree Bernstein basis function were used for the displacement approximation in all three coordinate directions. Brick distribution in the mosaic body is schematically shown in Fig. 3.4.

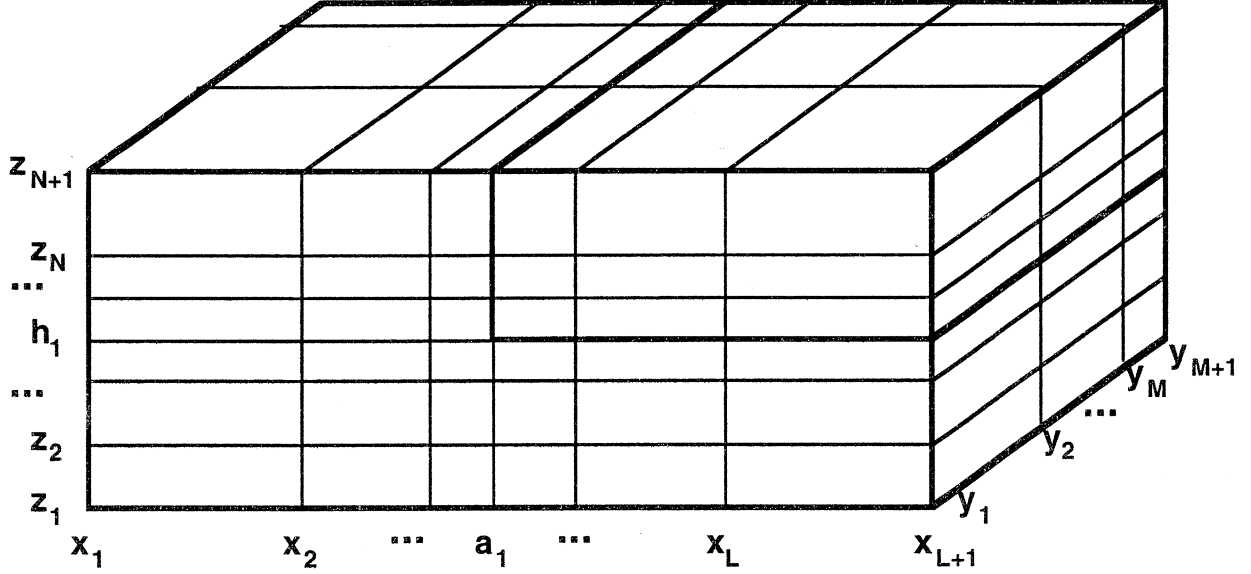


Fig. 3.4: Schematic of a nonuniform mesh of the bricks.

The coordinates $x_{l^*} = a_1$ and $z_{n^*} = h_1$ identify location of the boundaries between distinct material bricks (in this case between Al and the dummy material). The following parameters are further introduced to describe nonuniform brick meshes:

$$\xi_1 = \frac{x_l - x_{l-1}}{x_{l+1} - x_l} \quad \text{for } l = 2, 3, \dots, l^* - 1; \quad \xi_2 = \frac{x_{l+2} - x_{l+1}}{x_{l+1} - x_l} \quad \text{for } l = l^*, l^* + 1, \dots, L - 1 \quad (4)$$

$$\eta = \frac{y_m - y_{m-1}}{y_{m+1} - y_m} \quad \text{for } m = 2, 3, \dots, M \quad (5)$$

$$\zeta_1 = \frac{z_n - z_{n-1}}{z_{n+1} - z_n} \quad \text{for } n = 2, 3, \dots, n^* - 1; \quad \zeta_2 = \frac{z_{n+2} - z_{n+1}}{z_{n+1} - z_n} \quad \text{for } n = n^*, n^* + 1, \dots, N - 1 \quad (6)$$

Specific values of $L, M, N, l^*, \xi_1, \xi_2, \eta, n^*, \zeta_1$ and ζ_2 are given for each computational variant in Table 3.1.

Table 3.1. Characteristics of the brick meshes used in the analysis

Mesh No.	L	M	N	l^*	ξ_1	ξ_2	η	n^*	ζ_1	ζ_2
1	10	1	8	6	6	6	-	5	6	6
2	10	1	8	6	4	4	-	5	4	4
3	12	1	8	7	4	4	-	5	4	4
4	10	1	10	6	4	4	-	6	4	4
5	12	1	10	7	4	4	-	6	4	4
6	12	1	10	7	6	6	-	6	6	6
7	8	1	8	5	6	6	-	5	4	4
8	8	2	8	5	6	6	5	5	4	4

Two types of strain gages have been used in the experimental studies of Dr. Ajit K. Roy:

Gage Type I (GTI) having length $g_l^I = 0.032in.$ (0.813mm) and width $g_w^I = 0.060in.$ (1.52mm) and

Gage Type II (GTII) having length $g_l^{II} = 0.015in.$ (0.381mm) and width $g_w^{II} = 0.020in.$ (0.508mm).

The strain gage placement is indicated in Fig. 3.5 (shown not in scale). The distance $\Delta x = 0.25in.$ (6.35mm) and $\Delta z = 0.02in.$ (0.508mm). Strain gages 1, 2 and 5 measure ϵ_z , while strain gages 3 and 4 measure ϵ_x . The experimental strain magnitudes have been normalized by the

measured value of “far field” longitudinal strain ϵ_x^0 in the thin part of the specimen, and the analytical strains have been normalized by the analogous far field longitudinal strain.

When comparing experimental and analytical results, the computed strains have been *averaged* over the respective strain gage area. For GTI this area is $g_A^I = g_l^I \times g_w^I = 0.032in. \times 0.060in.$ and for GTII this is $g_A^{II} = g_l^{II} \times g_w^{II} = 0.015in. \times 0.020in.$ Selected strain distributions are shown together with the bars indicating the respective averaging intervals for GTI in Figs. 3.6 - 3.8. The curves plotted in Figs. 3.6 and 3.7 correspond to the “corner level” $z = h_1$. Keeping in mind that the averaging has been performed along some finite interval in the z -direction, showing strain variations for one z value may be not sufficient. Thus, additional illustration of the strain variations corresponding to different z levels is presented in Figs. 3.9 and 3.10. Indeed, even at some small distance from the level $z = h_1$ the strain variations change dramatically. Hence, the magnitudes of *averaged* strains should be rather insensitive to the strain values at the point $\{ x = a_1, y = b, z = h_1 \}$.

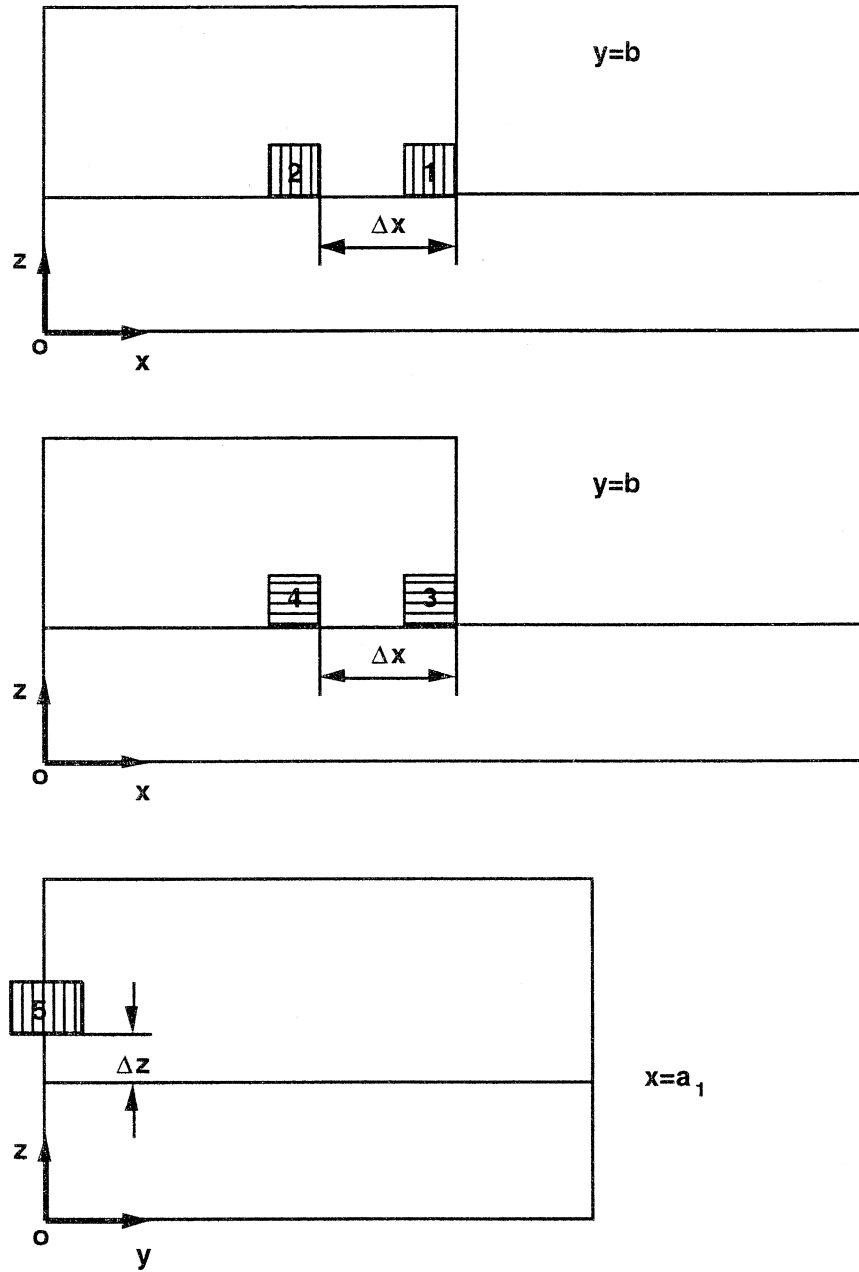


Fig. 3.5: Schematic of the strain gage placement (not in scale).

Analytical and experimental results for strain gages 1-5 are presented in Table 3.2. It is seen that there is no significant difference among the analytical results obtained with Meshes 1-7 (all these meshes contain only one brick in the y -direction). Analytical predictions are rather close to the readings of strain gages 3, 4 and 5. The discrepancy is a little higher for strain gage 2. The

most substantial discrepancy is observed for strain gage 1 (of both types I and II): the analytical predictions are about 4-5 times higher than the experimental data.

Table 3.2. Experimental and analytical strains in the stepped specimen

Gage No. and Type	1 (GTI)	1 (GTII)	2 (GTI)	3 (GTI)	4 (GTI)	5 (GTI)
Specimen No.	Experimental Strains					
1	-0.01	0.05	-0.12	0.12	0.34	0.10
Mesh No.	Analytical Averaged Strains					
1	0.036	0.235	-0.227	0.160	0.444	0.075
2	0.039	0.239	-0.235	0.158	0.435	0.095
3	0.039	0.239	-0.235	0.158	0.435	0.094
4	0.037	0.237	-0.227	0.160	0.444	0.075
5	0.036	0.224	-0.220	0.149	0.405	0.086
6	0.035	0.213	-0.202	0.134	0.386	0.069
7	0.033	0.233	-0.222	0.157	0.435	0.093
8	0.007	0.129	-0.219	0.127	0.432	0.094

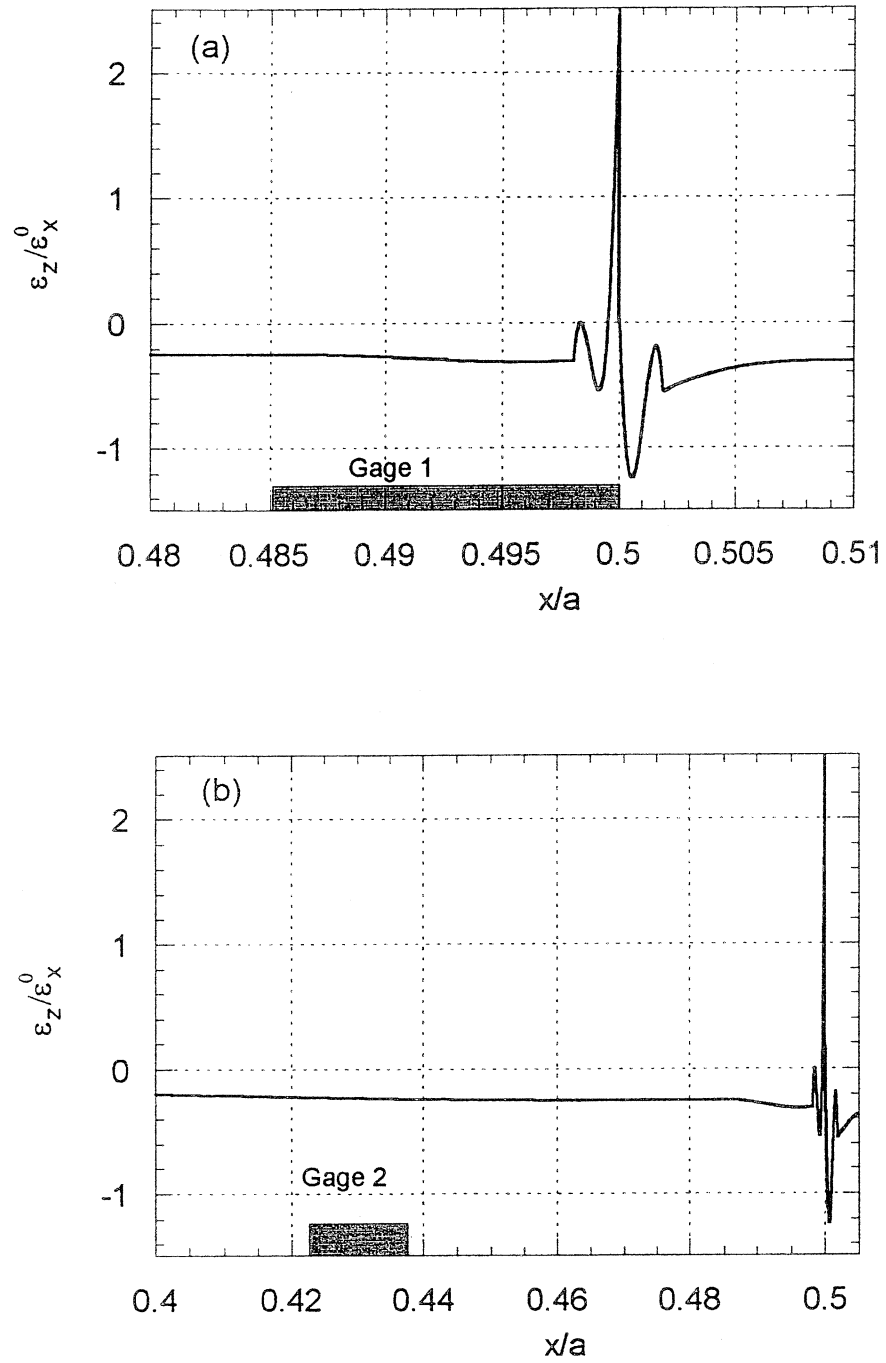


Fig. 3.6. Variations of $\varepsilon_z/\varepsilon_x^0$ in the x direction at $y=b$, $z=h_1$ computed with mesh No.8. Black bars indicate width of gages 1 (a) and 2 (b).

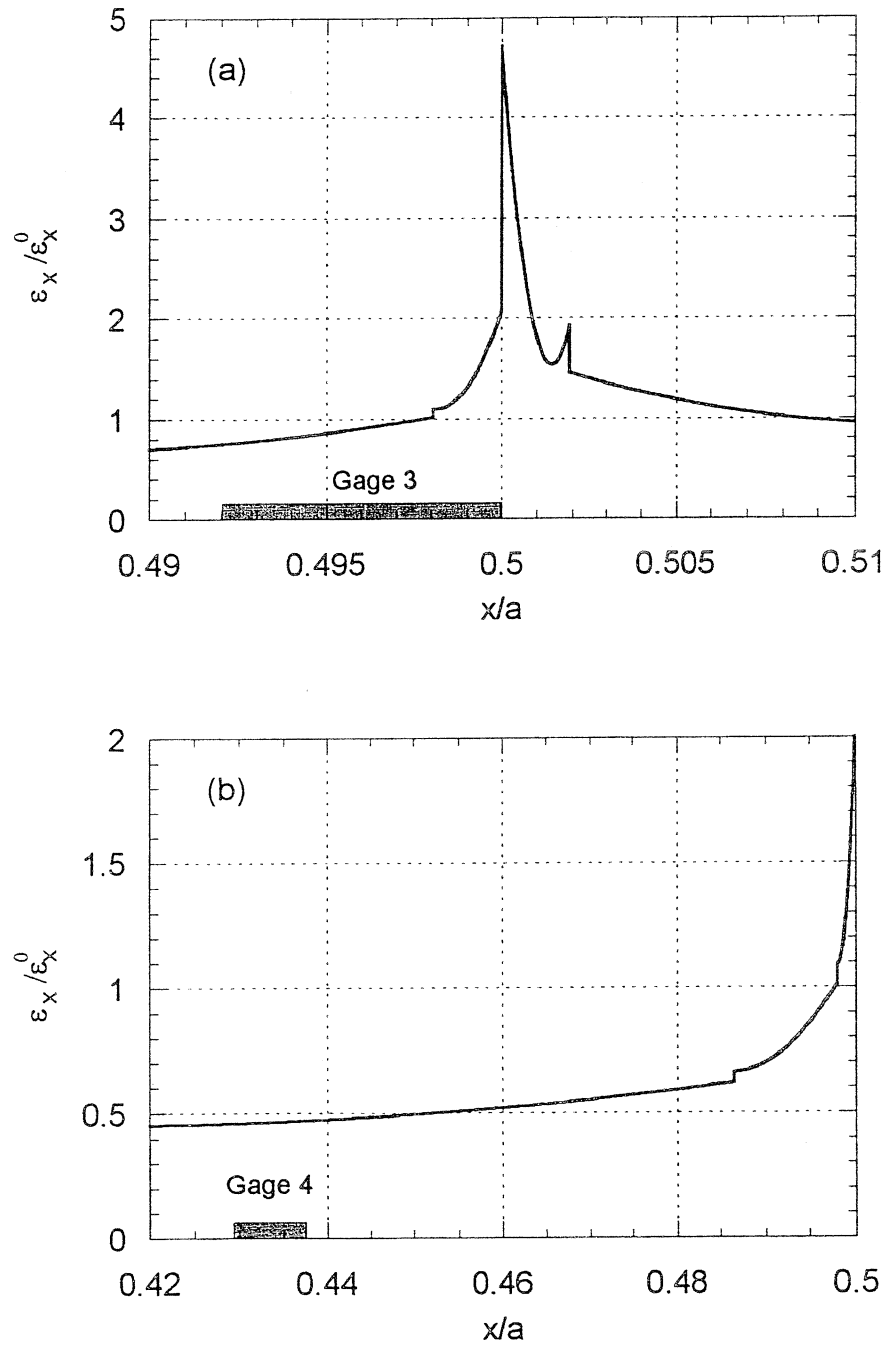


Fig. 3.7. Variations of $\varepsilon_x/\varepsilon_x^0$ in the x direction at $y=b$, $z=h_1$ computed with mesh No.8. Black bars indicate length of gages 3 (a) and 4 (b).

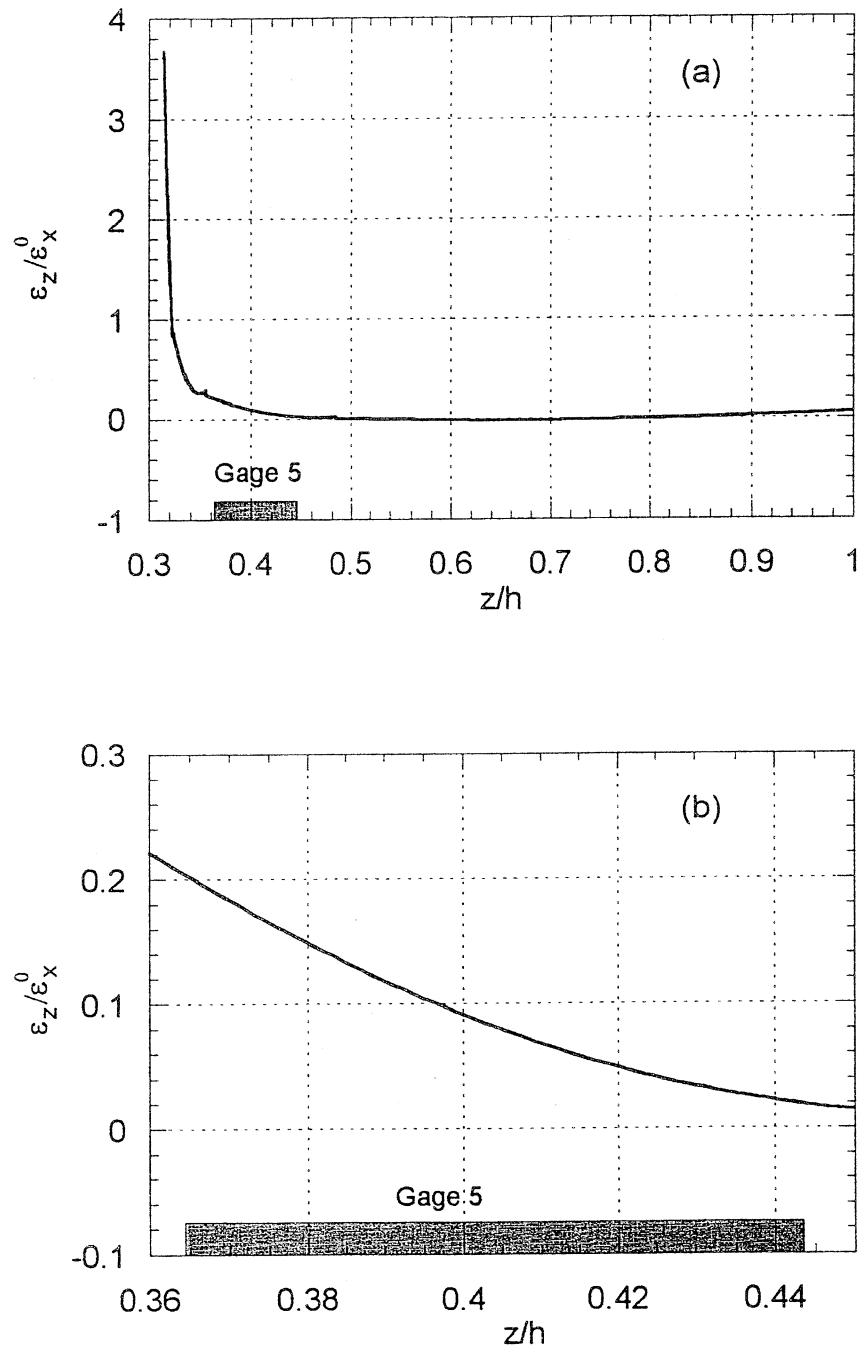


Fig. 3.8. Variations of $\varepsilon_z/\varepsilon_x^0$ in the z direction at $x = a_1$, $y = 0$ computed with mesh No.8. Black bars indicate length of gage 5 under two different magnifications.

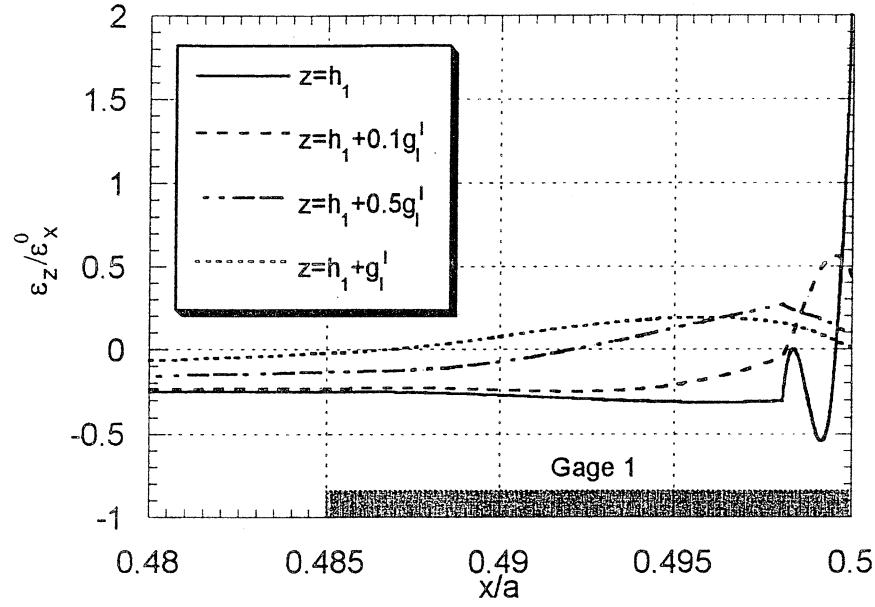


Fig. 3.9. Variations of $\varepsilon_z/\varepsilon_x^0$ in the x direction at $y = b$ and different z -levels computed with mesh No.8. Black bar indicates width of gage 1.

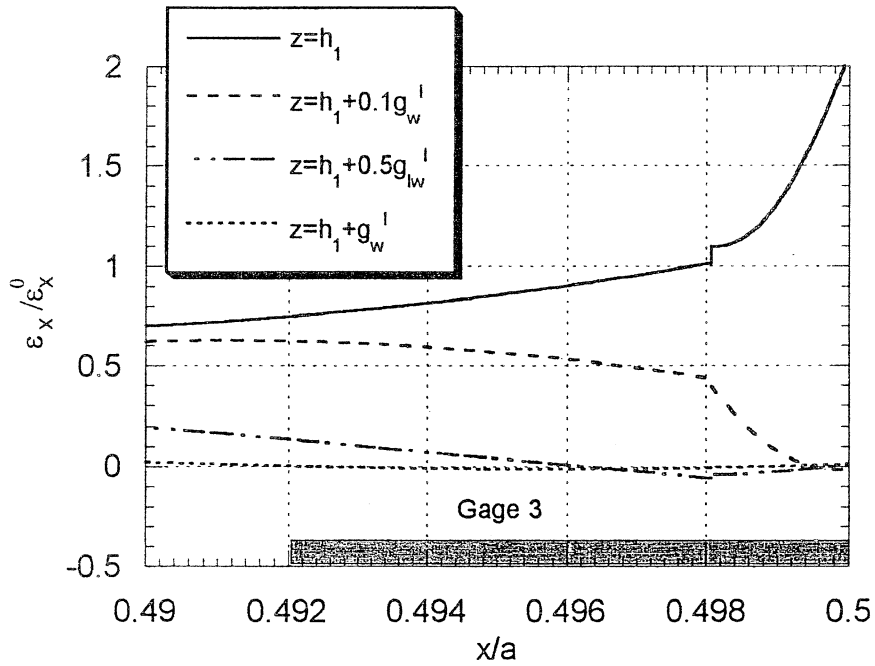


Fig. 3.10. Variations of $\varepsilon_x/\varepsilon_x^0$ in the x direction at $y = b$ and different z -levels computed with mesh No.8. Black bar indicates width of gage 3.

As is seen from Table 3.2, strain values for gage 1 (especially type 1) obtained with Mesh 8 are significantly lower than those obtained with Meshes 1-7. Results obtained with Mesh 8 are much closer to the experimental data for gages 1 and 3. So, it seems that using two bricks in the y -direction can significantly improve the analysis. To explain this effect, strain variations in the y -direction computed with Meshes 7 and 8 are compared in Figs. 3.11 and 3.12 for the x and z coordinates corresponding to the center of gage 1 (GTI). Surprisingly, the difference does not look significant. In order to further study this issue, additional illustrations are presented in Fig. 3.13. Variations of $\varepsilon_z / \varepsilon_x^0$ along the width of gage 1 (GTII) are shown for six values of z inside the gage length. Figs. 3.13(a-c) reveal that the *negative* strain values are considerably higher near the corner when using Mesh 8. And, keeping in mind that the averaged strain is *positive*, this may explain the aforementioned result. Possibly, if using more bricks in the y -direction, the discrepancy between analytical and experimental results can be further reduced.

It has to be emphasized that the ability of using finer discretizations in the y -direction is only possible in a 3-D analysis; there is no such opportunity when solving 2-D plane strain or plane stress problems.

3.4 A Comparison Of The Analytical And Experimental Results For Composite-To-Composite Adhesive Bonded Joint

Consider next a double-lap adhesive bonded joint of unidirectional composites shown in Fig. 3.14. Experimental specimens of this configuration have been tested in [5].

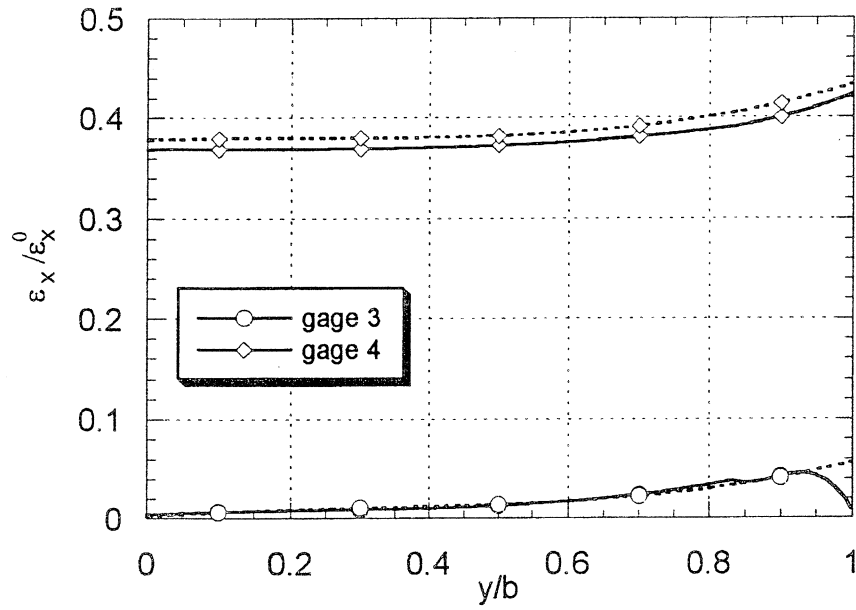


Fig. 3.11. Variations of $\varepsilon_x / \varepsilon_x^0$ along the y coordinate at $x = a_1 - g_l^I / 2$, $z = h_1 + g_w^I / 2$ computed with meshes 7 (-----) and 8 (——).

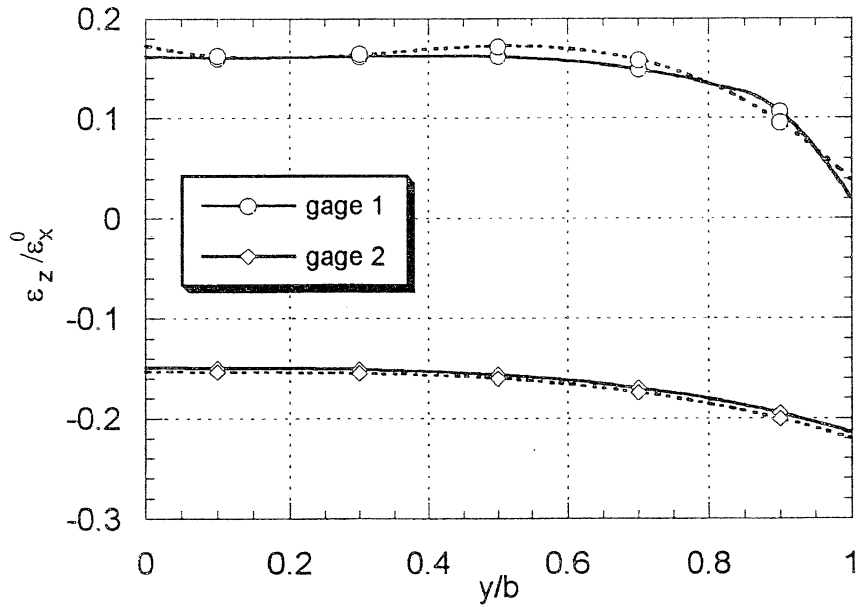


Fig. 3.12. Variations of $\varepsilon_z / \varepsilon_x^0$ along the y coordinate at $x = a_1 - g_w^I / 2$, $z = h_1 + g_l^I / 2$ computed with meshes 7 (-----) and 8 (——).

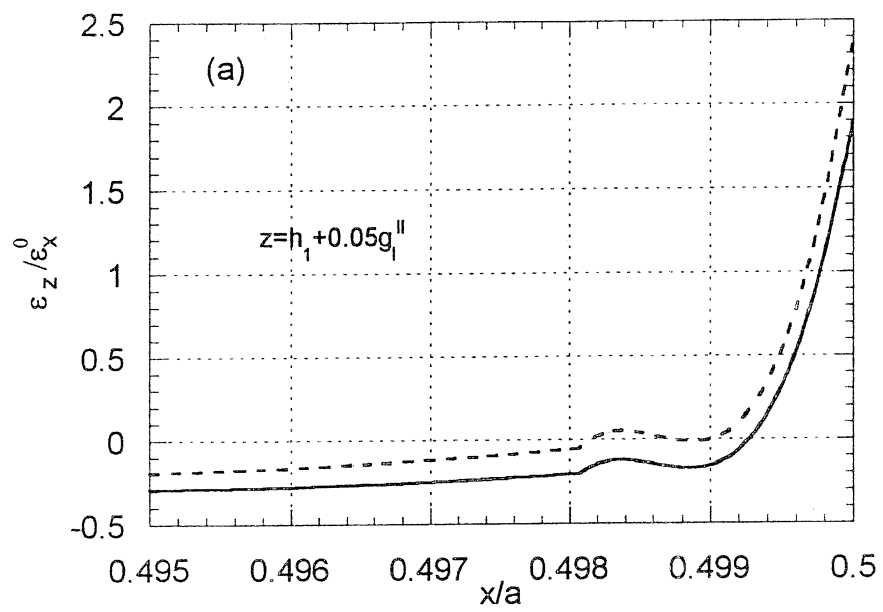


Fig. 3.13 a.

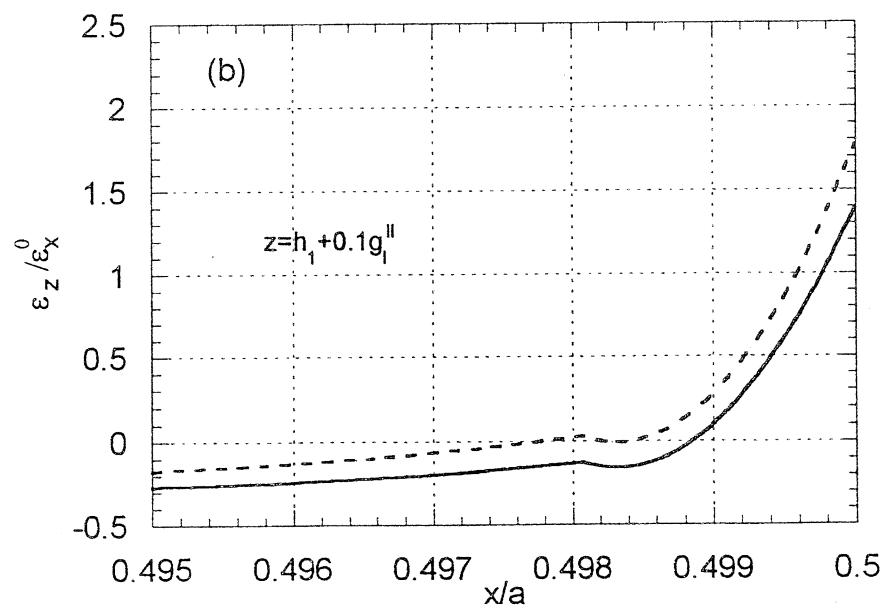


Fig. 3.13 b.

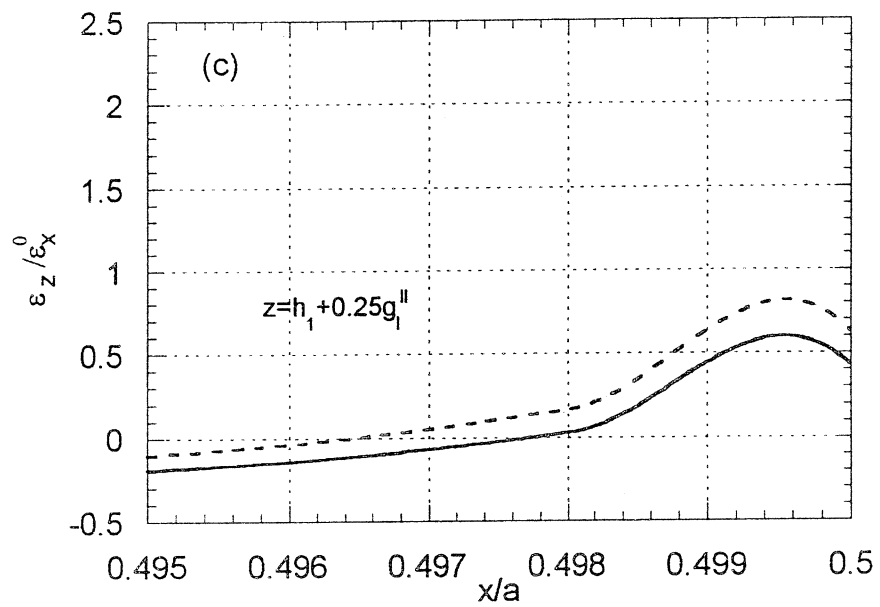


Fig. 3.13 c.

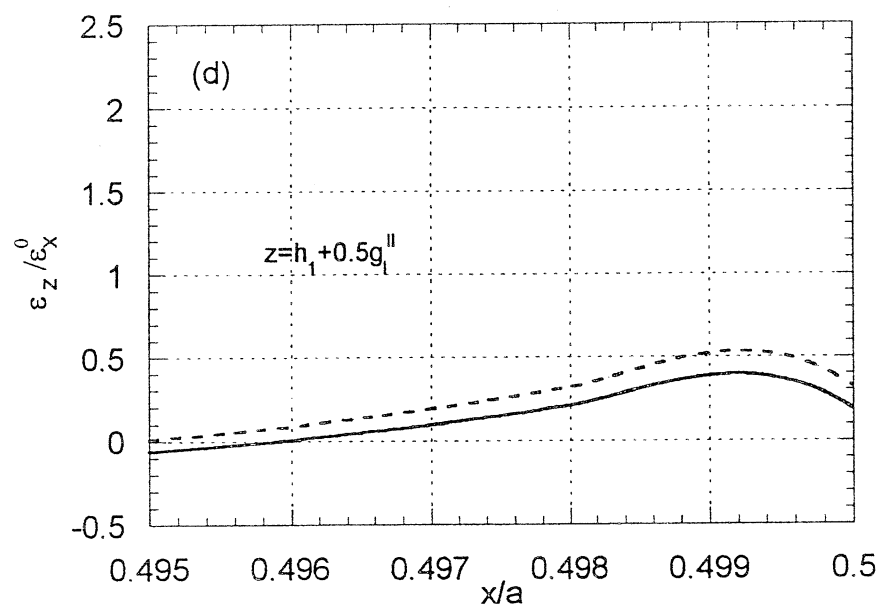


Fig. 3.13 d.

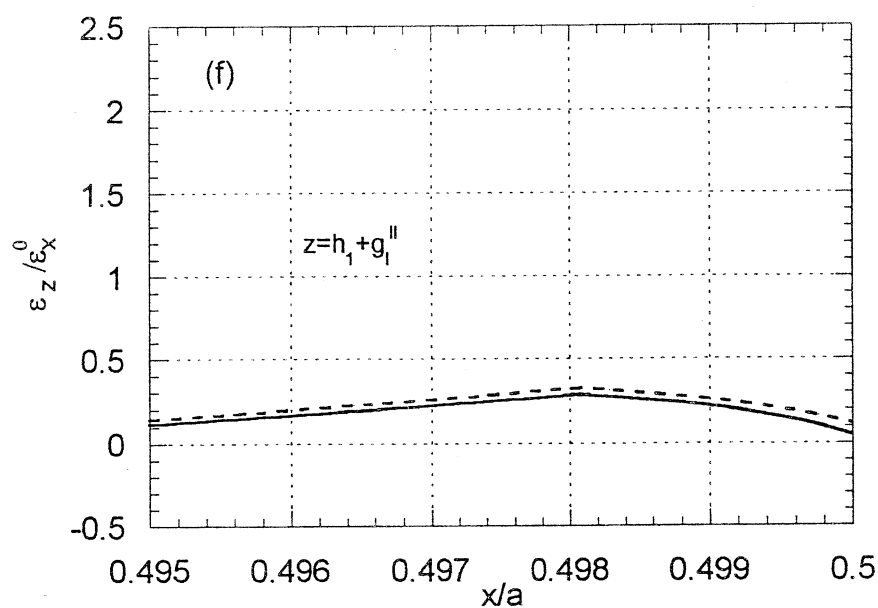
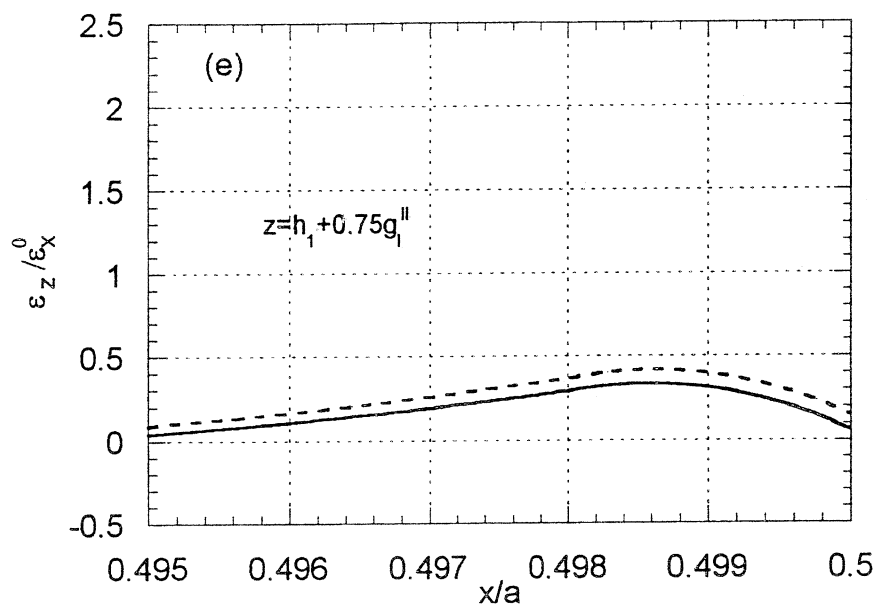


Fig. 3.13. Variations of $\varepsilon_z/\varepsilon_x^0$ along the x coordinate at $y = b$ and different z -levels computed with meshes 7 (.....) and 8 (—).

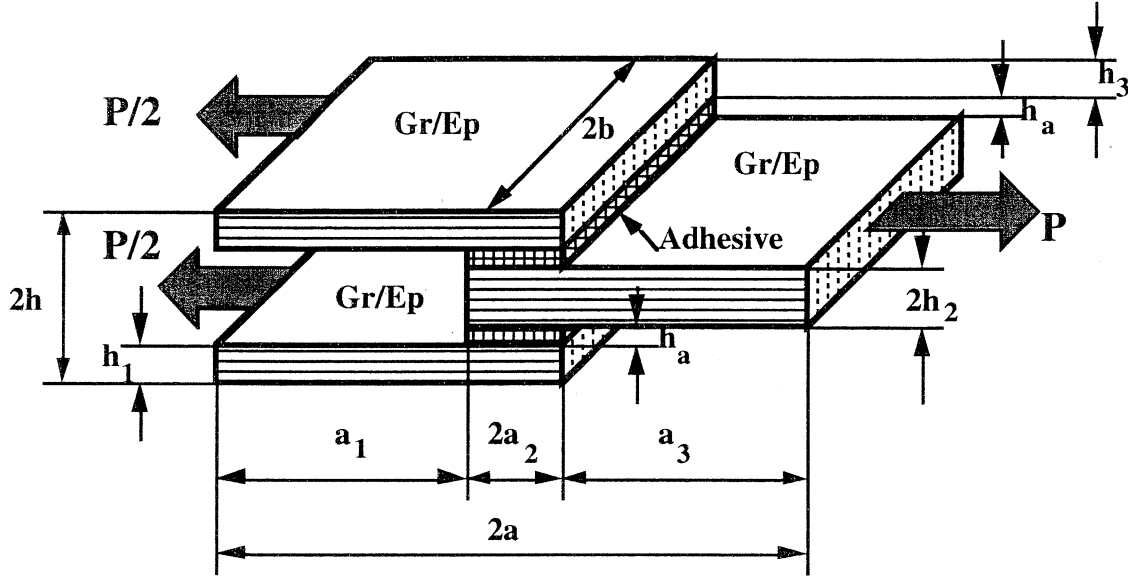


Fig. 3.14. Double-lap adhesive bonded joint specimen

The following geometric parameters have been used:

$$a_1 = a_3 = 2.25 \text{ in. (57.15 mm)}; \quad a_2 = 1 \text{ in. (25.4 mm)}; \quad 2a = a_1 + 2a_2 + a_3 = 6.5 \text{ in. (165.1 mm)}; \quad (7)$$

$$2b = 1 \text{ in. (25.4 mm)}; \quad h_1 = h_3 = 2h_2 = 0.09 \text{ in. (2.286 mm)}; \quad h_a = 0.005 \text{ in. (0.127 mm)}$$

All of the adherends are made from 16 plies of unidirectional Graphite/Epoxy tape AS4/3501-6; the following elastic characteristics have been adopted in the analysis:

$$E_L = 19.3 \text{ Msi (133 Gpa)}; \quad E_T = 1.55 \text{ Msi (10.7 Gpa)}; \quad G_L = 1.02 \text{ Msi (7.03 Gpa)} \quad (8)$$

$$G_T = 0.59 \text{ Msi (4.07 Gpa)}; \quad \nu_{LT} = 0.30$$

The bonding adhesive is Cytec FM300-2K film with 3% woven glass scrim with the following elastic characteristics:

$$E = 0.506 \text{ Msi } (3.47 \text{ GPa}); \quad \nu = 0.30 \quad (9)$$

In order to save computational time and required memory, it is suggested to simplify the problem by reducing analysis of the structure shown in Fig. 3.14 to its 1/8th part shown in Fig. 3.15.

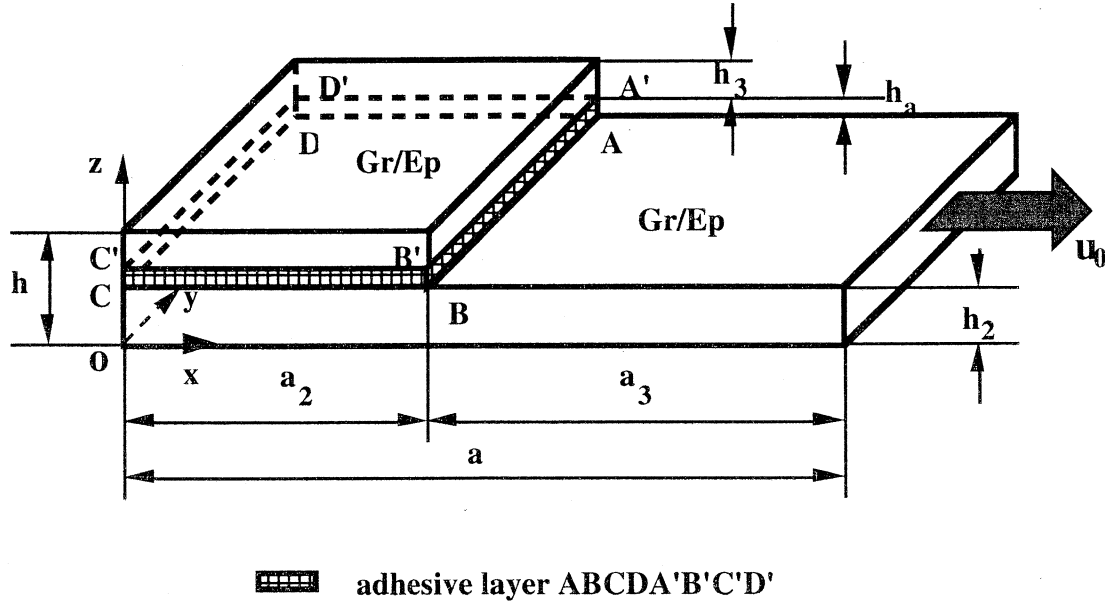


Fig. 3.15: The reduced bonded joint element.

This seems to be possible due to symmetry of the geometric configuration and material properties. Indeed, it is reasonable to assume that displacement u_x is zero along the cross-section perpendicular to the x -axis and passing through the center ($x=0$) of the structure. Also, displacement u_y is zero along the cross-section perpendicular to the y -axis and passing through the center of the structure, and displacement u_z is zero along the cross-section perpendicular to the z -axis and passing through the center of the structure. Besides, we substitute the static boundary condition at the right loaded end for the kinematic boundary condition, assuming that uniformly distributed displacement u_0 is applied there (it is easy to establish correspondence between applied

force and applied displacement). After that, the structural element shown in Fig. 3.15 has to be solved under the following set of boundary conditions:

$$u_x = 0 \text{ at } x = 0; \quad u_x = u_0 \text{ at } x = a; \quad u_y = 0 \text{ at } y = 0; \quad u_z = 0 \text{ at } z = 0 \quad (10)$$

Further, following the dummy material approach, the structural element of Figure 3.15 is replaced by the mosaic parallelepiped shown in Fig. 3.16. Thus, in this case we have an assembly of three different material bricks: unidirectional Gr/Ep composite, adhesive and dummy material. The problem is more complex than in Section 3.5. Specifically, there are two lines (AA' and BB') of *three* material junction, which are certainly suspects for the stress singularity. So, it is reasonable to use nonuniform computational meshes of bricks with higher refinement toward the lines AA' and BB'. The brick distribution applied in this analysis is schematically shown in Fig. 3.17. Due to small thickness of the adhesive layer, uniform brick mesh is used through its thickness in all variants.

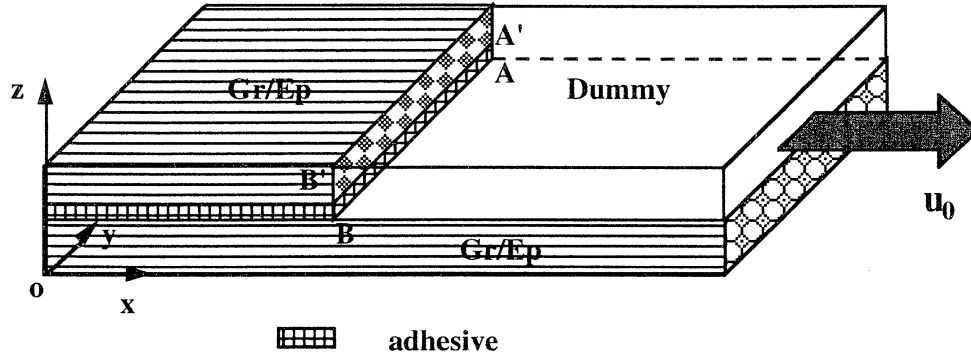


Fig. 3.16: Mosaic representation of the bonded joint structural element.

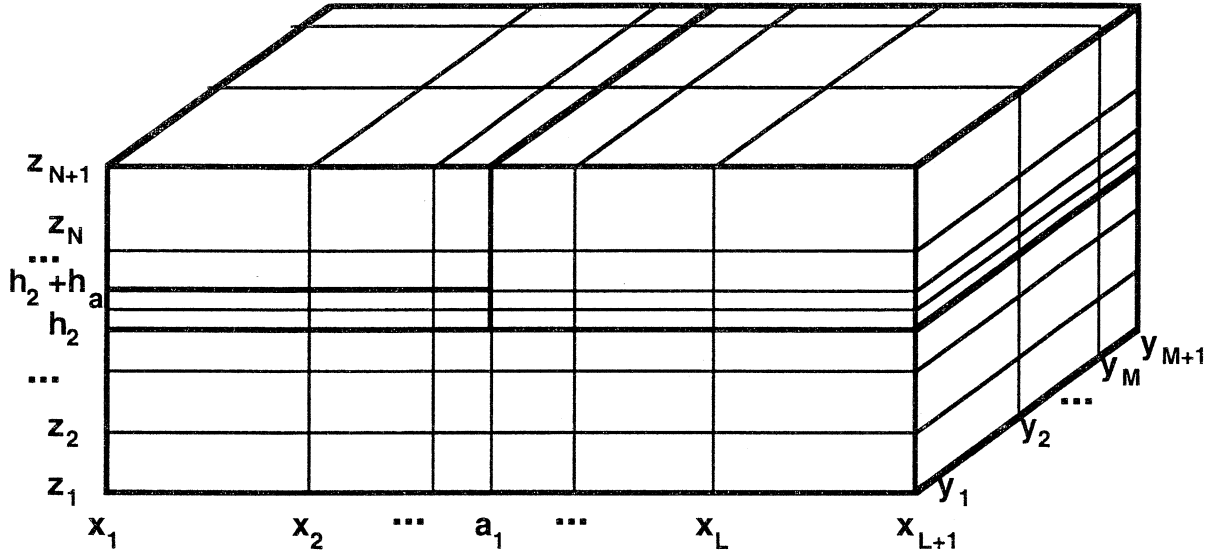


Fig. 3.17. Schematic of the brick mesh.

The mesh parameters introduced by (4) and (5) still can be utilized, but the following should be applied in place of (6):

$$\zeta_1 = \frac{z_n - z_{n-1}}{z_{n+1} - z_n} \text{ for } n = 2, 3, \dots, n^* - 1; \quad \zeta_2 = 1 \text{ for } n = n^*, n^* + 1, \dots, n^{**} - 1; \quad (11)$$

$$\zeta_3 = \frac{z_{n+2} - z_{n+1}}{z_{n+1} - z_n} \text{ for } n = n^{**}, n^{**} + 1, \dots, N - 1$$

where $z_{n^*} = h_2$ and $z_{n^{**}} = h_2 + h_a$. Specific values of $L, M, N, l^*, \xi_1, \xi_2, \eta, n^*, n^{**}, \zeta_1$ and ζ_3 are given for each computational variant in Table 3.3. Third degree Bernstein basis functions have been used for all three coordinate directions (e.g., $I = J = K = 3$) with the Meshes 1, 2 and 4, while with the Mesh 3 it was taken $I = K = 4, J = 3$.

Table 3.3. Characteristics of the brick meshes used in the analysis.

Mesh No.	L	M	N	l^*	ξ_1	ξ_2	η	n^*	n^{**}	ζ_1	ζ_3
1	10	1	10	6	5	5	-	5	7	5	5
2	8	1	15	5	6	6	-	5	9	6	2.5
3	8	1	8	5	6	6	-	4	6	6	6
4	8	2	8	5	6	6	6	4	6	6	6

In the experimental studies reported in [5], strain gages of Type II (GTII) have been used. Placement of transverse gages 1 and 2 (measuring ε_z) and longitudinal gages 3 and 4 (measuring ε_x) is schematically shown in Fig. 3.18. The distance Δx is 0.25in. (6.35mm).

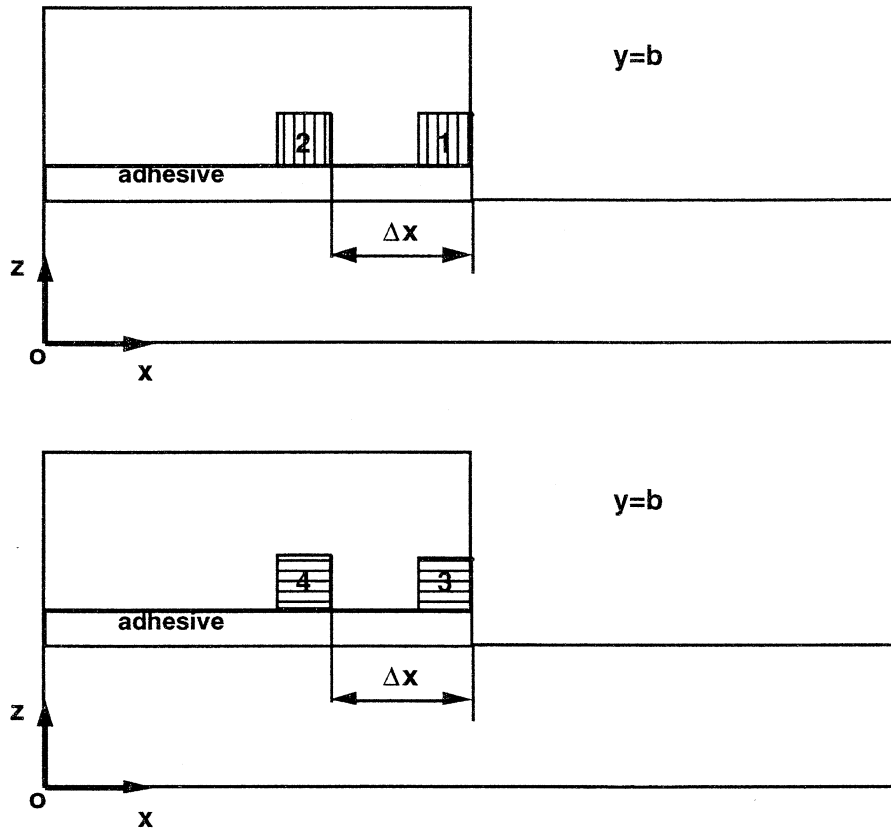


Fig. 3.18: Schematic of the strain gage placement (not in scale).

Variations of the transverse and longitudinal strains in the x -direction along the *interface* between upper adherend and adhesive and two other z -levels computed with Mesh 1 are shown in Figs. 3.19 and 3.20. It is seen that gages 2 and 4 are located in the zone of rather smooth strain variation, though the strain values are still sensitive to the distance from the interface. So, even at some distance from the corner, the *averaged* strains may significantly differ from the strains computed *exactly* at the interface. As seen in Figs. 3.19b and 3.20b, gages 1 and 3 cover the region of highest strain gradients. Here, strain variations change severely along the gage length (in the case of gage 1) or width (in the case of gage 3). So, the *averaged* strains may severely differ from the strains computed *exactly* at the interface. Accordingly, readings of gages 1 and 3 should be highly sensitive to the gage size and any small misplacement of the gage in the x or z -direction.

The obtained analytical results are compared to the experimental data from [5] in Table 3.4.

Table 3.4. Experimental and analytical strains in the double-lap joint specimen.

Gage No.	1	2	3	4
Specimen No.	Experimental Strains [5]			
1	0.050	-0.193	0.246	0.393
2	0.201	-0.193	0.192	0.310
Mesh No.	Analytical Averaged Strains			
1	0.517	-0.217	0.034	0.340
2	0.515	-0.209	0.035	0.335
3	0.527	-0.223	0.035	0.345
4	0.527	-0.214	0.037	0.350

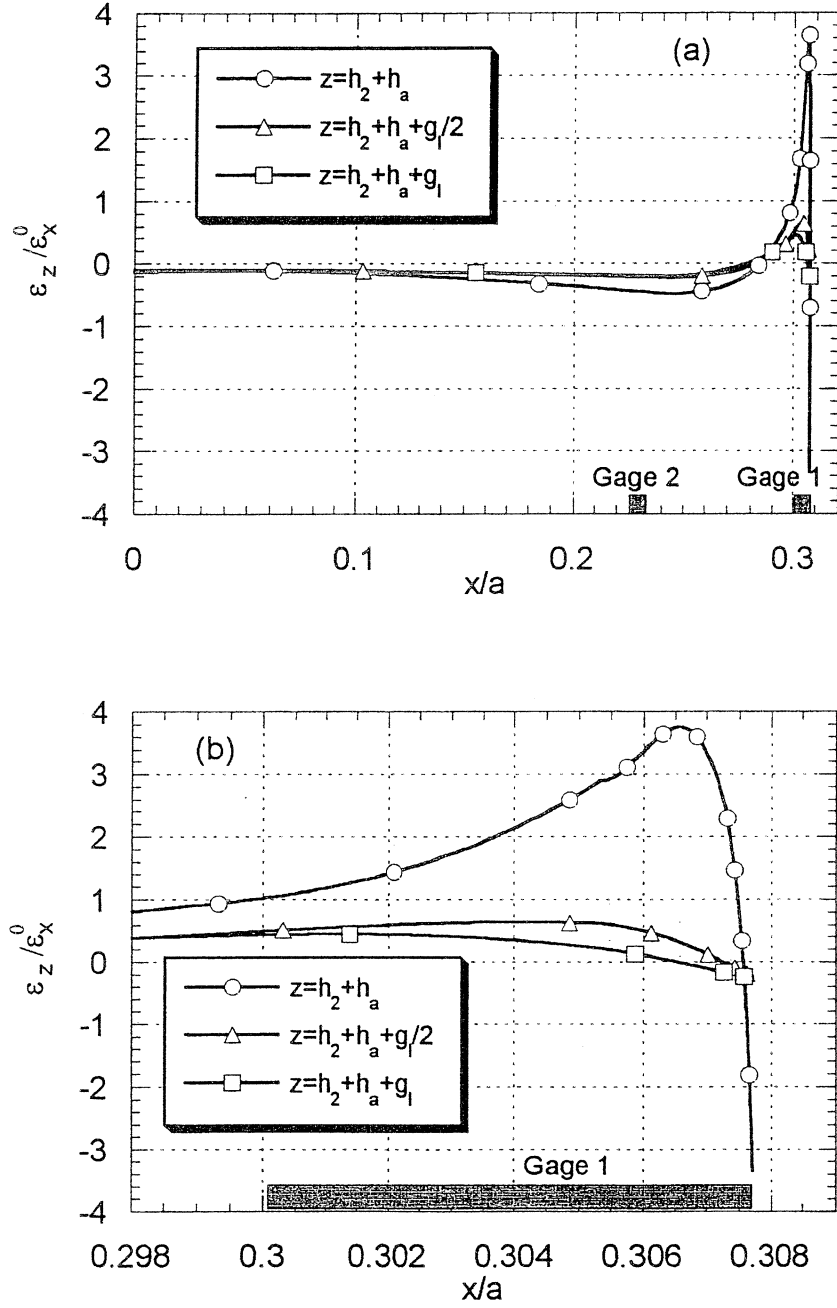


Fig. 3.19. Variations of $\varepsilon_z/\varepsilon_x^0$ in the x direction at $y=b$ and three z -levels. Black bars indicate width and location of gages 1 and 2.

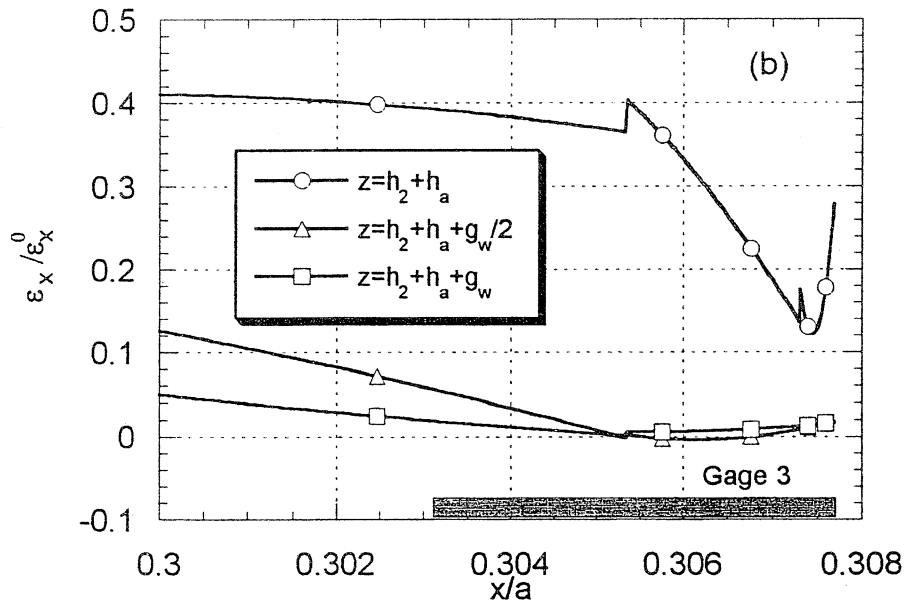
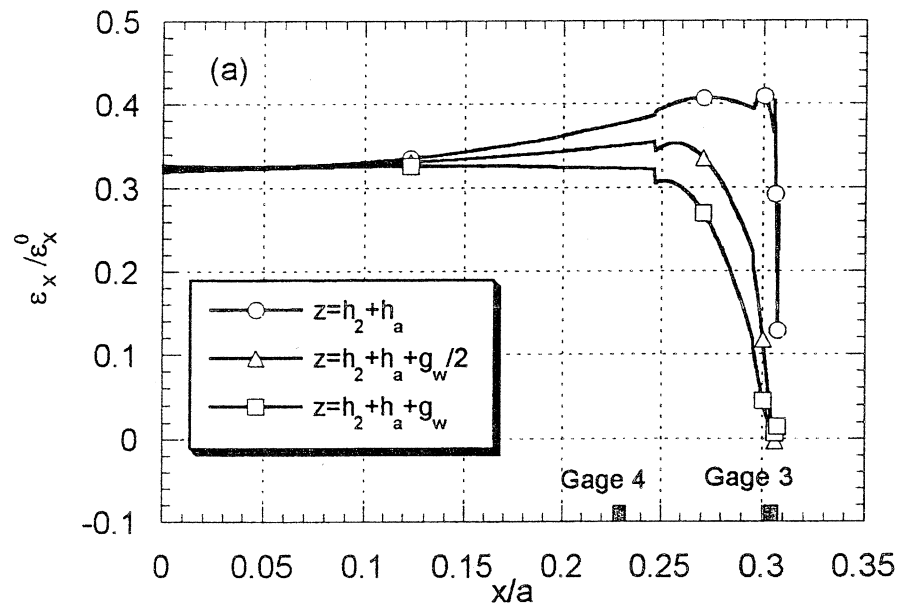


Fig. 3.20. Variations of $\varepsilon_x/\varepsilon_x^0$ in the x direction at $y = b$ and three z -levels. Black bars indicate length and location of gages 1 and 2.

When considering results for gage 1, it is seen that experimental data for two (supposedly identical) specimens differ by a factor of 4. The analytical results are about 4 times *higher* than the mean experimental strain between specimens 1 and 2. At the same time, the analytical results themselves are very consistent; their mutual variation is only about 2% when changing number of bricks in all three coordinate directions, mesh density near the corner and the interface, and even degree of the basis functions. We do not have an explanation why there is a substantial difference between experimental data and analytical predictions for gage 1. Note that the experimental data and analytical prediction for gage 2 are very close.

When considering experimental results from gage 3, the difference between specimens 1 and 2 is not so significant. Again, the obtained analytical predictions are mutually consistent and, at the same time, they are about 6 times *lower* than the mean experimental strain. Finally, it is recognized that all of the analytical predictions for gage 4 fit in the middle between the experimental data for specimens 1 and 2.

The presented comparison of analytical and experimental data shows that the developed 3-D analysis provides very accurate strain predictions for a double-lap composite-to-composite adhesive bonded joint, with the exception of a very small region near the end of the overlap zone. The revealed strain discrepancy in that region requires further investigation.

3.5 The Concept Of 3-D Progressive Failure Analysis

The Mosaic Model variational approach described in Sections 1 and 2 and applied for stress/strain analysis of composite bonded joints in this section, can be further developed for the analysis of progressive failure processes in composite structures. Obviously, in order to develop predictive methodology capable to *conjointly* account for a dispersed progressive damage and various types of developing cracks, the failure models and analytical tools should be very diverse. It is on demand to predict damage and crack initiation, growth, accumulation and ultimate failure of composite structures. The models should be able to identify failure modes corresponding to each

local failure event during the mechanical loading history. It is important to emphasize that both the *intralaminar* and *interlaminar* types of failure should be covered by the required analysis approach.

For a generic illustration, we can use a mosaic parallelepiped considered in Section 1. Assuming that each brick may have distinct elastic and strength characteristics, and that the mosaic body is exposed to a nonuniform stress/strain state, it is clear that progressive failure modeling is a complicated task. Once a local initial failure occurs at some site inside the parallelepiped, the displacements, strains and stresses may significantly redistribute in the whole mosaic body due to the local reduction of elastic properties. Consequently, the stresses are relieved within the damaged brick and, at the same time, elevated in all other bricks in the body. Indeed, such a stress elevation will affect mostly the adjacent bricks which become the primary suspects for the subsequent failure occurrence. Following this pattern, failure may propagate under the fixed load level (due to the successive stress redistributions around the growing zone of damaged material) or under the increasing load (due to the increasing stresses in all of the bricks). This process might involve a single failure mode (matrix cracking, fiber breakage, fiber-matrix debond, etc.) as well as several failure modes simultaneously. Since a composite structure will usually not survive extensive fiber failures, the progressive *intralaminar* failure is often limited to the gradual dispersed matrix damage.

The progressive *interlaminar* failure is usually related to the growing delamination. In this case the modeling approach should be rather different than for the case of an intralaminar failure. Delamination means that some free surface is created between two distinct materials. Again, in terms of the Mosaic Model, this effect can be accounted as the separation of two adjacent bricks along their boundary. Thus, formulation of the boundary value problem for a mosaic body presented in Sections 1 and 2 have to be modified by relaxing some of the displacement continuity conditions between the bricks. Creation of the initial delamination zone can be predicted (arguably, indeed) using some stress/strain based phenomenological failure criterion, while analysis of the growing delamination requires involvement of some fracture mechanics tools and criteria.

Generally, the intralaminar and interlaminar failure processes are not separable. It is well known that one possible cause of delamination is a matrix crack reaching the interface. On the other hand, delamination interacts not only with the matrix cracks, but may also cause fiber buckling, debond from the matrix and failure. Thus, in order to realistically predict ultimate failure of a composite structural part and identify its corresponding failure modes, both the intralaminar damage and interlaminar failure should be considered *interactively*.

First, a 3-D stress/strain analysis is needed for the originally undamaged structure. Next, an initial failure criterion for the composite material has to be chosen. This is a very important issue that was discussed in a number of special review papers. In particular, some authors has stated that the simplest maximum stress/strain criteria typically overestimates the strength of the lamina, because the interaction of stress components is neglected. On the other hand, the “interactive” tensor polynomial criterion which relates all *six* stress components in a *single* equation, has been recently criticized (see, for example, a discussion on this issue of Hart-Smith [6]) as having no mechanical substantiation and contradicting some obvious physical phenomena. Besides, when applying this type of phenomenological failure criterion it is not possible to identify the failure mode, which is of the primary value in any progressive failure analysis.

Experimental observations of failure in unidirectional fiber composites indicate that there are two primary modes: a “fiber” mode in which the composite fails due to fiber rupture in tension or fiber buckling in compression, and a “matrix” mode in which multiple planar or curved cracks parallel to the fibers or inclined with respect to the fibers, occur. A rather simple failure criterion introduced by Hashin [7] separates these two principal failure modes and also accounts for distinct failure mechanisms in tension and compression in the fiber direction as well as in tension and compression in the transverse direction. Importantly, the same type failure criterion can be used to predict the delamination initiation. Hashin's failure criterion seems to be suitable for the purpose of this study. Also, some newly introduced failure criteria of Hart-Smith [6] can be tried.

Next aspect of progressive failure analysis is to model damaged material, which is commonly viewed as the reduction of its elastic characteristics. This is still a challenging issue,

because any reasonable stiffness reduction approach of an anisotropic composite requires certain substantiation from the standpoint of micromechanics. It has to be noted that the existing methodologies of modeling damaged composites on a micro-level are still very limited. Due to this, the instantaneous stiffness reduction to zero is still the most common approach in the structural analysis. Another rather simple stiffness reduction approach usually called “Ply Discount Method” (PDM) also finds applications. However, there are several drawbacks of the PDM discussed in literature. The PDM neglects out-of-plane stress components and disregards the ability of load redistribution through the inter-ply boundary. Accordingly, the ply-by-ply interface failure mechanisms are discarded through the independently applied failure criterion. For example, when applied to cross-ply laminates, the PDM cannot describe the experimentally observed dependence of the laminate stiffness reduction on the transverse crack density. It is a common opinion that the PDM is not sophisticated enough to accurately characterize progressive matrix damage processes.

Some other models assume that the failure will not extend throughout the entire 90° layers but localize in regions distributed lengthwise. So, outside the failed regions, the 90° layers are still effective in supporting the load, while in the failed regions only the 0° layers are able to carry the load. A number of theoretical approaches have been developed in last 10 years to characterize constrained matrix cracking and stiffness reductions both in cross-ply and angle-ply laminates. Some comparisons with experimental data revealed that the elastic moduli calculated by the PDM provide good approximations to the observed residual elastic moduli of cross-ply laminates at the crack *saturation* state. In particular, it was found in [8] that the effective Young’s modulus of a $[0/90_n]_s$ laminated specimen in the axial direction *approaches asymptotically* the solution provided by the PDM under the condition that matrix cracks are *saturated*. Typically, the PDM overestimates the longitudinal modulus reduction, and this overestimate increases with increasing transverse constraints on the cracks.

Most of the theoretical works in composites damage mechanics have been focused on predicting the threshold stress for the onset of cracking and the spacing between the cracks. Crack density in each layer has been considered the major variable that characterizes the effect of matrix

cracks on stiffness reductions. The “Characteristic Damage State” that consists of nearly uniform spacings between the cracks in individual off-axis plies was introduced in [9]. These crack spacings were found to depend on ply thickness, fiber orientations, stacking sequence, etc. Another characterization, using the “Internal State Variables” was presented in [10]. One of the limitations for these variables is that the matrix crack size and spacing should be *uniform*. However, due to a random nature of the transverse cracking, existence of curved transverse cracks and partially angled transverse cracks, the uniformly distributed planar transverse crack assumption may be not realistic. It was observed experimentally that there are more curved than planar transverse cracks with increasing 90° layer thickness of a cross-ply composite.

A common concern is how to obtain the required stiffness reduction parameters needed in any progressive damage modeling approach. For example, the ratio of the total length of failed regions to the length of the specimen should be given in order to implement the Gradual Failure Model of Hahn and Tsai [11]. It is not clear how to obtain this value directly. The transverse crack *density* was used in a number of other theories. This input parameter has to be defined as a function of load value for any specific lamina material and ply lay-up, which seems impractical experimental task. On the other hand, in order to define this parameter theoretically, one have to solve a complex micro-mechanics problem. Another possible approach was proposed in [12]: to use four phenomenological material constants for the characterization of intralaminar cracking. It was suggested in the above work to perform set of experimental measurements of the moduli changes for known crack densities in a given laminate.

It follows from the existing literature study that serious difficulties are expected when attempting to apply any scientifically sound method, which is more sophisticated than the PDM, for the progressive damage modeling of composite structural elements exposed to *nonuniform* stress/strain fields. As mentioned above, the PDM, being asymptotically correct, overestimates the stiffness reductions. So, when using this approach, the safety factor would be increased, what is acceptable for many practical designs.

Another problem that seems to be important in the context of our task is obtaining the *whole* set of reduced elastic constants, which is needed in the structural analysis. However, a few works are known where the reduction of more than one constant (namely, the transverse elastic modulus) was reported. The importance to reasonably reduce other elastic constants was illustrated in [13], where it was shown that in the case of highly constrained transverse cracking in $[0/90^\circ]_{4s}$ graphite/epoxy laminate, the Poisson's ratios may change significantly, although a comparatively little change may occur in the Young's moduli.

One possible scheme (compatible with the maximum stress failure criterion) for the reduction of the in-plane elastic properties of a composite lamina is presented in Table 3.5 [14]. Here, $\bar{\sigma}_1$, $\bar{\sigma}_2$ and $\bar{\tau}_{12}$ are the in-plane stress components normalized by their *ultimate* values (used in the maximum stress criterion); E_1^0 , E_2^0 and G_{12}^0 are elastic and shear moduli of undamaged material; \tilde{E}_1 , \tilde{E}_2 and \tilde{G}_{12} are elastic and shear moduli of the damaged material. Here, index "1" corresponds to the fiber direction and "2" to the transverse direction. Parameters $\alpha_1 < 1$, $\alpha_2 < 1$, $\alpha_3 < 1$ and $\alpha_3' < 1$ characterize reduction of the moduli (as the simplest guess, those can be set zero). They can be considered independent or dependent on the corresponding strain components. Rigorously, these parameters are functions of the matrix crack density, fiber break density or other variables characterizing the damaged state of the lamina. Note that in the presence of cracks the undamaged (transversely isotropic) material becomes an orthotropic material (if all cracks are aligned in the directions 1 and 2) or even monoclinic material (if there are off-axis cracks). Thus, additional elastic constants may appear in the analysis.

It is possible, though not trivial to generalize the above stiffness reduction scheme for the 3-D case. Accordingly, more reduction coefficients will be involved, and in the presence of inclined cracks the damaged unidirectional lamina will represent a generally anisotropic material characterized with 21 independent elastic constants.

Table 3.5.Reduction scheme for the elastic characteristics of a composite lamina [14]

Variant No.	Failure Mode	\tilde{E}_1 / E_1^0	\tilde{E}_2 / E_2^0	$\tilde{G}_{12} / G_{12}^0$
1	$\bar{\sigma}_1 \geq 1$	α_1	α_2	α_3
2	$\bar{\sigma}_1 \leq -1, \bar{\sigma}_2 \geq 0$	α_1	α_2	α_3
3	$\bar{\sigma}_1 \leq -1, \bar{\sigma}_2 < 0$	α_1	1	α_3
4	$\bar{\sigma}_2 \geq 1$	1	α_2	α_3
5	$\bar{\sigma}_2 \leq -1$	1	α_2	α_3
6	$\bar{\tau}_{12} \geq 1, \bar{\sigma}_2 \geq 0$	1	α_2	α_3
7	$\bar{\tau}_{12} \geq 1, \bar{\sigma}_2 < 0$	1	1	α_3

The problem how to determine $\alpha_1, \alpha_2, \alpha_3, \alpha_3'$ and other analogous parameters that will additionally appear in the full 3-D analysis was discussed above. One rather common approach is to voluntarily set some of them zero or prescribe some nonzero values. When used in any structural analysis, this approach would allow to reflect some qualitative features of the gradual failure process, however this seems too coarse for the purpose of the ultimate failure predictions. The major drawback is that there is no relation to the micromechanical characteristics of any specific composite material.

Another possible approach is to adopt the Ply Discount Method. This asks to assume that at the stress level which corresponds to the failure initiation, the crack *saturation* state is

instantaneously achieved through the entire volume of the first failed brick. This assumption may result in an overestimated reduction of the elastic characteristics, but would allow one to reasonably incorporate the damaged state parameters without concerning about the actual crack density at each load level.

At the next level of complexity, the stiffness reduction parameters may be directly related to the actual state of damaged material by using some information from the micromechanics analysis. And, finally, those can be evaluated from the experimental data. The expected practical difficulties when applying these two approaches have been outlined above.

Another important aspect of the analysis is how to define dimensions of the initial damage zone (e.g., how to establish the first damaged brick)? This issue is directly related to the specific boundary value problem and, accordingly, to the stress/strain fields inside the brick. In any practical structural analysis situation (and especially for bonded joints), high stress/strain gradients will take place. Therefore, when using any first-ply failure criterion, the strains/stresses should be first averaged for the entire brick volume. Definitely, there is no general recipe how to choose the initial damaged brick as well as the subsequent damaged bricks during the progressive failure analysis. In each step, the decision should be made considering specific stress/strain variations, available computer facilities, time limitations, etc.

After the dimensions and the reduced elastic properties of the first damaged brick have been established, a new 3-D distribution of stresses/strains can be computed inside the whole mosaic body, and the second step of the progressive failure analysis can be performed. By applying again the chosen failure criterion to the newly averaged stress/strain fields in all of the bricks, one or more additional damaged bricks and corresponding failure modes may appear. Accordingly, the stiffnesses have to be reduced in all those bricks, and the analysis will go to the next cycle. This process can be continued till some ultimate state of damage (fiber breakage in all of the plies, specifically) is achieved.

The prototype of the described analysis approach have been developed and illustrated on the example of 3-D progressive failure of cross-ply laminated plates exposed to transverse bending

in [14]. The most interesting feature of the results presented there is the revealed dramatic change, after each failure event, in the stress fields computed for the damaged bricks and considerably elevated stresses in their undamaged neighbors. A novel advanced algorithm and computer code aimed at 3-D progressive failure analysis of mosaic composite structures, which utilizes the described *intralaminar* progressive failure approach, is under development.

As mentioned above, there is another aspect of progressive failure prediction methodology, namely, the *interlaminar* failure analysis. In terms of the Mosaic Model this means that cracks propagating between the bricks have to be analyzed. This problem necessarily requires to apply some fracture mechanics tools and crack propagation criteria. The major steps of this analysis can be briefly formulated as follows:

- (a) introduce initial debond crack between two bricks (made from the same or distinct materials) in the zone of highest transverse stresses; this is accomplished by relaxing the displacement continuity conditions along the corresponding surface element;
- (b) perform stress/strain analysis of the mosaic structure containing the crack(s) using 3-D Mosaic Model with the altered internal continuity conditions;
- (c) compute potential energies of each brick and the whole mosaic structure in the presence of the debond crack(s);
- (d) give some increment to the crack length and repeat steps (b) and (c) for a larger crack;
- (e) evaluate energy release rate using results of (c) and (d);
- (f) apply the critical energy release rate criterion and define if the crack growth guess was correct; if yes, then give another increment to the crack; if no, then increase the load level.

One specific problem illustrating application of the developed 3-D variational analysis to the interlaminar crack propagation modeling is presented next.

3.6 3-D Analysis Of An Interlaminar Crack Propagation

In general, fracture analysis includes two basic steps: (a) fracture initiation, and (b) fracture propagation. Appropriate fracture initiation criterion is required for each specific situation. Here, only step (b) is analyzed assuming that some initial crack of given length already exists. One specific problem of the interlaminar crack propagation under opening (mode I) will be analyzed in this section as to illustrate the application of 3-D Mosaic Model to linear fracture mechanics.

Consider a composite beam delaminated along its midplane over a length and loaded at the ends by peel displacement u_0 as shown in Fig. 3.21. Strain energy of the whole specimen is calculated as

$$P = \sum_s P^{(s)} \quad (12)$$

where $P^{(s)}$ is the strain energy of the s^{th} brick evaluated according to (1.12). The strain energy release rate is defined as

$$G_I = \frac{P(a_2) - P(a_2 + \Delta a)}{2b\Delta a} = \frac{\Delta P}{2b\Delta a} \quad (13)$$

where $P(a_2)$ is strain energy of the specimen with an interlaminar crack of length a_2 ; Δa is the virtual crack extension length, and $2b$ is width of the beam. Crack growth occurs when the strain energy release rate reaches its critical value G_{Ic} .

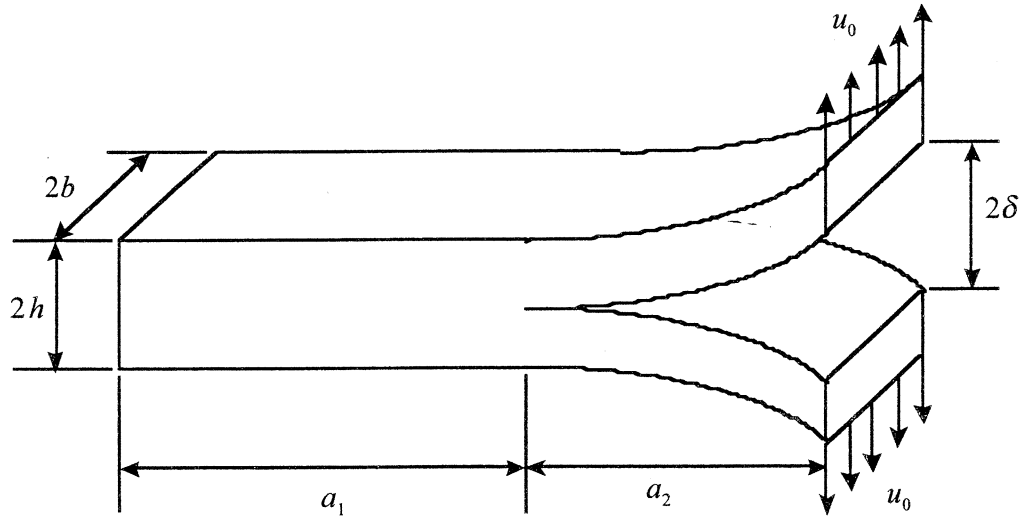


Fig. 3.21: Double cantilever beam under peel mode loading.

To analyze delamination growth, the problem shown in Fig. 3.21 need to be solved. Due to symmetry, the problem can be reduced to 1/4th part of the double cantilever beam as shown in Fig. 3.22. The boundary conditions are formulated as follows:

$$u_x|_{x=0} = 0 \quad (14)$$

$$u_y|_{y=0} = 0, \quad u_z|_{0 \leq x \leq a_1, z=0} = 0 \quad (15)$$

$$u_z|_{x=a_1+a_2, z=h} = u_0 \quad (16)$$

where u_0 is the applied peel displacement. Boundary condition (14) implies that the left side of the specimen is fixed, conditions (14) are result of the problem symmetry, and (16) is the external peel loading condition. Note that no conditions are imposed at the surface of the crack defined as $a_1 < x \leq a_1 + a_2, z = 0$.

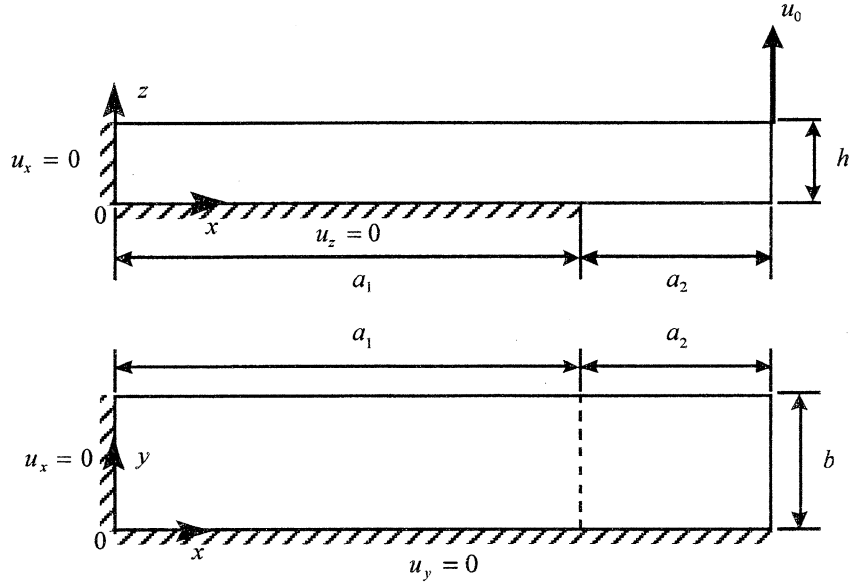


Fig. 3.22. Schematic of the 1/4th part of the double cantilever beam specimen

The following geometric parameters are used in the analysis:

$$a = a_1 + a_2 = 230 \text{ mm}, \quad 2b = 25.4 \text{ mm}, \quad 2h = 3 \text{ mm} \quad (17)$$

Elastic properties of AS4/3501-6 carbon/epoxy composite used in the analysis are taken as (8); the following value of critical strain energy release rate is used:

$$G_{Ic} = 200 \text{ J/m}^2 \quad (18)$$

Third degree Bernstein basis function were used for the displacement approximation in all three coordinate directions. Ten bricks in the x -direction ($L=10$), one brick in the y -direction ($M=1$), and four bricks in the z -direction ($N=4$) were used in the simulation. Brick mesh is refined in the vicinity of the crack. The farther away from the crack, the coarser brick mesh becomes, as illustrated in Fig. 3.23. The parameters of the nonuniform brick mesh are as following:

$$\xi_1 = \frac{x_l - x_{l-1}}{x_{l+1} - x_l} = 4 \quad \text{for } l = 2, 3, 4, 5; \quad \xi_2 = \frac{x_{l+2} - x_{l+1}}{x_{l+1} - x_l} = 4 \quad \text{for } l = 6, 7, 8, 9; \quad (19)$$

$$\zeta = \frac{z_{n+2} - z_{n+1}}{z_{n+1} - z_n} = 5 \quad \text{for } n = 1, 2, 3$$

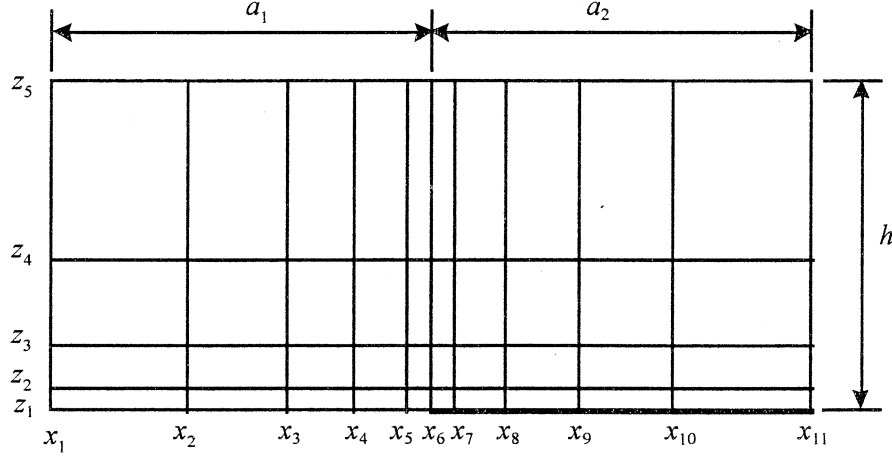


Fig. 3.23: Schematic of the brick mesh pattern.

The distribution of the strain energy density over the beam volume is shown in Fig. 3.24. Strain energy density of the s^{th} brick is evaluated as

$$p^{(s)} = \frac{P^{(s)}}{V^{(s)}} \quad (20)$$

where $V^{(s)}$ is the volume of the s^{th} brick. It is seen that strain energy is highly concentrated near the crack tip. Specifically, referring to Figs. 3.23 and 3.24, the strain energy density in the region $0 \leq x \leq x_4$ (occupied by the bricks 1-3, 11-13, and 31-33) is negligibly small. On the other hand, according to (17) and (19), this region covers 98.5% of the specimen volume located to the left from the crack (bricks 1-5, 11-15, and 31-35). The strain energy localization is, obviously, the result of the stress concentration in that region.

The dependencies of the strain energy release rate (SERR) on the applied peel displacement u_0 are shown in Fig. 3.25 for different lengths of the crack. A virtual crack extension length $\Delta a = 0.5 \text{ mm}$ was used for the evaluation of SERR. Actually, just one simulation is needed for a full characterization of the SERR relation to the applied displacement. For example, assume that the SERR value G' has been obtained at some magnitude u'_0 of the applied peel displacement. Then, SERR at an arbitrary value u_0 is calculated as

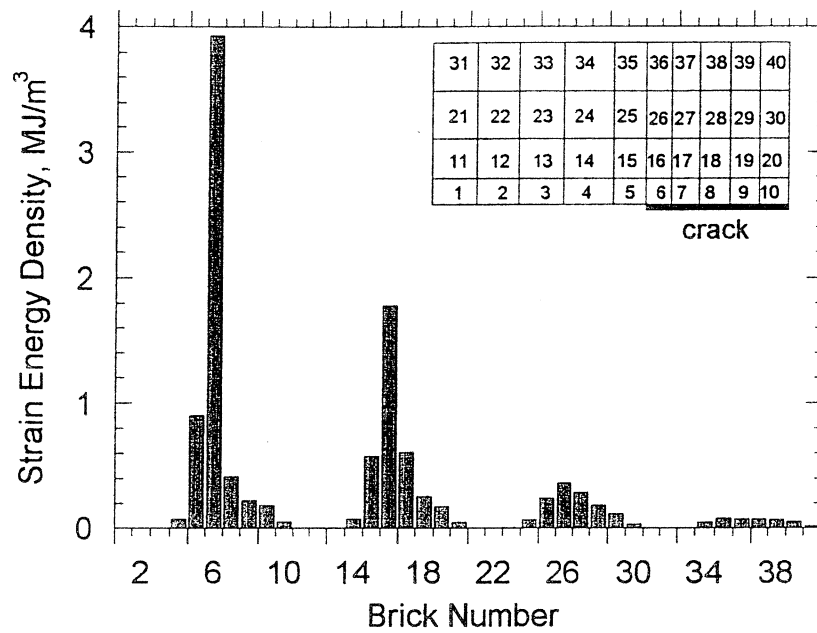


Figure 3.24. Distribution of the strain energy density inside the specimen. Crack size $a_2 = 10 \text{ mm}$, applied peel displacement $u_0 = 0.175 \text{ mm}$. The insert shows the nomenclature of the bricks.

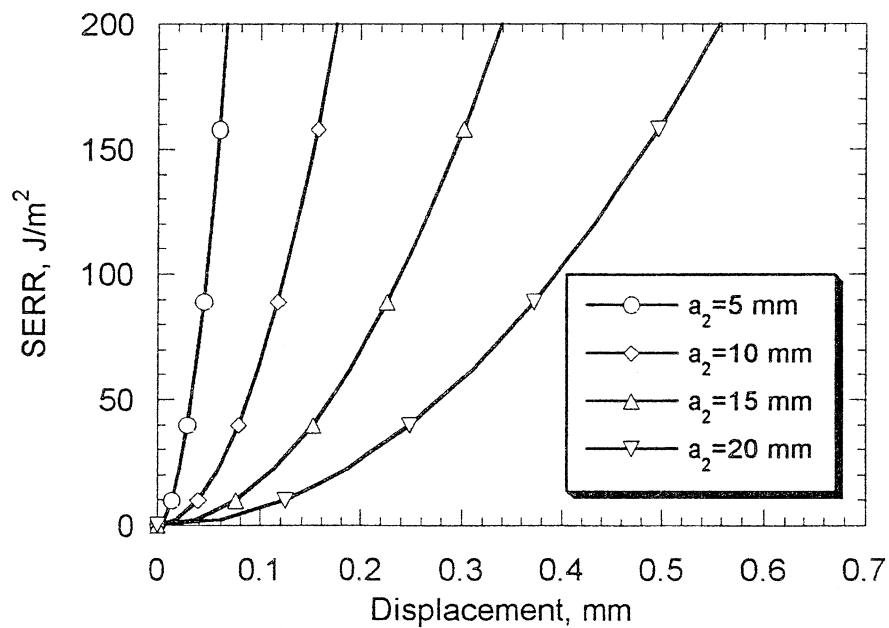


Figure 3.25. Variation of the strain energy release rate on the applied peel displacement u_0 at different crack sizes.

$$G = (u_0/u'_0)^2 \cdot G' \quad (21)$$

Eq. (21) is the consequence of a quadratic form of the strain energy relation to the displacement approximation coefficients $U_{ijk}^{m(s)}$, see Section 1, Eq. (12), and a linear form of the relations between $U_{ijk}^{m(s)}$ and the applied displacement u_0 .

The crack propagation process can be described using results presented in Fig. 3.25. For the specimen with initial crack length $a_2 = 5mm$, the increase of the applied peel displacement, u_0 , results in a monotonous increase of the SERR. At $u_0 \approx 0.066mm$, the SERR reaches the assumed critical value (18), and the crack starts to grow, releasing the accumulated strain energy. The growth continues until the crack reaches its new “stable” state corresponding to the length $a_2 = 10mm$. At the applied displacement magnitude $u_0 \approx 0.066mm$, the value of SERR corresponding to a new stable state drops to the level $G_I \approx 30J/m^2$. Further increase of the applied displacement leads to the increase of the SERR; this remains “safe” up to the peel displacement magnitude $u_0 \approx 0.175mm$, when the SERR reaches its critical value (18) again, and the crack gains another increment. The accumulated strain energy is then released, the SERR drops to the level $G_I \approx 50J/m^2$, and the process repeats, but at the higher level of the applied peel displacement.

The described discrete crack growth process which assumes some set of stable crack lengths is, of course, simplified and was presented here only for the sake of illustration how the Mosaic Model can be applied to the delamination growth problem. In a more rigorous analysis, which is the objective of our future work, each next stable crack length should be not assumed, but rather computed from the analysis itself.

To further illustrate results of the present analysis, Figs. 3.26 and 3.27 show variations of the crack length and strain energy density of the entire specimen upon the applied peel displacement. The strain energy density of the entire specimen volume is defined as

$$p = \sum_s p^{(s)} \quad (22)$$

where $p^{(s)}$ is the strain energy density of the s^{th} brick calculated from (3.20). It can be observed from Figs. 3.26 and 3.27 that the length of the initial crack remains unchanged till the applied peel displacement reaches its critical level u_{cr} . Below that level, the strain energy density of the specimen continuously increases. Further increase of the peel displacement above the level u_{cr} causes crack growth which is accompanied by the release of the accumulated strain energy and, accordingly, by the reduction of the total strain energy of the specimen.

It has to be noted that the difference between the *applied* peel displacement u_0 and the *computed* crack opening deflection δ at the end $x = a_1 + a_2$ is very small. Indeed, u_0 is about 6% higher than δ at the crack length $a_2 = 5\text{mm}$, and the difference is less than 0.06% at the crack length $a_2 = 20\text{mm}$.

In the example considered here the boundary value problem was formulated in terms of applied peel displacement. However, it is possible to formulate the reciprocal problem assuming that the peel force is applied to the double-cantilever specimen. An equivalency between the applied peel displacement u_0 and peel force F_0 can be established by comparing results of the numerical analyses.

Figure 3.28 shows variation of the crack opening deflection δ on the statically equivalent peel force. It is seen that the peel force increases till the delamination crack starts propagating. After that the peel force descends. It is also observed that as the initial crack length a_2 increases, the peel force required to increase the crack decreases. These analytical results are in a qualitative agreement with the experimental observations reported in [15] - [17]. Shape of the curve “crack length vs. applied displacement” shown in Fig. 3.26 is similar to those presented in [17].

The considered rather simple example shows capability of the developed Mosaic Model approach to predict propagation of initial cracks between the bricks in a 3-D composite body. The methodology is readily applicable to adhesive bonded joints of composite structural elements. A study of some example problems of this type is underway.

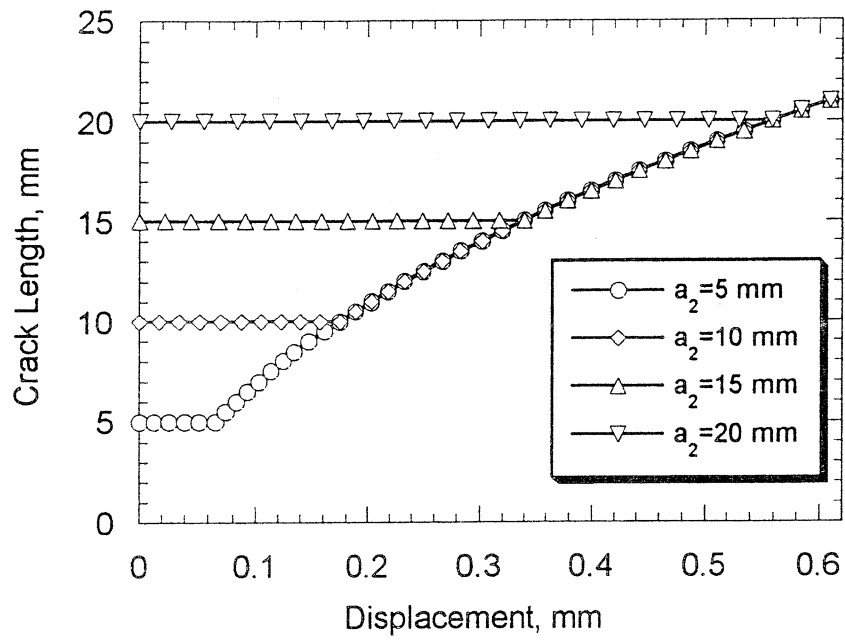


Figure 3.26. Dependence of the actual crack length on the applied peel displacement u_0 for different initial crack lengths a_2 .

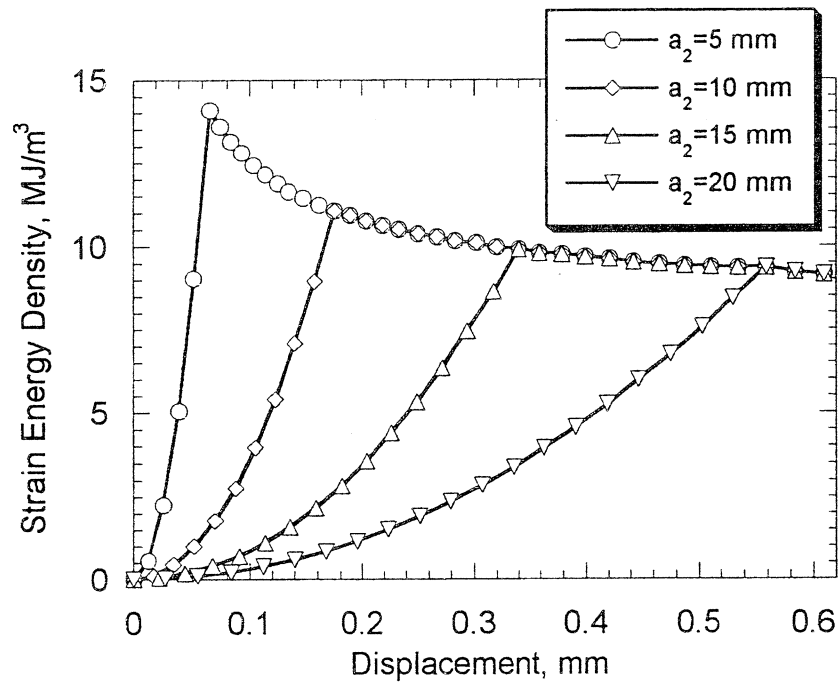


Figure 3.27. Dependence of the strain energy density on the applied peel displacement u_0 for different initial crack lengths a_2 .

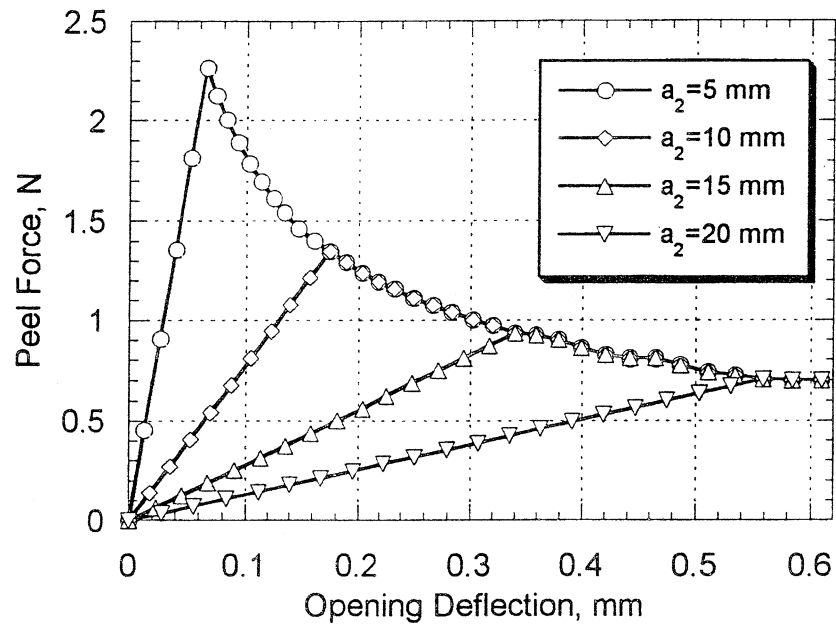


Figure 3.28. Dependence of the crack opening deflection δ on applied peel force for different initial crack sizes a_2 .

4.0 3-D FINITE ELEMENT ANALYSIS OF COMPOSITE-TO-METAL AND COMPOSITE-TO-COMPOSITE BONDED JOINTS

4.1 Introduction

Application of three-dimensional solid finite elements gains increasing interest in numerical analysis of composite structures. During the 1960s and early 1970s, the development of 3-D solid elements was one of the major points of interest in the finite element methodology. A variety of 3-D elements have been derived on the basis of previously developed 2-D elements. Among the most popular types of solid elements is the family of rectangular hexahedra: 8-node (linear displacement) element with 24 degrees of freedom (d.o.f.); 20-node (quadratic displacement) "serendipity" element with 60 d.o.f.; 27-node "full Lagrange" type (quadratic displacement) element with 81 d.o.f.; 32-node (incomplete cubic displacement) element with 96 d.o.f.; 64-node (complete cubic displacement) element with 192 d.o.f.; 8-node (incomplete quintic displacement) element with 96 d.o.f.; "Hermite" type element with both displacements and displacement derivatives as d.o.f., etc.

Several types of 3-D numerical analyses have been applied to bonded joints in [1]-[4]. The finite difference analysis of double-lap joints presented in [1] have addressed specifics of the 3-D stress variations, double-edge effect at the corner points and inability of capturing it by a 2-D plane strain analysis, the effect of adhesive layer treated as distinct 3-D entity, and discussion on the failure criteria and fracture mechanics applicability. However, not all of the suggestions and conclusions (specifically, those regarding stress singularities) have not been validated due to the difficulties to satisfy some boundary conditions and absence of a convergence study. An 8-node hexahedron finite element developed in [2] for bonded joint analysis contains substantial simplifications, which deprive many features of the full 3-D analysis. A 3-D finite element analysis of single-lap joints was reported in [3]. A 3-D finite element analysis using submodeling technique has been applied in [4]. This chapter presents a comprehensive

numerical study of composite-to-metal and composite-to-composite double-lap joints originated in the latter work.

The library of 3-D solid elements in ABAQUS contains first- and second-order isoparametric elements [5]. The first-order (linear displacement) element is the 8-node hexahedron. The second order (quadratic displacement) elements are: the 20-node “serendipity” hexahedron and the 27-node “full Lagrange” hexahedron. In the latter element, the full Lagrange interpolation employs product forms of the one-dimensional Lagrange polynomials. Our experience of utilizing all three aforementioned elements showed that the 27-node element is most accurate and computationally efficient. This element (C3D27 by the ABAQUS convention) will be further utilized in this study.

The major difficulty faced when performing 3-D analysis of bonded joints is that there are several zones of high stress gradients, and also several *lines* of possible singularities. Obviously, an accurate stress characterization near the lines of singularity with the use of *uniform* element mesh would require extremely high refinement and, accordingly, huge computational expenses. On the other side, when using *nonuniform* element meshes (for example, by applying “parametric refinement” available in ABAQUS), the element aspect ratio may become very high and thus cause so-called “zero or negative element volume error”. Both these computational obstacles have been faced when directly using C3D27 element in the analysis of double-lap joints. Particularly, the attempts to accurately compute stresses in relatively thick adhesively bonded joints with thin adhesive layer (which was modeled as distinct 3-D elastic entity) revealed severe limitations. Accuracy of the computed stresses was questionable. Thus, a more sophisticated capabilities available in ABAQUS have to be explored. The global-local type “submodeling” technique available in the recent versions of ABAQUS showed to be a viable approach.

4.2 The Concept of Submodeling

The idea how to apply submodeling technique to the bonded joint problems can be basically explained using specific example shown in Fig. 4-1a. Only those regions of the structure have to be analyzed in great detail (i.e., using fine element meshes), which are close to the corner lines AB and CD. Accordingly, the stress fields can be defined in several steps, by successively performing 3-D analysis for smaller and smaller local regions. When using this multi-step approach, the computed nodal displacements from some “predecessor” local analysis are used as the input geometric boundary conditions for the “successor” local analysis. If this methodology is implemented correctly, then each next step should provide increasingly accurate stresses in the zones of high stress gradients. Ultimately, if it is known that the stresses are finite everywhere in the structure, their values can be computed with any prescribed accuracy after some number of submodeling steps. In principle, the number of consecutive local analyses is limited only by patience of the analyst and physical time allocated for the specific problem. An experienced analyst can easily optimize the submodeling strategy.

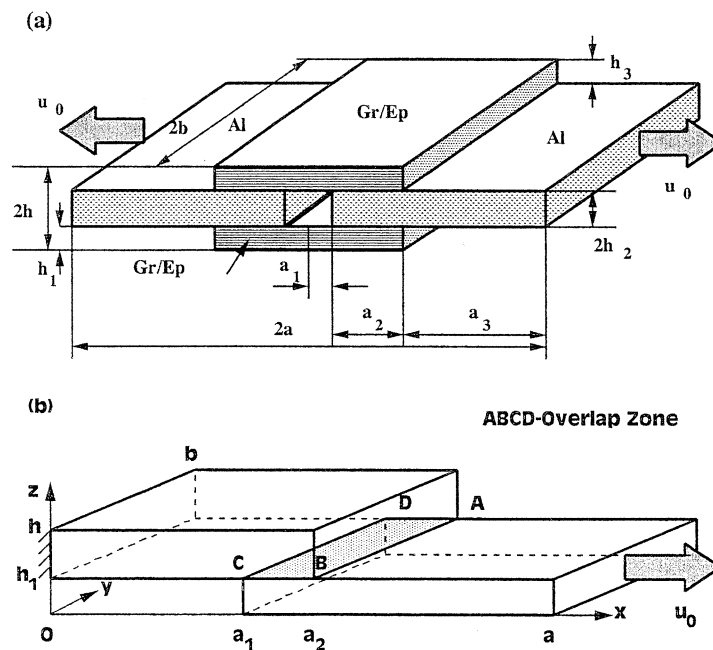


Fig. 4-1: Schematic of a double-lap joint (a) and its 1/8th part (b) considered in the analysis.

Another important feature of this methodology (which is, indeed, a common place for any global-local type analysis) is that after the first step (i.e., global analysis) has been accomplished, different local regions of the structure are “disconnected” and each of them is further analyzed *independently*. This is illustrated in Fig. 4-2, where the side view, x - z , and top view, x - y , of the structure are shown. In the local analyses, regions 1 and 2 are solved independently, and the number of d.o.f. used for the analysis of each local region may be even lower than in the initial global analysis. In the other words, instead of performing stress analysis of the whole structure in one step, the analysis of its small portions is performed in several independent steps.

After these general remarks we will perform first four steps of the submodeling analysis, i.e., the initial (global) analysis and three consecutive local analyses. The focus will be at the stress convergence study near the ends and *exactly* at the ends of the overlap zone. After that,

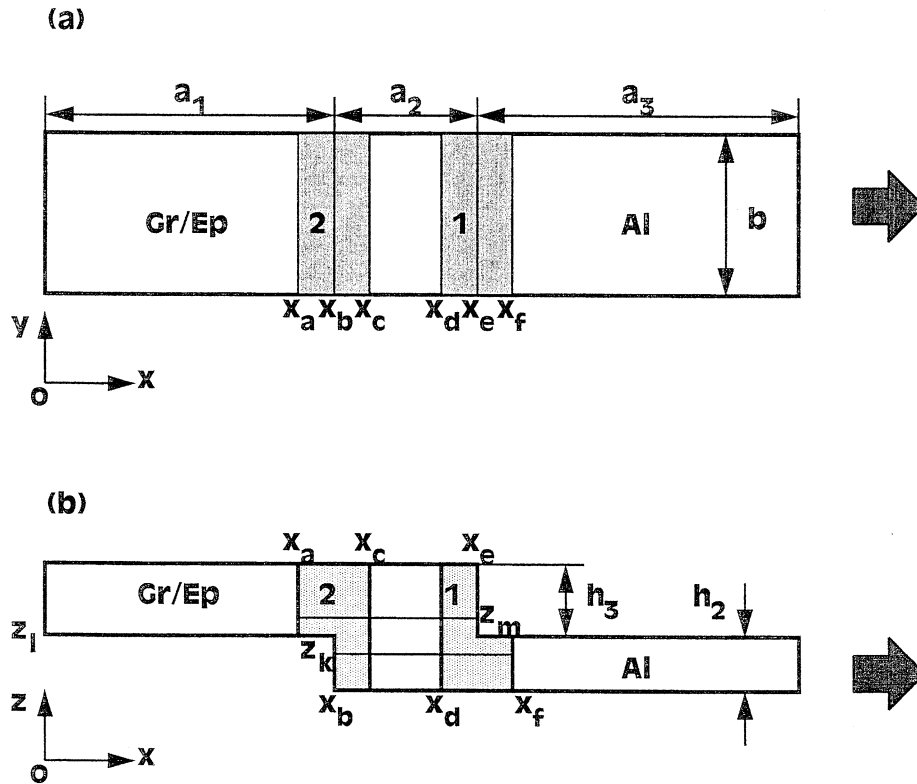


Fig. 4-2: Schematic of the local region locations.

submodeling technique will be illustrated on the example of double-lap joint with initial debond crack.

4.3 Problem Formulation

Consider double-lap bonded joint shown in Fig. 4-1a. The structure is exposed to uniform uniaxial extension. The displacement u_x having some known value u_0 is applied uniformly at the right and left ends of the middle adherends.

It is expected in the problem under consideration that some stress components may be singular at the lines AB and CD (see, Fig. 4-1a) which belong to the interface between the upper and middle adherends and the line DA which belongs simultaneously to the interface and free edge. It is important to emphasize that the cause of possible singularities at the lines AB and CD is different than at the line DA. Stress singularity at the line DA may be caused by the material property mismatch at the flat edge (similar to the classical free edge effect problem), while stress singularities at the lines AB and CD may be caused by both the material property mismatch and the step-wise geometry variation.

Further, it is assumed for simplicity that both the upper and lower adherends are made from the same material and have identical geometric characteristics. Also, it is assumed that both the right and left middle adherends are made from the same material, have identical geometric parameters and placed symmetrically with respect to the plane which is perpendicular to the x -axis and passes through the center points of the upper and lower adherends. These assumptions allow one to apply symmetry conditions in all three coordinate directions and, accordingly, reduce the structure to be analyzed to 1/8th part of the full structure, as shown in Fig. 4-1b. Accordingly, the full set of boundary conditions is formulated as following:

$$u_x = 0 \text{ at } x = 0; \quad u_x = u_0 \text{ at } x = a; \quad u_y = 0 \text{ at } y = 0; \quad u_z = 0 \text{ at } z = 0 \quad (1)$$

The upper and lower adherends are made from unidirectional graphite/epoxy (Gr/Ep)

composite with the following elastic properties:

$$\begin{aligned} E_L &= 164 \text{ GPa} \text{ (23.86 Msi)}, & E_T &= 9.82 \text{ GPa} \text{ (1.426 Msi)}, \\ G_L &= 6.78 \text{ GPa} \text{ (0.9825 Msi)}, & G_T &= 3.66 \text{ GPa} \text{ (0.5306 Msi)}, \\ \nu_{LT} &= 0.24 \end{aligned} \quad (2)$$

Direction of the reinforcement in the composite adherends is along the x -axis. The middle adherends are made from aluminum (Al) with the following properties:

$$E = 73.7 \text{ GPa} \text{ (10.7 Msi)}, \nu = 0.25 \quad (3)$$

Geometric parameters used in the analysis are:

$$a/a_1 = a/a_2 = a/b = 4, a/h_1 = a/h_2 = a/h_3 = 20 \quad (4)$$

It is further assumed that adhesive material provides perfect bonding, but due to a small thickness of adhesive layers those are not explicitly considered in this analysis. The effect of adhesive layers treated as distinct 3-D isotropic elastic solids will be studied in Sections 4.11 thru 4.13.

4.4 Global Analysis

The initial step is to perform global analysis of $1/8^{\text{th}}$ part of the structure shown in Fig. 4-1b using successively refined meshes of elements in the x , y and z -directions. It is questioned in this study if it is possible to obtain converged displacements and stresses at any point of the structure? For brevity of the element mesh description, the following notations of the number of elements in the x -direction are introduced:

$$\begin{aligned} N_{0a}^x &\text{ for } 0 \leq x/a \leq x_a/a, \quad N_{ab}^x \text{ for } x_a/a \leq x/a \leq x_b/a, \quad N_{bc}^x \text{ for } x_b/a \leq x/a \leq x_c/a, \\ N_{cd}^x &\text{ for } x_c/a \leq x/a \leq x_d/a, \quad N_{de}^x \text{ for } x_d/a \leq x/a \leq x_e/a, \\ N_{ef}^x &\text{ for } x_e/a \leq x/a \leq x_f/a, \quad N_{f1}^x \text{ for } x_f/a \leq x/a \leq 1 \end{aligned} \quad (5)$$

Number of elements in the y -direction inside the interval $0 \leq y/b \leq 1$ is denoted N_{0l}^y , and numbers of elements in the z -direction are denoted as

$$\begin{aligned} N_{0l}^z \text{ for } 0 \leq z/h \leq z_l/h, \quad N_{l1}^z \text{ for } z_l/h \leq z/h \leq 1, \quad N_{0k}^z \text{ for } 0 \leq z/h \leq z_k/h, \\ N_{kl}^z \text{ for } z_k/h \leq z/h \leq z_l/h, \quad N_{lm}^z \text{ for } z_l/h \leq z/h \leq z_m/h, \quad N_{m1}^z \text{ for } z_m/h \leq z/h \leq 1 \end{aligned} \quad (6)$$

Specific values of x_b , x_e and z_l are prescribed by the particular structural configuration. Coordinates x_a , x_c , x_d , x_f , z_k and z_m will be later on used for determining boundaries of the local regions. Their choice is dictated by the analyst's intuition. On one side, it is desirable to take them as close as possible to the corner lines AB and CD, because solving smaller local regions will reduce number of required steps of submodeling and, therefore, reduce pre-processing and post-processing effort, as well as the computational time. On the other side, the coordinate values should be at some reasonable distance away from the corner lines AB and CD, because if the local regions are too small, the global analysis has to be huge as to provide converged displacements and stresses at the boundaries of the local regions. The following specific numerical values have been adopted in the analysis:

$$\begin{aligned} x_a/a = 0.21, \quad x_b/a = 0.25, \quad x_c/a = 0.29, \quad x_d/a = 0.46, \quad x_e/a = 0.50, \quad x_f/a = 0.54, \\ z_k/h = 0.4, \quad z_l/h = 0.5, \quad z_m/h = 0.6 \end{aligned} \quad (7)$$

Tables 4-1 thru 4-3 present full description of the element meshes used in the global analysis. For all variants described in Table 4-1, uniform meshes were applied inside each of the intervals in the x -direction. The nonuniform meshes were applied in the y and z -directions (parametric mesh refinement was used for this purpose). The element next to the mid-plane, $y=0$, was always chosen the largest of all elements in the y -direction. The element next to the free edge, $y=b$, was always chosen the smallest of all elements in the y -direction. The lengths ratio of the largest to smallest elements in this direction was taken 40. In the z -direction, the largest element

in Al adherend is next to the mid-plane, $z = 0$, and the smallest element is next to the interface, $z = 0.5h$. Their lengths ratio in this direction was taken 8. Analogously, the largest element in the Gr/Ep adherend is next to the top surface, $z = h$, and the smallest element is next to the interface, $z = h_1$. Their lengths ratio in the z -direction is taken 8. For all variants described in Table 4-2, uniform meshes were used inside each interval in the x and y -directions; parametric mesh with the element ratio 8 was used in the z -direction. For all variants of Table 4-3, uniform meshes were applied in all of the intervals and for all of the coordinate directions.

Table 4-1: Element meshes used in the global analysis for the x -direction convergence study.

No. of mesh	N_{0a}^x	N_{ab}^x	N_{bc}^x	N_{cd}^x	N_{de}^x	N_{ef}^x	N_{f1}^x	N_{01}^y	N_{0l}^z	N_{l1}^z	Total d.o.f.
G.1	2	2	2	4	2	2	2	4	4	4	11,691
G.2	4	4	4	8	4	4	4	4	4	4	22,923
G.3	4	8	8	8	8	8	4	4	4	4	34,155
G.4	4	12	12	8	12	12	4	4	4	4	45,387
G.5	4	16	16	8	16	16	4	4	4	4	56,619
G.6	4	20	20	8	20	20	4	4	4	4	67,851

Table 4-2: Element meshes used in the global analysis for the y -direction convergence study.

No. of mesh	N_{0a}^x	N_{ab}^x	N_{bc}^x	N_{cd}^x	N_{de}^x	N_{ef}^x	N_{f1}^x	N_{01}^y	N_{0l}^z	N_{l1}^z	Total d.o.f.
G.7	4	8	8	8	8	8	4	5	2	2	41,745
G.8	4	8	8	8	8	8	4	10	2	2	79,695

Table 4-3: Element meshes used in the global analysis for the z-direction convergence study.

No. of mesh	N_{0a}^x	N_{ab}^x	N_{bc}^x	N_{cd}^x	N_{de}^x	N_{ef}^x	N_{f1}^x	N_{01}^y	N_{0k}^z	N_{kl}^z	N_{lm}^z	N_{ml}^z	Total d.o.f.
G.9	4	8	8	8	8	8	4	5	2	2	2	2	41,745
G.10	4	8	8	8	8	8	4	5	3	3	3	3	61,017
G.11	4	8	8	8	8	8	4	5	4	4	4	4	80,289

As was pointed out above, major objective of the global analysis is to obtain converged displacements $u_x(x,y,z)$, $u_y(x,y,z)$ and $u_z(x,y,z)$ at all points of the structure. As expected, it should be most difficult to accomplish this task for the corner lines AB and CD. The performed convergence study performed for all three displacements is illustrated in Table 4-4 for one point of the line AB. If applying the simplest convergence criterion, namely, a monotonous decrease of the error factor with the mesh refinement, it can be concluded that convergence of u_x and u_y is very fast and can be achieved with a rather coarse element mesh, but obtaining converged u_z requires much finer element meshes. This effect is, probably, related to the specific deformation pattern of the double-lap joints.

4.5 Local Analysis - Submodel 1

In the next step, local regions 1 and 2 shown in Fig. 4-2, which are especially interesting due to the expected high stress gradients there and possible singularities at the lines AB and CD, are solved separately using nodal displacement values calculated in the global analysis as the input data. The same 27-node element is used in all local analyses and for both local regions. In principle, any number of successive submodeling steps can be applied, using converged displacements computed in some preceding step for more accurate stress computation in the successive step. This should consistently increase accuracy of the stress predictions inside the local regions 1 and 2.

Table 4-4: Normalized displacements at, $x = 0.5a, y = 0.8b, z = 0.5h$ computed with the element meshes described in Tables 4-1 thru 4-3.

Displacement	u_x / u_0	u_y / u_0	u_z / u_0
G.1	0.34079	-0.05446	0.00180
G.2	0.34100	-0.05445	0.00264
G.3	0.34107	-0.05447	0.00306
G.4	0.34110	-0.05447	0.00319
G.5	0.34111	-0.05448	0.00325
G.6	0.34112	-0.05448	0.00328
G.7	0.34108	-0.05445	0.00317
G.8	0.34102	-0.05446	0.00308
G.9	0.34069	-0.05444	0.00298
G.10	0.34111	-0.05445	0.00319
G.11	0.34135	-0.05446	0.00328

First, consider local region 1, which length is defined by $x_d / a = 0.46$ and $x_f / a = 0.54$. Element meshes used in the first local analysis are described in Table 4-5. The x -direction meshes are nonuniform (parametric) with the ratio of the largest to smallest elements $l_x = L_x^{\max} / L_x^{\min} = 20$. The largest elements are next to the vertical planes passing through x_d and x_f , and the smallest elements are on both sides of the vertical plane passing through x_e . All meshes in the y and z -directions are uniform inside each of the intervals, i.e., $l_y = L_y^{\max} / L_y^{\min} = 1$ and $l_z = L_z^{\max} / L_z^{\min} = 1$.

Table 4-5: Element meshes used in the Submodel 1 analyses; $l_x = 20$, $l_y = 1$, $l_z = 1$

No. of mesh	N_{de}^x	N_{ef}^x	N_{01}^y	N_{0k}^z	N_{kl}^z	N_{lm}^z	N_{ml}^z	Total d.o.f.
L1.1	8	8	5	4	4	4	4	27,489
L1.2	10	10	5	4	4	4	4	34,089
L1.3	4	4	10	4	4	4	4	27,279
L1.4	6	6	10	4	4	4	4	39,879
L1.5	8	8	10	4	4	4	4	52,479
L1.6	10	10	10	4	4	4	4	65,079
L1.7	12	12	10	4	4	4	4	77,679
L1.8	8	8	10	4	8	8	4	77,679

Results for all three displacements calculated at $y=0.8b$ and $y=b$ with the meshes L1.1-L1.8 of Table 4-5 are presented in Tables 4-6 and 4-7. When comparing variant L1.1 with L1.2-L1.7, which have different number of elements in the x -direction, it is seen that the displacement values practically do not change if the number of elements is more than $N_{de}^x = N_{ef}^x = 6$. When comparing results obtained for variants L1.1 and L1.5 or results obtained for variants L1.2 and L1.6 (these correspond to different number of elements in the y -direction), it is seen that the effect of mesh refinement is more substantial, especially at the point $y=b$. The effect of z -direction mesh refinement is also considerable, especially for u_z , as seen from the comparison of L1.5 and L1.8.

Further, when comparing results presented in Table 4-6 for variants L1.3-L1.8 with the data obtained in the most refined global analysis (see Table 4-4), it is recognized that the local mesh refinements do not affect u_x and u_y , while u_z is changing considerably. So, for this displacement component the element mesh near the line $x=0.5a$, $z=0.5h$ should be very fine.

The slowest convergence is at the point $x = 0.5a$, $y = b$, $z = 0.5h$, as indicated by Table 4-7.

Next consider results for the normalized stress components σ_x/σ_0 , σ_z/σ_0 and τ_{xz}/σ_0 . The normalization factor $\sigma_0 = 0.961\text{GPa}$ (0.1393Msi) is the nominal longitudinal stress calculated at $x = a$ from Hooke's law, assuming that the longitudinal strain $\varepsilon_0 = 1\%$ at $x = a$; this corresponds to $u_0 = 0.01a$. Explanation to our choice to focus on stress components σ_x , σ_z and τ_{xz} in this study is that σ_x is the major in-plane stress in the loading case under consideration, and σ_z and τ_{xz} are traditionally considered as the most dangerous stresses for bonded joints. Numerical results obtained with the meshes L1.3-L1.7 of Table 4-5 are presented in Tables 4-8 and 4-9. Again, if applying the convergence criterion of a monotonous decrease of the error factor, it can be concluded that for both values of the y -coordinate, in both the materials, all three stress components under consideration show *very slow* convergence. Additional validation of this conclusion can be obtained using parametric mesh refinement in the x -direction.

Table 4-6: Normalized displacements at $x = 0.5a$, $y = 0.8b$, $z = 0.5h$ computed with the element meshes of Table 4-5.

Displacement	u_x/u_0	u_y/u_0	u_z/u_0
L1.1	0.34140	-0.05446	0.00363
L1.2	0.34140	-0.05446	0.00363
L1.3	0.34140	-0.05446	0.00363
L1.4	0.34134	-0.05446	0.00353
L1.5	0.34134	-0.05446	0.00354
L1.6	0.34134	-0.05446	0.00355
L1.7	0.34134	-0.05446	0.00355
L1.8	0.34175	-0.05446	0.00382

Table 4-7: Normalized displacements at $x = 0.5a$, $y = b$, $z = 0.5h$ computed with the element meshes of Table 4-5.

Displacement	u_x / u_0	u_y / u_0	u_z / u_0
L1.1	0.35126	-0.07507	0.00522
L1.2	0.35126	-0.07507	0.00523
L1.3	0.35126	-0.07506	0.00522
L1.4	0.35145	-0.07627	0.00573
L1.5	0.35145	-0.07627	0.00573
L1.6	0.35145	-0.07627	0.00574
L1.7	0.35145	-0.07627	0.00574
L1.8	0.35183	-0.07633	0.00600

Table 4-8. Normalized stresses in Al and Gr/Ep adherends at $x = 0.5a$, $y = 0.8b$, $z = 0.5h$ computed with the element meshes of Table 4-5.

Adherend	Al			Gr/Ep		
Stress	σ_x / σ_0	σ_z / σ_0	τ_{xz} / σ_0	σ_x / σ_0	σ_z / σ_0	τ_{xz} / σ_0
L1.3	3.8853	1.7952	-1.4412	4.2574	2.2144	-1.2825
L1.4	3.9532	1.8532	-1.5292	4.2060	2.2305	-1.2965
L1.5	3.9825	1.8779	-1.5892	4.1732	2.2350	-1.3052
L1.6	3.9959	1.8894	-1.6312	4.1519	2.2365	-1.3112
L1.7	4.0050	1.8961	-1.6637	4.1371	2.2365	-1.3158

Table 4-9: Normalized stresses in Al and Gr/Ep adherends at $x = 0.5a, y = b, z = 0.5h$ computed with the element meshes of Table 4-5.

Adherend	Al			Gr/Ep		
Stress	σ_x / σ_0	σ_z / σ_0	τ_{xz} / σ_0	σ_x / σ_0	σ_z / σ_0	τ_{xz} / σ_0
L1.3	3.5386	1.6561	-1.3270	3.9617	2.0263	-1.1943
L1.4	3.6008	1.7096	-1.4071	3.9139	2.0412	-1.2072
L1.5	3.6276	1.7325	-1.4619	3.8834	2.0454	-1.2151
L1.6	3.6399	1.7431	-1.5003	3.8637	2.0468	-1.2205
L1.7	3.6482	1.7493	-1.5299	3.8499	2.0474	-1.2248

Next consider results obtained with different meshes in the y -direction. Most interesting here is to study stresses at the point $x = 0.5a, y = b, z = 0.5h$, which belongs simultaneously to the *interface* and *free edge*. In order to develop efficient computational strategies, the interval $0 \leq y/b \leq 1$ was first divided into two subintervals. Accordingly, the following notations of the number of elements have been introduced: N_{0g}^y for $0 \leq y/b \leq 0.8$ and N_{g1}^y for $0.8 \leq y/b \leq 1$. Uniform meshes inside each of these intervals were applied in the first step; the number of elements used is given in Table 4-10. All mesh parameters in the x and z -directions were taken the same as in variant L1.5 of Table 4-5. In the next step, uniform meshes were used for the interval $0 \leq y/b \leq 0.8$ and parametric meshes for the interval $0.8 \leq y/b \leq 1$. The mesh parameters for this case are given in Table 4-11. Results for the stresses calculated with the element meshes of Tables 4-10 and 4-11 are presented in Tables 4-12 thru 4-15. It can be concluded from these data that even at the point $x = 0.5a, y = b, z = 0.5h$ all three stress components seem to be converging with the mesh refinement in the y -direction.

Table 4-10: Uniform meshes in the y -direction used in Submodel 1 analysis; $l_x = 20$, $l_z = 1$

No. of mesh	N_{0g}^y	N_{g1}^y	Total d.o.f.
L1.5	8	2	52,479
L1.9	4	1	27,489
L1.10	4	2	32,487
L1.11	4	4	42,483
L1.12	4	6	52,479
L1.13	4	8	62,475

Table 4-11: Parametric meshes in the y -direction used in Submodel 1 analysis; $l_x = 20$, $l_z = 1$

No. of mesh	N_{0g}^y	N_{g1}^y	l_y in $0.8 \leq y/b \leq 1$
L1.11	4	4	1
L1.14	4	4	10
L1.15	4	4	20
L1.16	4	4	40
L1.17	4	4	80
L1.18	4	4	160

Table 4-12: Normalized stresses in Al and Gr/Ep adherends at $x = 0.5a, y = b, z = 0.5h$ computed with the element meshes of Table 4-10.

Adherend	Al			Gr/Ep		
Stress	σ_x/σ_0	σ_z/σ_0	τ_{xz}/σ_0	σ_x/σ_0	σ_z/σ_0	τ_{xz}/σ_0
L1.5	3.6276	1.7325	-1.4619	3.8834	2.0454	-1.2151
L1.9	3.7244	1.7672	-1.4920	3.9515	2.0915	-1.2358
L1.10	3.6277	1.7325	-1.4619	3.8835	2.0454	-1.2151
L1.11	3.5152	1.7037	-1.4380	3.8081	2.0097	-1.1954
L1.12	3.4414	1.6918	-1.4303	3.7594	1.9962	-1.1854
L1.13	3.3841	1.6853	-1.4285	3.7210	1.9893	-1.1791

Table 4-13: Normalized stresses in Al and Gr/Ep adherends at $x = 0.5a, y = 0.8b, z = 0.5h$ computed with the element meshes of Table 4-10.

Adherend	Al			Gr/Ep		
Stress	σ_x/σ_0	σ_z/σ_0	τ_{xz}/σ_0	σ_x/σ_0	σ_z/σ_0	τ_{xz}/σ_0
L1.5	3.9825	1.8779	-1.5892	4.1732	2.2350	-1.3052
L1.9	3.9669	1.8717	-1.5820	4.1520	2.2265	-1.3005
L1.10	3.9833	1.8780	-1.5892	4.1739	2.2352	-1.3052
L1.11	3.9920	1.8787	-1.5897	4.1790	2.2360	-1.3056
L1.12	3.9920	1.8786	-1.5897	4.1790	2.2360	-1.3056
L1.13	3.9920	1.8785	-1.5897	4.1790	2.2360	-1.3056

Table 4-14: Normalized stresses in Al and Gr/Ep adherends at $x = 0.5a, y = b, z = 0.5h$ computed with the element meshes of Table 4-11.

Adherend	Al			Gr/Ep		
Stress	σ_x/σ_0	σ_z/σ_0	τ_{xz}/σ_0	σ_x/σ_0	σ_z/σ_0	τ_{xz}/σ_0
L1.11	3.5152	1.7037	-1.4388	3.8081	2.0097	-1.1954
L1.14	3.2098	1.6709	-1.4384	3.5948	1.9763	-1.1655
L1.15	3.0852	1.6560	-1.4500	3.4945	1.9687	-1.1594
L1.16	2.9824	1.6317	-1.4572	3.4096	1.9629	-1.1561
L1.17	2.9317	1.6141	-1.4593	3.3647	1.9603	-1.1554
L1.18	2.9249	1.6091	-1.4599	3.3535	1.9614	-1.1564

Table 4-15: Normalized stresses in Al and Gr/Ep adherends at $x = 0.5a, y = 0.8b, z = 0.5h$ computed with the element meshes of Table 4-11.

Adherend	Al			Gr/Ep		
Stress	σ_x/σ_0	σ_z/σ_0	τ_{xz}/σ_0	σ_x/σ_0	σ_z/σ_0	τ_{xz}/σ_0
L1.11	3.9920	1.8787	-1.5897	4.1790	2.2360	-1.3056
L1.14	3.9859	1.8790	-1.5895	4.1781	2.2359	-1.3054
L1.15	3.9857	1.8790	-1.5893	4.1755	2.2358	-1.3053
L1.16	3.9853	1.8789	-1.5891	4.1747	2.2356	-1.3051
L1.17	3.9847	1.8788	-1.5887	4.1735	2.2352	-1.3049
L1.18	3.9838	1.8785	-1.5883	4.1720	2.2347	-1.3045

4.6 Local Analysis - Submodel 2

Next step is to study stress convergence with refining element mesh in the z -direction. For this purpose, another local region is introduced. This is confined between the planes $z_k/h = 0.4$ and $z_m/h = 0.6$ and has the same dimensions in the x and y -directions as the local region considered in Submodel 1. The displacement values obtained from Submodel 1 analysis with element mesh L1.17 have been used as the nodal displacement input in the Submodel 2 analysis. Number of elements in the z -direction is described in Tables 4-16 and 4-17. The other parameters for the meshes described in Table 16 are: $N_{de}^x = 8$, $N_{ef}^x = 8$, $l_x = 20$ for both intervals $0.46 \leq x/a \leq 0.5$ and $0.5 \leq x/a \leq 0.54$; $N_{0g}^y = 4$, $l_y = 1$ for $0 \leq y/b \leq 0.8$; $N_{g1}^y = 4$, $l_y = 80$ for $0.8 \leq y/b \leq 1$; $l_z = 1$ for both intervals $0.4 \leq z/h \leq 0.5$ and $0.5 \leq z/h \leq 0.6$. The other parameters of the meshes described in Table 4-17 are: $l_z = 2$ or 4 for each of the intervals, $0.4 \leq z/h \leq 0.5$ and $0.5 \leq z/h \leq 0.6$ (size of the elements decrease toward $z/h = 0.5$). All other parameters are the same as for the meshes of Table 4-16.

Table 4-16: Uniform element meshes in the z -direction used in Submodel 2 analysis.

No. of mesh	N_{kl}^z	N_{lm}^z	Total d.o.f.
L2.1	4	4	22,083
L2.2	6	6	32,283
L2.3	8	8	42,483
L2.4	10	10	52,683

Table 4-17: Element meshes, nonuniform in the z -direction, used in Submodel 2 analysis.

No. of mesh	N_{kl}^z	N_{lm}^z	l_z	Total d.o.f.
L2.5	10	10	2	52,683
L2.6	10	10	4	52,683

Numerical results for the stresses at two points on the line AB are presented in Tables 4-18 and 4-19. In the case L2.6, violation of the allowable element aspect ratio has been indicated. However, even considering variants L2.1-L2.5 it is clear that the stresses *do not converge* at both points of the structure under consideration. Thus, mesh refinement in the z -direction indicates stress singularity at the corner line AB.

Table 4-18: Normalized stresses in Al and Gr/Ep adherends at $x = 0.5a$, $y = 0.8b$, $z = 0.5h$, computed with the element meshes of Tables 4-16 and 4-17.

Adherend	Al			Gr/Ep		
Stress	σ_x/σ_0	σ_z/σ_0	τ_{xz}/σ_0	σ_x/σ_0	σ_z/σ_0	τ_{xz}/σ_0
L2.1	3.9847	1.8788	-1.5887	4.1735	2.2352	-1.3049
L2.2	4.5425	2.1731	-1.7528	4.8838	2.6772	-1.5061
L2.3	4.9397	2.3687	-1.8600	5.4712	3.0212	-1.6636
L2.4	5.2337	2.5021	-1.9387	5.9740	3.2998	-1.7953
L2.5	5.6650	2.6698	-2.0602	6.8812	3.7666	-2.0353
L2.6	6.0350	2.7662	-2.1728	7.9627	4.2546	-2.3450

Table 4-19: Normalized stresses in Al and Gr/Ep adherends at $x = 0.5a$, $y = b$, $z = 0.5h$ computed with the element meshes of Tables 4-16 and 4-17.

Adherend	Al			Gr/Ep		
Stress	σ_x/σ_0	σ_z/σ_0	τ_{xz}/σ_0	σ_x/σ_0	σ_z/σ_0	τ_{xz}/σ_0
L2.1	2.9317	1.6141	-1.4593	3.3535	1.9614	-1.1564
L2.2	3.3443	1.9078	-1.6398	3.8974	2.3755	-1.3130
L2.3	3.6522	2.1184	-1.7543	4.3609	2.7049	-1.4336
L2.4	3.8874	2.2720	-1.8329	4.7726	2.9756	-1.5326
L2.5	4.2424	2.4822	-1.9371	5.5438	3.4378	-1.7123
L2.6	4.5522	2.6178	-2.0013	6.4947	3.9354	-1.9467

Further numerical results correspond to the point which is slightly below the corner line AB (Table 4-20) and slightly above the corner line AB (Table 4-21). These results clearly show convergence of the stresses. Note that, ideally, the stresses σ_x and τ_{xz} should be zero at $x = 0.5a$, $z = 0.6h$. Numerical results of Table 4-21 show that these stresses are very small compared to the nominal value σ_0 . Also, it is seen in Tables 4-20 and 4-21 that the magnitudes of σ_z/σ_0 at $z = 0.4h$ and at $z = 0.6h$ are very small compared to the magnitudes of σ_z/σ_0 in a proximity of the corner line AB (compare with Table 4-19).

Table 4-20: Normalized stresses in Al adherend at, $x = 0.5a$, $y = b$, $z = 0.4h$ computed with the element meshes of Table 4-16.

Adherend	Al		
Stress	σ_x / σ_0	σ_z / σ_0	τ_{xz} / σ_0
L2.1	0.8753	0.3626	-0.1790
L2.2	0.8808	0.3790	-0.1824
L2.3	0.8824	0.3838	-0.1830
L2.4	0.8835	0.3870	-0.1833

Table 4-21: Normalized stresses in Gr/Ep adherend at $x = 0.5a$, $y = b$, $z = 0.6h$ computed with the element meshes of Table 4-16.

Adherend	Gr/Ep		
Stress	σ_x / σ_0	σ_z / σ_0	τ_{xz} / σ_0
L2.1	0.0008	0.0543	-0.0014
L2.2	0.0009	0.0548	0.0040
L2.3	0.0009	0.0549	0.0038
L2.4	0.0009	0.0548	0.0036

Additional comparison between numerical results obtained in the global and local analyses is presented in Figs. 4-3 thru 4-5. The global analysis results correspond to the element mesh G.11 of Table 4-3 and the Submodel 2 analysis results correspond to the element mesh L2.5 of Table 4-17. The effect of using submodeling technique is similar for all three stress components and can be summarized as following:

- (i) stress values near the peaks are considerably higher in the case of Submodel 2 analysis than in the case of the global analysis (keep in mind that according to the above convergence study, the peak values tend to infinity with the mesh refinement);
- (ii) stress variations are smoother in the case of Submodel 2 analysis;
- (iii) Submodel 2 analysis provides practically zero values of σ_z and τ_{xz} everywhere at the traction-free surface of the middle adherend, except a small region near the corner line $x/a = 0.5$, while the global analysis does not satisfy these boundary conditions with such a high accuracy;
- (iv) starting at some distance from the corner line $x/a = 0.5$, the results obtained from the global and local analyses become practically indistinguishable;
- (v) the global and local analyses provide practically identical results at the ends of the local region, $x/a = 0.46$ and $x/a = 0.54$.

It is also seen that σ_z is tensile and its values near the corner line AB are higher than the nominal stress σ_0 . Moreover, τ_{xz} also exceeds σ_0 near the corner line. This confirms that these transverse stresses should be of a primary concern when predicting failure initiation in the joint.

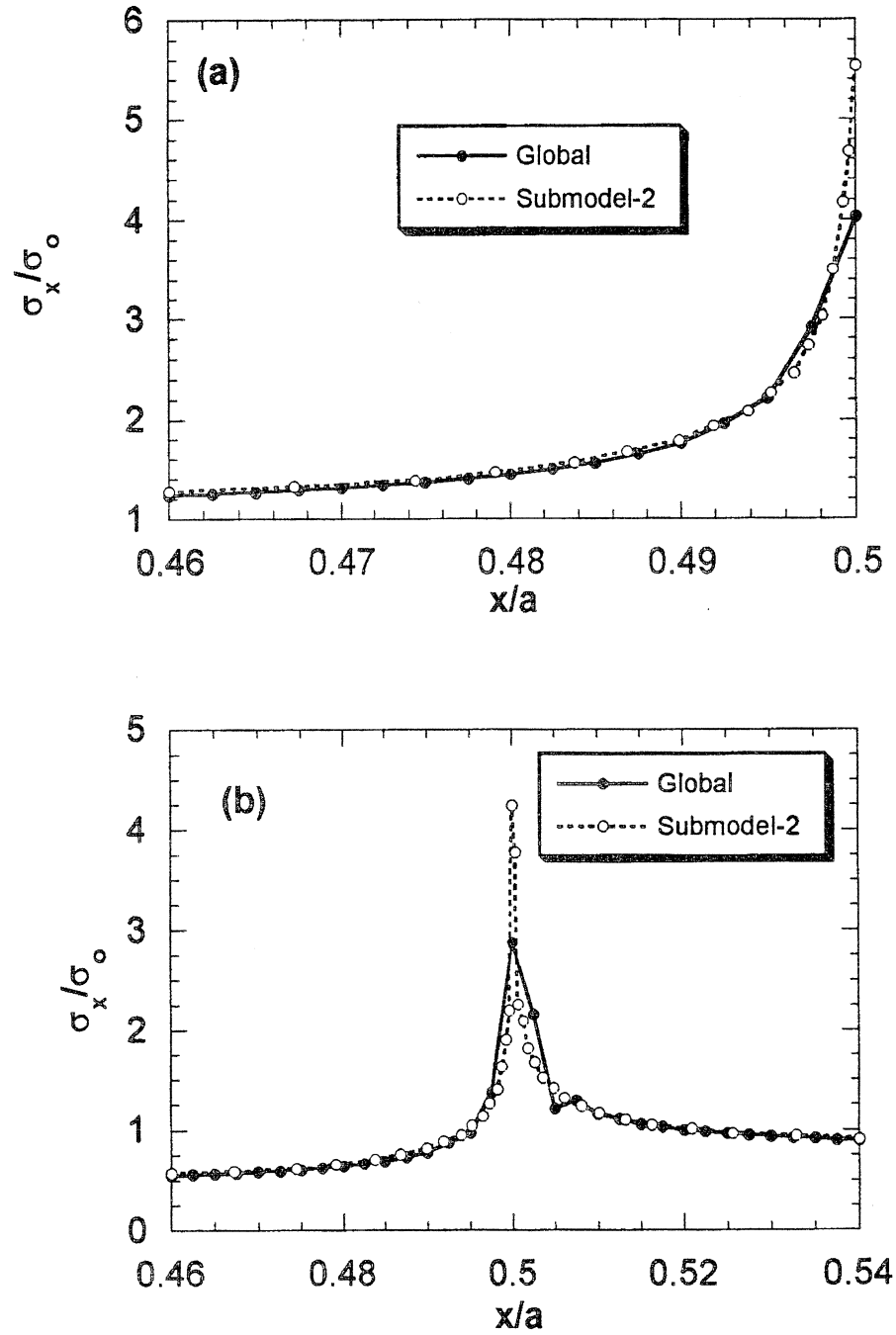


Fig. 4-3: Variations of σ_x / σ_0 in Gr/Ep (a) and Al (b) adherends in local region 1 at $y/b = 1$, $z/h = 0.5$.

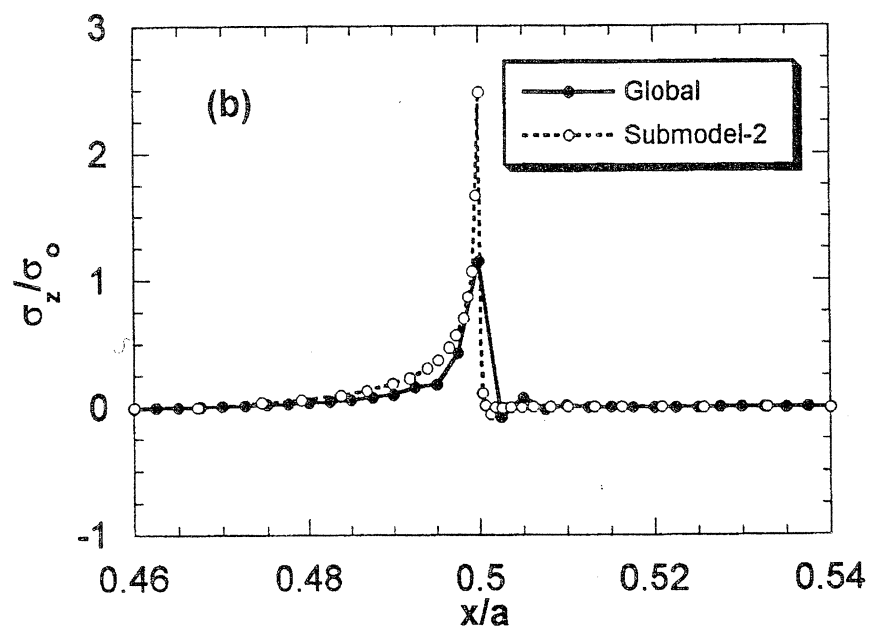
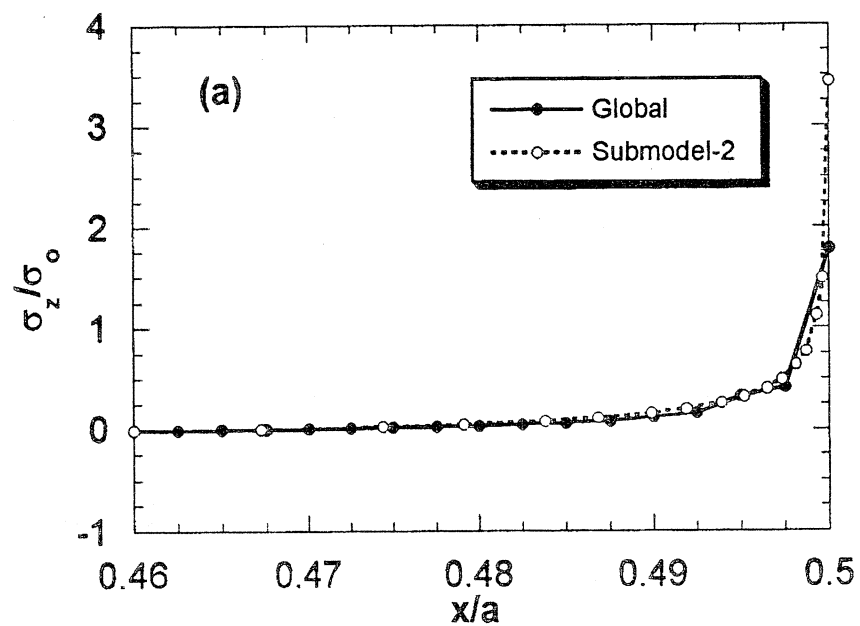


Fig. 4-4: Variation of σ_z / σ_0 in Gr/Ep (a) and Al (b) adherendas in local region 1 at $y/b=1$, $z/h = 0.5$.

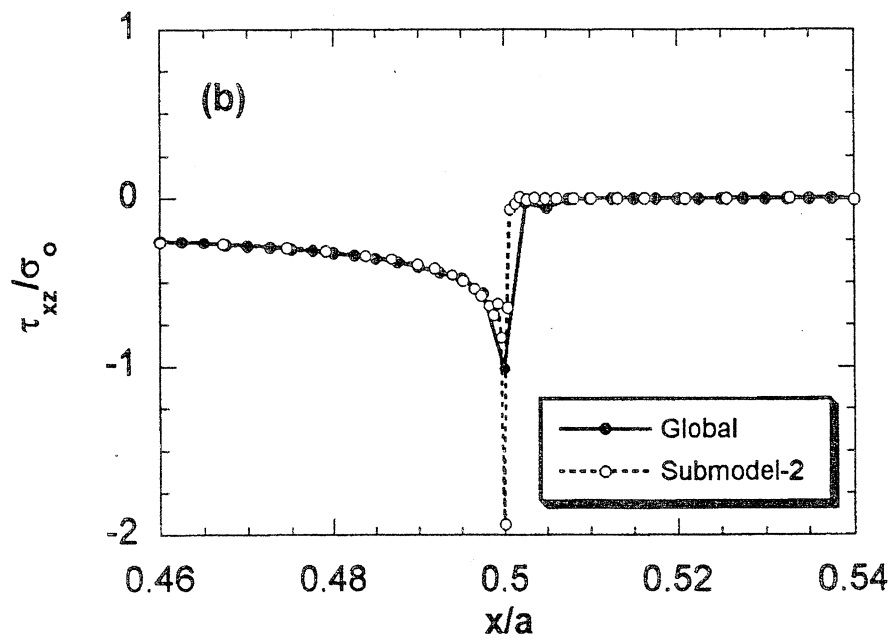
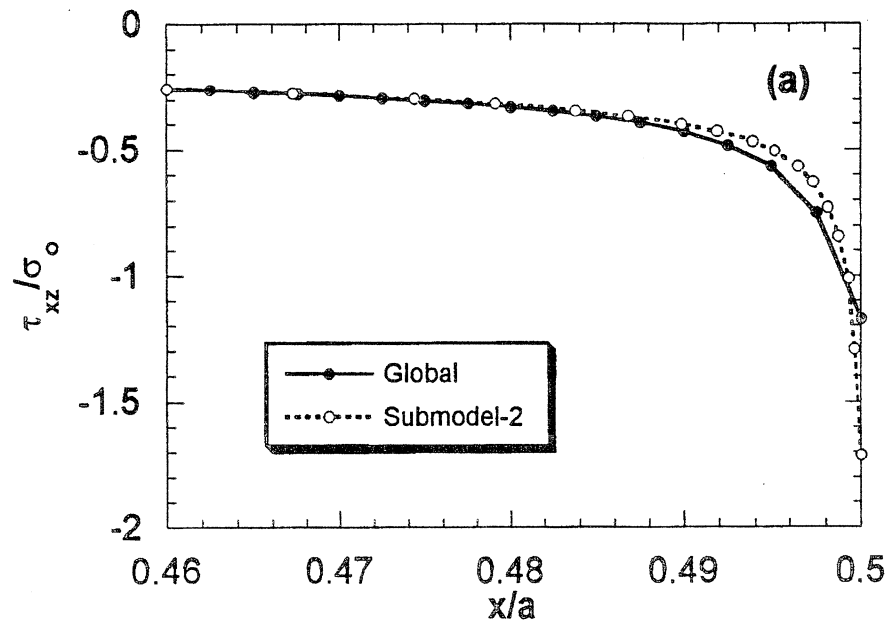


Fig. 4-5: Variations of τ_{xz}/σ_0 in Gr/Ep (a) and Al (b) adherends in local region 1 at $y/b = 1$, $z/h = 0.5$

4.7 Local Analysis - Submodel 3

When considering results of the element mesh refinement in the x -direction (see Tables 4-8 and 4-9), it is difficult to make certain conclusion about the stress convergence. A more detailed study is performed here in attempt to clarify this issue. Another local region is introduced, which has the same dimensions in the y and z -directions as the local region considered in Submodel 2, but of a smaller size in the x -direction. This newly introduced local region is confined between the planes $x_d/a = 0.49$ and $x_d/a = 0.51$. The displacement values obtained from the Submodel 2 analysis with element mesh L2.5 have been used as the boundary conditions in all variants of Submodel 3 analysis. The meshes are described in Table 4-22. In addition to those data, the following parameters were taken: $N_{de}^x = 8$, $N_{ef}^x = 8$ for both intervals $0.49 \leq x/a \leq 0.5$ and $0.5 \leq x/a \leq 0.51$; $N_{0g}^y = 4$, $l_y = 1$ for $0 \leq y/b \leq 0.8$; $N_{g1}^y = 4$, $l_y = 80$ for $0.8 \leq y/b \leq 1$; $N_{kl}^z = 10$, $N_{lm}^z = 10$ and $l_z = 2$ for both intervals $0.4 \leq z/h \leq 0.5$ and $0.5 \leq z/h \leq 0.6$. In all cases, the smallest elements are next to the interface.

Table 4-22: Element meshes, nonuniform in the x -direction, used in Submodel 3 analysis.

No. of mesh	l_x	Total d.o.f.
L3.1	1	52,683
L3.2	2	52,683
L3.3	4	52,683
L3.4	8	52,683
L3.5	16	52,683

Stress values obtained in Submodel 3 analysis are presented in Tables 4-23 and 4-24. These results are still not allowing to make any certain conclusion about stress convergence at the corner line AB for both the Al and Gr/Ep adherends. It seems that any further convergence study

using this methodology would be meaningless. Nevertheless, our major objective, to illustrate how the submodeling technique can be used for the stress convergence study, has been accomplished.

Table 4-23: Normalized stresses in Al and Gr/Ep adherends at, $x = 0.5a$, $y = 0.8b$, $z = 0.5h$ computed with the element meshes of Table 4-22.

Adherend	Al			Gr/Ep		
Stress	σ_x / σ_0	σ_z / σ_0	τ_{xz} / σ_0	σ_x / σ_0	σ_z / σ_0	τ_{xz} / σ_0
L3.1	5.0191	2.2150	-1.7895	6.7997	3.4777	-2.0002
L3.2	5.4725	2.5304	-1.9741	6.8812	3.6917	-2.0231
L3.3	5.8826	2.8347	-2.1772	6.8501	3.8426	-2.0545
L3.4	6.1870	3.0695	-2.4081	6.7449	3.9207	-2.0918
L3.5	6.3340	3.1890	-2.6333	6.6255	3.9448	-2.1263

Table 4-24: Normalized stresses in Al and Gr/Ep adherends at, $x = 0.5a$, $y = b$, $z = 0.5h$ computed with the element meshes of Table 4-22.

Adherend	Al			Gr/Ep		
Stress	σ_x / σ_0	σ_z / σ_0	τ_{xz} / σ_0	σ_x / σ_0	σ_z / σ_0	τ_{xz} / σ_0
L3.1	3.8183	2.1409	-1.6540	5.5658	3.2021	-1.6628
L3.2	4.1169	2.3785	-1.8469	5.5660	3.3761	-1.6946
L3.3	4.3866	2.6041	-2.0578	5.5038	3.5013	-1.7390
L3.4	4.5914	2.7786	-2.2915	5.4163	3.5682	-1.7911
L3.5	4.6972	2.8729	-2.5123	5.3384	3.5907	-1.8372

4.8 Local Stress Analysis In The Corner Region 2

Next consider local stress analysis results obtained for the left corner region 2, which is confined between the planes $x_a / a = 0.21$ and $x_c / a = 0.29$ (see Fig. 4-2). The global analysis

results, which have been used as the displacement boundary conditions for this local analysis, were taken from variant G.11 of Table 4-3. The mesh used in the local analysis is the same as L1.1 (see Table 4-5) with N_{de}^x replaced by N_{ab}^x and N_{ef}^x replaced by N_{bc}^x .

Stress variations in the interval $0.21 \leq x/a \leq 0.29$ at $y/b = 1$ and $z/h = 0.5$ obtained from the global analysis and Submodel 1 local analysis are compared in Figs. 4-6 thru 4-8. The variations of σ_x are very close, with slightly higher stress values near the peak shown by the local analysis. The variations of σ_z are considerably smoother in the case of the local analysis. The most severe distinction is seen in Fig. 4-8b, where the global and local analyses predict very different behavior of τ_{xz} near the point $x/a = 0.25$. The global analysis predicts maximum of τ_{xz} exactly at the corner point $x/a = 0.25$, while the local analysis predicts its maximum at some distance from the corner point, and descending stress approaching zero toward the corner point. The latter trend is consistent with the traction-free surface condition. However, at some rather small distance from the corner point, the variations obtained from the global and local analyses become practically indistinguishable for all three stress components.

It is interesting to compare stress variations near the right corner point (see Figs. 4-3 thru 4-5) and the left corner point (see Figs. 4-6 thru 4-8). As is seen from Figs. 4-3a and 4-6a, σ_x in Gr/Ep adherend is tensile near both corner points, but its values near the right corner point are higher. Comparison of Figs. 4-3b and 4-6b shows that σ_x in Al adherend is tensile at both corner points, but its values are higher near the right corner point. When comparing σ_z in Gr/Ep adherend (see Figs. 4-4a and 4-7a), it is seen that the stress is tensile near the right corner point and compressive near the left corner point. Analogous situation is observed in Al adherend (see Figs. 4-4b and 4-7b), where σ_z has high tensile values near the right corner point and much lower compressive values near the left corner point. The τ_{xz} variations (see Figs. 4-5 and 4-8) are very distinct near the right and left corner points. The values of this stress component are

much higher near the right corner point. The above results clearly indicate that the right corner line AB is the most probable site of initial failure. It can be expected (due to comparatively high peel stress and high transverse shear stress near this line) that debonding would be the likely mode of initial failure.

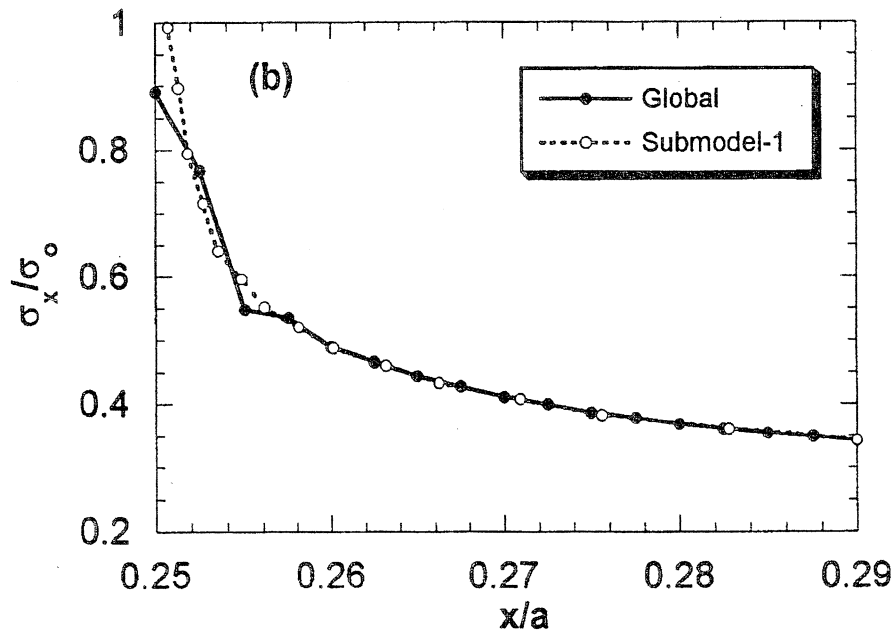
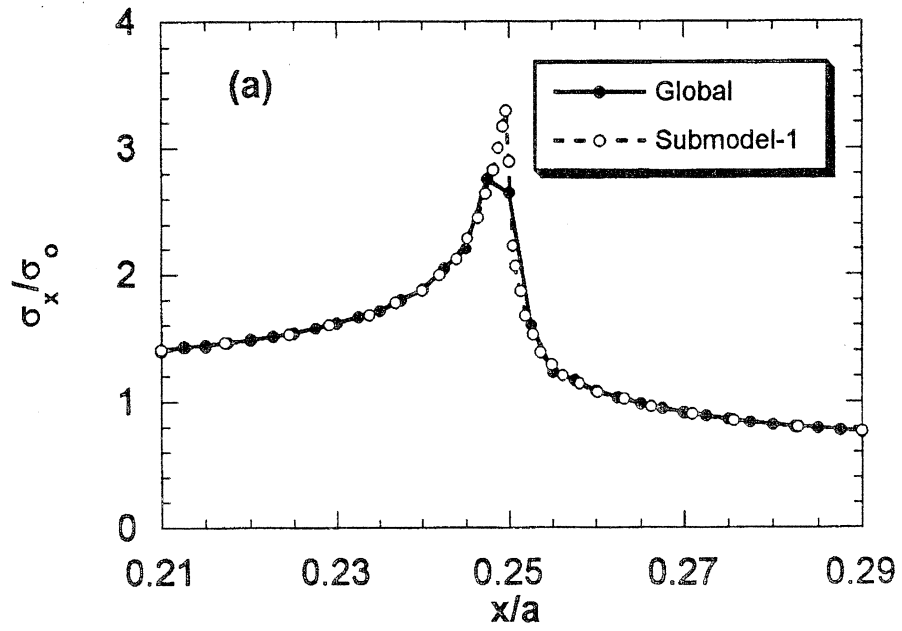


Fig. 4-6: Variations of σ_x / σ_0 in Gr/Ep (a) and Al (b) adherends in local region 2 at $y/b = 1$, $z/h = 0.5$.

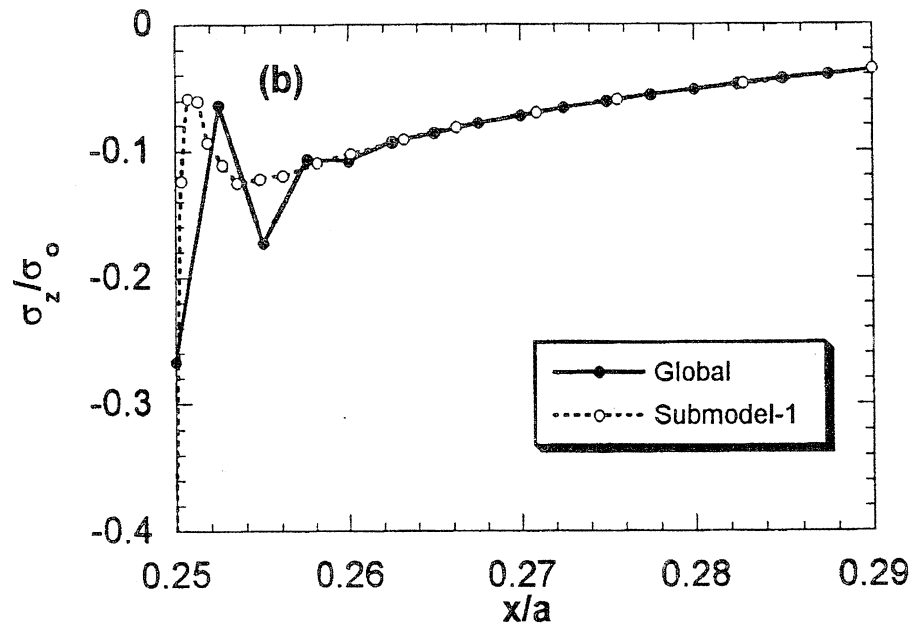
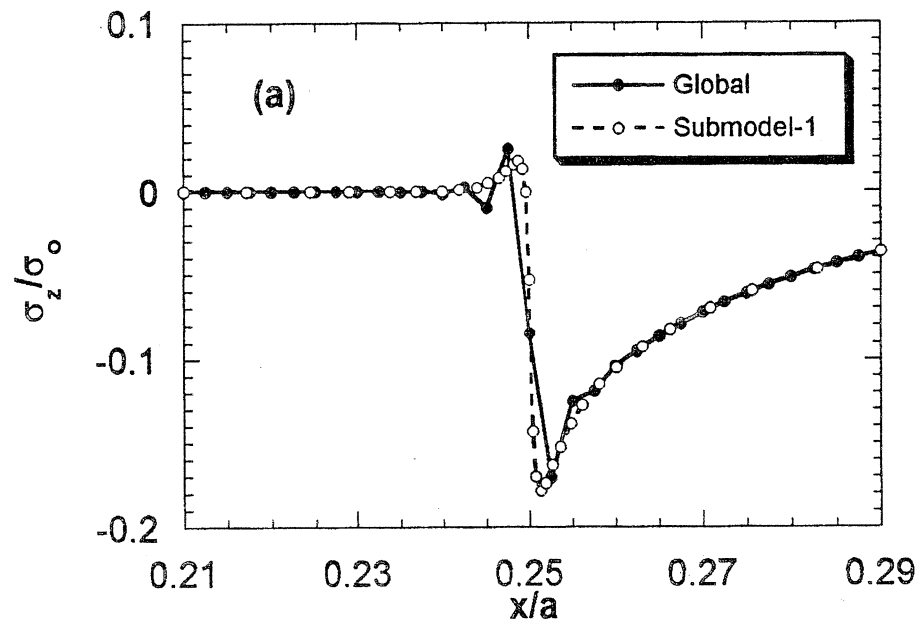


Fig. 4-7: Variations of σ_z/σ_0 in Gr/Ep (a) and Al (b) adherends in local region 2 at $y/b = 1$, $z/h = 0.5$.

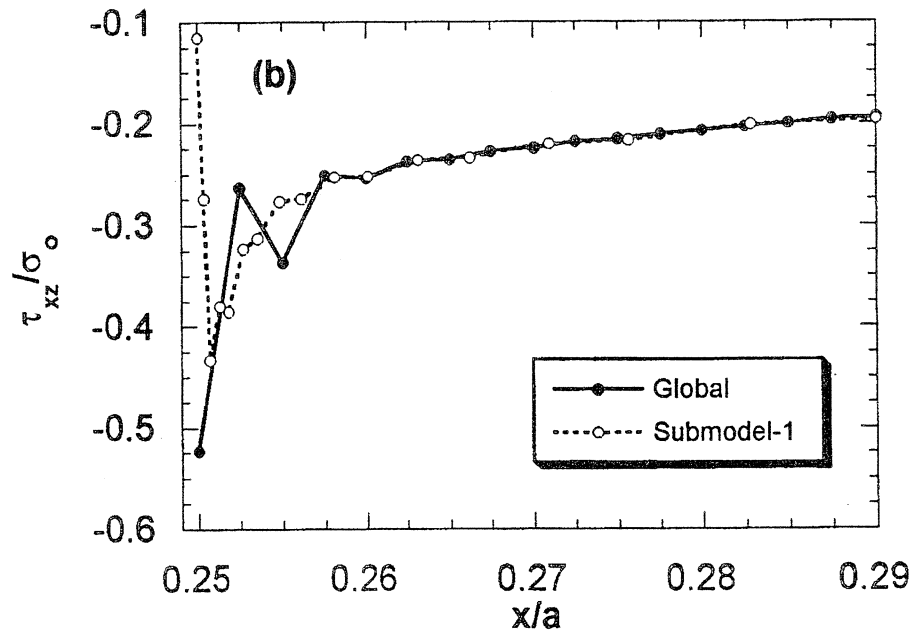
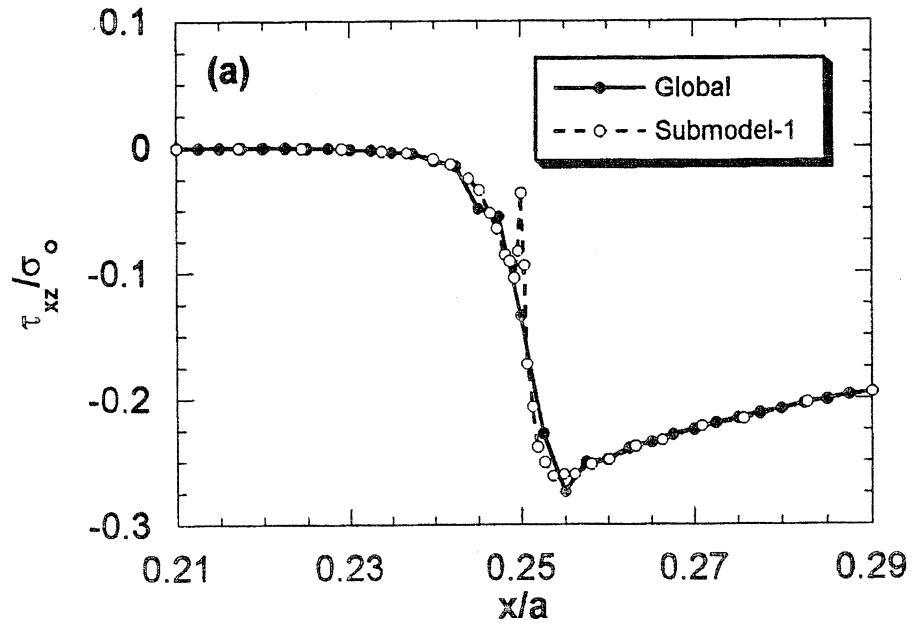


Fig. 4-8: Variations of τ_{xz}/σ_0 in Gr/Ep (a) and Al (b) adherends in local region 21 at $y/b = 1$, $z/h = 0.5$.

4.9 Stress Variations in the Width and Thickness Directions

Illustration of the stress variations in the y and z -directions for the local region 1 is presented here. The results were obtained with Submodel 2 analysis, using element mesh L2.4 (see Table 4-16). Total number of elements in the local region was taken 16, 8 and 20 in the x , y and z -directions, respectively. The nonuniform element meshes in the x and y -directions described in Section 4.6 are applied; the z -direction mesh is taken uniform.

Variations of σ_x , σ_z and τ_{xz} in the y -direction for half-width of the joint structure are shown in Fig. 4-9. The coordinate value $y/b = 1$ corresponds to the free edge. Results are presented for $x/a = 0.5$, $z/h = 0.5$ (corner line AB). It is seen that for the main part (about 90%) of the interval, all three stress components are practically constant, while near the free edge there is a considerable stress variation. It is interesting to note that the stresses *descend* towards the free edge. The results also indicate that σ_z and τ_{xz} computed from the sides of Al and Gr/Ep

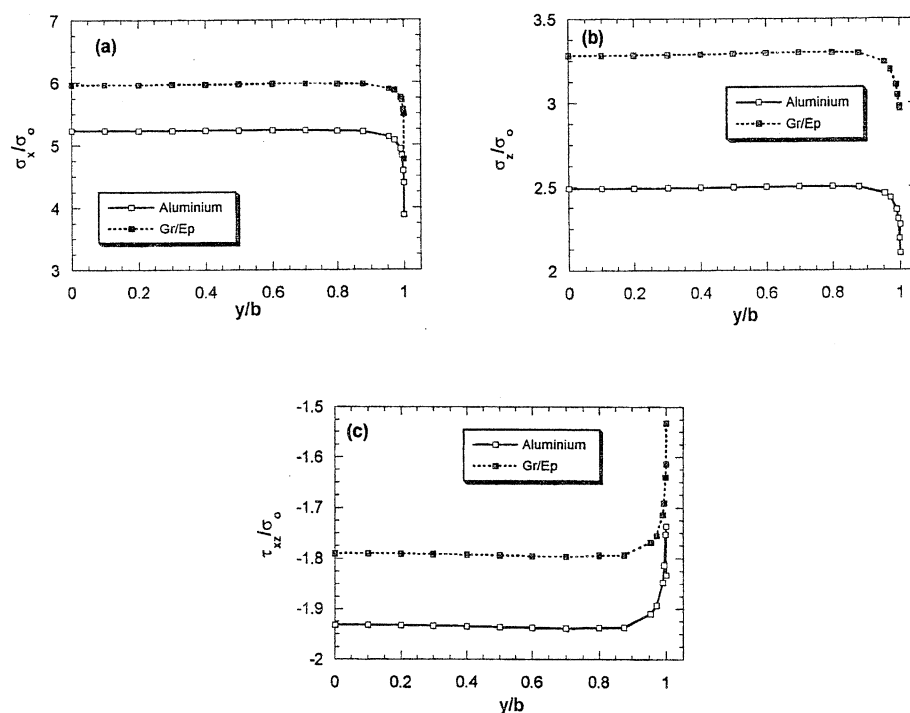


Fig. 4-9: Variations of σ_x/σ_0 (a), σ_z/σ_0 (b) and τ_{xz}/σ_0 (c) in the width direction for Gr/Ep and Al adherends in local region 1 at $x/a = 0.5$, $z/h = 0.5$.

adherends have considerable jumps at the interface along the whole width of the joint. Ideally, the stress values indicated by the square corresponding to the interface from the side of Al adherend and by the square corresponding to the interface from the side of Gr/Ep adherend should be equal. However, the transverse stress continuity is violated. Thus, the results show that it is not possible to achieve the required stress continuity even with very fine element meshes used for a very small local region. The revealed drawback seems to be intrinsic for the finite element analysis used here.

Variations of σ_x , σ_z and τ_{xz} in the z -direction for half-width of the joint structure are shown in Fig. 4-10. The coordinate value $z/h = 0.5$ corresponds to the interface between Al and Gr/Ep materials. The results are shown for $x/a = 0.5$, $y/b = 1$, i.e., the vertical corner line at the double-free edge. It is seen that σ_x is practically zero along the major part of Gr/Ep adherend, and only near the interface the traction-free surface condition is violated. At the other end of the

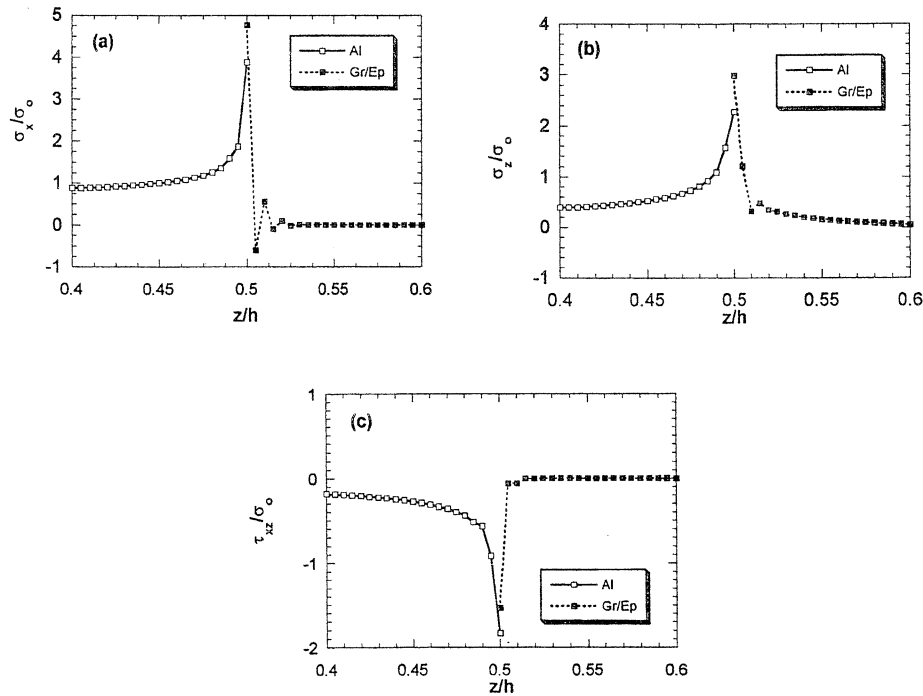


Fig. 4-10: Variations of σ_x/σ_0 (a), σ_z/σ_0 (b) and τ_{xz}/σ_0 (c) in the thickness direction for Gr/Ep and Al adherends in local region 1 at $x/a = 0.5$, $y/b = 1$.

interval, $z = 0.4$, σ_x is indistinguishable from the nominal value σ_0 . Variations of σ_z and τ_{xz} show that they reach maximums at the interface and that there are considerable jumps between the maximums.

4.10 Stress Analysis in the Presence of Initial Debond Crack

As indicated by the stress convergence study presented in the above sections, some stress components seem to be singular at the corner line AB. This means that if considering failure as the phenomenon occurring at some *point* of the structure (which is physically unreasonable but implied in the customary mathematical failure criteria), then *initial failure* must simultaneously occur at all points of the line AB under an infinitesimal load. In the case of double-lap bonded joint this means that initial failure in the form of debond cracks should be observed *immediately* after the load is applied. Thus, prediction of the failure initiation following a rigorous point-wise approach for this class of problems is an impossible task. The following two alternative approaches are visible to avoid this obstacle: (i) to compute *average* stresses along some finite width area near the line AB or (ii) to introduce some *initial* debond crack along the interface between Al and Gr/Ep adherends, which should start at the line AB and extend for some distance in the negative direction of the x -axis. The latter approach would allow to reformulate the boundary value problem and obtain solution in which singular stresses take place not at the end of the overlap zone but at the crack tip.

An analysis with debond crack can be computationally performed using existing capabilities of 3-D ABAQUS elements: the debond crack of given length can be introduced by detaching certain nodes which belong to the interface. Consequently, a number of double nodes would be created, one of them belonging to the Gr/Ep adherend and the other one to Al adherend. If this is performed only for that part of the interface where σ_z is tensile, then the adherends should separate along the whole area of detached nodes. This means that the debond crack, which

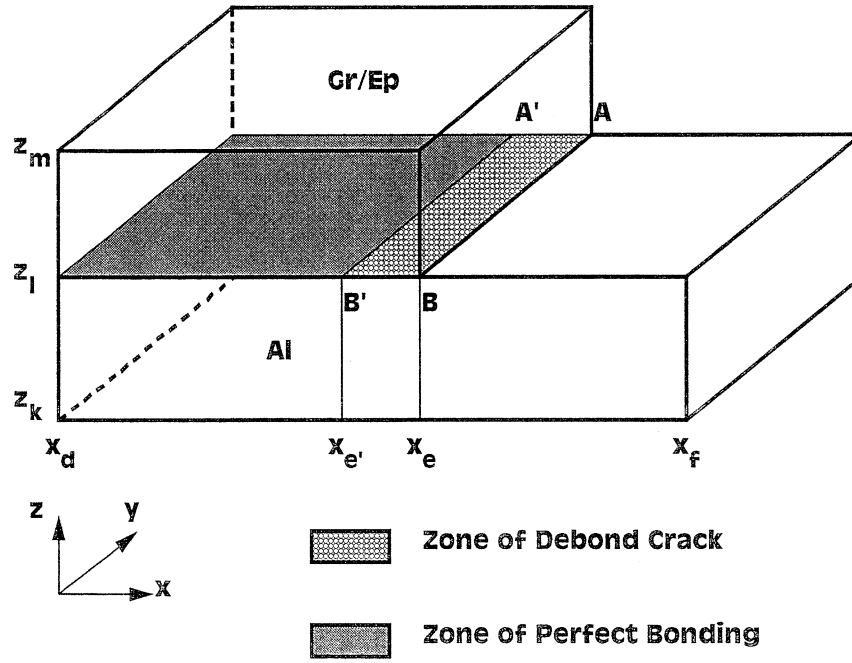


Figure 4-11: Initial debond crack at the end of the overlap zone.

configuration is defined by the area of detached nodes, will open under the applied *in-plane* load. Taking into consideration that the stresses are singular along the whole corner line AB, it is reasonable to detach the nodes along some area AA'B'B, as shown in Fig. 4-11. Length of the initial debond crack, denoted $\Delta x = x_e - x_d$, can be chosen arbitrarily.

Two numerical examples are considered for illustration of the described approach. Those correspond to the cases of nodes detached along the area AA'B'B with $x_d/a = 0.498$ (further referred as Crack 1) and $x_d/a = 0.495$ (Crack 2); recall that $x_e/a = 0.5$. The nodal displacements obtained from the Submodel 2 analysis without debond crack (corresponding to the element mesh L2.5 of Table 4-17) were used as boundary conditions for the Submodel 3 analysis with debond crack. Two local analysis variants were performed for the above crack lengths; they are further referred as C.1 and C.2. The respective element meshes are described in Table 4-25. The following mesh characteristics have been taken: $l_x = 5$ has been applied for the intervals $0.49 \leq x/a \leq 0.498$ and $0.498 \leq x/a \leq 0.5$ in the case C.1 and for the intervals

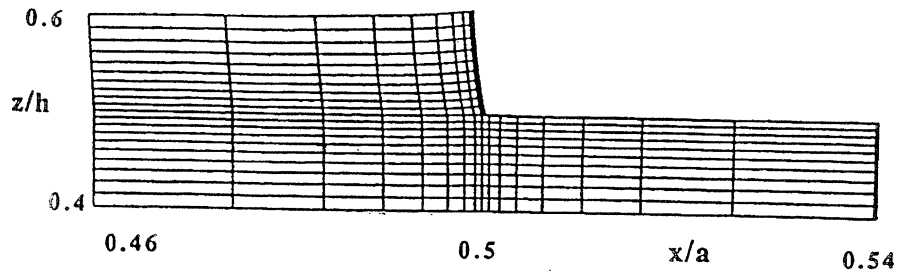
$0.49 \leq x/a \leq 0.495$ and $0.495 \leq x/a \leq 0.5$ in the case C.2. In both cases, the highest mesh refinement was applied near the crack tip, $x/a = 0.498$ for C.1 and $x/a = 0.495$ for C.2. The uniform x -direction mesh was used for the interval $0.5 \leq x/a \leq 0.51$. Other mesh parameters are the same as in variant L2.5 of Table 4-17. Results obtained with Submodel 2 (using element mesh L2.5) without debond crack are used for a comparison.

Table 4-25: Element meshes used in Submodel 3 analyses with the debond cracks; other parameters explained in the text.

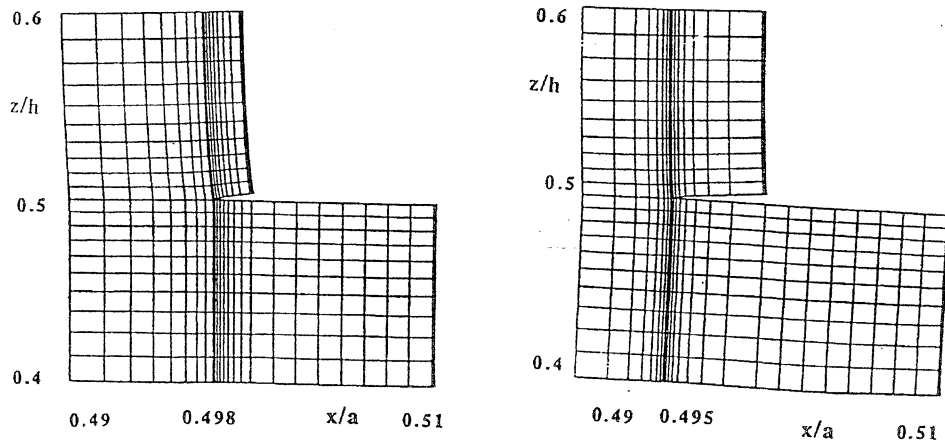
No. of mesh	x_e / a	N_{de}^x	N_{ee}^x	N_{ef}^x	Total d.o.f.
C.1	0.498	8	8	8	89,097
C.2	0.495	8	8	8	89,097

In order to provide better visual image of the deformed configuration of the bonded joint solved without and with initial debond crack, three magnified element meshes, distorted by the loading, are shown in Fig. 4-12 for the cross-section x - z , at $y=0$. The distorted mesh corresponding to the Submodel 2 region without crack is shown in Fig. 4-12a. The distorted meshes obtained with the cracks C.1 and C.2, which were computed for the Submodel 3 region, are shown in Figs. 4-12b and 4-12c. The latter figures illustrate that the separation of the adherends in the zones of detached nodes have occurred. It is also observed in Figs. 4-12b and 4-12c that major distortion of the displacement field is now at the crack tip.

Variations of σ_x , σ_z and τ_{xz} in the x -direction computed without crack, with Crack 1 and with Crack 2 are shown in Figs. 4-13 and 4-14. It is seen in Fig. 4-13 that variation of σ_x in Gr/Ep adherend radically changes in the presence of debond crack. In addition to the tensile peak there is also a compressive peak. When the crack length increases, the compressive peak is growing, while tensile peak is descending. Note that σ_x is practically zero at the location $x/a = 0.5$ when using analysis with debond crack, while that was not achievable in the analysis



(a)



(b)

Fig. 4-12: The element mesh distortions in the x -plane without crack (a) and with initial debond crack of different length (b,c).

without crack (compare with Fig. 4-3a). Thus, σ_x at the right edge of the upper adherend is released in the presence of initial debond crack.

When considering σ_x in Al adherend shown in Fig. 4-13b, it is seen that the stress is tensile along the whole interval. The stress peak (which is now reached at the crack tip) is considerably higher than in the joint without crack. Besides, the peak grows when increasing the initial crack length.

Variations of σ_z in the x -direction are shown in Fig. 4-14. For both the Gr/Ep and Al adherends this stress component is tensile in all three cases. Its peak monotonously descend in

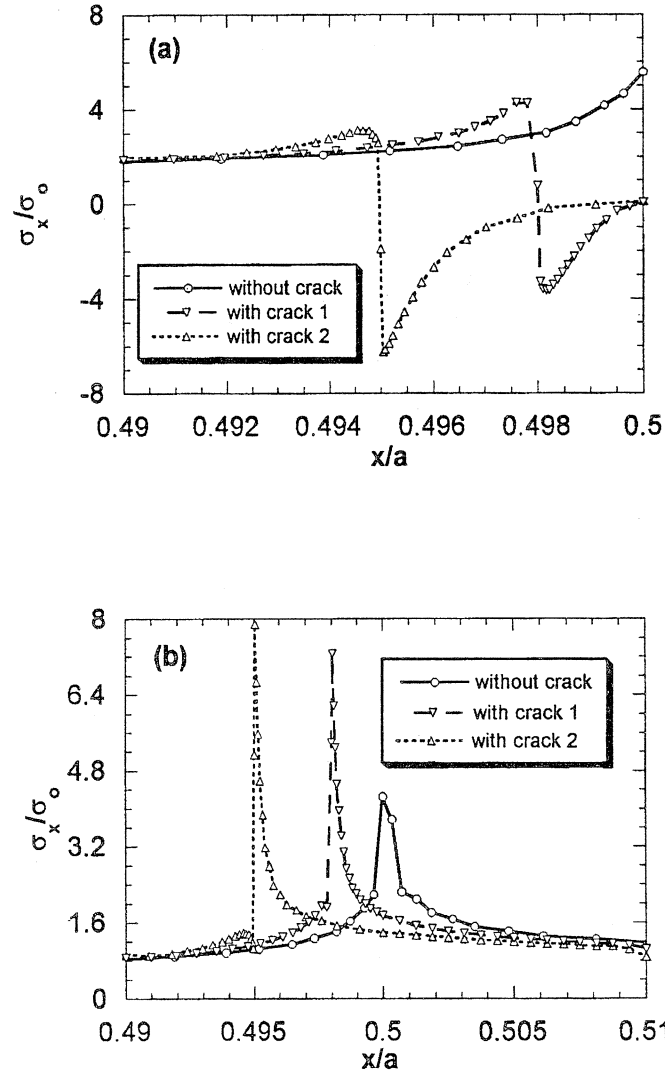


Fig. 4-13: Variations of σ_x/σ_0 in Gr/Ep (a) and Al (b) adherends at $y/b = 1$, $z/h = 0.5$ without crack and with initial debond crack of two different lengths.

the upper adherend with increasing length of the crack. However, in the lower adherent the trend is quite different: there is some crack length which provides the highest peak. It is worth mentioning that for both the debond crack cases, σ_z in both the adherends is very small along the whole crack length, so the stress has been released from the end of the overlap zone.

Variations of τ_{xz} in the x -direction are shown in Fig. 4-15. In the upper adherend these variations are radically different for the cases with and without debond crack. There are both positive and negative peaks, while only one peak with monotonous stress variation was obtained

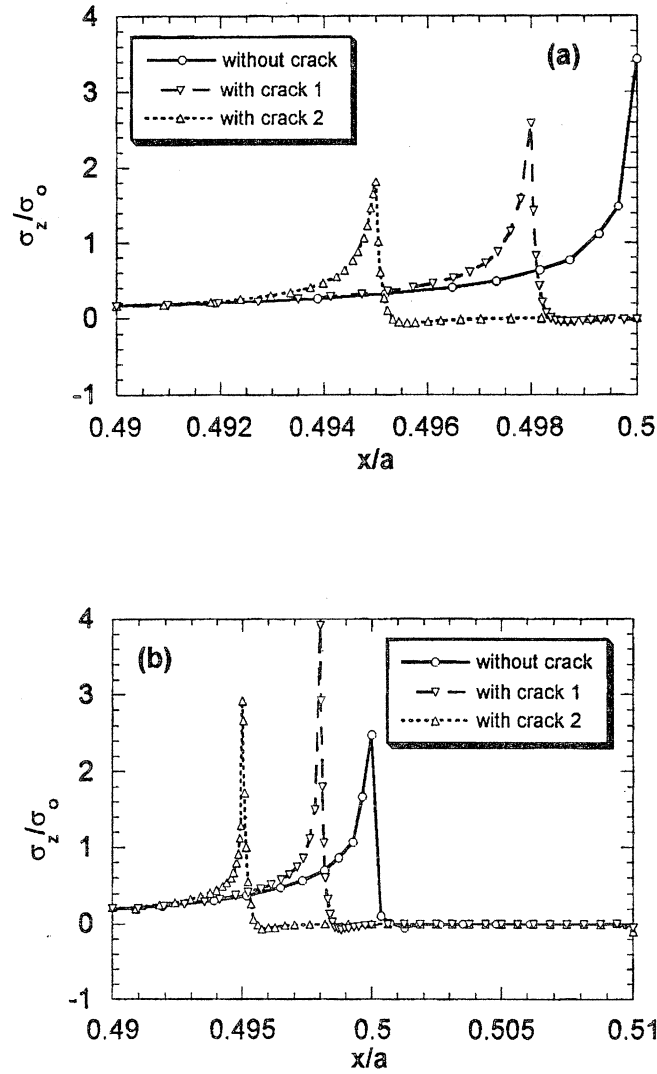


Fig. 4-14: Variations of σ_z/σ_0 in Gr/Ep (a) and Al (b) adherends at $y/b = 1$, $z/h = 0.5$ without crack and with initial debond crack of two different lengths

in the analysis without debond crack. For the middle adherend, the highest peak is observed in the case of Crack 1, similarly to the trend for σ_z (see, Fig. 4-14a). It is also seen that τ_{xz} values at the traction-free crack surface are very close to zero in the upper adherend and slightly deviate from zero in the middle adherend.

Presented results reveal some basic features of the stress variations in perfectly bonded composite-to-metal joint having small initial debond crack. At least qualitatively, the results are reasonable and reflect the expected trend: high peaks of the transverse stresses are released from

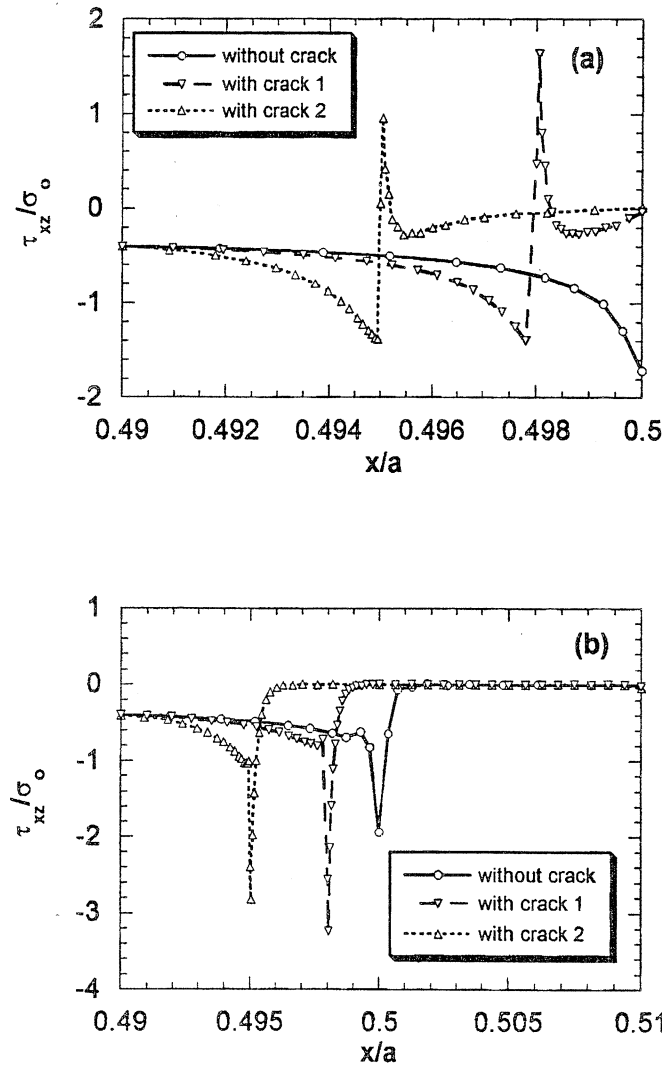


Fig. 4-15: Variations of τ_{xz}/σ_0 in Gr/Ep (a) and Al (b) adherends at $y/b = 1$, $z/h = 0.5$ without crack and with initial debond crack of two different lengths.

the end of the overlap zone and shifted to the debond crack tip.

Now, the other boundary value problem emerges, namely, the problem of debond crack propagation. A number of analytical and numerical fracture mechanics approaches are known for analyzing crack growth conditions, however specifics of the stress fields in bonded joints, e.g., presence of at least *three* significant stress components (σ_x , σ_z and τ_{xz}) which should contribute to the crack propagation process and, in addition to that, an extremely high nonuniformity of the stresses, would create definite challenges when developing a 3-D fracture

analysis of bonded joints.

4.11 Analysis of Composite-to-Composite Adhesive Bonded Joint

In the previous sections it was assumed that the structure shown in Fig. 4-1 is perfectly bonded, but adhesive layers have zero thickness and, therefore, those were not included in the analysis as physical entities. Here we will focus on the effect of a finite-thickness adhesive layer in the analogous double-lap joint problem. Schematic of a structural element under consideration is shown in Fig. 4-16a. As before, the structure is exposed to uniform uniaxial extension. The

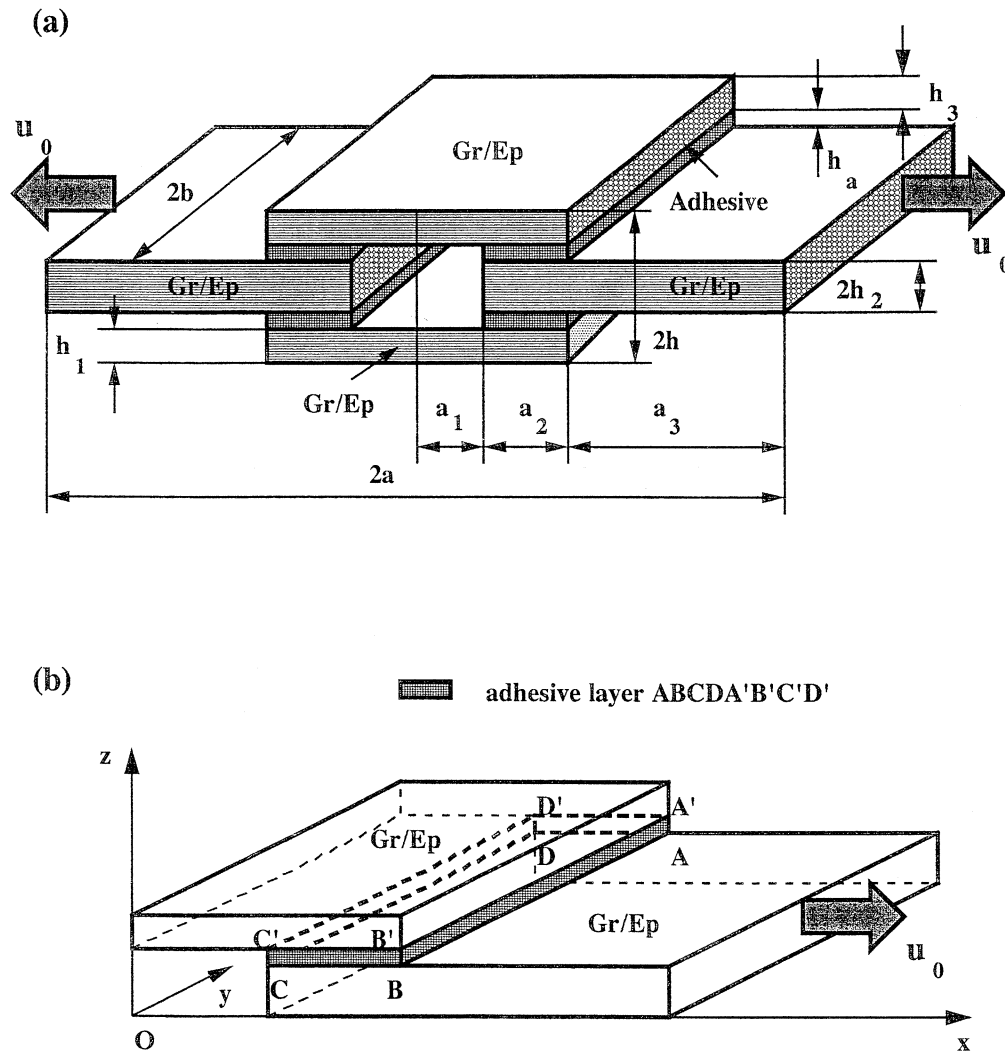


Figure 4-16. Schematic of a composite-to-composite adhesive bonded joint (a) and its $1/8^{\text{th}}$ part (b) considered in the analysis.

displacement u_x , having known value u_0 , is applied uniformly at the right and left ends of the middle adherends. All four adherends are made from the same material and have equal thickness. It is also assumed that both the right and left middle adherends are of equal length and placed symmetrically with respect to the plane perpendicular to the x -axis and passing through the center points of the upper and lower adherends. Further, it is assumed that all four adhesive layers have the same elastic properties and identical geometric parameters. The above assumptions are allowing to apply symmetry conditions in all three coordinate directions and, accordingly, reduce analysis to $1/8^{\text{th}}$ part of the full structure, as shown in Fig. 4-16b. Thus, the full set of geometric boundary conditions is exactly the same as in (4-1).

All of the adherends are made from 16 layers of unidirectional graphite/epoxy Hercules AS4/3501-6 tape having the following elastic properties:

$$E_L = 137 \text{ GPa} \ (20.0 \text{ Msi}), \ E_T = 10.57 \text{ GPa} \ (1.54 \text{ Msi}), \ \nu_{LT} = 0.30, \quad (8)$$

$$G_L = 5.15 \text{ GPa} \ (0.750 \text{ Msi}), \ G_T = 3.47 \text{ GPa} \ (0.506 \text{ Msi})$$

All layers are placed in the x -direction. The bonding adhesive is Cytec FM300-2K film with 3% woven glass scrim considered as isotropic material with the following properties:

$$E = 3.43 \text{ GPa} \ (0.50 \text{ Msi}), \ \nu = 0.30 \quad (9)$$

Geometric parameters used in the analysis are:

$$a = 45.72 \text{ cm} \ (18.0 \text{ in}), \ a_1 = a_3 = 20.32 \text{ cm} \ (8.0 \text{ in}), \ a_2 = 5.08 \text{ cm} \ (2.0 \text{ in}), \ b = 1.27 \text{ cm} \ (0.5 \text{ in}),$$

$$h = 0.3556 \text{ cm} \ (0.14 \text{ in}), \ h_1 = h_3 = 0.2286 \text{ cm} \ (0.09 \text{ in}), \ h_2 = 0.1143 \text{ cm} \ (0.045 \text{ in}), \quad (10)$$

$$h_a = 0.0127 \text{ cm} \ (0.005 \text{ in})$$

It is seen from the above geometric characteristics that the aspect ratios are $a/h = 129$ for the overall joint and $a_2/h_a = 400$ for the adhesive layers. Clearly, a direct 3-D stress analysis of the

structure with this kind of geometric configuration would be a serious challenge.

Another important specific feature of the problem under consideration is that there are multiple sites of high stress gradients and also several lines of possible stress singularities. Specifically, the following lines marked in Fig. 4-16b are under suspicion:

- corner line AB which belongs to the interface between adhesive layer and middle adherend;
- corner line C'D' which belongs to the interface between upper adherend and adhesive;
- lines BC, CD and DA, each of them belonging to the interface between the adhesive layer and middle adherend and, at the same time, to the free edge;
- lines A'B', B'C' and D'A', each of them belonging to the interface between the adhesive layer and upper adherend and, at the same time, to the free edge.

Each of these lines is a potential site of stress singularity. It should be pointed out that the nature of singularity at the lines AB and C'D' is different than at the other six lines. Stress singularity at AB and C'D' may be due to the material property mismatch together with the corner-wise geometry variation. Stress singularity at A'B', CD, A'D', AD, C'B', and CB may be only caused by the material property mismatch, similarly to the case of classical free edge effect.

Due to the aforementioned very high aspect ratios and presence of several lines of possible singularities in the problem under consideration, an accurate stress computation by the direct use of 3-D finite elements seems hardly possible task. Indeed, if utilizing uniform element meshes, a huge number of elements will be required. On the other side, if using nonuniform element meshes, the *element aspect ratio* may become too high; this is indicated in ABAQUS as “zero or

negative element volume error”.

Both the uniform and nonuniform types of element meshes have been tried. The results undoubtedly showed that the aforementioned geometric parameters cause *real* computational problems when C3D27 solid element is directly applied for the stress analysis of adhesive bonded joints. The conclusion has been drawn that the best outcome one can expect from a global analysis is to accurately predict 3-D displacement fields. In order to obtain sufficiently accurate stresses, a global-local type analysis should be used. The submodeling technique described in Section 4.2 will be further explored in the next two sections on the example of 3-D stress analysis of thin composite-to-composite adhesive bonded joints.

4.12 Global Analysis

An initial step is to perform global analysis of $1/8^{\text{th}}$ of the structure which is shown in Fig. 4-16b, using successively refined meshes of elements. The objective here is to illustrate that the displacement convergence can be achieved at any point of the structure, but the same cannot be said regarding the stress convergence. The following notations of the number of elements in the x -direction are introduced (these are slightly modified compared to (5)):

$$\begin{aligned}
 &N_{0a}^x \text{ for } 0 \leq x/a \leq x_a/a, \quad N_{ab}^x \text{ for } x_a/a \leq x/a \leq x_b/a, \quad N_{bc}^x \text{ for } x_b/a \leq x/a \leq x_c/a, \\
 &N_{cd}^x \text{ for } x_c/a \leq x/a \leq x_d/a, \quad N_{de}^x \text{ for } x_d/a \leq x/a \leq x_e/a, \quad N_{ef}^x \text{ for } x_e/a \leq x/a \leq x_f/a, \quad (11) \\
 &N_{fg}^x \text{ for } x_f/a \leq x/a \leq x_g/a, \quad N_{gl}^x \text{ for } x_g/a \leq x/a \leq 1
 \end{aligned}$$

Number of elements in the y -direction inside the interval $0 \leq y/b \leq 1$ is denoted N_{01}^y , and numbers of elements in the z -direction are denoted as following:

$$N_{0l}^z \text{ for } 0 \leq z/h \leq z_l/h, \quad N_{lm}^z \text{ for } z_l/h \leq z/h \leq z_m/h, \quad N_{m1}^z \text{ for } z_m/h \leq z/h \leq 1 \quad (12)$$

Specific values of x_b , x_f , z_l and z_m are defined by the structural configuration. These parameters are illustrated in Fig. 4-17.

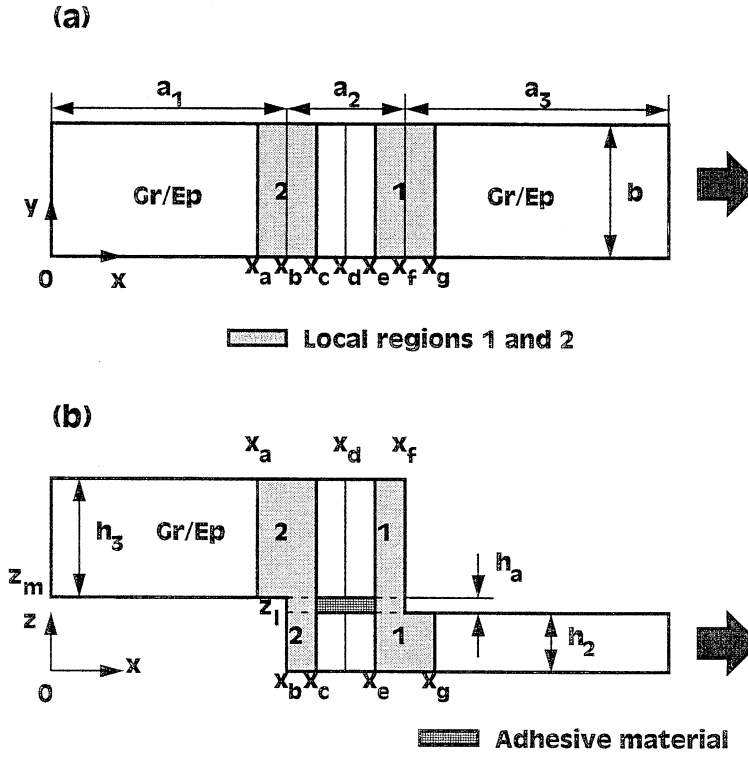


Fig. 4-17: Geometry of the global and local regions in the x - y (a) and x - z (b) planes.

According to (10), the following numerical values are adopted in the analysis:

$$x_b/a = 0.4444, x_f/a = 0.5556, z_l/h = 0.3214, z_m/h = 0.3571 \quad (13)$$

Coordinates x_a , x_c , x_e and x_g correspond to the boundaries of local analysis regions. The following specific numerical values are adopted in the analysis:

$$x_a/a = 0.4333, x_c/a = 0.4556, x_d/a = 0.5, x_e/a = 0.5444, x_g/a = 0.5667 \quad (14)$$

Table 4-26 provides description of the element meshes used in the five global analysis variants. For all of the variants uniform meshes were applied inside each of the intervals in the x -direction. The nonuniform meshes were applied in the y and z -directions (parametric mesh refinement was used for this purpose). Elements nearest to the mid-plane, $y=0$, were always

chosen the largest in the y -direction. The lengths ratio of the largest to smallest elements in this direction was taken 40. Elements in the middle adherend, nearest to the mid-plane, were chosen the largest, and elements nearest to the interface, $z_l/h = 0.3214$, the smallest in the z -direction. The lengths ratio of the largest to smallest elements in this direction was taken 8. For the upper adherend, the largest elements in the z -direction were the nearest to the top surface, $z/h = 1$, and the smallest were the nearest to the interface $z_m/h = 0.3571$. Their lengths ratio was taken 8.

Table 4-26: Element meshes used in the global analysis.

Mesh	N_{0a}^x	N_{ab}^x	N_{bc}^x	N_{cd}^x	N_{de}^x	N_{ef}^x	N_{fg}^x	N_{gl}^x	N_{0l}^y	N_{0l}^z	N_{lm}^z	N_{ml}^z	d.o.f.
GA.1	4	4	4	4	4	4	4	4	4	4	4	4	30,051
GA.2	4	6	6	4	4	6	6	4	4	4	4	4	37,395
GA.3	4	8	8	4	4	8	8	4	4	4	4	4	44,739
GA.4	4	6	6	4	4	6	6	4	5	4	4	4	45,705
GA.5	4	6	6	4	4	6	6	4	6	4	4	4	54,015

The slowest displacement convergence is expected at the aforementioned lines of possible singularities. The performed convergence study of all three displacements with the mesh refinement in the x -direction is illustrated in Tables 4-27 thru 4-29 for the following three x -coordinate values: $x = x_e, x = x_f$ and $x = x_g$ and four z -coordinate values: $z = 0, z = z_l, z = z_m$ and $z = h$.

Results of Table 4-27 show that the displacements have clearly converged at all four points under consideration. Same can be stated for the two points considered in Table 4-29. However, as follows from Table 4-28, there is a comparatively slow convergence of u_z at the points A and A', each of them belonging to the double-free edge and one of the interfaces (see, Fig. 4-16b). Thus, in order to obtain accurate transverse displacement values at these points even finer

element mesh in the x -direction should be used.

Table 4-27: Normalized displacements at $x = 0.5444a$, $y = b$ and four z -locations, computed with different x -direction element meshes of Table 4-26.

Mesh	u_x / u_0	u_y / u_0	u_z / u_0
	$z / h = 0$		
GA.1	0.0662	-0.8432×10^{-3}	0
GA.2	0.0662	-0.8438×10^{-3}	0
GA.3	0.0662	-0.8441×10^{-3}	0
	$z / h = 0.3214$		
GA.1	0.0657	-0.8099×10^{-3}	-0.2553×10^{-3}
GA.2	0.0657	-0.8105×10^{-3}	-0.2555×10^{-3}
GA.3	0.0657	-0.8107×10^{-3}	-0.2556×10^{-3}
	$z / h = 0.3571$		
GA.1	0.0653	-0.7978×10^{-3}	-0.2927×10^{-3}
GA.2	0.0653	-0.7983×10^{-3}	-0.2930×10^{-3}
GA.3	0.0653	-0.7985×10^{-3}	-0.2931×10^{-3}
	$z / h = 1$		
GA.1	0.0640	-0.6703×10^{-3}	-0.4330×10^{-3}
GA.2	0.0640	-0.6703×10^{-3}	-0.4330×10^{-3}
GA.3	0.0640	-0.6703×10^{-3}	-0.4330×10^{-3}

Table 4-28: Normalized displacements at $x = 0.5556a$, $y = b$ and four z -locations, computed with different x -direction element meshes of Table 4-26.

Mesh	u_x / u_0	u_y / u_0	u_z / u_0
	$z / h = 0$		
GA.1	0.0683	-0.1944×10^{-2}	0
GA.2	0.0683	-0.1942×10^{-2}	0
GA.3	0.0683	-0.1942×10^{-2}	0
	$z / h = 0.3214$		
GA.1	0.0679	-0.1927×10^{-2}	0.3584×10^{-3}
GA.2	0.0679	-0.1924×10^{-2}	0.3693×10^{-3}
GA.3	0.0679	-0.1922×10^{-2}	0.3743×10^{-3}
	$z / h = 0.3571$		
GA.1	0.0665	-0.1748×10^{-2}	0.7250×10^{-3}
GA.2	0.0665	-0.1737×10^{-2}	0.7906×10^{-3}
GA.3	0.0665	-0.1731×10^{-2}	0.8292×10^{-3}
	$z / h = 1$		
GA.1	0.0642	-0.9020×10^{-3}	0.6304×10^{-3}
GA.2	0.0642	-0.9020×10^{-3}	0.6337×10^{-3}
GA.3	0.0642	-0.9020×10^{-3}	0.6370×10^{-3}

Table 4-29: Normalized displacements at, $x = 0.5667a$, $y = b$ and two z -locations, computed with different x -direction element meshes of Table 4-26.

Mesh	u_x / u_0	u_y / u_0	u_z / u_0
	$z / h = 0$		
GA.1	0.0709	-0.2005×10^{-2}	0
GA.2	0.0709	-0.2004×10^{-2}	0
GA.3	0.0709	-0.2004×10^{-2}	0
	$z / h = 0.3214$		
GA.1	0.0709	-0.2005×10^{-2}	-0.1861×10^{-3}
GA.2	0.0709	-0.2005×10^{-2}	-0.1861×10^{-3}
GA.3	0.0709	-0.2005×10^{-2}	-0.1861×10^{-3}

The displacement convergence study with mesh refinement in the y -direction is illustrated in Tables 4-30 thru 4-32 considering the same ten points as in Tables 4-27 thru 4-29. Convergence of u_y is clear for all of the points. Results of Table 4-31 show that again, the slowest convergence of u_y and u_z is obtained for the corner points A and A'.

Table 4-30: Normalized displacements at, $x = 0.5444a$, $y = b$ and four z -locations, computed with different y -direction element meshes of Table 4-26.

Mesh	u_x/u_0	u_y/u_0	u_z/u_0
	$z/h = 0$		
GA.2	0.0662	-0.8438×10^{-3}	0
GA.4	0.0662	-0.8430×10^{-3}	0
GA.5	0.0662	-0.8424×10^{-3}	0
	$z/h = 0.3214$		
GA.2	0.0657	-0.8105×10^{-3}	-0.2555×10^{-3}
GA.4	0.0657	-0.8089×10^{-3}	-0.2568×10^{-3}
GA.5	0.0657	-0.8077×10^{-3}	-0.2576×10^{-3}
	$z/h = 0.3571$		
GA.2	0.0653	-0.7983×10^{-3}	-0.2930×10^{-3}
GA.4	0.0653	-0.7969×10^{-3}	-0.2942×10^{-3}
GA.5	0.0653	-0.7958×10^{-3}	-0.2948×10^{-3}
	$z/h = 1$		
GA.2	0.0640	-0.6703×10^{-3}	-0.4330×10^{-3}
GA.4	0.0642	-0.6688×10^{-3}	-0.4334×10^{-3}
GA.5	0.0642	-0.6685×10^{-3}	-0.4330×10^{-3}

Table 4-31: Normalized displacements at $x = 0.5556a$, $y = b$, and four z -locations, computed with different y -direction element meshes of Table 4-26.

Mesh	u_x/u_0	u_y/u_0	u_z/u_0
	$z/h = 0$		
GA.2	0.0683	-0.1942×10^{-2}	0
GA.4	0.0683	-0.1949×10^{-2}	0
GA.5	0.0683	-0.1954×10^{-2}	0
	$z/h = 0.3214$		
GA.2	0.0679	-0.1924×10^{-2}	0.3693×10^{-3}
GA.4	0.0679	-0.1943×10^{-2}	0.3670×10^{-3}
GA.5	0.0679	-0.1957×10^{-2}	0.3659×10^{-3}
	$z/h = 0.3571$		
GA.2	0.0665	-0.1737×10^{-2}	0.7906×10^{-3}
GA.4	0.0665	-0.1755×10^{-2}	0.7805×10^{-3}
GA.5	0.0665	-0.1768×10^{-2}	0.7730×10^{-3}
	$z/h = 1$		
GA.2	0.0642	-0.9020×10^{-3}	0.6337×10^{-3}
GA.4	0.0642	-0.8932×10^{-3}	0.6283×10^{-3}
GA.5	0.0642	-0.8899×10^{-3}	0.6282×10^{-3}

Table 4-32: Normalized displacements at $x = 0.5667a$, $y = b$ and two z -locations, computed with different y -direction element meshes of Table 4-26.

Mesh	u_x/u_0	u_y/u_0	u_z/u_0
	$z/h = 0$		
GA.2	0.0709	-0.2004×10^{-2}	0
GA.4	0.0709	-0.2005×10^{-2}	0
GA.5	0.0709	-0.2005×10^{-2}	0
	$z/h = 0.3214$		
GA.2	0.0709	-0.2005×10^{-2}	-0.1861×10^{-3}
GA.4	0.0709	-0.2005×10^{-2}	-0.1863×10^{-3}
GA.5	0.0709	-0.2005×10^{-2}	-0.1864×10^{-3}

It is also important to assure that *converged stresses* can be obtained from global analysis at the *boundaries* of the local region. Illustrative results obtained with the global element meshes of Table 4-26 are presented in Tables 4-33 thru 4-36 for the following two points in the lower adherend, $\{x = x_e, y = b, z = z_l\}$ and $\{x = x_g, y = b, z = z_l\}$, and one point in the adhesive, $\{x = x_e, y = b, z = z_l\}$ (see Fig. 4-17b for the notations). All stress magnitudes were normalized by the factor $\sigma_0 = 1.93\text{GPa}$ (0.28Msi) which represents nominal longitudinal stress calculated at $x = a$ from Hooke's law, assuming that the loaded end is free in the y and z -directions and that the applied longitudinal displacement is $u_0 = 0.01a$ ($\varepsilon_0 = 1\%$).

It is seen from Table 4-33 that all three stresses at the selected points in the lower adherend practically do not change with the x -direction mesh refinement. Results of Table 4-34 indicate that all three stresses in the adhesive layer have converged at the selected point. Results presented in Tables 4-35 and 4-36 for the y -direction mesh refinement indicate similar trend, e.g., that all three stresses have converged at the selected points for both the materials. These results

prove that it is correct to further perform *local* stress analysis for the region 1 (see Fig. 4-17), using output displacements computed with the mesh GA.3, for example, as the input data. Indeed, the displacements have been accurately calculated *everywhere* in the local region, and stresses have been calculated accurately at least at the *exterior* of the region, where the boundary conditions would be applied. So, the task of increasing stress computation accuracy *inside* the local region seems reasonable.

Table 4-33: Normalized stresses in the lower adherend at $y = b$, $z = 0.3214h$ and two x -locations, computed with different x -direction element meshes of Table 4-26.

Mesh	σ_x / σ_0	σ_z / σ_0	τ_{xz} / σ_0
	$x/a = 0.5444$		
GA.1	0.5440	-0.0126	-0.0537
GA.2	0.5446	-0.0126	-0.0538
GA.3	0.5449	-0.0126	-0.0539
	$x/a = 0.5667$		
GA.1	0.9884	-0.0001	-0.0004
GA.2	0.9881	-0.0001	-0.0004
GA.3	0.9879	-0.0001	-0.0004

Table 4-34: Normalized stresses in the adhesive layer at $x / a = 0.5444$, $y = b$, $z = 0.3214h$, computed with different x -direction element meshes of Table 4-26.

Mesh	σ_x / σ_0	σ_z / σ_0	τ_{xz} / σ_0
GA.1	0.0091	-0.0125	-0.0533
GA.2	0.0091	-0.0126	-0.0534
GA.3	0.0091	-0.0126	-0.0535

Table 4-35: Normalized stresses in the lower adherend at $y = b$, $z = 0.3214h$ and two x -locations, computed with different y -direction element meshes of Table 4-26.

Mesh	σ_x / σ_0	σ_z / σ_0	τ_{xz} / σ_0
	$x/a = 0.5444$		
GA.2	0.5446	-0.0126	-0.0538
GA.4	0.5469	-0.0124	-0.0539
GA.5	0.5483	-0.0123	-0.0539
	$x/a = 0.5667$		
GA.2	0.9881	-0.0001	-0.0004
GA.4	0.9883	-0.0001	-0.0004
GA.5	0.9885	-0.0001	-0.0004

Table 4-36. Normalized stresses in the adhesive layer at $x/a = 0.5444$, $y = b$, $z = 0.3214h$ computed with different y -direction element meshes of Table 4-26.

Mesh	σ_x / σ_0	σ_z / σ_0	τ_{xz} / σ_0
GA.2	0.0091	-0.0126	-0.0534
GA.4	0.0093	-0.0124	-0.0539
GA.5	0.0094	-0.0123	-0.0539

4.13 Numerical Comparison of the Global and Submodel Analyses

In the next steps, local regions 1 and 2 shown in Fig. 4-17 can be solved separately using nodal displacement values calculated in global analysis as the input data. The same 27-node element is used for the local analysis. In principle, any number of successive submodeling steps can be applied, using converged displacements computed in some preceding step for more accurate stress computation in the successive step. This should consistently increase accuracy of the stress predictions in the local regions 1 and 2.

Consider local region 1 shown in Fig. 4-17 with the geometric parameters given in (14). As follows from the previous section, the global analysis provided converged displacements for all points of this region. The displacements computed with global mesh GA.3 have been used as input data in the local analysis.

In the local analysis, the following numbers of elements were used: $N_{ef}^x = 16$, $N_{fg}^x = 16$, $N_{0l}^y = 4$, $N_{0l}^z = 4$, $N_{lm}^z = 4$ and $N_{ml}^z = 4$. The x -direction mesh was taken nonuniform with the ratio of the largest to smallest elements $l_x = L_x^{\max} / L_x^{\min} = 20$. The largest elements are those nearest to the vertical planes passing through coordinates x_e and x_g , and the smallest elements are those nearest to the vertical plane passing through coordinate x_f . All meshes in the y and z -directions were taken uniform inside each of the intervals.

Variations of the normalized stresses σ_x / σ_0 , σ_z / σ_0 and τ_{xz} / σ_0 in the x direction obtained from the global analysis and submodel analysis are shown in Figs. 4-18 thru 4-20 for the lower interface and in Figs. 4-21 thru 4-23 for the upper interface.

As seen in Fig. 4-18a, in the adhesive the difference between results near the corner point is considerable: the submodel analysis provides smooth stress variation and much higher peak value. On the contrary, results for the adherend in Fig. 4-18b are very close. Note that at the right end σ_x in adherend tends to σ_0 , and at the left end it tends to $\sigma_0 / 2$. It has to be pointed out that the region of high stress gradients is very small compared to the length of the overlap zone.

Analogous trends are seen in Fig. 4-19 for σ_z / σ_0 : in the adhesive there is significant difference between the results, while in the adherend they are very close. It has only to be mentioned that, as seen in Fig. 4-19b, the submodel analysis allows to satisfy the free-surface boundary condition more accurately.

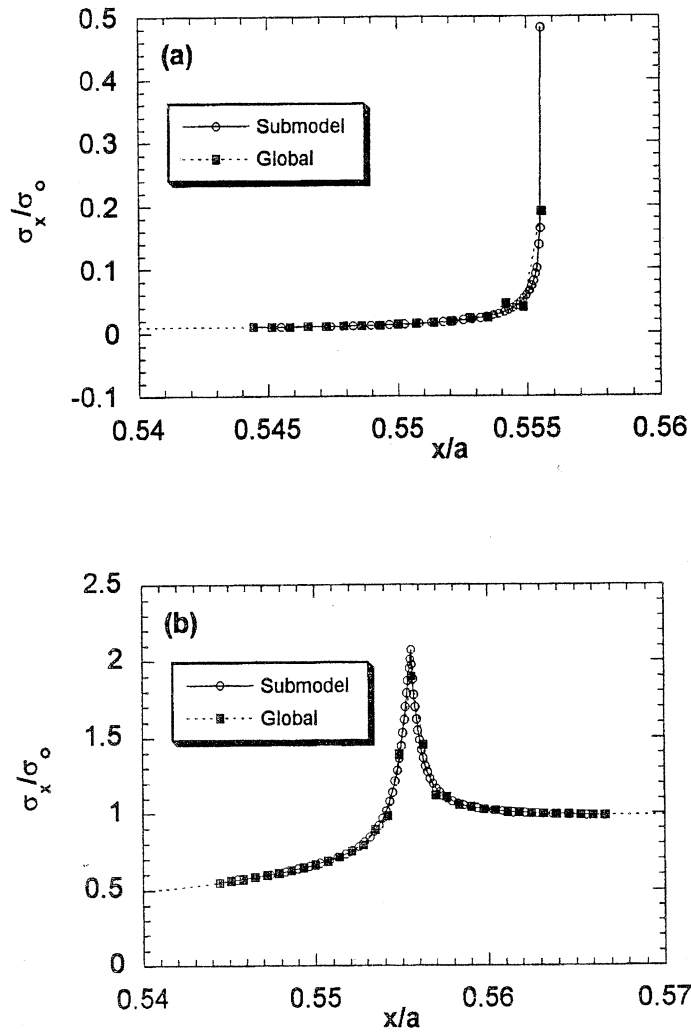


Fig. 4-18: Variations of σ_x/σ_0 in the adhesive (a) and middle adherend (b) along the interface at $y/b = 1$, $z/h = 0.3214$.

The τ_{xz}/σ_0 variations in the adhesive shown in Fig. 4-20a are rather close; the minor difference is that near the corner point the submodel analysis provides smoother variation of the stress and higher peak value. However, Fig. 4-20b shows that results for τ_{xz}/σ_0 in the adherend are very different near the corner point: a characteristic “double peak” is barely seen in the global analysis results, but is very obvious in the submodel results.

Results presented in Figs. 4-21 thru 4-23 for the upper interface, which is at some (very small, indeed) distance from the corner point show that the difference between results of the

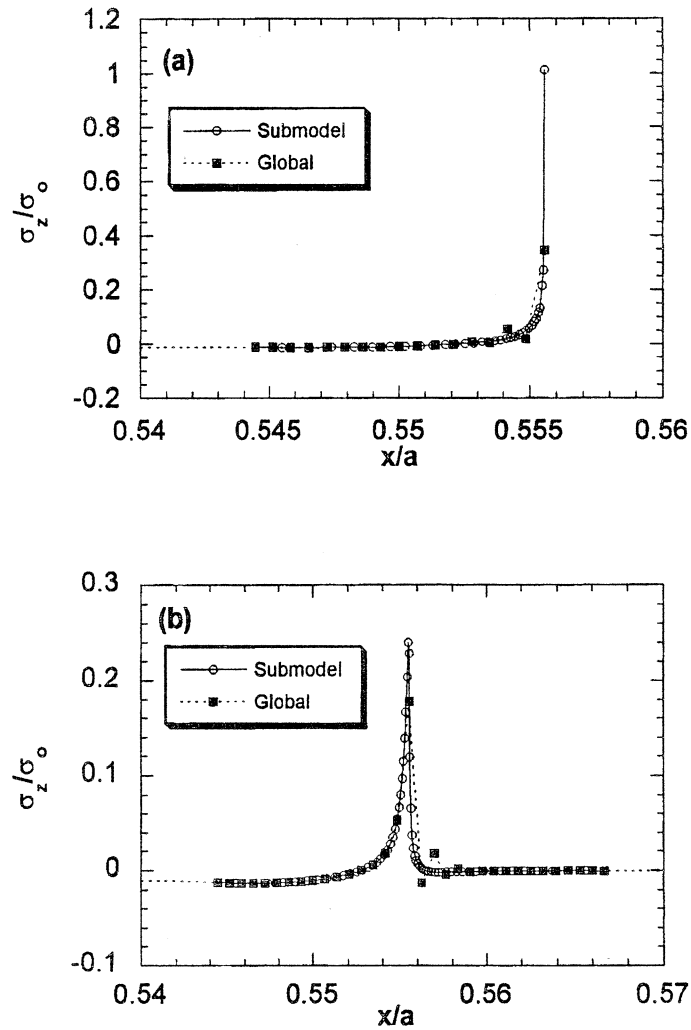


Fig. 4-19: Variations of σ_z/σ_0 in the adhesive (a) and middle adherend (b) along the interface at $y/b = 1$, $z/h = 0.3214$.

global and submodel analyses for all three stress components is only quantitative. In each case the submodel analysis shows smoother stress variation near the corner point and higher peak value. However, there are some problems in both the analysis approaches. Namely, Fig. 4-21a indicates that the very right point of σ_x variation in the adhesive does not tend to zero, as it supposed to be according to the free surface boundary condition (which was not, of course, imposed in the finite element solution). Though, as is seen in Fig. 4-21b, the very right point of σ_x variation in the adherend is close to zero, it may be occasional. Where will this point move with further mesh refinement? Possibly, to higher and higher negative value. Same questions

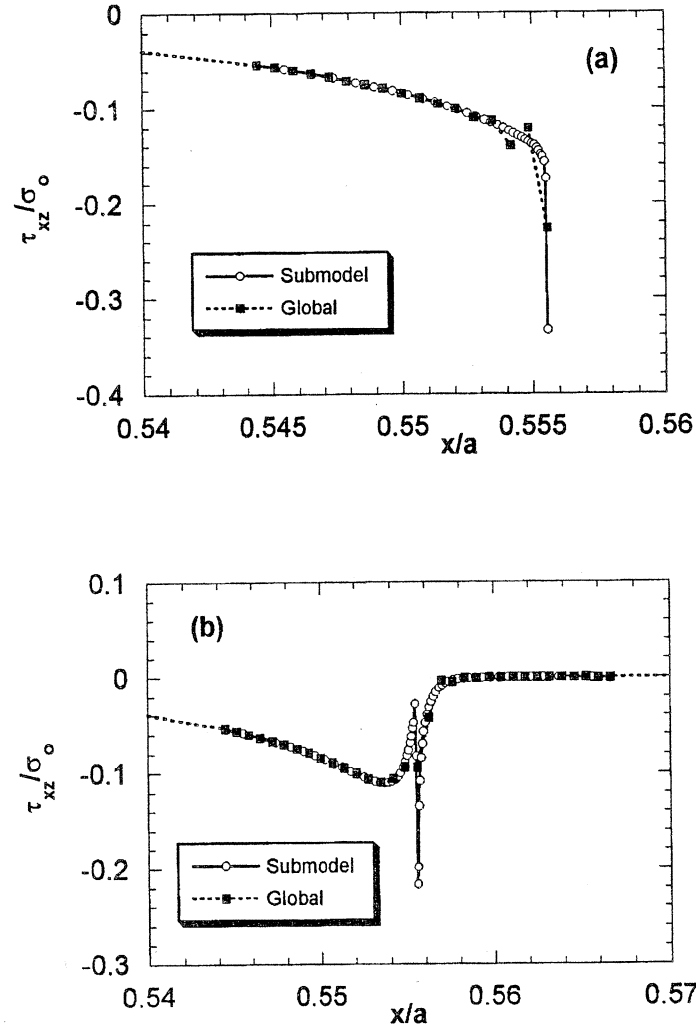


Fig. 4-20: Variations of τ_{xz}/σ_0 in the adhesive (a) and middle adherend (b) along the interface at $y/b = 1$, $z/h = 0.3214$.

arise when analyzing results in Fig. 4-22. Ideally, τ_{xz} should be zero at the very right points of the stress variations in the adhesive and adherend. However, it seems that their trend is to take some negative values which will probably grow with further mesh refinement.

The conclusion may be drawn from the above results that even at some very small distance from the corner point, the stresses computed with the global analysis and with submodeling technique are practically indistinguishable. The difference appears only in a small vicinity of the corner point, where submodeling definitely improves results for the stresses. However, even by

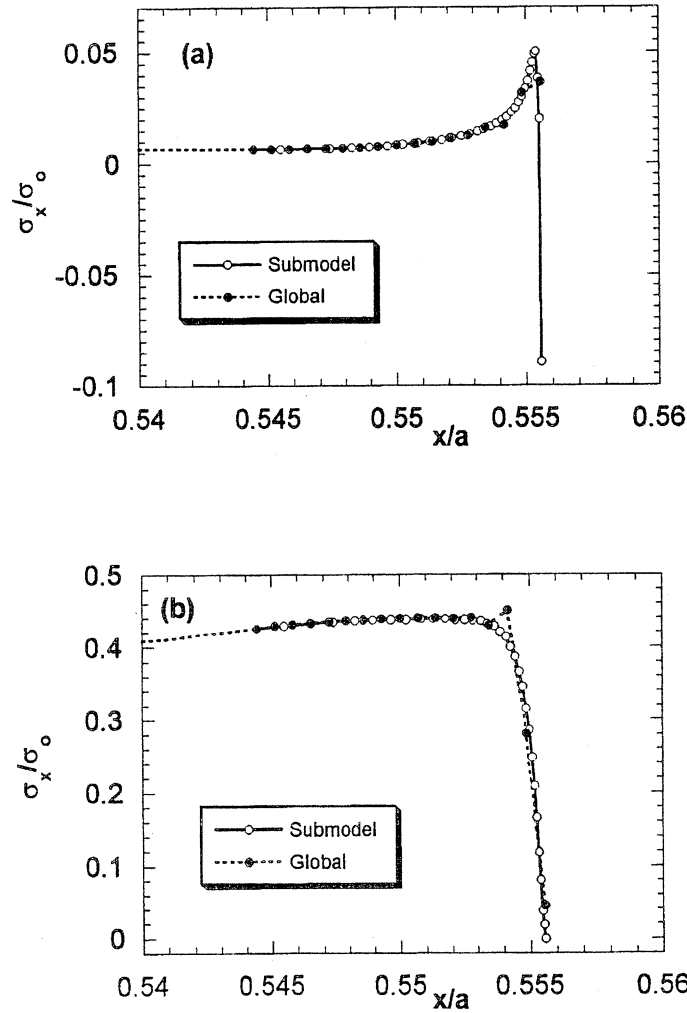


Fig. 4-21: Variations of σ_x/σ_0 in the adhesive (a) and upper adherend (b) along the interface at $y/b = 1, z/h = 0.3571$.

using more and more refined local analyses, it seems impossible to satisfy all of the required stress boundary conditions in a proximity of the corner. In our opinion, this problem seems to be of a purely academic interest, because *exactly* at the corner the stresses are *singular* anyway, so failure mechanics is not applicable and, accordingly, *failure initiation* prediction is impossible. On the other hand, if applying *averaging* of the computed stresses along some finite area, their *exact* distribution in a proximity of the corner may be of absolutely no importance.

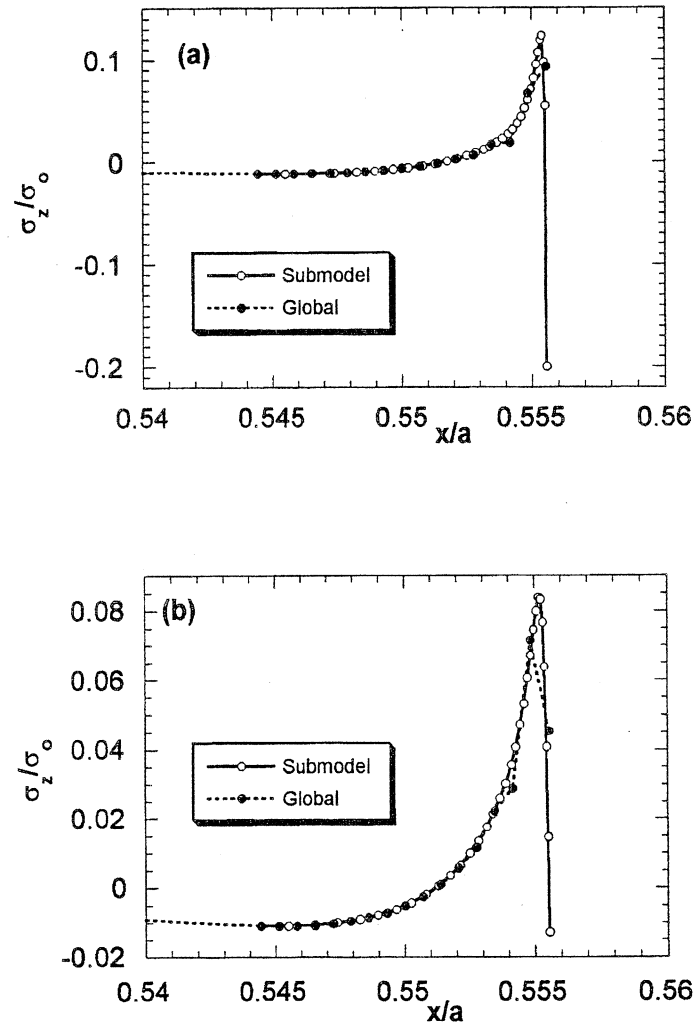


Fig. 4-22: Variations of σ_z/σ_0 in the adhesive (a) and upper adherend (b) along the interface at $y/b=1$, $z/h=0.3571$.

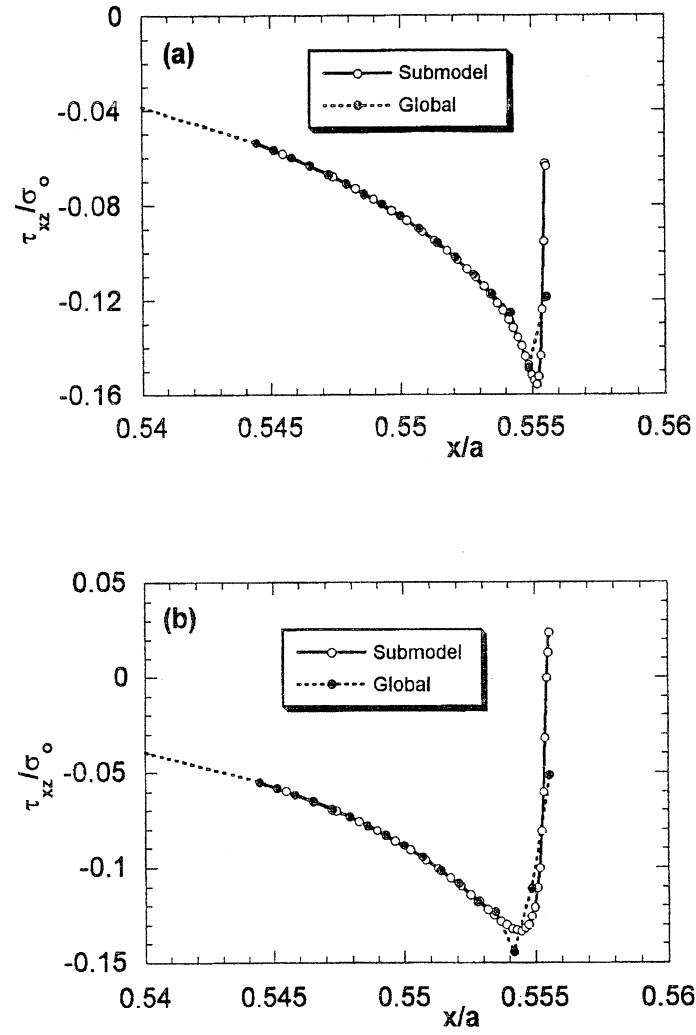


Fig. 4-23: Variations of τ_{xz}/σ_0 in the adhesive (a) and upper adherend (b) along the interface at $y/b = 1$, $z/h = 0.3571$.

4.14 Comparison of the Finite Element and Mosaic Model Results

A comparison between numerical data obtained with 3-D finite element and 3-D Mosaic Model analyses is presented here. Now we return to the example of Gr/Ep-Al bonded joint (see, Fig. 4-1) described in Sections 4.2 and 4.3. Three variants of the finite element analysis are used for comparison: global analysis of $1/8^{\text{th}}$ of the structure shown in Fig. 4-1b with the element mesh G.11 described in Table 4-3 (about 80,000 d.o.f.); Submodel 2 analysis of local region 1 characterized in Section 4.6 with the element mesh L2.5 described in Table 4-17 (this was the *third* consecutive step of analysis with about 52,000 d.o.f.), and Submodel 1 analysis of local region 2 described in Section 4.8 with the element mesh identical to L1.1 of Table 4-5 (this was the *second* consecutive step of analysis with about 27,000 d.o.f.).

The mosaic model analysis has been performed for $1/8^{\text{th}}$ of the structure shown in Fig. 4-1b. Third degree Bernstein polynomials were used for the displacement approximation in all three coordinate directions. Strain/stress continuity between the same material bricks was not enforced in this analysis. The following number of bricks was taken: 12 in x -direction, 1 in y -direction and 6 in z -direction. Total number of d.o.f. is about 14,000. Distribution of 72 bricks in the x - z plane is schematically shown in Fig. 4-24.

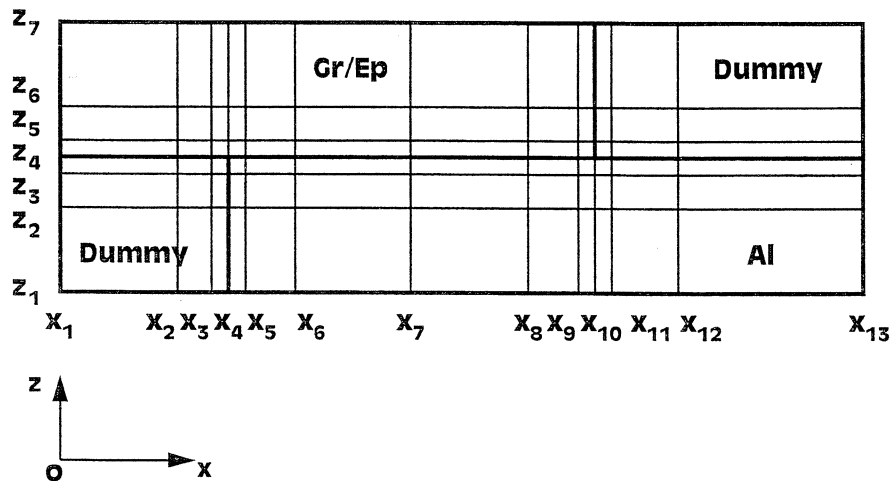


Fig. 4-24: Illustration of the brick distribution used in the Mosaic Model analysis.

The brick dimensions have been chosen according to the rule

$$\begin{aligned}
 x_2 - x_1 &= 4(x_3 - x_2) = 16(x_4 - x_3), & x_7 - x_6 &= 4(x_6 - x_5) = 16(x_5 - x_4), \\
 x_8 - x_7 &= 4(x_9 - x_8) = 16(x_{10} - x_9), & x_{13} - x_{12} &= 4(x_{12} - x_{11}) = 16(x_{11} - x_{10}), \\
 z_2 - z_1 &= 4(z_3 - z_2) = 16(z_4 - z_3), & z_7 - z_6 &= 4(z_6 - z_5) = 16(z_5 - z_4)
 \end{aligned} \tag{15}$$

Computed stresses are presented in Figs. 4-25 thru 4-31. Variations of σ_x obtained with Mosaic Model and with global FEA shown in Fig. 4-25 are practically indistinguishable. A comparison between the σ_x variations in the local region 2 shown in Fig. 4-26 and in the local region 1 shown in Fig. 4-27 also reveals only minor differences. For example, FEA results in Fig. 4-27b show higher peak stress value, however overall variations are very close.

Results for σ_z obtained with Mosaic Model and global FEA shown in Fig. 4-28 are also hardly distinguishable. A comparison of the σ_z variations in local region 1 shown in Fig. 4-29 reveals some quantitative distinctions near the peak, however overall shape of the variations is similar.

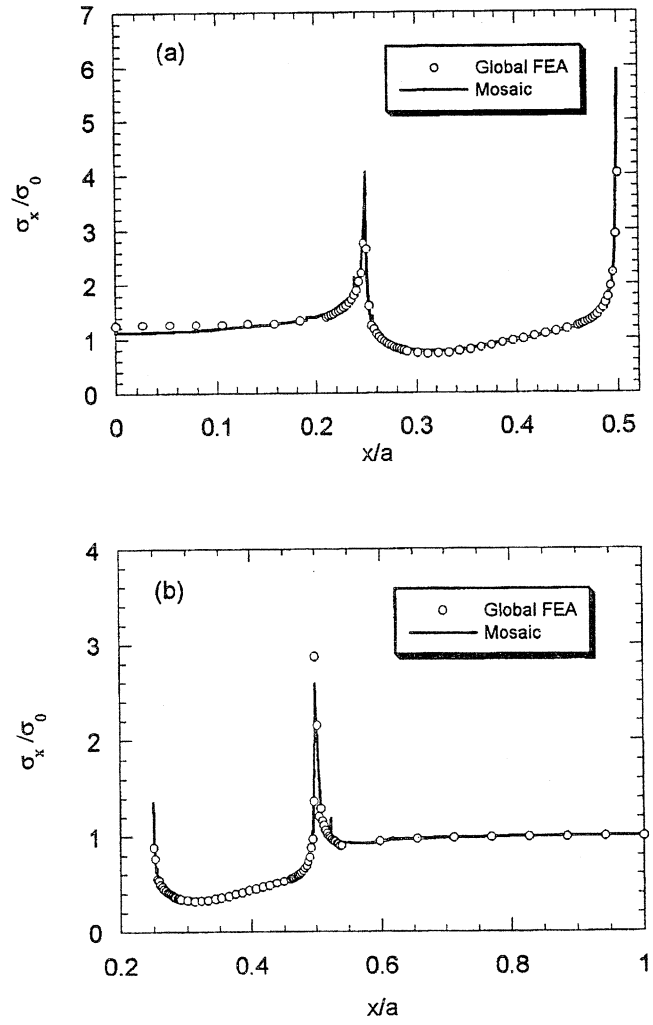


Fig. 4-25: Variations of σ_x / σ_0 in Gr/Ep (a) and Al (b) adherends in the x -direction for the global region at $y/b = 1$, $z/h = 0.5$.

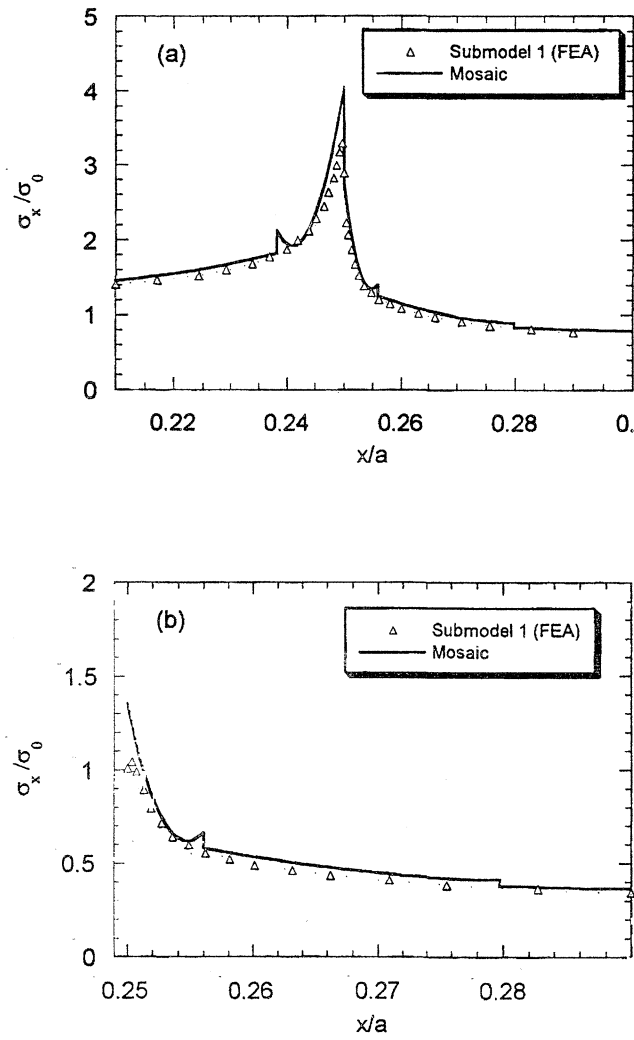


Fig. 4-26: Variations of σ_x / σ_0 in Gr/Ep (a) and Al (b) adherends in the x -direction for the local region 2 at $y/b = 1$, $z/h = 0.5$

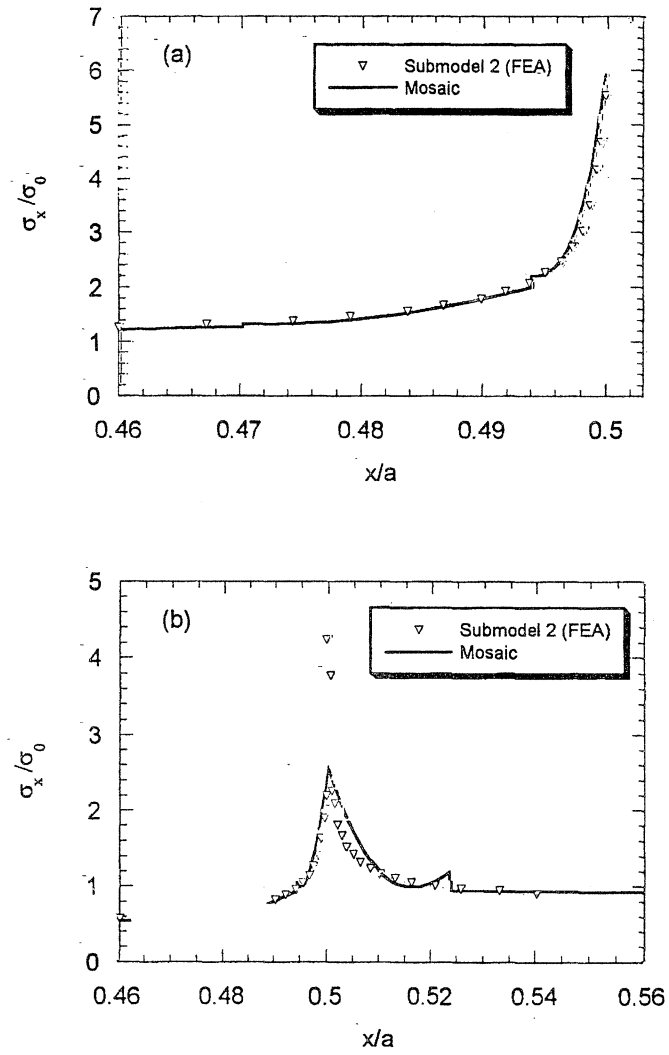


Fig. 4-27: Variations of σ_x / σ_0 in Gr/Ep (a) and Al (b) adherends in the x -direction for the local region 1 at $y/b = 1$, $z/h = 0.5$.

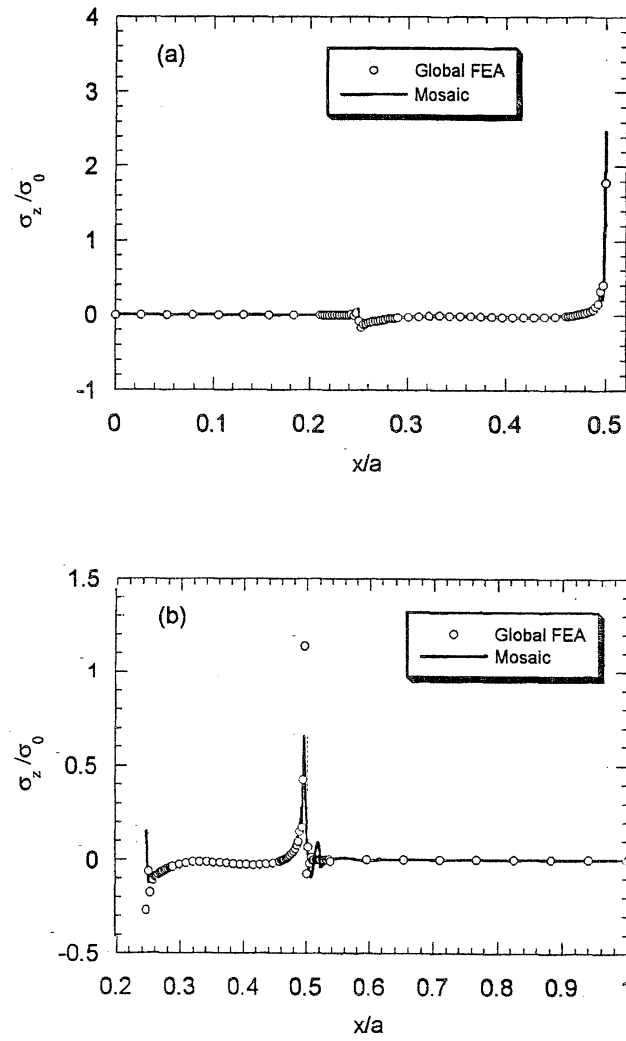


Fig. 4-28: Variations of σ_z / σ_0 in Gr/Ep (a) and Al (b) adherends in the x -direction for the global region at $y/b = 1$, $z/h = 0.5$.

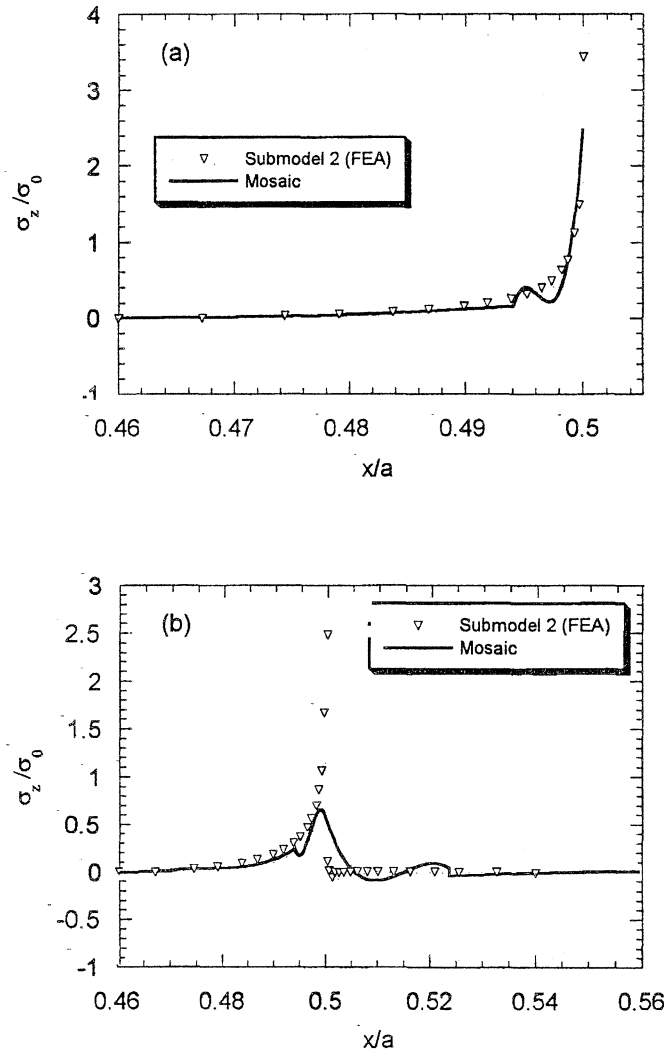


Fig. 4-29: Variations of σ_z / σ_0 in Gr/Ep (a) and Al (b) adherends in the x -direction for the local region 1 at $y/b = 1$, $z/h = 0.5$.

Results for τ_{xz} obtained with Mosaic Model and with global FEA shown in Fig. 4-30 are, again, very close. A comparison between the τ_{xz} variations in the local region 1 presented in Fig. 4-31 shows only some quantitative distinctions near the peak, with similar overall shape of the variations.

It has to be emphasized that Mosaic Model has been applied in a *single* step, for the whole global region, and with considerably smaller amount of d.o.f. than either in the global FEA or in the Submodel 1 and 2 analyses. Nevertheless, the results are comparable even near the stress

peaks. When moving at some small distance away from the peaks, Mosaic Model provides practically the same stress data as submodeling technique, which requires a lot of pre-processing and post-processing effort and, besides, is more computationally expensive.

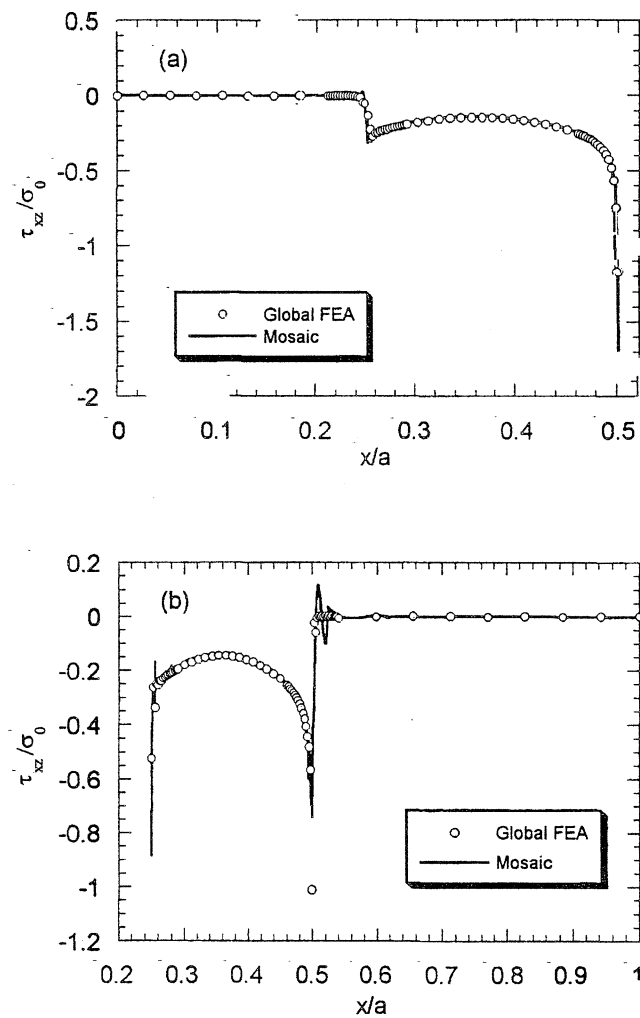


Fig. 4-30: Variations of τ_{xz}/σ_0 in Gr/Ep (a) and Al (b) adherends in the x-direction for the global region at $y/b = 1$, $z/h = 0.5$.

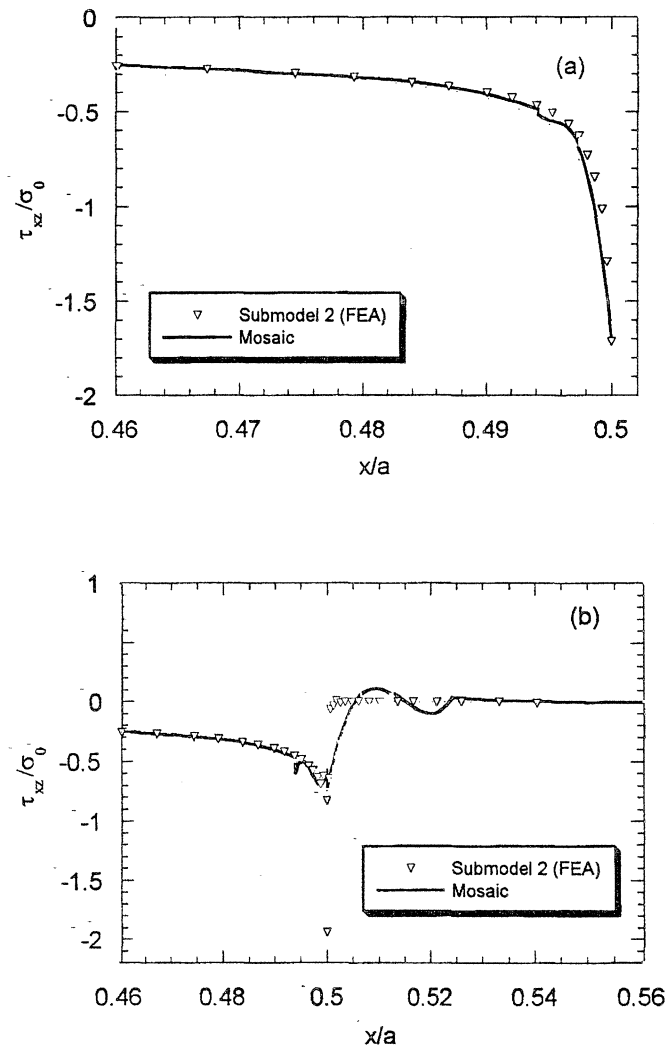


Fig. 4-31: Variations of τ_{xz} / σ_0 in Gr/Ep (a) and Al (b) adherends in the x -direction for the local region 1 at $y/b = 1$, $z/h = 0.5$.

REFERENCES

- (1) E. Alms, "Three-Dimensional Singularities in Double Lap Joints," *Engineering Fracture Mechanics*, 1985, Vol. 21, pp. 1097-1112.
- (2) W. W. Sable and P. Sharifi, "Structural Analysis of Bonded Joints Using the Finite Element Method," *Proceedings of ICCM-8, Honolulu, HI*, July 15-19, 1991. SAMPE, Covina, CA, pp. 9-F-1 - 9-F-11.
- (3) M. Y. Tsai and J. Morton, "Three-Dimensional Deformations in a Single-Lap Joint," *J. of Strain Analysis*, 1994, Vol. 29, pp. 137-145.
- (4) A. E. Bogdanovich and I. Kizhakkethara, "Three-Dimensional Finite Element Analysis of Adhesively Bonded Plates," *Collection of Techn. Pap. 38th AIAA/ASME/ASCE/AHS/ASC Conf. and Exhibit*, April 7-10, 1997, Kissimmee, FL. AIAA-97-1120, Pt. 3, pp. 1984-1993.
- (5) ABAQUS, *Version 5.5, Theory Manual*. Hibbitt, Karlsson & Sorensen, Inc., 1995.

5.0 THREE-DIMENSIONAL ANALYSIS OF CRACK PROPAGATION IN DOUBLE-LAP COMPOSITE BONDED JOINTS

5.1 Introduction

Adhesively bonded composite structures have gained increasing interest in the aircraft and aerospace industries. At the same time, there is still a lack of understanding of their fracture and progressive failure mechanisms and scientifically sound analysis tools enabling to quantify the variety of possible fracture processes and predict the ultimate failure.

It is well accepted today that adhesive joints usually fail by progressive growth of various type cracks and, hence, any realistic ultimate failure prediction should incorporate the fracture mechanics analysis. Starting with the early works [1]-[6], the scientific concepts, experimental and analytical methods of fracture mechanics have been extensively applied to adhesive bonded joints of metal structures. In one of pioneering works in this area [2] it was pointed out that “Cracks arise at the ends of the overlaps where stresses are maximal. The theory enables one to follow the development of the cracks without dealing with the problem of their generation which should be treated separately. The failing loads for the body as a whole are independent of the original crack size and can markedly exceed the loads corresponding to crack initiation.” Another important methodological aspect has been emphasized in [5]: “Since bonded joints always fail by progressive crack extension, no gross or average stress criteria are adequate to describe their structural performance. Accordingly, designs must be based on a fracture criterion”. Many subsequent theoretical and experimental studies of fracture of adhesively bonded metals (see, for example, reviews in [7], [8]) have justified that the crack propagation analysis is primarily important for predicting the joint strength.

Increasing application of bonded joints with composite adherends made the problem of analytical strength prediction even more complex. Due to anisotropy and inhomogeneity of composites, the variety of possible failure modes which can be realized in their bonded joints

increases tremendously. It can be expected *a priori* that in this case, delamination and various intra-ply failure modes can develop simultaneously or even precede the adhesive or cohesive crack propagation. Many experimental results obtained in the long course of studying composite bonded joints confirm such an expectation.

In one of the earliest experimental studies of bonded joints of unidirectional and angle-ply S-glass fiber reinforced plastics bonded by Hysol EA951 adhesive [9], a resin failure inside the composite adherend was observed. Another experimental study [10] showed that for carbon fiber composites bonded by a toughened epoxy adhesive Ciba-Geigy XD 911, all of the tested joints appeared to fail by interlaminar fracture inside the inner adherend. In experimental study [11] performed for bonded ARALL-1 single-lap and double-lap joints, it was systematically observed that the crack usually started in the spew fillet, but then penetrated into the prepreg layer closest to the adhesive. Such a crack then propagated inside the laminated adherend and caused the ultimate failure. It was even found that a small piece of aluminum remained on the failed surface, so the piece was fully separated from the aluminum layer during failure of the joint. This symptomatic result indicates that the crack can find a rather unusual penetration path: through a relatively strong aluminum layer of the adherend to a weak interface behind the layer. Certainly, such mode of failure can not be observed in the case of homogeneous metal adherends, simply because there are no interfaces.

Recent experimental studies [12], [13] conducted for double-lap bonded joints of unidirectional and cross-ply composites have shown similar general trends. The adherends were made from Hercules AS4/3501-6 tape, and FM-300 adhesive was used. The observed cracks were typically initiated at the end of the overlap, where the transverse normal and shear stresses reach their maximum (rigorously, infinite) values. The initial crack was detected when the load reached about 70% of the ultimate failure load. The crack was then propagating to

approximately the middle of the overlap. Upon careful examination under the SEM it was concluded that the crack propagation occurred within the laminated adherends, just several fiber diameters from the adhesive border. At some instant another crack was initiated at the other end of the overlap and propagated into the joint. The two cracks then linked via a third, inclined, crack which crossed the adhesive, and this caused final failure of the joint.

The aforementioned experimental observations of the failure peculiarities of composite bonded joints have not yet found their theoretical explanation. Various fracture mechanics approaches have been applied to metal bonded joints, but at this time no methodology exists which could account for the variety of failure modes and fracture processes characteristic for composite bonded joints and predict their ultimate failure (this is evident, particularly, from reviews of existing analysis methods and computer codes [10], [14]).

In section 1.4, a novel 3-D variational Mosaic Model analysis of crack propagation in composite structures has been proposed and illustrated on the example of modeling growing planar delamination in a double cantilever beam. This Section presents an extension of this analysis approach to 3-D crack propagation modeling in adhesive bonded joints of unidirectional and cross-ply laminated composite adherends. Some preliminary results of this study were reported in [16].

5.2 A Synopsis of 3-D Mosaic Model and Variational Analysis Approach

The purpose of 3-D Mosaic Model, which was originated in [17], is to develop a *unified* 3-D stress/strain, fracture and damage predictions tools applicable to a variety of composite structural elements. The simplest examples of structural elements which can be treated in the Cartesian coordinates are: rectangular laminated and sandwich plates, their single-lap and double-lap bonded joints, rectangular plates stiffened in one or two orthogonal directions with bonded rectangular stiffeners (the examples are illustrated in Figs. 5-1a, 5-2a and 5-3a). As shown in

Figs. 1b, 2b and 3b, when adding the necessary blocks of a “soft” material in each of these cases, the structural elements can be “filled up” to the full mosaic parallelepipeds. In all cases of Figs. 5-1 thru 5-3 the parallelepipeds contain four distinct materials, and thus possess the step-wise property variations in *two* coordinate directions. It is easy to imagine various more complex structural elements (an orthogonally stiffened panel, for example), which can be represented through the mosaic parallelepiped with the material property variation in all *three* coordinate directions.

Thus, a practically important set of structural elements can be treated in a unified manner, by the use of a generic Mosaic Model shown in Fig. 5-4. The model can incorporate any number of bricks; each of them may have distinct material properties, or some may have identical properties. It has to be emphasized that “soft” material bricks are only added for the convenience of analytical work and simplicity of the input and output routines. At some stage of the algorithmic derivations they are eliminated by simply renumbering the actual material bricks. A detailed description of the model and analysis approach is in sections 1 thru 4. In this section we

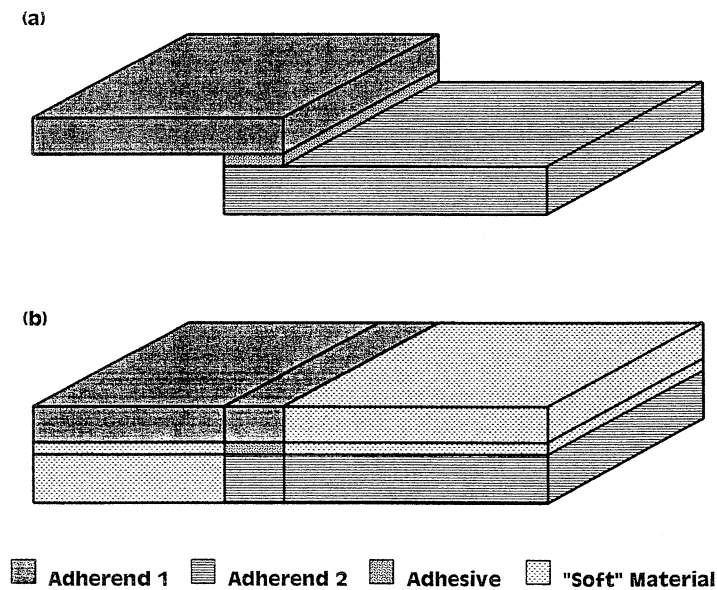


Fig. 5-1: A single-lap adhesive bonded joint (a) and its mosaic model (b).

present a brief description of the analysis approach which is necessary to further explain its application to the crack propagation problems.

A build-up of the mosaic body shown in Fig. 5-4 is fully defined by three sets of orthogonal planes $x = x_l$, $y = y_m$ and $z = z_n$ ($l = 2, \dots, L$, $m = 2, \dots, M$, $n = 2, \dots, N$). There are l anisotropic bricks in the body, each of them characterized by 21 elastic constants. Those discretization planes which separate distinct material bricks have a physical meaning while those which separate the same material bricks have purely computational meaning. At the first step of the algorithmic derivations it is suitable to not distinguish between the physical and computational discretization planes. The number of planes belonging to any of these types in the model is only limited by the computer capabilities.

The stress-strain relations for the s^{th} brick are written in the conventional form

$$\sigma_i^{(s)}(\mathbf{r}) = C_{ij}^{(s)} \varepsilon_j^{(s)}(\mathbf{r}), \quad i, j = 1, \dots, 6 \quad (1)$$

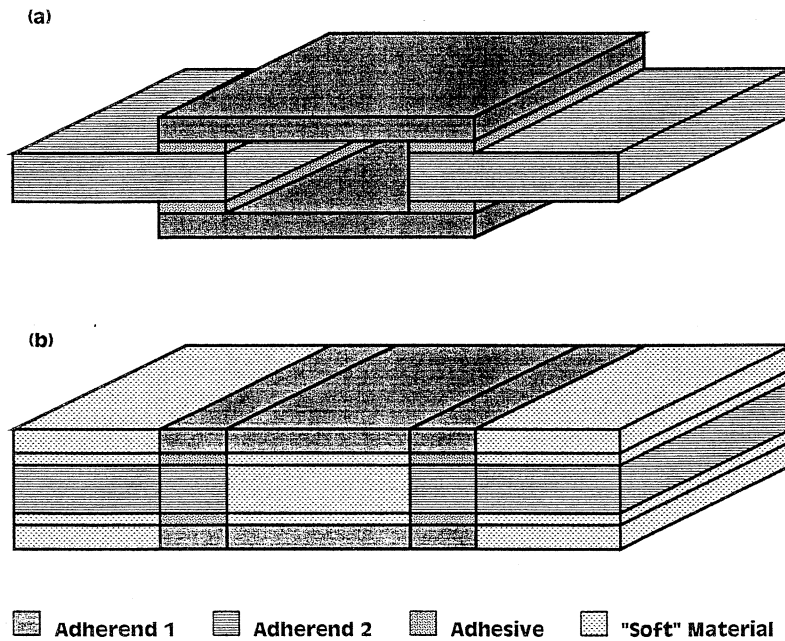


Fig. 5-2. A double-doubler adhesive bonded joint (a) and its mosaic model (b).

where $\sigma_i^{(s)}$ and $\varepsilon_j^{(s)}$ are stresses and strains, $C_{ij}^{(s)}$ are stiffness matrix components, and $\mathbf{r} = \{x, y, z\}$ is a position vector. In the present version of the analysis, the above strains are related to the displacements $u_1(x, y, z)$, $u_2(x, y, z)$ and $u_3(x, y, z)$, which correspond to the x , y and z directions, through the equations of linear 3-D elasticity:

$$\begin{aligned} \varepsilon_1^{(s)} &= \frac{\partial u_1^{(s)}}{\partial x}, \quad \varepsilon_2^{(s)} = \frac{\partial u_2^{(s)}}{\partial y}, \quad \varepsilon_3^{(s)} = \frac{\partial u_3^{(s)}}{\partial z}, \quad \varepsilon_4^{(s)} = \frac{\partial u_2^{(s)}}{\partial z} + \frac{\partial u_3^{(s)}}{\partial y}, \\ \varepsilon_5^{(s)} &= \frac{\partial u_1^{(s)}}{\partial z} + \frac{\partial u_3^{(s)}}{\partial x}, \quad \varepsilon_6^{(s)} = \frac{\partial u_1^{(s)}}{\partial y} + \frac{\partial u_2^{(s)}}{\partial x} \end{aligned} \quad (2)$$

The variational analysis developed for the Mosaic Model is based on the principle of minimum total potential energy written for the entire mosaic body:

$$\delta \Pi = \delta(P - W) = 0 \quad (3)$$

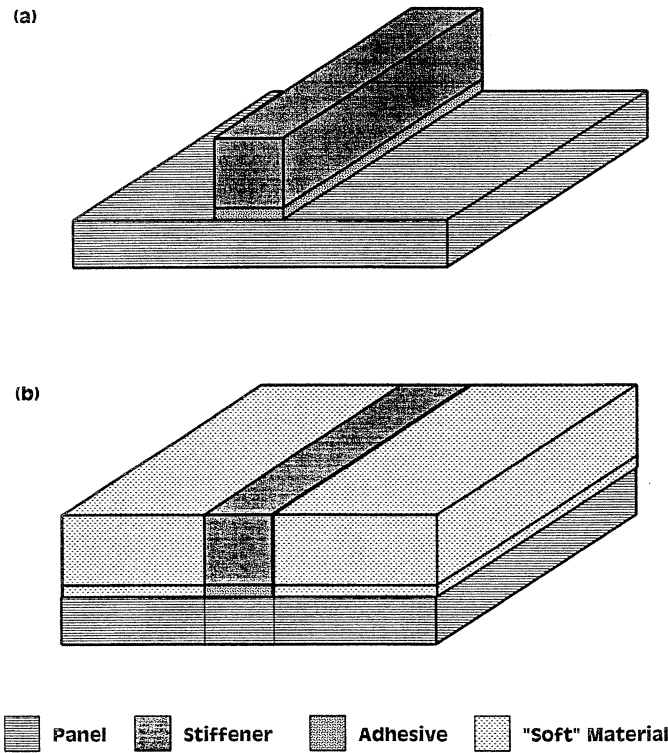


Fig. 5-3: A panel with adhesively bonded stiffener (a) and its mosaic model (b).

where P is strain energy and W is work of external surface forces. The total potential energy Π is further represented as the sum of potential energies $\Pi^{(s)}$ of all bricks in the body

$$\Pi = \sum_{s=1}^S \Pi^{(s)} = \sum_{s=1}^S (P^{(s)} - W^{(s)}) \quad (4)$$

where $S = LMN$. To further proceed with the evaluation of (4), it is necessary to use the stress-strain equations (1), the strain-displacement equations (2), and also to specify the assumed form of 3-D displacement field. Here we represent the displacement field in the s^{th} brick through the following triple series:

$$u_a^{(s)}(x, y, z) = \sum_{i=0}^I \sum_{j=0}^J \sum_{k=0}^K U_{ijk}^{a(s)} X_i(x) Y_j(y) Z_k(z); \quad a = 1, 2, 3 \quad (5)$$

where integer values I , J and K define number of degrees of freedom (d.o.f.) contained in the model; $U_{ijk}^{a(s)}$ are undetermined coefficients; $X_i(x)$, $Y_j(y)$ and $Z_k(z)$ are three sets of basis functions. At this point we do not need to specify them. Note that according to (5) the primary number of d.o.f. is $3S(I+1)(J+1)(K+1)$. Having the displacement field representation (5) it is

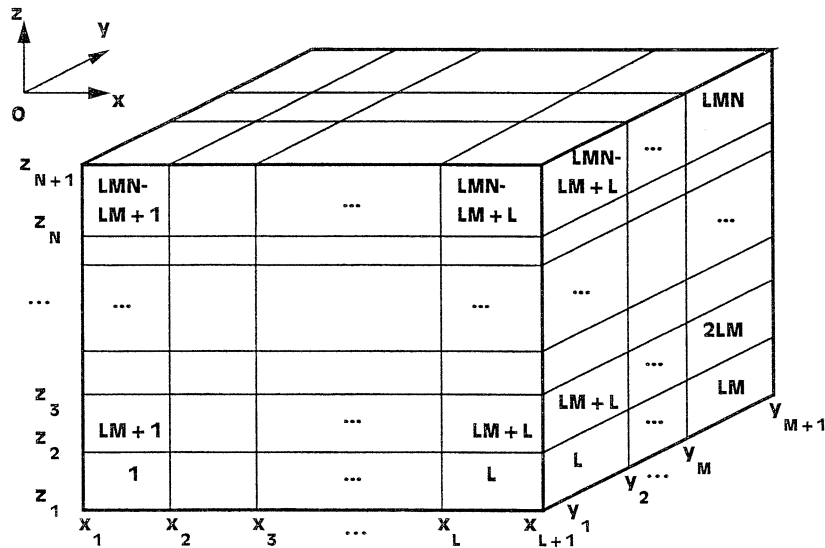


Fig. 5-4: Brick nomenclature in the mosaic body model.

possible to analytically derive expressions of $P^{(s)}$ and $W^{(s)}$ entering in (4).

One significant step of the algorithmic derivation is to define the *kinematically admissible* displacement field. This means that for each specific set of kinematic boundary conditions, the primary displacement approximation (5) has to be modified. Specifically, after imposing some external kinematic boundary conditions, certain coefficients from the primary set $U_{ijk}^{\alpha(s)}$ become known values (particularly, some of them may be zero). The corresponding “reduced” set of undetermined coefficients is further denoted $\tilde{U}_{ijk}^{\alpha(s)}$. After that the running indices i, j, k in (5) can be rearranged for the convenience, in order to maintain their starting value 0. The upper summation limits in the displacement series may now differ from those in the primary form (5); the new summation limits are denoted $I_\alpha^{(s)} \leq I$, $J_\alpha^{(s)} \leq J$, and $K_\alpha^{(s)} \leq K$ ($\alpha = 1, 2, 3$). Accordingly, the displacement field is now represented in the form

$$u_\alpha^{(s)}(x, y, z) = \sum_{i=0}^{I_\alpha^{(s)}} \sum_{j=0}^{J_\alpha^{(s)}} \sum_{k=0}^{K_\alpha^{(s)}} \tilde{U}_{ijk}^{\alpha(s)} X_i(x) Y_j(y) Z_k(z) + \sum_{i=J_\alpha^{(s)}+1}^I \sum_{j=J_\alpha^{(s)}+1}^J \sum_{k=K_\alpha^{(s)}+1}^K \hat{U}_{ijk}^{\alpha(s)} X_i(x) Y_j(y) Z_k(z) \quad (6)$$

where $\hat{U}_{ijk}^{\alpha(s)}$ are known values. The total number of d.o.f. in the model is now

$$d.o.f. = \sum_{s=1}^S \sum_{\alpha=1}^3 (I_\alpha^{(s)} + 1)(J_\alpha^{(s)} + 1)(K_\alpha^{(s)} + 1) \quad (7)$$

Note that the above modification of the primary displacement representation (5) is, essentially, analogous to the “condensation” procedure of a conventional finite element analysis. Importantly, the form of displacement field (6) may contain different number of undetermined coefficients for different bricks while the primary form (5) assumed equal number of them for all of the bricks.

Using the primary displacement representation (5), the total potential energy function (4) is written in the form

$$\Pi = \sum_{s=1}^S \Pi^{(s)}(U_{ijk}^{a(s)}) = \sum_{s=1}^S [P^{(s)}(U_{ijk}^{a(s)}) - W^{(s)}(U_{ijk}^{a(s)})] \quad (8)$$

where it is emphasized by the arguments in parentheses that the strain energy and work of external surface forces are fully defined in terms of the displacement approximation coefficients.

The following expressions of $P^{(s)}$ and $W^{(s)}$ are then obtained:

$$P^{(s)} = \frac{1}{2} \mathbf{U}^{(s)T} \mathbf{A}^{(s)} \mathbf{U}^{(s)} \quad (9)$$

$$W^{(s)} = \mathbf{U}^{(s)T} \mathbf{Q}^{(s)} \quad (10)$$

where

$$\mathbf{U}^{(s)} = \begin{Bmatrix} \{U_{ijk}^{1(s)}\} \\ \{U_{ijk}^{2(s)}\} \\ \{U_{ijk}^{3(s)}\} \end{Bmatrix}; \quad \mathbf{Q}^{(s)} = \begin{Bmatrix} \{Q_{ijk}^{1(s)}\} \\ \{Q_{ijk}^{2(s)}\} \\ \{Q_{ijk}^{3(s)}\} \end{Bmatrix}; \quad \mathbf{A}^{(s)} = \begin{bmatrix} a_{ijk,pqr}^{11(s)} & a_{ijk,pqr}^{12(s)} & a_{ijk,pqr}^{13(s)} \\ a_{ijk,pqr}^{21(s)} & a_{ijk,pqr}^{22(s)} & a_{ijk,pqr}^{23(s)} \\ a_{ijk,pqr}^{31(s)} & a_{ijk,pqr}^{32(s)} & a_{ijk,pqr}^{33(s)} \end{bmatrix}; \quad (11)$$

Explicit expressions of $a_{ijk,pqr}^{\alpha\beta(s)}$ and $Q_{ijk}^{\alpha(s)}$ can be found in [15].

To accomplish the condensation procedure, the vectors and matrix in (1.11) are substructured as following:

$$\mathbf{U}^{(s)} = \begin{Bmatrix} \mathbf{U}_a^{(s)} \\ \mathbf{U}_b^{(s)} \end{Bmatrix}; \quad \mathbf{Q}^{(s)} = \begin{Bmatrix} \mathbf{Q}_a^{(s)} \\ \mathbf{Q}_b^{(s)} \end{Bmatrix}; \quad \mathbf{A}^{(s)} = \begin{bmatrix} \mathbf{A}_{aa}^{(s)} & \mathbf{A}_{ab}^{(s)} \\ \mathbf{A}_{ba}^{(s)} & \mathbf{A}_{bb}^{(s)} \end{bmatrix} \quad (12)$$

where $\mathbf{U}_a^{(s)}$ and $\mathbf{Q}_a^{(s)}$ correspond to

$$i = 0, 1, \dots, I_\alpha^{(s)}; \quad j = 0, 1, \dots, J_\alpha^{(s)}; \quad k = 0, 1, \dots, K_\alpha^{(s)} \quad (13)$$

and $\mathbf{U}_b^{(s)}$ and $\mathbf{Q}_b^{(s)}$ correspond to

$$i = I_\alpha^{(s)} + 1, \dots, I; \quad j = J_\alpha^{(s)} + 1, \dots, J; \quad k = K_\alpha^{(s)} + 1, \dots, K \quad (14)$$

Accordingly, $\mathbf{A}_{aa}^{(s)}$, $\mathbf{A}_{ab}^{(s)}$, $\mathbf{A}_{ba}^{(s)}$ and $\mathbf{A}_{bb}^{(s)}$ correspond to the following combinations of the indices:

$$\mathbf{A}_{aa}^{(s)} \text{ to } i, p = 0, 1, \dots, I_\alpha^{(s)}; \quad j, q = 0, 1, \dots, J_\alpha^{(s)}; \quad k, r = 0, 1, \dots, K_\alpha^{(s)} \quad (15)$$

$$\mathbf{A}_{ab}^{(s)} \text{ to } i = 0, 1, \dots, I_\alpha^{(s)}; \quad p = I_\alpha^{(s)} + 1, \dots, I; \quad j = 0, 1, \dots, J_\alpha^{(s)}; \quad q = J_\alpha^{(s)} + 1, \dots, J; \quad (16)$$

$$k = 0, 1, \dots, K_\alpha^{(s)}; \quad r = K_\alpha^{(s)} + 1, \dots, K$$

$$\mathbf{A}_{ba}^{(s)} \text{ to } i = I_\alpha^{(s)} + 1, \dots, I; \quad p = 0, 1, \dots, I_\alpha^{(s)}; \quad j = J_\alpha^{(s)} + 1, \dots, J; \quad q = 0, 1, \dots, J_\alpha^{(s)}; \quad (17)$$

$$k = K_\alpha^{(s)} + 1, \dots, K; \quad r = 0, 1, \dots, K_\alpha^{(s)}$$

and $\mathbf{A}_{bb}^{(s)} \text{ to } i, p = I_\alpha^{(s)} + 1, \dots, I; \quad j, q = J_\alpha^{(s)} + 1, \dots, J; \quad k, r = K_\alpha^{(s)} + 1, \dots, K \quad (18)$

The following expressions are then obtained from (9) and (10) with the use of (12):

$$P^{(s)} = \frac{1}{2} \left(\mathbf{U}_a^{(s)T} \mathbf{A}_{aa}^{(s)} \mathbf{U}_a^{(s)} + \mathbf{U}_a^{(s)T} \mathbf{A}_{ab}^{(s)} \mathbf{U}_b^{(s)} + \mathbf{U}_b^{(s)T} \mathbf{A}_{ba}^{(s)} \mathbf{U}_a^{(s)} + \mathbf{U}_b^{(s)T} \mathbf{A}_{bb}^{(s)} \mathbf{U}_b^{(s)} \right) \quad (19)$$

$$\mathcal{W}^{(s)} = \mathbf{U}_a^{(s)T} \mathbf{Q}_a^{(s)} + \mathbf{U}_b^{(s)T} \mathbf{Q}_b^{(s)} \quad (20)$$

It is worth mentioning that the first term in (19) is a quadratic form of the undetermined coefficients, the second and third terms are their linear forms, and the fourth term is a constant. The first term in (20) is a linear form of the undetermined coefficients, and the second term is a constant.

It is known that one of the consequences of the variational principle (3) are Ritz-type equations which are, in our case, written in the following form:

$$\sum_{s=1}^S \left(\frac{\partial P^{(s)}}{\partial U_a^{(s)}} - \frac{\partial \mathcal{W}^{(s)}}{\partial U_a^{(s)}} \right) = 0 \quad (21)$$

where $^{(s)}$ and $^{(s)}$ are defined in (19) and (20). Before imposing connectivity of the bricks,

(21) provides S separate systems of linear simultaneous equations, each containing

$\sum_{\alpha=1}^3 (I_{\alpha}^{(s)} + 1)(J_{\alpha}^{(s)} + 1)(K_{\alpha}^{(s)} + 1)$ unknowns. The s^{th} system of linear simultaneous equations

derived from (19)-(21) with account for the symmetry of matrix \mathbf{A} (that has been shown in [15]) is then written as following

$$\mathbf{A}_{aa}^{(s)} \mathbf{U}_a^{(s)} = \mathbf{Q}_a^{(s)} - \mathbf{A}_{ab}^{(s)} \mathbf{U}_b^{(s)} \quad (22)$$

Note that the right hand side of the above system contains both the external surface forces and external displacements acting on the brick.

The above result allows one to solve any 3-D elasticity problem for an anisotropic brick with prescribed displacements, surface forces or any appropriate combinations of thereof. It has to be pointed out that no *a priori* assumptions have been made yet regarding specific type of basis functions in the displacement approximation (5) or regarding the number of basis functions determined by the values I, J and K . A specific choice of basis functions can be motivated by their preferable order of continuity, analytical convenience, higher convergence rate, computational stability, and other considerations.

Further development of the theory needs to address the internal geometric and static boundary conditions between the bricks. With the use of the brick nomenclature introduced earlier (see Fig. 5-4), a full set of the displacement continuity conditions in the mosaic body can be formulated as following. For the inter-brick boundaries perpendicular to the x -, y - and z -axis, respectively, it is obtained:

$$u_{\alpha}^{s(l,m,n)}(x_l, y, z) = u_{\alpha}^{s(l+1,m,n)}(x_l, y, z) \quad (23)$$

$$u_{\alpha}^{s(l,m,n)}(x, y_m, z) = u_{\alpha}^{s(l,m+1,n)}(x, y_m, z) \quad (24)$$

$$u_{\alpha}^{s(l,m,n)}(x, y, z_n) = u_{\alpha}^{s(l,m,n+1)}(x, y, z_n) \quad (25)$$

where $\alpha = 1, 2, 3$ in all three equations and

$$s(l, m, n) = 1 + (l - 2) + (m - 2)L + (n - 2)LM \quad (26)$$

The following values of l , m and n apply:

$$l = 2, \dots, L; \quad m = 2, \dots, M + 1; \quad n = 2, \dots, N + 1 \quad (27)$$

in (23),

$$l = 2, \dots, L + 1; \quad m = 2, \dots, M; \quad n = 2, \dots, N + 1 \quad (28)$$

in (24) and

$$l = 2, \dots, L + 1; \quad m = 2, \dots, M + 1; \quad n = 2, \dots, N \quad (29)$$

in (25).

Further, considering continuity conditions of transverse stresses at the inter-brick boundaries, the following is obtained for the boundaries perpendicular to the x -, y - and z -axes, respectively (double-index notations $\sigma_{11} = \sigma_1$, $\sigma_{22} = \sigma_2$, $\sigma_{33} = \sigma_3$, $\sigma_{23} = \sigma_4$, $\sigma_{31} = \sigma_5$, $\sigma_{12} = \sigma_6$ are used below for conciseness):

$$\sigma_{1\alpha}^{s(l, m, n)}(x_l, y, z) = \sigma_{1\alpha}^{s(l+1, m, n)}(x_l, y, z) \quad (30)$$

$$\sigma_{2\alpha}^{s(l, m, n)}(x, y_m, z) = \sigma_{2\alpha}^{s(l, m+1, n)}(x, y_m, z) \quad (31)$$

$$\sigma_{3\alpha}^{s(l, m, n)}(x, y, z_n) = \sigma_{3\alpha}^{s(l, m, n+1)}(x, y, z_n) \quad (32)$$

As before, $\alpha = 1, 2, 3$; the variation of index s is defined by (1.26), and the indices l , m , n run the values (27), (28) and (29) for the cases (30), (31) and (32), respectively. Equations (23)-(32) formulate a complete set of the displacement and stress continuity conditions between the bricks in the Mosaic Model, and thus can be used for any structural element allowing for such a modeling.

Next step of the solution procedure is to express these conditions in terms of undetermined coefficients of the displacement approximation. However, this step can be only accomplished after the basis functions are fully defined. In the present analysis the following basis functions are taken for the brick located between the planes x_l and x_{l+1} , y_m and y_{m+1} , n and z_{n+1} :

$$X_i(x) = \begin{cases} B_i^I(x) = \frac{I!}{i!(I-i)!} \left(\frac{x-x_l}{x_{l+1}-x_l} \right)^i \left(\frac{x_{l+1}-x}{x_{l+1}-x_l} \right)^{I-i} & \text{for } x \in [x_l, x_{l+1}] \\ 0 = \text{else} \end{cases} \quad (33)$$

$$Y_j(y) = \begin{cases} B_j^J(y) = \frac{J!}{j!(J-j)!} \left(\frac{y-y_m}{y_{m+1}-y_m} \right)^j \left(\frac{y_{m+1}-y}{y_{m+1}-y_m} \right)^{J-j} & \text{for } y \in [y_m, y_{m+1}] \\ 0 = \text{else} \end{cases} \quad (34)$$

$$Z_k(z) = \begin{cases} B_k^K(z) = \frac{K!}{k!(K-k)!} \left(\frac{z-z_n}{z_{n+1}-z_n} \right)^k \left(\frac{z_{n+1}-z}{z_{n+1}-z_n} \right)^{K-k} & \text{for } z \in [z_n, z_{n+1}] \\ 0 = \text{else} \end{cases} \quad (35)$$

In this manner, the triad l , m and n define the basis functions for all of the bricks.

The Bernstein polynomials possess certain valuable properties which make them suitable for developing elegant mathematical solutions and computational algorithms for various types of boundary value problems of elasticity. One of the properties is that it is possible to *identically* satisfy a practically important class of the external kinematic boundary conditions, namely *uniformly* distributed displacements applied over the exterior surface of the structure or some part of thereof (see Section 1-4 for details). Another property, which may be of a special importance from the standpoint of the computational efficiency, is that the Bernstein polynomials yield *smooth* approximants [18], e.g., they provide *simultaneous* approximation for the function and its *derivatives*.

It is easy to show that with the use of (33)-(35) the displacement continuity conditions (23)-(25) can be expressed in terms of the undetermined coefficients as

$$U_{ijk}^{\alpha,s(l,m,n)} = U_{0jk}^{\alpha,s(l+1,m,n)}, U_{ijk}^{\alpha,s(l,m,n)} = U_{i0k}^{\alpha,s(l,m+1,n)}, U_{ijk}^{\alpha,s(l,m,n)} = U_{ij0}^{\alpha,s(l,m,n+1)} \quad (36)$$

for all respective i, j and k . The values of s, l, m and n in (36) are defined by (26) and (27)-(29). If all of the relations (36) are satisfied, then the solution of any specific boundary value problem provides continuous displacement field *everywhere* in the mosaic body, regardless of the material properties of individual bricks.

Further, with the use of basis functions (33)-(35) it is possible to analytically formulate the conditions of strain and stress continuity between adjacent bricks made from the same material. The corresponding relations are obtained in the following:

$$U_{1jk}^{\alpha,s(\bar{l}+1,\bar{m},\bar{n})} = \frac{x_{\bar{l}+1} - x_{\bar{l}-1}}{x_{\bar{l}} - x_{\bar{l}-1}} U_{ijk}^{\alpha,s(\bar{l},\bar{m},\bar{n})} - \frac{x_{\bar{l}+1} - x_{\bar{l}}}{x_{\bar{l}} - x_{\bar{l}-1}} U_{i-1jk}^{\alpha,s(\bar{l},\bar{m},\bar{n})}; j = 0,1,\dots,J; k = 0,1,\dots,K \quad (37)$$

$$U_{i1k}^{\alpha,s(\bar{l},\bar{m}+1,\bar{n})} = \frac{y_{\bar{m}+1} - y_{\bar{m}-1}}{y_{\bar{m}} - y_{\bar{m}-1}} U_{ijk}^{\alpha,s(\bar{l},\bar{m},\bar{n})} - \frac{y_{\bar{m}+1} - y_{\bar{m}}}{y_{\bar{m}} - y_{\bar{m}-1}} U_{ij-1k}^{\alpha,s(\bar{l},\bar{m},\bar{n})}; i = 0,1,\dots,I; k = 0,1,\dots,K \quad (38)$$

$$U_{ij1}^{\alpha,s(\bar{l},\bar{m},\bar{n}+1)} = \frac{z_{\bar{n}+1} - z_{\bar{n}-1}}{z_{\bar{n}} - z_{\bar{n}-1}} U_{ijk}^{\alpha,s(\bar{l},\bar{m},\bar{n})} - \frac{z_{\bar{n}+1} - z_{\bar{n}}}{z_{\bar{n}} - z_{\bar{n}-1}} U_{ijk-1}^{\alpha,s(\bar{l},\bar{m},\bar{n})}; i = 0,1,\dots,I; j = 0,1,\dots,J \quad (39)$$

In the present analysis, the conditions of continuity of transverse stresses at the interfaces between *distinct* material bricks are not imposed, but rather expected to be accurately satisfied in a “soft” sense, as the natural boundary conditions. Accordingly, the notations \bar{l} , \bar{m} and \bar{n} in (37)-(39) emphasize that not all values from the sets $\{l\}$, $\{m\}$ and $\{n\}$ apply, but only those which correspond to the boundaries between the same material bricks.

After a full set of the displacement and stress continuity relations for the inter-brick boundaries in the mosaic body has been formulated in terms of the displacement approximation coefficients, the next necessary step of the analytical development is to incorporate them into the computational algorithm, which requires another condensation. Description of this procedure is omitted here due to its algorithmic complexity. It can only be mentioned that after

accomplishing this algorithmic step, the unknowns contained in (22), which correspond to different brick numbers, s , become mutually interrelated. Hence, the coupled system of linear simultaneous equations is obtained, which usually contains significantly less unknowns than all of the unrelated systems (22) together. Numerical solution of the system may be performed following common routines. This provides numerical values to some part of the displacement approximation coefficients $\tilde{U}_{ijk}^{\alpha(s)}$. The rest of them is then obtained from the continuity relations (36)-(39).

After all coefficients in the displacement approximation (6), $\tilde{U}_{ijk}^{\alpha(s)}$ and $\hat{U}_{ijk}^{\alpha(s)}$, have been defined, the summation of the respective triple series can be conducted to result in the displacement values for any given combination of the coordinates x , y and z . Further, the strains can be obtained by substituting (6) in (2). Finally, the stresses can be computed through the strains by the use of (1). Note that the displacements, strains and stresses are calculated *directly* from their analytical expressions for any *given point* of the structure, including interfaces, without applying any extrapolation to the nodes, smoothing, or other commonly used finite element postprocessing procedures. Output of the analysis provides displacements, strains and stresses at any point of the structure or their 2-D and 3-D plots along the coordinates.

5.3 3-D Crack Propagation Analysis Using Mosaic Model Approach

Having the theory presented in the previous section, our next objective is to develop fracture mechanics approach aimed at analyzing the propagation of 2-D planar cracks in the mosaic body. Assuming that a general 3-D state of stress takes place, including both the normal and shear stresses, the following additions should be made in order to introduce the crack:

- (a) In the case of a *tensile* normal stress between the bricks in that location where the crack is introduced, the crack opening and, possibly, also sliding would take place. In other words, the respective free surface would be created. The corresponding continuity

relations from the sets (36)-(39) should be then identified and eliminated.

- (b) In the case of a *compressive* normal stress between the bricks there is no crack opening but may be sliding. Again, the respective continuity relations from the sets (36)-(39) should be identified and eliminated. In addition to that, the non-penetration conditions have to be incorporated in this case. Also, it is possible to incorporate friction forces, assuming that the coefficient of friction between the bricks is known.

The described approach allows one to solve various problems concerning a planar crack propagation in any of the three orthogonal directions, either between distinct materials or inside the same material. It is further assumed that the crack is allowed to grow in discrete steps; this requirement means that only two adjacent bricks may be separated at each crack increment. Dimensions of the separated bricks, which determine the crack area increase, are defined by the chosen computational brick mesh. It is worth mentioning that unlike in the known finite element methodologies, where the displacement continuity conditions are relaxed only for the *nodes*, the present methodology allows one to relax the continuity conditions along the entire *surface element* in each step of the crack propagation modeling.

The total potential energy release rate can be then evaluated directly from expressions (8)-(10) by applying them to two consecutive states of the body with the crack. If the total potential energy at some state “ K ” is Π_K and at the state “ $K+1$ ” this is Π_{K+1} , then the energy release rate corresponding to the K^{th} crack propagation step is

$$G_{K,K+1} = \frac{\Pi_K - \Pi_{K+1}}{\Delta S_{K,K+1}} \quad (40)$$

where $\Delta S_{K,K+1}$ is the area between two bricks which have been separated in this step. The value of $G_{K,K+1}$ is defined entirely by the change of the coefficients $U_{ijk}^{\alpha(s)}$ when the crack propagates from the state K to $K+1$.

The main algorithmic steps of the developed crack propagation analysis can thus be summarized as following:

- (i) a single starter planar crack or multiple starter cracks between the specified bricks are introduced; this is accomplished by relaxing the respective continuity conditions from the sets (1.36)-(1.38);
- (ii) stress/strain analysis of the mosaic structure containing the starter crack(s) is conducted;
- (iii) the total potential energy in the presence of the starter crack(s) is computed;
- (iv) the surface increment is given to the starter crack(s), and the steps (ii) and (iii) are repeated; the brick mesh is adjusted to the change of location of the crack tip;
- (v) the energy release rate (ERR) is calculated using results of steps (iii) and (iv);
- (vi) the critical energy release rate (CERR) criterion is applied as the crack growth condition; if the CERR criterion is satisfied, then another crack increment is applied; if the CERR criterion is not satisfied, then the external load/displacement magnitude is increased, and the loop (ii)-(vi) is repeated.

It has to be pointed out that the described crack propagation analysis approach is based on the total potential energy evaluation at different states of the cracked mosaic body. The evaluation is performed using expressions (8)-(10) which, as mentioned before, only utilize the displacement approximation coefficients and do not assume any information about the strain and stress fields. The roots of this methodology, though discussed in the context of the finite element analysis, can be found in [19], where two different options of the strain energy evaluation were considered. It was pointed out in that work that using the straightforward approach to calculate strain energy in terms of the strain and stress fields may be disadvantageous, because these fields “cannot be as accurate as the original output from the finite element computer program which is

displacements”. It has been further recommended in the aforementioned work that “ it would be more accurate to use the original stiffness matrices, force vectors, and displacement vectors to calculate strain energy.” The present analysis complies with this approach. However, various other numerical approaches to the evaluation of ERR in adhesive bonded joints are known in literature; a summary of them can be found in [20].

Next two sections are devoted to numerical examples illustrating application of the developed analysis approach.

5.4 Analysis of Double-Lap Joint with Unidirectional Composite Adherends

Consider a double-lap adhesive bonded joint shown in Fig. 5-5a. Geometric parameters adopted in the analysis are:

$$\begin{aligned} a_1 = a_3 = 57.15mm (2.25in.), \quad a_2 = 25.4mm (1in.), \quad 2a = a_1 + 2a_2 + a_3 = 165.1mm (6.5in.), \\ 2b = 25.4mm (1in.), \quad h_1 = h_3 = 2h_2 = 2.286mm (0.09in.), \quad h_a = 0.127mm (0.005in.) \end{aligned} \quad (41)$$

All adherends are made from 16 plies of unidirectional Graphite/Epoxy tape AS4/3501-6; the following elastic characteristics are used:

$$\begin{aligned} E_L = 133 \text{ GPa} (19.3Msi), \quad E_T = 10.7 \text{ GPa} (1.55Msi), \quad G_L = 7.03 \text{ GPa} (1.02Msi), \\ G_T = 4.07 \text{ GPa} (0.59 \text{ Msi}), \quad \nu_{LT} = 0.30 \end{aligned} \quad (42)$$

The bonding adhesive is Cytac FM300-2K film (containing 3% woven glass scrim) with the following elastic characteristics:

$$E = 3.47GPa (0.506Msi); \quad \nu = 0.30 \quad (43)$$

Processing and testing of the described bonded joint specimens was reported in [12], [13].

In order to save computational time and memory, the following simplifications of the problem have been applied. Due to symmetry of the geometric configuration and material

properties, displacement u_x must be zero along the whole cross-section perpendicular to the x -axis and passing through the point $x = 0$ of the joint (see Fig. 5-5b). Also, displacement u_y should be zero along the cross-section perpendicular to the y -axis and passing through the center of the joint, and displacement u_z should be zero along the cross-section perpendicular to the z -axis and passing through the center of the joint. The respective symmetry conditions reduce analysis of the structure shown in Fig. 5-5a to its $1/8^{\text{th}}$ part which is shown in Fig. 5-5b. After that, following the “soft” material concept we fill-up the structural element of Fig. 5-5b to the mosaic parallelepiped shown in Fig. 5-5c. Now, the structural element to be solved contains three distinct materials: unidirectional Gr/Ep composite of the upper and middle adherends, Cytec FM300-2K adhesive material and a “soft” material. As mentioned before, the latter one is introduced only for convenience of the brick nomenclature and computational mesh description. The respective soft material bricks are eliminated from the actual computations.

In the experimental studies [12], [13] the force-controlled regime has been applied. In this theoretical study we consider both the displacement-controlled and force-controlled regimes. In the former case, the kinematic boundary condition of uniformly distributed displacement \bar{R}_0 is imposed at the right (loaded) end of the middle adherend. Thus, the full set of kinematic boundary conditions is formulated as following

$$u_x = 0 \text{ at } x = 0; \quad u_x = u_0 \text{ at } x = a; \quad u_y = 0 \text{ at } y = 0; \quad u_z = 0 \text{ at } z = 0 \quad (44)$$

Schematic of 3-D computational brick mesh used in the analysis is shown in Fig. 5-6. For convenience, the following notations of the intervals are introduced: in the x -direction $[x^{(p)}, x^{(p+1)}]$ with $p = 0, 1, 2, 3$; in the y -direction $[y^{(q)}, y^{(q+1)}]$ with $q = 0, 1$; in the z -direction $[z^{(r)}, z^{(r+1)}]$ with $r = 0, 1, \dots, 5$. Numbers of bricks in these intervals are denoted L_{p+1} , M_{q+1} and N_{r+1} , respectively (note that $L = \sum_p L_{p+1}$, $M = \sum_q M_{q+1}$ and $N = \sum_r N_{r+1}$). Now, the

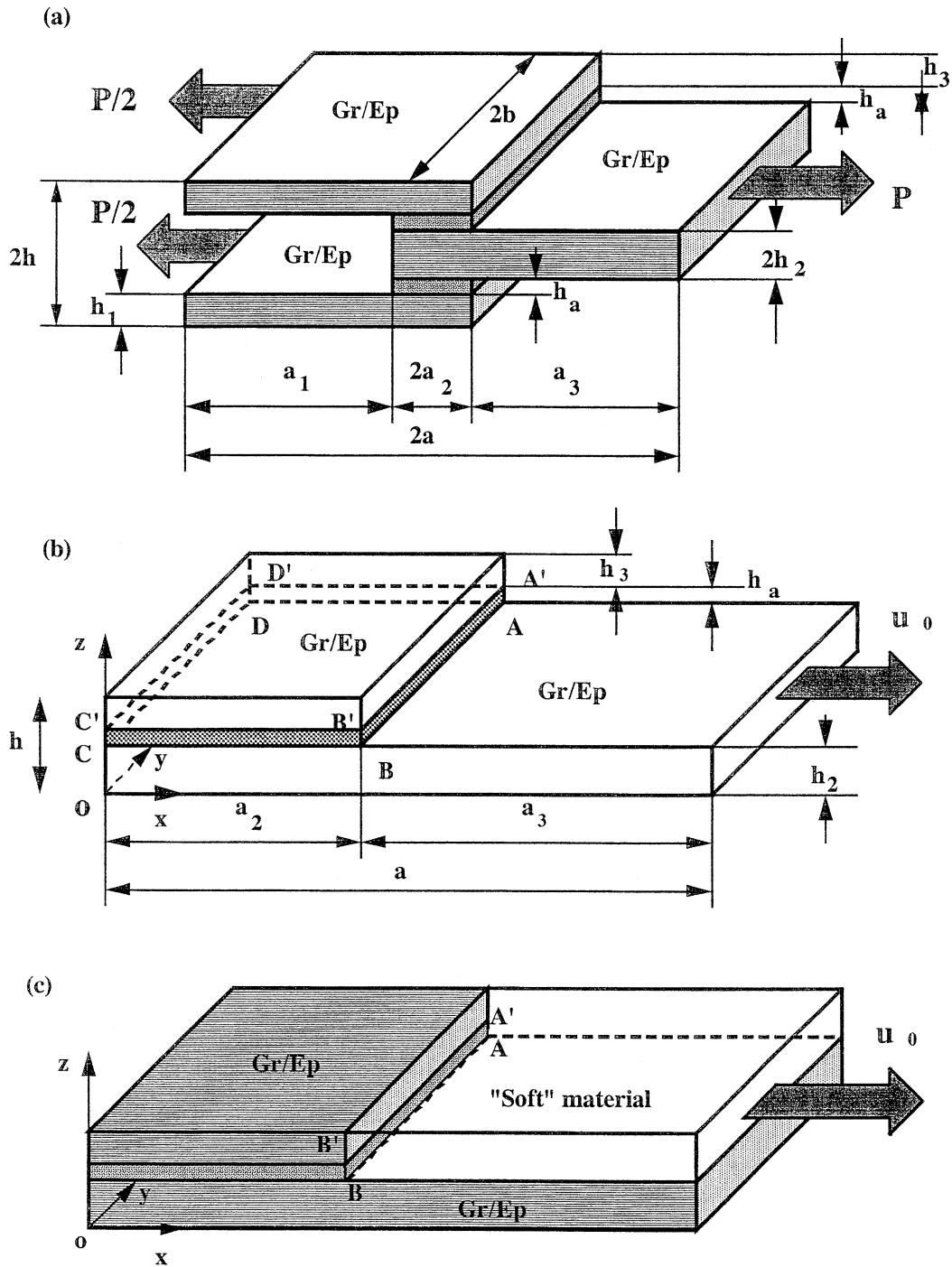


Fig. 5-5. Double-lap composite bonded joint (a), its 1/8th part (b) and mosaic model (c).

following relations are established between the newly introduced coordinates with superscripts and the coordinates with subscripts shown in Fig. 5-4: $x^{(p)} = x_p$, $y^{(q)} = y_q$, $z^{(r)} = z_r$, where

$$P = 1 + \sum_{i=1}^p L_i, \quad Q = 1 + \sum_{j=1}^q M_j \quad \text{and} \quad R = 1 + \sum_{k=1}^r N_k.$$

Further, to characterize nonuniformity of the brick meshes the following parameters are introduced:

$$\xi_{p+1} = \frac{x_{l_p+1} - x_{l_p}}{x_{l_p+2} - x_{l_p+1}}, \quad \eta_{q+1} = \frac{y_{m_q+1} - y_{m_q}}{y_{m_q+2} - y_{m_q+1}}, \quad \chi_{r+1} = \frac{z_{n_r+1} - z_{n_r}}{z_{n_r+2} - z_{n_r+1}} \quad (45)$$

where sets of numbers $\{l_p\}$, $\{m_q\}$ and $\{n_r\}$ are defined as follows

$$\{l_p\} = \sum_{i=1}^p L_i + 1, \dots, \sum_{i=1}^{p+1} L_i - 1; \quad \{m_q\} = \sum_{j=1}^q M_j + 1, \dots, \sum_{j=1}^{q+1} M_j - 1; \quad \{n_r\} = \sum_{k=1}^r N_k + 1, \dots, \sum_{k=1}^{r+1} N_k - 1 \quad (46)$$

Thus, the following set of input parameters fully characterizes the computational brick mesh: $p, q, r, L_{p+1}, M_{q+1}, N_{r+1}, \xi_{p+1}, \eta_{q+1}$, and χ_{r+1} . The mesh pattern can be adjusted to various other problems by simply changing the sets of numbers $\{p\}$, $\{q\}$ and $\{r\}$.

A detailed description of nine 3-D meshes used in this study is given in Tables 5-1 thru 5-4. Third degree Bernstein basis functions, corresponding to $I = J = K = 3$ in (33)-(35) have been

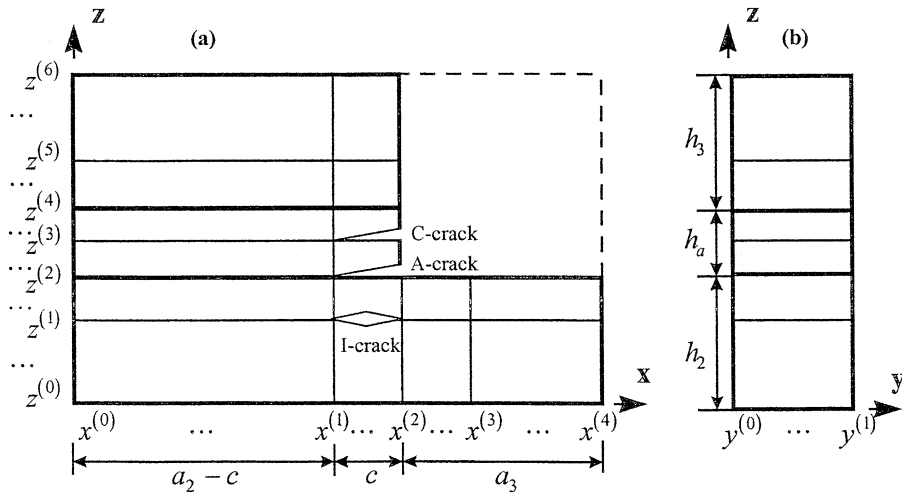


Fig. 5-6: Mesh design in the x - z (a) and y - z (b) planes.

taken for all three coordinate directions.

Table 5-1: Characteristics of the brick meshes in the x -direction

Mesh in x	L_1	ξ_1	L_2	ξ_2	L_3	ξ_3	L_4	ξ_4
X1	4	3.35	1	-	1	-	3	0.14
X2	4	3.35	2	1	2	1	3	0.14
X3	4	3.35	3	1	3	1	3	0.14
X4	3	5.25	2	0.5	1	-	3	0.14

Table 5-2: Characteristics of the brick meshes in the y -direction

Mesh in y	M_1	η_1
Y1	1	-
Y2	2	1
Y3	2	4

Table 5-3: Characteristics of the brick meshes in the z -direction

Mesh in z	N_1	χ_1	N_2	χ_2	N_3	χ_3	N_4	χ_4	N_5	χ_5	N_6	χ_6
Z1	3	1.5	1	-	1	-	1	-	1	-	3	0.5
Z2	3	1.5	2	1	2	1	1	-	1	-	3	0.5
Z3	3	1.5	3	1	3	1	1	-	1	-	3	0.5
Z4	3	1.5	1	-	1	-	1	-	1	-	3	0.5
Z5	3	2	1	-	1	-	1	-	1	-	3	0.3

Table 5-4: Computational variants used in the analysis

Variant No.	Mesh in x	Mesh in y	Mesh in z
1	X1	Y1	Z1
2	X2	Y1	Z1
3	X3	Y1	Z1
4	X1	Y1	Z2
5	X1	Y1	Z3
6	X1	Y2	Z1
7	X1	Y3	Z1
8	X4	Y1	Z4
9	X4	Y1	Z5

First consider numerical results illustrating distributions of the potential energy density of the bricks, defined as $D^{(s)} = \Pi^{(s)} / V^{(s)}$, for the following four cases: (i) without any crack, (ii) with “I-crack” (interlaminar crack) introduced in the middle adherend between the first and second layers closest to the adhesive, (iii) with “A-crack” (adhesive crack) located at the interface between the middle adherend and adhesive, and (iv) with “C-crack” (cohesive crack) located at the mid-thickness of the adhesive layer. Length of all three cracks is taken $c = 0.143mm$ ($0.0056in.$), which corresponds to the thickness of a single unidirectional ply in the adherends, h_p . In all the above cases the cracks occupy entire width of the joint.

Schematic of the brick distribution in the x - z plane is shown in Fig. 5-7. The brick mesh variant No. 1 of Table 5-4 has been used in these computations. The horizontal dimension of Bricks 32 and 33 as well as the vertical dimension of Bricks 32 and 59 are equal to the ply thickness h_p . By noting this the mesh description is completed.

Histograms presented in Fig. 5-8 reveal some interesting features of the potential energy

density distributions $D^{(s)}$ in the joint and its sensitivity to the presence of the interlaminar, adhesive and cohesive cracks. When considering the lower row of bricks, Nos. 1-8, it is seen in Fig. 5-8a that the $D^{(s)}$ is relatively small, its variation is shallow, and it reaches maximum at the loaded end of the middle adherend. Besides, the $D^{(s)}$ distribution is not visibly affected by the cracks. For the second row of bricks, Nos. 10-18, see Fig. 5-8b, the trends are similar. End of the overlap makes a more pronounced effect on the third row of bricks, Nos. 19-27, as seen in Fig. 1.8c. However, the crack effect is still barely visible.

Further, when considering the fourth row of bricks, it is seen in Fig. 1.8d that the maximum of $D^{(s)}$ corresponds to Bricks 32 and 33 which are closest to the corner point. The presence of the C-crack slightly increases $D^{(s)}$ in Bricks 30 and 31 (those gain some extra load) and, at the same time, decreases $D^{(s)}$ in Bricks 32-34. The A-crack effect on the bricks belonging to the same row is quite different: Bricks 30-32 get overloaded while Brick 33 gets significantly unloaded. At the same time the effect of the I-crack is negligible: only Bricks 32 and 33 get slightly overloaded.

Considering the fifth row, see Fig. 5-8e, which contains five bricks of the adhesive, Nos. 37-41 (Nos. 42-45 were prescribed to soft material bricks), it is seen that the highest $D^{(s)}$ is reached

82	83	84	85	86				
73	74	75	76	77				
64	65	66	67	68				
55	56	57	58	59				
46	47	48	49	50				
37	38	39	40	41				
28	29	30	31	32	33	34	35	36
19	20	21	22	23	24	25	26	27
10	11	12	13	14	15	16	17	18
1	2	3	4	5	6	7	8	9

Fig. 5-7: Brick nomenclature for the mesh variant 1 of Table 5-4.

in Brick 41 in both the cases, without cracks or with the I-crack. However, in the presence of the C-crack this brick is partly unloaded, and the maximum of $D^{(s)}$ moves to Brick 40. The effect is even stronger in the presence of the A-crack: Brick 41 stores very little energy while most of the energy is stored in Brick 40.

Results presented for the sixth row of bricks in Fig. 5-8f show again that the I-crack makes a negligible effect. The effect of the A-crack is also very small, except for Brick 50 which now is almost unloaded. The maximum of $D^{(s)}$ is reached in Brick 49 in all four cases. In the presence of the C-crack this brick gets some overload while Brick 50 is almost fully unloaded. Finally, it is seen in Figs. 1.8g and 1.8h that the seventh and eighth rows of bricks store very small portion of the total potential energy, and there is no visible crack effect on the respective $D^{(s)}$ distributions.

All of the discussed details of the energy density distributions seem reasonable from the mechanistic standpoint. Indeed, one could have anticipated *a priori* that the most overloaded part of the joint should be near the corner point, i.e., Bricks 32, 33, 40, 41 and 49, and that the highest potential energy density should be in Brick 40. This expectation is exactly confirmed by the obtained results. Further, one could anticipate that the effect of the I-crack should be most pronounced on Bricks 23, 32 and 33, and this is seen in Figs. 5-8c and 5-8d. The most pronounced effect of the A-crack could have been expected on Bricks 31, 32, 33, 40, 41 and 50 which is clearly shown by Figs. 5-8d, 5-8e and 5-8f. Finally, one could predict that the C-crack would mainly affect Bricks 31, 32, 33, 40, 41, 49 and 50, and this is also evident from Figs. 5-8d, 5-8e and 5-8f. The performed potential energy density analysis is useful for identifying the most loaded sites of the structure and their relocation with the propagation of I-, A- and C-cracks.

Next we present results of the convergence study conducted in this work. Three meshes in the x -direction (see variants 1-3 of Table 5-4) and three meshes in the z -direction (variants 1, 4

and 5) were employed. Numerical results obtained for various structural response characteristics are presented in Tables 5-5 and 5-6 for the analysis cases without any crack and with the A-crack having length $c = h_p$. The following characteristics are given in Table 5-5: $D = \Pi/V$, where Π is total potential energy and V is volume of the structure shown in Fig. 5-5b; $D_\gamma = \Pi_\gamma/V_\gamma$, $\gamma = 1,2,3$, where Π_γ and V_γ are potential energies and volumes of the following regions: $x \in [x^{(1)}, x^{(2)}]$, $z \in [z^{(1)}, z^{(2)}]$ (termed Region 1, corresponds to $\gamma = 1$); $x \in [x^{(2)}, x^{(3)}]$, $z \in [z^{(1)}, z^{(2)}]$ (Region 2, $\gamma = 2$); $x \in [x^{(1)}, x^{(2)}]$, $z \in [z^{(2)}, z^{(3)}]$ (Region 3, $\gamma = 3$). In all three cases $y \in [0, b]$. Further, a sum of the above values, $D_{1-3} = D_1 + D_2 + D_3$, is also presented. Also, the normalized displacements computed exactly at the corner point $(x = x^{(2)}, y = 0, z = z^{(2)})$ are shown in Table 5-5.

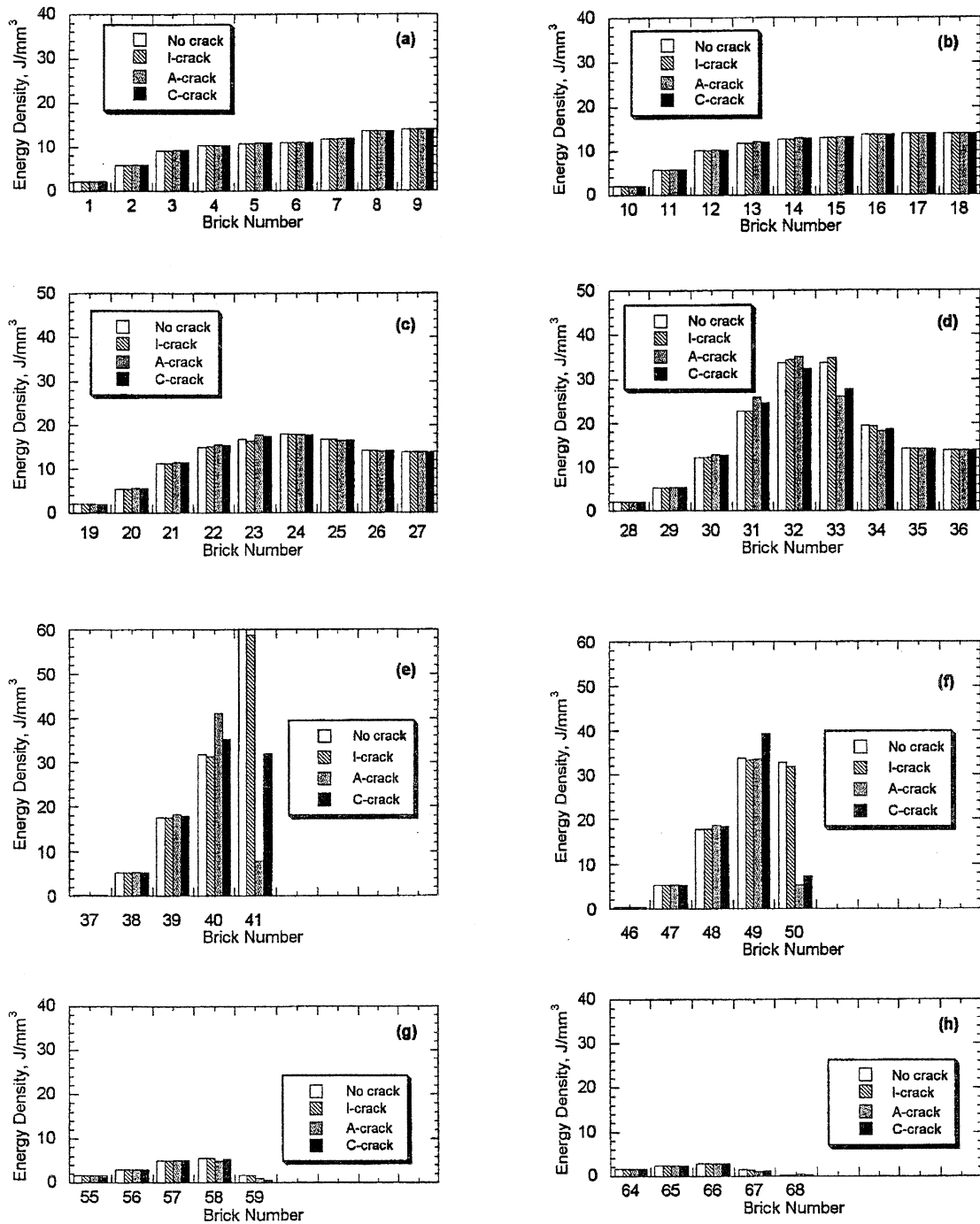


Fig. 5-8: Histogram of the potential energy density distribution in the double-lap bonded joint with unidirectional adherends

Table 5-5. Convergence of the global and local potential energy densities and displacements at the corner point with the mesh refinement in the x- and z-directions.

Mesh variant	D J/mm^3	D_1 J/mm^3	D_2 J/mm^3	D_3 J/mm^3	D_{1-3} J/mm^3	$\frac{u_x(x^{(2)}, 0, z^{(2)})}{u_0}$	$\frac{u_z(x^{(2)}, 0, z^{(2)})}{u_0}$
Without crack							
1	3.7479	34.065	34.613	63.146	131.82	0.1668	0.01111
2	3.7479	34.317	34.468	62.750	131.54	0.1668	0.01105
3	3.7479	34.374	34.437	62.683	131.49	0.1668	0.01103
4	3.7479	34.114	34.696	62.770	131.58	0.1668	0.01125
5	3.7479	34.129	34.708	62.696	131.53	0.1668	0.01128
With the A-crack							
1	3.7435	36.071	26.380	7.7789	70.230	0.1691	0.00457
2	3.7435	36.013	26.362	7.3635	69.739	0.1691	0.00461
3	3.7435	36.002	26.361	7.2962	69.659	0.1691	0.00461
4	3.7435	36.092	26.394	7.7133	70.199	0.1692	0.00455
5	3.7435	36.101	26.386	7.6982	70.185	0.1692	0.00455

Table 5-6 presents three stress components which were averaged over the aforementioned Regions 1, 2 and 3 (the subscript value indicate number of the region) and normalized by the factor

$$\sigma_0 = \frac{1}{bh_2} \int_0^b \int_0^{h_2} \sigma_x(a, y, z) dy dz \quad (47)$$

Table 5-6: Convergence of the averaged stresses computed for local Regions 1, 2 and 3.

Mesh variant	$\frac{\bar{\sigma}_x^{(1)}}{\sigma_0}$	$\frac{\bar{\sigma}_z^{(1)}}{\sigma_0}$	$\frac{\bar{\tau}_{xz}^{(1)}}{\sigma_0}$	$\frac{\bar{\sigma}_x^{(2)}}{\sigma_0}$	$\frac{\bar{\sigma}_z^{(2)}}{\sigma_0}$	$\frac{\bar{\tau}_{xz}^{(2)}}{\sigma_0}$	$\frac{\bar{\sigma}_x^{(3)}}{\sigma_0}$	$\frac{\bar{\sigma}_z^{(3)}}{\sigma_0}$	$\frac{\bar{\tau}_{xz}^{(3)}}{\sigma_0}$
Without crack									
1	1.431	0.1797	0.0917	1.418	0.0684	0.1477	0.0925	0.2248	0.1601
2	1.432	0.1812	0.0920	1.417	0.0663	0.1471	0.0911	0.2241	0.1591
3	1.432	0.1815	0.0922	1.417	0.0660	0.1470	0.0903	0.2239	0.1588
4	1.430	0.1809	0.0916	1.419	0.0681	0.1474	0.0918	0.2243	0.1596
5	1.430	0.1809	0.0918	1.419	0.0680	0.1471	0.0916	0.2242	0.1595
With the A-crack									
1	1.445	0.0843	0.1422	1.328	0.0146	0.0835	-.05093	0.0126	0.0327
2	1.444	0.0832	0.1419	1.328	0.0149	0.0835	-.05003	0.0108	0.0326
3	1.444	0.0830	0.1419	1.328	0.0148	0.0835	-.05028	0.0102	0.0327
4	1.443	0.0844	0.1421	1.328	0.0143	0.0833	-.05076	0.0125	0.0326
5	1.443	0.0841	0.1417	1.328	0.0144	0.0832	-.05071	0.0125	0.0326

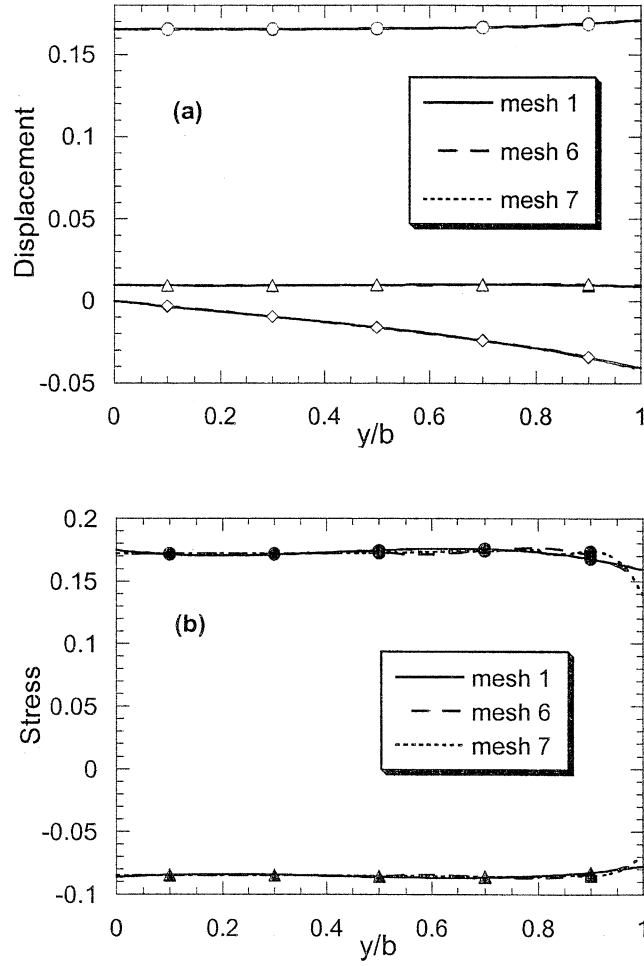


Fig. 5-9: Distributions of the displacements (a) u_x/u_0 (\circ), u_y/u_0 (\diamond) and u_z/u_0 (\triangle) and stresses (b) σ_z/σ_0 (\bullet), τ_{xz}/σ_0 (\blacktriangle) along the y -coordinate at $x = a_2 - h_p/2$, $z = h_2 - h_p/2$ calculated with mesh variants 1, 6, and 7 of Table 5-4.

Results presented in Tables 5-5 and 5-6 clearly show convergence of all of the considered characteristics. Interestingly, the total potential energy density, D , is absolutely insensitive to the mesh refinement. This is not a surprise, because this is the objective function minimized in the present variational analysis. Local potential energy densities, D_1 , D_2 , D_3 and D_{1-3} , show small fluctuations. The displacements at the corner point, where stresses may be singular, show clear convergence. Moreover, for all three local regions considered, the averaged stresses have undoubtedly converged. Thus, if desired, these computed stresses can be utilized for the purpose

of local failure prediction, by applying them in conjunction with some mathematical failure criterion (the maximum stress criterion and numerous variants of the tensor polynomial criterion can be mentioned as examples).

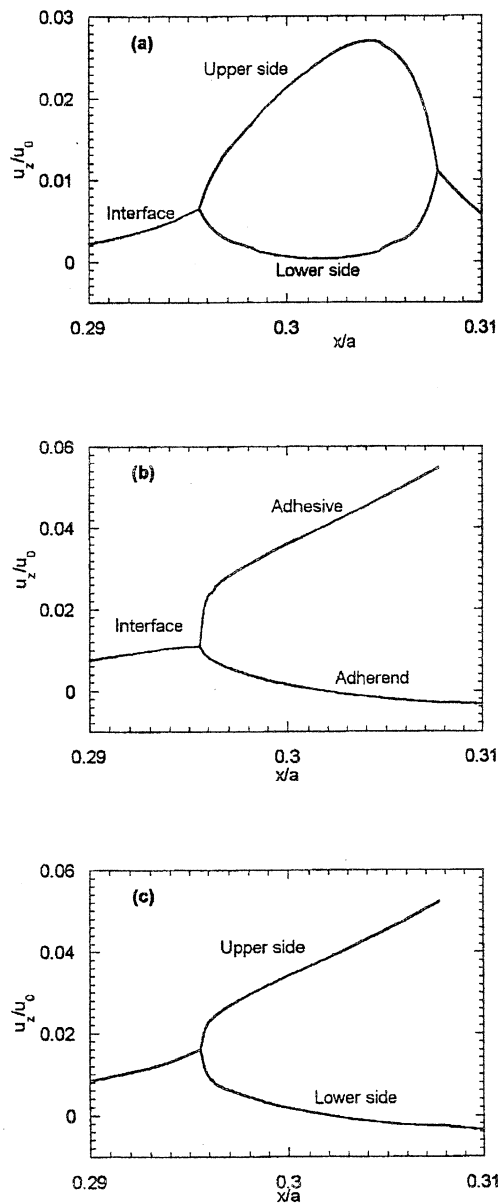


Fig. 5-10: Variations of the displacement corresponding to the I-crack (a), A-crack (b) and C-crack (c) opening in the case of unidirectional adherends

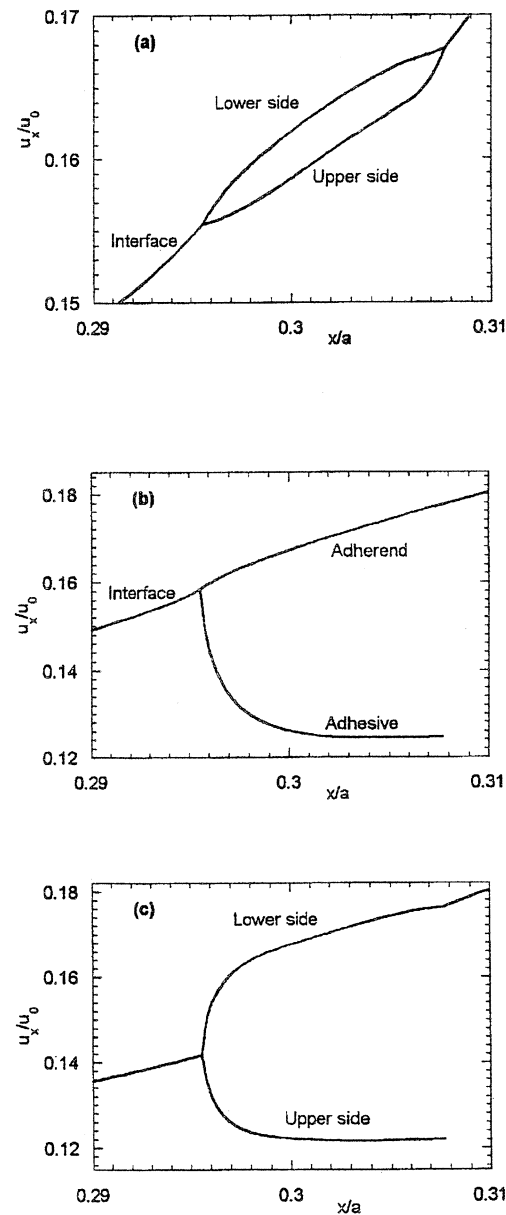


Fig 5-11: Variation of the displacements corresponding to the I-crack (a), A-crack (b) and C-crack (c) sliding in the case of unidirectional adherends

In order to illustrate a 3-D capability of the developed analysis, numerical results showing variations of the normalized displacements and stresses along the y -coordinate are presented in Fig. 5-9 for the meshes of bricks 1, 6 and 7 of Table 5-4. It is seen that the mesh refinement does not visibly affect the displacement variations, however the nonuniform mesh (variant No. 7) makes some effect on the stress variations. Note that the displacements u_x and u_z show very small variation along the y -coordinate while the variation of u_y is close to a linear function (this is owed to the absence of any constraint at the lateral surface $y = b$). It has to be pointed out that the edge effect is more pronounced for the stresses.

Our next objective is to proceed with the crack propagation analysis. First, it has to be mentioned that, according to the obtained prediction, the starter cracks introduced at the end of the overlap would open under the loading. Local distributions of the opening (Mode I) displacement u_z and sliding (Mode II) displacement u_x are shown in Figs. 5-10 and 5-11 for the above three types of crack. The starter I-crack was placed in the middle adherend at the interface between the first and second layers nearest to the adhesive. In the case of the A-crack the displacements were plotted for the adhesive-adherend interface from the side of middle adherend, $z = h_2 - 0$, and from the side of adhesive, $z = h_2 + 0$. In the case of the C-crack the displacements are shown for the mid-thickness of the adhesive layer. The results indicate that both the opening and sliding fracture modes take place for all three types of crack at the end of the overlap. The magnitudes of opening displacements for the cases of A- and C-cracks are close while the I-crack opening is about twice smaller. Also, it is seen that for all three types of crack the sliding and opening mode displacements are of the same order of magnitude. This indicates that in the problem under consideration the fracture Modes I and II are both significant. Thus, the example reveals a typical case of Mixed Mode I-II fracture.

The dependencies of the calculated ERR are shown for the same three types of crack in Fig.

5-12. The applied displacement magnitude is taken $u_0 = 0.2mm$. It is seen that the ERR values for the A- and C-cracks are very close and, at the same time, have much higher magnitudes than that for the I-crack. This shows that the propagation of a starter I-crack can only be expected if there is a very poor bonding between the composite layers. The cohesive crack propagation is also unlikely, because its CERR, G_c , is significantly higher than that of an adhesive crack (in particular, this was shown by experimental results [21] for the same bonded composite material and adhesive system as considered here). Thus, the highest possibility of failure in the initial stage of the process should be attributed to the adhesive crack propagation.

It is seen in Fig. 5-12 that the ERR variation with the crack length is qualitatively different for the I-crack than for the A- and C-cracks. In the case of the I-crack, a maximum of G variation is reached for about $0.5mm$ long crack, then at the crack length $1.4mm$ there is a G minimum, after which a monotonic growth takes place. For the other two types of crack there is only a maximum of G which corresponds to approximately $1.8mm$ long crack. This result may be helpful in understanding the advanced stage of the joint failure, where the I-crack propagation has been observed as the dominating failure mode [12].

The developed analysis enables predicting some other useful characteristics of the progressive failure process. In particular, variation of the “global” (averaged) longitudinal stiffness of the joint, which is defined according to the formula

$$\langle C_x \rangle = \frac{a}{u_0} \frac{1}{bh_2} \int_0^b \int_0^{h_2} \sigma_x(a, y, z) dy dz = \sigma_0 \frac{a}{u_0} \quad (48)$$

have been computed as function of the crack length for the I-, A- and C-crack cases. The results presented in Fig. 5-13 show that the global stiffness reduction is very small for the I-crack and more pronounced for the A- and C-cracks. However, even for the cracks $5mm$ long, the global stiffness reduction of the joint is only about 4%. This may be explained by the in-plane loading

direction and the in-plane crack orientation in the problem under consideration.

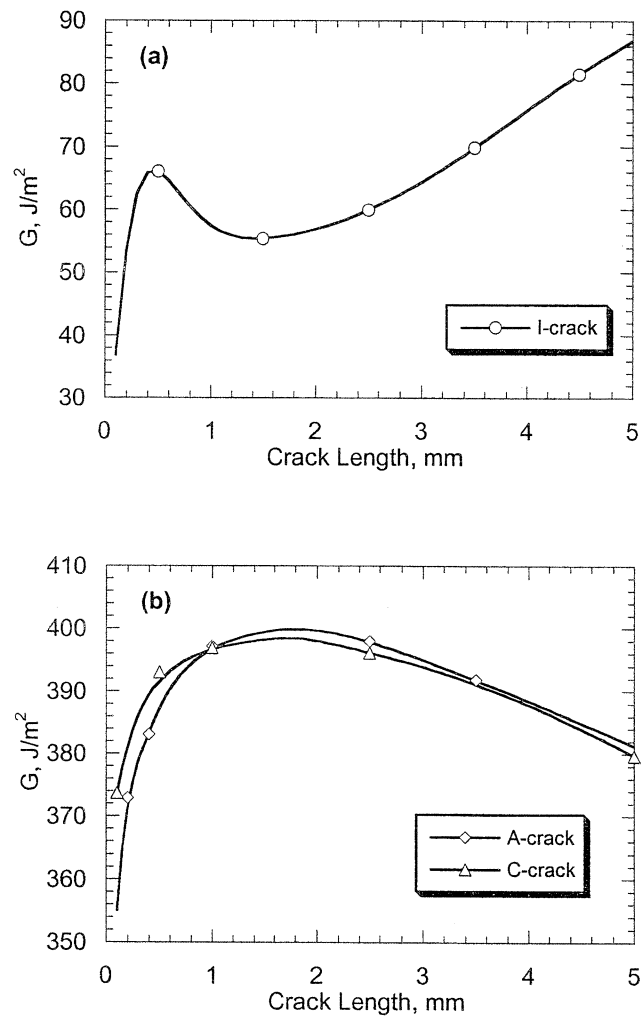


Fig. 5-12: Dependencies of the energy release rate on the crack length at $u_0 = 0.2 \text{ mm}$ in the case of unidirectional adherends.

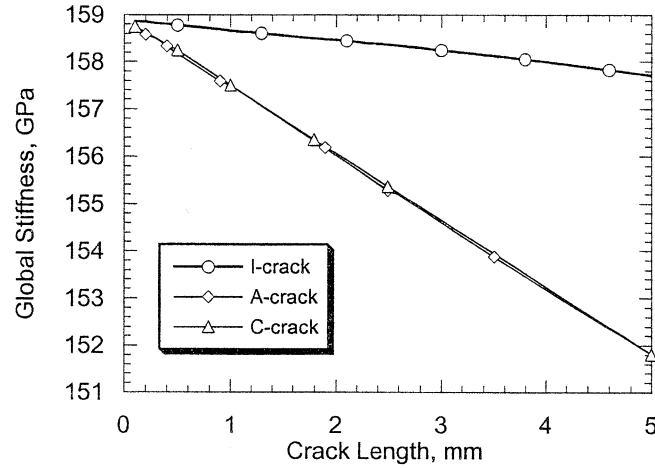


Fig. 5-13: Variations of the global stiffness (1.48) with the crack length in the case of unidirectional adherends.

Further, Fig. 5-14 illustrates variation of the “critical” applied displacement u^* as a function of crack length. The above critical displacement is defined as such value of u_0 which drives the starter crack to the given length. Due to the uncertainty in experimental values of the CERR for all three types of crack under consideration (and, especially, keeping in mind that a Mixed Mode I-II fracture has been predicted), the curves in Fig. 5-14 were plotted for several values of CERR. A similar type of illustration, but for the case of applied stress, is shown in Fig. 5-15. The “critical” applied stress, σ^* , is defined as such magnitude of σ_0 (48) under which the starter crack propagates to a given length. The above results allow one to evaluate various possibilities of the crack propagation, under the prescribed displacement or load, and to also define the critical displacement and critical stress magnitudes assuming that the required CERR values are known. However, if those are not known exactly, a bunch of curves shown in Figs. 5-14 and 5-15 may be of use.

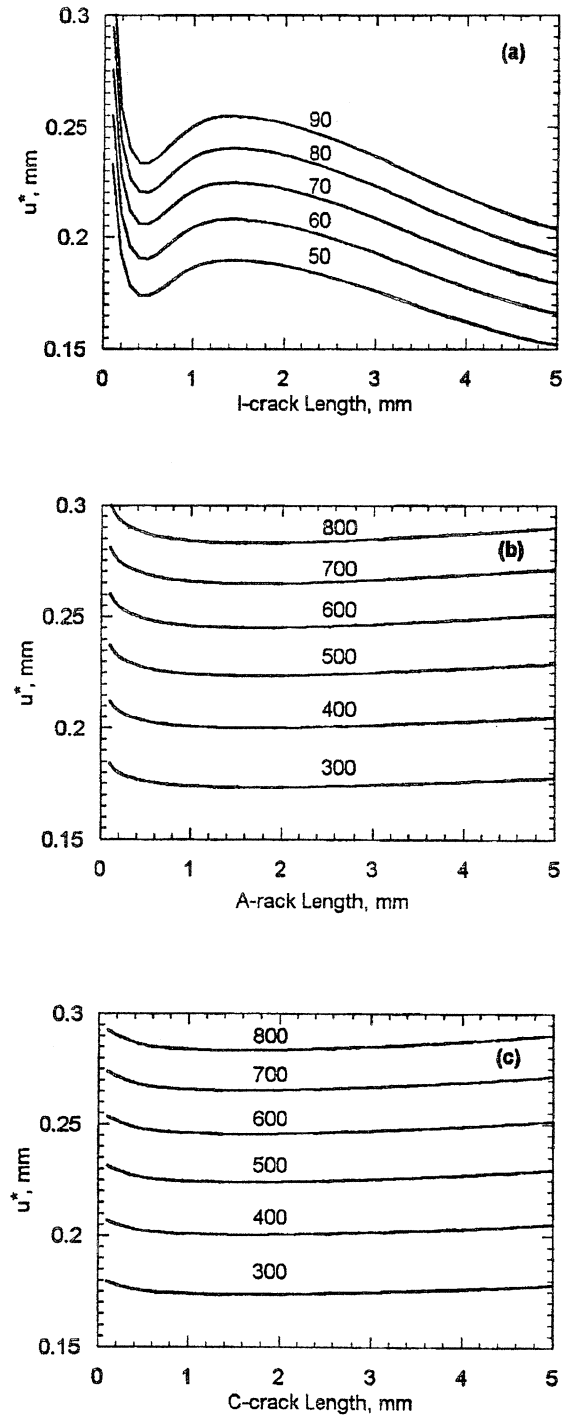


Fig. 5-14: Dependencies of the critical applied displacement on the crack length for the I-crack (a), A-crack (b) and C-crack (c) in the case of unidirectional adherends. Values at the curves indicate the critical strain energy release rate in J/m^2 .

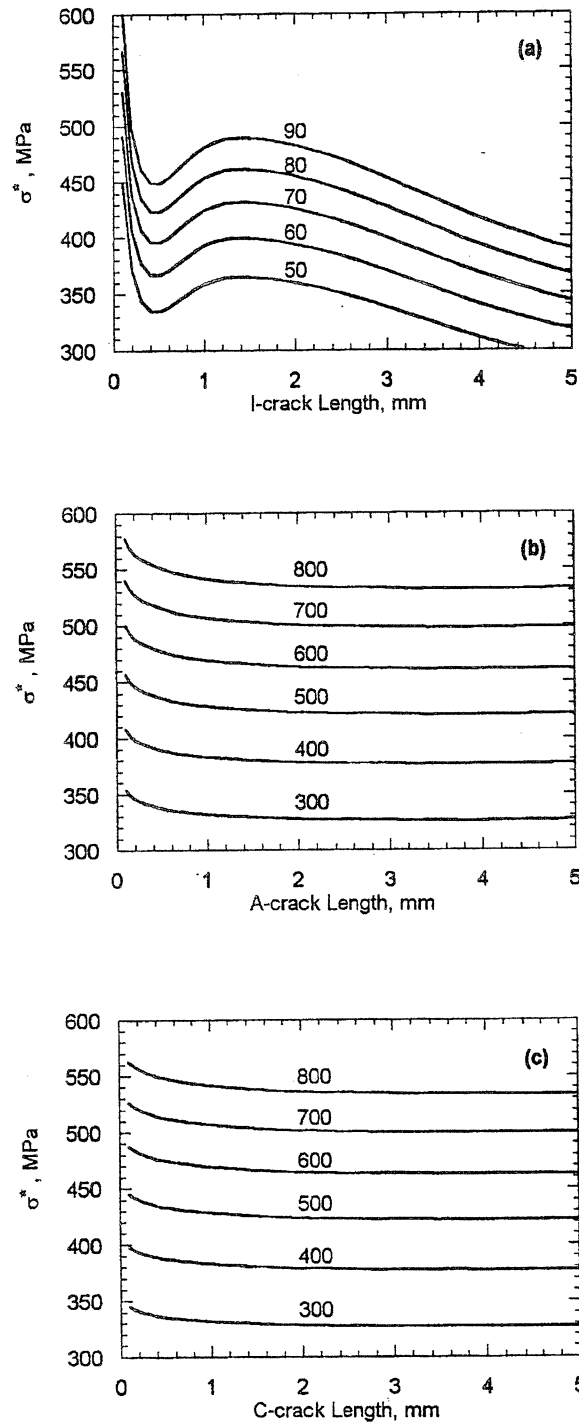


Fig. 5-15: Dependencies of the critical applied stress on the crack length for the I-crack (a), A-crack (b) and C-crack (c) in the case of unidirectional adherends. Values at the curves indicate the critical strain energy release rate in J/m^2 .

Results of the experimental study aimed at defining CERR for bonded unidirectional T300/5208 composites with FM-300 adhesive have been reported in [21]. According to those, the CERR for the adhesive type of crack is about $500J/m^2$. Hence, referring to Figs. 5-14b and 5-15b, the adhesive starter crack having length $1mm$ should propagate under the applied displacement value $0.225mm$ or applied stress value $425MPa$. If the applied displacement is kept constant, the starter crack propagates until it reaches $4mm$ length, and then stops. To a contrary, the crack does not stop if the stress level is kept constant.

The CERR value for a cohesive crack type is, according to [21], significantly higher than $500J/m^2$. Accordingly, results shown in Figs. 5-14b and 5-14c indicate that the A-crack propagation would be a more likelihood event. Further, the I-crack propagation, according to Fig. 5-14a, can not be expected in the whole considered range of the applied displacement magnitudes, because experimental values of the CERR for the interlaminar fracture of unidirectional T300/5208 composite, according to different authors, is in the range between 250 and $300J/m^2$.

Our next objective is to compare the predicted failure loads with the experimental data of [12], where the following ultimate failure stress values were obtained for different surface preparation techniques: $501MPa$ (acetone wash), $439MPa$ (hand sanding), $469MPa$ (grinding), and $453MPa$ (grit blasting). It is seen that all of them are higher than the stress value $425MPa$ which corresponds to the predicted A-crack propagation at the initial stage of failure. On the other hand, it was observed in [12] that initial cracks appeared at about 70% of the ultimate load which yields, in the case of acetone wash, $350MPa$. Thus, the predicted fracture initiation load is in the interval between the experimental fracture initiation load and the ultimate failure load. At this point we cannot present a more precise comparison due to the following reasons:

- (a) as was shown above, the Mixed Mode I-II fracture is predicted for the structure under

consideration; however, the respective CSERR values are not available;

- (b) the analysis results reported here did not account for a mutual interaction between the I-, A- and C-cracks;
- (c) as was observed in [12], the major crack propagated *inside* the top layer of the middle adherend; rigorously, that crack is not the same as the I-crack considered in the analysis;
- (d) the analysis did not consider possible intra-ply damage in the adherends, which would favourably affect the I-crack propagation.

The issue (a) can be only resolved by conducting suitable experiments. The issues (b) and (c) can be studied by analytical tools presented here. In order to address issue (d), it is necessary to incorporate in the analysis some damage mechanics approach (specifically, a reasonable local stiffness reduction scheme). It is anticipated that if taking into account the effects (b)-(d), a more precise and complete comparison between the experimental phenomena observed in [12] and theoretical predictions will be obtained, and this will reduce the gap between the experimental and analytical failure loads.

5.5 Analysis of Double-Lap Joint with Cross-Ply Composite Adherends

Next example considers the same double-lap bonded joint having geometric parameters (41), but with the cross-ply symmetric adherend lamination. Like before, each adherend is made from 16 plies of unidirectional Graphite/Epoxy tape AS4/3501-6 having elastic characteristics (42). The outer plies in all adherends are reinforced in the x -direction. The same adhesive film Cytec FM300-2K with elastic properties (43) is considered. The geometric boundary conditions (44) apply. An experimental study of this kind of the bonded joint specimens was performed in [13].

In order to reduce computational size of the problem, we apply here a partial “smearing” of the laminated adherends. A 16-ply, $[0/90^\circ]_{4s}$, laminate is reduced to a 3-layer laminate having the same total thickness, but composed from two original plies maintaining their actual orientations, 0° and 90° , and the third, thick “smeared” layer representing 14 other plies as a homogeneous orthotropic material. Effective stiffnesses of the latter one have been calculated using equations (5.50) of [22]. Structure of the upper half of the joint with the partially smeared cross-ply laminated adherends is shown in Fig. 5-16.

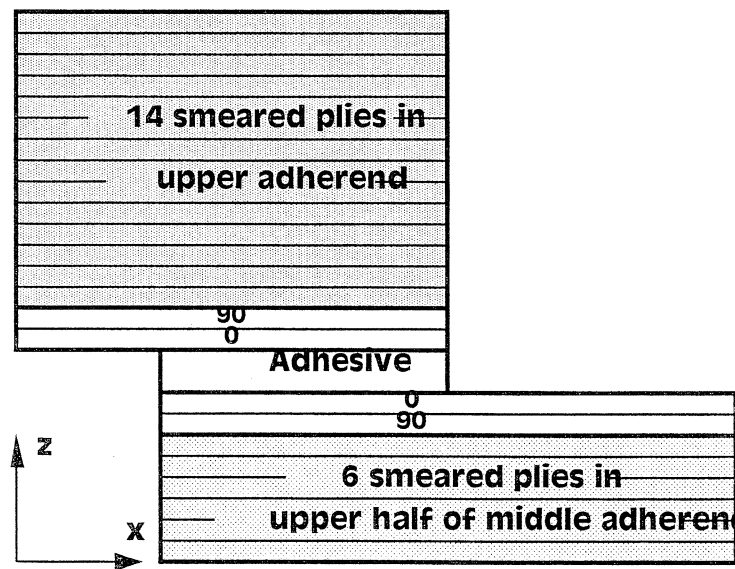


Fig. 5-16: Smearing scheme of the laminated adherends.

Results presented in this section were obtained using the mesh variant No. 9 of Table 1.4. The normalized opening and sliding displacements at the end of the overlap are given in Figs. 1.17 and 18. When comparing these results with the respective results in Figs. 1.9 and 1.10 it is seen that the adherend lamination has very little effect on the A- and C-crack openings. A slight difference is observed only for the interlaminar crack, which has smaller sliding displacements and also smaller crack opening in the case of the cross-ply lamination. Like in the case of unidirectional adherends, the joint with cross-ply adherends show Mixed Mode I-II fracture for all three types of crack.

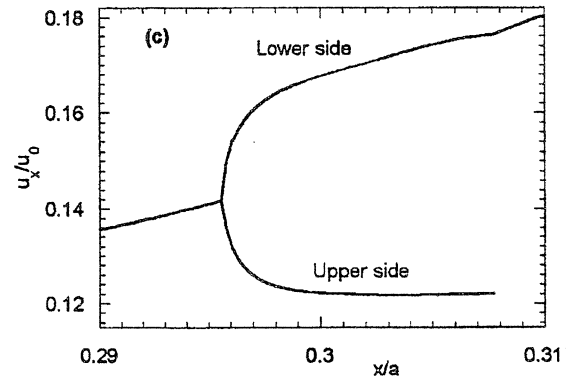
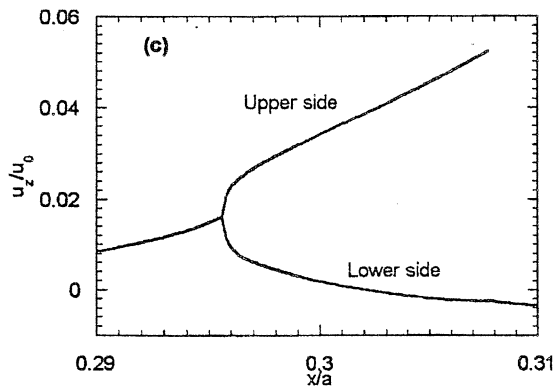
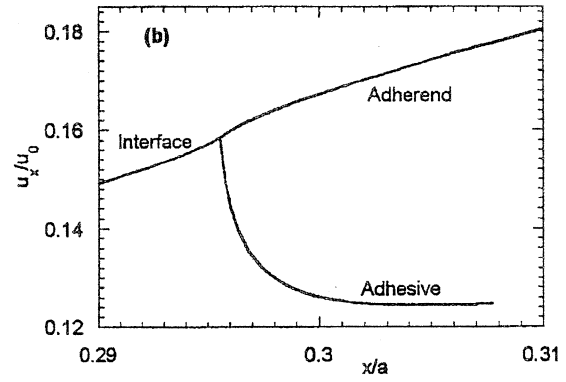
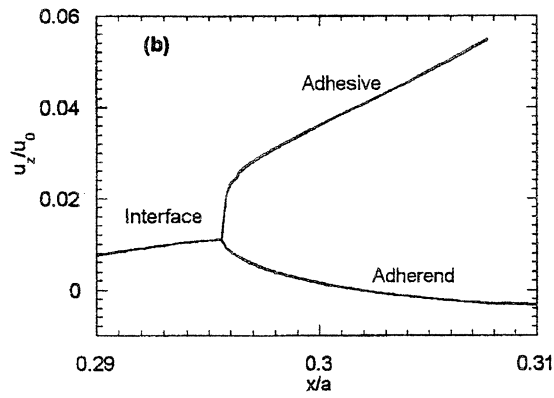
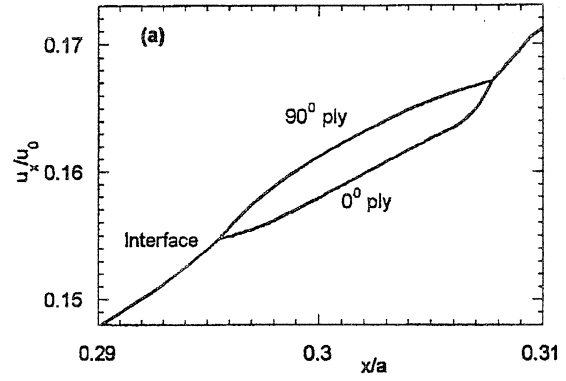
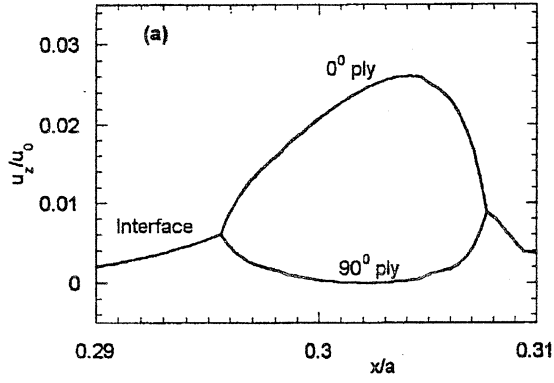


Fig. 5-17: Variations of the displacements corresponding to the crack opening mode for the I-crack (a), A-crack (a0 and C-crack (c) in the case of $[0^\circ / 90^\circ]_{45}$ adherends

Fig. 5-18: Variations of the displacements corresponding to the crack sliding mode for the I-crack (a), A-crack (a0 and C-crack (c) in the case of $[0^\circ / 90^\circ]_{45}$ adherends

Variations of the “global” stiffness of the joint, defined earlier by (1.48), versus the I- and A-crack lengths are shown in Fig. 5-19. Similarly to the case of unidirectional adherends (see Fig. 5-12), the effect of the I-crack is very small while the 7mm long A-crack reduces this structural characteristic by 3%.

A comparison of the variations of the ERR with increasing length of the I- and A-cracks is shown in Fig. 5-20. Similarly to the case of unidirectional adherends (see Fig. 5-11), the G values in the case of cross-ply adherends are significantly higher for the A-crack than for the I-crack, however the difference in Fig. 5-20 is relatively smaller than in Fig. 5-11. Again, it is noticed that the G -variation has only a maximum in the case of the A-crack while both the maximum and minimum are present in the case of the I-crack. This qualitatively distinct behavior can be useful for an explanation of the advanced stage of crack propagation. Indeed, as seen in Fig. 5-21a, if one had assumed the CERR for the I-crack being $200J/m^2$ and for the A-crack being $500J/m^2$, then the predicted crack propagation process would occur as a mixture of the A- and I-crack growths. Specifically, below the applied displacement $0.35mm$ no crack growth is predicted. If the applied displacement were $0.39mm$ then the starter A-crack having length $0.2mm$ would grow to the length $3mm$ and then stop. With the applied displacement $0.42mm$ both the A- and I-cracks would grow: the A-crack to the length $4mm$ and the starter I-crack having length $0.2mm$ to the length $0.8mm$. If the applied displacement were $0.42mm$, then the A-crack would grow to $7mm$ and stop while the I-crack would show an unstable growth. It is also seen from Fig. 5-21b that if a very poor interlaminar bonding of the composite were assumed, say $100J/m^2$, then an unstable I-crack propagation would occur under the applied displacement $0.37mm$ while the A-crack would only propagate from the length $0.4mm$ to $2.4mm$. Analogous trends are recognized in the case of the applied stress, see Fig. 5-22.

Experimental results reported in [13] show that the ultimate failure load for the adherends with cross-ply lamination $[0/90^\circ]_{4s}$, which was solved in the above analytical example, is 337MPa . Similarly to the case of unidirectional adherends, the major crack observed in this type of experimental specimen has grown within the middle adherend in the upper 0° ply, near the adhesive interface. The present theoretical predictions for the failure initiation loads are: 380MPa (the A-crack propagation) if assuming the CERR values as in Fig. 5-22a, and 300MPa (the I-crack propagation) if assuming the CERR values as in Fig. 5-22b. This comparison just

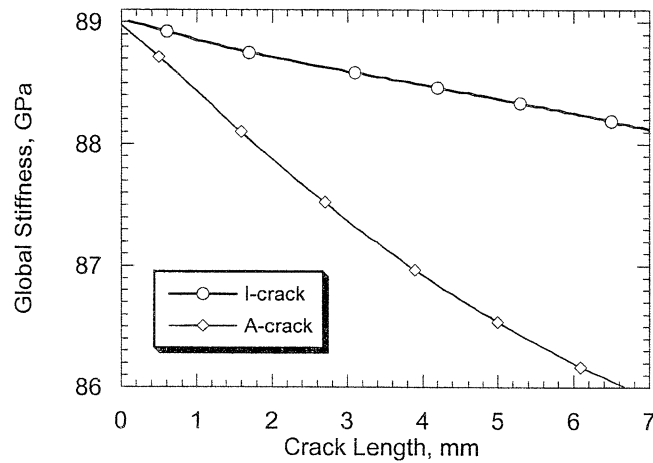


Fig. 5-19: Variations of the global stiffness (48) on the crack length in the case of $[0^\circ / 90^\circ]_{4s}$ adherends.

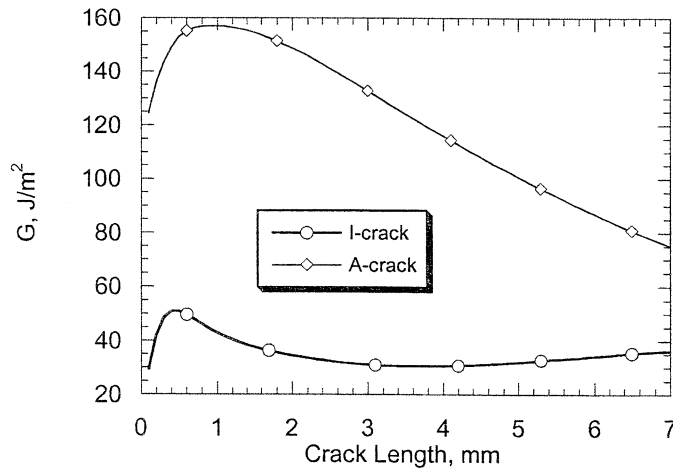


Fig. 5-20: Dependencies of the energy release rate on the crack length at $u_0 = 0.2 \text{ mm}$ in the case of $[0^\circ / 90^\circ]_{4s}$ adherends.

indicate that the experimental ultimate failure load and the predicted failure initiation load are in the same range. A more detailed comparison will be possible after conducting additional analytical and experimental work, as discussed in the previous section.

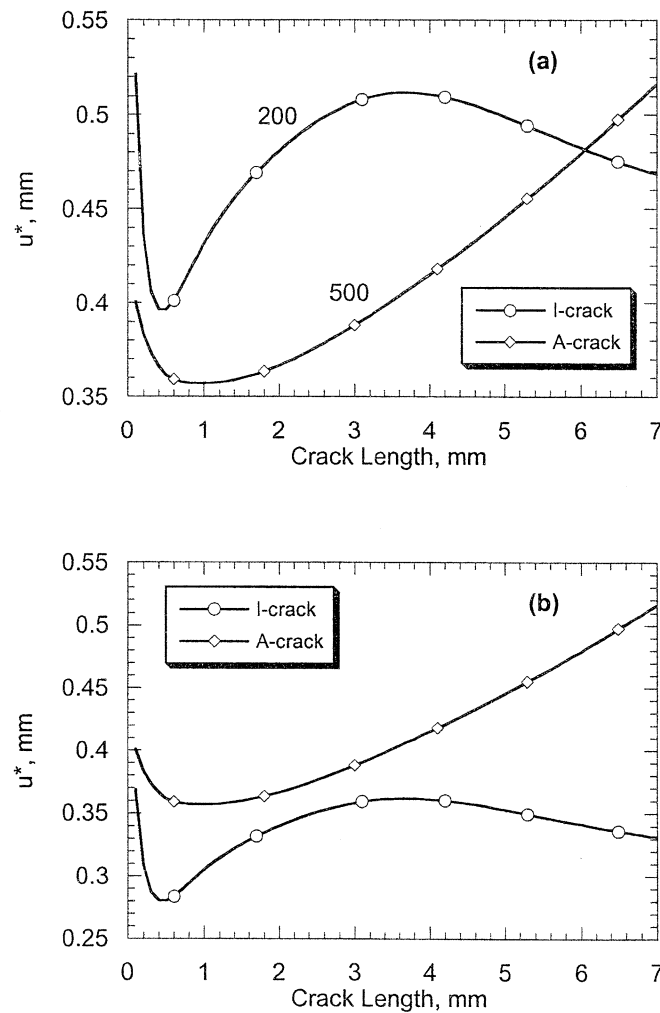


Fig. 5-21: Dependencies of the critical applied displacement on the crack length for the I- and A-cracks in the case of $[0^\circ / 90^\circ]_{4s}$ adherends. Values at the curves indicate the critical strain energy release rate in J/m^2 .

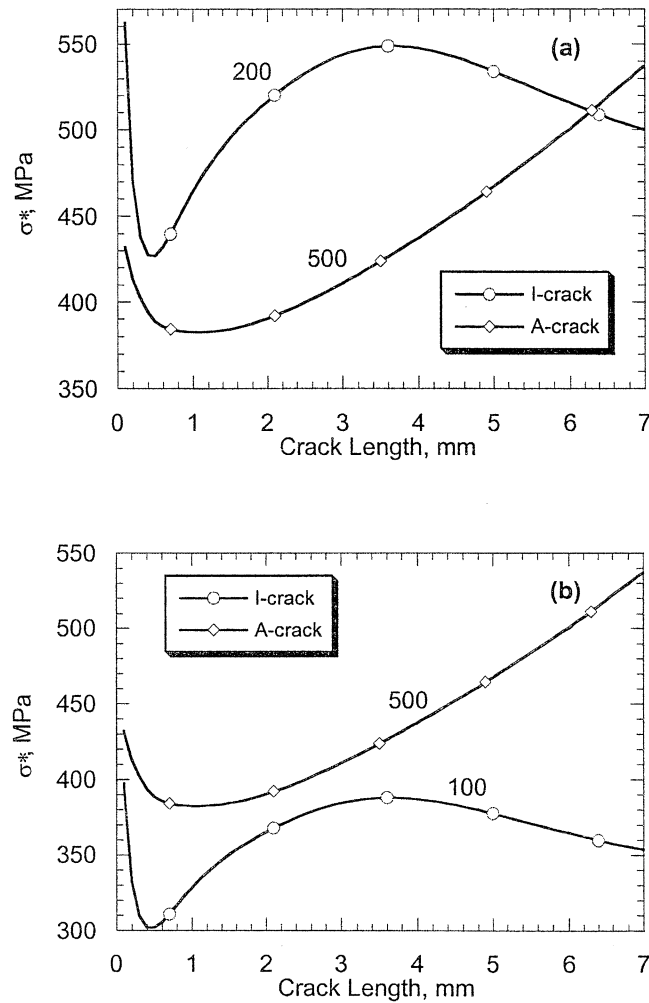


Fig. 5-22. Dependencies of the critical applied stress on the crack length for the I-and A-cracks in the case of $[0^\circ / 90^\circ]_{4s}$ adherends. Values at the curves indicate the critical strain energy release rate in J/m^2 .

5.6 Conclusions

The developed variational 3-D Mosaic Model analysis enables solving various problems of a planar crack propagation in composite structures and, particularly, in composite bonded joints, by numerically evaluating the total potential energy release rate and further applying the critical energy release rate criterion.

Specific results obtained for the double-lap adhesive bonded joints with unidirectional and cross-ply composite adherends show that there are significant qualitative distinctions between the

adhesive or cohesive crack propagation on one side, and the interlaminar crack propagation on the other side. Also, it has been revealed that during the initial stage of failure, the adhesive crack is more likely to propagate than the cohesive or interlaminar cracks. However, the interlaminar crack propagation may become a dominant failure mechanism at the advanced stage of failure, especially if accompanied by such effects as the crack interaction and dispersed damage in the composite adherends.

A preliminary quantitative comparison of the obtained theoretical predictions with the available experimental data for the unidirectional and cross-ply composite bonded joints show that there is certain correspondence between the analytical and experimental results, though the problem is far from being solved. Further theoretical developments and comprehensive numerical studies, along with a more detailed experimental investigation of failure processes in composite bonded joints are needed.

An extensive set of numerical results presented in this report for the energy density distributions, locally averaged stresses, crack opening and sliding displacements, variations of the energy release rates with the crack length, global stiffness reductions due to the crack growth, as well as the computed critical applied displacement and stress magnitudes, can be useful for the numerical comparisons of other analysis methodologies and computer codes.

REFERENCES

- (1) Ripling, E. J., Mostovoy, S., and Patrick, R. L., Application of Fracture Mechanics to Adhesive Joints, in: *Adhesion, ASTM STP 360*, ASTM, Philadelphia, PA, 1963, 5-19.
- (2) Malyshev, B. M. and Salganik, R. L., The Strength of Adhesive Joints Using the Theory of Cracks, *Int. J. of Fracture*, 1965, **1**, 114-128.
- (3) Irwin, G. R., Fracture Mechanics Applied to Adhesive Systems, Chapter 7 in: *Treatise on Adhesion and Adhesives, Vol. I: Theory* (Edited by R. L. Patrick), Marcel Dekker, New York, 1967, 233-267.

- (4) Ripling, E. J., Mostovoy, S., and Corten, H., Fracture Mechanics: A Tool for Evaluating Structural Adhesives, *J. Adhesion*, 1971, **3**, 107-123.
- (5) Mostovoy, S., Ripling, E. J., and Bersch, C. F., Fracture Toughness of Adhesive Joints, *J. Adhesion*, 1971, **3**, 125-144.
- (6) Anderson, G. P., Devries, K. L., and Williams, M. L., Finite Element in Adhesion Analysis, *Int. J. of Fracture*, 1973, **9** (4), 421-435.
- (7) Kinloch, A. J., Interfacial Fracture Mechanical Aspects of Adhesive Bonded Joints-A Review, *J. Adhesion*, 1979, **10**, 193-210.
- (8) Kinloch, A. J. and Shaw, S. J., A Fracture Mechanics Approach to the Failure of Structural Joints, Chapter 3 in: *Developments in Adhesives -2* (Edited by A. J. Kinloch), Applied Science Publishers, London and New Jersey, 1981, 83-124.
- (9) Renton, J. W. and Vinson, J. R., On the Behavior of Bonded Joints in Composite Material Structures, *Engnr. Fracture Mechanics*, 1975, **7**, 41-60.
- (10) Adams, R. D., Strength Predictions for Lap Joints, Especially with Composite Adherends. A Review, *J. Adhesion*, 1989, **30**, 219-242.
- (11) Long, R. S., Static Strength of Adhesively Bonded ARALL-1 Joints, *J. of Composite Materials*, 1991, **25**, 391-415.
- (12) Donaldson, S. L. and Roy, A. K., Experimental Studies on Composite Bonded Joints, *Proc. of ICCM-11, Gold Coast, Australia*, 14-18 July 1997, **V**, pp. 444-455.
- (13) Roy, A. K., Donaldson, S. L., and Schoeppner, G. A., Bonded Joints of Unidirectional and Cross-Ply Laminates: An Experimental Study, *A Collection of Technical Papers, 38th AIAA/ASME/ASCE/AHS /ASC Structures, Structural Dynamics, and Materials Conference*, April 7-10, 1997, Kissimmee, FL, **Pt. 3**, AIAA paper 97-1121, pp. 1994-2003.
- (14) Venkayya, V. B. and Tischler, V. A., A Review of Composite Joint Analysis Programs, *The 83rd Meeting of the AGARD Structures and Materials Panel, Florence, Italy, 2-3 September 1996, Conference Proceedings 590, Bolted/Bonded Joints in Polymeric Composites*, NATO publication, pp. 3.1-3.

- (15) Bogdanovich, A. E. and Yushanov, S. P. "Three Dimensional Variational Analysis of Paganos' Problems for Laminated Composite Plates," *Journal of Composites Science and Technology*, 2000, in press.
- (16) Bogdanovich, A. E. and Yushanov, S. P., 3-D Progressive Failure Analysis of Bonded Composite Joints, *A Collection of Technical Papers*, 39th AIAA/ASME/ASCE/AHS/ASC Structures, Structural Dynamics, and Materials Conference, April 20-23, 1998, Long Beach, CA, AIAA paper 98-1888.
- (17) Bogdanovich, A. E., Three-Dimensional Analysis of Anisotropic Spatially Reinforced Structures, *Fiber-Tex 1992, The Sixth Conference on Advanced Engineering Fibers and Textile Structures for Composites* (Edited by John D. Buckley), Philadelphia, PA, 1992, NASA Conference Publication 3211, pp. 271-304; also *Composites Manufacturing*, 1993, 4, 173-186.
- (18) Davis, P. J., *Interpolation & Approximation*, Dover Publications, New York, 1975.
- (19) Cook, W. A., The Calculation of Strain Energy Using Finite Element Computer Programs, Appendix 1 of paper "Finite Element in Adhesion Analyses" by G. P. Anderson, K. L. Devries, and M. L. Williams, *International Journal of Fracture*, 1973, 9 (4), 431-432.
- (20) Johnson, W. S., Stress Analysis of the Cracked-Lap-Shear Specimen: An ASTM Round Robin, *Journal of Testing and Evaluation*, 1987, 15, 303-324.
- (21) Mall, S. and Johnson, W. S., Characterization of Mode I and Mixed-Mode Failure of Adhesive Bonds Between Composite Adherends, in: *Composite Materials: Testing and Design, Seventh Conference, ASTM STP 8* American Society for Testing and Materials, Philadelphia, PA, 1986, 322-334.
- (22) Bogdanovich, A. E. and Pastore, C. M., *Mechanics of Textile and Laminated Composites*, Chapman & Hall, London, 1996.
- (23) Kinloch, A. J., *Adhesion and Adhesives. Science and Technology*, Chapman & Hall, London-New York, 1987.

6.0 FINITE ELEMENT ANALYSIS OF COMPOSITE BONDED JOINTS WITH ACCOUNT OF A SPEW FILLET

6.1 Introduction

The 3-D finite element analysis results presented in Section 4, Part B were obtained using submodeling technique available in ABAQUS. It was assumed that the adhesive terminates in a square end of the overlap. In reality, a fillet of adhesive (called the spew) exists in any bonded joint. As was noted in [1], it would be difficult to completely remove the spew by machining without machining either of the adherends. Moreover, machining would also initiate cracks in the adhesive. Thus, considering adhesive layer with a perfect square edge without cracks in the adhesive has to be viewed as the mathematical abstraction which can be hardly realized in practice.

The effect of spew fillet on the stress/strain distributions in adhesive bonded joints has been studied both theoretically and experimentally [1]-[8]. All of the known theoretical work was performed using finite element method. Specifically, various 2-D plane strain elements were applied, while the only 3-D analysis can be found in [7], where constant strain element has been used. Aluminium adherends were considered in most of the above works, with the exception of [5] where the adherends were steel and carbon fiber composites, [6] where the adherends were ARALL-1 laminates with various fractions of the aluminium and composite layers, and [8] where laminated graphite/epoxy adherends were used. Single-lap bonded joints were studied in [1], [2], [4], [6], [7], [8], while double-lap bonded joints were considered in [3], [5] and [6]. The loading case in all of the above studies was uniaxial in-plane tension.

This chapter presents stress analysis of double-lap composite bonded joint solved using submodeling technique available with ABAQUS finite elements. Details of its application to the problems of adhesive bonded joints can be found in Section 1 thru 4. The problem is treated in a 2-D formulation with the use of rectangular and triangular plane stress elements.

6.2 Analysis Approach

A double lap composite bonded joint under consideration is illustrated in Fig. 6-1. Schematic of the conventional spew models is shown in Fig. 6-2. Usually, it is assumed that the spew is a 45° triangle which may cover the full thickness of the adhesive and upper adherend (case G-D), only the adhesive layer (case E-B) or have any intermediate height (case F-C). The angles other than 45° have also been considered in [5].

From the analysis standpoint, the problems of adhesive bonded joint with square end of the overlap and with the spew fillet are quite different. Indeed, in the case EA, point A is the major suspect for stress singularity (that was confirmed by a comprehensive finite element study) and, accordingly, for the failure initiation. However, in the presence of a spew, this point does not play any special role. Rather, the locus of stress singularity can now be anticipated at one of the points B, C or D, depending on the particular spew model. Also, the stress character at point E is obviously different in the case EA versus EB or FC. In addition, points F and G should gain attention. Hence, a very different stress distribution in this local region can be expected.

When briefly summarizing results of the previous analytical and experimental studies, it has first to be mentioned that the predicted stress distributions in the adhesive at the end of the overlap, were found very different when taking into account the spew fillet than in the case of the square end. The most significant stress peak has been predicted at point E, and a lower peak at point D (in the model GD) or B (in the model EB), see [3], [4] and [5]. The maximum tensile stress has been predicted at point E at an angle of approximately 45° to the loading direction [1]. Accordingly, the cracks are forming at this angle, as observed in the failed joints. It was found that the failure initiation takes place in the adhesive within the spew fillet, and the cracks run close to the corner of the “unloaded” adherend [1]. The experimental observations [3] showed that in the single-lap joints these cracks appeared to propagate immediately along the joint to

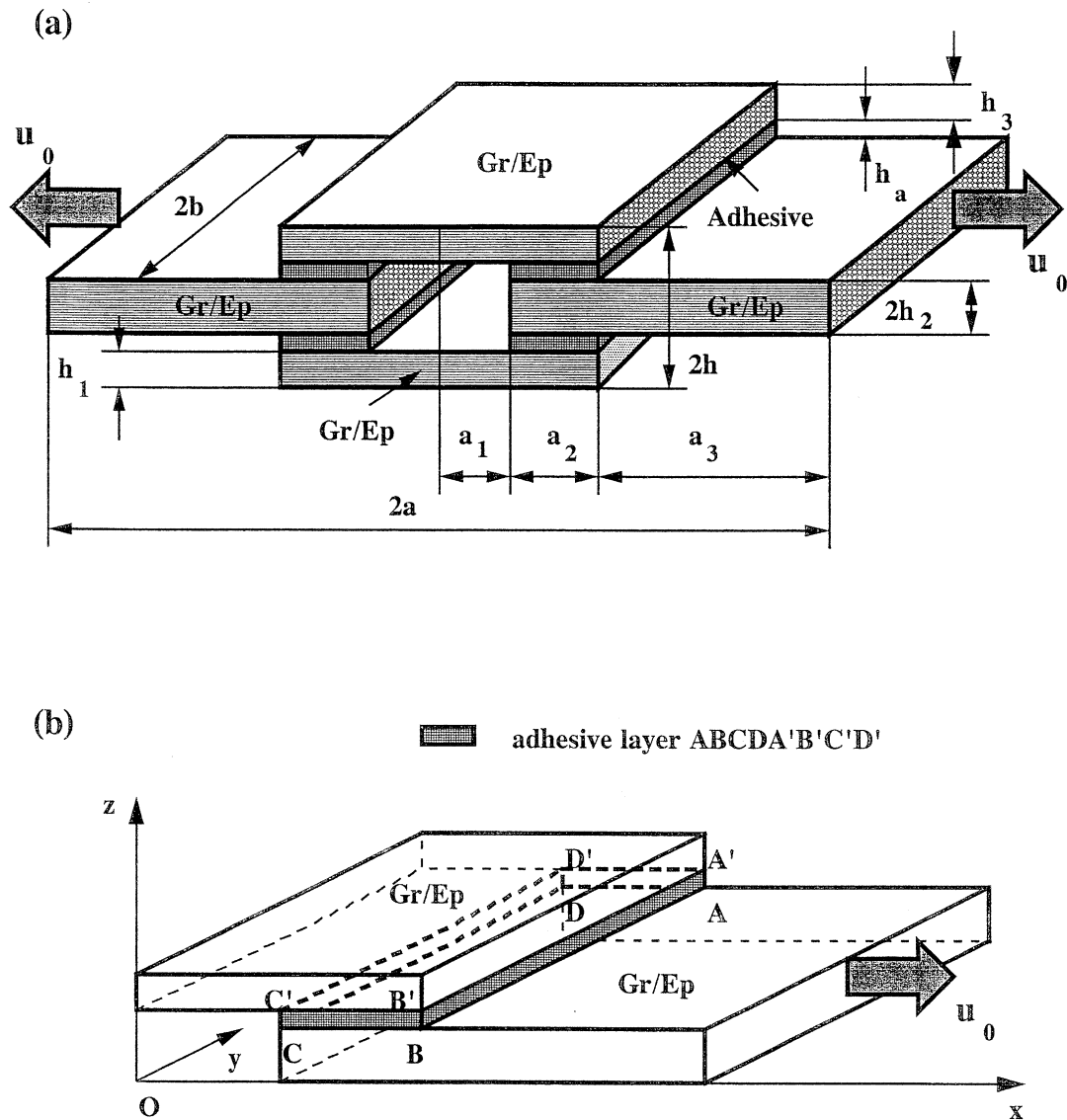


Fig.6-1: A double-lap composite bonded joint under consideration (a) and its 1/8-th part analyzed (b).

cause catastrophic failure. However, this was not always the case with the double-lap joints, where sometimes the crack was arrested at the interface and did not propagate until a higher load was applied.

The aforementioned failure mode has not been found, however, the only one which can be realized in the joints with spew fillet. It was suggested in [1] that if the boundary of the adherend and adhesive is relatively weak, then the longitudinal crack can be created, and the spew fillet

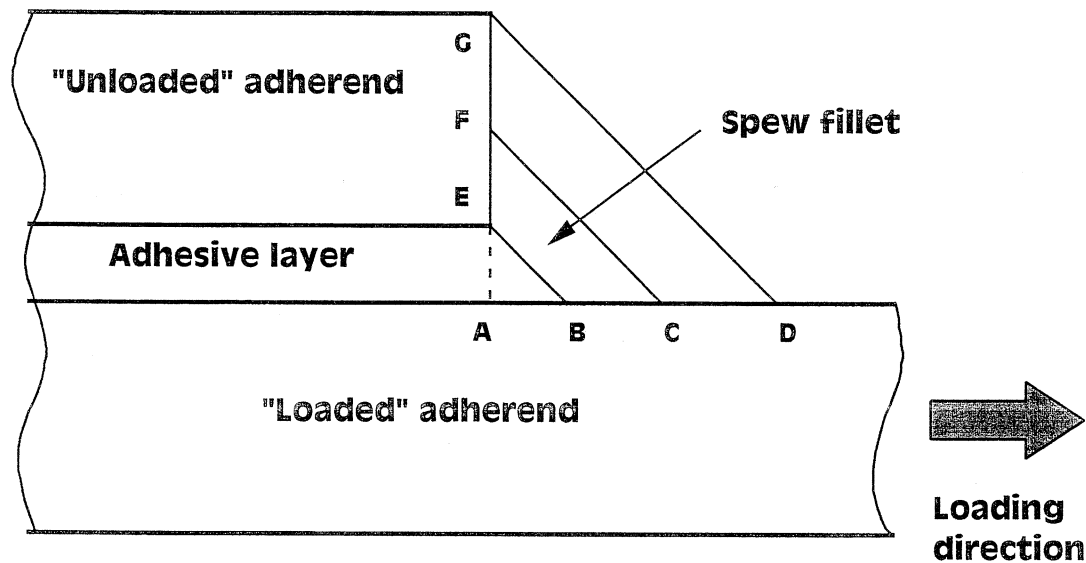


Fig. 6-2: Illustration of the spew fillet models in adhesive bonded joint.

can separate from the “loaded” adherend. Another possible failure mode has been suggested in [4], namely, formation of the transverse crack leading to the separation of the spew fillet from the “unloaded” adherend. Actually, the latter failure mode has been systematically observed in the experimental study [6]. It should be added that the author of [5] had observed experimentally that, despite the theoretical stress concentration at the corner of the “unloaded” adherend, the crack which initiates failure “rarely, if ever, cuts across the corner, but is usually about the same distance as the adhesive layer thickness away from it”.

Our objective here is to illustrate some effects of the spew fillet on stress distributions in adhesive bonded joint of unidirectional composite adherends analyzed earlier in Part B, Section 4. The same submodeling concept has been utilized in the present study, however with the use of 2-D plane stress elements. This simplification of the analysis was adopted because it allowed to use much finer meshes of elements in both the global and local analyses, as compared to the full 3-D analysis. Two types of elements were applied: 8-node plane stress quadrilaterals (CPS8 in the ABAQUS notation) for the rectangular regions of the adherends and adhesive and 6-node plane stress triangles (CPS6) for the spew fillet region. Unlike in most of the previously

published works, the spew fillet boundary is not modeled here as a straight line, but as the concave arc of radius h_a , as shown in Fig. 6-3. Such a spew model seems more realistic.

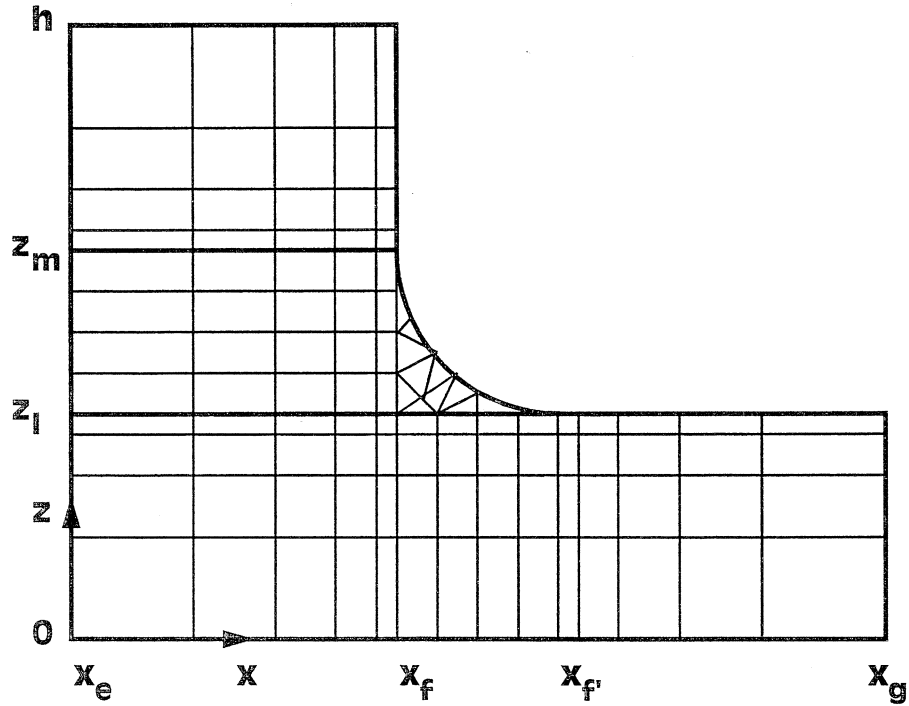


Fig. 6-3: Illustration of finite element mesh used in the local analysis with the spew fillet (not in scale); the mesh of triangle elements shown differs from the actual one generated by PATRAN.

6.3 Numerical Results

First, the global analysis was performed with the following numbers of quadrilateral elements in the x and z -directions (see Section 4.4, Part B for the notations):

$$N_{0a}^x = 4, N_{ab}^x = 8, N_{bc}^x = 8, N_{cd}^x = 4, N_{de}^x = 4, N_{ef}^x = 8, N_{fg}^x = 8, N_{g1}^x = 4 \quad (1)$$

$$N_{0l}^z = 4, N_{lm}^z = 4, N_{ml}^z = 4 \quad (2)$$

Nonuniform meshes of elements in both the x and z -directions were used for the adherends and also in the x -direction for the adhesive. The smallest elements in the x -direction were chosen near the lines $x = x_b$ and $x = x_f$. The smallest elements in the adherends in the z -direction were

chosen near the lines $z = z_l$ and $z = z_m$. A uniform z -direction mesh was used for the adhesive.

Then, the obtained nodal displacements were applied to the local analysis which was performed for the region defined by the coordinates $x_e / a = 0.5444$ and $x_g / a = 0.5667$. Element mesh used for the local region is schematically shown in Fig. 6-3. The following numbers of quadrilateral elements were taken in the x -direction:

$$N_{ef}^x = 16, N_{ff'}^x = 4, N_{f'g}^x = 16 \quad (3)$$

with the same numbers of elements in the z -direction (2) as used in the global analysis.

A comparison of local distributions of the stresses calculated with and without the spew fillet is presented in Figs. 6-4 and 6-5 for the lower interface (between middle adherend and adhesive) and in Figs. 6-6 and 6-7 for the upper interface (between upper adherend and adhesive). In this scale, the horizontal end of the spew fillet corresponds to the point $x_f / a = 0.55584$. When considering results for the lower interface in Figs. 6-4 and 6-5, it is seen that in all cases the stress peaks are located between the corner point of the square-ended joint, $x_f / a = 0.55556$, and horizontal end of the spew fillet, $x_f / a = 0.55584$. This result is in a qualitative agreement with the earlier finite element analysis results reported in [1], [3], [4] and [5]. It is also seen in Fig. 6-4 that in the adherend, there is a minor effect of the spew on the normal stress components σ_x and σ_z , and a more considerable effect on the shear stress component τ_{xz} . For all three stress components under consideration, the peak values in the adherend are lower in the presence of the spew.

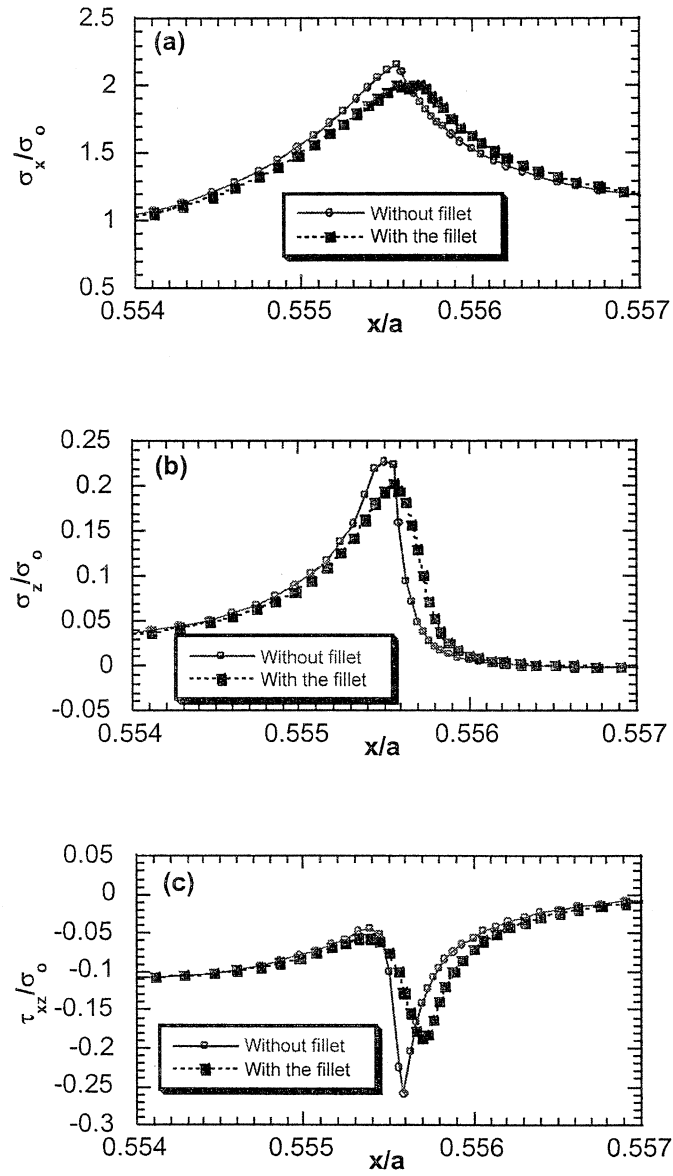


Fig. 6-4: Variations of σ_x / σ_0 (a), σ_z / σ_0 (b) and τ_{xz} / σ_0 (c) at the lower interface, $z/h = 0.3214$, from the side of adherend.

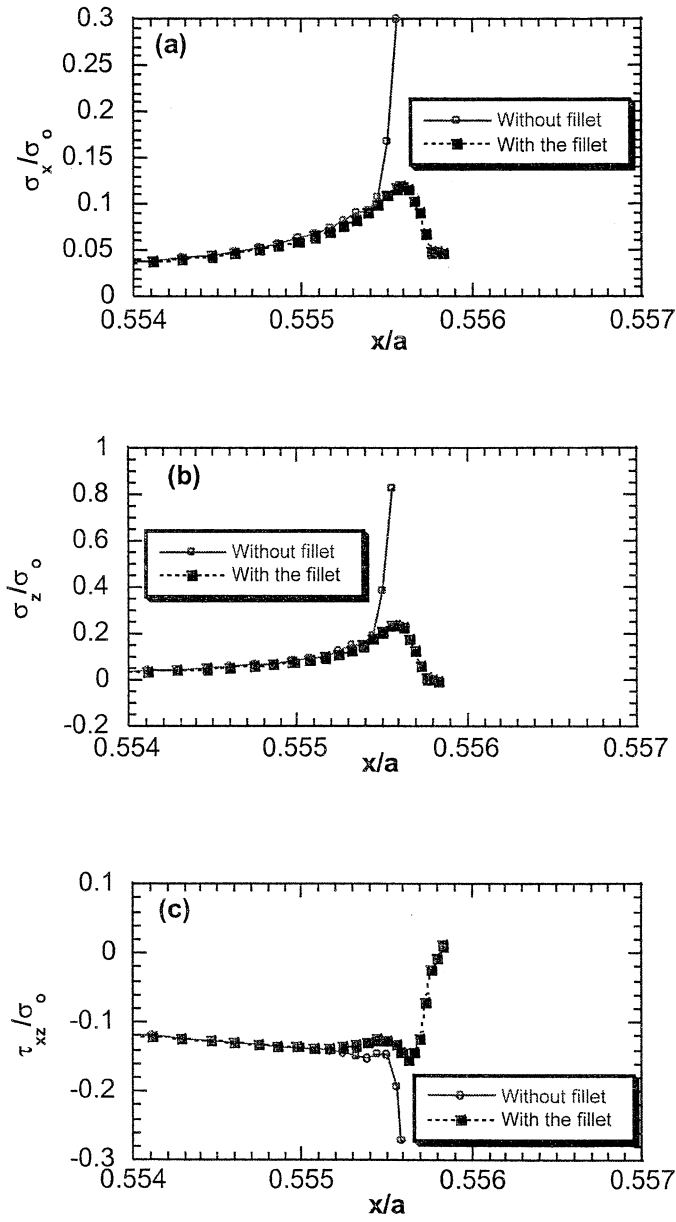


Fig. 6-5: Variations of σ_x / σ_0 (a), σ_z / σ_0 (b) and τ_{xz} / σ_0 (c) at the lower interface, $z/h = 0.3214$, from the side of adhesive.

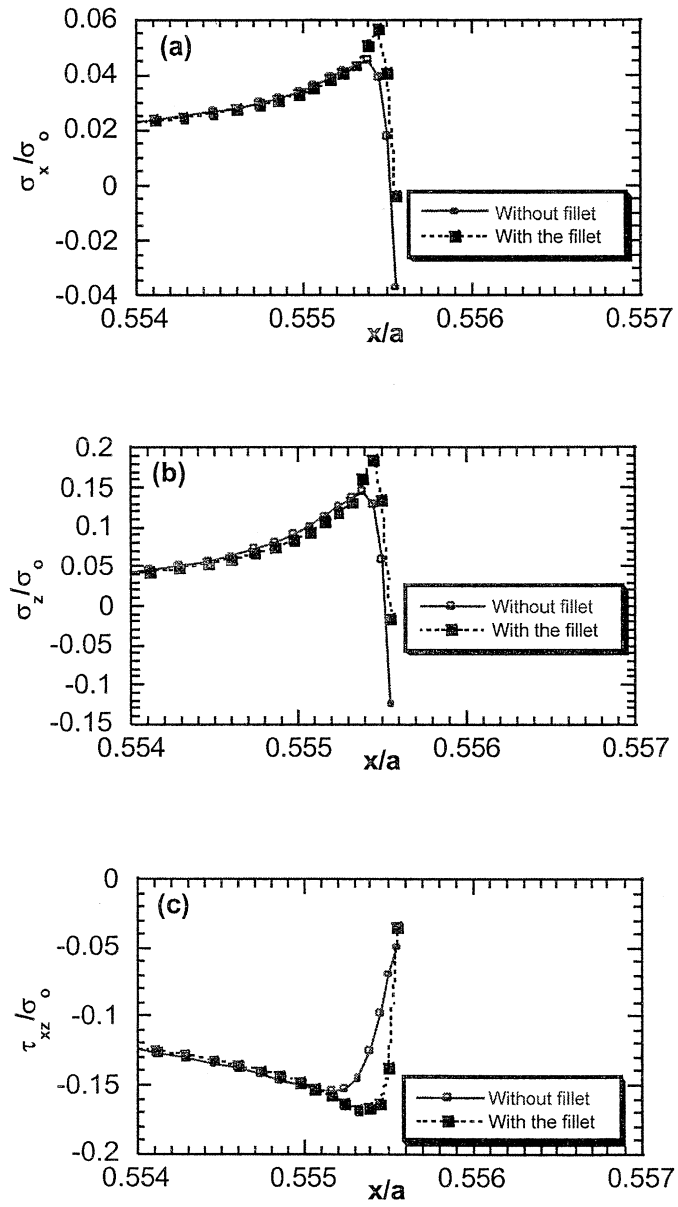


Fig. 6-6: Variations of σ_x / σ_0 (a), σ_z / σ_0 (b) and τ_{xz} / σ_0 (c) at the upper interface, $z/h = 0.3571$, from the side of adhesive

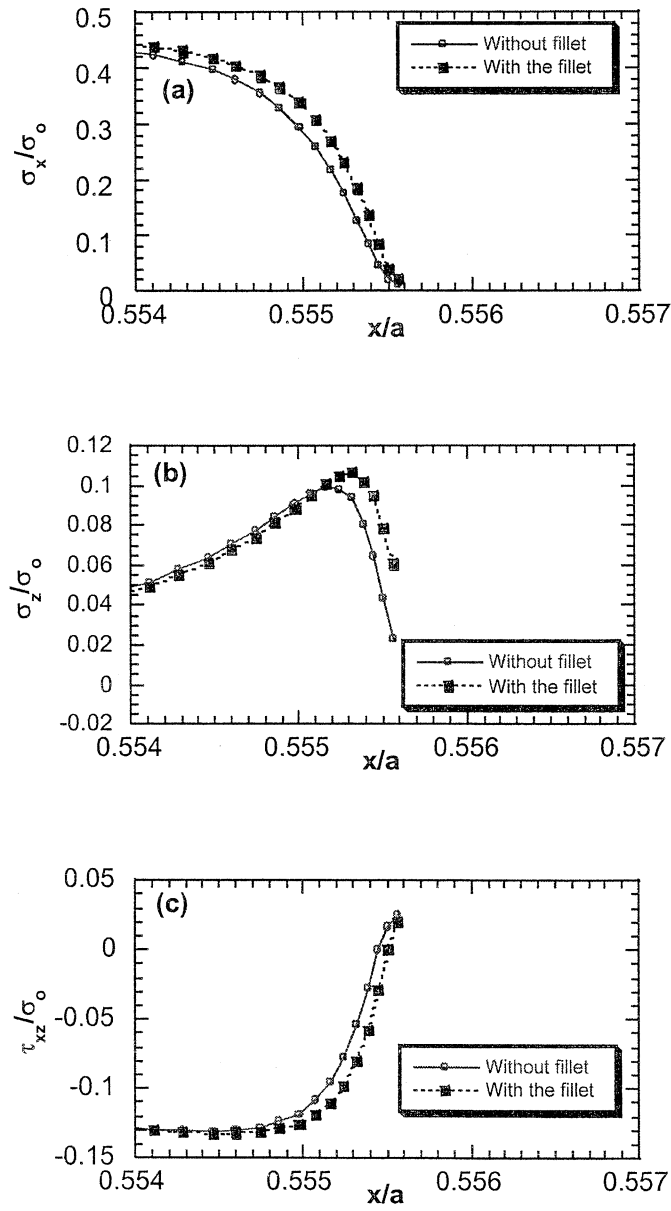


Fig. 6-7: Variations of σ_x / σ_0 (a), σ_z / σ_0 (b) and τ_{xz} / σ_0 (c) at the upper interface, $z/h = 0.3571$, from the side of adherend

The most significant effect is observed in Fig. 6-5 for the stresses σ_x and σ_z in the adhesive. These stress components do not tend to grow infinitely as in the case of the square edge, but reach their finite-valued maximums inside the spew zone. It is seen that σ_x tends to a rather small but clearly nonzero value at the end of the spew fillet, while σ_z and τ_{xz} tend to zero there. Also, when comparing the variations of σ_z and τ_{xz} in the adherend and adhesive in Figs. 6-4 and 6-5, it is seen that their continuity at the interface is accurately satisfied in the presence of the spew. Thus, it seems that the common computational problem caused by the stress singularity at point A of the square-edged joint can be successfully resolved by introducing the spew fillet. It needs to be further studied, if there is a significant stress concentration effect at the horizontal end of the spew fillet (some indications of that for the triangular spew fillet models can be seen in the results of [3]-[5]). However, such an effect seems unlikely to occur for the “smooth” spew fillet model used in the present work.

Now consider results for the upper interface presented in Figs. 6-6 and 6-7. First, it is noticed that shapes of all stress distributions are similar for the cases with and without the spew fillet. However, the peaks of all three stresses in the adhesive become even higher and sharper in the spew fillet case. The convergence study has not been performed for this problem, but it is anticipated that the stresses should be still singular at point E. Though the situation may be different when using the spew fillet model FC or GD (see, Fig. 6-2). Also, it is recognized in Fig. 6-7 that the effect of spew fillet on stress distributions in the upper adherend is not significant. It is also observed that the continuity of σ_z and τ_{xz} along the upper interface is not satisfied. Thus, introducing the spew fillet of the type shown in Fig. 6-3 does not fully resolve the analytical difficulties related to the corner point E. Further modification of the spew fillet model is required.

6.4 Conclusions

The previous as well as the present analytical results along with the experimental observations with moiré interferometry [8] lead to the major conclusion that the spew fillet radically changes the stress distributions in the *adhesive* along the lower interface near the end of the overlap. Consequently, it seems necessary to take into account this effect if one wishes to predict *failure initiation* of the joint.

Possibly, in some cases (especially for the single-lap joints), the failure initiation in the spew could be viewed as a close predecessor of the adhesive or cohesive crack propagation in the overlap region, and thus may provide a slightly conservative estimate of the ultimate failure load. However, it should not be taken as a rule that the crack formation in the spew or its separation from the adherends will cause immediate failure of the joint. Even in the case of metal adherends it is rather obvious that the spew, having very small volume, a relatively low elastic modulus and, at the same time, constrained to a rather low deformation by the adherends, can not play a major role in the *load transfer* between the adherend. The load transfer still takes place through some region of the overlap.

The effect of a spew fillet on the progressive failure of composite bonded joints is expected to be a rather insignificant. Indeed, in the case of laminated composite adherends, where progressive failure involves delamination and intralaminar damage (as discussed in Section 5 of this report), it seems unlikely that such modes of progressive failure can be considerably affected by the crack(s) created in a small volume of a relatively soft spew.

REFERENCES

- (1) R. D. Adams and N. A. Peppiatt "Stress Analysis of Adhesive-bonded Lap Joints", *Journal of Strain Analysis*, 1974, **9** (3), pp. 185-196.
- (2) A. D. Crocombe and R. D. Adams, "Influence of the Spew Fillet and Other Parameters on the Stress Distribution in the Single Lap Joint", *Journal of Adhesion*, 1981, **13**, pp. 141-155.
- (3) R. D. Adams, J. Coppendale, and N. A. Peppiatt, "Failure Analysis of Aluminium-Aluminium Bonded Joints", Chapter 7 in *Adhesion 2, 15th Annual Conference on Adhesion and Adhesives*, London, K. W. Allen (Editor), Applied Science Publ., Ltd., London, pp. 105-120.
- (4) J. A. Harris and R. D. Adams, "Strength Prediction of Bonded Single Lap Joints by Non-linear Finite Element Methods", *International Journal of Adhesion and Adhesives*, 1984, **4**, pp. 65-78.
- (5) R. D. Adams, "Strength Predictions for Lap Joints, Especially with Composite Adherends. A Review", *Journal of Adhesion*, 1989, **30**, pp. 219-242.
- (6) R. S. Long, "Static Strength of Adhesively Bonded ARALL-1 Joints", *Journal of Composite Materials*, 1991, **25**, pp. 391-415.
- (7) M. Y. Tsai and J. Morton, "Three-Dimensional Deformations in a Single-lap Joint", *Journal of Strain Analysis*, 1994, **29**, pp. 137-145.
- (8) M. Y. Tsai, J. Morton, and F. L. Matthews, "Experimental and Numerical Studies of a Laminated Composite Single-lap Adhesive Joint", *Journal of Composite Materials*, 1995, **29** (9), pp. 1254-1275.
- (9) S. L. Donaldson and A. K. Roy, "Experimental Studies on Composite Bonded Joints", *Proceedings of ICCM-11, Gold Coast, Australia*, 1997, Vol. V, pp. 444-455.
- (10) A. K. Roy, S. L. Donaldson, and G. A. Schoeppner, "Bonded Joints of Unidirectional and Cross-ply Laminates: An Experimental Study", *A Collection of Technical Papers, 38th AIAA/ASME/ASCE/AHS /ASC Structures, Structural Dynamics, and Materials Conference*, 1997, Kissimmee, FL, Part **3**, AIAA-97-1121, pp. 1994-2003.

7.0 THREE-DIMENSIONAL MOSAIC MODEL ANALYSIS WITH ACCOUNT OF THE ENVIRONMENTAL EFFECTS

7.1 Introduction

The earlier developed 3-D Mosaic Model analysis of stresses/strains and progressive failure (see, Section 5 of this Report) in composite structures and, particularly, adhesive bonded joints, allows one to solve various mechanical loading cases. However, the effects of environmental conditions (primarily, when changing temperature and/or humidity) are also of a great significance. This chapter presents methodology of incorporating two effects from this category, namely the linear thermal expansion and moisture swelling into the analysis of stresses/strain states and crack propagation in composite structures. It is assumed that the aforementioned effects can be characterized in terms of linear relations with respect to the temperature change and moisture change by weight. Besides, it is assumed that the aforementioned effects are not interrelated. The computer code realizing this approach had been developed and tested on some benchmark thermomechanical problems, though no numerical results of bonded joint analysis were obtained due to a stop work.

7.2 Incorporation of the Thermal Expansion and Moisture Swelling Effects into 3-D Mosaic Model

Theoretical development presented in this section is an extension of the equations given in Part B, Section 1. Those equations which are not changed by the temperature and moisture effects are not reproduced here.

Considering linear hygro-thermoelastic behavior of the s^{th} anisotropic brick, the stress-strain relations are written in the following concise form

$$\tilde{\sigma}_{\xi\psi}^{(s)}(\mathbf{r}) = \tilde{C}_{\xi\psi\zeta\eta}^{(s)} \tilde{\varepsilon}_{\zeta\eta}^{(s)}(\mathbf{r}) - \tilde{\beta}_{\xi\psi}^{(s)} \Delta T^{(s)}(\mathbf{r}) - \tilde{\gamma}_{\xi\psi}^{(s)} \Delta M^{(s)}(\mathbf{r}); \quad \xi, \psi, \zeta, \eta = 1, 2, 3 \quad (1)$$

where $\mathbf{r} = \{x, y, z\}$ is position vector, $\Delta T^{(s)}(\mathbf{r})$ and $\Delta M^{(s)}(\mathbf{r})$ are the temperature change and moisture change by weight, respectively, between two states of the s^{th} brick; they may be

any continuous functions of the coordinates. Further, $\tilde{\beta}_{\xi\psi}^{(s)}$ and $\tilde{\gamma}_{\xi\psi}^{(s)}$ are second rank tensors which are related to the tensors of thermal expansion $\tilde{\alpha}_{\zeta\eta}^{(s)}$ and moisture swelling $\tilde{\mu}_{\zeta\eta}^{(s)}$, respectively, through the relations

$$\tilde{\beta}_{\xi\psi}^{(s)} = \tilde{C}_{\xi\psi\zeta\eta}^{(s)} \tilde{\alpha}_{\zeta\eta}^{(s)}; \quad \tilde{\gamma}_{\xi\psi}^{(s)} = \tilde{C}_{\xi\psi\zeta\eta}^{(s)} \tilde{\mu}_{\zeta\eta}^{(s)} \quad (2)$$

It has to be pointed out that all of the above quantities with “~” are the tensorial ones. When introducing the respective “engineering” quantities and representing them in the 6 element column and 6x6 matrix format, equations (3.1) and (3.2) are obtained in the following form:

$$\sigma_{\phi}^{(s)}(\mathbf{r}) = C_{\phi\chi}^{(s)} \varepsilon_{\chi}^{(s)}(\mathbf{r}) - \beta_{\phi}^{(s)} \Delta T^{(s)}(\mathbf{r}); \quad \phi, \chi = 1, 2, \dots, 6 \quad (3)$$

$$\beta_{\phi}^{(s)} = C_{\phi\chi}^{(s)} \alpha_{\chi}^{(s)}; \quad \gamma_{\phi}^{(s)} = C_{\phi\chi}^{(s)} \mu_{\chi}^{(s)} \quad (4)$$

where $C_{\phi\chi}^{(s)}$ are conventional “engineering” stiffnesses;

$$\begin{aligned} \beta_1^{(s)} &= \tilde{\beta}_{11}^{(s)}, \beta_2^{(s)} = \tilde{\beta}_{22}^{(s)}, \beta_3^{(s)} = \tilde{\beta}_{33}^{(s)}, \beta_4^{(s)} = \tilde{\beta}_{23}^{(s)}, \beta_5^{(s)} = \tilde{\beta}_{13}^{(s)}, \beta_6^{(s)} = \tilde{\beta}_{12}^{(s)}; \alpha_1^{(s)} = \tilde{\alpha}_{11}^{(s)}, \alpha_2^{(s)} = \tilde{\alpha}_{22}^{(s)}, \\ \alpha_3^{(s)} &= \tilde{\alpha}_{33}^{(s)}, \alpha_4^{(s)} = 2\tilde{\alpha}_{23}^{(s)}, \alpha_5^{(s)} = 2\tilde{\alpha}_{13}^{(s)}, \alpha_6^{(s)} = 2\tilde{\alpha}_{12}^{(s)}, \end{aligned}$$

and

$$\begin{aligned} \gamma_1^{(s)} &= \tilde{\gamma}_{11}^{(s)}, \gamma_2^{(s)} = \tilde{\gamma}_{22}^{(s)}, \gamma_3^{(s)} = \tilde{\gamma}_{33}^{(s)}, \gamma_4^{(s)} = \tilde{\gamma}_{23}^{(s)}, \gamma_5^{(s)} = \tilde{\gamma}_{13}^{(s)}, \gamma_6^{(s)} = \tilde{\gamma}_{12}^{(s)}; \mu_1^{(s)} = \tilde{\mu}_{11}^{(s)}, \mu_2^{(s)} = \tilde{\mu}_{22}^{(s)}, \\ \mu_3^{(s)} &= \tilde{\mu}_{33}^{(s)}, \mu_4^{(s)} = 2\tilde{\mu}_{23}^{(s)}, \mu_5^{(s)} = 2\tilde{\mu}_{13}^{(s)}, \mu_6^{(s)} = 2\tilde{\mu}_{12}^{(s)}. \end{aligned}$$

Equation (3) can be viewed as a straightforward generalization of the stress-strain relations, Part B Sec 1 (3), with the temperature and moisture terms added. Note that similarly to the model adopted in [1], the contribution of moisture swelling is, essentially, of the same form as the one of the thermal expansion.

Now, strain energy of the s^{th} brick is defined as

$$P^{(s)} = \int_{V^{(s)}} \left[\frac{1}{2} C_{\phi\chi}^{(s)} \varepsilon_{\phi}^{(s)} \varepsilon_{\chi}^{(s)} - \beta_{\phi}^{(s)} \varepsilon_{\phi}^{(s)} \Delta T^{(s)} - \gamma_{\phi}^{(s)} \varepsilon_{\phi}^{(s)} \Delta M^{(s)} \right] dV \quad (5)$$

and for the whole mosaic body one obtains

$$\begin{aligned} P &= \sum_{s=1}^S \int_{V^{(s)}} \left[\frac{1}{2} C_{\phi\chi}^{(s)} \varepsilon_{\phi}^{(s)} \varepsilon_{\chi}^{(s)} - \beta_{\phi}^{(s)} \varepsilon_{\phi}^{(s)} \Delta T^{(s)} - \gamma_{\phi}^{(s)} \varepsilon_{\phi}^{(s)} \Delta M^{(s)} \right] dV \\ &= \sum_{s=1}^S \left(P^{E(s)} - P^{HT(s)} \right) = P^E - P^{HT} \end{aligned} \quad (6)$$

where P^E is “elastic” part of the total strain energy and P^{HT} its “hygro-thermal” part; the latter one is defined as

$$P^{HT} = \sum_{s=1}^S \int_{V^{(s)}} \left[\left(\beta_{\phi}^{(s)} \Delta T^{(s)} + \gamma_{\phi}^{(s)} \Delta M^{(s)} \right) \varepsilon_{\phi}^{(s)} \right] dV \quad (7)$$

Explicit expression of $P^{E(s)}$ is provided by equation (12), Part B Sec 1. The expressions of the work of external mechanical surface forces $A^{(s)}$, presented by (17) and (20), Part B Sec 1, hold.

The expression of $P^{HT(s)}$, when written explicitly, represents a linear form of the displacement approximation coefficients $U_{ijk}^{\alpha(s)}$:

$$P^{HT(s)} = \sum_{i=0}^{I_x} \sum_{j=0}^{J_x} \sum_{k=0}^{K_x} U_{ijk}^{1(s)} \Theta_{ijk}^{1(s)} + \sum_{i=0}^{I_y} \sum_{j=0}^{J_y} \sum_{k=0}^{K_y} U_{ijk}^{2(s)} \Theta_{ijk}^{2(s)} + \sum_{i=0}^{I_z} \sum_{j=0}^{J_z} \sum_{k=0}^{K_z} U_{ijk}^{3(s)} \Theta_{ijk}^{3(s)} \quad (8)$$

Note that there is an obvious similarity between expression (8) for $P^{HT(s)}$ and the expression (20), Part B Sec 1 for $A^{(s)}$. Besides, $P^{E(s)}$ is not related to the thermal expansion effect.

The following notations were introduced in (8):

$$\begin{aligned} \Theta_{ijk}^{1(s)} &= \Theta_{ijk}^{uuu(s)} + \Theta_{ijk}^{uuu(s)} + \Theta_{ijk}^{uuu(s)} \\ \Theta_{ijk}^{2(s)} &= \Theta_{ijk}^{vvv(s)} + \Theta_{ijk}^{vvv(s)} + \Theta_{ijk}^{vvv(s)} \end{aligned} \quad (9)$$

$$\Theta_{ijk}^{3(s)} = \Theta_{ijk}^{wtw(s)} + \Theta_{ijk}^{wv(s)} + \Theta_{ijk}^{v(s)}$$

with the integrals defined as follows

$$\begin{aligned} \Theta_{ijk}^{uuu(s)} &= \int_{x_l}^{x_{l+1}} \int_{y_m}^{y_{m+1}} \int_{z_n}^{z_{n+1}} [\beta_1^{(s)} \Delta T^{(s)}(x, y, z) + \gamma_1^{(s)} \Delta M^{(s)}(x, y, z)] \dot{X}_i^u(x) Y_j^u(y) Z_k^u(z) dx dy dz \\ \Theta_{ijk}^{uuu(s)} &= \int_{x_l}^{x_{l+1}} \int_{y_m}^{y_{m+1}} \int_{z_n}^{z_{n+1}} [\beta_5^{(s)} \Delta T^{(s)}(x, y, z) + \gamma_5^{(s)} \Delta M^{(s)}(x, y, z)] \dot{X}_i^u(x) Y_j^u(y) \dot{Z}_k^u(z) dx dy dz \\ \Theta_{ijk}^{uuu(s)} &= \int_{x_l}^{x_{l+1}} \int_{y_m}^{y_{m+1}} \int_{z_n}^{z_{n+1}} [\beta_6^{(s)} \Delta T^{(s)}(x, y, z) + \gamma_6^{(s)} \Delta M^{(s)}(x, y, z)] \dot{X}_i^u(x) \dot{Y}_j^u(y) Z_k^u(z) dx dy dz \\ \Theta_{ijk}^{vvv(s)} &= \int_{x_l}^{x_{l+1}} \int_{y_m}^{y_{m+1}} \int_{z_n}^{z_{n+1}} [\beta_2^{(s)} \Delta T^{(s)}(x, y, z) + \gamma_2^{(s)} \Delta M^{(s)}(x, y, z)] \dot{X}_i^v(x) \dot{Y}_j^v(y) Z_k^v(z) dx dy dz \\ \Theta_{ijk}^{vvv(s)} &= \int_{x_l}^{x_{l+1}} \int_{y_m}^{y_{m+1}} \int_{z_n}^{z_{n+1}} [\beta_4^{(s)} \Delta T^{(s)}(x, y, z) + \gamma_4^{(s)} \Delta M^{(s)}(x, y, z)] \dot{X}_i^v(x) \dot{Y}_j^v(y) \dot{Z}_k^v(z) dx dy dz \\ \Theta_{ijk}^{vvv(s)} &= \int_{x_l}^{x_{l+1}} \int_{y_m}^{y_{m+1}} \int_{z_n}^{z_{n+1}} [\beta_6^{(s)} \Delta T^{(s)}(x, y, z) + \gamma_6^{(s)} \Delta M^{(s)}(x, y, z)] \dot{X}_i^v(x) Y_j^v(y) Z_k^v(z) dx dy dz \\ \Theta_{ijk}^{www(s)} &= \int_{x_l}^{x_{l+1}} \int_{y_m}^{y_{m+1}} \int_{z_n}^{z_{n+1}} [\beta_3^{(s)} \Delta T^{(s)}(x, y, z) + \gamma_3^{(s)} \Delta M^{(s)}(x, y, z)] \dot{X}_i^w(x) Y_j^w(y) \dot{Z}_k^w(z) dx dy dz \\ \Theta_{ijk}^{www(s)} &= \int_{x_l}^{x_{l+1}} \int_{y_m}^{y_{m+1}} \int_{z_n}^{z_{n+1}} [\beta_4^{(s)} \Delta T^{(s)}(x, y, z) + \gamma_4^{(s)} \Delta M^{(s)}(x, y, z)] \dot{X}_i^w(x) \dot{Y}_j^w(y) Z_k^w(z) dx dy dz \\ \Theta_{ijk}^{www(s)} &= \int_{x_l}^{x_{l+1}} \int_{y_m}^{y_{m+1}} \int_{z_n}^{z_{n+1}} [\beta_5^{(s)} \Delta T^{(s)}(x, y, z) + \gamma_5^{(s)} \Delta M^{(s)}(x, y, z)] \dot{X}_i^w(x) Y_j^w(y) Z_k^w(z) dx dy dz \end{aligned} \tag{3.10}$$

The Ritz equations (9), Part B Sec 1, are modified to the form

$$\sum_{s=1}^S \left[\frac{\partial \mathcal{P}^{E(s)}}{\partial \mathcal{U}_{pqr}^{\alpha(f)}} - \frac{\partial (A^{(s)} + P^{HT(s)})}{\partial \mathcal{U}_{pqr}^{\alpha(f)}} \right] = 0, \quad \alpha = 1, 2, 3 \quad (11)$$

Further, by substituting expressions (12) and 20), Part B Sec 1, together with expression (8), in (11) one obtains the following system of linear simultaneous equations for the s^{th} brick:

$$\sum_{i=0}^{I_x} \sum_{j=0}^{J_x} \sum_{k=0}^{K_x} a_{ijk,pqr}^{11(s)} U_{ijk}^{1(s)} + \sum_{i=0}^{I_y} \sum_{j=0}^{J_y} \sum_{k=0}^{K_y} a_{ijk,pqr}^{12(s)} U_{ijk}^{2(s)} + \sum_{i=0}^{I_z} \sum_{j=0}^{J_z} \sum_{k=0}^{K_z} a_{ijk,pqr}^{13(s)} U_{ijk}^{3(s)} = Q_{pqr}^{1(s)}$$

for $p = 0, 1, \dots, I_x$; $q = 0, 1, \dots, J_x$; $r = 0, 1, \dots, K_x$

$$\sum_{i=0}^{I_x} \sum_{j=0}^{J_x} \sum_{k=0}^{K_x} a_{ijk,pqr}^{21(s)} U_{ijk}^{1(s)} + \sum_{i=0}^{I_y} \sum_{j=0}^{J_y} \sum_{k=0}^{K_y} a_{ijk,pqr}^{22(s)} U_{ijk}^{2(s)} + \sum_{i=0}^{I_z} \sum_{j=0}^{J_z} \sum_{k=0}^{K_z} a_{ijk,pqr}^{23(s)} U_{ijk}^{3(s)} = Q_{pqr}^{2(s)} + \Theta_{pqr}^{2(s)} \quad (3.12)$$

for $p = 0, 1, \dots, I_y$; $q = 0, 1, \dots, J_y$; $r = 0, 1, \dots, K_y$

$$\sum_{i=0}^{I_x} \sum_{j=0}^{J_x} \sum_{k=0}^{K_x} a_{ijk,pqr}^{31(s)} U_{ijk}^{1(s)} + \sum_{i=0}^{I_y} \sum_{j=0}^{J_y} \sum_{k=0}^{K_y} a_{ijk,pqr}^{32(s)} U_{ijk}^{2(s)} + \sum_{i=0}^{I_z} \sum_{j=0}^{J_z} \sum_{k=0}^{K_z} a_{ijk,pqr}^{33(s)} U_{ijk}^{3(s)} = Q_{pqr}^{3(s)} + \Theta_{pqr}^{3(s)}$$

for $p = 0, 1, \dots, I_z$; $q = 0, 1, \dots, J_z$; $r = 0, 1, \dots, K_z$.

It is seen that these equations represent the generalization of equations (22), Part B Sec1; they incorporate additional terms $\Theta_{pqr}^{1(s)}$, $\Theta_{pqr}^{2(s)}$ and $\Theta_{pqr}^{3(s)}$ defined by (9). Like before, the terms $Q_{pqr}^{1(s)}$, $Q_{pqr}^{2(s)}$ and $Q_{pqr}^{3(s)}$ are defined by equations (21), Part B Sec 1. The coefficients $a_{ijk,pqr}^{11(s)}$, ..., $a_{ijk,pqr}^{33(s)}$ are defined for the general case of anisotropy by equations (13), Part B Sec 1.

Thus, after replacing $Q_{pqr}^{1(s)}$ by $Q_{pqr}^{1(s)} + \Theta_{pqr}^{1(s)}$, $Q_{pqr}^{2(s)}$ by $Q_{pqr}^{2(s)} + \Theta_{pqr}^{2(s)}$ and $Q_{pqr}^{3(s)}$ by $Q_{pqr}^{3(s)} + \Theta_{pqr}^{3(s)}$, rest of the algorithm described in Sections 1 and 2, Part B does not change. Consequently, a 3-D hygro-thermomechanical stress/strain and failure analysis of bonded joints can be performed following the methodology presented in Section 3, Part B.

A simplified and more concise version of the above theory can be obtained using displacement approximation (5) assumed in Section 5 of this report, in place of the approximation (5), Part B Sec 1. In this case it is taken, $I_x = I_y = I_z = I$, $J_x = J_y = J_z = J$ and $K_x = K_y = K_z = K$. After incorporating the effects of thermal expansion and moisture swelling into equations of Section 1, the only change is that vector $\mathbf{Q}^{(s)}$ in (11) Part B Sec 1 has the following components:

$$\mathbf{Q}^{(s)} = \left\{ \begin{array}{l} \left\{ Q_{ijk}^{1(s)} + \Theta_{ijk}^{1(s)} \right\} \\ \left\{ Q_{ijk}^{2(s)} + \Theta_{ijk}^{2(s)} \right\} \\ \left\{ Q_{ijk}^{3(s)} + \Theta_{ijk}^{3(s)} \right\} \end{array} \right\} \quad (13)$$

where $\Theta_{ijk}^{1(s)}$, $\Theta_{ijk}^{2(s)}$ and $\Theta_{ijk}^{3(s)}$ are defined by (9). After that, the rest of the theory presented in Section 5 of this report, including all considerations regarding crack propagation analysis apply to the cases of thermal expansion, moisture swelling, mechanical loading, and any combination of thereof.

7.3 The Particular Case: Bricks Having One Plane of Elastic Symmetry

Consider now one particular case of the above theory, which would directly apply to the analysis of laminated plates. Assume that the mosaic structure is composed from orthotropic bricks having stiffnesses $\bar{C}_{11}^{(s)}$, $\bar{C}_{12}^{(s)}$, $\bar{C}_{13}^{(s)}$, $\bar{C}_{22}^{(s)}$, $\bar{C}_{23}^{(s)}$, $\bar{C}_{33}^{(s)}$, $\bar{C}_{44}^{(s)}$, $\bar{C}_{55}^{(s)}$, $\bar{C}_{66}^{(s)}$, coefficients of thermal expansion $\bar{\alpha}_1^{(s)}$, $\bar{\alpha}_2^{(s)}$, $\bar{\alpha}_3^{(s)}$ and moisture swelling $\bar{\mu}_1^{(s)}$, $\bar{\mu}_2^{(s)}$ and $\bar{\mu}_3^{(s)}$ ($\bar{\alpha}_4^{(s)} = \bar{\alpha}_5^{(s)} = \bar{\alpha}_6^{(s)} = \bar{\mu}_4^{(s)} = \bar{\mu}_5^{(s)} = \bar{\mu}_6^{(s)} = 0$), all of them referred to the principal axes of material symmetry \bar{x}_s , \bar{y}_s , \bar{z}_s . The quantities $\bar{\beta}_\phi^{(s)}$ and $\bar{\gamma}_\phi^{(s)}$ are then expressed as follows

$$\begin{aligned} \bar{\beta}_1^{(s)} &= \bar{C}_{11}^{(s)}\bar{\alpha}_1^{(s)} + \bar{C}_{12}^{(s)}\bar{\alpha}_2^{(s)} + \bar{C}_{13}^{(s)}\bar{\alpha}_3^{(s)}, \quad \bar{\beta}_2^{(s)} = \bar{C}_{12}^{(s)}\bar{\alpha}_1^{(s)} + \bar{C}_{22}^{(s)}\bar{\alpha}_2^{(s)} + \bar{C}_{23}^{(s)}\bar{\alpha}_3^{(s)}, \\ \bar{\beta}_3^{(s)} &= \bar{C}_{13}^{(s)}\bar{\alpha}_1^{(s)} + \bar{C}_{23}^{(s)}\bar{\alpha}_2^{(s)} + \bar{C}_{33}^{(s)}\bar{\alpha}_3^{(s)}, \quad \bar{\beta}_4^{(s)} = \bar{\beta}_5^{(s)} = \bar{\beta}_6^{(s)} = 0 \end{aligned} \quad (14)$$

and

$$\begin{aligned}\bar{\gamma}_1^{(s)} &= \bar{C}_{11}^{(s)} \bar{\mu}_1^{(s)} + \bar{C}_{12}^{(s)} \bar{\mu}_2^{(s)} + \bar{C}_{13}^{(s)} \bar{\mu}_3^{(s)}, \quad \bar{\gamma}_2^{(s)} = \bar{C}_{12}^{(s)} \bar{\mu}_1^{(s)} + \bar{C}_{22}^{(s)} \bar{\mu}_2^{(s)} + \bar{C}_{23}^{(s)} \bar{\mu}_3^{(s)}, \\ \bar{\gamma}_3^{(s)} &= \bar{C}_{13}^{(s)} \bar{\mu}_1^{(s)} + \bar{C}_{23}^{(s)} \bar{\mu}_2^{(s)} + \bar{C}_{33}^{(s)} \bar{\mu}_3^{(s)}, \quad \bar{\gamma}_4^{(s)} = \bar{\gamma}_5^{(s)} = \bar{\gamma}_6^{(s)} = 0\end{aligned}\quad (15)$$

If the angle between global axis x and local axis \bar{x}_s is denoted θ_s and $\bar{z}_s = z$, then by applying the respective transformation law to (14) and (15) one obtains

$$\begin{aligned}\beta_1^{(s)} &= \left(\bar{C}_{11}^{(s)} \bar{\alpha}_1^{(s)} + \bar{C}_{12}^{(s)} \bar{\alpha}_2^{(s)} + \bar{C}_{13}^{(s)} \bar{\alpha}_3^{(s)} \right) \cos^2 \theta_s + \left(\bar{C}_{12}^{(s)} \bar{\alpha}_1^{(s)} + \bar{C}_{22}^{(s)} \bar{\alpha}_2^{(s)} + \bar{C}_{23}^{(s)} \bar{\alpha}_3^{(s)} \right) \sin^2 \theta_s \\ \beta_2^{(s)} &= \left(\bar{C}_{11}^{(s)} \bar{\alpha}_1^{(s)} + \bar{C}_{12}^{(s)} \bar{\alpha}_2^{(s)} + \bar{C}_{13}^{(s)} \bar{\alpha}_3^{(s)} \right) \sin^2 \theta_s + \left(\bar{C}_{12}^{(s)} \bar{\alpha}_1^{(s)} + \bar{C}_{22}^{(s)} \bar{\alpha}_2^{(s)} + \bar{C}_{23}^{(s)} \bar{\alpha}_3^{(s)} \right) \cos^2 \theta_s \\ \beta_3^{(s)} &= \bar{C}_{13}^{(s)} \bar{\alpha}_1^{(s)} + \bar{C}_{23}^{(s)} \bar{\alpha}_2^{(s)} + \bar{C}_{33}^{(s)} \bar{\alpha}_3^{(s)} \\ \beta_4^{(s)} &= 0, \quad \beta_5^{(s)} = 0\end{aligned}\quad (16)$$

$$\beta_6^{(s)} = \left[\left(\bar{C}_{12}^{(s)} - \bar{C}_{11}^{(s)} \right) \bar{\alpha}_1^{(s)} + \left(\bar{C}_{22}^{(s)} - \bar{C}_{12}^{(s)} \right) \bar{\alpha}_2^{(s)} + \left(\bar{C}_{23}^{(s)} - \bar{C}_{13}^{(s)} \right) \bar{\alpha}_3^{(s)} \right] \sin \theta_s \cos \theta_s$$

and

$$\begin{aligned}\gamma_1^{(s)} &= \left(\bar{C}_{11}^{(s)} \bar{\mu}_1^{(s)} + \bar{C}_{12}^{(s)} \bar{\mu}_2^{(s)} + \bar{C}_{13}^{(s)} \bar{\mu}_3^{(s)} \right) \cos^2 \theta_s + \left(\bar{C}_{12}^{(s)} \bar{\mu}_1^{(s)} + \bar{C}_{22}^{(s)} \bar{\mu}_2^{(s)} + \bar{C}_{23}^{(s)} \bar{\mu}_3^{(s)} \right) \sin^2 \theta_s \\ \gamma_2^{(s)} &= \left(\bar{C}_{11}^{(s)} \bar{\mu}_1^{(s)} + \bar{C}_{12}^{(s)} \bar{\mu}_2^{(s)} + \bar{C}_{13}^{(s)} \bar{\mu}_3^{(s)} \right) \sin^2 \theta_s + \left(\bar{C}_{12}^{(s)} \bar{\mu}_1^{(s)} + \bar{C}_{22}^{(s)} \bar{\mu}_2^{(s)} + \bar{C}_{23}^{(s)} \bar{\mu}_3^{(s)} \right) \cos^2 \theta_s \\ \gamma_3^{(s)} &= \bar{C}_{13}^{(s)} \bar{\mu}_1^{(s)} + \bar{C}_{23}^{(s)} \bar{\mu}_2^{(s)} + \bar{C}_{33}^{(s)} \bar{\mu}_3^{(s)} \\ \gamma_4^{(s)} &= 0, \quad \gamma_5^{(s)} = 0\end{aligned}\quad (17)$$

$$\gamma_6^{(s)} = \left[\left(\bar{C}_{12}^{(s)} - \bar{C}_{11}^{(s)} \right) \bar{\mu}_1^{(s)} + \left(\bar{C}_{22}^{(s)} - \bar{C}_{12}^{(s)} \right) \bar{\mu}_2^{(s)} + \left(\bar{C}_{23}^{(s)} - \bar{C}_{13}^{(s)} \right) \bar{\mu}_3^{(s)} \right] \sin \theta_s \cos \theta_s$$

Thus, all of the input quantities required for the analysis have been expressed in terms of orthotropic elastic characteristics and coefficients of thermal expansion and moisture swelling of the bricks, assuming that those are given in the coordinate system related to principal axes of symmetry of the bricks.

Using the analysis methodology presented in this chapter, a computer code has been developed and applied to several benchmark thermomechanical problems which have known closed-form analytical solutions. The examples have been numerically studied, and it was found that the obtained results are in a full agreement with the exact ones.

REFERENCES

- (1) E. A. Humphreys and B. W. Rosen, "Properties Analysis of Laminates", in: *Engineered Materials Handbook, Vol. 1, Composites*, ASM International, Metals Park, Ohio, 1987, pp. 218-235.

